I. Kinetic Modeling of Surface Reactions
II. Computational Design of Organic Semiconductors

by

Changhae Andrew Kim

Sc.B. Chemical Physics, Brown University, 2017

Submitted to the Department of Chemistry
in partial fulfillment of the requirements for the degree of

Doctor of Philosophy in Chemistry

at the

MASSACHUSETTS INSTITUTE OF TECHNOLOGY

September 2022

Author .....
Department of Chemistry
June 6, 2022

Certified by .....
Troy Van Voorhis
Haslam and Dewey Professor of Chemistry
Thesis Supervisor

Accepted by .....
Adam P. Willard
Associate Professor of Chemistry
Graduate Officer

This doctoral thesis has been examined by a Committee of the Department of Chemistry as follows:

Professor Bin Zhang .....

Thesis Committee Chair

Pfizer-Laubach Career Development Associate Professor of Chemistry

Professor Troy Van Voorhis .....

Thesis Supervisor

Haslam and Dewey Professor of Chemistry

Professor Jianshu Cao .....

Thesis Committee Member

Professor of Chemistry

I. Kinetic Modeling of Surface Reactions

II. Computational Design of Organic Semiconductors

by

Changhae Andrew Kim

Submitted to the Department of Chemistry
on June 6, 2022, in partial fulfillment of the
requirements for the degree of
Doctor of Philosophy in Chemistry

Abstract

In Part I of this thesis, we propose moment closure methods to simulate the chemical kinetics of surface reactions. For systems with static disorder in the rate constants and short-range correlation in the densities of reactants, we propose the half heterogeneous pair approximation (HHPA). Combining the intuitions of the mean-field steady state (MFSS) method and the pair approximation (PA), we consider representative pairs of sites in a self-consistent bath of the average pairwise correlation. Preaveraging over the static disorder in one site of each pair makes HHPA efficient enough to simulate systems of several species and calibrate rate constants. For systems with long-range dynamic correlation, we propose the use of machine learning (ML) to construct system-specific moment closures. Using the lattice Lotka-Volterra model (LLVM) as a model system, we trained feedforward neural networks (FFNNs) on kinetic Monte Carlo (KMC) results at select values of rate constants and initial conditions. The ML moment closure (MLMC) gave drastic improvements in the simulated dynamics and descriptions of the dynamical regimes throughout the parameter space.

In Part II of this thesis, we propose new design principles to enhance the efficiencies of organic light-emitting diodes (OLEDs). In particular, we are interested in thermally activated delayed fluorescence (TADF) and triplet-triplet annihilation (TTA), which convert the nonemissive triplet excitons into emissive singlet excitons. First, we introduce a simple four-state model of TADF. The model predicts that it is possible to realize adiabatic singlet (S_1) and triplet (T_1) states with fast $T_1 \to S_1$ intersystem crossing (ISC) and $S_1 \to S_0$ radiative decay. Using molecular dynamics (MD) and the time-dependent density functional theory (TDDFT), we consider conformational variation as a means to sample the parameter space, and then we examine the potential of direct optimization to maximize the TADF rate. Second, we investigate the role of ISC in enhancing the efficiencies of TTA upconverters. We present computational evidence that the limit-breaking TTA efficiencies of certain annihilators might be attributed to the $T_2 \to S_1$ ISC. Furthermore, we propose strategies to enhance this ISC and provide experimental support of enhanced efficiencies.

Thesis Supervisor: Troy Van Voorhis
Title: Haslam and Dewey Professor of Chemistry

Acknowledgments

First and foremost, I would like to thank my advisor, Professor Troy Van Voorhis. His continuous support, encouragement, and insightful advice were pivotal to the successful completion of my graduate studies. In addition, I appreciated the multitude of opportunities and the freedom to work on a wide variety of projects.

Also, I would like to thank my thesis committe members, Professor Bin Zhang and Professor Jianshu Cao. Their encouragement and constructive advice helped to advance my research and career.

The members of the Van Voorhis group created a caring and supportive environment. Professor Zhou Lin and Professor Tianyu Zhu extended help and guidance when I was starting my research. Professor Piotr de Silva, it was a pleasure to work together, and I learned a lot in our discussions. Dr. Nathan D. Ricke, Dr. Hong-Zhou Ye, and Dr. Alexandra McIsaac provided pertinent suggestions on my research and guidance on my system administrator duties. Dr. Natasha Seelam offered knowledge that extended beyond the specialties of our group. Dr. Alexandra Raeber, Dr. Matthias Kick, Leah Weisburn, and Ezra Alexander provided help in maintaining the computer clusters and engaged me in many scientific and nonscientific dialogues. Shicheng Hu, I enjoyed the enthusiasm and the scientific curiosity when we worked together. Also, I appreciated the discussions, suggestions, and camaraderie of Dr. Ricardo Pedro, Dr. Tamar Goldzak, Dr. Yael Cytter, Dr. Jacqueline Tan, Dr. Oinam Meitei, Henry Tran, Kimberly Zhang, and Alex Byrne. Special thanks to Henry, Leah, and Ezra, who proofread this thesis.

I am grateful to my collaborators in the Baldo group. Professor Marc A. Baldo, Dr. Dong-Gwang Ha, and Dr. Ting-An Lin, I learned so much working together, and I enjoyed their enthusiasm and profound insights in experimental science.

Also, I am grateful to my friend, Eric Sung. He will be missed.

Last but not least, I would like to thank my parents and my grandmother. My parents' endless love, support, and encouraging advice gave me the strength to go through these trying times, and I am forever indebted to my grandmother who raised

me alongside my parents. This thesis is dedicated to them.

You should do research while you are young.

My mother

Contents

List of Figures

List of Tables

Part I

Kinetic Modeling of Surface Reactions

Chapter 1

Introduction

Kinetic models are a useful tool to translate our knowledge of microscopic processes into macroscopic observables or vice versa. However, there are a number of challenges in the kinetic modeling of surface reactions, such as static disorder in the rate constants and dynamic correlation in the densities of the reactants. In Part I of this thesis, we propose methods to capture the effects of static disorder and dynamic correlation in surface reactions. In this chapter, we develop the theoretical background that is required to understand the works in Part I. Assuming Markovian processes and an *a priori* knowledge of the rate constants, the chemical master equation (CME) gives an exact treatment of the chemical kinetics. However, the computational costs are intractable in most systems of practical relevance. While the kinetic Monte Carlo (KMC) method provides a way to sample the desired outcomes, the computational costs of these stochastic simulations can still be formidable. In this thesis, we consider moment closure approximations as a hierarchical approach to obtain qualitative and sometimes quantitative insight into the chemical kinetics.

1.1 Pathological Behaviors in Chemical Kinetics

Chemical kinetics of surface reactions can exhibit a wide range of pathological behaviors. Among the most dramatic examples are catalytic reactions that exhibit density oscillations [1], hysteresis loops [2, 3], spatiotemporal patterns [4, 5], and chaos [6, 7].

Horn and Jackson established that detailed balance precludes oscillations, bistabilities, and other irregular dynamics in chemical reactions. [8]. It stands to reason that these systems do not satisfy the necessary and sufficient conditions of detailed balance [9, 10], and many assumptions that are taken to be granted in chemical kinetics do not apply. Notably, the steady states of surface reactions are not always an equilibrium.

Even in mundane cases where the system exhibits a monotonic relaxation, the rates of elementary reactions are sometimes not described by first-order or second-order kinetics. According to the law of mass action, the rate of a unimolecular reaction is

$$\frac{d[A]}{dt} = -k[A] \tag{1.1}$$

and the rate of a bimolecular reaction is

$$\frac{d[A]}{dt} = -k[A][B] \tag{1.2}$$

where $[A]$ and $[B]$ are the densities of reactants A and B, respectively; and k is the rate constant. Solving the first-order kinetics gives

$$[A] = [A]_0 e^{-kt} \tag{1.3}$$

and solving the second-order kinetics gives

$$[A] = \frac{[A]_0}{1 + kt} \tag{1.4}$$

where we have assumed $[B] = [A]$. However, many surface reactions exhibit a stretched exponential kinetics [11–13].

$$[A] = [A]_0 \exp\left(-\frac{k_0 t^{1-h}}{(1-h)}\right) \tag{1.5}$$

where k_0 and $h < 1$ are parameters. This is not consistent with either first-order or second-order kinetics. Instead, the stretched exponential is known to arise when a

unimolecular reaction exhibits a time-dependent rate coefficient [14]

$$\frac{d[A]}{dt} = -\frac{k_0}{t^h}[A] \tag{1.6}$$

Alternatively, enforcing a time-independent rate coefficient and calibrating the reaction orders give noninteger reaction orders

$$\frac{d[A]}{dt} = -k[A]^\alpha[B]^\beta \tag{1.7}$$

Due to the influence of Kopelman [15, 16], the appearance of stretched exponentials or noninteger reaction orders often invokes the phrase "fractal kinetics" or "fractal-like kinetics" in the chemical literature. We do not condone the abuse of this terminology, since it implies that these pathological behaviors arise due to special geometries of the surface. In truth, they can be traced to a number of distinct origins. [17, 18].

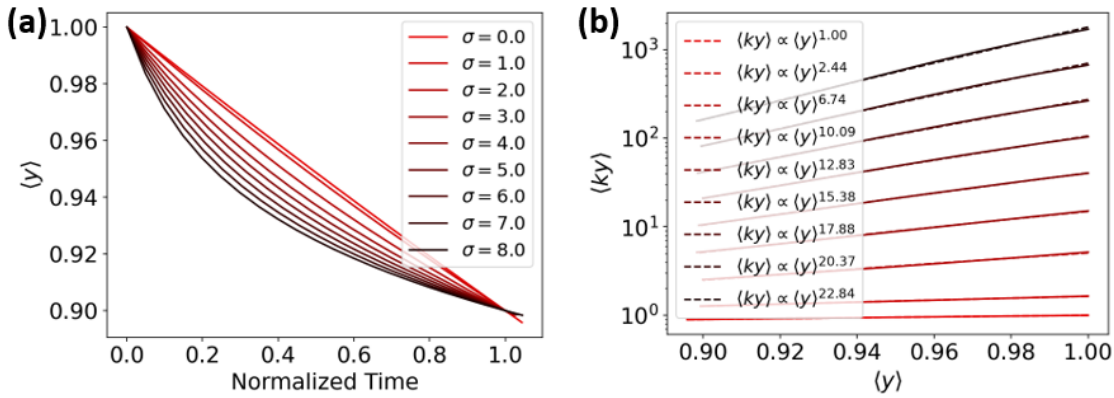

Figure 1-1: (a) Simulated kinetics of a unimolecular reaction with static disorder. The amount of static disorder σ is in units of k_BT. The time has been normalized with respect to the point when the ensemble-average density $\langle y \rangle$ reaches 90 % of its initial value. (c) Ensemble-average rates as functions of ensemble-average densities.

First, many surfaces are expected to exhibit static disorder, site-to-site variations in the rate constants due to defects in the crystal lattice or the amorphous structure of the surface. In systems with significant amounts of static disorder, employing a single-valued rate constant per elementary step is insufficient [19, 20], and static disorder can have a nontrivial effect on the chemical kinetics [21–24]. To demonstrate the

effects of static disorder, we consider the chemical kinetics of a unimolecular reaction

$$\frac{dy_k}{dt} = -ky_k \tag{1.8}$$

where the rate constants k have a log-normal distribution

$$\rho(k)dk = \frac{1}{(2\pi\sigma^2)^{1/2}} \exp\left[-\frac{(\log k - \mu)^2}{2\sigma^2}\right] \frac{dk}{k} \tag{1.9}$$

Since we can remove the mean μ by rescaling the time, the standard deviation σ is the tunable parameter. We are interested in the ensemble-average kinetics

$$\langle y(t) \rangle = \int y_k(t)\rho(k)dk \tag{1.10}$$

Solutions that correspond to a few values of σ are shown in Figure 1-1a. Normalizing the time with respect to the point when $\langle y \rangle$ reaches 90 % of its initial value, we can see that the kinetics become nonexponential as the amount of static disorder increases. This implies that this reaction is no longer described by first-order kinetics at the macroscopic level, even though it is unimolecular at the microscopic level. The ensemble-average rate is nonlinear in the ensemble-average density

$$\langle ky \rangle \approx k_{\text{eff}} \langle y \rangle^n \tag{1.11}$$

where k_{eff} and n are the effective rate constant and reaction order, respectively. As shown in Figure 1-1b, the effective reaction orders are unrecognizable as a unimolecular reaction, and they are noninteger in the presence of static disorder.

Second, surface reactions often exhibit spatial correlation, interdependence in the probabilities of finding reactants next to each other. Indeed, the law of mass action assumes perfect mixing of the reactants [25]. It is going to break down in the presence of spatial correlation. The nature of the correlation might be lateral interaction or dynamic correlation. Lateral interaction refers to attractive and repulsive interactions between adsorbates. Hence, it is thermodynamic in origin. It implies that

the activation energies and hence the rate coefficients are not constants but they can depend on the global surface coverages [3, 26], as well as the occupation of nearby sites [27, 28]. While capturing the effects of lateral interaction is an important issue in many systems, it is beyond the scope of this thesis.

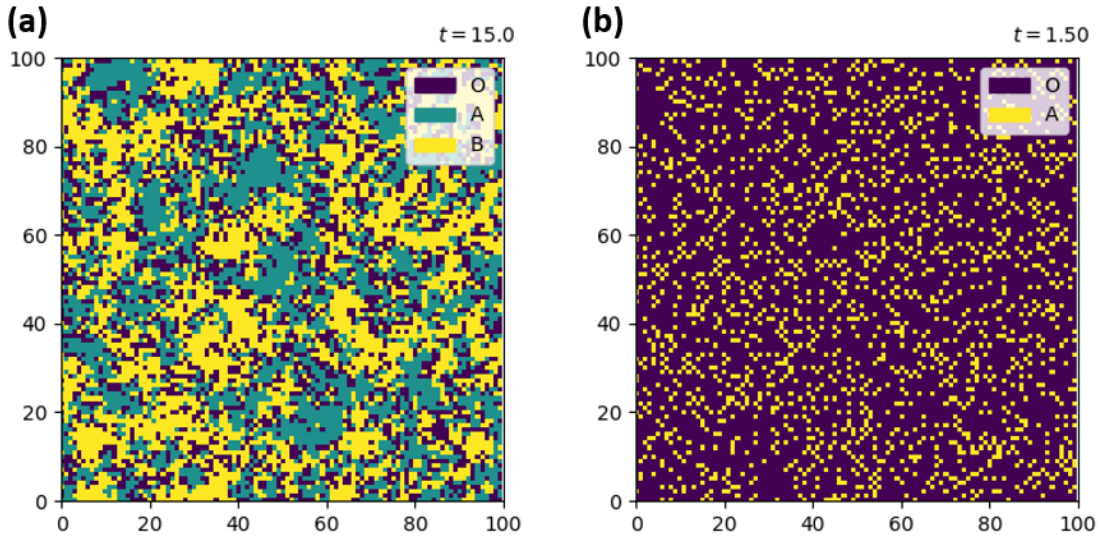

Figure 1-2: Stochastic simulation of (a) two-species and (b) one-species bimolecular reaction on a lattice. This is the same systems as the heterodimer and the homodimer formations in Section A.1.

Dynamic correlation arises due to a combination of bimolecular reactions and slow diffusion. Hence, it is kinetic in origin. The extent to which dynamic correlation can impact the system is quite shocking. In fact, one of the simplest examples gives the most dramatic results. Consider a two-species bimolecular reaction on the lattice

$$O \rightarrow A \tag{1.12}$$

$$O \rightarrow B \tag{1.13}$$

$$A + B \rightarrow O + O \tag{1.14}$$

where O is a vacancy; and A and B are the two reactants. We are not including any static disorder or lateral interaction, and the reactants are immobile on the lattice. As shown in Figure 1-2a, stochastic simulation of this system shows that species A and B arrange themselves into monospecific islands that extend over several sites in

diameter. Hence, the reaction rate is not proportional to the surface coverages of A and B, but it is proportional to the circumferences of the islands. These spatiotemporal patterns are quite insensitive to the incorporation of desorption and diffusion into the model [18].

Even when there are no apparent spatiotemporal patterns, annihilation of the reactants in pairs reduce the probabilities of finding reactants next to each other in unexpected ways. As a more mundane example, consider a one-species bimolecular reaction on the lattice

$$* \rightarrow A \tag{1.15}$$

$$A + A \rightarrow * + * \tag{1.16}$$

As shown in Figure 1-2b, this system gives rise to an altnernating array of vacancies and A molecules. Recently, Temel et al. demonstrated this effect in a realistic model of CO oxidation [29]. With the present understanding of chemical kinetics, the effects of dynamic correlation are quite unpredictable unless explicit configurations of the lattice are considered.

1.2 Chemical Master Equation

There is a duality in what various authors mean by the chemical master equation (CME). On the one hand, there are homogeneous systems, such as solutions and colloids, where the reactants and the products are assumed to be well mixed. In this case, the numbers of molecules are sufficient to define the state of the system, and the positions of the molecules are not explicit variables [30–34]. For a simple system of two species, the state of the system can be written as

$$\Psi = (n_A, n_B) \tag{1.17}$$

where n_A and n_B are the numbers of A and B molecules, respectively.

On the other hand, there are heterogeneous systems, such as surfaces and inter-

faces, where the reactants and the products are not well mixed due to slow diffusion or lateral interactions. Mapping the system on to a lattice, the state of the system is defined by the configurations of the lattice [27, 35, 36]. Hence, not only the numbers of molecules, but also their positions are explicit variables. For a two-species system on a 2×2 lattice, the states of the system include

$$\Psi \in \left\{ \cdots, \begin{array}{|c|c|}\hline & A \\ \hline B & \\ \hline \end{array}, \cdots, \begin{array}{|c|c|}\hline A & B \\ \hline & A \\ \hline \end{array}, \cdots \right\} \tag{1.18}$$

More generally, the state of the system can be written as

$$\Psi = \begin{array}{|c|c|}\hline \psi_1 & \psi_2 \\ \hline \psi_3 & \psi_4 \\ \hline \end{array} \tag{1.19}$$

where ψ_i is the occupant of site i, which might be a vacancy, A, or B.

In this thesis, we focus on heterogeneous systems. However, we continue to elaborate on homogeneous systems and the differences inbetween, because the theories and the terminologies in the two communities are related, which can be a source of miscommunication. In particular, it is worth noting that heterogeneous systems can be reformulated as a special case of homogeneous systems by treating members of the same species at different sites as distinct species. For example, Equation 1.19 can be rearranged to take the form

$$\Psi = (n_{A_1}, n_{B_1}, n_{A_2}, n_{B_2}, n_{A_3}, n_{B_3}, n_{A_4}, n_{B_4}) \tag{1.20}$$

where $n_{A_i} = 1$ if the occupant of site i is an A molecule, and 0 otherwise. Likewise, the microscopic processes that take place at different positions are treated as distinct processes. It stands to reason that any statement that is valid in homogeneous systems should have a counterpart in heterogeneous systems, though it is sometimes unclear whether such statements retain not only their mathematical validity, but also their physical interpretation.

In both the homogeneous and the heterogeneous systems, CME takes the form

$$\frac{dp_\Psi}{dt} = +\sum_\Phi k_{\Phi\to\Psi} p_\Phi - \sum_\Phi k_{\Psi\to\Phi} p_\Psi \tag{1.21}$$

where p_Ψ denotes the probability of finding the system in state Ψ; and $k_{\Phi\to\Psi}$ is the sum of the rate constants of the elementary steps, if any, that would take the system in state Φ to state Ψ. Hence, CME is a system of ordinary differential equations (ODEs) that propagates the probabilities of all possible states of the system.

Provided that the state-to-state transitions are Markovian and the rate constants of the elementary steps are known *a priori*, CME gives an exact description of the chemical kinetics. In particular, CME can give an exact treatment of both static disorder and dynamic correlation. Unfortunately, the computational costs of CME scale exponentially. In homogeneous systems, the dimensionality scales as the number of molecules raised to the number of species. In heterogeneous systems, the dimensionality scales as the number of species raised to the number of molecules (sites). Solving CME is intractable in all but the smallest systems.

1.3 Kinetic Monte Carlo

One way to extract details about the solution of CME involves stochastic sampling of trajectories through the state space. This method is called the stochastic simulation algorithm (SSA) in homogeneous systems [30] and the kinetic Monte Carlo (KMC) method in heterogeneous systems [27]. In principle, it is possible to approach the exact solution by averaging over a vast number of trajectories. In practice, we perform enough simulations to converge the desired outcome, such as the surface coverage or the reaction rate, to the desired precision. For a pedagogical introduction to KMC, see References [28, 37].

Broadly, the KMC algorithms can be classified into the rejection-free KMC and the rejection KMC. Both algorithms require an initial state as the starting point, and each step begins with the cataloging of possible reactions. The rejection-free KMC

computes the total rate of transition

$$R = \sum_r k_r \tag{1.22}$$

where k_r is the rate constant of possible reaction r. Then, one of the possible reactions is chosen with a probability k_r/R, and the time step is drawn out of a Poisson distribution with the mean R^{-1}. Depending on the source, this algorithm is also called the residence-time algorithm, the n-fold way, or the Bortz-Kalos-Lebowitz (BKL) algorithm [38]. For readers who are more familiar with SSA, it is worth noting that the rejection-free KMC uses the same time step as the Gillespie algorithm [30].

The rejection KMC chooses one of the possible reactions with a uniform probability. Then, the reaction is accepted with a probability k_r/k_0, where k_0 is the highest rate constant in the system, and the time step is drawn out of a Poisson distribution with the mean $(Nk_0)^{-1}$. Note that there is a chance that the reaction is rejected and nothing happens in a time step, which counteracts the uniform choice of possible reactions and the shorter time steps. Depending on the source, this algorithm is also called the "standard" algorithm. The two algorithms have been proven to give equivalent results [39], so the choice is a matter of the application and the computational resources. On the one hand, each step of the rejection KMC is cheaper than each step of the rejection-free KMC, since it is often possible to estimate k_0 without considering the rate constants of all possible reactions. On the other hand, the time steps are shorter, since we have $Nk_0 > R$.

Since the explicit configurations of the lattice are considered, KMC can give an exact treatment of static disorder and spatial correlation. However, there are a couple of caveats. The computational costs can be formidable in systems with a separation of time scales, which might be due to quasi-equilibrium or fast diffusion [40]. A number of approaches to mitigate the problem have been proposed. One approach involves weighting the transition probabilities or rescaling the rates to reduce the number of steps that are spent on the quasi-equilibrium processes [41, 42]. Another popular approach is τ-leaping [40], which reduces the number of rate calculations by allowing

multiple reactions to take place in one extended time step. In addition, there are active efforts to parallelize KMC [43–46].

More importantly, the size of the lattice and the number of trajectories that are required to converge the stochastic simulations make it impractical to use KMC in calibrating rate constants or finding critical points. Indeed, sampling enough trajectories to draw a qualitative conclusion is one matter; sampling enough trajectories to attain quantitative precision at many points in the parameter space can be problematic even when the system does not exhibit any separation of time scales.

1.4 Moment Closure Approximation

Since the desired outcome in chemical kinetics is often an ensemble average, such as the surface coverage or the reaction rate, we are motivated to write the kinetic equations in the occupation probabilities of n-site clusters (n-site probabilities)

$$[X] \equiv [X_i] = \sum_{\Psi} \delta_{\psi_i,X} p_{\Psi} \tag{1.23}$$

$$[XY] \equiv [X_i Y_j] = \sum_{\Psi} \delta_{\psi_i,X} \delta_{\psi_j,Y} p_{\Psi} \tag{1.24}$$

$$[XYZ] \equiv [X_i Y_j Z_k] = \sum_{\Psi} \delta_{\psi_i,X} \delta_{\psi_j,Y} \delta_{\psi_k,Z} p_{\Psi} \tag{1.25}$$

where i, j, and k are a string of adjacent sites on the lattice; and $\delta_{\psi_i,X} = 1$ if the occupant of site i is $\psi_i = X$ and 0 otherwise.

These n-site probabilities are special cases of moments. In chemistry, the use of the term *moment* is more common in homogeneous systems, where the moments are defined as

$$\langle n_X \rangle = \sum_{\Psi} n_X^{\Psi} p_{\Psi} \tag{1.26}$$

$$\langle n_X n_Y \rangle = \sum_{\Psi} n_X^{\Psi} n_Y^{\Psi} p_{\Psi} \tag{1.27}$$

$$\langle n_X n_Y n_Z \rangle = \sum_{\Psi} n_X^{\Psi} n_Y^{\Psi} n_Z^{\Psi} p_{\Psi} \tag{1.28}$$

where n_X^Ψ gives the number of X molecules in state Ψ. Indeed, we have $\delta_{\psi_i,X} = n_{X_i}$ as discussed in Section 1.2. However, the n-site probabilities are a strict subset of the nth-order moments, since the n-site probabilities only consider strings of adjacent sites on the lattice, whereas the nth-order moments consider all possible combinations of species.

The kinetic equations of one-site clusters are

$$\begin{aligned}\frac{d[X]}{dt} = &+ \sum_A k_{A\to X}[A] + N \sum_{YAB} k_{AB\to XY}[AB] \\ &- \sum_A k_{X\to A}[X] - N \sum_{YAB} k_{XY\to AB}[XY] \end{aligned} \tag{1.29}$$

where $k_{AB\to XY}$ is the rate constant of the elementary step, $A+B \to X+Y$, if it exists; and N is the number of nearest neighbors. For example, the first term describes the unimolecular reaction of the A to produce a X at its position, and the last term describes the bimolecular reaction of the X and a neighboring Y to produce a A and a B at their respective positions.

Observe that the equations are not closed. Unless the elementary steps consist of unimolecular reactions only, the equations of n-site clusters are going to depend on information about $(n+1)$-site clusters. In order to create a closed system of equations, we need a prescription to approximate the higher-order moments using only information about the lower-order moments – hence, a moment closure approximation. The simplest and the most popular closure is the mean-field (MF) approximation, $[XY] = [X][Y]$, which neglects any correlation that might exist between the sites.

To capture the effects of correlation, we need the kinetic equations of at least

two-site clusters

$$\begin{aligned}\frac{d[XY]}{dt} = &+ \sum_{BC} k_{BC\to XY}[BC] \\ &+ (N-1)\sum_{WAB} k_{AB\to WX}[ABY] + (N-1)\sum_{CDZ} k_{CD\to YZ}[XCD] \\ &- \sum_{BC} k_{XY\to BC}[XY] \\ &- (N-1)\sum_{WAB} k_{WX\to AB}[WXY] - (N-1)\sum_{CDZ} k_{YZ\to CD}[XYZ] \end{aligned} \tag{1.30}$$

For example, the first term describes the reaction of the BC pair to produce a XY pair at its position, and the last term describes the reaction of the Y in the XY pair and a neighboring Z to produce a C (making a XC pair) and a D at their respective positions. We have treated unimolecular reactions as special cases of bimolecular reactions where one of the reactants is a spectator.

Now, we need to approximate the three-site probabilities in terms of the two-site probabilities. Using the definition of conditional probability, we can write

$$[XYZ] \approx \frac{[XY][YZ]}{[Y]} \tag{1.31}$$

Known as the pair approximation (PA), this formula has been invented by independent workers in chemistry [47, 48], population biology [49, 50], and epidemiology [51].

In principle, the closed system of equations would become more accurate as higher-order moments are used as the basis of the moment closure approximation. Formally, one can interpret MF and PA as special cases of product approximations [52, 53], so it should be possible to generalize PA to n-site probabilities. Examples of these attempts include the triple approximation [54], the approximate master equations [55, 56], and the cluster mean-field approximation [35]. However, the derivation and the computation of the kinetic equations become challenging, as the geometries of the higher-order clusters are complicated, and the number of moments scales exponentially with the order.

A subset of the readers might be more familiar with stochastic closures, such as the normal [57, 58], Poisson [59], and log-normal closures [60], which are often used in homogeneous systems. The physical and mathematical arguments behind these closures are quite different, since the moments in homogeneous systems are expected numbers of molecules ($\in \mathbb{R}$), as opposed to occupation probabilities ($\in [0, 1]$). In short, stochastic closures assume that the numbers of molecules have a certin probability distribution. Applying stochastic closures to heterogeneous systems entails contradictions: we are considering a probability distribution of probabilities, and the distributions are defined on $\mathbb{R}$, as opposed to $[0, 1]$. Although it can be carried out with suitable adjustments, our experience indicates that stochastic closures encounter instabilities and unphysical values in heterogeneous systems that exhibit a strong spatial correlation.

Nonetheless, it is worth noting that the equations of nth moments in homogeneous systems are analogous to the equations of n-site clusters in heteogeneous systems. Only, the site indices and the number of nearest neighbors do not appear, and the ordering of species in the moments does not matter. Schnoerr et al. have a pedagogial paper on moment closure approximations in homogeneous systems [34]. Interested readers should refer to their work.

Next, we turn our attention to static disorder. Equations 1.29 and 1.30 neglect the effects of static disorder altogether, since the rate of an elementary step is described by the same rate constant throughout the lattice. This is a common practice to reduce the theoretical and the computational complexity. However, recent studies have demonstrated that static disorder can have a nontrivial effect on the chemical kinetics [19, 21, 23, 24]. To capture the effects of static disorder, we cannot drop the site indices in Equation 1.23, and the kinetic equation of one-site clusters becomes

$$\begin{aligned}\frac{d[X_i]}{dt} = &+ \sum_A k_{A_i \to X_i}[A_i] + \sum_{YAB} \sum_j k_{A_i B_j \to X_i Y_j}[A_i B_j] \\ &- \sum_A k_{X_i \to A_i}[X_i] - \sum_{YAB} \sum_j k_{X_i Y_j \to A_i B_j}[X_i Y_j] \end{aligned} \tag{1.32}$$

where X_i denotes species X at site i; j runs over the nearest neighbors of site i; and

$k_{A_iB_j \to X_iY_j}$ is the rate constant of the elementary step, $A + B \to X + Y$, with species A at site i and species B at site j, or zero if such step does not exist.

Equation 1.32 makes explicit treatment of the static disorder in the neighboring sites, so a large number of sites should be sampled to converge the average over the static disorder. These quench mean-field (QMF) approaches are useful in simulating quenched networks, such as single-atom catalysts on amorphous supports [21, 23] and the spread of infectious diseases [61–65]. However, it would be desirable to avoid sampling a large number of sites without sacrificing the ability to describe static disorder, since the tasks of calibrating rate constants or finding critical points require many iterations of these simulations. In this regard, previous works in our group have proposed an efficient strategy to capture the effects of static disorder: the mean-field steady state (MFSS) method, which considers a collection of representative sites in a self-consistent bath of the average environment [20, 22].

To our knowledge, static disorder and dynamic correlation have not been examined together in chemistry, though there have been attempts at related problems in epidemiology [66] and network theory [67].

1.5 Structure of Part I

The remainder of Part I is organized as follows:

In Chapter 2, we propose the half heterogeneous pair approximation (HHPA) to describe the effects of static disorder and dynamic correlation together. Combining the intuitions of MFSS and PA, we consider representative pairs of sites in a self-consistent bath of the average pairwise correlation. Preaveraging over the static disorder in one site of each pair makes HHPA efficient enough to simulate systems of several species and calibrate rate constants. We apply HHPA to simulate the chemical kinetics of methanol oxidation on the rutile $TiO_2(110)$ surface. In analyzing the results, we elucidate the role of static disorder in reproducing the stretched exponentials in the observed kinetics and the importance of dynamic correlation in calibrating the model parameters.

In Chapter 3, we show that machine learning (ML) can be used to construct accurate moment closures in chemical kinetics, using the lattice Lotka-Volterra model (LLVM) as a model system. We trained feedforward neural networks (FFNN) on KMC results at select values of rate constants and initial conditions. Given the same level of input as PA, the ML moment closure (MLMC) gives accurate predictions of the instantaneous three-site probabilities. Further, we explore the potential of MLMC to improve the simulated dynamics and descriptions of the dynamical regimes.

In Chapter 4, we summarize the key results of Part I and discuss future directions.

Chapter 2

Heterogeneous Pair Approximation of Methanol Oxidation

We propose a novel method to simulate the chemical kinetics of methanol oxidation on the rutile TiO_2(110) surface. Such a method must be able to capture the effects of static disorder (site-to-site variations in the rate constants), as well as dynamic correlation (interdependent probabilities of finding reactants next to each other). Combining the intuitions of the mean-field steady state (MFSS) method and the pair approximation (PA), we consider representative pairs of sites in a self-consistent bath of the average pairwise correlation. Preaveraging over the static disorder in one site of each pair makes this half heterogeneous pair approximation (HHPA) efficient enough to simulate systems of several species and calibrate rate constants. According to the simulated kinetics, static disorder in the hole transfer steps suffices to reproduce the stretched exponentials in the observed kinetics. The dominant hole scavengers are found to be temperature-dependent: the methoxy anion at 80 K and the methanol molecule at 180 K. Moreover, two distinct subpopulations of 5-coordinate titanium (Ti_{5c}) sites emerge, a high-activity group and a low-activity group, even though no such division exists in the rate constants. Since the division is quite insensitive to the details of static disorder, the emergence of the two groups might play a significant role in a variety of photocatalytic processes on TiO_2.

2.1 Introduction

Methanol reforming is a chemical reaction that converts methanol and water into carbon dioxide and hydrogen gas, which has promising applications in fuel cells [68–71]. The reaction can be photocatalyzed on a TiO_2 surface [72–74], where the first step is the oxidation of methanol to formaldehyde [73]. As both a practical reaction and a model system to emulate the decomposition of organic pollutants, the photocatalytic dissociation of methanol on the rutile $TiO_2(110)$ surface has been a subject of extensive research in both experimental [75–78] and theoretical [79–82] studies. Nonetheless, some aspects of the reaction mechanism remain enigmatic.

While it has been established that photogenerated holes play a central role in methanol oxidation [83–85], the identity of the hole scavenger continues to be debated. On the basis of density functional theory (DFT) and Bader charge analysis, it has been proposed that the cleavage of the OH bond is thermally activated, and the methoxy anion traps a hole to break the CH bond [79, 81]. Meanwhile, Migani and Blancafort used spin-polarized DFT to show that an exciton can be localized in the TiO_2 lattice underneath a methanol molecule [80]. The hole can migrate up to the methanol molecule in a proton-coupled electron transfer (PCET), whence the methoxy radical can either reduce to a methoxy anion or proceed to a formaldehyde radical anion. However, the precise role of photogenerated holes in the cleavage of the OH bond continues to be questioned [82].

Another mystery, the fraction of undissociated methanol decays as a stretched exponential of the irradiation time [75–77, 86], which is a signature of fractal kinetics [15, 16]. Fractal kinetics is a term that encompasses a wide range of pathological behaviors that arise in heterogeneous systems, which might be intrinsic to the reaction mechanism or due to the geometry of the interface [18]. Indeed, a couple of explanations have been proposed on the origin of the stretched exponentials [76, 77, 86]. On the one hand, methanol oxidation involves multiple, reversible steps [76, 79, 87]. Such a reaction network can give rise to an overall kinetics that is nonexponential. On the other hand, charge transport on the rutile $TiO_2(110)$ surface is disordered [12, 88]. As

the reactants on the most active sites are consumed, the effective rate coefficient might diminish over time. Feng et al. have measured the kinetics of methanol oxidation at multiple surface coverages and temperatures [77], but there is not a mathematical and mechanistic model that helps to support either of the explanations.

Indeed, we are not aware of attempts to answer these questions via kinetic modeling. This could be attributed to a couple of challenges. The first challenge is static disorder. For practical applications, the relevant surface is not the stoichiometric TiO_2, but rather the reduced TiO_{2-x} [89]. The nonstoichiometry entails surface and subsurface oxygen vacancies, which affect the electronic structure in their vicinity and the chemistry at the surface [90–92]. There would be site-to-site variations in the rate constants, and using a single-valued rate constant per elementary step might not be sufficient to describe the disordered kinetics. The second challenge is dynamic correlation. On the one hand, STM images show that the products of methanol oxidation tend to remain next to each other [75, 77, 87]. The uncorrelated products of probabilities, $[CH_3O^-][H]$ and $[CH_2O^{\cdot -}][H]$, are going to underestimate the rate of the reverse reaction. On the other hand, the diffusion of the formaldehyde at temperatures $\gtrsim 215\,\mathrm{K}$ inhibit the reverse reaction [87, 93]. Hence, the relative positions of the reactants and the products should be taken into account. In the chemical literature, the effects of static disorder have been analyzed in the contexts of grafted single-atom catalysts [19, 21, 23, 24], quantum dot solids [94], and organic light-emitting diodes (OLED) [22], as well as dynamic correlation in the contexts of metal and metal oxide surfaces [29, 35, 48]. To our knowledge, static disorder and dynamic correlation have not been examined together in chemistry, though there have been attempts at related problems in epidemiology [66] and network theory [67].

In this chapter, we propose a novel method to simulate the chemical kinetics of methanol oxidation on TiO_2. Combining the intuitions of the mean-field steady state (MFSS) method [20, 22] and the pair approximation (PA) [48–51], we take representative pairs of sites and place them in a self-consistent bath of the average pairwise correlation. Then, we preverage over the static disorder in one site of each pair, which gives a considerable reduction in the computational costs. This half

heterogeneous pair approximation (HHPA) is efficient enough to simulate systems of several species and calibrate rate constants. We demonstrate these capabilities using the experimental data of Feng et al [77].

Comparison of mechanistic models points to an alternative route to thermal activation that can break the OH bond. In fact, the identity of the dominant hole scavenger is found to be temperature-dependent – the methoxy anion at 80 K and the methanol molecule at 180 K. The simulated kinetics appear to be insensitive to the details of charge transport inside the TiO_2 lattice, and static disorder in the hole transfer to the methanol molecule and the methoxy anion suffices to reproduce the stretched exponentials in the observed kinetics. Remarkably, the static disorder gives rise to bimodal distributions in the coverages and the rates, even though the rate constants have a unimodal distribution. This implies that two groups of 5-coordinate titanium (Ti_{5c}) sites emerge with innate and disparate activities. Hence, there are not only two pathways that are active at different temperatures, but also two groups of Ti_{5c} sites that have different activities. Since the division appears to be quite insensitive to the type of static disorder and persist over a range of temperatures, the emergence of the two groups might play a significant role in a variety of photocatalytic processes on TiO_2.

2.2 Theory

2.2.1 Mathematical Methods

A sure way to capture the effects of static disorder and dynamic correlation is kinetic Monte Carlo (KMC) method [27, 30, 37]. However, the size of the lattice and the number of trajectories that are required to converge the stochastic simulation often make it impractical to calibrate rate constants using KMC. Besides, the desired outcomes of chemical kinetics simulations are often ensemble average quantities, such as surface coverages and reaction rates. Therefore, it makes sense to write the kinetic equations in the occupation probabilities of n-site clusters (n-site probabilities).

The kinetic equations of one-site clusters are given by

$$\begin{aligned}\frac{d[X_i]}{dt} = &+ \sum_A k_{A_i \to X_i}[A_i] + \sum_{YAB} \sum_j k_{A_i B_j \to X_i Y_j}[A_i B_j] \\ &- \sum_A k_{X_i \to A_i}[X_i] - \sum_{YAB} \sum_j k_{X_i Y_j \to A_i B_j}[X_i Y_j] \end{aligned} \tag{2.1}$$

where X_i denotes species X at site i; j runs over the nearest neighbors of site i; and $k_{A_i B_j \to X_i Y_j}$ is the rate constant of the elementary step, $A + B \to X + Y$, with species A at site i and species B at site j, or zero if such step does not exist. For example, the first term describes the unimolecular reaction of the A to produce a X at its position, and the last term describes the bimolecular reaction of the X and a neighboring Y to produce a A and a B at their respective positions. On a uniform surface, the sites would have the same rate constants and occupation probabilities, so the indices could be dropped. On a nonuniform surface, the indices are required to capture the effects of static disorder.

Theise equations are not closed, since two-site probabilities are required to describe bimolecular reactions. In general, the kinetic equations of n-site clusters depend on the $(n+1)$-site clusters. These n-site probabilities are special cases of moments, and we need a moment closure to approximate the higher-order moments using what we know about the lower-order moments. The simplest approximation is the mean-field (MF) approximation, $[X_i Y_j] \approx [X_i][Y_j]$, which treats the occupation of neighboring sites as independent, or uncorrelated.

To capture the effects of correlation, we need the kinetic equations of at least two-site clusters

$$\begin{aligned}\frac{d[X_i Y_j]}{dt} = &+ \sum_{BC} k_{B_i C_j \to X_i Y_j}[B_i C_j] \\ &+ \sum_{WAB} \sum_h k_{A_h B_i \to W_h X_i}[A_h B_i Y_j] + \sum_{CDZ} \sum_k k_{C_j D_k \to Y_j Z_k}[X_i C_j D_k] \\ &- \sum_{BC} k_{X_i Y_j \to B_i C_j}[X_i Y_j] \\ &- \sum_{WAB} \sum_h k_{W_h X_i \to A_h B_i}[W_h X_i Y_j] - \sum_{CDZ} \sum_k k_{Y_j Z_k \to C_j D_k}[X_i Y_j Z_k] \end{aligned} \tag{2.2}$$

where h runs over the nearest neighbors of i that are not j; and k runs over the nearest neighbors of j that are not i. For example, the first term describes the reaction of the BC pair to produce a XY pair at its position, and the last term describes the reaction of the Y in the XY pair and a neighboring Z to produce a C (making a XC pair) and a D at their respective positions. We have treated unimolecular reactions as special cases of bimolecular reactions where one of the reactants is a spectator.

Now, we need to approximate the three-site probabilities in terms of the two-site probabilities. Using the definition of conditional probability, we can write

$$[X_i Y_j Z_k] \approx \frac{[X_i Y_j][Y_j Z_k]}{[Y_j]} \tag{2.3}$$

Known as PA, this formula has been invented by independent workers in chemistry [48], population biology [49, 50], and epidemiology [51].

Some readers might be more familiar with stochastic closures, such as the normal [57], Poisson [58], and log-normal [59, 60] closures. However, stochastic closures are derived using physical and mathematical arguments that are more relevant to homogeneous systems (solutions and colloids), where the moments are expected numbers of molecules $\in \mathbb{R}$, as opposed to heterogeneous systems (surfaces and solids), where the moments are occupation probabilities of sites $\in [0, 1]$. Moreover, stochastic closures are prone to instabilities and unphysical values even in their native systems [34]. PA is robust once we assign an appropriate value to the removable discontinuity at zero. Thus, we do not further consider stochastic closures.

Next, we turn our attention to static disorder. Equations 2.1 and 2.2 make explicit treatments of the static disorder in the neighboring sites, so a large number of sites should be sampled to converge the average over the static disorder. These quench mean-field (QMF) approaches are useful in simulating quenched networks, such as single-atom catalysts on amorphous supports [21, 23] and the spread of infectious diseases [61–65]. In the present context, we expect that it would be more useful to replace the neighboring sites with a bath that reflects the average environment. Then, only a small number of representative sites would need to be treated in an explicit

manner, and a weighted average over these sites could be used to update the bath in a self-consistent manner. In other words, we want to replace

$$[B_j] \rightarrow \langle [B] \rangle = \frac{1}{M} \sum_{i=1}^{M} [B_i] = \int_k [B(k)] \rho(k) dk \approx \sum_k w_k [B_k] \tag{2.4}$$

where M is the number of sites on the lattice; $\rho(k)$ is the distribution of the rate constants; and w_k is a discretization of $\rho(k)dk$. Thus, we transform a sum over the sites of the lattice to an integral over the rate constants, which can be approximated as a weighted sum over some representative sites.

To simplify the transformation, we need a few assumptions. First, we assume that the static disorder can be represented as a one-dimensional distribution. If the effects of the static disorder are embodied in the height of a barrier, then the rates of the forward and the reverse reactions that cross this barrier are going to be modulated together. If the effects of the static disorder are embodied in the stability of a reactant, then the rate constants of the reactions that consume this reactant are going to be modulated together. Second, we assume that the static disorder is site-by-site. For unimolecular reactions, this means that the rate constants at sites i and j are independent. For bimolecular reactions, we assume that one of the reactants or the products dictates the reactivity, so the site that starts with the the reactant or ends with the product determines the rate constant. Hence, we write $k_{A_iB_j \rightarrow X_iX_j} \rightarrow k_{A_iB \rightarrow X_iY}$ or $k_{B_jA \rightarrow Y_jX}$.

Figure 2-1 gives graphical representations of the heterogeneous mean-field (HMF) approximation and HHPA. The HMF equations are

$$\begin{aligned} \frac{d[X_i]}{dt} = &+ \sum_A k_{A_i \rightarrow X_i} [A_i] + \sum_{YAB} N_{XY} k_{A_iB \rightarrow X_iY} [A_i] \langle [B] \rangle + \sum_{YAB} N_{XY} \langle k_{BA \rightarrow YX} [B] \rangle [A_i] \\ &- \sum_A k_{X_i \rightarrow A_i} [X_i] - \sum_{YAB} N_{XY} k_{X_iY \rightarrow A_iB} [X_i] \langle [Y] \rangle - \sum_{YAB} N_{XY} \langle k_{YX \rightarrow BA} [Y] \rangle [X_i] \end{aligned} \tag{2.5}$$

where N_{XY} is the number of nearest neighbors. The subscripts in N_{XY} are required to accommodate the anisotropy of the lattice, if any exists. In essence, we have taken

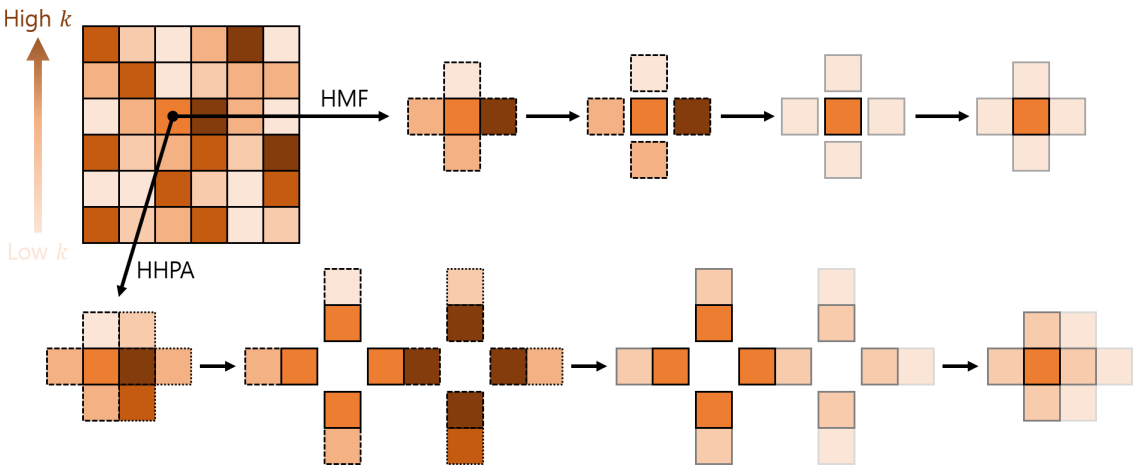

Figure 2-1: Schematics of HMF and HHPA.

the neighbors of the main site and replaced them with the ensemble average site. The mean-field steady state (MFSS) method can be obtained by setting the left hand side of the HMF equations to zero and solving to obtain the steady state probabilities [20, 22].

Terms of the form, $\langle k_{BA\to YX}[B]\rangle$, appear in the equations. These are not the same as $\langle k_{BA\to YX}\rangle\langle[B]\rangle$. The average of the product combines the effects of the static disorder on the rate constants and the effects of the rate constants on the occupation probabilities to give the effective rate. However, the product of the averages erases the dependence of the occupation probabilities on the rate constants.

As the MF part of its name indicates, HMF neglects the dynamic correlation of the main site with the neighboring sites. It replaces the neighboring sites with the ensemble average site that has no connection to the main site. Hence, the rates reflect neither the unlikelihood of finding reactants next to each other nor the likelihood of finding products next to each other due to the finite diffusivity of the adsorbates. To recover the effects of dynamic correlation, we need to write the kinetic equations in terms of higher-order clusters.

Naively, we might take the kinetic equation of two-site clusters and replace the

neighboring site terms with conditional averages, such as

$$[A_l B_i] \rightarrow \langle [B_i A] \rangle = \sum_k w_k [B_i A_k] \tag{2.6}$$

which gives the probability of finding species B at site i along with species A at a generic neighboring site. Similar methods have been successful in epidemiology [66] and network theory [67]. Unfortunately, the same approach is unlikely to be useful in chemical kinetics. The presence of two indices i and j in the main pair means that the number of equations is quadratic. If M sites with distinct rate constants are required to describe the distribution of rate constants at the one-site level, then $M(M+1)/2$ pairs are required at the two-site level. For a system of S species, the full heterogeneous pair approximation would contain $S^2 M(M+1)/2$ variables. This might not be a problem in systems of two to three species, such as the susceptible-infected-recovered (SIR) model [95] or the voter model [96]. However, chemists are often interested in systems containing multiple reactants, intermediates, and products.

To reduce the computational costs, we take advantage of the assumption that the static disorder is site-by-site. We preaverage over the static disorder in one of the main sites and change the variables, $[X_i Y_j] \rightarrow [X_i Y]$. Averaging over the static disorder does not amount to erasing dynamic correlation. The variables, $[X_i Y]$, are conditional averages in Equation 2.6, which consider the simultaneous occupation probabilities of site i and its generic neighbor. Hence, the effects of site i on its neighboring sites and vice versa are treated in an average sense. As a point of contrast, HMF reduces to uniform MF on a uniform surface, whereas HHPA reduces to uniform PA.

The HHPA equations are

$$\begin{aligned}
\frac{d[X_iY]}{dt} = &+ \sum_{BC} k_{B_iC\to X_iY}[B_iC] \\
&+ \sum_{BC} \frac{\langle k_{CB\to YX}[CB]\rangle}{\langle [CB]\rangle}[B_iC] \\
&+ \sum_{WAB} N_{WXY} k_{B_iA\to X_iW} \frac{[B_iA][B_iY]}{[B_i]} \\
&+ \sum_{WAB} N_{WXY} \frac{\langle k_{AB\to WX}[AB]\rangle}{\langle [AB]\rangle} \frac{[B_iA][B_iY]}{[B_i]} \\
&+ \sum_{CDZ} N_{XYZ} \left\langle k_{CD\to YZ} \frac{[CX][CD]}{[C]} \right\rangle \frac{[X_iC]}{\langle [CX]\rangle} \\
&+ \sum_{CDZ} N_{XYZ} \frac{\langle k_{DC\to ZY}[DC]\rangle}{\langle [DC]\rangle} \left\langle \frac{[CX][CD]}{[C]} \right\rangle \frac{[X_iC]}{\langle [CX]\rangle} \\
&- (ABCD \leftrightarrow WXYZ)
\end{aligned} \tag{2.7}$$

where N_{WXY} and N_{XYZ} are the numbers of nearest neighbors that are not one of the main sites; and the notation $(ABCD \leftrightarrow WXYZ)$ replicates the previous terms with the roles of the reactants and products exchanged. Namely, we have written down terms that produce an X_iY pair and gathered terms that consume an X_iY pair in $(ABCD \leftrightarrow WXYZ)$. In the first and third terms, the reactions are centered on site i, so the rates are described using the explicit rate constants, such as $k_{B_iC\to X_iY}$. In the second and fourth terms, the reactions involve site i but are centered on the neighboring site, so the rates are described using the effective rate coefficients, such as $\langle k_{AB\to WX}[AB]\rangle/\langle [AB]\rangle$. The fifth and sixth terms are formulated to preserve the equality, $\langle [XY]\rangle = \langle [YX]\rangle$, provided that the initial conditions satisfy it.

The assumption that the static disorder is site-by-site might break down in systems where point defects are not the dominant type of defects, or if the rate of reaction has intrinsic dependence on multiple sites. Even in systems where the site-by-site assumption holds, the preaveraged neighbor might not be sufficient to capture the effect of the neighboring sites on site i, if pairs with extreme values of rate constants on both sites have an important role on the kinetics. However, the same weaknesses also affect HMF. In Appendix A.1, we compare the performances of HMF and HHPA

on a number of simple model systems, and HHPA gives qualitative improvements over HMF in every case. Although PA is not satisfactory in systems with significant long-range correlation, it can exhibit semiquantitative accuracy in systems with only short-range correlation. Therefore, we expect HHPA to give a reasonable description of methanol oxidation on TiO_2.

We have implemented the above methods in a C code that computes the rates and the Jacobian of a user-input reaction mechanism using a choice of uniform MF, uniform PA, HMF, and HHPA. The code is available on GitHub (https://github.com/changhae-kim/hmca).

2.2.2 Mechanistic Model

For the purposes of simulating methanol oxidation, the rutile $TiO_2(110)$ surface can be regarded as a rectangular lattice with alternating rows of 5-coordinate titanium sites (Ti_{5c}) and bridging oxygen sites (O_b) [89, 97]. The nonstoichiometry of the reduced TiO_{2-x} implies that 9–10 % of the O_b sites are replaced with bridging oxygen vacancies (O_v) [77]. Methanol can adsorb on one of the two positions: the Ti_{5c} sites, where molecular adsorption is favored, and the O_v sites, where dissociative adsorption is favored [98–101]. The active sites in the photocatalytic dissociation of methanol appear to be the Ti_{5c} sites [75, 76], and Feng et al. only counted the adsorbates on the Ti_{5c} sites [77]. Therefore, we do not consider O_v sites in our model.

Figure 2-2 illustrates a mechanistic model of methanol oxidation. The model includes most reactions that have been proposed to take place during the irradiation of methanol on TiO_2, along with their reverse reactions [78–81, 93]. However, we do not consider the cross-coupling of methanol and formaldehyde, which has been shown to be negligible at coverages $\lesssim 0.15$ monolayer (ML) [102].

Along the bottom of Figure 2-2, the steps in blue represent the cleavage of the OH bond and the CH bond in the methanol molecule and the methoxy anion, respectively. The reactions do not involve photogenerated holes. For these *thermally activated* steps, a multitude of DFT studies have established the expected values of the activation energies. The OH bond cleavage is endothermic by 0.01–0.08 eV, and

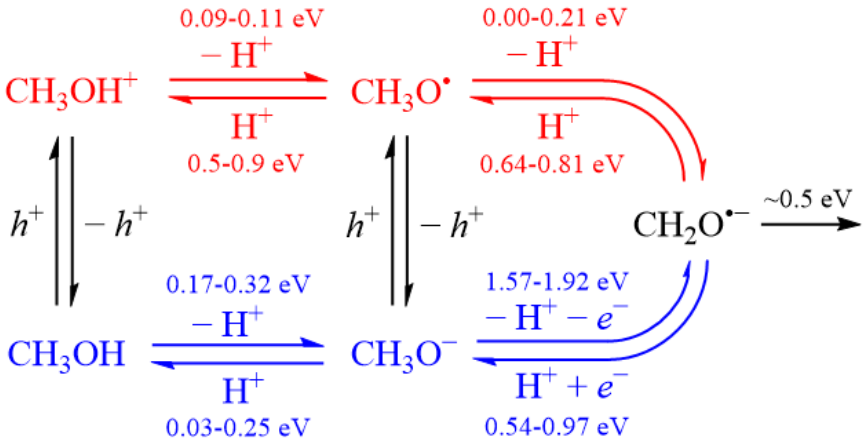

Figure 2-2: Mechanistic model of methanol oxidation on TiO_2. The expected values of the activation energies are based on a number of DFT studies [78–81, 93].

both the forward and the reverse reactions should be accessible, with the forward barrier of 0.17–0.32 eV and the reverse barrier of 0.03–0.25 eV [79–81]. In contrast, the CH bond cleavage is much more endothermic, and only the reverse reaction might be accessible, with the barrier of 0.54–0.97 eV [79, 81].

Along the top of Figure 2-2, the steps in red represent the cleavage of the OH bond and the CH bond in the methanol "cation" and the methoxy radical, respectively. Notice that the reactants have trapped a hole in some capacity. For these *hole-activated* steps, the feasibilities and the activation energies are debated. Indeed, it is uncertain whether the methanol molecule would trap a hole on itself. Given the mechanistic resolution of chemical kinetics, our model does not distinguish between a hole trapping at the methanol molecule and a hole trapping at a nearby position in the TiO_2 lattice. The reactant CH_3OH^+ might not be a methanol cation per se, but a methanol molecule with an exciton or a hole in the TiO_2 lattice underneath. According to computational studies that managed to place an exciton [80] or a hole [78] underneath the methanol molecule, the OH bond cleavage becomes exothermic, and the forward barrier decreases to 0.09–0.11 eV. Meanwhile, there is no dispute that the methoxy anion would trap a hole. Studies have found that the CH bond cleavage should be almost barrierless [78, 80], or it might have a modest activation energy of 0.21 eV [81].

The reactants of the thermally activated steps and the hole-activated steps can interchange via charge transfer, which are the vertical steps in Figure 2-2. Finally, the formaldehyde can diffuse along the Ti_{5c} rows with the activation energy $\sim 0.5\,eV$ [93], which prevents the recomposition of methanol [87].

According to the mechanistic model, the methanol molecule has a number of routes to the formaldehyde radical anion. Since the cleavage of the CH bond in the methanol anion should be inaccessible [79], we can dismiss the themally activated pathway: $CH_3OH \rightarrow CH_3O^- \rightarrow CH_2O^{\cdot -}$. Bader charge analysis indicated that the methanol molecule is unlikely to trap a hole [81, 82]. Shen and Henderson irradiated surfaces covered in methanol and methoxy, respectively, and found that the photocatalytic dissociation of methoxy is an order of magnitude faster than that of methanol at 100–120 K [103]. These results have motivated a pathway where the cleavage of the OH bond is thermally activated and then the methoxy anion traps a hole to break the CH bond: $CH_3OH \rightarrow CH_3O^- \rightarrow CH_3O^{\cdot} \rightarrow CH_2O^{\cdot -}$ [79, 81]. Meanwhile, Migani and Blancafort found that an exciton can be localized in the TiO_2 lattice underneath a methanol molecule [80]. Using scanning tunneling microscopy (STM), Tan et al. found that the direct injection of a hole into the TiO_2 surface can initiate one-step conversions of methanol to methoxy, methoxy to formaldehyde, and methanol to formaldehyde [78]. These results have motivated an alternative pathway where the hole mediates the cleavage of the OH bond and the CH bond: $CH_3OH \rightarrow CH_3OH^+ \rightarrow CH_3O^{\cdot} \rightarrow CH_2O^{\cdot -}$ [78, 80]. However, Jin et al. have proposed that the holes might only contribute vibrational energy in the cleavage of the OH bond [82].

In our model, the presence of CH_3OH^+ provides an alternative route to thermal activation, where the cleavage of the OH bond proceeds with a different set of rate constants. Again, CH_3OH^+ might be a methanol molecule with an exciton or a hole trapped underneath. The actual charge transfer onto the methanol molecule might be coupled to the OH bond cleavage. Even if the hole did not play a direct role in the OH bond cleavage, the charge transfer should be immediate or concurrent if the hole were just underneath the methanol molecule. Since the OH bond cleavage is expected to be fast in any case, the kinetic analysis might not be able to distinguish these two

cases. However, the hole-mediated cleavage of the OH bond is not reversible like the thermally activated cleavage, and whether the hole enters the equation before or after the OH bond cleavage makes a difference. Hence, we should be able to determine the dynamical relevance of photogenerated holes in the cleavage of the OH bond.

2.2.3 Model Parameters

Feng et al. measured the kinetics of methanol oxidation at a number of surface coverages between 0.01 ML and 0.11 ML and at the temperatures of 80 K and 180 K [77]. To calibrate the relevant parameters, we minimize the root mean square normalized error (RMSNE) of the simulated kinetics. That is, the error at each point is normalized to the uncertainty of the experimental data, which is a common practice in regression.

We assume that the rate constants of the molecular steps obey the transition state theory

$$k_r(T) = Q_r \frac{k_\mathrm{B}T}{h} e^{-\Delta E_r^\ddagger / k_\mathrm{B}T} \tag{2.8}$$

where $\Delta E_r^\ddagger$ is the activation energy and Q_r is the partition function. The expected values of the activation energies are summarized in Figure 2-2. In principle, the partition functions are temperature-dependent. However, we assume that they are almost constant and require that their values are 10^{-2}–10^2.

Meanwhile, we assume that the charge carrier dynamics take place at a faster time scale than the molecular dynamics. This implies that the charge transfer steps can be approximated as unimolecular reactions of the methanol and the methoxy adsorbates, with an effective rate constant $k_r = k_r'[h^+]$. Since these effective rate constants combine the effects of the charge carrier density and mobility, they might not have a simple dependence on temperature. The mobility of the charge carriers increases as the temperature increases, which in turn increases their recombination [104]. Hence, we treat the effective rate constants of charge transfer at the two temperature as independent parameters.

To describe the effects of static disorder, we apply a Boltzmann factor to the

effective rate constants of hole transfer to the methanol molecule and the methoxy anion

$$k_r^i(T) = k_r^0(T)e^{-\Delta E_i/k_\mathrm{B}T} \tag{2.9}$$

where ΔE_i represents the site-to-site variation in the trap energies. Indeed, we conjecture that the disparate abilities of sites to transfer a hole to the adsorbates arise due to hole trapping and detrapping. Given the 3.03 eV band gap of the rutile TiO_2 [105, 106], it is dubious whether the deep trap states in the middle of the band gap can participate in the photochemistry, so we focus on the shallow trap states that contribute to the band gap narrowing. Thus, we expect that ΔE_i would have a Poisson distribution, associated with the Urbach tail at the band edge of a disordered semiconductor [107]

$$\rho(\Delta E) \propto e^{-\Delta E/E_\mathrm{U}}, \Delta E > 0 \tag{2.10}$$

where E_U is the Urbach energy that controls the amount of static disorder. Since the static disorder affects the trap energies on the TiO_2 side only, we do not apply the Boltzmann factor in the back transfer of the hole to the lattice.

Overall, the mechanistic model has 27 parameters: 4 charge transfer rate constants at 80 K; 4 charge transfer rate constants at 180 K; 9 activation energies; 9 partition functions; and the Urbach energy.

One of the most undesirable outcomes in regression is overfitting. If a model is given too many degrees of freedom, then it starts fitting to irrelevant information, such as the noise in the experimental data. In a mechanistic model, the parameters have an intuitive interpretation due to the topology of the model, so overfitting would yield values that are inconsistent with the interpretation. Fortunately, our goal is not to find unknown values in the dark. Our model has an extensive collection of expected values, so it should not be difficult to detect signs of overfitting. It would give substantial confidence in the mechanistic model if a fit were obtained with the parameters in reasonable ranges.

2.3 Results and Discussion

2.3.1 Simulated Kinetics

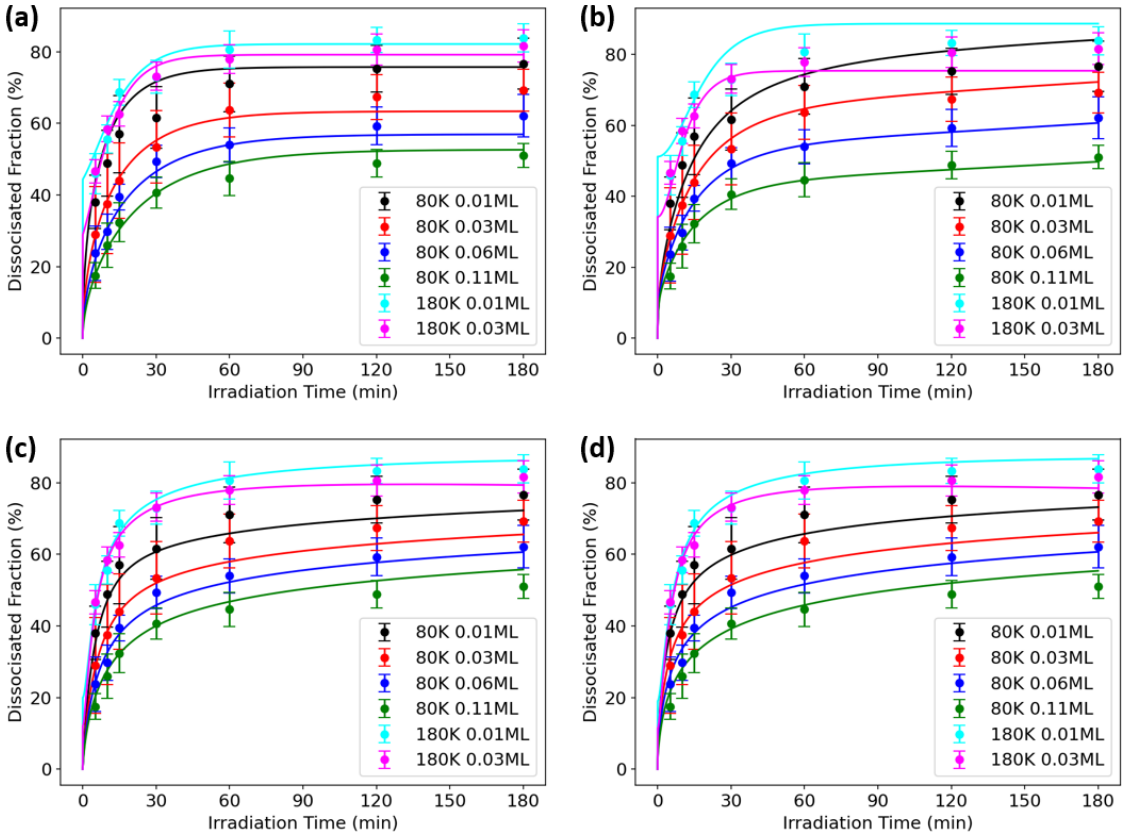

Figure 2-3: Time-dependent dissociation fractions in (a) MF, RMSNE = 0.781; (b) PA, RMSNE = 0.795; (c) HMF, RMSNE = 0.542; and (d) HHPA, RMSNE = 0.589.

Figure 2-3a,b shows the simulated kinetics in uniform MF and PA, respectively. RMSNEs are 0.781 in MF and 0.795 in PA, which means that the simulated kinetics tend to be within a standard deviation of the experimental kinetics. However, a visual inspection reveals a number of issues. In the short time, the simulated kinetics in both MF and PA exhibit a transient at 180 K, where the dissociation fraction jumps, switches to a concave growth, and then switches back to a convex growth. There is no evidence of such behavior in the STM images or the time-dependent two-photon photoemission (2PPE) spectra [75, 76, 86]. In the long time, the simulated kinetics in MF reach a steady state, and the simulated kinetics in PA also reach a steady state

at 180 K. Again, these are inconsistent with the observed kinetics, which slow down but do not reach a steady state after hours of irradiation [75, 76, 86].

Figure 2-3c,d shows the simulated kinetics in HMF and HHPA, respectively. RMSNEs have decreased to 0.542 in HMF and 0.589 in HHPA, and the simulated kinetics are now in good agreement with the experimental kinetics. In the short time, the transient at 180 K is suppressed to a point that it is inconspicuous. In the long time, the simulated kinetics slow down but do not reach a steady state in the simulation time, as desired. The improvements can be rationalized as follows. Due to the static disorder, there are sites with disparate rates of hole transfer. As the reactants on the most active sites are consumed, more and more inactive sites come to dominate the kinetics. Hence, the simulated kinetics in HMF and HHPA behave like a sum of multiple kinetics. On the one hand, there are the fast components that exhibit a rapid growth in the short time, so the transient must be suppressed to avoid overshooting the experimental kinetics. On the other hand, there are the slow components that make up the tail in the long time.

Even though the MF methods attain RMSNEs that are somewhat smaller than the PA methods, we emphasize that MF is not as faithful to the physical reality as PA, since the products of methanol oxidation tend to remain next to each other. To demonstrate that MF and PA simulate somewhat different realities, we entered the parameters that were calibrated using the MF methods into the PA methods and vice versa. In essence, entering the MF parameters into PA stretches the dynamics to the right, and entering the PA parameters into MF shrinks the dynamics to the left. The details can be found in Appendix A.2.

Comparing the simulated kinetics in the uniform and the heterogeneous methods, we propose that static disorder might be required to reproduce the observed kinetics. As discussed in Section 2.1, there have been a couple of explanations on the origin of the stretched exponentials in the observed kinetics. One explanation was that multiple, reversible steps give rise to an overall kinetics that is nonexponential, and the other explanation was that static disorder in the rate constants gives rise to an effective rate coefficient that diminishes over time. While it is true that the uniform

methods predict nonexponential kinetics, they do not resemble the stretched exponentials in the observed kinetics [75, 76, 86]. In particular, the short time behavior at 180 K containsa transient that is not observed in experiments. Meanwhile, assuming a simple distribution of trap energies is sufficient to give a good fit to the experimental kinetics and a suppression of the transient. Thus, the simulations seem to suggest that the static disorder in the hole transfer gives rise to the stretched exponentials.

It is also noteworthy that the simulated kinetics appear to be insensitive to the details of charge transport inside the TiO_2 lattice. As discussed in Section 2.2.3, we have assumed that the charge carrier dynamics take place at a faster time scale than the molecular dynamics and treated the charge transfer steps as unimolecular reactions of the methanol and the methoxy adsorbates with an effective rate constant. Thus, the simulations are oblivious to what the charge carriers are doing inside the TiO_2 lattice, except that the photogenerated holes favor certain sites over others. Furthermore, the static disorder in the charge transport is embodied in the Urbach energy, which is a shared parameter across different surface coverages and temperatures. Feng et al. have proposed that the differences in the observed kinetics at different surface coverages might be attributed to the adsorbates scattering the photogenerated holes [77]. We do not find evidence of such sophisticated interactions. Instead, the competitive inhibition due to the consumption of O_b sites appears to be sufficient to capture the coverage-dependence.

Since the role of photogenerated holes in the cleavage of the OH bond is controversial, we also considered a modified model where the methanol cation has been removed. We provide the details in Appendix A.3 and discuss the key results here. Using the modified model, we are unable to obtain RMSNE < 1 in uniform MF or PA, and the short time behavior again contains the transient at 180 K. HMF and HHPA also find higher RMSNEs of 0.910 and 0.981, respectively. As shown in Figure A-5c,d, the primary source of error appears to be the short time behavior at 180 K. The simulated kinetics at 180 K exhibit significant divergence at different surface coverages, whereas the experimental kinetics are almost on top of each other. Thus, including an alternative route to the OH bond cleavage entails a significant improvement in the

simulated kinetics, and the hole-activated cleavage of the OH bond appears to play an important role in methanol oxidation.

2.3.2 Rates and Rate Constants

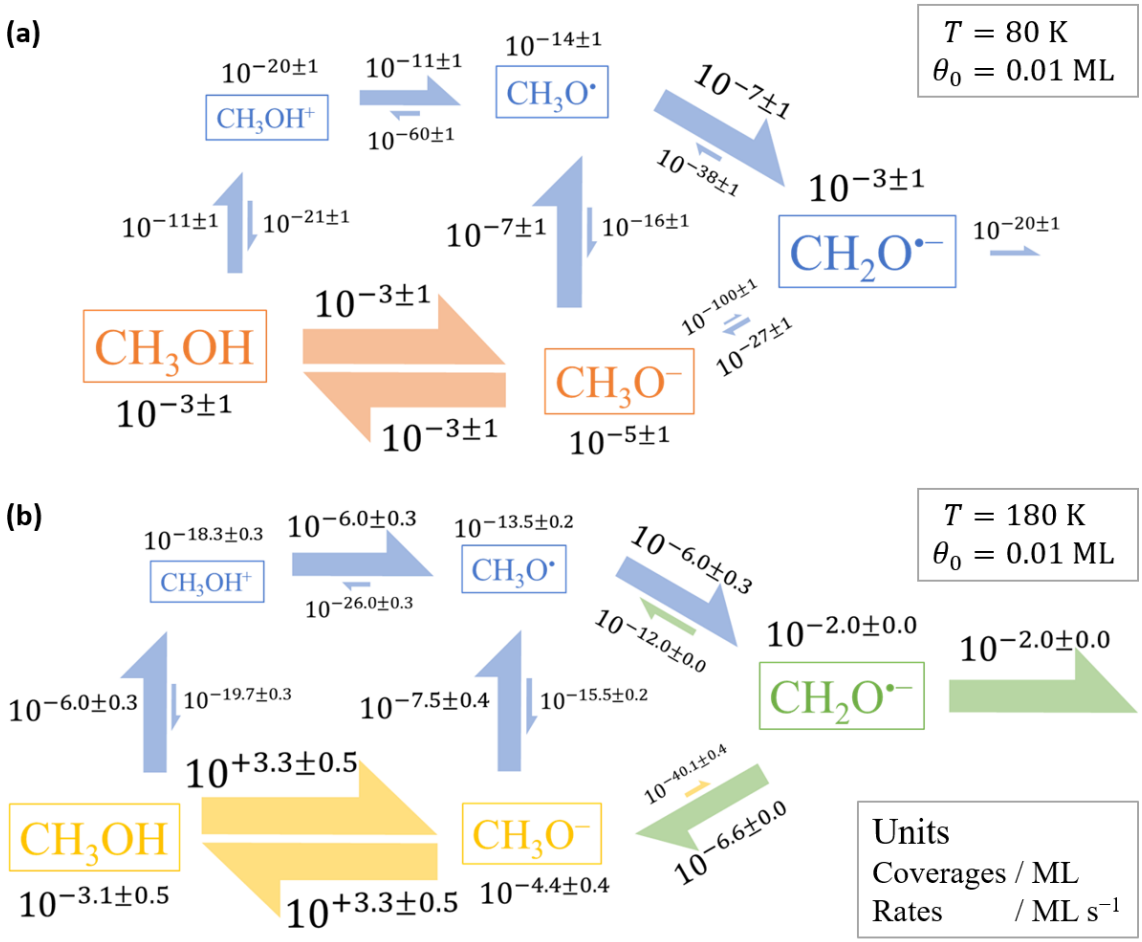

Figure 2-4: Time-averaged coverages and rates at (a) 80 K and (b) 180 K in HHPA. The sizes of the boxes and the arrows relate to the magnitudes of the coverages and the rates, respectively. The units of the coverages and the rates are ML and ML s^{-1}, respectively. The plus-minus values are the spreads in the coverages and the rates due to the static disorder, not uncertainties. The colors indicate different distributions: blue indicates a unimodal distribution, whereas orange, yellow, and green indicate bimodal distributions with different weights. For details, refer to Figure 2-5.

Figure 2-4a,b summarize the time-averaged coverages (occupation probabilities) and rates at 80 K and 180 K, respectively. These are rates and not rate constants. Furthermore, we note that the plus-minus values indicate the spreads in the coverages

and the rates due to the static disorder, not uncertainties.

The fastest steps at both temperatures are the thermally activated cleavage and reformation of the OH bond. Since the interconversion is orders of magnitude faster than any of the other steps, it gives rise to a quasi-equilibrium between the methanol molecule and the methoxy anion. Of course, fast is relative, and the interconversion is slow enough at 80 K to allow the methanol and the methoxy adsorbates to appear as distinct species in STM images. Meanwhile, the interconversion takes place at a monolayer per millisecond at 180 K. In fact, the transient in the simulated kinetics might be attributed to the rapid equilibration.

The dominant pathways of the forward reaction involve a hole transfer to the methoxy anion at 80 K and the methanol molecule at 180 K. In each case, the rates of the subsequent steps are almost equal to the rate of the hole transfer, which implies that the forward reaction almost always goes to completion once the hole transfer takes place. Hence, the hole transfer to the methoxy anion at 80 K and the methanol molecule at 180 K are the rate-limiting steps at the respective temperatures. In particular, it follows that the methanol molecule is the dominant hole scavenger at 180 K. Even though the thermally activated cleavage of the OH bond is orders of magnitude faster, the methoxy anion reverts to the methanol molecule, except in a fraction of cases when the methoxy anion traps a hole. Thus, the hole-activated cleavage of the OH bond, which is slower but takes the reaction to completion, has the potential to determine the overall kinetics.

The dominant pathway of the reverse reaction is thermally activated at both temperatures. Since the methoxy anion is in quasi-equilibrium with the methanol molecule, the thermally activated reformation of the CH bond is the rate-limiting step. Meanwhile, the diffusion of the formaldehyde is significant at 180 K, and it appears to outcompete the reverse reaction.

Our identification of the dominant hole scavengers is so far consistent with the experimental results of Shen and Henderson [103]. On the one hand, their experiments were conducted at 100–120 K only. On the other hand, Shen and Henderson considered surfaces covered in only one of methanol or methoxy, which gives a measure

of the rate constants rather than the rates. As shown in Figure 2-4, the methanol molecule is expected to be at least an order of magnitude more abundant than the methoxy anion. Thus, an accurate comparison would require taking the relative abundances into account. In fact, the reversibility of the thermally activated OH bond cleavage appears to explain why coadsorbed oxygen was required to prepare methoxy in the experiments [103, 108]. Thermal heating alone would not be effective at producing high yields of methoxy adsorbates, since the methoxy anion would revert to the methanol molecule in the absence of coadsorbates to harvest the hydrogen.

It is also important to note that the rate-limiting steps entail some ambiguities in interpreting the mechanistic model. As mentioned earlier, almost every time a hole transfer to the methanol molecule takes place, it is converted to the methoxy radical and then the formaldehyde. This implies that the overall kinetics of the dissociation fraction would be unaffected even if we replaced the two-step process ($CH_3OH + h^+ \rightarrow CH_3OH^+ \rightarrow CH_3O^{\cdot} + H^+$) with the one-step process ($CH_3OH + h^+ \rightarrow CH_3O^{\cdot} + H^+$). In fact, the same can be said about the hole-activated cleavage of the CH bond ($CH_3O^- + h^+ \rightarrow CH_3O^{\cdot} \rightarrow CH_2O^{\cdot -} + H^+$). This is a well-known property of a rate-limiting step: The final product is produced at the same rate as the rate-limiting step, as if it were the final step. Hence, this kinetic analysis is unable to ascertain whether the charge transfer and the proton transfer occur in a sequential or concerted manner during the hole-activated cleavage of the OH and CH bonds.

To establish the upper and the lower bounds on the calibrated parameters, we performed sensitivity analysis by perturbing each of the parameters and recording the response of RMSNE. We provide the details in Appendix A.4 and discuss the key results here. In the end, there are 9 parameters that have a well-defined optimum: the activation energies and the partition functions of the rate-limiting steps and the quasi-equilibrium steps, as well as the Urbach energy, which measures the amount of static disorder. The fast steps that follow a rate-limiting step do not matter as long as the rate constants are greater than the rate-limiting step, and the slow steps that compete with a rate-limiting step or a fast step do not matter as long as the rate constant is smaller than the relevant step. Thus, we can construct a compact

model, where we set most of the rate constants to zero or a large value. Again, we provide the details in Appendix A.5. The compact model gives RMSNEs on par with the original model, and the calibrated parameters tend to be within a narrow range of the parameter space, suggesting that the 9 parameters have an optimum not only when perturbed one at a time, but also in the multidimensional parameter space.

Interestingly, the effective rate constant of the hole transfer to the methoxy anion must be at least an order of magnitude smaller at 180 K than it is at 80 K, as shown in Table A.1. The non-Arrhenius behavior is not an artifact of the mechanistic model containing a back-transfer step. As discussed above, the rate constants of the back-transfer steps can be set to zero with no consequence on RMSNE, so the back transfer is not effective at counteracting the hole transfer. The non-Arrhenius behavior is also not an artifact of the mechanistic model containing the methanol cation. As shown in Table A.2, the modified model with no hole transfer to the methanol molecule also predicts that the effective rate constant of the hole transfer to the methoxy anion is orders of magnitude smaller at 180 K than it is at 80 K. Hence, the non-Arrhenius behavior appears to be intrinsic to the physics of the hole transfer.

We can make sense of the non-Arrhenius behavior using the expression of the effective rate constant

$$k_r(T) \propto [h^+(T)]e^{-\Delta E_r/k_\mathrm{B}T} \tag{2.11}$$

where ΔE_r is the activation energy; and $[h^+(T)]$ is the quasi-steady-state density of photogenerated holes at temperature T. As discussed in Section 2.2, the charge carrier recombination increases as the temperature increases, so the hole density is a decreasing function of the temperature. While the Boltzmann factor is an increasing function of the temperature, it remains at ≈ 1 if the activation energy is small enough. Indeed, computational studies have reported that it is easy to trap a hole at the methoxy adsorbate, and the hole transfer to the methoxy anion is downhill [78, 81]. Then, the hole transfer might have a small barrier. It is plausible that the "effective" rate constant of the hole transfer to the methoxy anion can decrease as the temperature increases.

Furthermore, taking the ratios of the effective rate constants at two temperatures gives

$$\exp\left[(\Delta E_{\mathrm{I}} - \Delta E_{\mathrm{II}})\left(\frac{1}{k_{\mathrm{B}}T_1} - \frac{1}{k_{\mathrm{B}}T_2}\right)\right] = \frac{k_{\mathrm{I}}(T_1)/k_{\mathrm{I}}(T_2)}{k_{\mathrm{II}}(T_1)/k_{\mathrm{II}}(T_2)} \tag{2.12}$$

Substituting I = [$CH_3OH \rightarrow CH_3OH^+$], II = [$CH_3O^- \rightarrow CH_3O^{\cdot}$], $T_1 = 80\,\mathrm{K}$, and $T_2 = 180\,\mathrm{K}$, we deduce that $\Delta E_{CH_3OH \rightarrow CH_3OH^+} - \Delta E_{CH_3O^- \rightarrow CH_3O^{\cdot}} \gtrsim 0.2\,\mathrm{eV}$. Incidentally, this value coincides with the *GW* results of Jin et al., which identified 3.91 eV and 3.70 eV as the excited states where the hole has a significant density on the methanol and the methoxy adsorbates, respectively [82]. While this is not sufficient evidence to conclude whether the methanol molecule can trap a hole as a methanol cation, it is important to remember that chemical kinetics might not always proceed according to the energetics. Per molecule, the hole transfer to the methanol molecule is slower than the hole transfer to the methoxy anion at both temperatures. However, the relative abundance of the methanol molecule and the slowdown of the hole transfer to the methoxy anion appear to enable the methanol molecule to be the dominant hole scavenger at 180 K.

2.3.3 Distributions of Coverages and Rates

In Section 2.3.2, we noted spreads in the coverages (occupation probabilities) and the rates due to the static disorder. As discussed in Section 2.2.3, only the effective rate constants of the hole transfer to the methanol molecule and the methoxy anion were assumed to differ site to site. Since the static disorder is contained in the hole transfer, the effects of the static disorder must be propagating throughout the reaction network. We have used colors to indicate the types of observed distributions in Figure 2-4.

Since the trap energies had a unimodal distribution, one might expect the coverages and the rates to also exhibit a unimodal dsitribution. Indeed, most of the coverages and the rates (blue in Figure 2-4) exhibit a unimodal distribution, as shown in Figure 2-5a. Remarkably, the coverages of the methanol molecule and the methoxy anion at 80 K (orange in Figure 2-4a) exhibit a bimodal distribution, as shown in Fig-

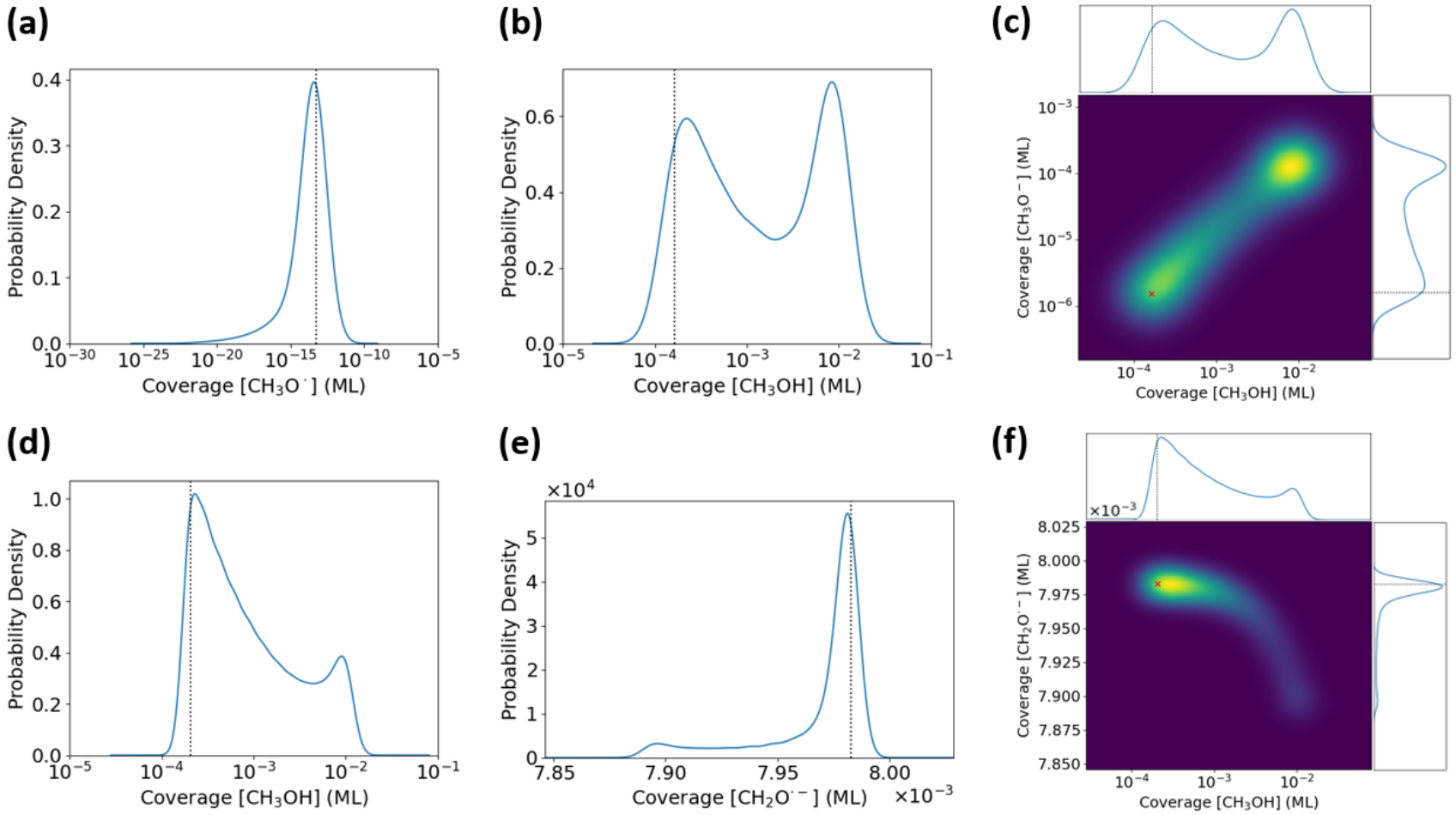

Figure 2-5: Time-averaged distributions of the coverages in HHPA: (a) methoxy radical at 80 K, blue in Figure 2-4; (b) methanol molecule at 80 K, orange in Figure 2-4a; (c) methanol molecule and methoxy anion at 80 K, both orange in Figure 2-4a; (d) methanol molecule at 180 K, yellow in Figure 2-4b; (e) formaldehyde at 180 K, green in Figure 2-4b; and (f) methanol molecule and formaldehyde at 180 K, yellow and green in Figure 2-4b, respectively. The dotted lines and the crosses mark the coverages of the site with $\Delta E_i = 0$, or $k_r^i = k_r^0$.

ure 2-5b. The sites with high and low coverages are divided into distinct groups, and the two groups appear to contain similar fractions of sites. Moreover, the sites with high and low coverages of the methanol molecule also have high and low coverages of the methoxy anion, respectively, as shown in Figure 2-5c. The correlation of the coverages might be attributed to the quasi-equilibrium of the methanol molecule and the methoxy anion.

The coverages of the methanol molecule and the methoxy anion at 180 K (yellow in Figure 2-4b) continue to exhibit a bimodal distribution, as shown in Figure 2-5d. Sites with low coverages are a majority, and sites with high coverages are a minority. The coverage of the formaldehyde at 180 K (green in Figure 2-4b) also exhibits a bimodal distribution, as shown in Figure 2-5e. For the formaldehyde, the weights are the opposite of the methanol molecule and the methoxy anion. Indeed, the sites with high and low coverages of the formaldehyde have low and high coverages of the methanol molecule, respectively, as shown in Figure 2-5f.

The bimodal distributions are not results of time-averaging. As shown in Figure 2-6a,b, the coverages of the methanol molecule and the methoxy anion exhibit bimodal distributions at each point in time regardless of the temperature. The case of the formaldehyde at 180 K can be deceptive, since Figure 2-6c shows only a pixel-thin curve. However, this is due to the narrow spread in the coverage of the formaldehyde (see the x-scale of Figure 2-5e). At each point in time, the distribution resembles Figure 2-5e. We provide a complete collection of the time-averaged and time-dependent distributions in Figures A-21–A-29. Furthermore, the corresponding coverages and rates in the modified model and the compact model also exhibit bimodal distributions, as shown in Figures A-30–A-49.

Effectively, two subpopulations of Ti_{5c} sites have emerged on the TiO_2 surface. On the high-activity sites, the hole transfer to the methanol molecule and the methoxy anion is rapid, so the reactants undergo rapid oxidation to the formaldehyde. On the low-activity sites, the hole transfer is slow, so the methanol molecule and the methoxy anion remain in quasi-equilibrium, with slow oxidation to the formaldehyde. Hence, the high-activity sites end up with low coverages of the methanol molecule, and vice

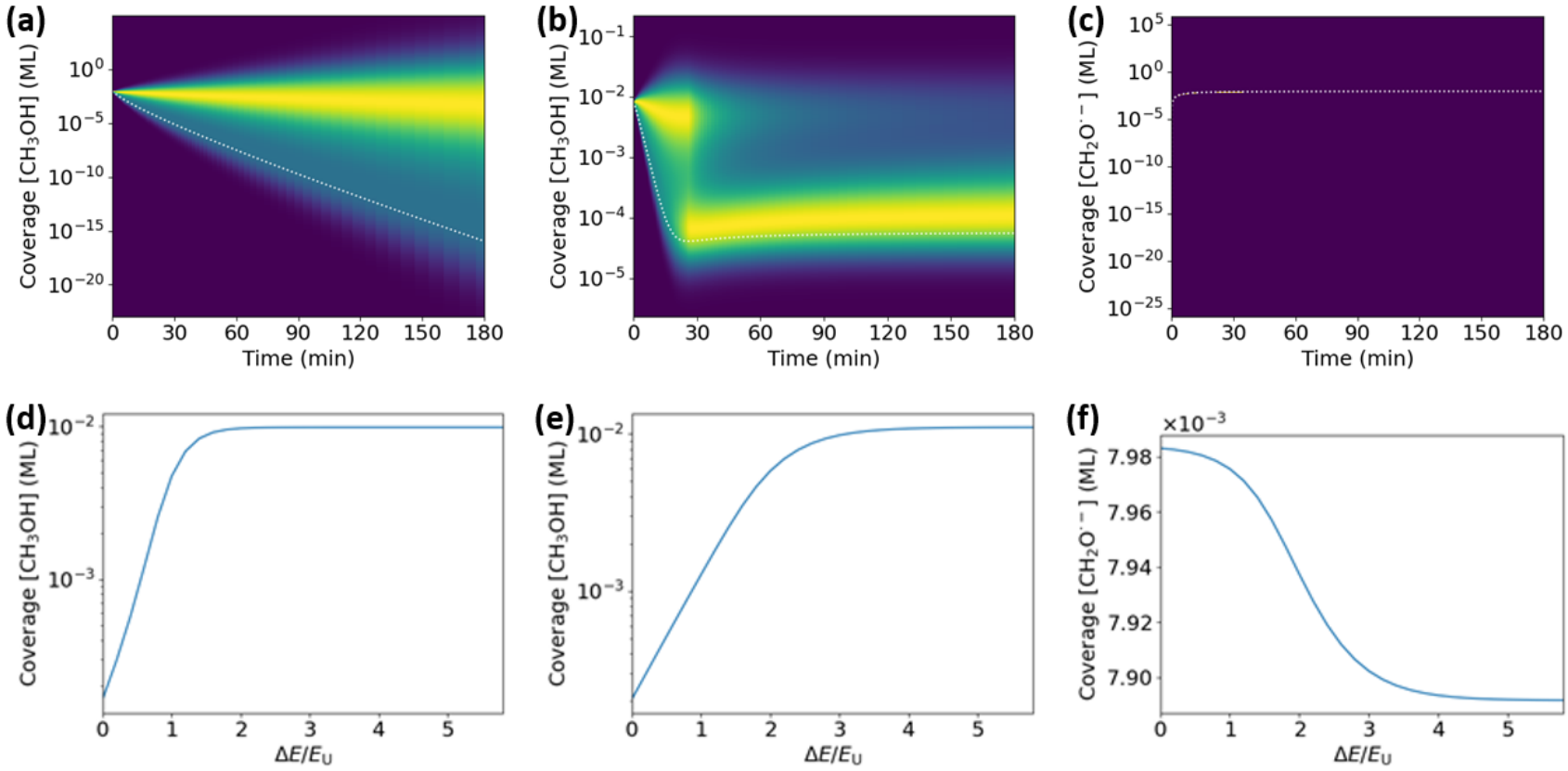

Figure 2-6: Time-dependent distributions of the coverages and time-averaged coverages as a function of the trap energy: (a,d) methanol molecule at 80 K; (b,e) methanol molecule at 180 K; and (c,f) formaldehyde at 180 K. The dotted curves mark the coverages of the site with $\Delta E_i = 0$, or $k_r^i = k_r^0$.

versa. The two groups of Ti_{5c} sites are not distinct in a discrete sense. They represent ranges on a continuum of rate constants, which might be attributed to continuous variables, such as the distances and the orientations of nearby defects. When the sites are not catalyzing a reaction, there might not be an obvious difference in the coordination or the structure. Indeed, the variations in the trap energies are within a few multiples of the Urbach energy $\sim 30\,\mathrm{meV}$, as shown in Table A.1. Then, it makes sense that the weight of the high-activity group increases at 180 K. A significant fraction of sites that are inactive at 80 K ($k_\mathrm{B}T \sim 6.9\,\mathrm{meV}$) can turn active at 180 K ($k_\mathrm{B}T \sim 15.5\,\mathrm{meV}$). At high enough temperatures, the low-activity group might be unpopulated altogether.

The peculiar part is that there are so few sites in the transition zone. A continuous change in the rate constants appears to give an abrupt change in the rates, akin to a dynamical transition or a bifurcation in the reaction network. Since a significant fraction of the sites have $\Delta E_i \sim k_\mathrm{B}T$, it is not a surprise that a distinct high-activity group should emerge. In Figure 2-5, we have marked the expected coverage of a site with $\Delta E_i = 0$, or $k_r^i = k_r^0$, which coincides with the high-activity group, as expected. Curiously, it follows that a wide range of sites with $\Delta E_i \gg k_\mathrm{B}T$ are ending up with similar coverages and give rise to the low-activity group. This is due to the limits on the coverages. As shown in Figures 2-6d,e, sites with only a few Urbach energies of trap energy are already so inactive that they retain the initial coverage of the methanol molecule. Likewise, the diffusion of the formaldehyde at 180 K enables some coverage of the formaldehyde even on the inactive sites, as shown in Figure 2-6f. Thus, we expect that most types of static disorder with a long tail of trap energies that extends into $\Delta E_i \gg k_\mathrm{B}T$ would yield a distinct low-activity group.

To establish the robustness of the division, we examined the normal, Poisson ($k = 2$), and hyperbolic secant distributions, in addition to the Poisson ($k = 0$) distribution of trap energies. We provide the details in Appendix A.7. The key result is that the division appears to be quite insensitive to the type of static disorder. Only the normal distribution predicts a significant reduction of the division in all of the coverages. However, the normal distribution evokes the deep trap states, which are

unlikely to participate in the photochemistry, which leads us to favor the Poisson distribution. In any case, the robustness of the division suggests that the emergence of the high-activity and the low-activity groups might be a staple feature in a variety of photocatalytic processes on TiO_2.

2.4 Conclusion

We have described a novel method to simulate the chemical kinetics of methanol oxidation on TiO_2. Combining the intuitions of MFSS and PA, HHPA can describe the effects of static disorder and dynamic correlation together. Furthermore, preaveraging over the static disorder in one site of each pair makes HHPA efficient enough to simulate systems of several species and calibrate rate constants.

The simulated kinetics indicate that the dominant hole scavengers are temperature-dependent: the methoxy anion at 80 K and the methanol molecule at 180 K. Even though the thermally activated cleavage of the OH bond is orders of magnitude faster, the methoxy anion tends to revert to the methanol molecule before it traps a hole. Thus, the hole-activated cleavage of the OH bond, which is slower but takes the reaction to completion, determines the overall kinetics at 180 K. Meanwhile, static disorder in the hole transfer steps appears to explain the stretched exponentials in the observed kinetics. Remarkably, two groups of Ti_{5c} sites emerge with innate and disparate activities, even though no such division exists in the underlying rate constants. Since the division appears to be quite insensitive to the type of static disorder and persist over a range of temperatures, the emergence of two groups might play a significant role in a variety of photocatalytic processes on TiO_2.

Furthermore, it is worth noting the role of dynamic correlation. While dynamic correlation did not appear to reduce the ability of HMF to reproduce the observed kinetics, HMF might be doing so with incorrect values of the parameters. Entering the parameters that were calibrated using the MF methods into the PA methods and vice versa resulted in simulated kinetics with qualitative deviations. Although HHPA can exhibit semiquantitative accuracy in systems with only short-range correlation,

such as methanol oxidation on TiO_2, its performance on a number of simple model systems revealed that PA is not satisfactory in systems with significant long-range correlation. In Chapter 3, we propose a scheme to overcome the weaknesses of simple moment closures in systems with significant long-range correlation.

On the basis of these results, we propose a number of directions that require attention in the future. Concerning TiO_2 and methanol oxidation in particular, it would be of both practical and theoretical interest to determine whether the high-activity sites and the low-activity sites retain their activities when the surface is cleaned and a new layer of adsorbates is deposited. Furthermore, there are few systematic studies of the chemical kinetics over ranges of temperatures, coverages, and defect densities that would help identify the mechanistic regimes that might exist. Concerning chemical kinetics in general, it might be worthwhile to identify and classify systems where a combination of static disorder and dynamic correlations has nontrivial effects on chemical kinetics.

2.5 Acknowledgements

Reprinted with permission from Ref. [109]. Copyright 2022 American Chemical Society. This work was supported by the ACS Petroleum Research Fund (60503-ND6).

2.6 Supplementary Information

The Supplementary Information is available in Appendix A: demonstration of HMF and HHPA on a number of simple model systems; cross-examination of calibrated parameters in the MF and the PA methods; simulated kinetics in the modified model; sensitivity analysis of the calibrated parameters in the original model and the modified model; construction and outcomes of the compact model; extended discussion on the origin of the bimodal distributions in the coverages and the rates; distributions of the coverages and the rates in the original, modified, and compact models; and normal,

Poisson ($k = 2$), and hyperbolic secant distributions of trap energies.

Chapter 3

Machine Learning Dynamic Correlation in Lattice Lotka-Volterra Model

Lattice models are a useful tool to simulate the chemical kinetics of surface reactions. Since it is expensive to propagate the probabilities of the entire lattice configurations, it is practical to consider the occupation probabilities of a typical site or a cluster of sites instead. This amounts to a moment closure approximation of the chemical master equation. Unfortunately, simple moment closures, such as the mean-field (MF) and the pair approximation (PA), exhibit weaknesses in systems with significant long-range correlation. In this chapter, we show that machine learning (ML) can be used to construct accurate moment closures in chemical kinetics, using the lattice Lotka-Volterra model (LLVM) as a model system. We trained feedforward neural networks (FFNNs) on kinetic Monte Carlo (KMC) results at select values of rate constants and initial conditions. Given the same level of input as PA, the ML moment closure (MLMC) gave accurate predictions of the instantaneous three-site occupation probabilities. Solving the kinetic equations in conjunction with MLMC gave drastic improvements in the simulated dynamics and descriptions of the dynamical regimes throughout the parameter space. In this way, MLMC is a promising tool to interpolate KMC simulations or construct pretrained closures that would enable researchers to

extract useful insight at a fraction of the computational costs.

3.1 Introduction

Machine learning (ML) is an important tool in computational chemistry. On the one hand, it has been used to accelerate the discovery of drugs and materials by deducing the electronic properties of molecules [110–114], reactivities of organic compounds [115–117], and secondary structures of proteins [118–120] using just the topologies of the molecules. On the other hand, it has been used to improve simulations by replacing the approximate right hand sides, such as density functionals [121, 122], electron densities [123, 124], and force fields [125–128], with ML models. Meanwhile, there have been a few applications of ML in chemical kinetics [36, 129, 130]. We believe that ML might provide a way to improve the solution of the chemical master equation (CME).

There is a duality in what various authors mean by CME. First, there are homogeneous systems where the state of the system is defined by the numbers of molecules [30–34] and the positions of the molecules are not explicit variables. Second, there are heterogeneous systems, where the state of the system is defined by the configuration of a lattice [27, 35, 36]. Hence, not only the numbers of molecules, but also their positions are explicit variables. In both cases, CME is a system of ordinary differential equations (ODEs) that propagates the probabilities of all possible states of the system, and the computational costs are exponential. Only, the homogeneous case scales as the number of molecules raised to the number of species, whereas the heterogeneous case scales as the number of species raised to the number of molecules. In this thesis, we focus on heterogeneous systems. Nonetheless, the mathematical commonalities imply that results that hold in heterogeneous systems might be also meaningful in homogeneous systems and vice versa.

Since the shear size of the state space often makes it impractical to solve the full CME, moment closure approximations have been considered an affordable approach to extract qualitative insight. The kinetic equations are written in terms of

n-species subsystems (homogeneous case) or n-site clusters (heterogeneous case), and the higher-order moments, which describe the interactions of the nth order moments with the rest of the system, are approximated using a moment closure. In homogeneous systems, the most popular closures are stochastic closures, such as the normal [57, 58], Poisson [59], and log-normal closures [60]. Recently, Smadbeck and Kaznessis proposed an alternative scheme that computes the higher-order moments and their probability distribution by maximizing the information entropy [33]. In heterogeneous systems, the most popular closures are the mean-field (MF) approximation and the pair approximation (PA) [47–51]. There have been attempts to go to higher-order moments, such as the triple approximation [54], the approximate master equations [55, 56], and the cluster mean-field approximation [35]. In principle, moment closure approximations become more accurate as higher-order moments are used as the basis. However, an increase in the order is accompanied by a steep rise in the computational costs.

Recently, Ernst et al. demonstrated that moment closures based on deep Boltzmann machines (DBMs) can obtain accurate dynamics of the Lotka-Volterra model on the lattice [36]. In analogy to the empirical construction of density functionals, we believe that ML could provide a breakthrough in overcoming the complexity-accuracy trade-off of moment closure approximations, provided that it can be formulated in a way that is intuitive and accessible to the chemical community.

In this chapter, we show that a simple ML architecture can be used to construct an accurate moment closure in chemical kinetics. Our choice of feedforward neural networks (FFNNs) has both theoretical and practical relevance. On the theoretical side, FFNNs are the simplest neural networks. They are oblivious of time, nor do they have memory of the previous inputs and outputs. Indeed, they are functions that approximate the instantaneous values of the higher-order moments using the instantaneous values of the lower-order moments. On the practical side, FFNNs are fast to train and evaluate. They might scale better to larger numbers of species and higher orders of moments. Moreover, FFNNs are already available in popular software libraries, such as TensorFlow [131] and scikit-learn [132]. Hence, it is an architecture

with which many chemists are already familiar.

The remainder of this chapter is organized as follows: We begin by reviewing the origin of moment closure approximations. Then, we introduce the lattice Lotka-Volterra model (LLVM) and use it as the model system to demonstrate the strengths and weaknesses of MF and PA. Next, we train FFNNs to estimate the instantaneous three-site occupation probabilities, using the results of kinetic Monte Carlo (KMC) simulations at select values of rate constants and initial conditions. At the same level of input as PA, the ML moment closure (MLMC) can reduce the absolute and relative errors in the three-site probabilities by an order of magnitude. Furthermore, MLMC gives drastic improvements in the simulated dynamics and improved descriptions of the dynamical regimes throughout the parameter space of the model system.

3.2 Theory

3.2.1 Chemical Master Equation and Moment Closure

Consider a chemical reaction on a lattice. The molecules can adsorb on a vacant site, desorb, diffuse to a neighboring site, or react with another molecule. Let p_Ψ denote the probability of finding the lattice in configuration Ψ. The chemical master equation (CME) is given by

$$\frac{dp_\Psi}{dt} = +\sum_\Phi k_{\Phi\to\Psi} p_\Phi - \sum_\Phi k_{\Psi\to\Phi} p_\Psi \tag{3.1}$$

where $k_{\Psi\to\Phi}$ is the sum of the rate constants of the elementary steps, if any, that would take a lattice in configuration Ψ to configuration Φ. Concrete examples of these terms can be found in Appendix B.1. Assuming Markovian processes and an *a priori* knowledge of the rate constants, CME gives an exact treatment of both static disorder (site-to-site variations that are reflected in the rate constants, $k_{\Psi\to\Phi}$) [20, 22] and dynamic correlation (segregation and self-organization of reactants that manifest on the explicit lattice configurations, Ψ) [15, 16, 18]. In the present investigation, we assume no static disorder and consider dynamic correlation only. Unfortunately, the

dimensionality of CME scales as S^L, where S is the number of species and L is the number of sites on the lattice, making CME intractable in many systems of practical relevance.

In princple, the kinetic Monto Carlo (KMC) [27, 30, 37] can recover the static disorder and dynamic correlation. A stochastic simulation of the lattice amounts to sampling a trajectory through the configuration space. By averaging over multiple simulations, one can approach the full CME results. However, the computational costs of the simulations can be formidable, especially if rapid equilibrium or diffusion is involved [27, 37, 40].

Since the desired outcome in chemical kinetics is often an ensemble average, such as the surface coverage or the reaction rate, we are motivated to rewrite the kinetic equations in the occupation probabilities of n-site clusters (n-site probabilities)

$$[X] \equiv [X_i] = \sum_{\Psi} \delta_{\psi_i,X} p_{\Psi} \tag{3.2}$$

$$[XY] \equiv [X_i Y_j] = \sum_{\Psi} \delta_{\psi_i,X} \delta_{\psi_j,Y} p_{\Psi} \tag{3.3}$$

$$[XYZ] \equiv [X_i Y_j Z_k] = \sum_{\Psi} \delta_{\psi_i,X} \delta_{\psi_j,Y} \delta_{\psi_k,Z} p_{\Psi} \tag{3.4}$$

where i, j, and k are a string of adjacent sites on the lattice; and $\delta_{\psi_i,X} = 1$ if the occupant of site i is $\psi_i = X$ and 0 otherwise. These n-site probabilities are special cases of moments.

The kinetic equations of one-site clusters are given by

$$\begin{aligned} \frac{d[X]}{dt} = &+ \sum_R k_{R\to X}[R] + N \sum_{YRS} k_{RS\to XY}[RS] \\ &- \sum_R k_{X\to R}[X] - N \sum_{YRS} k_{XY\to RS}[XY] \end{aligned} \tag{3.5}$$

where $k_{RS\to XY}$ is the rate constant of the elementary step, $R+S \to X+Y$, if it exists; and N is the number of nearest neighbors. For example, the first term describes the unimolecular reaction of the R to produce an X at its position, and the last term describes the bimolecular reaction of the X and a neighboring Y to produce an R

and an S at their respective positions.

Observe that the equations are not closed. Unless the elementary steps consist of unimolecular reactions only, the equations of n-site clusters are going to depend on information about $(n+1)$-site clusters. In order to create a closed system of equations, we need a prescription to approximate the higher-order moments using only information about the lower-order moments – hence, a moment closure approximation. The simplest and the most popular closure is the mean-field (MF) approximation, $[XY] = [X][Y]$, which neglects any correlation that might exist between the sites.

The next simplest closure, which incorporates some site-to-site correlation, is the pair approximation (PA). Consider the kinetic equations of two-site clusters

$$\begin{aligned}\frac{d[XY]}{dt} = &+ \sum_{RS} k_{RS\to XY}[RS] \\ &+ (N-1)\sum_{WQR} k_{QR\to WX}[QRY] + (N-1)\sum_{STZ} k_{ST\to YZ}[XST] \\ &- \sum_{RS} k_{XY\to RS}[XY] \\ &- (N-1)\sum_{WQR} k_{WX\to QR}[WXY] - (N-1)\sum_{STZ} k_{YZ\to ST}[XYZ] \end{aligned} \tag{3.6}$$

For example, the first term describes the reaction of the RS pair to produce an XY pair in their positions, and the last term describes the reaction of the Y in the XY pair and a neighboring Z to produce an S (making an XS pair) and a T at their respective positions. We have treated unimolecular reactions as a special case of bimolecular reactions where one of the participants is a spectator.

With the two-site probabilities, $[XY]$, as the variables, the kinetic equations now depend on the three-site probabilities, $[XYZ]$. PA estimates the three-site probabilities using the definition of conditional probability

$$[XYZ] = \frac{[XY][YZ]}{[Y]} \tag{3.7}$$

Due to its simple rationale, PA has been invented many times by independent workers in chemistry [47, 48], population biology [49, 50], and epidemiology [51].

In principle, the closed system of equations would become more accurate as higher-order moments are used as the basis of the moment closure approximation. Formally, one can interpret MF and PA as special cases of product approximations [52, 53], so it should be possible to generalize PA to n-site probabilities. Examples of these attempts include the triple approximation [54], the approximate master equations [55, 56], and the cluster mean-field approximation [35]. However, the derivation and the computation of the kinetic equations become challenging, as the geometries of the higher-order clusters are complicated, and the number of moments grows with the order as S^n.

A subset of the readers might be more familiar with stochastic closures, such as the normal [57, 58], Poisson [59], and log-normal closures [60], which are often used in homogeneous systems. The physical and mathematical arguments behind these closures are quite different, since the moments in the homogeneous case are expected numbers of molecules ($\in \mathbb{R}$), as opposed to occupation probabilities ($\in [0, 1]$). In short, stochastic closures assume that the numbers of molecules have a certin probability distribution. Applying stochastic closures to heterogeneous systems entails contradictions: we are considering a probability distribution of probabilities, and the distributions are defined on $\mathbb{R}$, as opposed to $[0, 1]$. Although it can be carried out with suitable adjustments, our experience indicates that stochastic closures encounter instabilities and unphysical values in heterogeneous systems that exhibit a strong spatial correlation, such as LLVM. PA is robust as long as the removable discontinuity at zero is assigned an appropriate value. Thus, we focus on PA.

Nonetheless, it is worth noting that the equations of nth moments in homogeneous systems are analogous to the equations of n-site clusters in heteogeneous systems. Only, the number of nearest neighbors does not appear, and the ordering of species in the moments does not matter in the homogeneous case. If ML can be used to construct accurate moment closures in heterogeneous systems, then there is a chance that a similar procedure could be used to construct accurate moment closures in homogeneous systems. Schnoerr et al. have a pedagogial paper on moment closure approximations in homogeneous systems [34]. Interested readers should refer to their

work.

3.2.2 Model System

The Lotka-Volterra model is a classic model system in which the activities of competing components lead to the emergence of oscillations. Originally, it was devised to describe autocatalytic chemical reactions [133], but its application has been extended to biological systems [134–136], where it had another intuitive interpretation. Our implementation of LLVM is given by

$$O + A \xrightarrow{k_1} A + A \tag{3.8}$$

$$A + B \xrightarrow{k_2} B + B \tag{3.9}$$

$$B \xrightarrow{k_3} O \tag{3.10}$$

where one often interprets O as the vacancy, A as the prey, and B as the predator. The kinetic equations at the levels of one-site and two-site clusters can be found in Appendix B.2. To our knowledge, there is no chemical reaction that follows this mechanism *per se*. However, it can be regarded as a coarse-grain approximation. In Appendix B.3, we discuss how the NO + CO reaction on the Pt(100)-(1×1) surface [3] might be coarse-grained on to LLVM.

Variations in LLVM have been a subject of interest in the physics community [137–139]. They are known to display a number of features that are insensitive to the implementation [140]. In particular, the collective activities of the prey and the predator give rise to spatiotemporal patterns [141], along with density oscillations [142] that average out in the thermodynamic limit [138, 139]. Some of the spatiotemporal patterns in our implementation are shown in Figure 3-1. It is interesting to see traveling wave patterns emerge. First, A grows into islands (Figure 3-1a,b). As the islands of A expand, B begins to grow (Figure 3-1c) and then proceeds to overrun the islands (Figure 3-1d,e). The cycle resets as B gives way to O (Figure 3-1f). We emphasize that the individual molecules are immobile in our implementation, but their formation and consumption as a collective give rise to the apparent pursuit-evasion

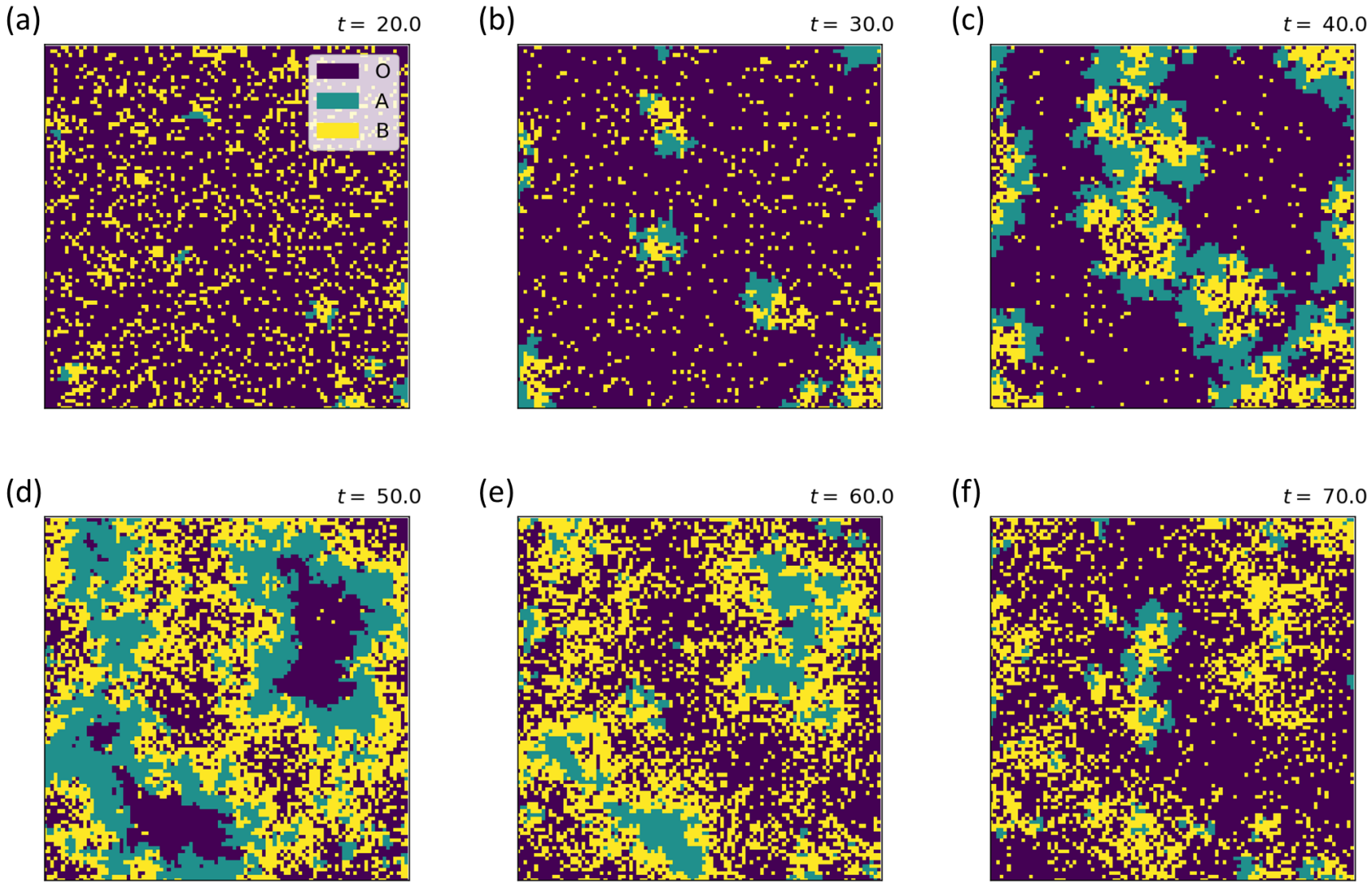

Figure 3-1: Snapshots of a KMC simulation. The snapshots are zooming into a 100×100 sublattice of the 500×500 lattice. The panels correspond to different times: (a) $t = 20.0$, (b) $t = 30.0$, (c) $t = 40.0$, (d) $t = 50.0$, (e) $t = 60.0$, and (f) $t = 70.0$. The rate constants were $(k_1, k_2, k_3) = (0.5, 0.3, 0.1)$, and the initial conditions were $([O], [A], [B]) = (0.2, 0.3, 0.5)$.

behavior.

Self-organization of reactants is not uncommon in surface reactions. Even the benign $A + B \rightarrow AB \uparrow$ model is known to result in monospecific islands of A and B [15, 16, 18], and numerous real-world examples can be found in heterogeneous catalysis [1]. Indeed, the NO + CO/Pt(100) reaction is one of them. Similar to LLVM, the NO + CO reaction gives rise to spatiotemporal patterns, and the dephasing of local oscillations [3, 143] leads to the damping of global oscillations [144]. The types of correlations in LLVM are quite relevant to chemical systems.

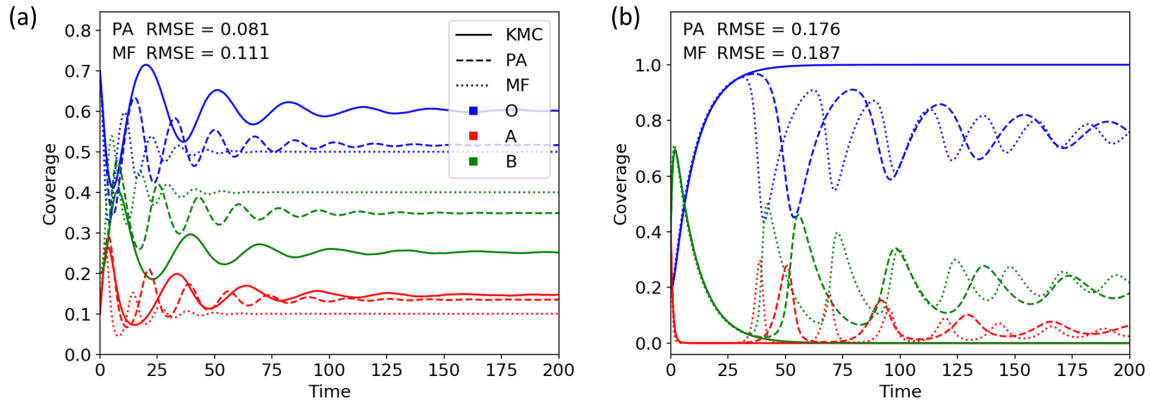

Figure 3-2: Time-dependent coverages in MF (dotted lines), PA (dashed lines), and KMC (solid lines). (a) The rate constants were $(k_1, k_2, k_3) = (0.4, 0.5, 0.2)$, and the initial conditions were $([O], [A], [B]) = (0.7, 0.1, 0.2)$. (b) The rate constants and the initial conditions were $(0.2, 0.7, 0.1)$ and $(0.2, 0.4, 0.4)$, respectively. Clearly, PA provides significant but not satisfactory improvement over MF in both cases.

In Figure 3-2, we demonstrate the strengths and weaknesses of PA on LLVM. Although PA (dashed lines) does give a noticeable improvement over MF (dotted lines), it still looks too much like MF as opposed to KMC (solid lines). In the oscillatory regime (Figure 3-2a), PA underestimates the amplitude and period. In the nonoscillatory regime, where $[A]$ and $[B]$ go to zero (Figure 3-2b), PA can still predict damped oscillations. Moreover, the steady-state coverages are mispredicted. The source of the error is the long-range correlation. Because PA only knows about the short-range (two-site) correlation, it is not able to anticipate the formation of islands or traveling waves that span a large number of sites. That is, not without information about the mechanism and the nature of the correlation built into the

approximation.

3.2.3 Machine Learning Moment Closure

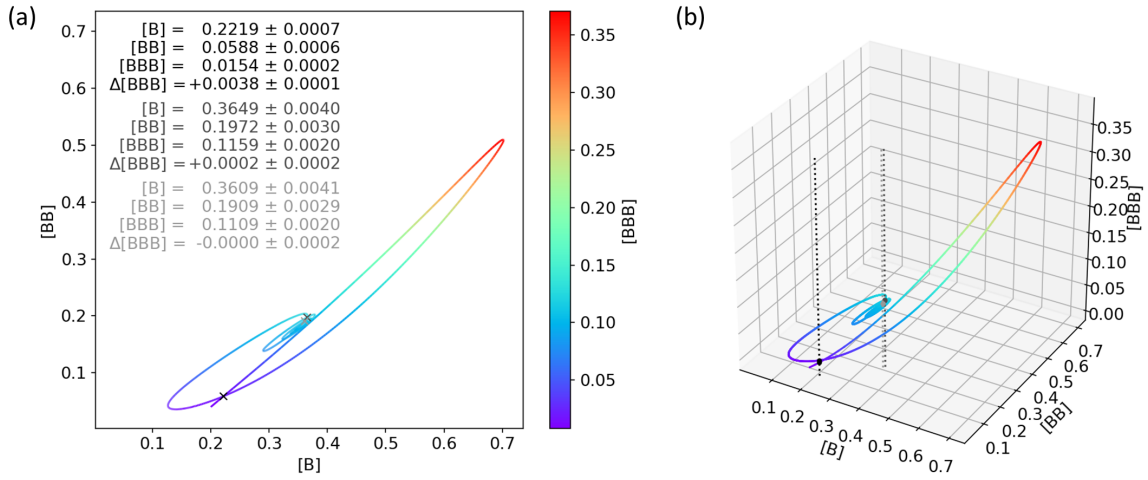

Figure 3-3: Self-crossings of the time-dependent one-site, two-site, and three-site probabilities. The curve was obtained as an average over 20 KMC simulations on a 1000×1000 lattice. (a) On the 2D plot, the self-crossings on the xy-plane are indicated by crosses, and the coordinates and the standard deviations are provided on the upper left. (b) On the 3D plot, the self-crossings on the xy-plane are indicated by bold dots, and the vertical dotted lines are visual aids. The rate constants were $(k_1, k_2, k_3) = (0.5, 0.3, 0.1)$, and the initial conditions were $([O], [A], [B]) = (0.2, 0.6, 0.2)$.

The goal of MLMC is a smarter closure that still takes low-order moments as the input but uses mechanism-specific information to give a more accurate output. However, what is the lowest order at which the moments can be expect to be predictive of the correlation? For the case of LLVM, Figure 3-3 gives some insight. Since the system is undergoing nonequilibrium dynamics, it is not possible in priciple to write the n-site probabilities as functions of the k-site probabilities ($k < n$). Indeed, Figure 3-3a shows that it is not plausible to write the two-site probability, $[BB]$, as a function of the one-site probability, $[B]$. Due to the oscillatory nature of the dynamics, the system returns to the same value of $[B]$ multiple times, and it is clear that the relationship between $[B]$ and $[BB]$ is not one-to-one. Hence, there is no function such that $[BB] = f([B])$.

On the other hand, there are far fewer points where the system returns to the same

values of $[B]$ and $[BB]$ at the same time. These appear as self-crossings of the curve in Figure 3-3a. Of course, there are still differences in the three-site probability, $[BBB]$, each time the curve crosses itself, so it is not possible to write $[BBB] = f([B], [BB])$ in strict terms. However, the numbers on the upper left of Figure 3-3a and the three-dimensional plot in Figure 3-3b indicate that the differences are small. In many cases, they are on the same order of magnitude as the statistical noise in the KMC simulations, and they can be negligible if the curve crosses itself with minimal time for the correlation to evolve. Similar results were obtained using other initial conditions and reference species (Figures B-1–B-3). Therefore, we conjecture that the three-site probabilities can be written to a good approximation as functions of the two-site probabilities. A viable ML model of the three-site probabilities could be constructed using no more than the two-site probabilities as the input.

3.2.4 Computational Details

The stochastic simulations were performed using rejection-free KMC [27, 37] with periodic boundary conditions. Unless otherwise mentioned, the KMC coverages in the figures were obtained as averages over ten simulations on a 500×500 lattice. The kinetic equations were integrated using the variable coefficient multistep backward differentiation formula (BDF) method [145–147] as implemented in the GNU Scientific Library 2.5 [148]. Unless otherwise mentioned, the equations were integrated using relative and absolute tolerances of 10^{-5} and 10^{-10}, respectively.

For the training data, we used the outcomes of KMC simulations at select values of rate constants and initial conditions. We ran the simulation only once at each combination of parameters. First, the the initial conditions were fixed at $([O], [A], [B]) = (0.4, 0.3, 0.3)$, and the rate constants were varied in $k_1, k_2, k_3 \in \{0.1, 0.3, 0.5, 0.7, 0.9\}$. The simulations were performed on a 200×200 lattice. At intervals of 0.1 unit time up to 200.0 unit time, we sampled the lattice configurations and counted the two- and three-site clusters, considering the symmetries, $[XY] = [YX]$ and $[XYZ] = [ZYX]$. Then, we chose seven combinations of rate constants that gave distinct dynamics, as shown in Table B.1. For each combination, the initial conditions were varied in

$[O], [A], [B] \in \{0.1, 0.2, ..., 0.9\}$ with the constraint $[O] + [A] + [B] = 1.0$. This time, the simulations were performed on a 500×500 lattice, and the configurations were sampled at intervals of 0.1 unit time up to 500.0 unit time. The $125 + 7 \times 36 = 377$ simulations yielded a total of 1 171 229 data points.

We found it useful to apply a log transform $y' = \log y$ to both the two-site probabilities, $[XY]$, and the three-site probabilities, $[XYZ]$, so that the ML models minimize the relative error, as opposed to the absolute error. Bounding the relative error ensures that the reaction rates and hence the dynamics would remain accurate when one or more of the probabilities are small. In applying the log transform, we took the data points containing zero-valued two-site probabilities and made three copies where the zero-valued two-site probabilities have been replaced with small values

$$\delta = \frac{10^{-p}}{2 \cdot 500^2} \tag{3.11}$$

where $p = 1$, 2, and 3, respectively. The denominator, $2 \cdot 500^2$, is the total number of two-site clusters on a 500×500 lattice, so the small values correspond to 1/10, 1/100, and 1/1000 of the smallest nonzero two-site probability that can be represented on the lattice. We removed the original zero-containing data points and inserted the modified data points. Meanwhile, the zero-valued three-site probabilities were replaced with PA estimates, using the nonzero two-site probabilities and the small values put in place of the zero-valued two-site probabilities. Even though the replacement might reduce the accuracy of the ML models in themselves, we found that it improves the robustness of the chemical kinetic simulations, as one or more of the probabilities approach zero. The treatment of the zeros increased the number of data points to 1 232 155. Finally, we standardized the input and output data with the mean $\mu = 0$ and standard deviation $\sigma = 1$.

The ML models were constructed and trained using TensorFlow 1.13 [131]. We trained a separate FFNN for each of the six three-site probabilities that appear in the kinetic equations. The FFNNs shared a simple architecture: $6 \to 100 \to 100 \to 75 \to 50 \to 25 \to 12 \to 1$ units on each layer, which were fully connected and had

a rectified linear unit (ReLU) activation, except the linear input and output. As a means of regularization, the data were shuffled and split into six sets, one of which was set aside as the test set, and the other five sets were utilized in a fivefold cross-validation (CV). At each cycle of the CV, a FFNN was trained by stochastic gradient descent (SGD) on the mean squared error (in the log space) via the Adam optimizer [149]. The SGD used a batch size of 10 000 and stopped at 150 iterations. At the end of the cycles, the FFNN that yielded the smallest loss on the test set was chosen as the final model. In addition to the CV, no further regularization methods were employed.

3.3 Results and Discussion

As detailed in Section 3.2.4, we trained FFNNs to predict the three-site probabilities in terms of the distinct two-site probabilities

$$[XYZ] = f([OO], [OA], [OB], [AA], [AB], [BB]). \tag{3.12}$$

Figure 3-4 demonstrates the accuracy of MLMC. Based on the spreads of the training sets and the test set, there does not appear to have been serious over-fitting. Moreover, there are qualitative improvements compared to PA (Figure 3-5). Not only is the off-diagonal spread of the data points narrower in general, but also the spread is narrower towards the smaller values in particular. This means that the absolute error decreased along with the predicted quantities. Hence, MLMC has bounded the relative error, as desired. For a quantitative evaluation, we computed two types of root mean-squared-error (RMSE) on the test set: the root-mean-squared *absolute* error and the root-mean-squared *relative* error. The values are shown on the upper left of Figures 3-4a-f and 3-5a-f. Indeed, MLMC gives an order-of-magnitude improvement over PA in both criteria.

Remarkably, the kinetic equations (Equation 3.6) employing MLMC can be integrated using a standard ODE solver [145–148]. The numerical integrability is non-

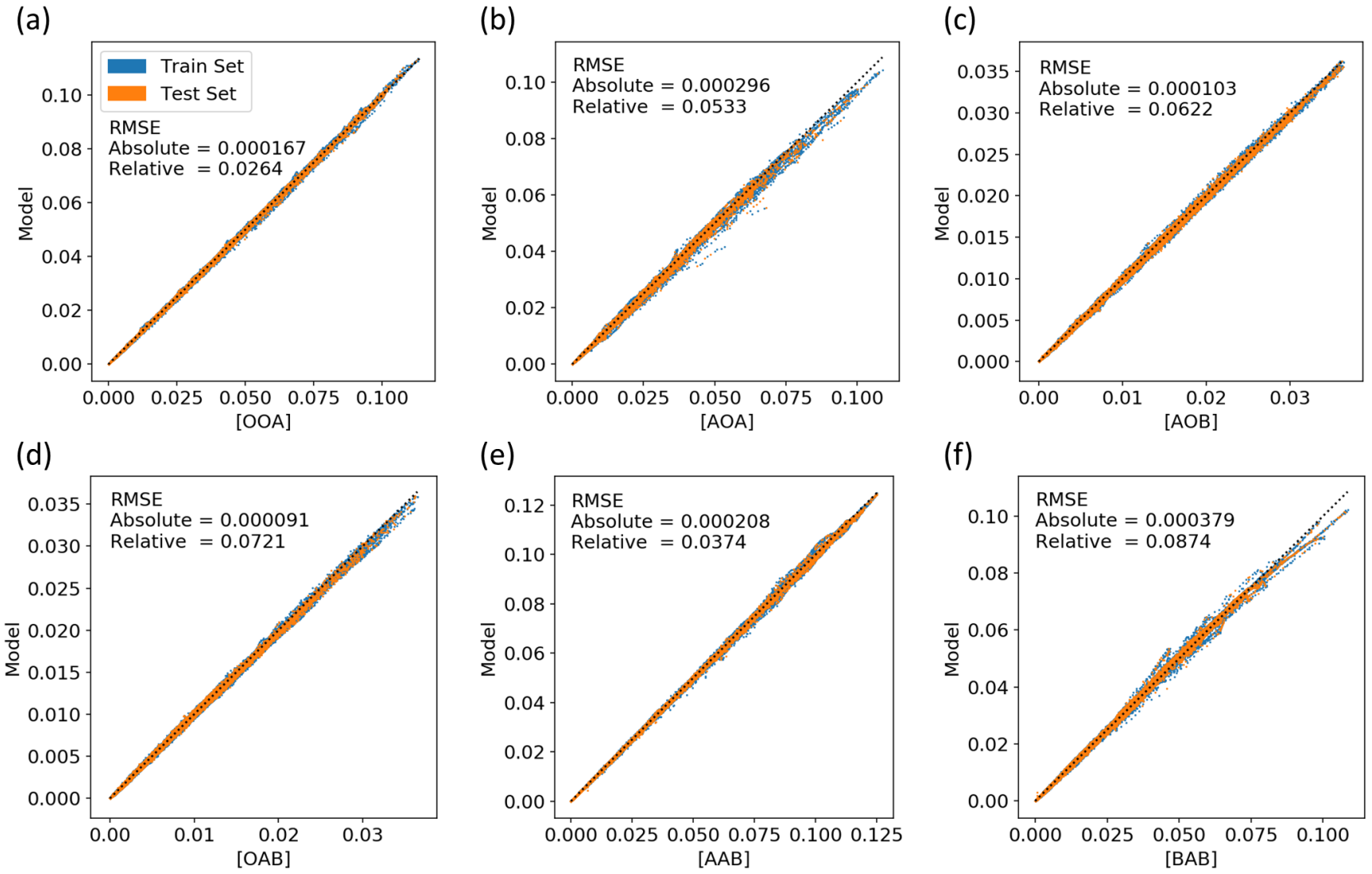

Figure 3-4: Scatter plots of the ML against the KMC three-site probabilities. The panels correspond to the distinct three-site probabilities: (a) $[OOA]$, (b) $[AOA]$, (c) $[AOB]$, (d) $[OAB]$, (e) $[AAB]$, and (f) $[BAB]$. The training set is plotted in blue dots, and the test set is plotted in orange dots.

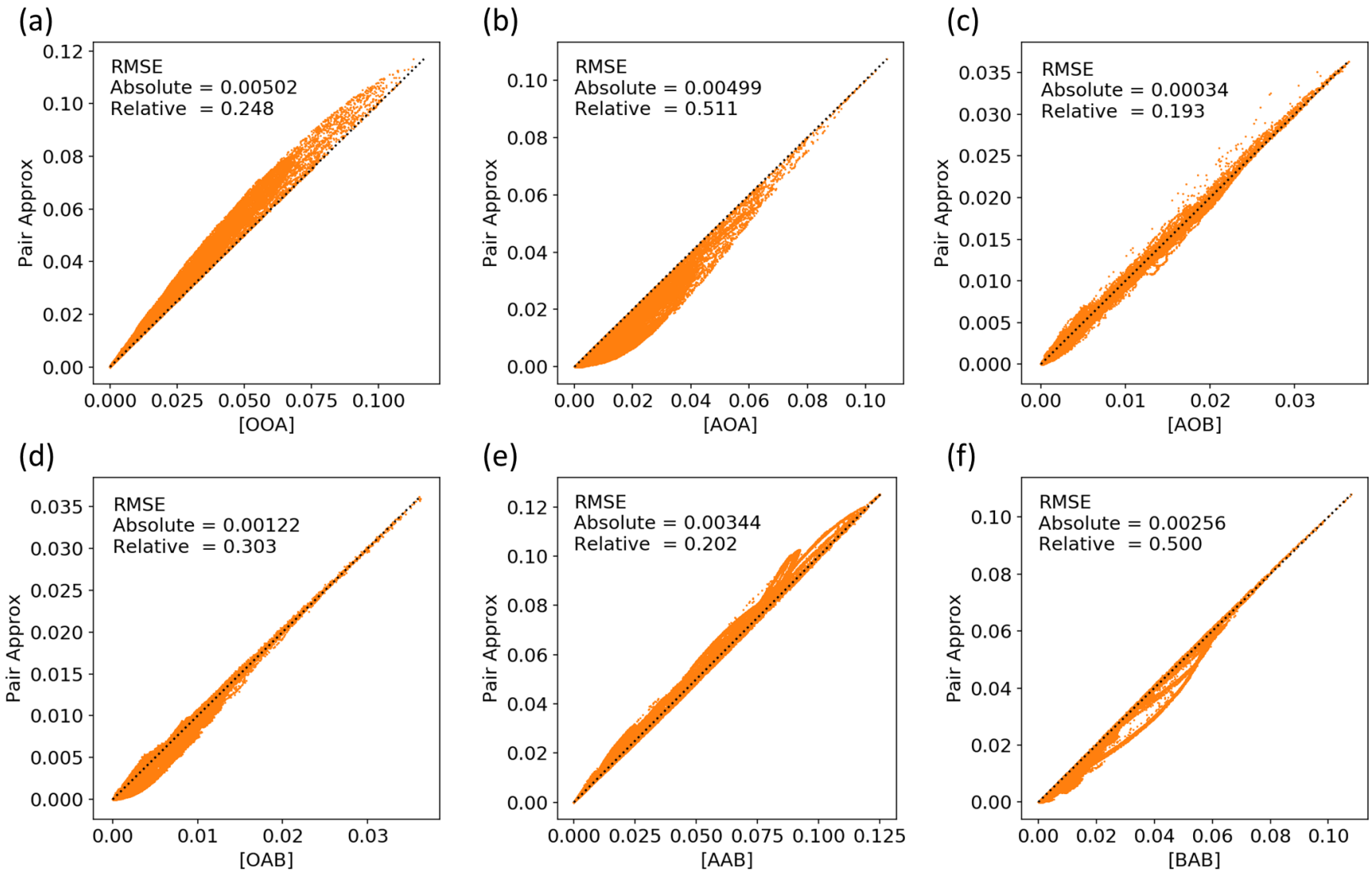

Figure 3-5: Scatter plots of the PA against the KMC three-site probabilities. The panels correspond to the distinct three-site probabilities: (a) $[OOA]$, (b) $[AOA]$, (c) $[AOB]$, (d) $[OAB]$, (e) $[AAB]$, and (f) $[BAB]$. Only the test set is plotted, since PA is not a trained model.

trivial in a number of ways. Even though our FFNNs should be continuous functions, there are a number of pathological properties that can make numerical integration difficult, such as wild oscillations and jaggedness. Moreover, while the FFNNs have been encoded with the symmetries, $[XY] = [YX]$ and $[XYZ] = [ZYX]$, they have not been encoded with the laws of probability, such as the equality, $\sum_Z [XYZ] = [XY]$, and the inequality, $[XYZ] \leq [XY]$. Indeed, numerical integration can be problematic if the inequality is violated, because overestimation of the three-site probabilities and hence the reaction rates can cause the two-site probabilities to overshoot zero and take negative values. The replacement of zero-valued probabilities in the training data with PA estimates helps mitigate the problem by guiding the FFNNs to go to zero as the probabilities go to zero.

Here, we note that it was our choice of methodology not to encode the laws of probability in the ML models. There are a variety of ways to impose equality and inequality constraints on neural networks [150, 151]. Employing some of these methods might be the topic of future investigation.

Figure 3-6 shows some of the dynamics that were obtained using MLMC. Additional examples are shown in Figure B-6. Overall, MLMC gives qualitative improvements over PA. In the oscillatory regime, MLMC gives accurate predictions of the amplitude and period (Figures 3-6a and B-6a), though it can underestimate the damping (Figure B-6b). The transition to the nonoscillatory regime also appears to be predicted with good accuracy (Figures 3-6b and B-6c,d). A challenging situation is when one or both of $[A]$ and $[B]$ are near zero. The minority species has a chance to recover or vanish altogether. In the recovering case, KMC has difficulties converging on the dynamics, because the dynamics hinges on a small number of seed molecules. Since the accuracy of MLMC is limited by KMC, MLMC also gives erratic dynamics (Figure 3-6c). Nonetheless, it is an improvement over the PA prediction of periodic oscillations. In the vanishing case, MLMC can capture the depletion of a species (Figures 3-6d and B-6e), but sometimes it predicts fictitious recovery with erratic oscillations (Figure B-6f). We suspect that the replacement of zero-valued probabilities in the training data with PA estimates might be contributing to the fictitious

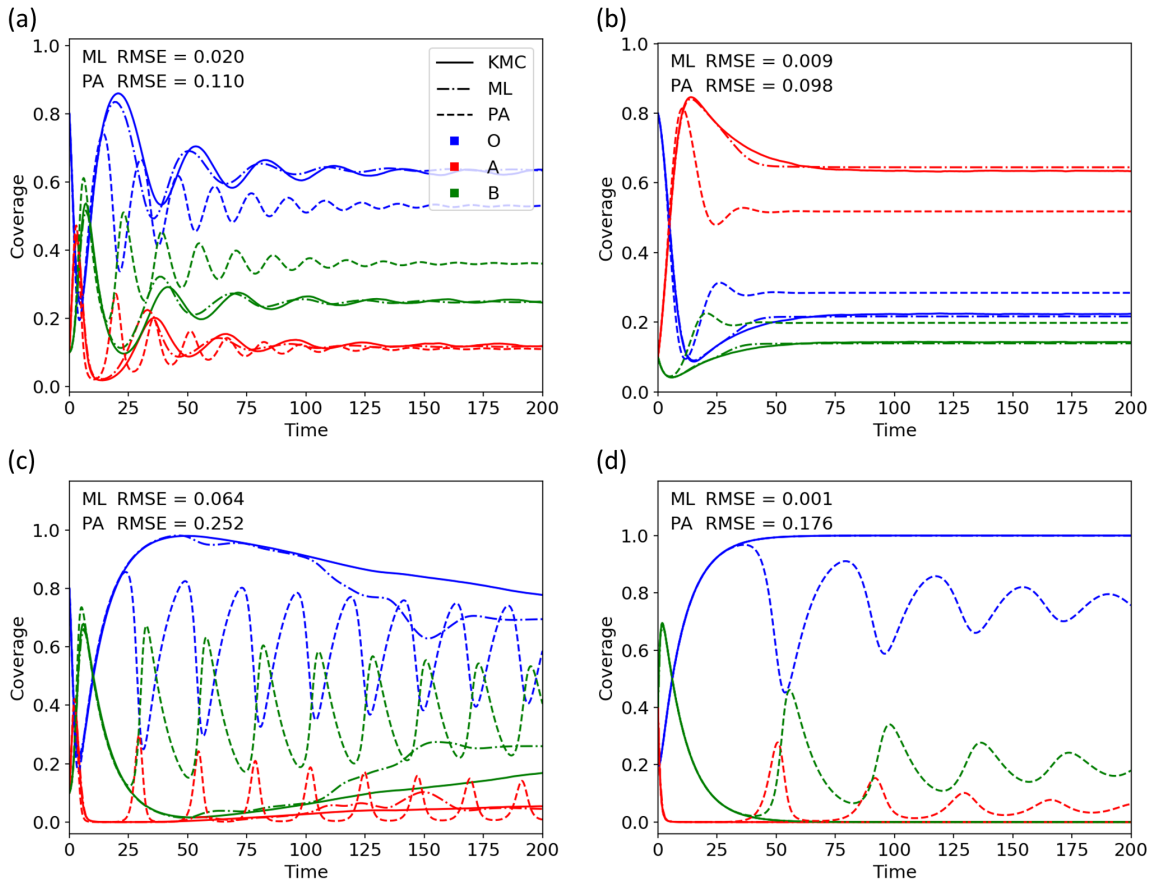

Figure 3-6: Time-dependent coverages in PA (dashed lines), ML (dashed-dotted lines), and KMC (solid lines). (a) The rate constants were $(k_1, k_2, k_3) = (0.5, 0.6, 0.2)$, and the initial conditions were $([O], [A], [B]) = (0.8, 0.1, 0.1)$. (b) The rate constants and the initial conditions were $(0.2, 0.3, 0.4)$ and $(0.8, 0.1, 0.1)$, respectively. (c) The rate constants and the initial conditions were $(0.8, 0.4, 0.1)$ and $(0.2, 0.1, 0.7)$, respectively. (d) The rate constants and the initial conditions were $(0.2, 0.7, 0.1)$ and $(0.2, 0.4, 0.4)$, respectively. In general, MLMC gives both qualitative and quantitative improvements over PA.

dynamics. Hence, there might be some trade-off between accuracy and robustness in our treatment of the zero-valued probabilities.

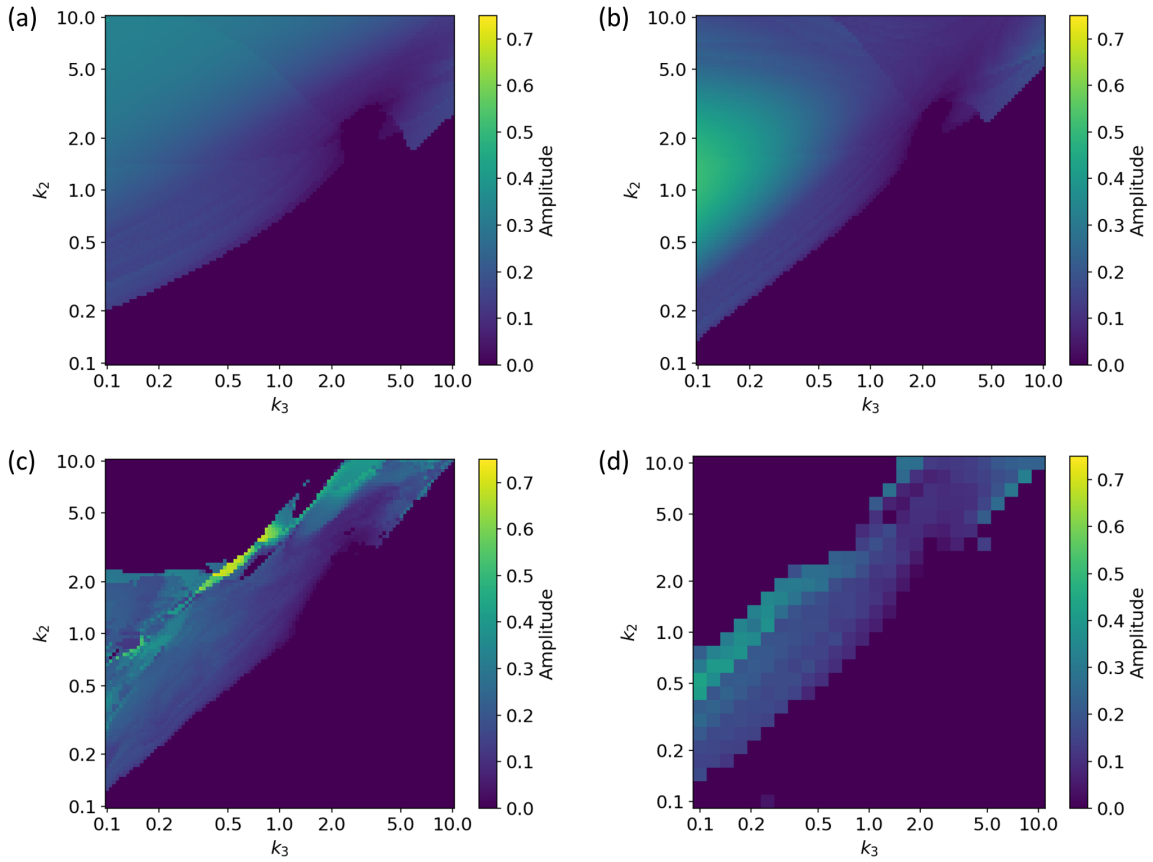

Figure 3-7: Contour maps of the nonlinear oscillation amplitudes in (a) MF, (b) PA, (c) ML, and (d) KMC. Given the nonlinear oscillation of the coverages, the amplitude was defined as the average crest-trough and trough-crest separation over the first two cycles (or three if resolvable). The rate constants were normalized to $k_1 = 1.0$, and the initial conditions were $([O], [A], [B]) = (0.5, 0.3, 0.2)$.

For a comprehensive overview of the method performances, we conducted a systematic survey of the rate constant space by fixing one of the rate constants ($k_1 = 1.0$) and varying the remaining rate constants ($k_2, k_3 \in [0.1, 10.0]$). Figures 3-7, B-7, and B-8 map the nonlinear oscillation amplitudes, frequencies, and damping ratios, respectively. Due to the time-consuming nature of KMC simulations, the plots of the KMC data are sparser than the others. Indeed, the 500×500 lattice simulations to create Figure 3-7d took 5 h per simulation. To make the plot at the same resolution as the other methods, KMC would have taken 50 000 h of CPU time, disregarding

repetitions to average out stochastic noise. Using MLMC, we could complete the task in 600 h of central processing unit (CPU) time: 500 h of KMC to prepare the data, 60 h of training, and 40 h of MLMC simulation.

Again, MLMC (Figure 3-7c) has qualitative resemblance to KMC (Figure 3-7d), whereas PA (Figure 3-7b) has more in common with MF (Figure 3-7a). MLMC predicts the accurate position of the lower boundary on the oscillatory regime ($k_2 \gtrsim k_3$) and an approximate position of the upper boundary ($k_2 \lesssim 5k_3$). Note a triangular region on the center left, where MLMC predicts oscillations in contrast to KMC. The dynamics in this region corresponds to the fictitious recovery discussed earlier (Figure B-6f). Because the fictitious oscillations are slow and sustained, the triangular region is almost invisible in the frequency plot (Figure B-7) and highlighted in the damping ratio plot (Figure B-8). We expect that more training data in that part of the parameter space would have mitigated the erroneous dynamics.

We emphasize that MLMC has not been trained to predict the dynamics. The FFNNs were optimized to predict the instantaneous three-site probabilities using the instantaneous two-site probabilities. On the one hand, it is not surprising that accurate estimates of the three-site probabilities could improve the dynamics. On the other hand, it is not obvious that using the best estimates of the three-site probabilities at each instant would yield the best estimate of the overall dynamics. MLMC has conceptual similarities to proposals of ML differential equations, where a ML model is trained on time-dependent data to extract the right hand side of the underlying equation [152–154]. The kinetic equations in terms of moments can be regarded as a special case, where the linear terms are known and the nonlinear terms have well known properties. In the future, it would be interesting to investigate training the FFNNs to output values that yield the best estimate of the dynamics, rather than the best estimate of instantaneous values.

Even though MLMC needs KMC data to be trained, we have shown that MLMC can be applied to rate constants and initial conditions to which it has not been exposed. The internal transferability suggests two practical applications of MLMC. In the short term, MLMC could be used to interpolate KMC simulations. Often, one

needs to run numerous simulations in a small region of the parameter space in order to obtain a phase diagram, locate a critical point, or fit rate constants. Considerable savings in computational costs can result if a select subset of the simulations were performed using KMC, and the gaps were filled using MLMC. In the long term, one can imagine pretrained closures that are aimed at classes of reaction mechanisms. Similar to the density functional theory (DFT), pretrained closures can help researchers extract useful insight about typical systems of interest at a fraction of the computational cost of KMC.

Of course, the application of MLMC to realistic models of chemical systems must surmount a couple of challenges. An intrinsic weakness of MLMC is that its accuracy depends on the quantity and quality of the training data. The noise in the KMC data can reduce the accuracy of MLMC, unless multiple simulations or large lattices are used to average out the stochastic fluctuations. In this work, the noise was problematic when the probabilities were near zero. The problem is expected to be more severe in realistic systems, where the rate constants can be on different orders of magnitude. On the one hand, the disparate time scales can slow down the KMC simulations, making it impractical to run multiple simulations or use large lattices. On the other hand, many of the probabilities are going to be comparable to or smaller than the inverse of the lattice size (the maximum precision of a KMC simulation). Indeed, another weakness of MLMC is our treatment of the vanishing probabilities. We have replaced the zero-valued three-site probabilities with PA estimates, which makes a specific assumption about the nature of the correlation. In principle, it is possible that the system retains a strong correlation even as the probabilities approach zero, and our approach would mispredict the correlation and hence the dynamics. A smarter scheme to handle the zero and near-zero probabilities might be required.

The previous point suggests a potential solution to the challenges. We conjecture that the correlation in many systems might have a limiting behavior as the rate constants grow more extreme. It is unlikely that a new type of correlation would be created once the rate constants are more than an order of magnitude apart. This might enable training the ML models on moderate combinations of rate constants,

where the probabilities are nonzero and the KMC simulations are affordable, whence we can extrapolate the correlation to more extreme combinations. In any case, we believe that the potential applications of MLMC warrant further research and development of the methodology.

3.4 Conclusion

We have explored the application of ML to derive moment closures in chemical kinetics. As demonstrated by the case of LLVM, PA exhibits weaknesses in systems with strong long-range correlation. In order to capture the long-range correlation at the same level of input as PA, we trained FFNNs to predict the instantaneous three-site probabilities using the instantaneous two-site probabilities. MLMC reduced the absolute and the relative errors in the three-site probabilities by an order of magnitude. Furthermore, MLMC gave drastic improvements in the simulated dynamics. The amplitude and the period in the oscillatory regime could be predicted to good accuracies, and the dynamical transitions to the nonoscillatory regime could be located to a reasonable precision. Based on these outcomes, we propose that MLMC could be used to interpolate KMC simulations or construct pretrained closures to avoid KMC in certain systems.

The next phase would be to demonstrate MLMC on realistic models of specific chemical systems. Given the proposal of pretrained closures, it would be desirable to construct MLMCs that are transferrable among similar reaction mechanisms. Further development of the ML model design might be necessary, such as data transforms and neural network architectures that enforce the laws of probability. Finally, it might be interesting to incorporate the effects of static disorder. This would yield a method that can capture both static disorder and dynamic correlation at a fraction of the computational costs of KMC.

3.5 Acknowledgements

Reproduced from Ref. [155], with the permission of AIP Publishing. Dr. Nathan D. Ricke provided the Python script to train neural networks. This work was supported by the U.S. Department of Energy Office of Basic Energy Sciences (DE-FG02-07ER46474).

3.6 Supplementary Information

The Supplementary Information is available in Appendix B: concrete examples of terms in CME; kinetic equations of LLVM at the levels of one-site and two-site clusters; coarse-graining of NO + CO / Pt(100)-(1 × 1) on to LLVM; 2D and 3D plots of three-site probabilities as functions of one-site and two-site probabilities; table of rate constants and initial conditions that were represented in the training data; scatter plots of the ML and the PA estimates of three-site probabilities in the log scale; additional examples of time-dependent coverages in PA, ML, and KMC; and contour plots of nonlinear oscillation frequencies and amplitude ratios.

Chapter 4

Conclusion

We summarize the key results of Part I and discuss future directions.

In Chapter 2, we developed and applied the half heterogeneous pair approximation (HHPA) to simulate the chemical kinetics of methanol oxidation on TiO_2. Combining the intuitions of the mean-field steady state (MFSS) method and the pair approximation (PA), HHPA can describe the effects of static disorder and dynamic correlation together. Furthermore, preaveraging over the static disorder in one site of each pair makes HHPA efficient enough to simulate systems of several species and calibrate rate constants. The simulated kinetics indicate that the identity of the dominant hole scavengers is temperature-dependent: the methoxy anion at 80 K and the methanol molecule at 180 K. Meanwhile, static disorder in the hole transfer steps appears to explain the stretched exponentials in the observed kinetics. In addition, two groups of Ti_{5c} sites emerge with innate and disparate activities, even though no such division exists in the underlying rate constants. Since the division appears to be quite insensitive to the type of static disorder and persist over a range of temperatures, the emergence of two groups might play a significant role in a variety of photocatalytic processes on TiO_2.

In Chapter 3, we explored the application of machine learning (ML) to construct accurate moment closures in chemical kinetics. To capture the long-range correlation at the same level of input as PA, we trained feedforward neural networks (FFNNs) to predict the instantaneous three-site probabilities using the instantaneous two-site

probabilities. The ML moment closure (MLMC) reduced the absolute and the relative errors in the three-site probabilities by an order of magnitude. Furthermore, MLMC gave drastic improvements in the simulated dynamics. The amplitude and the period in the oscillatory regime could be predicted to good accuracies, and the dynamical transitions to the nonoscillatory regime could be located to a reasonable precision. Based on these outcomes, we propose that MLMC could be used to interpolate kinetic Monte Carlo (KMC) simulations or construct pretrained closures to avoid KMC in certain systems.

There are a number of directions that require attention in the future. Concerning the chemistry of surfaces and interfaces, it should be worthwhile to identify and classify systems where static disorder and dynamic correlations have nontrivial effects on the chemical kinetics. In particular, we want to understand the nature and the origin of static disorder in these systems. Taking TiO_2 as an example, it would be of both practical and theoretical interest to determine whether the high-activity sites and the low-activity sites retain their activities when the surface is cleaned and a new layer of adsorbates is deposited. Furthermore, we need to investigate the chemical kinetics over ranges of temperatures, coverages, and defect densities to identify the mechanistic regimes that might exist.

Concerning the development of methods, we would like to demonstrate the benefits of MLMC on realistic models of specific chemical systems. Given the proposal of pretrained closures, it would be desirable to construct MLMCs that are transferrable among similar reaction mechanisms. Further development of the ML model design might be necessary, such as data transforms and neural network architectures that enforce the laws of probability. Finally, it would be interesting to incorporate the effects of static disorder into MLMC, whether in the framework of ML or in a mathematical method similar to HHPA. This would yield a method that can capture both static disorder and dynamic correlation at a fraction of the computational cost of KMC.

Part II

Computational Design of Organic Semiconductors

Chapter 5

Introduction

In Part II of this thesis, we propose design principles to enhance the efficiencies of organic light-emitting diodes (OLEDs). In this chapter, we develop the theoretical background that is required to understand the works in Part II. We begin by introducing common types of OLEDs. In particular, we are interested in thermally activated delayed fluorescence (TADF) and triplet-triplet annihilation (TTA), which are approaches to increase the efficiencies of OLEDs by converting the nonemissive triplet excitons into emissive singlet excitons. Next, we describe the theoretical tools to calculate the rates of transitions, such as fluorescence and intersystem crossing (ISC). These rates provide insight into the dynamics of excitons inside organic semiconductors and suggest ways to improve their efficiencies. Finally, we give an introduction to the Hartree-Fock (HF) method and the density functional theory (DFT), which we use to calculate the electronic structures of molecules.

5.1 Organic Light-Emitting Diodes

Organic light-emitting diodes (OLEDs) are a promising solution in digital displays and lighting applications. Since Tang and VanSlyke demonstrated the first OLED device in 1987 [156], OLEDs have attracted widespread research and development (R&D) efforts in both the academia and the industry. OLED displays exhibit supremacy in energy efficiency, image quality, response time, and compactness over conventional

technologies, such as liquid crystal displays (LCDs) [157–159]. In addition, OLEDs are expected to help reduce global energy consumption [160, 161] and yield new commercial products, such as transparent lighting panels and flexible displays [162, 163].

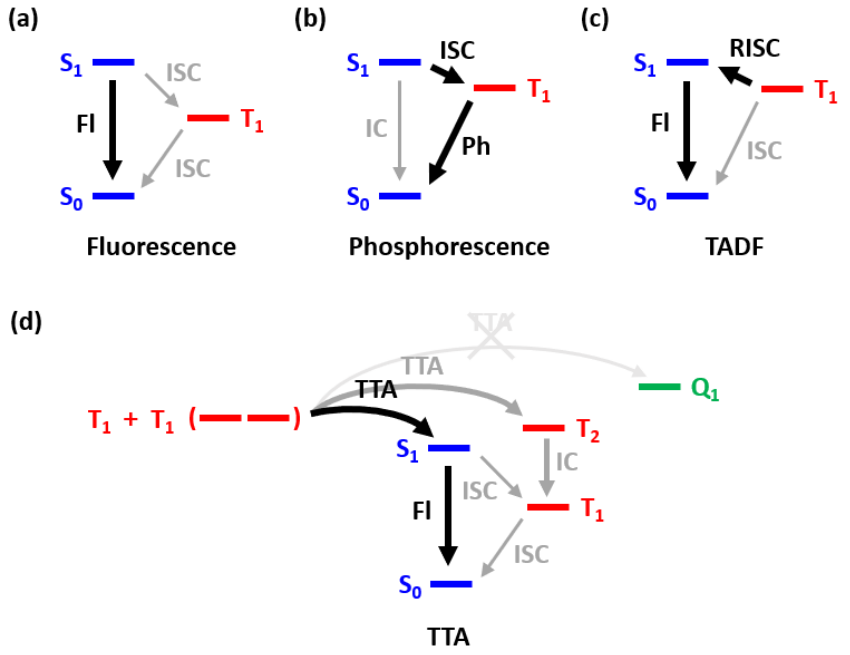

Figure 5-1: Schematics of (a) fluorescence, (b) phosphorescence, (c) TADF, and (d) TTA.

A key issue in developing more efficient OLEDs is overcoming the disadvantageous spin statistics. When electrons and holes are injected into the organic layer, they recombine in one of the four possible spin states with equal likelihoods: one singlet state and three triplet states. As shown in Figure 5-1a, the singlet excitons can emit a photon and decay to the singlet ground state, whereas the radiative decay of the triplet excitons is spin-forbidden, Most of the excitons are dissipated as heat, and the external quantum efficiency (EQE) of fluorescent OLEDs cannot exceed 25 %. In response, a number of approaches have been proposed to harvest the triplet excitons.

Baldo et al. introduced phosphorescent OLEDs (PhOLEDs), which activate the otherwise forbidden transition between the triplet excited state and the singlet ground state [164], as shown in Figure 5-1b. Using the strong spin-orbit coupling (SOC) in

heavy metal complexes, the rate of phosphorescence can be brought into the useful microsecond time scales [162, 165]. However, in spite of the commercial success of red and green PhOLEDs, an efficient and stable blue PhOLED remains out of reach [159, 166], and the rarity and the toxicity of heavy metals are also problematic.

Thermally activated delayed fluorescence (TADF) is an alternative approach that involves converting the nonemissive triplet excitons into emissive singlet excitons [167, 168]. In typical organic molecules, electron exchange stabilizes the first triplet excited state (T_1) with respect to the first singlet excited state (S_1). However, if the singlet-triplet (ST) energy gap is under a few k_BT, thermal fluctuations can drive the reverse intersystem crossing (RISC) of the T_1 population into the S_1 state, as shown in Figure 5-1c. Modulation of the exchange energy is accomplished by tuning the spatial overlap of the highest occupied molecular orbital (HOMO) and the lowest unoccupied molecular orbital (LUMO). In the first metal-free TADF OLED, Adachi et al. employed a donor-acceptor (DA) architecture to localize the HOMO and the LUMO on orthogonal moieties, creating S_1 and T_1 states of charge transfer (CT) character [169, 170]. Since then, a large number of TADF emitters have been designed on the same principle [171–175],

Unfortunately, the spatial separation of the HOMO and the LUMO not only reduces the ST gap, but also the TDM between the S_1 state and the ground state (S_0), which reduces both the prompt and the delayed fluorescence rates. In addition, according to El-Sayed's rule [176], the identical CT characters of the S_1 and the T_1 states are expected to lead to a vanishing SOC and hence a vanishing RISC rate. Therefore, the design principles of TADF OLEDs pose not only a practical problem, but also a theoretical paradox that needs to be resolved.

As yet another alternative, triplet-triplet annihilation (TTA) provides an upconversion (UC) pathway that combines two low-energy triplet excitons to produce one high-energy singlet exciton. When two triplets collide, the triplet-triplet (TT) pair attains singlet, triplet, and quintet spin multiplicities in a 1:3:5 ratio, as shown in Figure 5-1d. However, the quintet states of organic molecules are too high in energy, so the quintet TT pairs dissociate back into two triplets. Meanwhile, the higher triplet

states decay to the T_1 state. This gives $18\,T_1 \rightarrow 1\,S_1 + 3\,T_1 + 5 \times 2\,T_1$. Subtracting triplets that appear on both sides of the equation, we get that the theoretical limit on the efficiency of the TTA process is 20 % per triplet or 40 % per TT pair [177]. Interestingly, experimental studies have reported annihilators with TTA efficiencies that appear to exceed this limit, such as 9,10-diphenylanthracene (DPA) [178] and 5,6,11,12-tetraphenyltetracene (rubrene) [179].

Since the low energy of the T_1 excitons is conducive to the stability of the OLED device, TTA is a promising solution in blue OLEDs. Furthermore, TTA is a promising approach to photon upconversion, with applications in photovoltaics [180–182], photocatalysis [183–185], sensing [186, 187], bioimaging [188, 189], and controlled drug release [190]. Identifying the mechanism of enhanced TTA efficiencies in DPA and rubrene is imperative, as it could yield new design principles that impact a wide range of applications.

5.2 Transition Rates

5.2.1 Fluorescence

The rate of fluorescence can be estimated using the Einstein coefficient [191]

$$k_{\mathrm{F}} = \frac{e^2 {\omega_{10}}^2}{2\pi\varepsilon_0 m c^3} f_{10} \tag{5.1}$$

Even though its name suggests a classical origin, which is true in a historical sense, we can also derive Equation 5.1 in the framework of first-order time-dependent perturbation theory and quantization of the electromagnetic field. We provide the complete derivation in Appendix C and summarize the key steps here.

We begin with the Hamiltonian of a particle in an electromagnetic field

$$\hat{H} = \frac{1}{2m} \left(\hat{\mathbf{p}} + q\mathbf{A}(\hat{\mathbf{r}})\right)^2 + V(\hat{\mathbf{r}}) \tag{5.2}$$

where m and q are the mass and the charge of the particle, respectively; $\hat{\mathbf{p}}$ and $\hat{\mathbf{r}}$

are the momentum and the position operators, respectively; V is the (unperturbed) potential energy; and $\mathbf{A}$ is the vector potential

$$\mathbf{A}(\hat{\mathbf{r}}) = \sum_{\mathbf{k},\boldsymbol{\epsilon}} \left(\frac{\hbar}{2\varepsilon_0 \omega_{\mathbf{k}} L^3} \right)^{1/2} \left(\hat{a}_{\mathbf{k},\boldsymbol{\epsilon}} e^{+i\mathbf{k}\cdot\hat{\mathbf{r}}} \boldsymbol{\epsilon} + \hat{a}^\dagger_{\mathbf{k},\boldsymbol{\epsilon}} e^{-i\mathbf{k}\cdot\hat{\mathbf{r}}} \boldsymbol{\epsilon}^* \right) \tag{5.3}$$

where $\mathbf{k}$ and $\boldsymbol{\epsilon}$ are the wave number and the polarization vectors, respectively; $\omega_{\mathbf{k}}$ is the frequency corresponding to $\mathbf{k}$; L is the length of the cubic box enclosing the system (for normalization); and $\hat{a}_{\mathbf{k},\boldsymbol{\epsilon}}$ and $\hat{a}^\dagger_{\mathbf{k},\boldsymbol{\epsilon}}$ are the annihilation and the creation operators, respectively. We divide the full Hamiltonian into the unperturbed Hamiltonian and the first-order perturbation

$$\hat{H}^{(0)} = \frac{1}{2m} \hat{\mathbf{p}}^2 + V(\hat{\mathbf{r}}) \tag{5.4}$$

$$\hat{H}^{(1)} = \frac{q}{m} \mathbf{A}(\hat{\mathbf{r}}) \cdot \hat{\mathbf{p}} \tag{5.5}$$

To be precise, we are interested in emission, so we only need the part of the perturbation corresponding to the creation of a photon

$$\hat{H}^{(+)} = \sum_{\mathbf{k},\boldsymbol{\epsilon}} \frac{q}{m} \left(\frac{\hbar}{2\varepsilon_0 \omega_{\mathbf{k}} L^3} \right)^{1/2} \hat{a}^\dagger_{\mathbf{k},\boldsymbol{\epsilon}} e^{-i\mathbf{k}\cdot\hat{\mathbf{r}}} \boldsymbol{\epsilon}^* \cdot \hat{\mathbf{p}} \tag{5.6}$$

We calculate the transition amplitudes in the interaction picture

$$\begin{aligned} &\langle \mathrm{S}_0, n_{\mathbf{k},\boldsymbol{\epsilon}} + 1 | \psi(t) \rangle \\ &\qquad = \frac{1}{i\hbar} \int_0^t \langle \mathrm{S}_0, n_{\mathbf{k},\boldsymbol{\epsilon}} + 1 | H^{(+)}(t') | \mathrm{S}_1, n_{\mathbf{k},\boldsymbol{\epsilon}} \rangle \, dt' \\ &\qquad = -iq\omega_{10} \left(\frac{n_{\mathbf{k},\boldsymbol{\epsilon}} + 1}{2\varepsilon_0 \hbar \omega_{\mathbf{k}} L^3} \right)^{1/2} \boldsymbol{\epsilon}^* \cdot \langle \mathrm{S}_0 | \hat{\mathbf{r}} | \mathrm{S}_1 \rangle \, \frac{\sin((\omega_{\mathbf{k}} - \omega_{10})t/2)}{(\omega_{\mathbf{k}} - \omega_{10})/2} \, e^{i(\omega_{\mathbf{k}} - \omega_{10})t/2} \end{aligned} \tag{5.7}$$

where $\omega_{10} = (E_{\mathrm{S}_1} - E_{\mathrm{S}_0})/\hbar$; and $\langle \mathrm{S}_0 | \hat{\mathbf{r}} | \mathrm{S}_1 \rangle$ is the transition dipole moment (TDM). Since we are interested in spontaneous emission, we assume $n_{\mathbf{k},\boldsymbol{\epsilon}} = 0$. Then, we obtain the total $\mathrm{S}_1 \to \mathrm{S}_0$ transition probability by summing over the wave number and the

polarization vectors

$$
\begin{aligned}
|\langle \mathrm{S}_0|\psi(t)\rangle|^2 &= \sum_{\mathbf{k},\boldsymbol{\epsilon}} |\langle \mathrm{S}_0, n_{\mathbf{k},\boldsymbol{\epsilon}}+1|\psi(t)\rangle|^2 \\
&= \frac{q^2}{2\varepsilon_0 \hbar L^3} \sum_{\mathbf{k}} \frac{{\omega_{10}}^2}{\omega_{\mathbf{k}}} \left(\frac{\sin((\omega_{\mathbf{k}}-\omega_{10})t/2)}{(\omega_{\mathbf{k}}-\omega_{10})/2} \right)^2 \sum_{\boldsymbol{\epsilon}} |\boldsymbol{\epsilon}^* \cdot \langle \mathrm{S}_0|\hat{\mathbf{r}}|\mathrm{S}_1\rangle|^2 \\
&= \frac{q^2 {\omega_{10}}^3}{3\pi\varepsilon_0 \hbar c^3} |\langle \mathrm{S}_0|\hat{\mathbf{r}}|\mathrm{S}_1\rangle|^2 t
\end{aligned} \tag{5.8}
$$

where c is the speed of light. We rewrite this expression as

$$
|\langle \mathrm{S}_0|\psi(t)\rangle|^2 = \frac{q^2 {\omega_{10}}^2}{2\pi\varepsilon_0 m c^3} f_{10} t \tag{5.9}
$$

using the definition of the oscillator strength

$$
f_{10} = \frac{2m\omega_{10}}{3\hbar} |\langle \mathrm{S}_0|\hat{\mathbf{r}}|\mathrm{S}_1\rangle|^2 \tag{5.10}
$$

As desired, the rate of emission is the same as the Einstein coefficient.

5.2.2 Intersystem Crossing

The rate of intersystem crossing (ISC) can be estimated using Fermi's golden rule

$$
k_{R\to P} = \frac{2\pi}{\hbar} |\langle P|\hat{H}_{\mathrm{SO}}|R\rangle|^2 \rho_{R\to P} \tag{5.11}
$$

where R and P are the initial (reactant) and the final (product) states, respectively; $\langle P|\hat{H}_{\mathrm{SO}}|R\rangle$ is the spin-orbit coupling (SOC); and $\rho_{R\to P}$ is the Franck-Condon weighted density of states (FCWD). One of the simplest ways to estimate the FCWD is Marcus theory [192, 193]

$$
\rho_{R\to P} = \frac{1}{(4\pi\lambda_{\mathrm{M}} k_{\mathrm{B}} T)^{1/2}} \exp\left[-\frac{(\Delta E_{P-R} + \lambda_{\mathrm{M}})^2}{4\lambda_{\mathrm{M}} k_{\mathrm{B}} T} \right] \tag{5.12}
$$

The reorganization energy is defined as

$$\lambda_{\mathrm{M}} = E_P(\mathbf{q}_R) - E_P(\mathbf{q}_P) \tag{5.13}$$

where $E_P(\mathbf{q}_R)$ and $E_P(\mathbf{q}_P)$ are the energies of the final state at the initial and the final state minima, respectively.

A potent contribution that is missing in Marcus theory is the role of high-frequency, quantum-mechanical vibrational modes. While tunneling is negligible in many systems, it might be the dominant contribution when the crossing point of the initial and the final states is high enough in energy to prevent a classical passage. The simplest way to capture the effects of high-frequency vibrational modes is Marcus-Levich-Jortner (MLJ) theory [194]

$$\rho_{R\to P} = \frac{1}{(4\pi\lambda_{\mathrm{M}} k_{\mathrm{B}} T)^{1/2}} \sum_n \frac{S^n}{n!} e^{-S} \exp\left[-\frac{(\Delta E_{P-R} + \lambda_{\mathrm{M}} + n\hbar\omega)^2}{4\lambda_{\mathrm{M}} k_{\mathrm{B}} T}\right] \tag{5.14}$$

where S is the effective Huang-Rhys factor and ω is the effective frequency. These are obtained by mode-averaging

$$S = \sum_v S_v \tag{5.15}$$

$$\omega = \frac{1}{S} \sum_v S_v \omega_v \tag{5.16}$$

For each vibrational mode v, the Huang-Rhys factor is defined as

$$S_v = \frac{k_v (q_{R,v} - q_{P,v})^2}{2\hbar\omega_v} \tag{5.17}$$

where k_v is the spring constant of the mode; and $q_{R,v}$ and $q_{P,v}$ are the coordinates of the initial and the final state minima along the mode, respectively. For simplicity, we assume that the vibrational modes of the excited states are the same as the ground state. Later on, we explain why it might not be meaingful to go beyond this assumption. Using the harmonic approximation, we can rewrite $q_{P,v} - q_{R,v}$ in terms

of the gradients

$$\frac{dE_R}{dq_v} = \frac{dE_R}{dq_v}(q_v = q_{0,v}) + k_v(q_v - q_{0,v}) \tag{5.18}$$

$$\frac{dE_P}{dq_v} = \frac{dE_P}{dq_v}(q_v = q_{0,v}) + k_v(q_v - q_{0,v}) \tag{5.19}$$

where $q_{0,v}$ is some reference coordinate, which we choose to be the ground state minimum. The Huang-Rhys factors become

$$S_v = \frac{1}{2k_v\hbar\omega_v}\left(\frac{dE_P}{dq_v}(q_v = q_{0,v}) - \frac{dE_R}{dq_v}(q_v = q_{0,v})\right)^2 \tag{5.20}$$

In this manner, the rate in MLJ theory can be calculated with only a ground state vibrational mode analysis on top of the requirements in Marcus theory.

Marcus and MLJ theories were formulated to describe the rates of CT reactions [192–194]. Originally, Marcus theory was derived under the assumption that the donor and the acceptor do not undergo structural changes, such as the Fe^{2+}/Fe^{3+} redox reaction. Later, it was extended to describe the inner sphere reorganization of the donor and the acceptor in addition to the outer sphere reorganization of the solvent. Remarkably, Marcus and MLJ theories have been applied with some success to describe nonradiative electronic transitions of a molecule [195–198]. In Marcus theory, the potential energy surfaces (PESs) of the initial and the final states are approximated as identical harmonic oscillators whose minima are displaced by distance $q_P - q_R$ and energy gap ΔE_{P-R}. Then, the crossing point of the initial and the final state PESs is given by

$$\Delta E^{\ddagger}_{R\to P} = \frac{(\Delta E_{P-R} + \lambda_{\mathrm{M}})^2}{4\lambda_{\mathrm{M}}} \tag{5.21}$$

Substituting Equations 5.12 and 5.21 into Equation 5.11, we verify that the rate expression takes the familiar Arrhenius form

$$k_{R\to P} = A\exp\left(-\frac{\Delta E^{\ddagger}_{R\to P}}{k_{\mathrm{B}}T}\right) \tag{5.22}$$

For our purposes, Equation 5.21 embodies the most useful aspect of Marcus theory.

Finding the minimum energy crossing points (MECPs) of electronic states is difficult. It is much easier to optimize the geometries of the initial and the final states to obtain ΔE_{P-R} and λ_{M}.

There are a number of caveats in applying Marcus and MLJ theories to describe electronic transitions. Marcus theory approximates the initial and the final state PESs as identical harmonic oscillators. In general, PESs of molecules are not harmonic, and the vibrational modes of the various electronic states are not going to be the same. Moreover, Marcus and MLJ theories rely on the Condon approximation, which assumes that the electronic couplings are independent of the nuclear coordinates. As a result, the accuracies of Marcus and MLJ theories are going to depend on the system [198], and the absolute values of the transition rates should be take with a grain of salt. Nonetheless, Marcus and MLJ theories are useful to the extent that they provide a qualitative insight into the photophysics of molecules.

5.3 Electronic Structure

5.3.1 Wave Function Methods

The starting point of electronic structure theory is the time-independent Schrödinger equation

$$\hat{H}\Psi = E\Psi \tag{5.23}$$

where Ψ is the wave function, E is the total energy, and $\hat{H}$ is the Hamiltonian

$$\begin{aligned}\hat{H} = &-\sum_I \frac{\hbar^2}{2M_I}{\nabla_I}^2 - \sum_i \frac{\hbar^2}{2m}{\nabla_i}^2 \\ &+ \sum_{I<J} \frac{Z_I Z_J e^2}{4\pi\varepsilon_0 |\mathbf{R}_I - \mathbf{R}_J|} - \sum_{Ii} \frac{Z_I e^2}{4\pi\varepsilon_0 |\mathbf{R}_I - \mathbf{r}_i|} + \sum_{i<j} \frac{e^2}{4\pi\varepsilon_0 |\mathbf{r}_i - \mathbf{r}_j|}\end{aligned} \tag{5.24}$$

where i and j run over the electrons; and I and J run over the nuclei. In the order of their appearance, the terms in the Hamiltonain represent the kinetic energy of the nuclei, the kinetic energy of the electrons, the nucleus-nucleus repulsion, the nucleus-electron attraction, and the electron-electron repulsion.

Since the nuclei are much heavier and slower than the electrons, it is common to make the Born-Oppenheimer approximation [199], which assumes that the motions of the nuclei and the electrons are separable. Then, we can fix the nuclear coordinates, and the problem reduces to solving the electronic Hamiltonian

$$\hat{H}_{\text{el}} = -\sum_i \frac{\hbar^2}{2m}{\nabla_i}^2 - \sum_{Ii} \frac{Z_I e^2}{4\pi\varepsilon_0|\mathbf{R}_I - \mathbf{r}_i|} + \sum_{i<j} \frac{e^2}{4\pi\varepsilon_0|\mathbf{r}_i - \mathbf{r}_j|} \tag{5.25}$$

where the nuclear coordinates enter as parameters. Assuming that the wave function is normalized, the electronic energy can be found by

$$E_{\text{el}} = \int \Psi^\dagger(\mathbf{r}^n)\hat{H}_{\text{el}}\Psi(\mathbf{r}^n)d\mathbf{r}^n \tag{5.26}$$

and the total energy is given by

$$E_{\text{total}} = E_{\text{el}} + \sum_{I<J} \frac{Z_I Z_J e^2}{4\pi\varepsilon_0|\mathbf{R}_I - \mathbf{R}_J|} \tag{5.27}$$

From the perspective of nuclear motion, this "total" energy is the potential energy as a function of the nuclear coordinates, which is the starting point of ab initio molecular dynamics (AIMD) [200].

In principle, the n-electron wave function that solves the electronic Hamiltonian (Equation 5.25) is a generic function of the $3n$ electronic coordinates. In practice, this is too complicated to solve, so we try to approximate the n-electron wave function Ψ with a simpler function Φ. Requiring that Φ is normalized, we can optimize the parameters of Φ in accordance with the variational principle

$$\int \Phi^\dagger(\mathbf{r}^n)\hat{H}_{\text{el}}\Phi(\mathbf{r}^n)d\mathbf{r}^n \geq E_0 \tag{5.28}$$

where E_0 is the exact ground state energy.

The simplest approximation is the Hartree-Fock (HF) method. In essence, we want to assume that the n-electron wave function is separable. However, we need to take into account the Fermionic nature of electrons. The wave function is antisymmetric

with respect to the interchange of two electrons

$$\Psi(\mathbf{r}_1, ..., \mathbf{r}_i, ..., \mathbf{r}_j, ..., \mathbf{r}_n) = -\Psi(\mathbf{r}_1, ..., \mathbf{r}_j, ..., \mathbf{r}_i, ..., \mathbf{r}_n) \tag{5.29}$$

Hence, the n-electron wave function is approximated by a Slater determinant [201]

$$\Phi(\mathbf{r}^n) = \frac{1}{\sqrt{n!}} \begin{vmatrix} \phi_1(\mathbf{r}_1) & \phi_1(\mathbf{r}_2) & \cdots & \phi_1(\mathbf{r}_n) \\ \phi_2(\mathbf{r}_1) & \phi_2(\mathbf{r}_2) & \cdots & \phi_2(\mathbf{r}_n) \\ \vdots & \vdots & \ddots & \vdots \\ \phi_n(\mathbf{r}_1) & \phi_n(\mathbf{r}_2) & \cdots & \phi_n(\mathbf{r}_n) \end{vmatrix} \tag{5.30}$$

where ϕ_i are spin orbitals (molecular orbitals with spin). Physically, this amounts to the assumption that the n electrons reside in n spin orbitals. Inserting Equation 5.30 into Equation 5.28 and minimizing with respect to ϕ_i gives the HF equations

$$f(\mathrm{r}_1)\phi_i(\mathbf{r}_1) = \epsilon_i \phi_i(\mathbf{r}_1) \tag{5.31}$$

where $f(\mathrm{r}_1)$ is the Fock operator

$$f(\mathrm{r}_1) = h(\mathrm{r}_1) + \sum_j J_j(\mathbf{r}_1) - \sum_j K_j(\mathbf{r}_1) \tag{5.32}$$

where we have defined the one-electron Hamiltonian h, the Coulomb operator J_j, and the exchange operator K_j as

$$h(\mathrm{r}_1) = -\frac{\hbar^2}{2m}{\nabla_1}^2 + \sum_I \frac{Z_I e^2}{4\pi\varepsilon_0 |\mathbf{R}_I - \mathbf{r}_1|} \tag{5.33}$$

$$J_j(\mathbf{r}_1) = \int |\phi_j(\mathbf{r}_2)|^2 \frac{e^2}{4\pi\varepsilon_0 |\mathbf{r}_1 - \mathbf{r}_2|} d\mathbf{r}_2 \tag{5.34}$$

$$K_j(\mathbf{r}_1)\phi_i(\mathbf{r_1}) = \left[\int \phi_j^*(\mathbf{r_2}) \phi_i(\mathbf{r_2}) \frac{e^2}{4\pi\varepsilon_0 |\mathbf{r}_1 - \mathbf{r}_2|} d\mathbf{r}_2 \right] \phi_j(\mathbf{r_1}) \tag{5.35}$$

Instead of explicit electron-electron repulsion, each electron only feels the average field of the other electrons. This is why HF is called the mean-field method or the method of noninteracting electrons.

Again, it is convenient to approximate the spin orbitals with a simpler function. We introduce a set of basis functions such that

$$\phi_i = \sum_{\mu} C_{\mu i} \chi_{\mu} \tag{5.36}$$

A sensible choice of basis functions might be ones that resemble atomic orbitals. Due to the ease of analytical integration, it is common to approximate the exponential form of the atomic orbitals with a linear combination of gaussians [202]. Using this change of bases, we arrive at the Hartree-Fock-Roothan equations

$$\mathbf{FC} = \mathbf{SC}\boldsymbol{\epsilon} \tag{5.37}$$

where we have defined the Fock matrix $\mathbf{F}$ and the overlap matrix $\mathbf{S}$ as

$$F_{\mu\nu} = \langle \chi_{\mu} | f | \chi_{\nu} \rangle = \int \chi_{\mu}^{*}(\mathbf{r}_1) f(\mathrm{r}_1) \chi_{\nu}(\mathbf{r}_1) d\mathbf{r}_1 \tag{5.38}$$

$$S_{\mu\nu} = \langle \chi_{\mu} | \chi_{\nu} \rangle = \int \chi_{\mu}^{*}(\mathbf{r}_1) \chi_{\nu}(\mathbf{r}_1) d\mathbf{r}_1 \tag{5.39}$$

The problem of solving Equation 5.31 has been reduced to a generalized eigenvalue problem. However, the evaluation of the Fock matrix $\mathbf{F}$ depends on the coefficients $\mathbf{C}$, so Equation 5.37 must be solved in an iterative manner. This is why HF is called a self-consistent field (SCF) method.

It turns out that HF is poorish at predicting wave functions and energies. On the one hand, the wave functions of some systems, such as transition metal compounds and conical intersections, are not well described by a single Slater determinant. Fortunately, this strong electron correlation is not important in most organic molecules at their equilibrium geometries. On the other hand, the absence of explicit electron-electron repulsion implies that HF cannot capture the tendencies of electrons to avoid each other and reduce their energies. This weak electron correlation is present in all many-electron systems.

One approach to capture electron correlation involves writing the wave function as a linear combination of Slater determinants that correspond to different electronic

configurations. Then, the coefficients of the configurations are minimized in accordance with the variational principle (Equation 5.28). Since the HF determinant often represents the ground state electronic configuration, it is common to write the other determinants as excitations

$$\Phi = c_0\Phi_0 + \sum_{ia} c_i^a \Phi_i^a + \sum_{ijab} c_{ij}^{ab} \Phi_{ij}^{ab} + \cdots \tag{5.40}$$

where Φ_0, Φ_i^a, and Φ_{ij}^{ab} are the HF, singly excited, and doubly excited determinants, respectively. This approach is called configuration interaction (CI). As written, Equation 5.40 corresponds to the full CI (FCI). Due to the combinatorial number of terms, FCI is intractable in all but the smallest systems.

There are a couple of ways to reduce the number of terms. One approach restricts the excitations to a few frontier orbitals: the highest occupied orbitals and the lowest unoccupied orbitals. This method is the complete active space (CAS)-CI. While CAS-CI can be used to capture strong electron correlation, it is ineffective at capturing weak electron correlation. Another approach truncates the excitations at some multiplicity. For example, restricting to singly and doubly excited determinants gives the CI singles and doubles (CISD). These truncated CI methods are effective at capturing weak electron correlation. Unfortunately, CISD is still quite expensive, and it is impractical in applications that involve large system sizes or large numbers of electronic structure calculations.

5.3.2 Density Functional Theory

The theoretical foundation of the density functional theory (DFT) is the Hohenberg-Kohn theorems [203]:

1. The external potential is a unique functional of the electron density. Since the external potential determines the Hamiltonian, the many-electron ground state is a unique functional of the electron density.

2. The energy functional has a minimum at the ground state density associated

with the external potential.

In essence, there exists a universal functional of the electron density that can give the many-electron ground state of any molecule or material. Whereas the n-electron wave function is a function of the $3n$ electronic coordinates, the electron density is always a function of the 3 spatial coordinates. Hence, one might expect that employing the electron density reduces the computational complexity. Unfortunately, the form of this functional is unknown, nor is it obvious whether it has a closed form in the first place. Nonetheless, people have tried to write down various approximations.

One of the challenges in constructing an accurate functional is the kinetic energy. Today, practical implementations employ the Kohn-Sham density functional theory (KS-DFT), which considers a fictitious system of noninteracting electrons that has the same density as the actual system. The wave function is written as a single Slater determinant (Equation 5.30). Then, the electron density is given by

$$\rho(\mathbf{r}) = \sum_i |\phi_i(\mathbf{r})|^2 \tag{5.41}$$

The energy functional can be written as

$$E[\rho] = T_s[\phi^n] - V_{\mathrm{ne}}[\rho] + J[\rho] + E_{\mathrm{xc}}[\rho] \tag{5.42}$$

where we have defined the kinetic energy of the noninteracting system T_s, the nucleus-electron attraction V_{ne}, the Coulomb repulsion J, and the exchange-correlation (XC) energy E_{xc} as

$$T_{\mathrm{s}}[\phi^n] = -\sum_i \int \phi_i^*(\mathbf{r}) \frac{\hbar^2}{2m} \nabla^2 \phi_i(\mathbf{r}) d\mathbf{r} \tag{5.43}$$

$$V_{\mathrm{ne}}[\rho] = \sum_I \int \frac{Z_I e^2}{4\pi\varepsilon_0 |\mathbf{R}_I - \mathbf{r}|} \rho(\mathbf{r}) d\mathbf{r} \tag{5.44}$$

$$J[\rho] = \frac{1}{2} \iint \frac{e^2}{4\pi\varepsilon_0 |\mathbf{r}_1 - \mathbf{r}_2|} \rho(\mathbf{r}_1)\rho(\mathbf{r}_2) d\mathbf{r}_1 d\mathbf{r}_2 \tag{5.45}$$

$$E_{\mathrm{xc}}[\rho] = T[\rho] - T_s[\phi^n] + V_{\mathrm{ee}}[\rho] - J[\rho] \tag{5.46}$$

In short, we have gathered the error inside the XC energy. Although it might seem that we have only postponed the problem, the term that we need to approximate is much smaller now, since T_s and J capture most of the kinetic energy and the electron-electron repulsion, respectively.

Minimizing Equation 5.42 with respect to the orbitals ϕ_i gives the Kohn-Sham equation

$$\left[-\frac{\hbar^2}{2m}\nabla^2 + v_{\mathrm{s}}(\mathbf{r})\right]\phi_i(\mathbf{r}) = \epsilon_i\phi_i(\mathbf{r}) \tag{5.47}$$

where v_{s} is the effective potential

$$v_{\mathrm{s}}(\mathbf{r}) = \sum_I \frac{Z_I e^2}{4\pi\varepsilon_0|\mathbf{R}_I - \mathbf{r}|} + \int \frac{e^2}{4\pi\varepsilon_0|\mathbf{r} - \mathbf{r}'|}\rho(\mathbf{r}')d\mathbf{r}' + \frac{\delta E_{\mathrm{xc}}}{\delta\rho} \tag{5.48}$$

Equation 5.47 can be solved using a self-consistent field method similar to HF. Hence, KS-DFT can recover electron correlation at the computational costs of a mean-field method, provided that we have a good approximation of the XC functional (the last term in Equation 5.48). As a result, the design of XC functionals has attracted widespread research and development (R&D) efforts, and a myriad of functionals have been proposed [204, 205].

A useful extension of DFT is time-dependent density functional theory (TDDFT), which enables the calculation of excited states. The theoretical foundation of TDDFT is the Runge-Gross theorems [206], which are the time-dependent analogues of the Hohenberg-Kohn theorems [203]. In principle, the excited states are obtained by considering the response of the wave function to an electric field. In practice, this is transformed into an eigenvalue problem [207, 208]

$$\begin{bmatrix} \mathbf{A} & \mathbf{B} \\ \mathbf{B}^\dagger & \mathbf{A}^\dagger \end{bmatrix}\begin{bmatrix} \mathbf{X} \\ \mathbf{Y} \end{bmatrix} = \omega \begin{bmatrix} \mathbf{-1} & \mathbf{0} \\ \mathbf{0} & \mathbf{1} \end{bmatrix}\begin{bmatrix} \mathbf{X} \\ \mathbf{Y} \end{bmatrix} \tag{5.49}$$

Written in this way, the TDDFT equation has the same form as the time-dependent Hartree-Fock (TDHF). Interestingly, the CIS equation appears in an intact form inside

the TDHF equation

$$\mathbf{AX} = \omega\mathbf{X} \tag{5.50}$$

This analogy motivated the extraction of the **A** matrix in TDDFT, which gave rise to the Tamm-Dancoff approximation (TDA) [209]. Of course, the TDA results should be taken with a grain of salt, since the physical and mathematical arguments are heuristic. However, TDA is effective at avoiding imaginary roots that sometimes trouble the full TDDFT.

5.4 Structure of Part II

The remainder of Part II is organized as follows:

In Chapter 6, we introduce a simple quantum-mechanical model of thermally activated delayed fluorescence (TADF), where the Hamiltonian is written in the basis of four spin-mixed diabatic states representing pure charge transfer (CT) and local excitation (LE) states. The model predicts that it is possible to realize lowest-lying adiabatic singlet (S_1) and triplet (T_1) excited states with a small singlet-triplet (ST) gap, differing CT/LE contributions, and appreciable LE component in the S_1 state. These characteristics can explain the coexistence of rapid $T_1 \rightarrow$ S1 reverse intersystem crossing and $S_1 \rightarrow S_0$ radiative decay in some chromophores. We perform a Monte Carlo sampling of the parameter space to determine which parameters are decisive in TADF efficiency. This is followed by an ab initio exploration of the conformation space of a model donor-acceptor (DA) system.

In Chapter 7, we take the idea of conformational dependence to the next step. Given that the TADF rate of a molecule depends on its conformation, we hypothesize that there exists a conformation that maximizes the TADF rate. To test this idea, we use the time-dependent density functional theory (TDDFT) to simulate the TADF rates of several TADF emitters while shifting their geometries toward higher TADF rates in a select subspace of internal coordinates. We find that geometric changes in this subspace can increase the TADF rate up to three orders of magnitude with respect to the minimum energy conformation. Analyzing the maximum TADF conformation,

we extract a number of structural motifs that might provide a useful handle on the TADF rate of a DA system.

In Chapter 8, we work in collaboration with the group of Professor Marc A. Baldo to investigate the role of intersystem crossing (ISC) in enhancing the observed efficiencies of TTA upconverters. Experimental studies have reported molecules with triplet-triplet annihilation (TTA) efficiencies that appear to exceed the theoretical limit of 40 %. We present computational evidence that these limit-breaking TTA efficiencies might be attributed to the $T_2 \rightarrow S_1$ ISC. Furthermore, we propose strategies to enhance this ISC and provide experimental support of enhanced efficiencies.

In Chapter 9, we summarize the key results of Part II and discuss future directions.

Chapter 6

Simple Four-State Model of TADF

We introduce a simple quantum-mechanical model of thermally activated delayed fluorescence (TADF). The Hamiltonian is written in the basis of four spin-mixed diabatic states that represent pure charge transfer (CT) and local excitations (LE). The model predicts that it is possible to realize lowest-lying adiabatic singlet (S_1) and triplet (T_1) excited states with a small singlet-triplet (ST) gap, differing CT/LE contributions, and appreciable LE component in the S_1 state. These characteristics can explain the coexistence of rapid $T_1 \rightarrow S_1$ reverse intersystem crossing (RISC) and $S_1 \rightarrow S_0$ radiative decay in some chromophores. Through the sampling of the parameter space and statistical analysis of the data, we show which parameter combinations contribute the most to the TADF efficiency. We also show that conformational fluctuations of a single model donor-acceptor (DA) system sample a significant region of the parameter space and can enhance the TADF rate by almost three orders of magnitude. This study provides new guidelines for the optimization of TADF emitters by the means of electronic structure and conformational engineering.

6.1 Introduction

Thermally activated delayed fluorescence (TADF) [167, 210] is believed to be one of the most promising routes to increase the efficiency of organic light-emitting diode (OLED) devices [168–170, 211–213]. Harvesting of normally nonemissive triplet ex-

citons is achieved through design of molecular emitters that can undergo an efficient thermally activated intersystem crossing to a singlet manifold, followed by a radiative relaxation to the ground state. To date, this idea has enabled a large number of metal-free organic emitters [163, 171–175, 214–218], and the technology is becoming competitive with already commercially deployed phosphorescent OLEDs [163, 173, 175, 218–220].

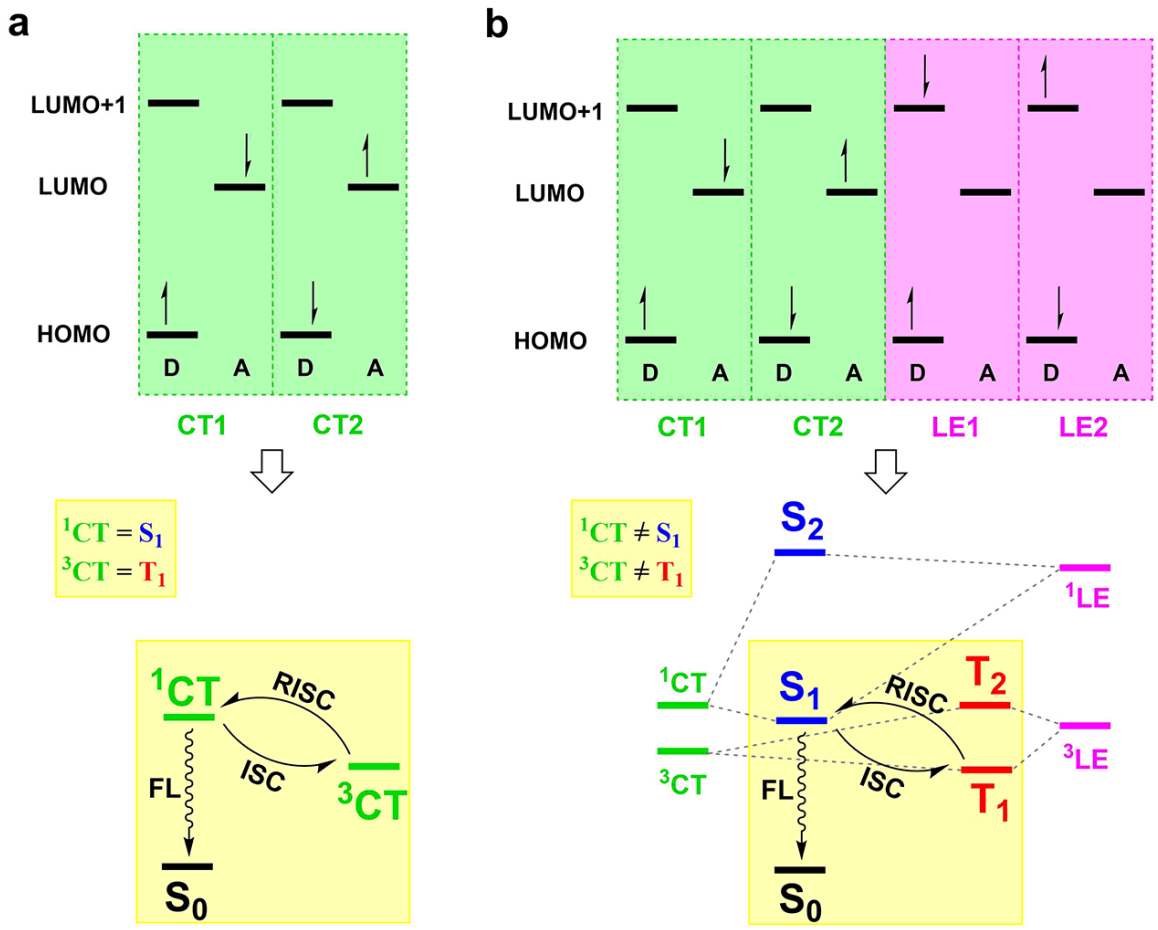

Figure 6-1: Comparison of electronic configurations and resulting energy diagrams in (a) the two-state model and (b) the four-state model.

In an OLED device, 25 % of the generated excitons end up in the first excited singlet state S_1 and 75 % in the first excited triplet state T_1. Due to electron exchange interactions, the dark T_1 state has lower energy than the bright S_1 state (Figure 6-1a). In the canonical model of TADF, the triplet exciton needs to be thermally activated to become isoenergetic with the S_1 state. Subsequently, spin-orbit coupling

(SOC) can convert it into a singlet state, from which photon emission is a spin-allowed process. This reverse intersystem crossing (RISC) mechanism is a thermally activated process, so its efficiency critically depends on the energy barrier, i.e. the singlet-triplet (ST) gap ΔE_{ST}. Additionally, the rate of transition depends on the SOC between the relevant states $\langle \mathrm{S}_1 | H_{\mathrm{SO}} | \mathrm{T}_1 \rangle$. This highlights that efficient RISC can proceed, assuming small but nonvanishing SOC, only if S_1 and T_1 are energetically close.

To date, there have been many ab initio studies of TADF emitters, initially focusing on calculations of the ST gaps [221–227]. High-throughput screening approaches have been proposed [228–230] to find new emitters with an effective trade-off between small ΔE_{ST} and fast radiative decay. Further experimental [174, 231–233] studies have shown that for many TADF molecules the lowest triplet state is not a charge transfer (CT) but a local excitation (LE), which indicated that the understanding of the TADF mechanism is incomplete and known design strategies are not optimal. Since then, a number of theoretical works have analyzed the mixed CT/LE nature of the excited states [197, 234–238], importance of vibronic effects [239–243], and influence of the interactions with the environment [244–247], including the importance of static and dynamic disorder [248, 249]. Several recent review articles summarize the computational and theoretical developments in the field [250–253].

In this chapter, we propose a new four-state model for TADF that generalizes the canonical model by including both the CT and the LE states. We examine the behavior of this model as a function of its microscopic parameters, i.e. the energy gap and electronic couplings between the states. In Section 6.2, we begin by summarizing the canonical two-state model and then introduce the four-state generalization. Next, in Section 6.3, we perform a Monte Carlo sampling of the parameter space to determine which parameters are decisive in TADF efficiency. This is followed by an ab initio exploration of the conformation space of a model donor-acceptor (DA) system. The study allows us to formulate new guidelines for the design of efficient TADF materials.

6.2 Theory

6.2.1 Two-State Model of TADF

The standard two-state model for TADF [170] can be described as an electron transfer from the HOMO localized on the donor (D) moiety to the LUMO on the acceptor (A) moiety. This picture gives rise to two isoenergetic spin-mixed charge-transfer states CT1 and CT2

$$|\mathrm{CT1}\rangle = \frac{1}{\sqrt{2}}|\phi_{\mathrm{H}}(1)\alpha(1)\phi_{\mathrm{L}}(2)\beta(2)| \tag{6.1}$$

$$|\mathrm{CT2}\rangle = -\frac{1}{\sqrt{2}}|\phi_{\mathrm{H}}(1)\beta(1)\phi_{\mathrm{L}}(2)\alpha(2)| \tag{6.2}$$

The electronic coupling between these two states is known as the exchange integral

$$\langle \mathrm{CT1}|\hat{H}|\mathrm{CT2}\rangle = (\phi_{\mathrm{H}}(D)\phi_{\mathrm{L}}(A)|\phi_{\mathrm{L}}(D)\phi_{\mathrm{H}}(A)) = K_{\mathrm{HL}} \tag{6.3}$$

and the corresponding eigenfunctions of the Hamiltonian are spin-pure states $|^1\mathrm{CT}\rangle = \frac{1}{\sqrt{2}}(|\mathrm{CT1}\rangle + |\mathrm{CT2}\rangle)$ and $|^3\mathrm{CT}\rangle = \frac{1}{\sqrt{2}}(|\mathrm{CT1}\rangle - |\mathrm{CT2}\rangle)$. The energies of these states can be written as

$$E_{\mathrm{S}_1} = h_{\mathrm{H}} + h_{\mathrm{L}} + J_{\mathrm{HL}} + K_{\mathrm{HL}} \tag{6.4}$$

$$E_{\mathrm{T}_1} = h_{\mathrm{H}} + h_{\mathrm{L}} + J_{\mathrm{HL}} - K_{\mathrm{HL}} \tag{6.5}$$

where h_{H} and h_{L} are the HOMO and the LUMO integrals, respectively; and J_{HL} is the Coulomb two-electron integral $(\phi_{\mathrm{H}}(D)\phi_{\mathrm{H}}(D)|\phi_{\mathrm{L}}(A)\phi_{\mathrm{L}}(A))$. From Equations 6.4 and 6.5 results that the ST gap is simply twice the exchange integral

$$\Delta E_{\mathrm{ST}} = 2K_{\mathrm{HL}} \tag{6.6}$$

which immediately suggests that minimizing the exchange integral by spatial separation of the HOMO and the LUMO is a reasonable design strategy for TADF emitters.

This design principle has been realized in many TADF emitters which are based

on the DA architecture [163, 218]. The large dihedral angle between the donor and the acceptor units causes spatial localization of the HOMO and the LUMO and consequently small exchange integral K_{HL}. Despite these early successes, it has been realized that the two-state model has several deficiencies. First, a pure ^{1}CT state would have a very small oscillator strength, so efficient luminescence following efficient RISC would not be possible. This is because there is a single variable (HOMO-LUMO overlap) that governs both the oscillator strength and the ST gap. Efficient TADF requires both large oscillator strength (large HOMO-LUMO overlap) and a small singlet triplet gap (small HOMO-LUMO overlap). There is thus an inescapable trade-off – one cannot have high oscillator strength and small gaps at the same time – and so TADF rates are fundamentally limited to a theoretical maximum of $\approx 1\,\mu\mathrm{s}^{-1}$. The second deficiency of the two-state model is that ISC between two states of the same electronic character is very inefficient as the spin flip needs to be offset by a change of the orbital angular momentum so that the total angular momentum is conserved [176, 254]. This means that the SOC between two pure CT states vanishes $\langle {}^1\mathrm{CT}|\hat{H}_{\mathrm{SO}}|{}^3CT\rangle = 0$ and the intersystem crossing is impossible irrespective of how small the energy gap is. Finally, it has been noticed that TADF efficiency does not always correlate with the small ST gap [214]. Relatively high efficiencies have been observed for emitters with large apparent gaps. Also, donor-acceptor-donor (DAD) architectures have been shown to be more efficient compared to DA systems despite having similar ST gaps [171, 213, 255]. Recently, several new approaches to the design of TADF emitters [173, 256, 257] and increasing the efficiency of the devices [219, 258, 259] have been proposed.

6.2.2 Four-State Model of TADF

In the two-state model, efficient TADF is limited because of the trade-off between small ST gaps and large oscillator strengths due to the CT character of the states involved. On the other hand, there is experimental evidence that a local triplet (^{3}LE) state that is energetically close to both CT states plays a role in RISC [174, 231–233]. In particular, it has been suggested that vibronic nonadiabatic effects are responsible

for the interaction between CT and LE states and efficient RISC [239–241, 243, 254, 260–262]. Here we propose a model that generalizes the two-state model to include also LE states. This model bypasses the need for nonadiabatic effects to explain efficient TADF; however, it does not preclude this mechanism to be operational in some cases.

As the starting point, we assume that the active space is composed of three orbitals. To focus the discussion, we assume that the HOMO and the LUMO + 1 are localized on the donor, and the LUMO is localized on the acceptor (2 electrons in 3 orbitals); however, the model works for any three orbitals that can describe one-electron CT and LE (e.g. the HOMO on donor; the HOMO − 1 and the LUMO on acceptor – 4 electrons in 3 orbitals). Consideration of all possible single excitations within the active space gives four electron configurations illustrated in the top panel of Figure 6-1b. These configurations correspond to the conceptual picture of excitations as the electron transfer between spatially localized molecular orbitals.

Note that these states are diabatic states with a well-defined electronic character, so they can be classified as charge-transfer (CT1 and CT2) or local (LE1 and LE2) excitations, and that they are not eigenfunctions of the spin operator. For these reasons, the Hamiltonian in the $(|\mathrm{CT1}\rangle, |\mathrm{CT2}\rangle, |\mathrm{LE1}\rangle, |\mathrm{LE2}\rangle)$ basis is not diagonal and, to a good approximation (discussed in Appendix D.1), takes the following form

$$\hat{H} = \begin{pmatrix} 0 & K_{\mathrm{CT}} & t & K_{\mathrm{X}} \\ K_{\mathrm{CT}} & 0 & K_{\mathrm{X}} & t \\ t & K_{\mathrm{X}} & \Delta E & K_{\mathrm{LE}} \\ K_{\mathrm{X}} & t & K_{\mathrm{LE}} & \Delta E \end{pmatrix} \tag{6.7}$$

The parameters of the Hamiltonian are ΔE, the energy gap between CT and LE states, where the energy of the CT states is arbitrarily set to 0; the exchange integrals

$$K_{\mathrm{CT}} = \langle \mathrm{CT1}|\hat{H}|\mathrm{CT2}\rangle = (\phi_{\mathrm{H}}(D)\phi_{\mathrm{L}}(A)|\phi_{\mathrm{L}}(A)\phi_{\mathrm{H}}(D)) \tag{6.8}$$

$$K_{\mathrm{LE}} = \langle \mathrm{LE1}|\hat{H}|\mathrm{LE2}\rangle = (\phi_{\mathrm{H}}(D)\phi_{\mathrm{L+1}}(D)|\phi_{\mathrm{L+1}}(D)\phi_{\mathrm{H}}(D)) \tag{6.9}$$

are a sum of a one-electron hopping integral and a two-electron integral

$$\begin{aligned} t = & \langle \mathrm{CT1}|\hat{H}|\mathrm{LE1}\rangle = t' + K'_{\mathrm{X}} \\ = & \langle \phi_{\mathrm{L}}(A)|\hat{h}|\phi_{\mathrm{L+1}}(D)\rangle + (\phi_{\mathrm{H}}(D)\phi_{\mathrm{H}}(D)|\phi_{\mathrm{L}}(A)\phi_{\mathrm{L+1}}(D)) \end{aligned} \tag{6.10}$$

where $\hat{h}$ is the one-electron partof the Hamiltonian, and a two-electron integral

$$K_{\mathrm{X}} = \langle \mathrm{CT1}|\hat{H}|\mathrm{LE2}\rangle = (\phi_{\mathrm{H}}(D)\phi_{\mathrm{L+1}}(D)|\phi_{\mathrm{L}}(A)\phi_{\mathrm{H}}(D)) \tag{6.11}$$

The Hamiltonian in Equation 6.7 can be block-diagonalized in the basis of diabatic spin-pure states

$$\left|{}^1\mathrm{CT}\right\rangle = \frac{1}{\sqrt{2}}(|\mathrm{CT1}\rangle + |\mathrm{CT2}\rangle) \tag{6.12}$$

$$\left|{}^3\mathrm{CT}\right\rangle = \frac{1}{\sqrt{2}}(|\mathrm{CT1}\rangle - |\mathrm{CT2}\rangle) \tag{6.13}$$

$$\left|{}^1\mathrm{LE}\right\rangle = \frac{1}{\sqrt{2}}(|\mathrm{LE1}\rangle + |\mathrm{LE2}\rangle) \tag{6.14}$$

$$\left|{}^3\mathrm{LE}\right\rangle = \frac{1}{\sqrt{2}}(|\mathrm{LE1}\rangle - |\mathrm{LE2}\rangle) \tag{6.15}$$

which leads to two 2×2 Hamiltonians operating in the singlet and triplet subspaces

$$\hat{H}_{\mathrm{S}} = \begin{pmatrix} K_{\mathrm{CT}} & t + K_{\mathrm{X}} \\ t + K_{\mathrm{X}} & \Delta E + K_{\mathrm{LE}} \end{pmatrix} \tag{6.16}$$

$$\hat{H}_{\mathrm{T}} = \begin{pmatrix} -K_{\mathrm{CT}} & t - K_{\mathrm{X}} \\ t - K_{\mathrm{X}} & \Delta E - K_{\mathrm{LE}} \end{pmatrix} \tag{6.17}$$

Diagonalizing these Hamiltonians gives closed form expressions for the energies of the adiabatic states E_{S_1}, E_{S_2}, E_{T_1}, and E_{T_2}, as well as for the coefficients of the eigenvectors in the basis of spin-pure diabatic states (see Appendix D.2). In particular, the

expression for the ST energy gap ΔE_{ST} is the following

$$\begin{aligned}\Delta E_{\mathrm{ST}} =& K_{\mathrm{LE}} + K_{\mathrm{CT}} \\ &- \sqrt{\frac{1}{4}(\Delta E + K_{\mathrm{LE}} + K_{\mathrm{CT}})^2 - (\Delta E + K_{\mathrm{LE}})K_{\mathrm{CT}} + (t + K_{\mathrm{X}})^2} \\ &+ \sqrt{\frac{1}{4}(\Delta E - K_{\mathrm{LE}} - K_{\mathrm{CT}})^2 + (\Delta E - K_{\mathrm{LE}})K_{\mathrm{CT}} + (t - K_{\mathrm{X}})^2}\end{aligned} \tag{6.18}$$

which is significantly more complicated than simply twice the exchange integral within the two-state model. The gap ΔE_{ST} depends on all the parameters of the model, and it is clear that the design principle based on the minimization of the HOMO-LUMO spatial overlap is not the only way to obtain a small ST gap. The first square root in Equation 6.18 reduces the gap, while the second acts in the opposite direction, so the final outcome depends on the interplay between ΔE and the different coupling elements. While the exchange couplings and ΔE affect the energy separation between CT and LE diabatic states, the mixing of these diabats is determined by $|t + K_{\mathrm{X}}|$ and $|t - K_{\mathrm{X}}|$ for singlet and triplet manifolds, respectively. This means that CT and LE states of different multiplicities have different mixing strengths, which will result in dif ferent electronic characters of the respective energy states. Due to the different contributions of CT and LE states, the SOC between the S_1 and the T_1 states could be appreciable without the mediation of the T_2 state via nonadiabatic coupling. The efficiency of this direct pathway will depend on the relative signs and values of t and K_{X}, as well as values of ΔE and exchange integrals. Coupling of ^{1}CT and ^{1}LE through the $(t + K_{\mathrm{X}})$ element also means that the S_1 state is a mixture of the CT and LE diabats rather than a pure CT state, which explains how TADF molecules can have an appreciable dipole coupling to the ground state and be efficient light emitters (see Figure 6-1b).

At this point, the four-state model explains why efficient TADF is possible in organic molecules: In principle, the right electronic Hamiltonian can simultaneously yield a small ST gap ΔE_{ST} together with qualitatively different contributions of LE and CT states in the S_1 and T_1 adiabats, which enable efficient intersystem crossing,

as well as a significant LE contribution in the S_1 state, which enables high quantum yields. This clearly demonstrates that the trade-off between minimizing the HOMO-LUMO overlap for small ST gaps and maximizing it for efficient fluorescence is not a physical limitation, but merely an artifact of the oversimplified two-state model. Our result also highlights the role of both CT and LE diabatic states and demonstrates that consideration of the lowest adiabatic states of each spin multiplicity can be sufficient for efficient RISC.

While the model suggests that nonadiabatic coupling is not necessary for efficient RISC, it does not preclude its relevance. It is plausible that coherent mixing of T_1 and T_1 states enhances the RISC rate in the vicinity of conical intersections or avoided crossings, where the $T_1 - T_2$ gap is very small. Another possibility for importance of molecular vibrations is their contribution through non-Condon effects. Within the Condon approximation, all the matrix elements in Equation 6.7 are constant and independent of the molecular geometry. However, molecular vibrations can lead to large variations in instantaneous couplings, effectively modulating both RISC and fluorescence. In this case, the rates depend only on nuclear positions, but not momenta, which is also consistent with the proposed conformational dependence [216] of TADF efficiency. Nevertheless, it is important to stress that neither nonadiabatic nor non-Condon effects are *necessary* for efficient TADF from the perspective of the four-state model.

6.3 Results

6.3.1 Parameter Space Exploration

The four-state model depends on five parameters which determine the relative energetics and character of the first two excited states within singlet and triplet manifolds. We will focus on three quantities predicted by the model, which can be optimized to boost the overall TADF efficiency. First, the ST gap ΔE_{ST} (Equation 6.18) needs to be minimized to ensure a significant thermally induced population of vibrational

states of the T_1 electronic state, which are isoenergetic with the S_1 state. Second, in order to maximize the fluorescence rate, the transition dipole moment between S_1 and S_0 states needs to be as large as possible. While this quantity cannot be calculated within the four-state model without introducing the one-electron basis explicitly, we note that quantum yield correlates with the LE character of the S_1 state, which is assumed to be bright. Therefore, we consider the quantity $S_1^{\mathrm{LE}} = |\langle {}^1\mathrm{LE}|\mathrm{S}_1\rangle|^2$ as a proxy for fluorescence efficiency. Finally, appreciable SOC is a prerequisite for fast RISC even in the small ΔE_{ST} limit. The SO coupling cannot be directly calculated from the model; however, according to El-Sayed's rule it is only nonvanishing between states with substantially different electronic character. Therefore, as the proxy for efficient SO we use the unsigned difference between CT contributions in the S_1 and T_1 states: $\Delta\mathrm{CT} = \left||\langle {}^1\mathrm{CT}|\mathrm{S}_1\rangle|^2 - |\langle {}^3\mathrm{CT}|\mathrm{T}_1\rangle|^2\right|$.

The analytical expressions for ΔE_{ST}, S_1^{LE}, and $\Delta\mathrm{CT}$ can be obtained directly by diagonalizing the model Hamiltonians in Equations 6.16 and 6.17; however, their dependence on the parameters is rather complicated (compare with states' coefficients in Appendix D.2). To better understand how manipulating different parameters can lead to changes in the TADF efficiency, we performed a Monte Carlo sampling of the parameter space. To this end, we made some a priori assumptions about the relevant ranges of values (see Appendix D.3.1). We sampled random 106 points from the parameter space and calculated the corresponding ΔE_{ST}, S_1^{LE}, and $\Delta\mathrm{CT}$ values. Histograms of these quantities are presented in Figure 6-2.

The distribution of ST gaps (Figure 6-2a) resembles a bell-shaped curve, which reflects the complex dependence on several uniformly distributed parameters (see Equation 6.18). The average of ΔE_{ST} is 1.25 eV, and the standard deviation is 1.10 eV. This is in stark difference with the twostate model for which $\Delta E_{\mathrm{ST}} = 2K_{\mathrm{CT}}$. An interesting feature of the distribution is that there is a significant number of points with $\Delta E_{\mathrm{ST}} < 0$. This appears as perhaps an unphysical result, because negative ST gaps are normally not observed in practice. However, based on constrained DFT calculations, Difley et al. have found exciplex systems that exhibit negative gaps [263], which was explained by the kinetic exchange effect which stabilizes singlet

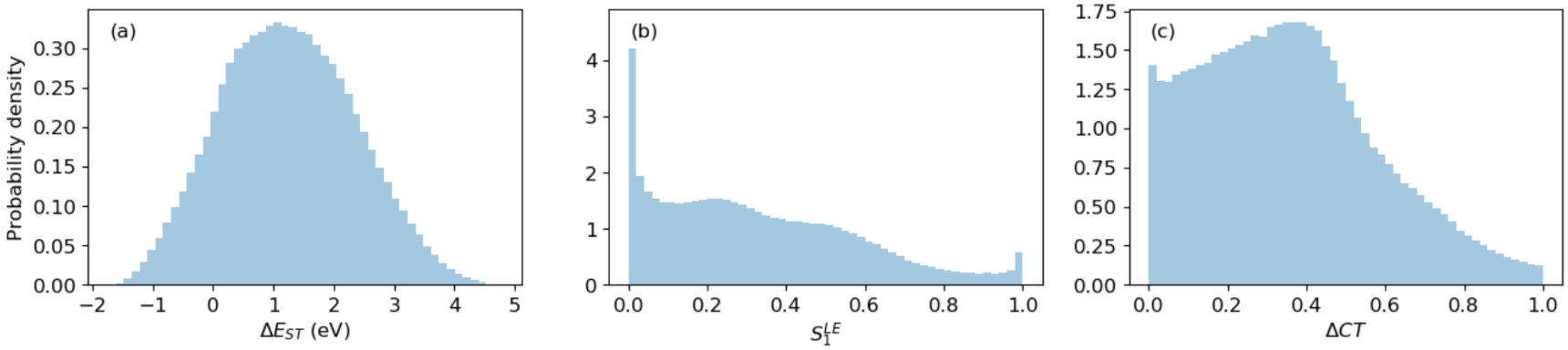

Figure 6-2: Distributions of ΔE_{ST}, $\mathrm{S}_1^{\mathrm{LE}}$, and ΔCT calculated by random sampling of the parameter space.

states. Recently Olivier et al [248]. also reported negative ΔE_{ST} resulting from stronger stabilization of the singlet state by the polarizable environment. Neither of these mechanisms is operational in our four-state model, which could mean that we are sampling the regions of the parameter space which are unphysical or exceedingly difficult to realize in real molecules. Nevertheless, this is not a problem of the model itself, and a general conclusion can still be drawn from these results. In particular, it is clear that relatively many combinations of parameters can lead to small ST gaps, which is beneficial for fast RISC in TADF molecules.

The distribution of $\mathrm{S}_1^{\mathrm{LE}}$ (Figure 6-2b) shows that the first singlet excited state is usually dominated by the CT character ($\mathrm{S}_1^{\mathrm{LE}} < 0.5$). This is the case for 75 % of the sampled parameter vectors and corresponds well with the experimental observations about TADF emitters. Nevertheless, the figure shows also that there are many parameter combinations which yield a significant component of the LE state in S_1, which should lead to appreciable fluorescence efficiency. Figure 6-2c illustrates how likely it is to find parameters that lead to S_1 and T_1 states that differ in their electronic character. The maximum of the distribution is at 0.4, and more often than not these two states are appreciably different. This is again in line with many reports on TADF emitters, where the lowest triplet state is found to have a substantial LE component. This in turn opens up a possibility for significant SOC, which would be otherwise prevented by El-Sayed's rule.

To gain more insight into which parameters control TADF efficiency, we filtered the data and retained only 17 706 out 10^6 solutions satisfying the criteria $\Delta E_{\mathrm{ST}} < 0.1\,\mathrm{eV}$, $\mathrm{S}_1^{\mathrm{LE}} > 0.25\,\mathrm{eV}$, and $\Delta\mathrm{CT} > 0.4$, which are likely to represent efficient TADF emitters (see Appendix D.3.2 for details). This filtering naturally selects parameter values that are beneficial for TADF and rejects parameter values that are harmful. The resulting distributions of parameters are shown in Figure 6-3. Figure 6-3a suggest that the small energy offset between the CT and the LE states is beneficial for TADF; however, the distribution is rather broad with a standard deviation of approximately 0.5 eV and either energetic ordering of states is possible. There is some preference for smaller values of K_{CT} (Figure 6-3b), but many solutions can be found even with

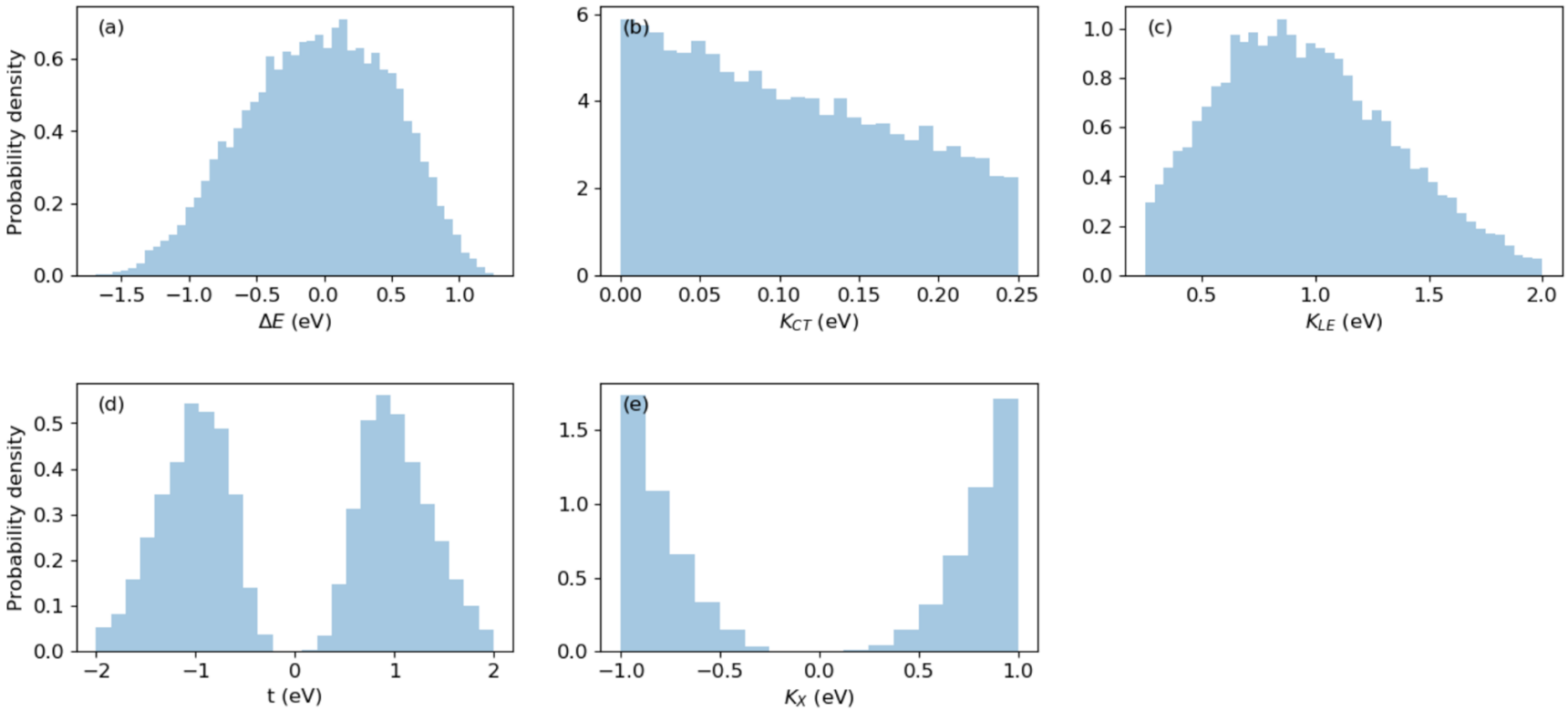

Figure 6-3: Histograms of the model Hamiltonian parameters after filtering the data.

relatively large CT exchange integrals. The distribution of LE exchange integrals (Figure 6-3c) is also broad, with the mean 1 eV and standard deviation 0.4 eV. Figure 6-3d,e shows that both t and K_{X} have to be nonvanishing. In particular, the larger the K_{X} the more likely it is for the solutions to represent efficient TADF, and the distribution of the hopping integrals t has a maximum at ± 1 eV. While all the parameters were uncorrelated in the original set, filtering is expected to introduce some correlations, and revealing them should provide guidelines for parameter combinations that yield efficient TADF activity. First, we note that while the signs of t and K_{X} were random and uncorrelated in the original set, now all these parameters are of the same sign; therefore, this condition appears as a prerequisite for efficient TADF. Note that flipping the phase of either the ϕ_{L} or the $\phi_{\mathrm{L+1}}$ orbital will change the sign of both parameters, so only nontrivial changes in the orbital shape can influence the relative sign. Based on the above observations, the most critical design parameters for fast TADF are the magnitude and relative sign of t and K_{X}. The fact that two heretofore unrecognized parameters are more important than K_{CT}, which had been previously thought to dominate TADF rates, suggests that some previous design efforts may have succeeded partly by serendipity. For example, rotation of a dihedral angle will typically change K_{CT} (which was thought to be most important) and also the magnitude and sign of t and K_{X} (which are typically even more important).

To extract more nuanced correlations, we performed a principal component analysis (PCA) of the covariance matrix. The detailed analysis is in Appendix D.3.3, but the main conclusion is that small values of $t - K_{\mathrm{X}}$ and to a lesser extent moderately negative $\Delta E - K_{\mathrm{LE}}$ are necessary for efficient TADF activity. The analysis of analytical solutions of the four-state model sheds some light on the importance of $t - K_{\mathrm{X}}$ and $\Delta E - K_{\mathrm{LE}}$. The energy of the S_1 state is stabilized by $|t + K_{\mathrm{X}}|$ while T1 is stabilized by $|t - K_{\mathrm{X}}|$, so small values of the latter parameter lead to shrinking of the ST gap, which is always beneficial for TADF efficiency. Small $|t - K_{\mathrm{X}}|$ also favors stronger LE character of the T_1 state relative to S_1 and consequently leads to larger ΔCT values. The energies of the ^{3}LE and ^{3}CT states are $\Delta E - K_{\mathrm{LE}}$ and $-K_{\mathrm{CT}}$, respectively. Therefore, for LE to be the dominant component in T_1, the condition

$\Delta E - K_{\mathrm{LE}} < -K_{\mathrm{CT}}$ must hold. At the same time, the energy gap between these states cannot be too large to allow effective mixing, which explains why moderately negative values of $\Delta E - K_{\mathrm{LE}}$ are beneficial for efficient TADF. By a similar argument, appreciable S_1^{LE} and efficient fluorescence requires that $\Delta E + K_{\mathrm{LE}}$ is not much larger than K_{CT} on the scale of the coupling element $t + K_{\mathrm{X}}$. This suggests that, contrary to the prediction of the conventional two-state model, minimization of K_{CT} is not necessarily the best strategy for maximizing TADF efficiency.

6.3.2 Conformation Space Exploration

In order to apply the design principles from the four-state model, it would be ideal to explore the parameter space of ΔE, t, K_{X}, K_{CT}, and K_{LE} in candidate TADF molecules. However, this is challenging for two reasons. First, the parametrization of the four-state Hamiltonian from ab initio calculations requires explicit construction of the diabatic states (CT1, CT2, LE1, and LE2) and accurate evaluation of the related energies and couplings. Although the latter could be achieved through methods such as constrained DFT [264–267] or ΔSCF [268, 269], how to define the relevant states in these frameworks is not straightforward. Second, optimization in the chemical space is difficult due to its discreteness. While carrying out such optimization would be part of the long-term goal that leads to new emitters, we choose at this point to explore parameter space by varying the conformation of a single DA system (i.e. the distance and relative orientation between the donor and the acceptor moieties), which has the practical benefit of being continuous.

Our model system is based on a DA exciplex with a TPA (triphenylamine) donor and a TRZ (2,4,6-triphenyl-1,3,5-triazine) acceptor, both of which are common moieties in TADF design [163, 172, 212, 229, 270]. The exciplex is known to possess intermolecular CT excited states and great conformational flexibility [175]. The lowest excited states have a dominant CT character due to the fact that LE states are high-lying excited states in a typical exciplex. Meanwhile, according to the four-state model, we want the T_1 and S_1 states of the exciplex to have a mixed CT/LE character. Therefore, we make two modifications to the TPA/TRZ exciplex. First, we

link an extra donor CZ (carbazole) to the TRZ group to form CZ-TRZ. CZ-TRZ is a well-known fluorophore and has been used as a parent compound for several high-efficiency deep-blue TADF materials [217, 220]. Using CZ-TRZ as the acceptor in the exciplex introduces low-lying excited states with LE character, while excited states with CT character are due to excitations between TRZ and TPA moieties. Second, we add chlorine groups to TPA to form TPA-Cl. This further tunes the energetics of the CT excites states so that lowest CT and LE states are close enough, which corresponds to a small ΔE parameter in the four-state model. The final structures of TPA-Cl (donor) and CZ-TRZ (acceptor) are shown in Figure 6-4.

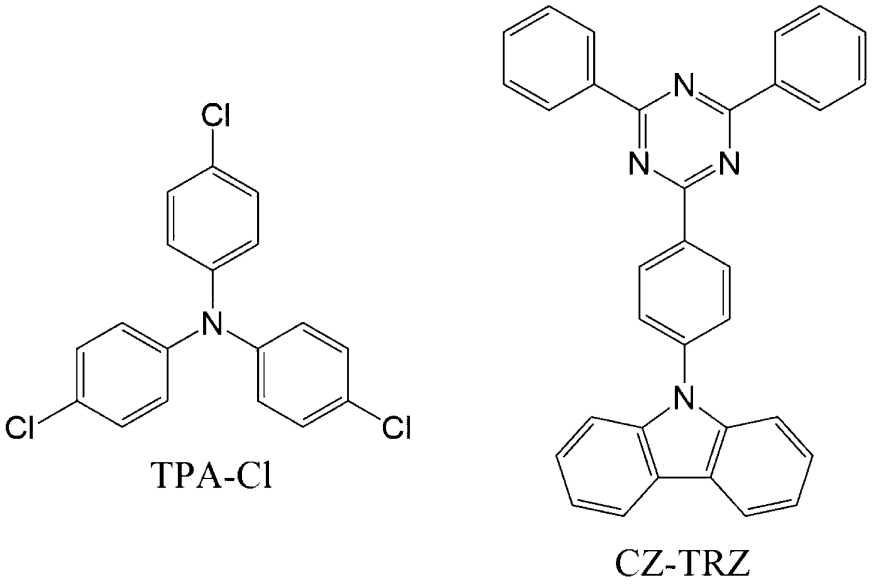

Figure 6-4: Structures of TPA-Cl (donor) and CZ-TRZ (acceptor).

Arbitrary conformations were generated as snapshots of molecular dynamics (MD) simulations, using the OPLS-aa force field [271]. In order to obtain exhaustive sampling of the conformation space, we found it necessary to modify the van der Waals parameters for the monomers. Further details can be found in Appendix D.4. As a result, the conformational space we explore is significantly different than the thermally accessible conformation space. To be clear, this is intentional: the aim of the calculations is to ascertain whether some configuration (which may or may not be thermally accessible for this donor and acceptor) could display dramatically accelerated TADF. If so, this observation would provide strong evidence that the four-state

model is actually relevant for TADF in real molecules. The excited states in the selected conformations were computed in the framework of TDDFT, using the B3LYP exchange-correlation functional [272–277] and the 6-31+G* basis set [278–280]. It is well-known [208, 281] that standard hybrid functionals, such as B3LYP, give inadequate descriptions of CT states. Although the use of optimally tuned range-separated hybrids [224, 225] has been found to be a practical solution that works well for TADF emitters, the goal was not to make quantitative predictions about individual conformers, which may or may not be possible to synthesize in the laboratory but to show that the TADF rate of a given system can undergo substantial improvements as parameters like t and K_{X} vary with conformation. Hence, it was desirable to choose a functional that could reproduce qualitative trends at a minimal computational cost.

Given the TDDFT results, the rate of prompt fluorescence was estimated using the Einstein coefficient [191]

$$k_{\mathrm{F}} = \frac{e^2 {\omega_{10}}^2}{2\pi\varepsilon_0 m c^3} f_{10} \tag{6.19}$$

where e and m are the electron charge and mass, respectively; c is the speed of light; and ω_{10} and f_{10} are the $\mathrm{S}_1 - \mathrm{S}_0$ transition frequency and oscillator strength, respectively. The TADF rate was estimated using the formula [215]

$$k_{\mathrm{TADF}} = \frac{k_{\mathrm{F}}[\mathrm{S}_1]}{[\mathrm{S}_1] + [\mathrm{T}_1]} = \frac{k_{\mathrm{F}}}{1 + K} \tag{6.20}$$

$$K \equiv \frac{[\mathrm{T}_1]}{[\mathrm{S}_1]} = 3 \exp\left(\frac{\Delta E_{\mathrm{ST}}}{k_{\mathrm{B}} T}\right) \tag{6.21}$$

where k_{B} is the Boltzmann constant and the temperature T was taken to be 298 K. The last formula assumes that the excited state populations have thermalized and that only the S_1 and the T_1 states are populated to a significant extent. Since TADF time scales are on the order of microseconds, the first assumption would hold, provided that there exists an efficient ISC pathway. Meanwhile, the second assumption should be valid in most conformations of interest. Among the conformers that exhibited the largest oscillator strengths ($> 10^{-3}$) and the smallest ΔE_{ST} (< 100 meV), the T_2 state was almost always higher in energy than the S_1 state. If the T_2 state were lower

in energy than the S_1 state, then the T_2 state should be included in the denominator, and such cases can be found in Appendix D.6. However, the correction was neglected in the main discussion, because taking the T_2 state into consideration did not alter the statistics in a meaningful way. In general, the formula provides an upper bound to the TADF rate, since RISC might not be fast enough to replenish the S_1 state.

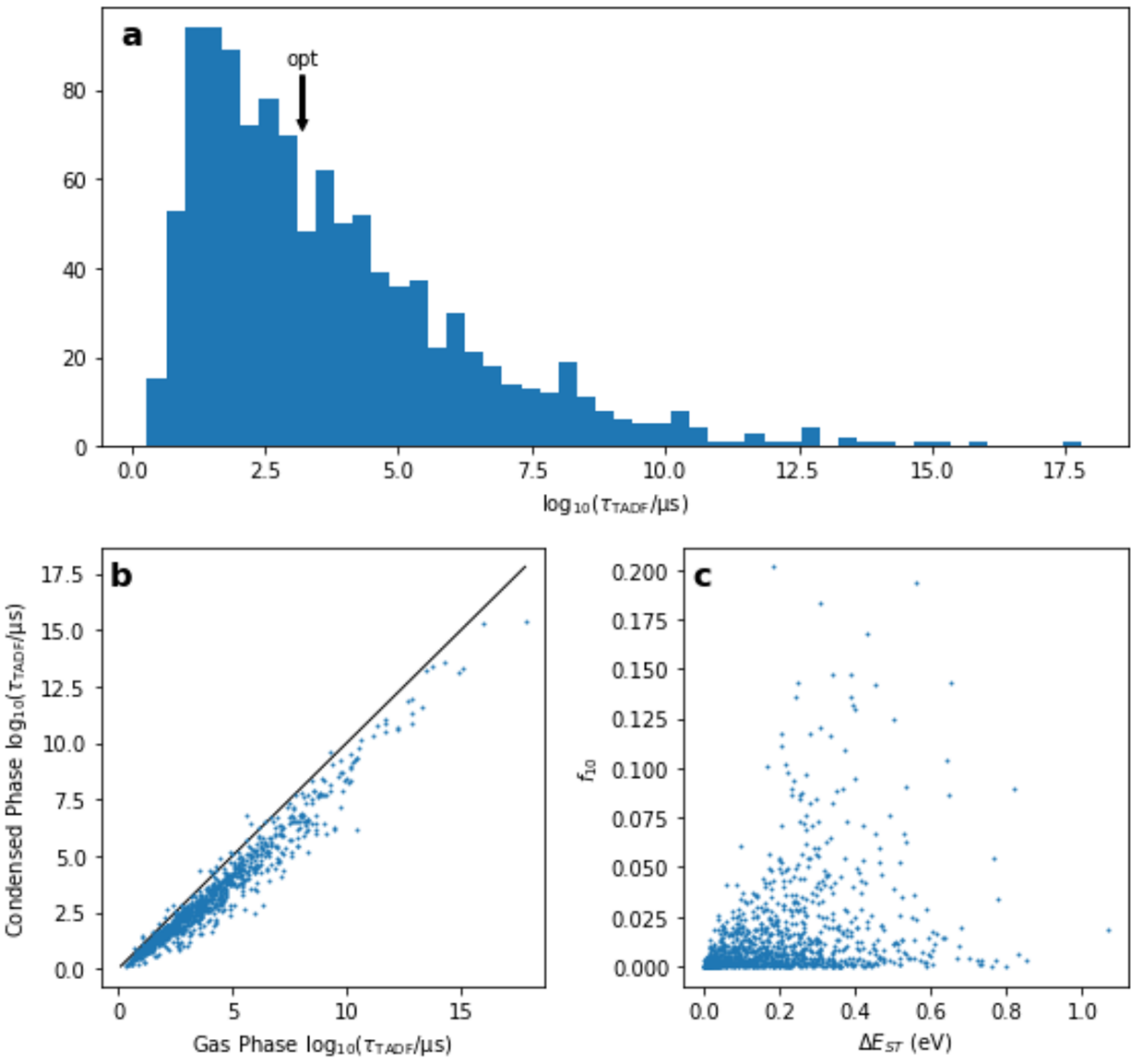

Figure 6-5: (a) Histogram of the TADF lifetimes. The TADF lifetime at the DFT optimized geometry is marked as "opt." (b) Scatter plot of the condensed phase against the gas phase TADF lifetimes. The solid black line has a unit slope ($y = x$). (c) Scatter plot of the $S_1 - S_0$ oscillator strength against ΔE_{ST}.

The results have been summarized in Figure 6-5, and the numerical output on the most relevant conformers has been provided in Appendix D.6. Figure 6-5a is a

histogram of the TADF lifetimes. It is clear that the DFT optimized geometry is not the optimal conformation in terms of TADF. Since there was a selection bias toward high TADF rates, the distribution is skewed, but a significant number of conformations were found to exhibit higher TADF rates than the DFT optimized geometry. A TADF lifetime as short as 2.0 µs (oscillator strength of 1.4×10^{-2} and ΔE_{ST} of 0.02 eV), an 800-fold improvement over the DFT optimized geometry, has been obtained. Condensed phase effects were gauged at the level of linear-response conductor-like polarizable continuum model (LR-CPCM) [282, 283], the details of which have been provided in Appendix D.7. Figure 6-5b is a scatterplot of the condensed phase against the gas phase TADF rates. While LR-CPCM tended to stabilize the S_1 state, decrease ΔE_{ST}, and increase the oscillator strength, the effects were insufficient to induce qualitative changes in the TADF rates. Hence, the remainder of the discussion will proceed based on the gas phase results. Finally, Figure 6-5c is a scatterplot of the oscillator strength against the ΔE_{ST}, testing the fundamental trade-off predicted by the two-state model, in which a single variable (HOMO-LUMO overlap) determines both quantities. The correlation between the two variables is weaker than would be expected based on the conventional two-state model [170]. The distribution may suggest an upper bound on the oscillator strength that can be achieved at a given ΔE_{ST} for this exciplex, but if so the slope is quite steep, allowing a sizable oscillator strength to coexist with a small ΔE_{ST}. This is fairly strong evidence that, by inducing large conformational changes, one can influence TADF through factors beyond the simple electron-hole overlap term that dominates the two-state model. One obvious explanation for this is that different conformations are probing variations in $t - K_{\mathrm{X}}$ by varying the relative phase of these contributions.

For two of the conformers that exhibited high TADF rates ($\tau_{\mathrm{TADF}} < 10$ µs), the dominant pairs of natural transition orbitals (NTOs) [284] in the S_1 and the T_1 states have been visualized in Figure 6-6. Notice that the second conformer exhibits a linear conformation, with the donor moiety next to the TRZ group of the acceptor moiety, as opposed to a stacked conformation that would be expected in the equilibrium geometry. In both conformers, the spatial separation of the hole and the particle

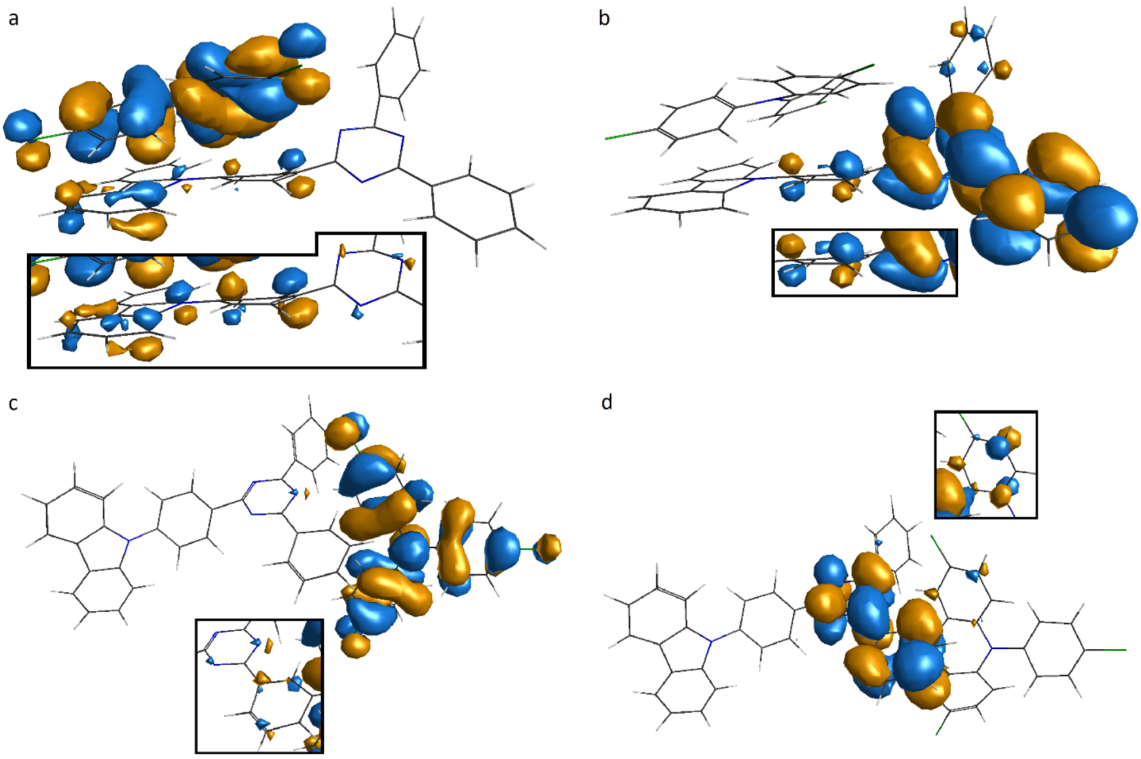

Figure 6-6: (a,c) Hole and (b,d) particle orbitals of the S_1 state. The insets are the corresponding NTOs of the T_1 state.

orbitals is consistent with the strong CT character of the S_1 and the T_1 excitations, but parts of the hole orbitals, as well as the particle orbital in the second conformer, can be seen delocalized onto the opposite moiety, which indicates also a non-negligible LE contribution. As a result, a substantial oscillator strength could be obtained, even when the donor and the acceptor molecules were not in a stacked conformation. Further note the differences between the NTOs of the S_1 and the T_1 states, which are most obvious in the delocalized lobes of the hole and the particle orbitals. In particular, the T_1 excitation appears to have a stronger LE character than the S_1 excitation. Again, this is consistent with the predictions of the four-state model, where differential mixing of CT and LE states is possible in the singlet and triplet manifolds. We suspect that the differences between the S_1 and the T_1 states for this dimer would be even more pronounced in reality and that their apparent similarity is due to the abovementioned shortcoming of the B3LYP functional favoring CT states. Other conformers also exhibited varying degrees of CT/LE mixture in the S_1 and the T_1 states, and more examples have been provided in Appendix D.8 (Figures D-3 and D-4). A more detailed comparison of the S_1 and the T_1 states based on the Kohn-Sham orbitals can also be found in Appendix D.8.

All in all, a more sophisticated computational method or an experiment could reveal most of the found conformers to be poor TADF emitters. For the purposes of this study, however, it sufficed to show that a large oscillator strength, a small ΔE_{ST}, and a substantial SOC can coexist in the framework of a reasonable density functional. A priori, it should be no easier to optimize a set of properties in the DFT world than it is in the real world. The *in silico* discovery of efficient TADF via SOC should motivate a search for such systems *in vitro*.

6.4 Discussion

Turning to the ensemble statistics of the conformers, the most obvious feature is the order-of-magnitude variations in the oscillator strengths and the energy gaps, indicating strong non-Condon effects in the context of the four-state model. Although

the conformations may be unrealistic as equilibrium geometries, they are realistic as snapshots in time. Further assuming the validity of the Born-Oppenheimer approximation, the TADF rates based on the TDDFT results are just the instantaneous rates at the corresponding times along the trajectory. Hence, the results support the proposition that the instantaneous TADF rate of a system can be maximized at some nonequilibrium geometry. There might even exist a system where most accessible conformations have a higher TADF rate than that of the equilibrium geometry. The existence of such a system would help explain the experimental account of Ward and collaborators [255] that TADF in a DAD system diminished when the motion of the donor and the acceptor moieties was hindered. Indeed, constraining the geometry would be detrimental if thermal motion gave access to an ensemble of conformations with higher TADF rates. On the other hand, it would also be possible to harness the conformational dependence by freezing an emitter in the conformation or the range of conformations that maximizes the rate. Such a design strategy becomes viable in light of the four-state model's implication that the rates depend only on the nuclear positions and not on the momenta.

Of course, there are some questions that must be answered before conformational variation can lead to the improvement of real TADF emitters. First, there is the theoretical problem of determining the structural features that facilitate TADF. In the model system, there did not appear to be a particular distance, torsion, or orientation that could be conclusively associated with high TADF rates. Perhaps it was to be expected, considering the intricate interplay of several variables in the four-state model. Then, there is the experimental problem of synthesizing molecules in a specific conformation. While there have been efforts to tune the conformation of TADF emitters using steric hindrance [217, 255], there does not appear to be an established method or guideline to date. Nevertheless, conformational variation introduces a new dimension over which TADF emitters can be optimized. Further theoretical and experimental efforts should be directed to elucidating the structural features that facilitate TADF and the synthetic techniques of enforcing these structures on real molecular systems.

6.5 Conclusions

We have proposed a simple four-state model which explains the key prerequisites of efficient TADF in organic DA systems. The four spin-mixed diabatic states constitute the conceptual basis to discuss the electronic structure of TADF emitters. We show that the resulting adiabatic T_1 and S_1 excited states can have the necessary characteristics to ensure efficient TADF. These characteristics are a small ST gap, different electronic characters of S_1 and T_1, and a significant LE component in S_1. The first two conditions enable fast reverse intersystem crossing, while the last one enables appreciable quantum yields. The model suggests that nonadiabatic effects are not necessary for efficient TADF; however, it does not rule out their contribution completely.

Monte Carlo sampling reveals that the conditions for efficient TADF are relatively easy to satisfy in the parameter space; however, it does not mean that it is equally easy to realize them in real molecular systems. The statistical analysis of the data filtered for TADF activity reveals that a close mutual alignment of some pairs of parameters of the model is a prerequisite for TADF, while their magnitude fine-tunes its efficiency. This observation provides new design principles for optimization of organic emitters, which should aim at satisfying the parameter alignment criteria.

Establishing the structure-property relationships between different molecular architectures and model parameters should be the next step in the exploration of the four-state model, which would lead eventually to the exploration of the chemical space. The most straightforward way to achieve this is to parametrize the four-state Hamiltonian based on ab initio calculations or experimental data. This would allow correlations between different molecular designs and model parameters to be extracted and eventually guide the development of new emitters with improved efficiencies. The optimal parametrization strategy and its exploitation will be a subject of further investigations. In the meantime, by the means of combined MD and TDDFT simulations for model exciplex systems, we showed that significant increase of the TADF efficiency can be also obtained by exploration of the conformation space. This supports

the vibronic mechanism for TADF, in which the non-Condon effects modulate the instantaneous TADF rates and maximize them for some nonequilibrium conformations. Additionally, our study suggests that optimization of condensed-phase molecular conformations, e.g. through controlled exploitation of steric hindrance or application of pressure, may be a practical design strategy for improved OLED materials.

6.6 Acknowledgements

Reprinted with permission from Ref. [285]. Copyright 2019 American Chemical Society. Professor Piotr de Silva proposed the four-state model of TADF and performed the Monte Carlo analysis of the parameter space. Dr. Tianyu Zhu designed the DA exciplex. This work was supported by the U.S. Department of Energy Office of Basic Energy Sciences (BES ER46474).

6.7 Supplementary Information

The Supplementary Information is available in Appendix D: approximations behind the four-state Hamiltonian; eigenvalues and eigenvectors of the four-state Hamiltonian; details of the Monte Carlo sampling, principal component analysis, and MD simulations; images of natural transition orbitals; analysis of the orbital transitions; further details on the TADF rate expression; numerical outputs of TDDFT calculations; and details and results of the LR-CPCM/TDDFT calculations.

Chapter 7

Maximizing TADF via Conformational Optimization

We investigate a new strategy to enhance thermally activated delayed fluorescence (TADF) in organic light-emitting diodes (OLEDs). Given that the TADF rate of a molecule depends on its conformation, we hypothesize that there exists a conformation that maximizes the TADF rate. To test this idea, we use the time-dependent density functional theory (TDDFT) to simulate the TADF rates of several TADF emitters while shifting their geometries toward higher TADF rates in a select subspace of internal coordinates. We find that geometric changes in this subspace can increase the TADF rate up to three orders of magnitude with respect to the minimum energy conformation, and the simulated TADF rate can even be brought into the submicrosecond time scales under the right conditions. Furthermore, the TADF rate enhancement can be maintained with a conformational energy that might be within the reach of modern synthetic chemistry. Analyzing the maximum TADF conformation, we extract a number of structural motifs that might provide a useful handle on the TADF rate of a donor-acceptor (DA) system. The incorporation of conformational engineering into the TADF technology could usher in a new paradigm of OLEDs.

7.1 Introduction

Organic light-emitting diodes (OLEDs) are a promising solution in digital displays and lighting applications. Since Tang and VanSlyke demonstrated the first OLED device in 1987 [156], OLEDs have attracted widespread research and development (R&D) efforts in both the academia and the industry. OLED displays exhibit supremacy in energy efficiency, image quality, response time, and compactness over conventional technologies, such as liquid crystal displays (LCDs) [157–159]. In addition, OLEDs are expected to help reduce global energy consumption [160, 161] and yield new commercial products, such as transparent lighting panels and flexible displays [162, 163].

A key issue in developing more efficient OLEDs is overcoming the disadvantageous spin statistics. When electrons and holes are injected into the organic layer, they recombine in one of the four possible spin states with equal likelihoods: one singlet state and three triplet states. Whereas the singlet excitons can emit a photon and decay to the likewise singlet ground state, radiative decay of the triplet excitons is spin-forbidden. Most of the excitons are dissipated as heat, and the external quantum efficiency (EQE) of fluorescent OLEDs cannot exceed 25 %. As a way to harvest the triplet excitons, Baldo et al. introduced phosphorescent OLEDs (PhOLEDs), which activate the otherwise forbidden transition between the triplet excited state and the singlet ground state [164]. Using the strong spin-orbit coupling (SOC) in heavy metal complexes, the rate of phosphorescence can be brought into the useful microsecond time scales [162, 165]. However, in spite of the commercial success of red and green PhOLEDs, an efficient and stable blue PhOLED remains out of reach [159, 166], and the rarity and the toxicity of heavy metals are also problematic.

Thermally activated delayed fluorescence (TADF) is an alternative approach that involves converting the nonemissive triplet excitons into emissive singlet excitons [167, 168]. In typical organic molecules, electron exchange stabilizes the first triplet excited state (T_1) with respect to the first singlet excited state (S_1). However, if the singlet-triplet (ST) energy gap is under a few $k_B T$, thermal fluctuations can drive the reverse

intersystem crossing (RISC) of the T_1 population into the S_1 state. Modulation of the exchange energy can be accomplished by tuning the spatial overlap of the highest occupied molecular orbital (HOMO) and the lowest unoccupied molecular orbital (LUMO). In the first metal-free TADF OLED, Adachi et al. employed a donor-acceptor (DA) architecture to localize the HOMO and the LUMO on orthogonal moieties, creating S_1 and T_1 states of charge transfer (CT) character [169, 170]. Since then, a large number of TADF emitters have been designed on the same principle [171–175], and high-throughput screening approaches with the aid of machine learning techniques have been employed to give extensive surveys of the relevant chemical space [228, 286]. As a culmination of the R&D efforts, the efficiencies of TADF OLEDs are becoming competitive with commercial PhOLEDs [220, 287–289].

Unfortunately, the spatial separation of the HOMO and the LUMO also diminishes the transition dipole moment (TDM) between the S_1 state and the ground state (S_0). A decrease in the TDM entails a decrease in both the prompt and the delayed fluorescence rates. The trade-off between a small ST gap and a large TDM is manifest even in the outcomes of high-throughput screening studies [228, 286]. In addition, according to El-Sayed's rule [176], the identical CT characters of the S_1 and the T_1 states are expected to lead to a vanishing SOC and hence a vanishing RISC rate. However, the trade-off might not be an intrinsic limitation of TADF but an artifact of the design principles based on an oversimplified model. Indeed, recent studies have demonstrated that the T_1 state of many TADF molecules has significant contributions of local excitation (LE) [174, 290, 291] and that higher triplet states might also have an important role in the RISC step [240, 241, 290]. The two-state model of TADF does not provide the requisite insight to guide the development of trend-breaking emitters.

In Chapter 6, a four-state model of TADF was proposed that might provide a way to overcome the trade-off. According to the four-state model, the ST gap contains additional terms that can counter the effects of electron exchange, enabling the co-existence of a small ST gap and a large TDM in the same molecule. Furthermore, the adiabatic S_1 and T_1 wave functions contain different fractions of diabatic CT and

LE wave functions, enabling the coexistence of a vanishing ST gap and a nonvanishing SOC. Although the mathematical forms of the S_1 and T_1 energies and wave functions do not render themselves to straightforward interpretation, exploring the conformation space of TADF emitters has been proposed as a practical approach to discovering new design principles. Using molecular dynamics (MD) to sample the conformation space and the time-dependent density functional theory (TDDFT) to simulate the electronic excitations, we showed that a DA complex can achieve up to an 800-fold enhancement of the TADF rate with respect to the minimum energy conformation. Indeed, a number of theoretical studies have shown that the conformation of a molecule can modulate the excitation energies and state-to-state couplings that contribute to the TADF rate [244, 292, 293]. It would be reasonable to believe that the TADF rate has a strong dependence on the conformation.

In this chapter, we take the idea of conformational dependence to the next step and examine the potential of direct optimization to maximize the TADF rate. Using a number of known TADF emitters, we show that the TADF rate can be enhanced up to three orders of magnitude and can even be brought into the submicrosecond time scales via suitable changes of conformation. The maximum TADF conformation is free of thermal fluctuations that plague MD snapshot geometries, and one can extract specific hints, as well as general principles that can boost the performance of TADF OLEDs. Furthermore, we find that taking a small subset of the conformational variables suffices to gain substantial control over the TADF rate, and the relevant variables seem to overlap with degrees of freedom (DOFs) that might be tunable via steric hindrance or mechanical strain. Hence, conformational optimization appears to herald a new paradigm of TADF OLEDs.

7.2 Theory

The TADF rate was estimated using the formulation of Adachi et al [215]. First, the rate of TADF is understood to mean the quasi-steady-state rate at which the excited

states are depopulated via fluorescence

$$k_{\mathrm{TADF}} \equiv \frac{k_{\mathrm{F}}[\mathrm{S}_1]}{[\mathrm{S}_1] + [\mathrm{T}_1] + [\mathrm{T}_2]} \tag{7.1}$$

where we have assumed that internal conversion (IC) is fast enough that only the S_1, T_1, and T_2 states have significant populations. In our experience, omission of the T_2 state can lead to an overestimation of the TADF rate when the T_2 energy is below the S_1 energy. Assuming that the forward and reverse intersystem crossing (ISC and RISC) are fast compared to the radiative and nonradiative decay processes, the formula reduces to

$$k_{\mathrm{TADF}} = \frac{k_{\mathrm{F}}}{1 + K_1 + K_2} \tag{7.2}$$

where K_n is the equilibrium constant between the S_1 state and the T_n state

$$K_n = 3 \exp\left(\frac{\Delta E_{\mathrm{S}_1 - \mathrm{T}_n}}{k_B T}\right) \tag{7.3}$$

The fluorescence rate is estimated by the Einstein coefficients [191]

$$k_{\mathrm{F}} = \frac{e^2 {\omega_{10}}^2}{2\pi\epsilon_0 m_e c^3} f_{10} \tag{7.4}$$

where e and m_e are the electron charge and mass, respectively; c is the speed of light; and ω_{10} and f_{10} are the $S_1 \to S_0$ energy gap and oscillator strength, respectively. In the final objective function, we added a penalty to damp the increase in the conformational energy (the DFT energy with respect to the energy minimum) and byproduct features that might arise in the optimization

$$\Phi = k_{\mathrm{TADF}} - \Lambda \Delta E_{\mathrm{DFT}} \tag{7.5}$$

where Λ is a tunable parameter and ΔE_{DFT} is the change in the DFT energy with respect to the minimum energy conformation. We chose the tunable parameter to be on the order $\Lambda \sim 1\,\mu\mathrm{s}^{-1} {E_{\mathrm{h}}}^{-1}$.

We need to emphasize a couple of points regarding the objective function. First,

Equation 7.2 attempts to describe a single conformer of definite geometry. There are theories that enable the inclusion of geometric relaxation (or reorganization) [192, 193] and vibrational effects [194] in estimating the rates of RISC and fluorescence, and these would be the proper way to describe a dynamical ensemble of conformers [247, 294, 295]. However, the TADF rate maximization is a geometry optimization where we maximize the TADF rate instead of minimizing the energy, which necessitates the evaluation of the TADF rate at a definite geometry. Hence, consideration of nuclear dynamics is incompatible with the present investigation.

Second, Equation 7.2 represents an upper bound on the TADF rate. In the real universe, nonradiative decay and a finite RISC rate would entail a slowdown in addition to the fluorescence rate and the thermodynamic cap on the S_1 population. Nonetheless, the formula appeals to our purposes in a number of ways. In the first place, we are only interested in good TADF emitters, where TADF dominates over nonradiative decay, so it makes sense to compute the TADF rate by itself and verify after the fact that TADF proceeds on a feasible time scale. Moreover, Brédas et al. calculated the RISC rates of several TADF emitters and found that RISC rates on the microsecond time scale are not uncommon [290]. We expect that RISC would not be a severe bottleneck in most cases and that the formula would provide a tight upper bound on the TADF rate. Indeed, we found that the RISC only makes quantitative corrections and does not alter the qualitative trends in our model systems. The computational details and numerical results have been provided in Appendix E.2.

The electronic structure calculations were performed using the B3LYP exchange-correlation functional [272–277] and the 6-31+G* basis set [278–280, 296], as implemented in the Q-Chem 5.1 software package [297]. The geometries were visualized in Avogadro 1.2.0 [298], and the natural transition orbitals (NTOs) [284] were visualized in MacMolPlt 7.7 [299]. Standard hybrid functionals are known to underestimate the excitation energy and overestimate the CT character of CT-like states [208, 281]. We are also neglecting the dielectric environment, which is known to stabilize the CT-like states [247], and the dielectric stabilization is not, in principle, equivalent to the CT error [294]. However, our objective was not to make quantitative predictions of TADF

rates but to extract qualitative trends that can guide the design of TADF emitters. Since analytical derivatives of the TDM are not available, the TADF rate maximization entails much higher computational costs than the usual energy minimization. Thus, it was desirable to use a functional that can reproduce the qualitative trends at minimal costs.

To establish that conformational dependence is not an artifact of B3LYP, the electronic structures at the key geometries were recalculated using PBE0 [300–302], M06-2X [303], and LRC-ω^*PBE [304–306]. The asterisk indicates ionization potential-electron affinity(IPEA)-tuning of the range-separation parameter, which we did at the minimum energy conformation in vacuum. Solvent effects were examined in the cases of M06-2X and LRC-ω^*PBE, using the integral equation formalism polarizable continuum model (IEF-PCM) [307–309] and first order, perturbative state-specific (ptSS) [283] treatment of the excited states. We used the dielectric constant and optical dielectric constant of toluene at room temperature: $\varepsilon = 2.379$ and $\varepsilon_\infty = 2.232$ [310].

The TADF rate maximization was performed using a variation of the Nelder-Mead simplex method [311, 312]. Since there are multiple versions of the method, we have outlined our algorithm in Appendix E.1. The geometries of the molecules were represented in the Z-matrix coordinates. We have included the Z-matrices of the model systems at the key geometries in Appendix E.5. To reduce the computational costs and contain the geometric changes in the meaningful regions of the conformation space, a subset of the bond lengths, bond angles, and dihedral angles were chosen to be varied, while the others were constrained to the values at the minimum energy conformation. Since peripheral hydrogens should not have strong effects on the electronic structure and aromatic ring systems should be resistant to distortions, we chose the geometries of the single bonds that connect the aromatic ring systems as the variables. For a complete range of motion, six DOFs are required per bond: one bond length, two bond angles, and three dihedral angles. Hence, the number of variables in each of the model systems could be reduced to 30 or fewer Z-matrix coordinates. To assess the extent to which our choices of variables were justified, a

constrained energy minimization was performed at the end of the TADF rate maximization, where we relaxed the bond lengths and angles that had been fixed in the TADF rate maximization.

7.3 Results and Discussion

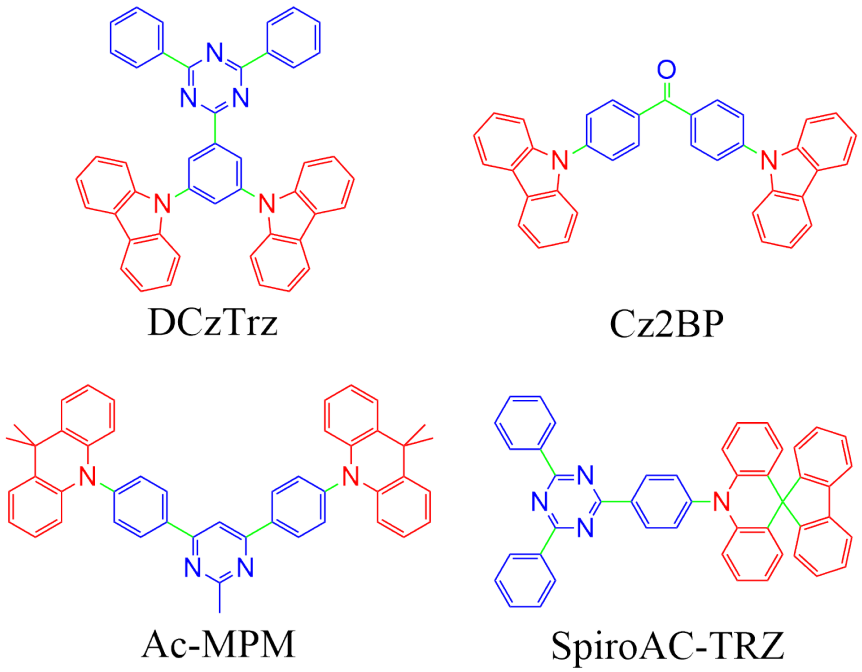

Figure 7-1: Structures of DCzTrz, Cz2BP, Ac-MPM, and SpiroAC-TRZ. The donor and acceptor groups are indicated in red and blue, respectively. Shown in green are the single bonds whose geometries were varied in the TADF rate maximization.

As model systems, we chose a number of TADF emitters that have been reported to exhibit high EQE in blue: DCzTrz [287], Cz2BP [313], Ac-MPM [314], and SpiroAC-TRZ [289]. The skeletal structures of the model systems are shown in Figure 7-1. We are going to examine the case of DCzTrz in detail and use the other emitters to assess the extent to which the results can be generalized.

7.3.1 DCzTrz

Table 7.1 summarizes the energetics of DCzTrz at the maximum TADF geometries with various energy penalties. Between the energy minimum ($\Lambda = \infty$) and the

Λ ($\mu s^{-1} {E_h}^{-1}$)	ΔE_{DFT} (kJ mol^{-1})	EE (eV) S$_1$ / T$_1$ / T$_2$	f_{10}	k_{TADF} (μs^{-1})
∞	0	2.84 / 2.71 / 2.74	0.017	0.0094
8.0	211	2.86 / 2.83 / 2.93	0.026	0.88
4.0	278	2.94 / 2.91 / 3.00	0.029	1.06
2.0	409	2.86 / 2.84 / 2.95	0.026	1.08
0.0	594	2.79 / 2.77 / 2.90	0.028	1.07

Table 7.1: Conformational energies, excitation energies, oscillator strengths, and TADF rates of DCzTrz at the maximum TADF geometries with various energy penalties. The case of $\Lambda = \infty$ corresponds to the energy minimum, and the case of $\Lambda = 0$ corresponds to the TADF maximum with no energy penalty.

TADF maximum with no energy penalty ($\Lambda = 0$), the TADF rate increases over two orders of magnitude from 9.4 ms^{-1} to 1.07 μs^{-1}. Moreover, the enhancement is not a result of trade-off between a small ST gap and a large TDM: the S$_1$-T$_1$ gap decreases from 0.13 eV to 0.02 eV, and f_{10} increases from 0.017 to 0.028. The simultaneous improvement of what are supposed to be contraindicated properties confirms that conformational optimization has achieved more than modulation of the HOMO-LUMO overlap. Although the conformational energy also undergoes a gigantic increase of 594 kJ mol^{-1}, the results with energy penalty reveal that much of the energy is irrelevant to improving the TADF rate. Using $\Lambda = 4.0\,\mu s^{-1} {E_h}^{-1}$, the conformational energy can be halved with negligible loss in the TADF rate. Using $\Lambda = 8.0\,\mu s^{-1} {E_h}^{-1}$, further damping to 211 kJ mol^{-1} is possible with less than 20 % loss of the TADF rate enhancement. The stability of the TADF rate against an energy penalty affirms that the maximum TADF conformation is not an absurdity, but its essential features are those that one may hope to reproduce using suitable techniques in the real universe.

Figure 7-2a shows the minimum energy conformation with arrows indicating the DOFs that participate in the TADF rate maximization. It is obvious that the TADF maximum in Figure 7-2b is a strained conformation. The carbazole (Cz, donor) groups have popped above and below the plane of the 2,4,6-triphenyl-1,3,5-triazine (Trz, acceptor) group by $-33.4°$ (left) and $3.7°$ (right), respectively. To be precise, two of the phenyl rings have twisted with respect to the triazine ring, so the Trz group

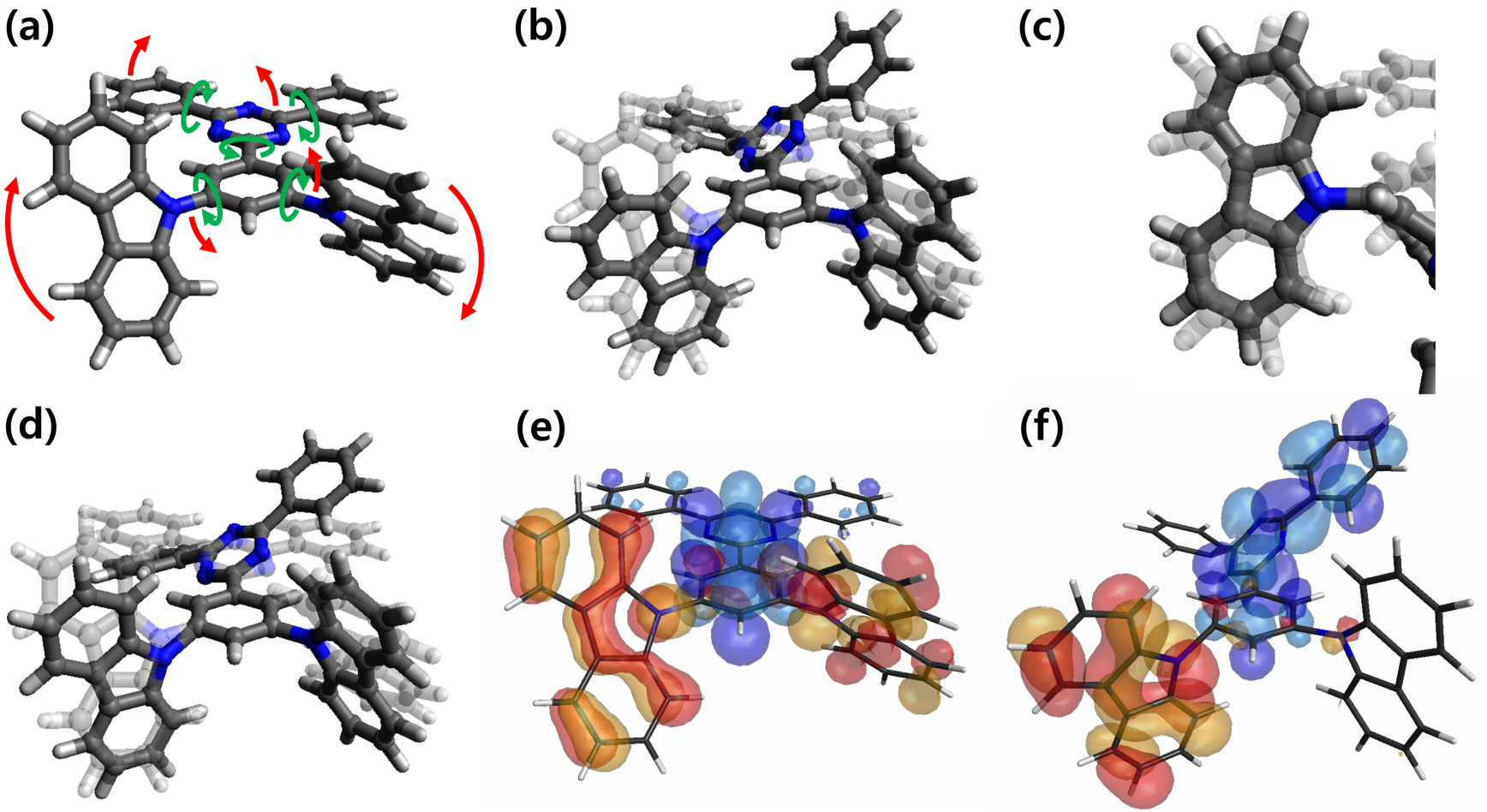

Figure 7-2: Geometries of DCzTrz: (a) the energy minimum, $\Lambda = \infty$; (b) the TADF maximum with no energy penalty, $\Lambda = 0$; (c) a magnified view of the donor-acceptor bond; and (d) the TADF maximum with energy penalty, $\Lambda = 8.0\,\mu s^{-1} {E_h}^{-1}$. Also, the NTO pairs of the S_1 state: (e) the energy minimum, $\Lambda = \infty$; and (f) the TADF maximum with no energy penalty, $\Lambda = 0$. The arrows in panel (a) indicate the DOFs that are the most active in the TADF rate maximization, and the translucent geometries in the background of panels (b-d) are the minimum energy conformation. In panels (e-f), the hole orbitals are shown in red and orange, respectively, and the electron orbitals are shown in sky blue and indigo. ISO value: 0.025.

is no longer planar, so these angles are with respect to the phenyl ring that bridges the Cz groups to the rest of the Trz group. Also, the Cz groups have rotated to become more orthogonal to the Trz group. The Cz groups are 92.7° (left) and 79.8° (right) to the Trz group, respectively, in contrast to 57.3° (left) and 56.5° (right) at the energy minimum. Increasing the dihedral angle between the donor and acceptor moieties is a known strategy to reduce the HOMO-LUMO overlap and hence the ST gap [217, 315, 316]. The fact that the same motif appears at the TADF maximum of DCzTrz is an encouraging sign that useful design principles can be extracted.

Indeed, a strange feature comes to attention. After popping above and below the plane of the Trz group, the Cz groups tilt back toward the Trz group, as shown in Figure 7-2c. The lower and upper C_{Cz}-N_{Cz}-C_{Trz} angles at each Cz group differ by 17.7° (left) and −19.5° (right), respectively, whereas the C_{Cz}-N_{Cz}-C_{Trz} angles at the energy minimum are the same $125.7 \pm 0.2°$. Though the differences in the angles change to 23.8° (left) and −6.5° (right), the gooseneck persists even with an energy penalty of $\Lambda = 8.0\,\mu s^{-1} {E_h}^{-1}$. Hence, the gooseneck cannot be a side product of the optimization but a feature relevant to TADF. Though the physical intuition is unclear, it might be associated with the additional terms in the four-state model. or the dissimilar forms of the integrands in the exchange integral $\langle {r_{12}}^{-1} \rangle$ and the transition dipole integral $\langle r_1 \rangle$. After all, the ST gap and the TDM should depend not only on the overlap but also on the orientation of the HOMO and the LUMO.

Meanwhile, the twist in the Trz group tends to dissipate with energy penalty. As shown in Figure 7-2d, the phenyl rings return to a more coplanar arrangement to the triazine ring in what appears to be a concerted manner. However, the planarity of the Trz group remains quite disturbed even with an energy penalty of $\Lambda = 8.0\,\mu s^{-1} {E_h}^{-1}$. The phenyl rings to the front center and the back left are 30.2° and 30.6° to the triazine ring, respectively, which are 41.6° and 61.3° in the absence of energy penalty. We conjecture that the twist in the Trz group controls the distribution of the LUMO so that it gets neither too close to nor too far away from to the HOMO. Comparing the dominant NTO pairs of the S_1 state at the energy minimum (Figure 7-2e) and the TADF maximum (Figure 7-2f), the distribution of the S_1 hole is indeed impacted.

The NTOs of the T_1 state are similar (Figure E-4). This would also explain why the twist appears to unroll in a concerted manner as energy penalties are imposed. Overall, the twist in the Trz group appears to help enhance the TADF rate, but a balance must be struck with the conformational energy.

7.3.2 Other Model Systems

	Λ ($\mu s^{-1} E_h^{-1}$)	ΔE_{DFT} (kJ mol^{-1})	EE (eV) S_1 / T_1 / T_2	f_{10}	k_{TADF} (μs^{-1})
Cz2BP	inf	0	2.99 / 2.67 / 2.78	0.345	1.9×10^{-4}
	8.0	162	2.67 / 2.63 / 2.64	0.061	0.66
	4.0	181	2.66 / 2.62 / 2.62	0.062	0.69
	0.0	193	2.64 / 2.60 / 2.61	0.060	0.69
Ac-MPM	inf	0	2.47 / 2.46 / 2.47	3.4×10^{-5}	0.0012
	8.0	51	2.51 / 2.49 / 2.49	0.036	0.59
	4.0	365	2.54 / 2.51 / 2.67	0.022	0.58
	0.0	420	2.55 / 2.52 / 2.61	0.028	0.63
SpiroAC-TRZ	inf	0	2.41 / 2.41 / 2.66	7.9×10^{-6}	4.2×10^{-4}
	8.0	104	2.56 / 2.54 / 2.75	0.012	0.49
	4.0	294	2.48 / 2.46 / 2.75	0.017	0.50
	0.0	475	2.50 / 2.48 / 2.67	0.019	0.61

Table 7.2: Conformational energies, excitation energies, oscillator strengths, and TADF rates of Cz2BP, Ac-MPM, and SpiroAC-TRZ at the maximum TADF geometries with various energy penalties. The case of $\Lambda = \infty$ corresponds to the energy minimum, and the case of $\Lambda = 0$ corresponds to the TADF maximum with no energy penalty.

Table 7.2 summarizes the energetics of Cz2BP, Ac-MPM, and SpiroAC-TRZ. The TADF rates start in the millisecond time scale at the energy minimum and end in the microsecond time scale at the TADF maximum, suggesting that TADF rate enhancements over two to three orders of magnitude might be typical in the conformational optimization of TADF emitters. Cz2BP undergoes the largest enhancement in the TADF rate, a factor of 3000. However, the improvement is a result of trade-off between a small ST gap and a large TDM: both the S_1-T_1 gap and f_{10} decrease from 0.32 eV to 0.04 eV and from 0.345 to 0.060, respectively. The cases of Ac-MPM and SpiroAC-TRZ might be more complicated. Whereas the increases in the S_1-T_1 gaps of 0.02 eV are comparable to the uncertainty, the increases in the f_{10} of Ac-MPM

and SpiroAC-TRZ span three orders of magnitude from 3.4×10^{-5} to 0.028 and from 7.9×10^{-6} to 0.019, respectively. The disproportionate trade-off suggests that conformational optimization might have had a nontrivial impact on the electronic structure. In any case, simultaneous improvement of the ST gap and the TDM might be a rare occurrence, which might also explain why DCzTrz was the only model system whose TADF rate reached the submicrosecond regime.

Notice that the minimum energy conformations of Ac-MPM and SpiroAC-TRZ have a tiny ST gap. In particular, the ST gap of SpiroAC-TRZ is near vanishing. The two-state model would suggest that the SOC must vanish, since both the S_1 and T_1 states must be CT states [176]. Surprisingly, the RISC step does not appear to be the most severe bottleneck. The f_{10} and SOC are 7.9×10^{-6} and $0.0063\,\mathrm{cm}^{-1}$, respectively, which correspond to a fluorescence rate of $2.0\,\mathrm{ms}^{-1}$ and a RISC rate of $2.9\,\mathrm{ms}^{-1}$ (Table E.1). This makes sense in light of the four-state model. The S_1 and T_1 states contain different fractions of the diabatic CT and LE states, and the electron exchange favors the S_1 state as the more CT-like state. Hence, the fluorescence step can end up slower than the RISC step.

In each of the model systems, a suitable energy penalty can reduce the conformational energy with minimal loss in the TADF rate. Even with no energy penalty, the TADF maximum of Cz2BP has a conformational energy of $194\,\mathrm{kJ\,mol}^{-1}$, less than half of the other model systems. With an energy penalty of $\Lambda = 8.0\,\mu\mathrm{s}^{-1}{E_\mathrm{h}}^{-1}$, Ac-MPM and SpiroAC-TRZ reduce their conformational energies to $53\,\mathrm{kJ\,mol}^{-1}$ and $102\,\mathrm{kJ\,mol}^{-1}$, respectively, while retaining more than 90 % and 80 % of the TADF rates. Though these conformational energies might seem daunting, synthetic chemists have created and stabilized molecules with strain energies over $300\,\mathrm{kJ\,mol}^{-1}$ [317, 318]. For certain TADF emitters, the maximum TADF conformation might be synthesizable using suitable modifications in the real universe.

Figure 7-3 shows the geometries of Cz2BP, Ac-MPM, and SpiroAC-TRZ at the TADF maximum with no energy penalty ($\Lambda = 0$). The maximum TADF geometries with energy penalties and a detailed discussion of their relations to the energetics can be found in Appendix E.3. Here, we summarize the key results. First, the

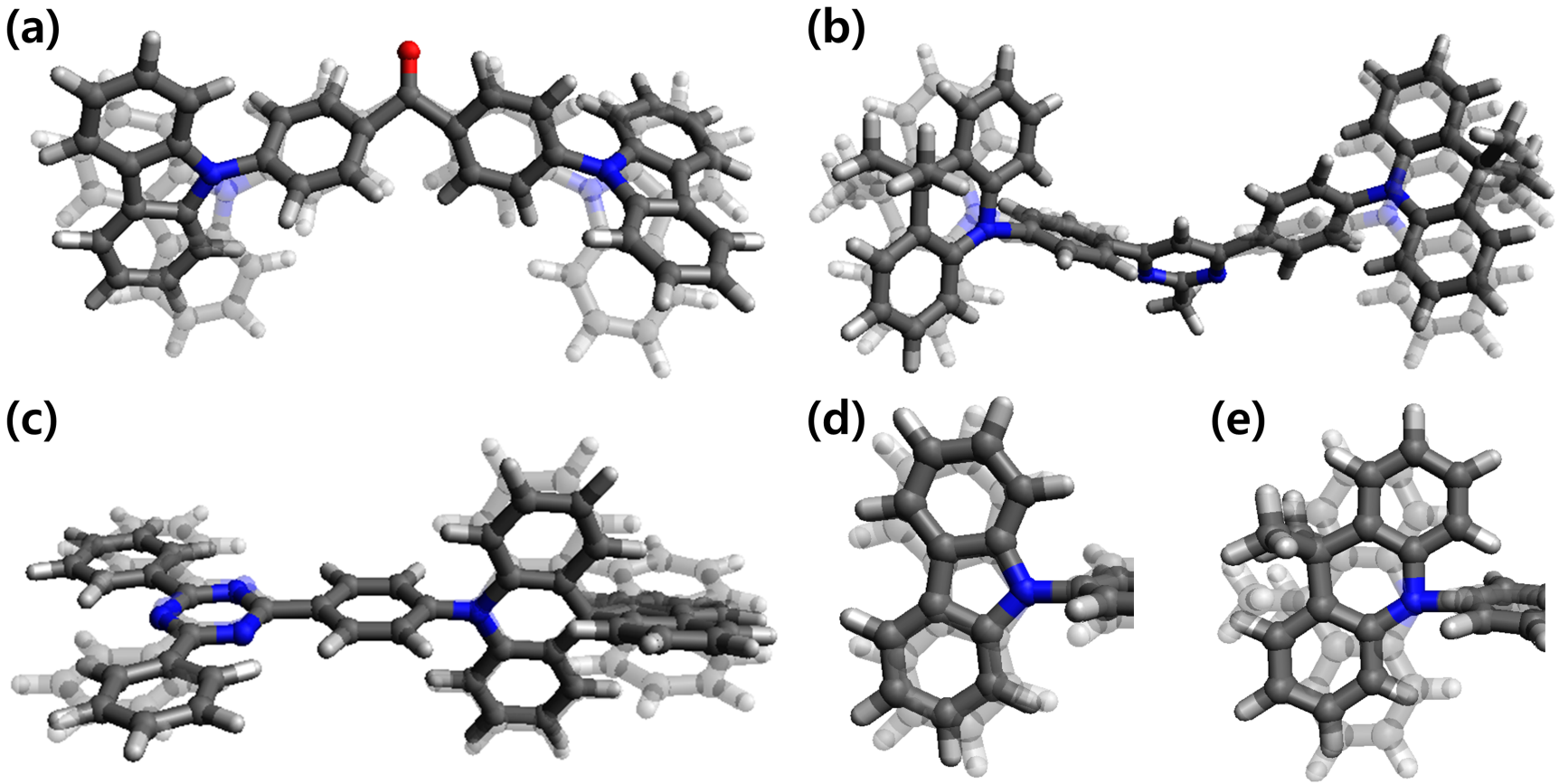

Figure 7-3: Geometries of (a) Cz2BP; (b) Ac-MPM; and (c) SpiroAC-TRZ at their respective TADF maxima with no energy penalty ($\Lambda = 0$). Also, magnified views of the donor-acceptor bonds in (d) Cz2BP and (e) Ac-MPM. The translucent geometries in the background are the minimum energy conformations.

dihedral angles between the donor and acceptor groups increase in Cz2BP (Figure 7-3a), while they decrease in Ac-MPM (Figure 7-3b) and SpiroAC-TRZ (Figure 7-3c). The dihedral angle changes are consistent with the outcome that both the ST gap and the TDM decrease in Cz2BP and increase in Ac-MPM and SpiroAC-TRZ. Second, SpiroAC-TRZ is the only model system that does not develop a gooseneck. The donor groups of Cz2BP (Figure 7-3d) and Ac-MPM (Figure 7-3e) both pop above and below the plane of the acceptor group and then tilt back toward the acceptor group. Third, the acceptor groups of Cz2BP and Ac-MPM become twisted, albeit in different ways from both DCzTrz and each other. In Cz2BP, the phenyl rings become more orthogonal to each other. In Ac-MPM, one of the phenyl rings twists out of plane, while the other maintains a moderate angle to the pyrimidine ring. The gooseneck and the twist in the acceptor group tend to persist even with energy penalties.

Remarkably, three out of the four model systems developed a gooseneck at the DA bond and a twist in the acceptor group. We suspect that these motifs might provide a useful handle on the TADF rate in general DA systems. Unfortunately, there is a need for theoretical intuition and experimental evidence at this point. In spite of abundant efforts to manipulate the DA dihedral angles [217, 315, 316], we are not aware of prior studies that have considered out-of-plane displacement of the donor and the acceptor moieties. As discussed earlier, the gooseneck might be associated with the mathematical forms of the integrals that enter the TADF rate, but it is unclear which integrals are affected in what way.

The twist in the acceptor group is also obscure. While it is not hard to rationalize how the twist might change the distribution of the LUMO, it is not always clear why a particular distribution should be more conducive to TADF than another, nor does there appear to be a pattern in how the acceptor groups become distorted. For example, Ac-MPM appears to push the LUMO toward just one of the donor groups, while Cz2BP remains much more symmetric. The dominant NTO pairs of the S_1 and T_1 states can be found in Appendix E.4. Perhaps, the absence of a trend is due to the small number of model systems. The twist might not be a single motif but a

collection of motifs that concern specific families of emitters.

On the other hand, the lack of physical intuition attests to the true value of conformational optimization: discovery of design principles that do not render themselves to deduction.

7.3.3 Choice of Density Functional

To assess the functional dependence of the results, we took the maximum TADF geometries optimized using B3LYP and recalculated the electronic structures using PBE0, M06-2X, and LRC-ω^*PBE. To our surprise, the generalized gradient approximation (GGA) global hybrid, the meta-GGA global hybrid, and the range-separated hybrid (RSH) exhibited similar patterns. Since tuned RSHs have been shown to be effective at predicting the excited-state properties of TADF emitters [224, 294], we focus on LRC-ω^*PBE as the primary subject of comparison. The complete set of results can be found in Appendix E.2.

	Λ ($\mu s^{-1} E_h^{-1}$)	ΔE_{DFT} (kJ mol^{-1})	EE (eV) S$_1$ / T$_1$ / T$_2$	f_{10}	k_{TADF} (μs^{-1})
DCzTRZ (vacuum)	inf	0	3.39 / 3.07 / 3.14	0.0310	1.5×10^{-5}
	8.0	202	3.49 / 3.27 / 3.29	0.0133	2.8×10^{-4}
	4.0	267	3.49 / 3.26 / 3.27	0.0018	2.4×10^{-5}
	2.0	394	3.37 / 3.15 / 3.20	3.5×10^{-4}	7.1×10^{-6}
	0.0	573	3.33 / 2.93 / 3.11	3.9×10^{-4}	1.1×10^{-8}
DCzTRZ (toluene)	inf	0	3.30 / 3.07 / 3.08	0.0312	3.1×10^{-4}
	8.0	199	3.37 / 3.27 / 3.27	0.0146	0.024
	4.0	262	3.39 / 3.27 / 3.27	0.0021	0.0019
	2.0	389	3.28 / 3.14 / 3.21	4.2×10^{-4}	2.5×10^{-4}
	0.0	568	3.24 / 2.93 / 3.12	3.4×10^{-4}	2.7×10^{-7}
Ac-MPM (toluene)	inf	0	3.04 / 3.09 / 3.06	5.0×10^{-5}	0.0073
	8.0	48	2.97 / 2.98 / 3.07	0.031	3.8
	4.0	341	3.02 / 2.89 / 3.02	0.034	0.026
	0.0	393	3.08 / 2.82 / 3.08	0.0059	3.4×10^{-5}

Table 7.3: Conformational energies, excitation energies, oscillator strengths, and TADF rates of DCzTrz and Ac-MPM recomputed with LRC-ω^*PBE/IEF-PCM at the maximum TADF geometries optimized with B3LYP. The case of $\Lambda = \infty$ corresponds to the energy minimum, and the case of $\Lambda = 0$ corresponds to the TADF maximum with no energy penalty.

Table 7.3 summarizes the LRC-ω^*PBE energetics of DCzTrz at the B3LYP ge-

ometries. Interestingly, the TADF rates in LRC-ω^*PBE seem to increase with the energy penalty at small values of Λ. The TADF rate reduces to $0.011\,\mathrm{s}^{-1}$ at the geometry optimized with no energy penalty ($\Lambda = 0$), which is smaller than $15\,\mathrm{s}^{-1}$ at the energy minimum. On the other hand, the maximum TADF rate is $280\,\mathrm{s}^{-1}$ at the geometry optimized with $\Lambda = 8.0\,\mu\mathrm{s}^{-1}{E_\mathrm{h}}^{-1}$, which is an order of magnitude greater. A toluene-like environment stabilizes the S_1 state by 0.1–0.2 eV, increasing the maximum TADF rate to $24\,\mathrm{ms}^{-1}$ at the geometry optimized with $\Lambda = 8.0\,\mu\mathrm{s}^{-1}{E_\mathrm{h}}^{-1}$, which is now two orders of magnitude greater than $0.31\,\mathrm{ms}^{-1}$ at the energy minimum. The other molecules exhibit similar trends, as shown in Tables E.4 and E.6.

Remarkably, LRC-ω^*PBE predicts much more favorable TADF properties in Ac-MPM and SpiroAC-TRZ. Table 7.3 shows the energetics of Ac-MPM in a toluene-like environment as computed using LRC-ω^*PBE/IEF-PCM. Notice that Ac-MPM exhibits a simultaneous improvement of the ST gap and TDM and a TADF rate in the submicrosecond time scales at the geometry optimized with $\Lambda = 8.0\,\mu\mathrm{s}^{-1}{E_\mathrm{h}}^{-1}$. As shown in Table E.6, SpiroAC-TRZ also exhibits a simultaneous improvement at $\Lambda = 4.0\,\mu\mathrm{s}^{-1}{E_\mathrm{h}}^{-1}$, though the TADF rate is the greatest at $\Lambda = 8.0\,\mu\mathrm{s}^{-1}{E_\mathrm{h}}^{-1}$. The TADF rates of Ac-MPM and SpiroAC-TRZ are $3.8\,\mu\mathrm{s}^{-1}$ and $2.9\,\mu\mathrm{s}^{-1}$ at the respective geometries optimized with $\Lambda = 8.0\,\mu\mathrm{s}^{-1}{E_\mathrm{h}}^{-1}$. Again, we emphasize that we have not reoptimized the geometries using LRC-ω^*PBE/IEF-PCM. It stands to reason that we could have gotten even more drastic enhancements if we had.

Hence, various functionals corroborate the enhancement of TADF rates in the B3LYP geometries, provided that the objective function contained sufficient energy penalty. We suspect that the TADF rate maximization had a propensity to exploit the quirks of the B3LYP universe and that the energy penalty helped the optimizer to remain in the safe region of the conformation space. The existence of such quirks is not surprising, since B3LYP is just an approximation to the exact density functional. However, B3LYP is not special in this regard. In fact, we might have encountered the same issue even if we had optimized the geometries using a different functional. Suppose that we had done the TADF rate maximization using LRC-ω^*PBE/IEF-PCM. We would have obtained drastic enhancements only to have those results be

brought into question by the other functionals. For practical purposes, it would make sense to perform the TADF rate maximization using an inexpensive method and verify the improvements using more sophisticated methods.

We recapitulate the noteworthy commonalities in the energetics predicted by B3LYP and the other functionals. First, there exists a conformation where the TADF rate is orders of magnitude greater than at the minimum energy conformation. Moreover, the maximum TADF conformation in B3LYP and in the other functionals cannot be too far apart, considering that a moderate energy penalty is sufficient to arrive at a geometry that exhibits TADF rate enhancement in all of the functionals. These observations reaffirm that the maximum TADF conformation not only exists but also can be determined to a reasonable precision. Second, one or more of the model systems exhibit a simultaneous improvement of the ST gap and TDM. These are DCzTrz in B3LYP and PBE0 and Ac-MPM and SpiroAC-TRZ in M06-2X/IEF-PCM and LRC-ω^*PBE/IEF-PCM. When a simultaneous improvement of the ST gap and TDM occurs, the maximum TADF rate can be impressive. The TADF rate of DCzTrz in B3LYP and the TADF rates of Ac-MPM and SpiroAC-TRZ in M06-2X/IEF-PCM and LRC-ω^*PBE/IEF-PCM reach the submicrosecond time scales. It is possible but difficult to think that the simultaneous improvement is just a quirk in each of the functionals, given that the last two methods predicted simultaneous improvement in geometries optimized using a different functional. The results cast a serious doubt on the conventional wisdom that the trade-off is an inherent property of TADF emitters.

7.3.4 Choice of Conformational Variables

So far, we have assumed that the variables in the TADF rate maximization corresponded to the most flexible DOFs in the model systems. While the assumption does not affect the existence of conformations that maximize the TADF rate, it does affect the extent to which we can expect the maximum TADF conformation to be reproducible in the real universe. If our choice of conformational variables were appropriate, then the changes in the geometry and the consequent changes in the TADF rate would be minimal even if we relaxed the complementary DOFs. Hence, we took

the maximum TADF geometries and performed a constrained energy minimization to relax the hydrogen atoms and the aromatic ring systems, which had been fixed in the TADF rate maximization.

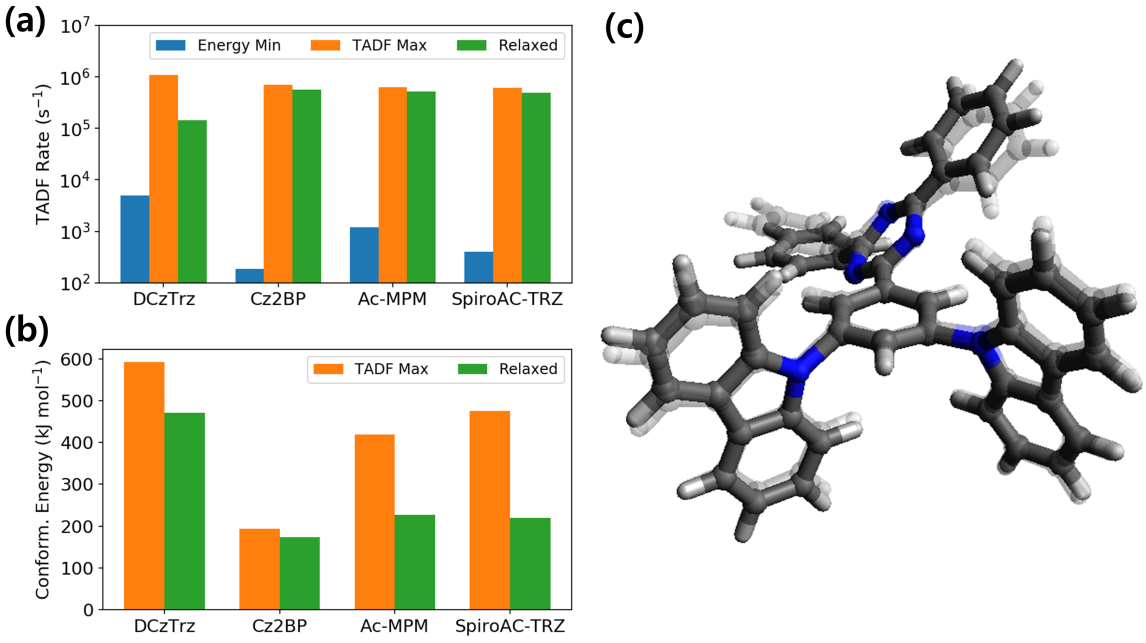

Figure 7-4: (a) TADF rates and (b) DFT energies of DCzTrz, Cz2BP, Ac-MPM, and SpiroAC-TRZ at the energy minimum, at the TADF maximum ($\Lambda = 0$), and after the relaxation of the hydrogen atoms and the aromatic ring systems. (c) Geometry of DCzTrz after the relaxation of the hydrogen atoms and the aromatic ring systems.

Figure 7-4 summarizes the energetics of the maximum TADF geometries before and after the constrained energy minimization. The effects of the relaxation depend on the system. For example, DCzTrz undergoes an order-of-magnitude decrease in the TADF rate from $1.07\,\mu s^{-1}$ to $0.14\,\mu s^{-1}$, and a noticeable decrease in the DFT energy from $594\,kJ\,mol^{-1}$ to $472\,kJ\,mol^{-1}$, as shown in Figures 7-4a,b, respectively. It appears that our choice of variables included too many rigid DOFs or the geometric changes might have been severe enough to obscure the distinction of flexible and rigid DOFs. Figure 7-2c reveals that the constrained energy minimization causes distortions in the phenyl and the triazine rings that tend to restore the planarity of the Trz group. These changes agree with the conjecture that the twist in the acceptor group imparts a considerable strain on DCzTrz. Also, it makes sense that unrolling the twist in the acceptor group in an unconcerted manner would be detrimental to

the TADF rate, since the distortion controls the distribution of the LUMO.

With the exception of DCzTrz, the TADF rate enhancement is quite stable against the relaxation of the hydrogen atoms and the aromatic ring systems. Cz2BP shows minimal changes in both the TADF rate and the DFT energy, meaning that our choice of variables captured both the most flexible DOFs and the DOFs that are the most relevant to the TADF rate. In the cases of Ac-MPM and SpiroAC-TRZ, the conformational energies are halved, but the TADF rates remain at $0.52\,\mu s^{-1}$ and $0.49\,\mu s^{-1}$, respectively. The geometries of Cz2BP, Ac-MPM, and SpiroAC-TRZ after the constrained energy minimization have been provided in Section E.3. In addition to affirming our choice of variables, the stability of the TADF rate suggests a substantial overlap between the most flexible DOFs and the DOFs that determine the TADF rate in the model systems. The outcome is consistent with our proposition that the essential features of the maximum TADF conformation might be synthesizable using suitable modifications in the real universe.

How to synthesize the maximum TADF conformers is beyond the scope of this work, but we can suggest some basic examples. The textbook chemist's approach would be to attach bulky groups that constrain the rotation of certain bonds – the same approach has been used to modulate the donor-acceptor dihedral angles in TADF emitters [217, 315, 316]. We can also imagine placing the organic layer under mechanical stress or pressure to crowd the molecules together. In the first place, it is not necessary to have every OLED molecule in the maximum TADF conformation. For most practical purposes, it would suffice to increase the population of molecules that have a higher TADF rate than the equilibrium ensemble of the original emitter. We expect that a myriad of techniques in enzyme design might prove applicable to the conformational engineering of TADF OLEDs.

7.4 Conclusion

To demonstrate the potential of conformational optimization to assist the development of trend-breaking TADF OLEDs, we studied direct maximization of the TADF

rate in the conformation spaces of several TADF emitters. As desired, one of the model systems (DCzTrz) achieved a simultaneous improvement of the ST gap and the TDM, and its simulated TADF rate could be brought into the submicrosecond time scales. Even model systems that exhibited trade-off between a small ST gap and a large TDM were found to undergo TADF rate enhancements by two to three orders of magnitude. The conformational energy required to maximize the TADF rate can be as small as $193\,\mathrm{kJ\,mol^{-1}}$ even in the absence of energy penalty (Cz2BP), and the conformational energy can be as small as $51\,\mathrm{kJ\,mol^{-1}}$ with minimal loss in the TADF rate enhancement (Ac-MPM). Furthermore, the maximum TADF conformations of the model systems shared a number of structural motifs, such as the gooseneck at the DA bond and the concerted rotation of the aromatic rings in the acceptor group. Although the physical intuition behind these motifs remains obscure, the opacity itself demonstrates the true value of conformational optimization: discovery of design principles that do not render themselves to deduction.

The conformational dependence of the TADF rate motivates the incorporation of conformational engineering into the TADF technology. Based on the results of TADF rate maximization with energy penalties and constrained energy minimization, the maximum TADF conformation of certain molecules, or another conformation that contains its essential features, might be synthesizable, given the high levels of strain that are within the reach of modern synthetic chemistry. Since the minimum energy conformation is not the best geometry in terms of the TADF rate, it would be desirable to manipulate the conformation in a way that enhances the TADF rate. Although the proposition might seem unorthodox in physical or organic chemistry, changing the properties of a molecule by changing its conformation is a standard in fields such as enzyme design. In the future, we hope to connect conformational optimization with experimental efforts and demonstrate that the electronic structures of TADF emitters can be improved in the real universe.

7.5 Acknowledgements

Reprinted with permission from Ref. [319]. Copyright 2021 American Chemical Society. This work was supported by the U.S. Department of Energy Office of Basic Energy Sciences (DE-FG02-07ER46474).

7.6 Supplementary Information

The Supplementary Information is available in Appendix E: our version of the Nelder-Mead simplex method; calculation of the RISC rate and evaluation of its effects on the TADF rate; recalculation of the electronic structures using PBE0, M06-2X, LRC-ω*PBE, M06-2X/IEF-PCM and LRC-ω*PBE/IEF-PCM; geometries of Cz2BP, Ac-MPM, and SpiroAC-TRZ at the TADF maximum with various energy penalties and after the relaxation of DOFs that had been fixed in the TADF rate maximization; NTO pairs of DCzTrz, Cz2BP, Ac-MPM, and SpiroAC-TRZ in the S_1 and T_1 states; Z-matrices thereof.

Chapter 8

Enhancing TTA Upconversion via High-Level Intersystem Crossing

Experimental studies have reported molecules with triplet-triplet annihilation (TTA) efficiencies that appear to exceed the theoretical limit of 40 %. We present computational evidence that these limit-breaking TTA efficiencies might be attributed to the $T_2 \rightarrow S_1$ intersystem crossing (ISC). Furthermore, we propose strategies to enhance this ISC and provide experimental support of enhanced efficiencies.

8.1 Introduction

Triplet-triplet annihilation (TTA) provides an upconversion (UC) pathway that combines two low-energy triplet excitons to produce one high-energy singlet exciton. It is a promising approach to photon upconversion, with applications in photovoltaics [180–182], photocatalysis [183–185], sensing [186, 187], bioimaging [188, 189], and controlled drug release [190]. In addition, TTA is a promising solution for organic light-emitting diodes (OLEDs) in the blue region, since the low energy of the triplets is conducive to the device stability [320–322].

When two triplets collide, the triplet-triplet (TT) pair attains singlet, triplet, and quintet spin multiplicities in a 1:3:5 ratio, as shown in Figure 8-1. However, the quintet states of organic molecules are too high in energy, so the quintet TT pairs

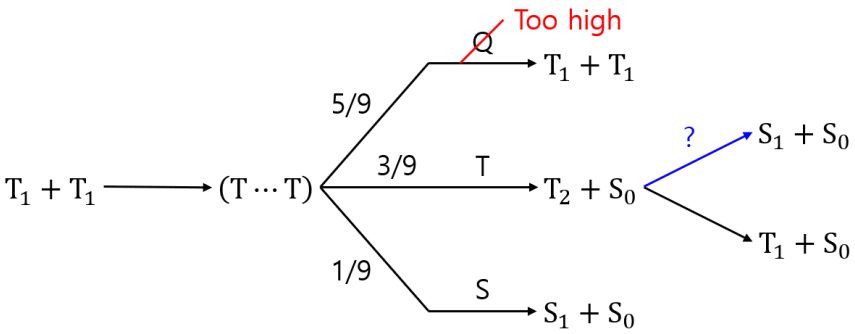

Figure 8-1: Schematic of TTA with $T_2 \rightarrow S_1$ ISC.

dissociate back into two triplets. Meanwhile, the higher triplet states decay to the T_1 state. This gives $18\,T_1 \rightarrow 1\,S_1 + 3\,T_1 + 5 \times 2\,T_1$. Subtracting triplets that appear on both sides of the equation, we get that the theoretical limit on the TTA efficiency is 20 % per triplet or 40 % per TT pair [177]. Interestingly, experimental studies have reported annihilators with efficiencies that appear to exceed this limit, such as 9,10-diphenylanthracene (DPA) [178] and 5,6,11,12-tetraphenyltetracene (rubrene) [179].

A number of mechanisms have been proposed. First, the T_2 state might be higher in energy than twice the T_1 energy [177]. Then, the triplet TT pair might dissociate like the quintet TT pair. For example, the TTA efficiencies of perylene derivatives have been shown to depend on the T_2 energy [323, 324]. Second, the T_2 exciton might undergo ISC to the S_1 state [177]. This does not increase the efficiency of TTA per se, but it increases the observed efficiency. Indeed, experimental studies found evidence of $T_2 \rightarrow S_1$ ISC in rubrene [325]. In addition, second-order perturbation terms [326] and intermolecular factors [325] have been proposed to be relevant.

8.2 Theory

To determine whether the T_2 state is higher in energy than twice the T_1 energy, we calculated the excited states of DPA, rubrene, and their parent molecules using time-dependent density functional theory (TDDFT) with the B3LYP exchange-correlation functional [272–277] and the 6-31G* basis set [278, 279, 335, 336] as implemented in the Q-Chem 5.1 software package [297]. The excitation energies are summarized

Molecule	B3LYP / 6-31G*			Experiment		
	S_1	T_1	T_2	S_1	T_1	T_2
Anthracene	3.28	1.80	3.30	3.3 [327]	1.85 [327, 328]	3.25 [327, 329]
DPA	3.16	1.73	3.27	3.14 [330]	1.77 [328]	
Tetracene	2.49	1.12	2.51	2.6 [327]	1.26 [327]	2.55 [327, 329]
Rubrene	2.19	0.95	2.33	2.35 [331]	1.15 [332, 333]	
DPBF	2.93	1.52	3.10	2.98 [334]	1.48 [333]	

Table 8.1: Computational and experimental excitation energies. The computational values correspond to vertical excitation at the S_0 geometry. The experimental values represents combinations of UV-Vis absorption [327, 330, 331, 334] emission [327], signlet-triplet absorption using oxygen perturbation [328], triplet-triplet absorption [329], and energy transfer [332, 333].

in Table 8.1, along with the values in the experimental literature [327–334]. Since the computational values correspond to vertical excitation, whereas the experimental values represent combinations of various techniques, a direct comparison might not be appropriate, and there might be reorganization energies of 0.1–0.2 eV [195, 196]. Nonetheless, the computational values appear to be good proxies of the experimental values. Only, TDDFT underestimates the T_1 energies of tetracene and rubrene by 0.2 eV. We could not find the T_2 energies of DPA and rubrene in the experimental literature, but we extrapolate using anthracene and tetracene that TDDFT predicts accurate T_2 energies.

The results in Table 8.1 indicate that the T_2 state is not higher than twice the T_1 energy in these molecules. Even in tetracene and rubrene, the T_2 state should be about twice the T_1 energy, considering the 0.2 eV underestimation of the T_1 energy in TDDFT. Hence, there is no energetic reason that the triplet TT pair must dissociate into two triplets.

Meanwhile, the S_1 state is 0.1 eV lower than the T_2 state in DPA and rubrene. If the $T_2 - S_1$ spin-orbit coupling (SOC) were strong enough, then a significant portion of the T_2 exciton might undergo ISC to the S_1 state rather than internal conversion (IC) to the T_1 state.

We calculated the $T_2 \rightarrow S_1$ ISC rates in the frameworks of Marcus theory [192, 337] and Marcus-Levich-Jortner (MLJ) theory [194]. We provide the details in Supplementary Section F.1. As shown in Figure 8-2a, the $T_2 - S_1$ SOC is 7 and 60 times stronger

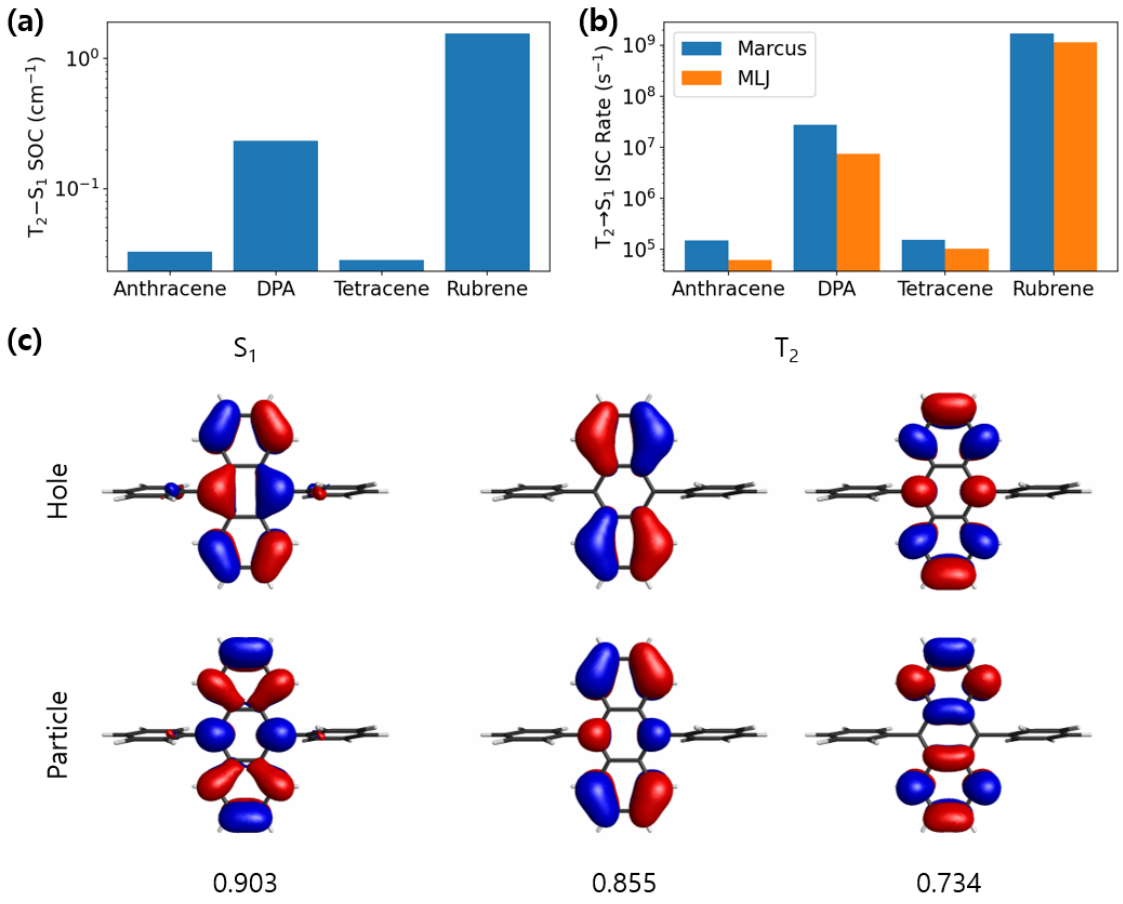

Figure 8-2: (a) $T_2 - S_1$ SOC; (b) $T_2 \rightarrow S_1$ ISC rates; and (c) NTO pairs of the S_1 and the T_2 states in DPA and their eigenvalues.

in DPA and rubrene than anthracene and tetracene, respectively. Together with adjustments of the S_1 and the T_2 energies, this gives $T_2 \rightarrow S_1$ ISC rates that are 10^2 and 10^4 times higher, respectively, as shown in Figure 8-2b. The absolute values of these rates should be taken with caution, since they rely on the harmonic approximation and the Franck-Condon (FC) approximation. However, the order-of-magnitude enhancements in the ISC rates might explain the observed TTA efficiencies of DPA and rubrene.

The SOC enhancement in DPA can be explained in terms of the excitation characters. According to El-Sayed's rule, the SOC of two states is nonzero only if they have different characters [176]. We conjecture that increasing the character difference might increase the SOC. See the natural transition orbital (NTO) pairs [284] of the S_1 and the T_2 states of DPA in Figure 8-2c. The orbitals on the anthracene core is identical to anthracene. However, the S_1 hole and particle delocalize on to the phenyl rings, whereas the T_2 exciton shows no such delocalization. This increases the $S_1 - T_2$ character difference. If our conjecture is correct, then we should be able to further enhance the SOC by pulling S_1 on to the phenyl rings.

We substituted the electron-withdrawing (EW) amide and the electron-donating (ED) amine groups at the $4'$ and $4''$ positions of DPA, as shown in Figure 8-3a. These do not appear to affect the delocalization of the T_2 exciton, but the amine group pulls the the S_1 hole on to the phenyl rings, as shown in Figure 8-3b. As expected, the $T_2 - S_1$ SOC and ISC rate have increased, as shown in Figure 8-3c,d. Meanwhile, the amide group reduces the SOC and the ISC rate, though there is no visible effect on the delocalization. These results support that the enhanced SOC in DPA are due to the differences in the excitation characters. Moreover, they suggest a more potent annihilator – $4', 4''$-diamino-9, 10-diphenylanthracene (Diamine).

As shown in Figure F-2, the qualitative trends in the $T_2 - S_1$ SOC and ISC rates are corroborated by a wide range of density functionals. Interestingly, rubrene appears to have a different mechanism that enhances the $T_2 - S_1$ SOC. The analysis of rubrene will be the topic of a separate study.

Another popular way to increase the SOC in organic molecules is using heavy

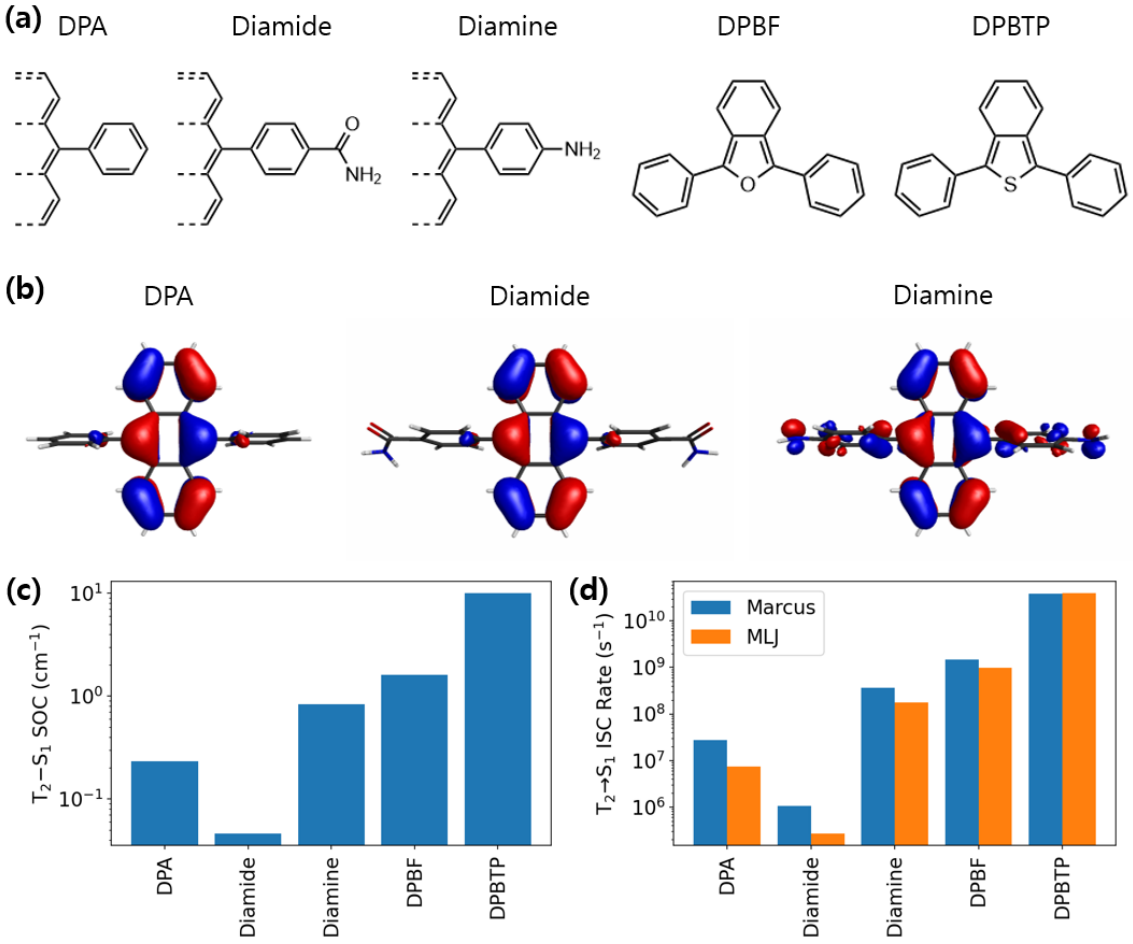

Figure 8-3: (a) Structures of the DPA and the DPBF derivatives; (b) S_1 holes of the DPA derivatives; (c) $T_2 - S_1$ SOC; and (d) $T_2 \rightarrow S_1$ ISC rates.

atoms. In this approach, the heavy atom should be near the core of the molecule to ensure excitation densities on the heavy atom. A well-known annihilator that satisfies this criterion is 1,3-diphenylisobenzofuran (DPBF). We substituted the oxygen in DPBF with a sulfur, as shown in Figure 8-3a. This 1,3-diphenylisobenzothiophene (DPBTP) exhibits a 6-fold enhancement in the $T_2 - S_1$ SOC and a 30-fold enhancement in the $T_2 \rightarrow S_1$ ISC rate. In particular, the $T_2 \rightarrow S_1$ ISC rate is predicted to enter the picosecond timescales.

8.3 Experiment

To verify the enhancement in the proposed molecules, we characterized the TTA efficiencies of Diamine, DPBTP, and their parent molecules. Photon upconversion in these systems is realized by introducing a triplet sensitizer, a molecule with rapid $S_1 \rightarrow T_1$ ISC, which generates and transfers a triplet to the annihilators upon photoexcitation, as shown in Figure 8-4a [180, 338, 339]. Based on the triplet energies of the candidates, platinum(II) octaethylporphyrin (PtOEP) was chosen as the sensitizer in DPA and Diamine, and platinum(II) tetraphenyltetrabenzoporphyrin (PtTPBP) in DPBF and DPBTP. The photon upconverters are thin films of annihilator:0.5 wt.% sensitizer:10 wt.% polystyrene. We provide the details in Supplementary Section F.2. As shown in Figure 8-4b, upconverted emissions are obvious when the PtOEP and the PtTPBP-sensitized upconverters are excited at $\lambda = 532\,\text{nm}$ and $\lambda = 635\,\text{nm}$, respectively.

We extracted the TTA efficiency by measuring the efficiencies of the other processes in Figure 8-4a. The efficiency of upconversion (ϕ_{UC}) is

$$\phi_{\text{UC}} = \frac{1}{2}\phi_{\text{ISC}} \times \phi_{\text{DET}} \times \phi_{\text{TTA}} \times (1 - \phi_{\text{BT}}) \times \phi_{\text{PL}} \tag{8.1}$$

where ϕ_{ISC} is the ISC efficiency of the sensitizer, ϕ_{DET} is the efficiency of triplet transfer to the annihilator, ϕ_{TTA} is the TTA efficiency of the annihilator, ϕ_{BT} is the singlet back transfer from the annihilator, and ϕ_{PL} is the photoluminescence quantum

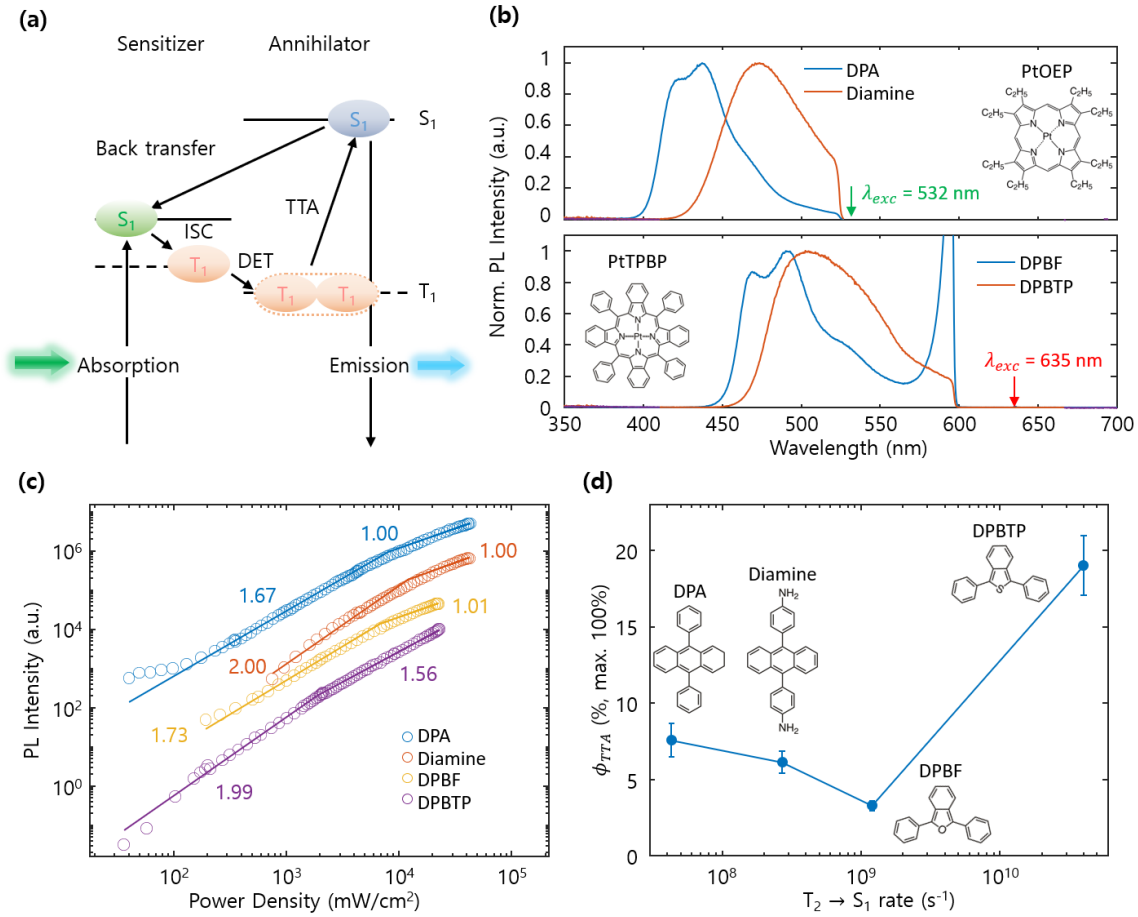

Figure 8-4: (a) Schematic of photon upconversion. (b) Upconverted PL spectra of DPA:PtOEP, Diamine:PtOEP, DPBF:PtTPBP, and DPBTP:PtTPBP. Inset: molecular structures of the sensitizers. The PtOEP-sensitized and the PtTPBP-sensitized upconverters were excited at 532 nm and 635 nm, respectively. A 532 nm notch filter and a 635 nm shortpass filter were applied to exclude the laser signal in the respective systems. (c) Plots of the upconverted PL intensity against the incident intensity. The numbers indicate the power laws. The absence of the linear regime in DPBTP indicates that the measured TTA efficiency is an underestimate of the optimal performance. (d) Plots of the observed TTA efficiency against the predicted $T_2 \rightarrow S_1$ ISC rate.

yield (PLQY) of the annhilator film. The factor of 1/2 reflects the convention of defining $\phi_{\mathrm{TTA}} = 100\,\%$ when $2\,\mathrm{T}_1 \rightarrow 1\,\mathrm{S}_1$.

Since no singlet emission is observed in PtOEP and PtTPBP, we assume $\phi_{\mathrm{ISC}} = 100\,\%$, We measured ϕ_{UC} and ϕ_{PL} with an integrating sphere via de Mello's method [340]. Next, ϕ_{DET} was estimated by

$$\phi_{\mathrm{DET}} = 1 - \frac{\phi_{\mathrm{PL}}(\lambda_{\mathrm{sen}})}{\phi_{\mathrm{PL,sen}}} \tag{8.2}$$

where $\phi_{\mathrm{PL,sen}}$ is the PLQY of the sensitizer and $\phi_{\mathrm{PL}}(\lambda_{\mathrm{sen}})$ is the PLQY of the upconverter at the wavelength of the sensitizer emission. In a similar manner, ϕ_{BT} was determined by

$$\phi_{\mathrm{BT}} = 1 - \frac{\phi_{\mathrm{PL}}}{\phi_{\mathrm{PL,ann}}} \tag{8.3}$$

where $\phi_{\mathrm{PL,ann}}$ is the PLQY of the annihilator and ϕ_{PL} is the PLQY of the upconverter at the wavelength of the annihilator emission. Due to the inhomogeneities of the films, we measured multiple spots on each sample and took the average of the calculated ϕ_{TTA} at every point. The results are summarized in Tables 8.2.

The intensity of upconverted PL due to TTA is known to exhibit a transition from quadratic to linear dependence as the incident intensity increases, where ϕ_{TTA} is optimized in the linear regime [341]. We provide the details in Supplementary Section F.3. As shown in Figure 8-4c, we were able to increase the excitation intensity until all but one of the upconverters attained a power law of 1. The exception, DPBTP, attains a minimum power law of 1.56, which implies that the measured ϕ_{TTA} is an underestimate of the optimal performance. Also, the devices have not undergone extensive optimization, so we focus on the relative values of ϕ_{TTA}.

As shown in Figure 8-4d, increasing the $\mathrm{T}_2 \rightarrow \mathrm{S}_1$ ISC rate does not always increase ϕ_{TTA}. In particular, ϕ_{TTA} is smaller in Diamine than DPA. Indeed, ϕ_{TTA} represents a competition of multiple channels. On the one hand, TTA competes with the nonradiative decay of the T_1 exciton. Modifications to increase the desirable $\mathrm{T}_2 \rightarrow \mathrm{S}_1$ SOC also increase the undesirable $\mathrm{T}_1 \rightarrow \mathrm{S}_0$ SOC, as shown in Figure F-3. In particular, the $\mathrm{T}_1 \rightarrow \mathrm{S}_0$ ISC rate is only 3 times higher in DPA than anthracene, whereas

	DPA:PtOEP	Diamine:PtOEP	DPBF:PtTPBP	DPBTP:PtTPBP
ϕ_{UC} (%)	0.69 ± 0.09	0.11 ± 0.01	$(6.78 \pm 0.74) \times 10^{-2}$	0.53 ± 0.06
$\phi_{\mathrm{PL,ann}}$ (%)	54.0 ± 1.16 (365 nm)	20.1 ± 0.36 (365 nm)	22.3 ± 0.86 (405 nm)	30.4 ± 0.57 (405 nm)
ϕ_{PL} (%)	10.39 ± 2.82	2.84 ± 0.12	4.97 ± 1.29	5.61 ± 2.55
ϕ_{BT} (%)	58.4	82.3	77.7	81.6
ϕ_{DET} (%)	85.0 ± 1.48	98.0 ± 0.50	82.7 ± 4.91	98.4 ± 0.23
ϕ_{TTA} (%)	7.58 ± 1.12	6.14 ± 0.74	3.30 ± 0.33	19.0 ± 1.96

Table 8.2: Experimental results.

it is 300 times higher in Diamine than DPA. Hence, we can rationalize why ϕ_{TTA} increases from anthracene to DPA, but not from DPA to Diamine.

On the other hand, the $T_2 - S_1$ ISC competes with the decay of the T_2 exciton. Again, these do not affect the efficiency of TTA per se, but they affect the "external" efficiency that we measure. Though *ab initio* calculation of IC rates is challenging [342–344], experimental values in related systems range in the picosecond [345–348] to nanosecond [349] timescales. On the order of tens to hundreds of picoseconds, the $T_2 \rightarrow S_1$ ISC might be one of the fastest photophysical processes in DPBTP. Hence, the ϕ_{TTA} enhancement from DPBF to DPBTP makes sense given the scales of the $T_2 \rightarrow S_1$ ISC rates.

8.4 Conclusion

Our results demonstrate the potential importance of the $T_2 \rightarrow S_1$ ISC in TTA UC. The energies of the S_1, T_1, and T_2 states are not sufficient to explain the limit-breaking TTA efficiencies in DPA and rubrene. Instead, there appears to be a correlation between the $T_2 \rightarrow S_1$ ISC rate and ϕ_{TTA}. Of course, a higher $T_2 \rightarrow S_1$ ISC rate does not guarantee a higher ϕ_{TTA} due to competition with the non-radiative decay of the T_1 and the T_2 excitons. We expect that these competing channels can be suppressed by optimizing the fabrication process and the choices of functional groups. Tuning the $T_2 \rightarrow S_1$ ISC rate might provide a strategy to systematic improvement of TTA materials.

8.5 Acknowledgements

The contents of this chapter have not been published yet. Ting-An Lin carried out the fabrication and the characterization of the photon upconverters. Shicheng Hu performed the electronic structure and transition rate calculations in the non-B3LYP functionals. This study was supported by the U.S. Department of Energy Office of Basic Energy Sciences (DE-FG02-07ER46474).

8.6 Supplementary Information

The Supplementary Information is available in Appendix F: calculation of ISC rates in the frameworks of Marcus theory and MLJ theory; fabrication of photon upconverters; dependence of the upconverted PL intensity on the incident intensity.

Chapter 9

Conclusion

We summarize the key results of Part II and discuss future directions.

In Chapter 6, we proposed a simple four-state model which explains the key prerequisites of efficient thermally activated delayed fluorescence (TADF) in organic donor-acceptor systems. The four spin-mixed diabatic states representing pure charge transfer (CT) and local excitations (LE) constitute the conceptual basis to discuss the electronic structure of TADF emitters. We show that the resulting lowest-lying adiabatic triplet (T_1) and singlet (S_1) excited states can have the necessary characteristics to ensure efficient TADF: a small singlet-triplet (ST) gap, different electronic character of S_1 and T_1, and a significant LE component in S_1.

Monte Carlo sampling reveals that the conditions for efficient TADF are relatively easy to satisfy in the parameter space. The statistical analysis of the data filtered for TADF activity reveals that a close mutual alignment of some pairs of parameters of the model is a prerequisite for TADF, while their magnitude fine-tunes its efficiency. This observation provides new design principles for optimization of organic emitters, which should aim at satisfying the parameter alignment criteria. In addition, by the means of combined molecular dynamics (MD) and time-dependent density functional theory (TDDFT) simulations for model exciplex systems, we showed that significant increase of TADF efficiency can be also obtained by exploration of the conformation space. This supports the vibronic mechanism for TADF, in which the non-Condon effects modulate the instantaneous TADF rates and maximize them for some nonequilibrium

conformations.

In Chapter 7, we studied direct maximization of the TADF rate in the conformation spaces of several TADF emitters. As desired, one of the model systems (DCzTrz) achieved a simultaneous improvement of the ST gap and the transition dipole moment (TDM), and its simulated TADF rate could be brought into the submicrosecond time scales. Even model systems that exhibited trade-off between a small ST gap and a large TDM were found to undergo TADF rate enhancements by two to three orders of magnitude. The conformational energy required to maximize the TADF rate can be as small as $193\,\mathrm{kJ\,mol^{-1}}$ even in the absence of energy penalty (Cz2BP), and the conformational energy can be as small as $51\,\mathrm{kJ\,mol^{-1}}$ with minimal loss in the TADF rate enhancement (Ac-MPM). Furthermore, the maximum TADF conformations of the model systems shared a number of structural motifs, such as the gooseneck at the donor-acceptor (DA) bond and the concerted rotation of the aromatic rings in the acceptor group. Although the physical intuition behind these motifs remains obscure, the opacity itself demonstrates the true value of conformational optimization: discovery of design principles that do not render themselves to deduction.

The conformational dependence of the TADF rate motivates the incorporation of conformational engineering into the TADF technology. Based on the results of TADF rate maximization with energy penalties and constrained energy minimization, the maximum TADF conformation of certain molecules, or another conformation that contains its essential features, might be synthesizable, given the high levels of strain that are within the reach of modern synthetic chemistry. Since the minimum energy conformation is not the best geometry in terms of the TADF rate, it would be desirable to manipulate the conformation in a way that enhances the TADF rate. Although the proposition might seem unorthodox in physical or organic chemistry, changing the properties of a molecule by changing its conformation is a standard in fields such as enzyme design. In the future, we hope to connect conformational optimization with experimental efforts and demonstrate that the electronic structures of TADF emitters can be improved in the real universe.

In Chapter 8, we worked in collaboration with the group of Professor Marc A.

Baldo to investigate the role of intersystem crossing (ISC) in enhancing the observed efficiency of triplet-triplet annihilation (TTA). Our results demonstrate the potential importance of $T_2 \rightarrow S_1$ ISC in TTA upconversion (UC). The energies of the S_1, T_1, and T_2 states are not sufficient to explain the limit-breaking TTA efficiencies in DPA and rubrene. Instead, there appears to be a correlation between the $T_2 \rightarrow S_1$ ISC rate and ϕ_{TTA}. Of course, a higher $T_2 \rightarrow S_1$ ISC rate does not guarantee a higher ϕ_{TTA} due to competition with the non-radiative decay of the T_1 and T_2 excitons. We expect that these competing channels can be suppressed by optimizing the fabrication process and the choices of functional groups. Tuning the $T_2 \rightarrow S_1$ ISC rate might provide a strategy to systematic improvement of TTA materials.

Based on these results, there are a couple of directions that require attention. First, we aim to find more ways to tune the $T_2 - S_1$ SOC and the rate of $T_2 \rightarrow S_1$ ISC. In particular, rubrene appears to have a different mechanism that enhances the $T_2 - S_1$ SOC than DPA (differential delocalization of the S_1 and the T_2 states) and DPBF (heavy atoms). Second, we want to explain the slow rate of $T_2 \rightarrow T_1$ internal conversion (IC). The rate of $T_2 \rightarrow T_1$ IC must be quite slow to enable the enhancement of observed TTA efficiencies via $T_2 \rightarrow S_1$ ISC. Exploring the electronic structures of the T_1 and the T_2 states in the vicinity of their minimum energy crossing point (MECP) might provide an explanation to the longevity of the T_2 state and suggest ways to further reduce the rate of $T_2 \rightarrow T_1$ IC.

Appendix A

Supplementary Information: Heterogeneous Pair Approximation of Methanol Oxidation

A.1 HMF and HHPA on Simple Model Systems

We compare the performances of HMF and HHPA on a number of simple model systems. In each model system, we assign one of the rate constants to a log-normal distribution of values, or a normal distribution of activation energies

$$\rho(k) \propto \frac{1}{k} \exp\left(-\frac{(\log k - \mu)^2}{2\sigma^2}\right) \tag{A.1}$$

where μ controls the position of the maximum; and σ controls the spread. We varied the mean and the spread of the rate constant, while the other rate constants were set to 1. Note that the mean of the log-normal distribution is

$$\langle k \rangle = \exp\left(\mu + \frac{\sigma^2}{2}\right) \tag{A.2}$$

which we took into account when choosing the value of μ.

The first model system is a *homodimer formation*

$$O_i \rightarrow A_i \tag{A.3}$$

$$A_i + A_j \xrightarrow{k_i} O_i + O_j \tag{A.4}$$

where we can interpret O as a vacancy and A as a monomer.

The second model system is a *heterodimer formation*

$$O_i \rightarrow A_i \tag{A.5}$$

$$O_i \rightarrow B_i \tag{A.6}$$

$$A_i + B_j \xrightarrow{k_i} O_i + O_j \tag{A.7}$$

where we can interpret O as a vacancy; and A and B as monomers.

The third model system is a *self-assembly*

$$O_i + A_j \xrightarrow{k_i} A_i + A_j \tag{A.8}$$

$$A_i \rightarrow O_i \tag{A.9}$$

where we can interpret O as a vacancy and A as a monomer.

The fourth model system is a *catalysis*

$$O_i \rightarrow B_i \tag{A.10}$$

$$B_i + A_j \xrightarrow{k_i} O_i + A_j \tag{A.11}$$

where we can interpret O as a vacancy; A as a catalyst; and B as a substrate.

In each model system, the bimolecular step correlates the probabilities of finding reactants (and products) next to each other. Even in the absence of static disorder, spatiotemporal patterns can emerge on the lattice. In the homodimer formation (Figure A-2a), the annihilation of AA pairs leaves alternating arrays of $AOAO$. In the heterodimer formation (Figure A-2b), the annihilation of AB pairs gives rise to monospecific islands of A and B. In the self-assembly (Figure A-2c), the deposition of

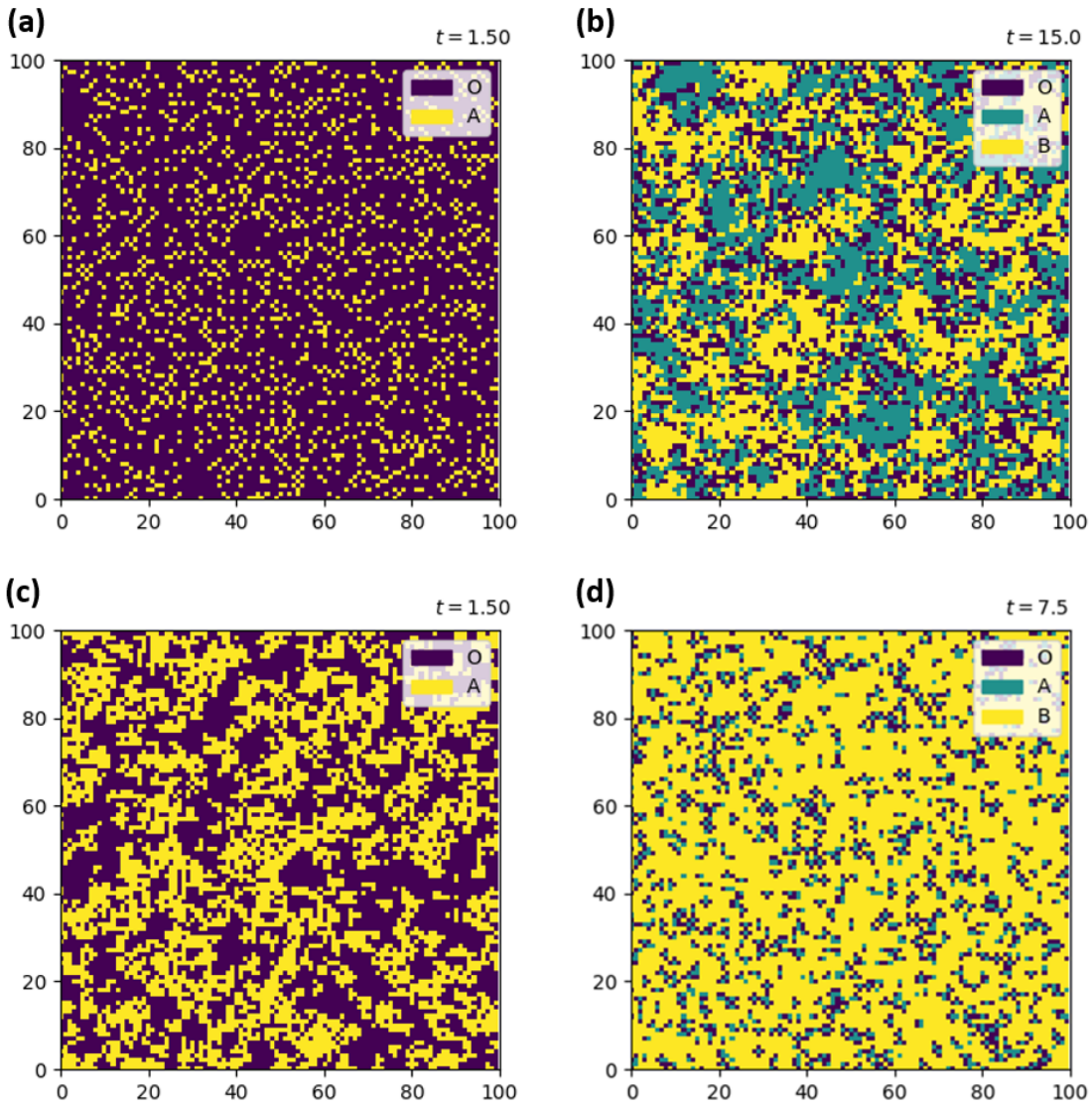

Figure A-1: Snapshots of KMC simulations on a 100×100 lattice: (a) homodimer formation at $k = 10$; (b) heterodimer formation at $k = 1$; (c) self-assembly at $k = 1$; and (d) catalysis at $k = 1$ and $[A] = 0.1$. There was no static disorder in the rate constants, and these are spatial correlations that are inherent to the reaction mechanism.

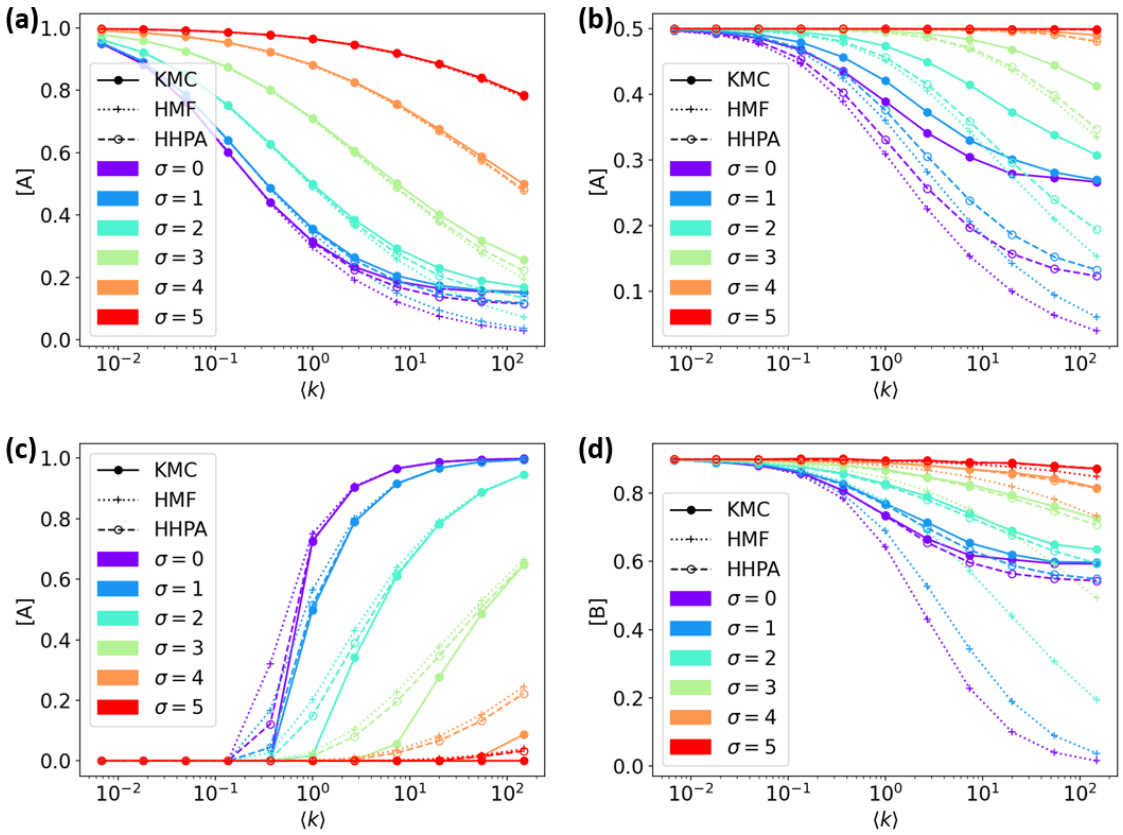

Figure A-2: Steady state coverages in HMF (crosses and dotted lines), HHPA (empty circles and dashed lines), and KMC (solid circles and solid lines): (a) homodimer formation; (b) heterodimer formation; (c) self-assembly; and (d) catalysis. The KMC coverages are averages of 20 or more simulations on independent 200×200 lattices.

A on top of existing clusters gives rise to snowflakes. In the catalysis (Figure A-2d), the annihilation of B next to A leaves O only in the vicinity of A. Since PA captures correlation upto and including pairs of sites, we expect that it would be accurate in systems with only short-range correlation, such as the homodimer formation and the catalysis, but become less accurate in systems with significant long-range correlation, such as the heterodimer formation and the self-assembly.

We compared the steady state coverages of the reactants in KMC, HMF, and HHPA. In the homodimer formation (Figure A-2a) and the catalysis (Figure A-2d), HHPA gives a semiquantitative approximation of the KMC coverages. In the heterodimer formation (Figure A-2b) and the self-assembly (Figure A-2c), HHPA gives results that are closer to HMF than KMC. These results are as expected given the nature of the correlation in these systems. Nonetheless, HHPA captures the qualitative behavior of the heterodimer formation (Figure A-2b). In the limit of high rate constant, the coverage asymptotes at a finite value, instead of vanishing altogether. Indeed, species A and B can coexist on the lattice if they can remain segregated. This kind of correlation cannot be described in HMF, but it can be recovered to some extent in HHPA. On a similar note, HMF also predicts a vanishing coverage in the catalysis (Figure A-2d). The coverage should asymptote at a finite value, since only the substrates in the vicinity of the catalysts can be annihilated. HHPA captures this short-range correlation and gives a qualitative improvement over HMF.

Samples of the time-dependent coverages are shown in Figure A-3. Mostly, the time-dependent coverages exhibit the same trends as the steady state coverages. In the homodimer formation (Figure A-3a) and the catalysis (Figure A-3d), HHPA gives a semiquantitative approximation of the KMC coverages. In the heterodimer formation (Figure A-3b) and the self-assembly (Figure A-3c), HHPA gives results that are closer to HMF than KMC. Only, HHPA does not capture the overshoot transient in the homodimer formation (Figure A-3a). The discrepancies between HHPA and KMC might be attributed to the missing long-range correlation in HHPA.

It is clear that methanol oxidation on TiO_2 would have significant short-range, but negligible long-range correlation. The longest-range correlation arises when two

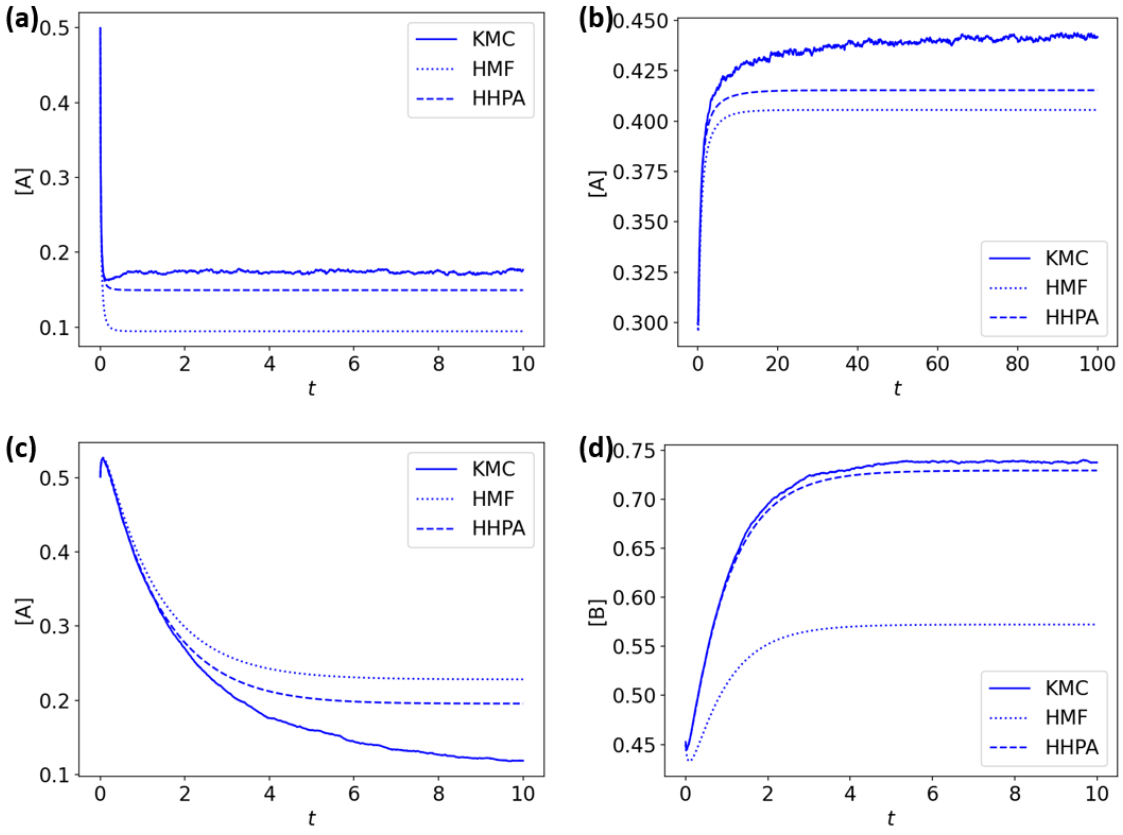

Figure A-3: Time-dependent coverages in HMF (crosses and dotted lines), HHPA (empty circles and dashed lines), and KMC (solid circles and solid lines): (a) homodimer formation at $\langle k \rangle = 3$ and $\sigma = 1$; (b) heterodimer formation at $\langle k \rangle = 1$ and $\sigma = 2$; (c) self-assembly at $\langle k \rangle = 2$ and $\sigma = 3$; and (d) catalysis at $\langle k \rangle = 2$ and $\sigma = 2$. These time-dependent coverages are single trajectories on a 200×200 lattice, and they have not been averaged like the steady state coverages in Figure A-2.

methanol molecules are neighboring the same O_b site. If one of the methanol molecules deposits a hydrogen on the O_b site, then the other methanol molecule cannot remove more than one hydrogen. This appears to have more in common with the alternating arrays of $AOAO$ in the homodimer formation than the monospecific islands of A and B in the heterodimer formation. Therefore, we expect HHPA to give a reasonable description of methanol oxidation on TiO_2.

A.2 Cross-Examination of Calibrated Parameters

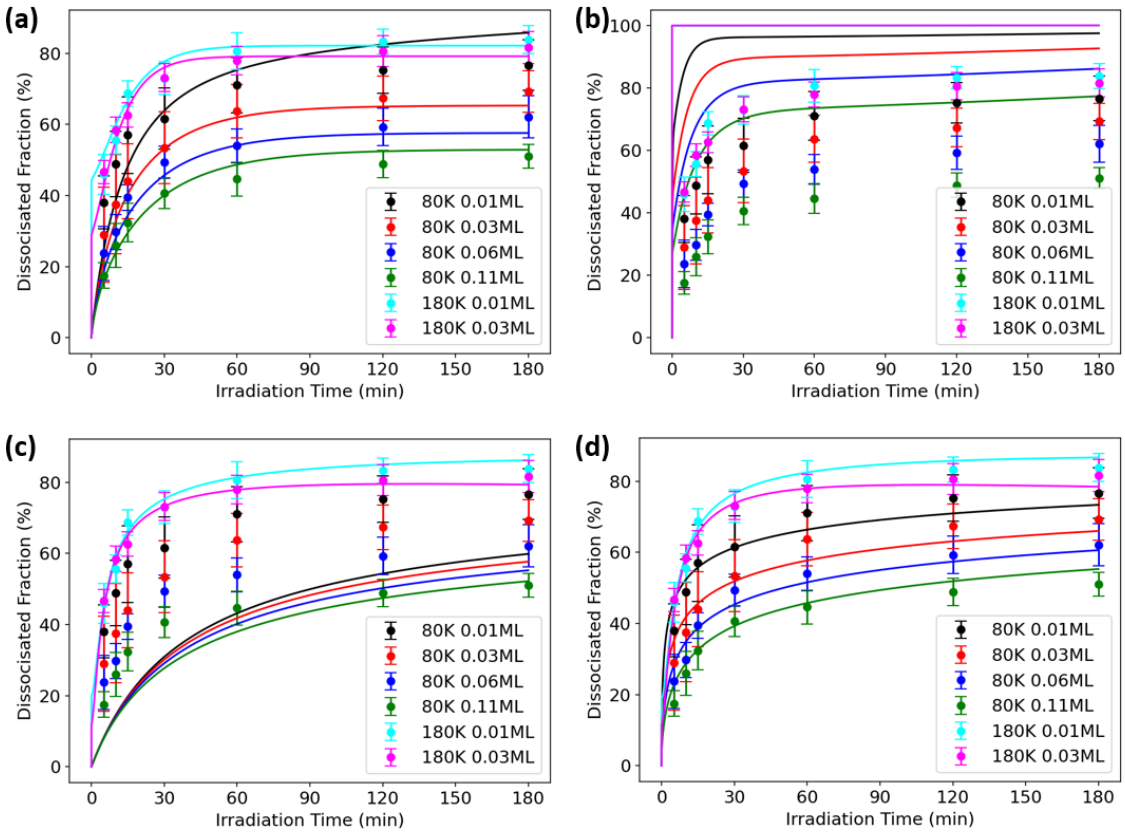

Figure A-4: Cross-examination of the calibrated parameters: (a) entering the MF parameters into PA, RMSNE = 0.753; (b) entering the PA parameters into MF, RMSNE = 6.587; (c) entering the HMF parameters into HHPA, RMSNE = 2.346; and (d) entering the HHPA parameters into HMF, RMSNE = 0.637.

Even though the MF methods attain root mean square normalized errors (RMSNEs) that are somewhat smaller than the PA methods, we emphasize that MF is not as faithful to the physical reality as PA, since the products of the methanol oxidation tend to remain next to each other. To demonstrate that MF and PA simulate somewhat different realities, we entered the parameters that were calibrated in HMF into HHPA and vice versa. As shown in Figure A-4a,b, respectively, entering the MF parameters into PA stretches the dynamics to the right, and entering the PA parameters into MF shrinks the dynamics to the left. Figure A-4c,d show similar patterns in HMF and HHPA. These trends make sense, since MF would underestimate the rate of the reverse reaction in the simulations and thus overestimate the rate constants in the regression. Interestingly, the simulated kinetics at 80 K tend to be impacted more than the simulated kinetics at 180 K. The errors in MF might be reduced at 180 K, as the diffusion of formaldehyde erases much of the correlation.

A.3 Modified Model

The modified model eliminates the steps going into and out of CH_3OH^+ in the original model (Figure 2-2). This reduces the number of parameters to 19: 2 charge transfer rate constants at 80 K; 2 charge transfer rate constants at 180 K; 7 activation energies; 7 partition functions; and the Urbach energy.

Figure A-5a,b show the simulated kinetics in uniform MF and PA, respectively. RMSNEs are 1.443 in MF and 1.381 in PA, which means that the simulated kinetics tend to be outside a standard deviation of the experimental kinetics. Using the modified model, we are unable to obtain RMSNE < 1 in uniform MF or PA. Visual inspection reveals serious issues in the simulated kinetics. In addition to the short time transient and the long time behavior that are also problematic in the original model, the simulated kinetics at 180 K exhibit significant divergence at different surface coverages, whereas the experimental kinetics are almost on top of each other.

Figure A-5c,d show the simulated kinetics in HMF and HHPA, respectively. RMSNEs are 0.910 in HMF and 0.981 in HHPA, which are again higher than the original

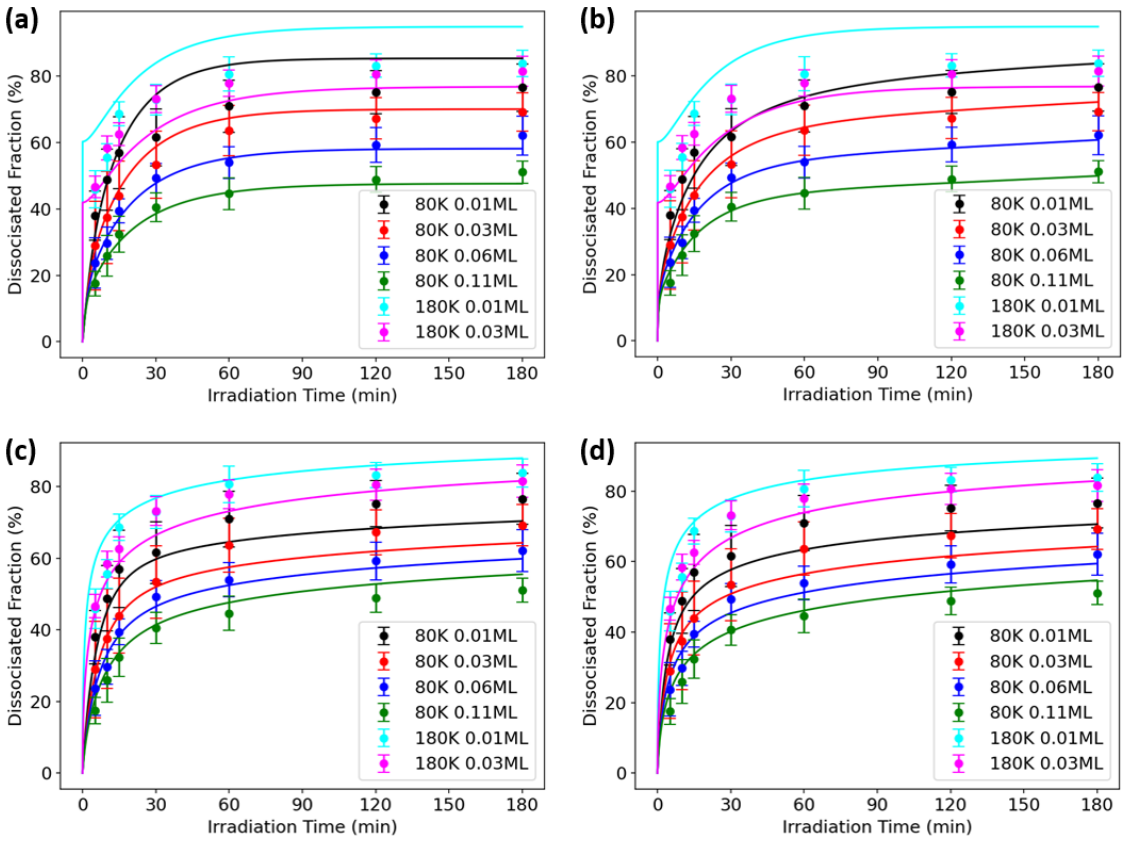

Figure A-5: Time-dependent dissociation fractions in the modified model with (a) MF, RMSNE = 1.443; (b) PA, RMSNE = 1.381; (c) HMF, RMSNE = 0.910; and (d) HHPA, RMSNE = 0.981.

model. The primary source of error appears to be the short time behavior at 180 K. Albeit not as severe as uniform MF and PA, the simulated kinetics at 180 K exhibit significant divergence at different surface coverages. Nonetheless, HMF and HHPA suppress the transient at 180 K, and the simulated kinetics resemble stretched exponentials, which slow down but do not reach a steady state in the simulation time.

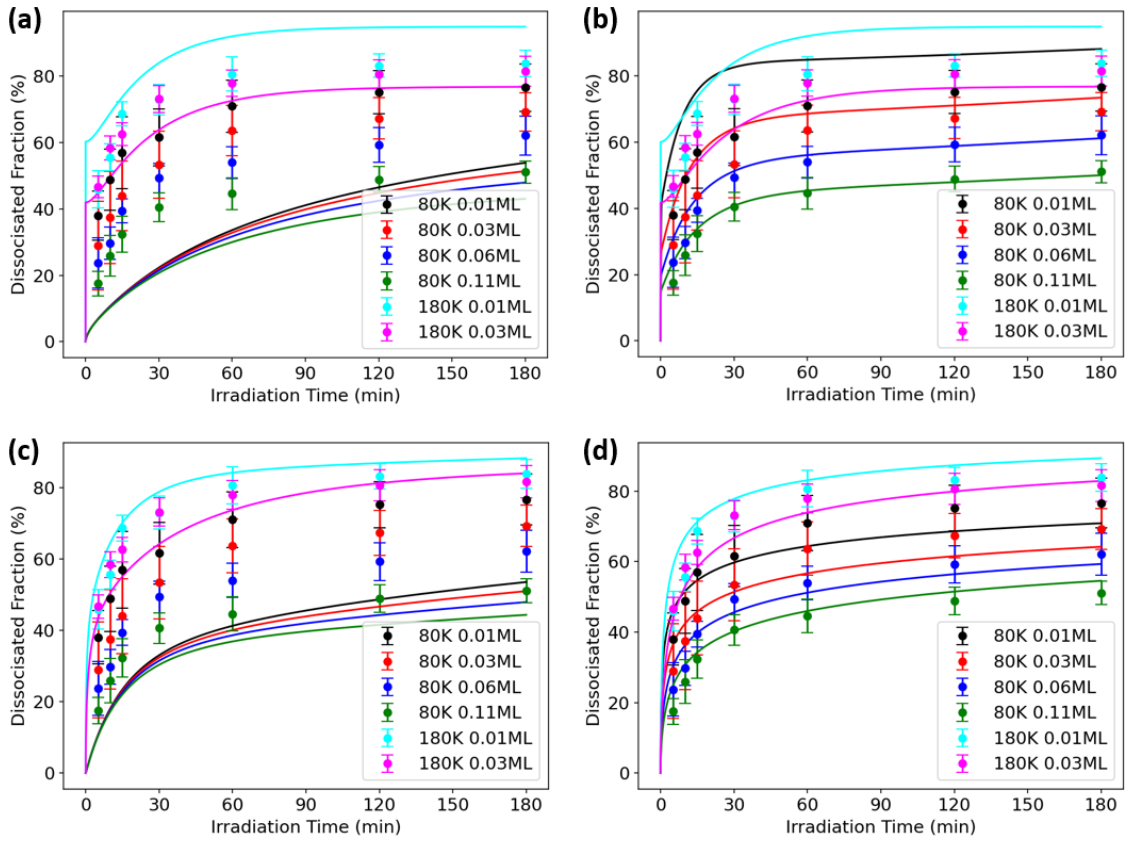

Figure A-6: Cross-examination of the calibrated parameters in the modified model: (a) entering the MF parameters into PA, RMSNE = 3.384; (b) entering the PA parameters into MF, RMSNE = 1.681; (c) entering the HMF parameters into HHPA, RMSNE = 2.471; and (d) entering the HHPA parameters into HMF, RMSNE = 1.025.

Figure A-6 shows the cross-examination of the calibrated parameters. Like the original model, entering the MF parameters into PA stretches the dynamics to the right, and entering the PA parameters into MF shrinks the dynamics to the left. Again, the simulated kinetics at 80 K tend to be impacted more than the simulated kinetics at 180 K.

On the one hand, most of the observations that we made in the original model are reiterated in the modified model. This shows that our findings, such as the relevance of static disorder in reproducing the observed kinetic and the differences of the simulated realities in the MF and the PA methods, do not depend on an elementary step whose feasibility is controversial. On the other hand, the quality of the fit in the modified model is much worse than the original model. Thus, including an alternative route to the OH bond cleavage entails a significant improvement in the simulated kinetics, and the hole-activated cleavage of the OH bond appears to play an important role in methanol oxidation.

A.4 Sensitivity Analysis

A.4.1 Original Model

The minimization of RMSNE appears to have multiple solutions. For the most part, the multiplicity can be attributed to parameters that do not have a well-defined optimum and do not matter as long as they are greater than or smaller than a certain value. Since the solutions give activation energies and partition functions that are within the expected value ranges, we have no means to identify the true answer. Thus, we use the solution with the smallest RMSNE as a starting point.

To establish the upper and the lower bounds on the calibrated parameters, we perturbed each of the parameters and recorded the response of RMSNE. The graphs of RMSNE in HMF are shown in Figures A-7–A-9, and the graphs of RMSNE in HHPA are shown in Figures A-10–A-12. There is no qualitative difference between HMF and HHPA. For most parameters, the perturbation causes RMSNE to increase on one side or both sides, as the parameter takes more and more undesirable values. In the cases of the formaldehyde diffusion (Figure A-10i,j) and the thermally activated reformation of the OH bond (Figure A-12g,h), RMSNE stops increasing at a finite value as the activation energies increases or the partition function decreases. This makes sense since the forward reaction embodies the primary features of methanol

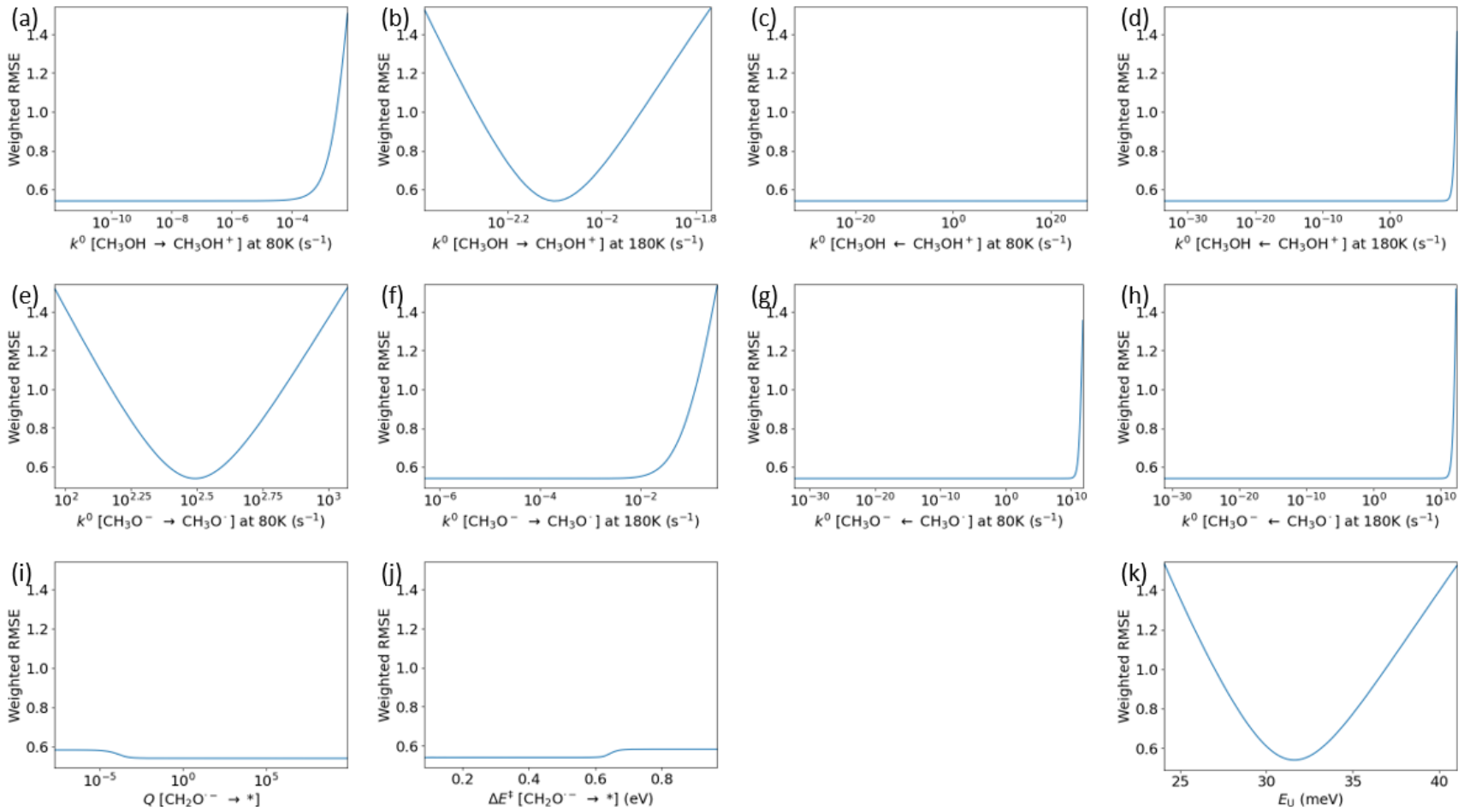

Figure A-7: Graphs of RMSNE in HMF (1/3).

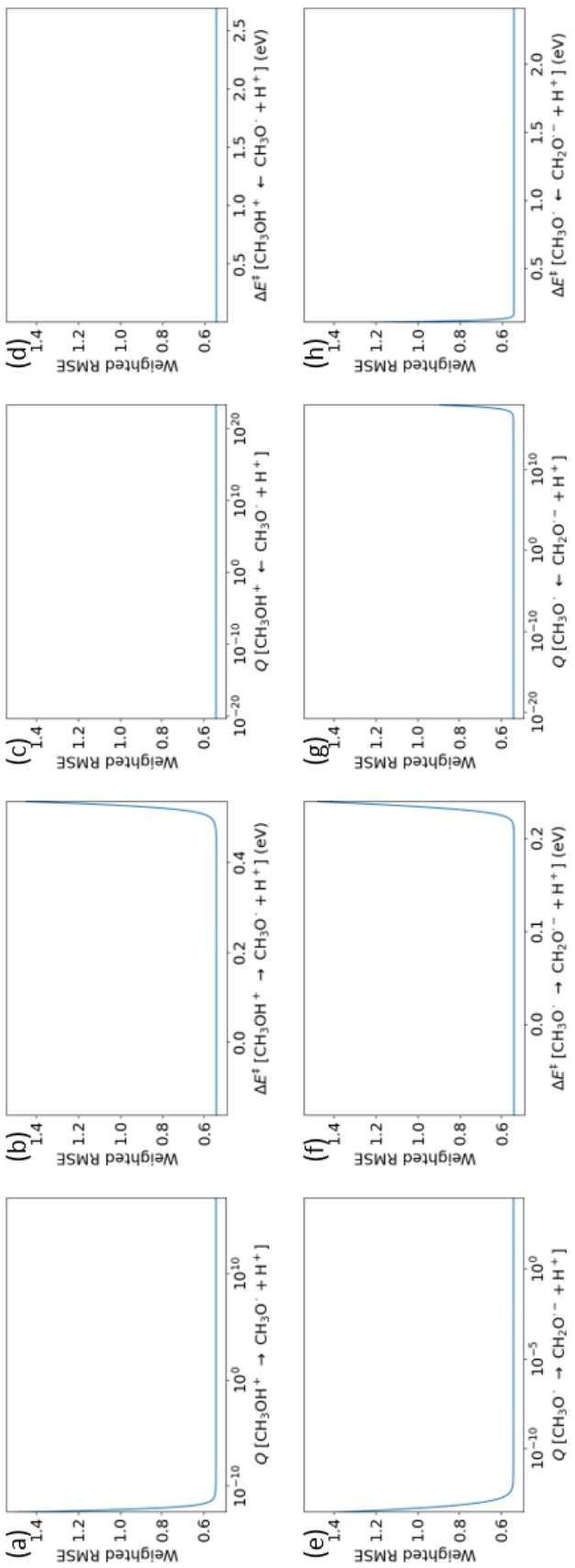

Figure A-8: Graphs of RMSNE in HMF (2/3).

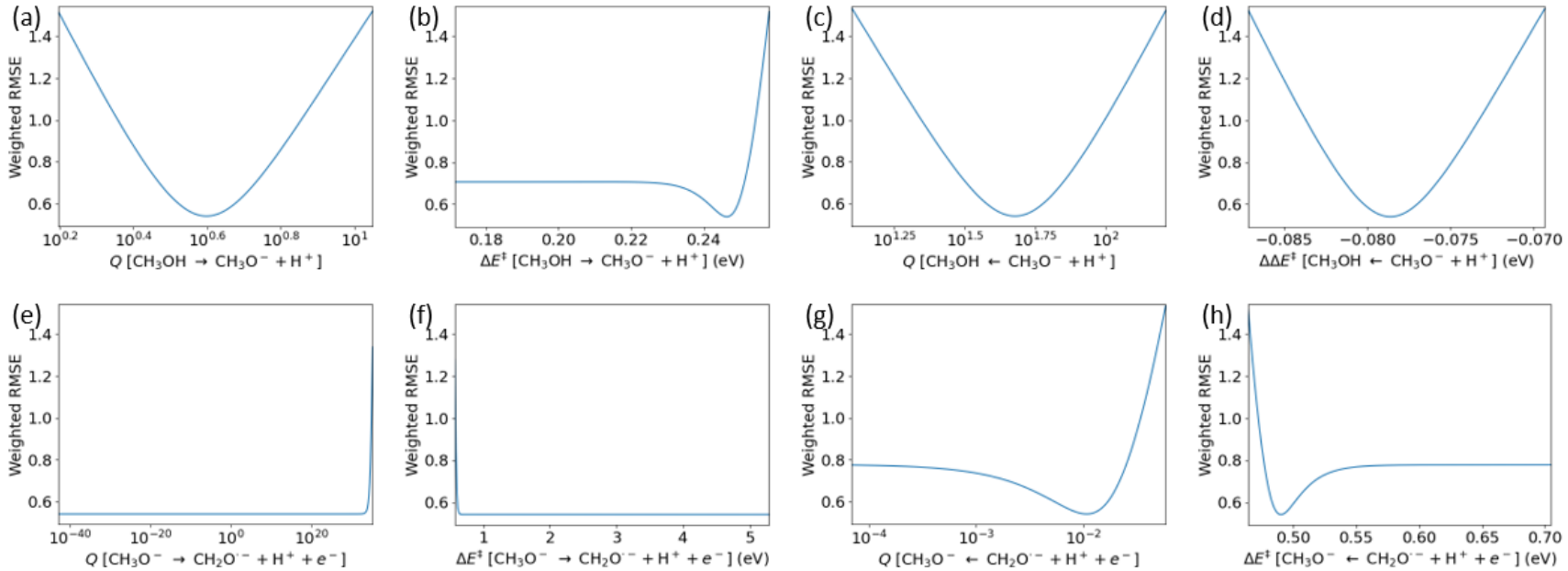

Figure A-9: Graphs of RMSNE in HMF (3/3). Notice that we are using the reverse barrier (perturbed) minus the forward barrier (fixed) as the x-axis in panel (d) – hence, the double delta.

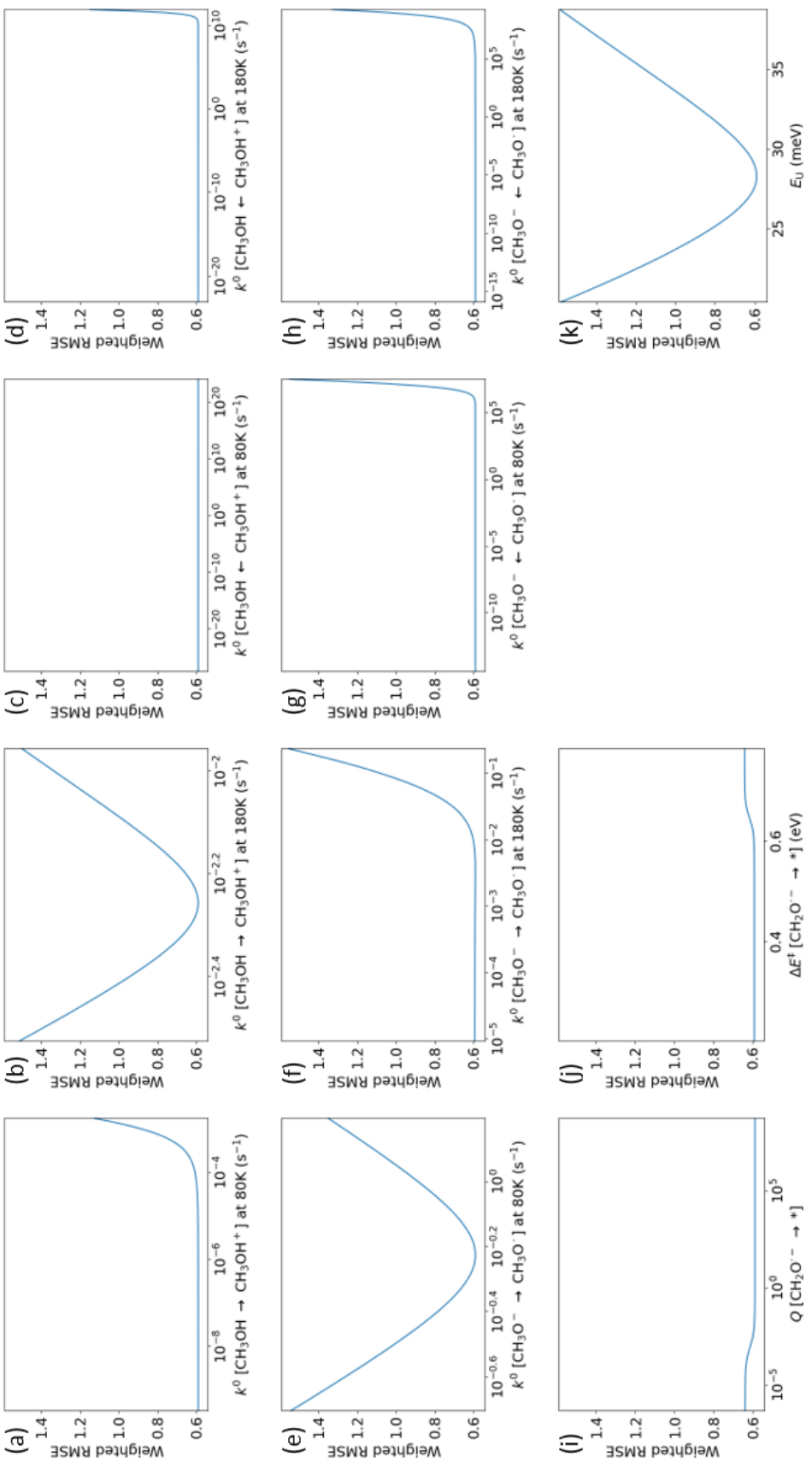

Figure A-10: Graphs of RMSNE in HHPA (1/3).

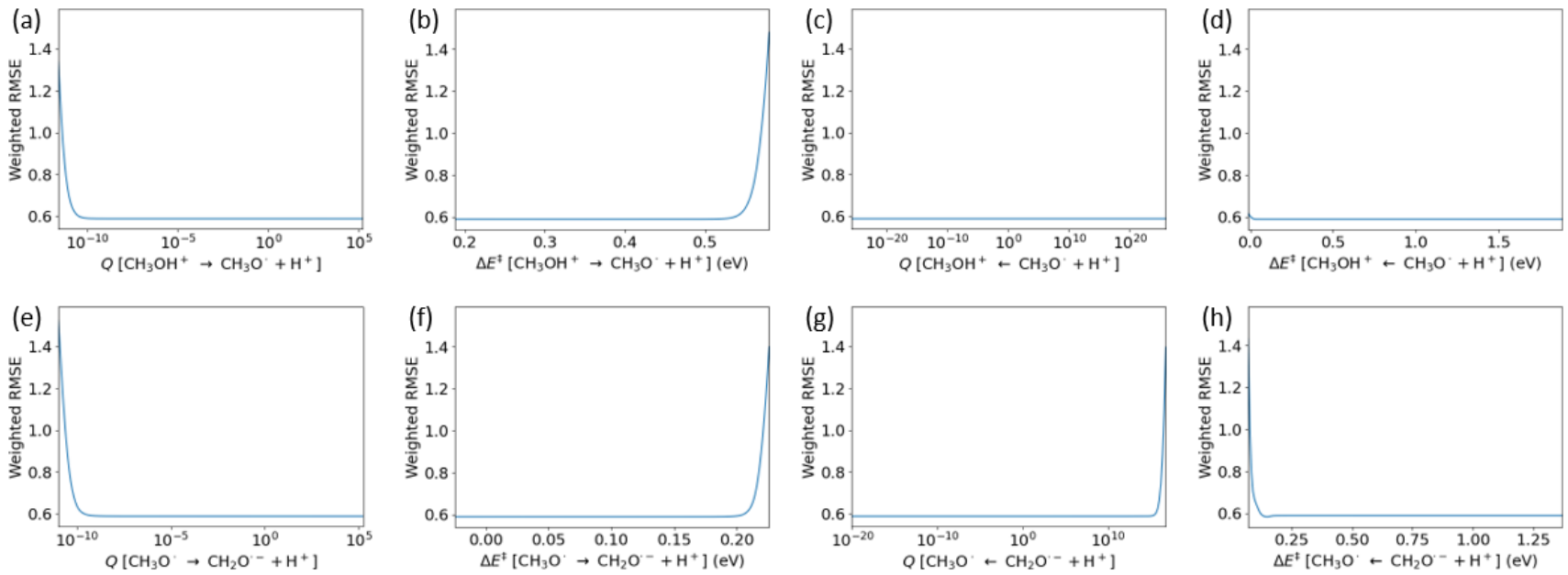

Figure A-11: Graphs of RMSNE in HHPA (2/3).

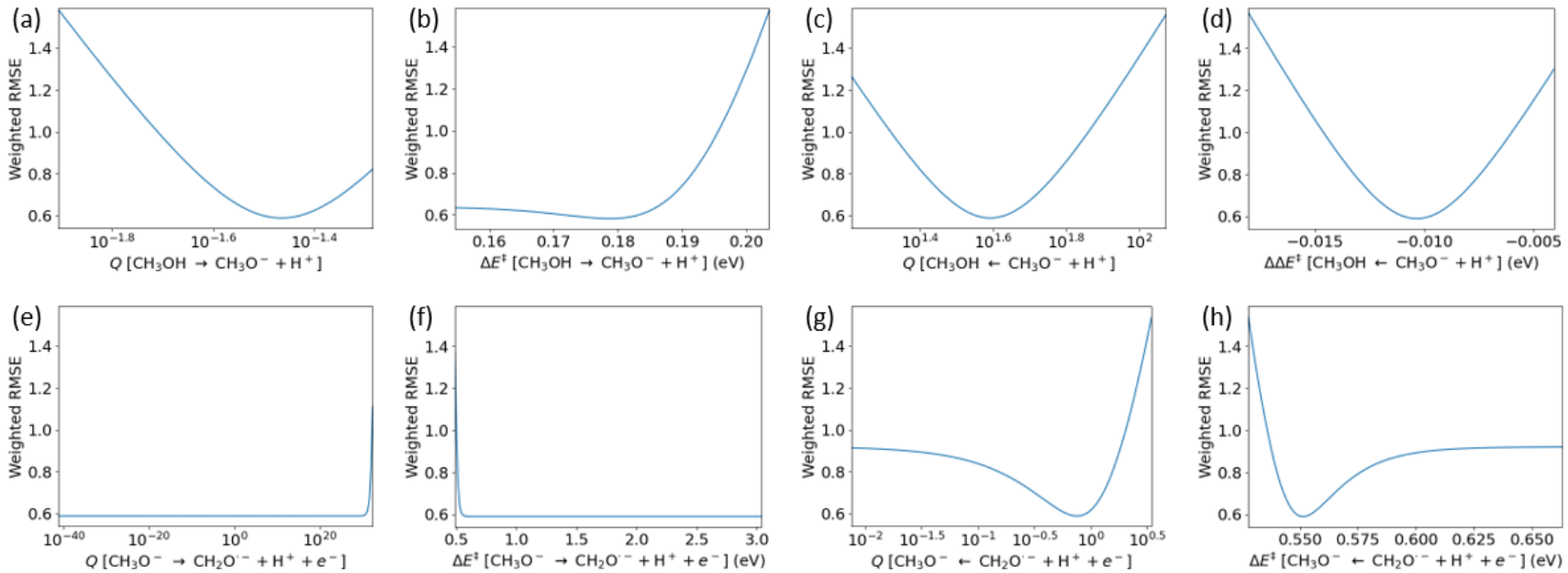

Figure A-12: Graphs of RMSNE in HHPA (3/3). Notice that we are using the reverse barrier (perturbed) minus the forward barrier (fixed) as the x-axis in panel (d) – hence, the double delta.

oxidation, and the reverse reaction and the diffusion are secondary.

Reaction	Parameter	HMF		HHPA	
		Forward	Reverse	Forward	Reverse
CH_3OH	$k^0(80\,\mathrm{K})$ (s^{-1})	$\lesssim 10^{-5}$	-	$\lesssim 10^{-5}$	-
$\rightleftharpoons CH_3OH^+$	$k^0(180\,\mathrm{K})$ (s^{-1})	$\approx 10^{-2.1}$	$\lesssim 10^{8}$	$\approx 10^{-2.3}$	$\lesssim 10^{10}$
CH_3O^-	$k^0(80\,\mathrm{K})$ (s^{-1})	$\approx 10^{2.5}$	$\lesssim 10^{10}$	$\approx 10^{-0.2}$	$\lesssim 10^{6}$
$\rightleftharpoons CH_3O^{\cdot}$	$k^0(180\,\mathrm{K})$ (s^{-1})	$\lesssim 10^{-2}$	$\lesssim 10^{10}$	$\lesssim 10^{-2}$	$\lesssim 10^{5}$
$CH_2O^{\cdot -} + Ti_{5c}$	Q	$\gtrsim 10^{-2}$		$\gtrsim 10^{-1}$	
$\rightarrow Ti_{5c} + CH_2O^{\cdot -}$	$\Delta E^{\ddagger}$ (eV)	$\lesssim 0.6$		$\lesssim 0.6$	
$CH_3OH^+ + O_b$	Q	$\gtrsim 10^{-10}$	-	$\gtrsim 10^{-10}$	-
$\rightleftharpoons CH_3O^{\cdot} + H^+$	$\Delta E^{\ddagger}$ (eV)	$\lesssim 0.5$	-	$\lesssim 0.5$	$\gtrsim 0.0$
$CH_3O^{\cdot} + O_b$	Q	$\gtrsim 10^{-12}$	$\lesssim 10^{16}$	$\gtrsim 10^{-9}$	$\lesssim 10^{15}$
$\rightleftharpoons CH_2O^{\cdot -} + H^+$	$\Delta E^{\ddagger}$ (eV)	$\lesssim 0.2$	$\gtrsim 0.2$	$\lesssim 0.2$	$\gtrsim 0.1$
$CH_3OH + O_b$	Q	$\approx 10^{0.6}$	$\approx 10^{1.7}$	$\approx 10^{-1.5}$	$\approx 10^{1.6}$
$\rightleftharpoons CH_3O^- + H^+$	$\Delta E^{\ddagger}$ (eV)	≈ 0.25	≈ 0.17	≈ 0.18	≈ 0.17
$CH_3O^- + O_b$	Q	$\lesssim 10^{33}$	$\approx 10^{-2.0}$	$\lesssim 10^{30}$	$\approx 10^{-0.1}$
$\rightleftharpoons CH_2O^{\cdot -} + H^+$	$\Delta E^{\ddagger}$ (eV)	$\gtrsim 0.7$	≈ 0.49	$\gtrsim 0.6$	≈ 0.55
Urbach energy	E_U (meV)	≈ 32		≈ 28	

Table A.1: Calibrated parameters.

Table A.1 summarizes the results of the sensitivity analysis. The activation energies and the partition functions are bounded in a way such that the bounds on the rate constants are unambiguous. If the activation energy is less than a certain value, then the partition function is greater than a certain value, and vice versa. There are a few parameters that do not have a bound in a reasonable range. Given that these parameters seem to have no consequence on the simulated kinetics, we suspect that the corresponding rate constants are bounded above in principle. To make sense of why the parameters are bounded as they are, we must cross-examine the rates of the reactions in Figure 2-4.

The dominant pathway of the forward reaction involves a hole transfer to the methoxy anion at 80 K and the methanol molecule at 180 K. In each case, the rates of the subsequent steps are almost equal to the rate of the hole transfer, which implies that the forward reaction almost always goes to completion once the hole transfer

takes place. Hence, the hole transfer to the methoxy anion at 80K and the methanol molecule at 180K are the rate-limiting steps at the respective temperatures. It makes sense that the rate constants of these steps have a well-defined optimum. Meanwhile, the subsequent hole-activated cleavages of the OH and the CH bonds do not matter as long as they are fast enough, so the rate constants are only bounded below. Since the quasi-equilibrium connects the methanol molecule and the methoxy anion into a single reservoir, the thermally activated cleavage of the CH bond and the hole transfer to the methanol molecule at 80 K and the methoxy anion at 180 K are competing with the rate-limiting steps at the respective temperatures. Because the competing steps must be slow enough to avoid altering the overall kinetics, the rate constants are only bounded above.

The dominant pathway of the reverse reaction is thermally activated at both temperatures. Since the reformation of the CH bond is the rate-limiting step, the rate constant has a well-defined optimum. On the other hand, the hole-activated pathway is competing with the thermally activated pathway, so the hole-activated reformation of the OH and the CH bonds and the back transfer of hole must be slow enough. As a result, the rate constants of these steps are only bounded above. Meanwhile, the diffusion of formaldehyde is significant at 180 K, and it might inhibit the reverse reaction. However, the rate constant is only bounded below, because it does not matter as long as the diffusion starts at some point between 80 K and 180 K and it is fast enough to outcompete the reverse reaction.

We now return to the thermally activated cleavage and reformation of the OH bond. It makes sense that the relative values of the activation energies and the partition functions have a well-defined optimum, since the rate-limiting steps depend on the methanol molecule at 80 K and the methoxy anion at 180 K. However, it is not obvious that the absolute values should have a well-defined optimum. In steady state kinetics, only the equilibrium constant and not the individual rate constants matter in a quasi-equilibrium step. In time-dependent kinetics, this is not true any more, because rapid equilibration can manifest as a transient. Indeed, the simulated kinetics in uniform MF and PA had an obvious transient at 180 K, and the simulated

kinetics in HMF and HHPA also had a transient, however inconspicous. On top of the lower bound which is needed to maintain the quasi-equilibrium, there must be an upper bound on the rate constants to suppress the transient. Furthermore, the interactions between the hole transfer steps and the thermally activated cleavage of the OH bond might help restrict the activation energies and the partition functions in the multidimensional space.

To verify that the 9 parameters have an optimum not only when perturbed one at a time, but also in the multidimensional parameter space, we constructed the compact model using just the 9 parameters. We continue this discussion in Section A.5.

A.4.2 Modified Model

Reaction	Parameter	HMF		HHPA	
		Forward	Reverse	Forward	Reverse
CH_3O^-	$k^0(80\,\mathrm{K})$ (s^{-1})	$\approx 10^{5.5}$	$\lesssim 10^{7}$	$\approx 10^{3.6}$	$\lesssim 10^{8}$
$\rightleftharpoons CH_3O^{\cdot}$	$k^0(180\,\mathrm{K})$ (s^{-1})	$\approx 10^{1.6}$	$\lesssim 10^{10}$	$\approx 10^{-0.6}$	$\lesssim 10^{9}$
$CH_2O^{\cdot -} + Ti_{5c}$	Q	-		-	
$\rightarrow Ti_{5c} + CH_2O^{\cdot -}$	$\Delta E^{\ddagger}$ (eV)	-		-	
$CH_3O^{\cdot} + O_b$	Q	$\gtrsim 10^{-7}$	$\lesssim 10^{14}$	$\gtrsim 10^{-11}$	$\lesssim 10^{16}$
$\rightleftharpoons CH_2O^{\cdot -} + H^+$	$\Delta E^{\ddagger}$ (eV)	$\lesssim 0.2$	$\gtrsim 0.2$	$\lesssim 0.2$	$\gtrsim 0.1$
$CH_3OH + O_b$	Q	$\approx 10^{1.2}$	$\approx 10^{1.5}$	$\approx 10^{-0.7}$	$\approx 10^{1.7}$
$\rightleftharpoons CH_3O^- + H^+$	$\Delta E^{\ddagger}$ (eV)	≈ 0.22	≈ 0.12	≈ 0.19	≈ 0.11
$CH_3O^- + O_b$	Q	$\lesssim 10^{36}$	$\lesssim 10^{-3}$	$\lesssim 10^{29}$	$\lesssim 10^{-7}$
$\rightleftharpoons CH_2O^{\cdot -} + H^+$	$\Delta E^{\ddagger}$ (eV)	$\gtrsim 0.5$	$\gtrsim 0.6$	$\gtrsim 0.6$	$\gtrsim 0.5$
Urbach energy	E_U (meV)	≈ 37		≈ 33	

Table A.2: Calibrated parameters in the modified model.

The graphs of RMSNE in HMF are shown in Figures A-13 and A-14, and the graphs of RMSNE in HHPA are shown in Figures A-15 and A-16. Table A.2 summarizes the results of sensitivity analysis on the modified model.

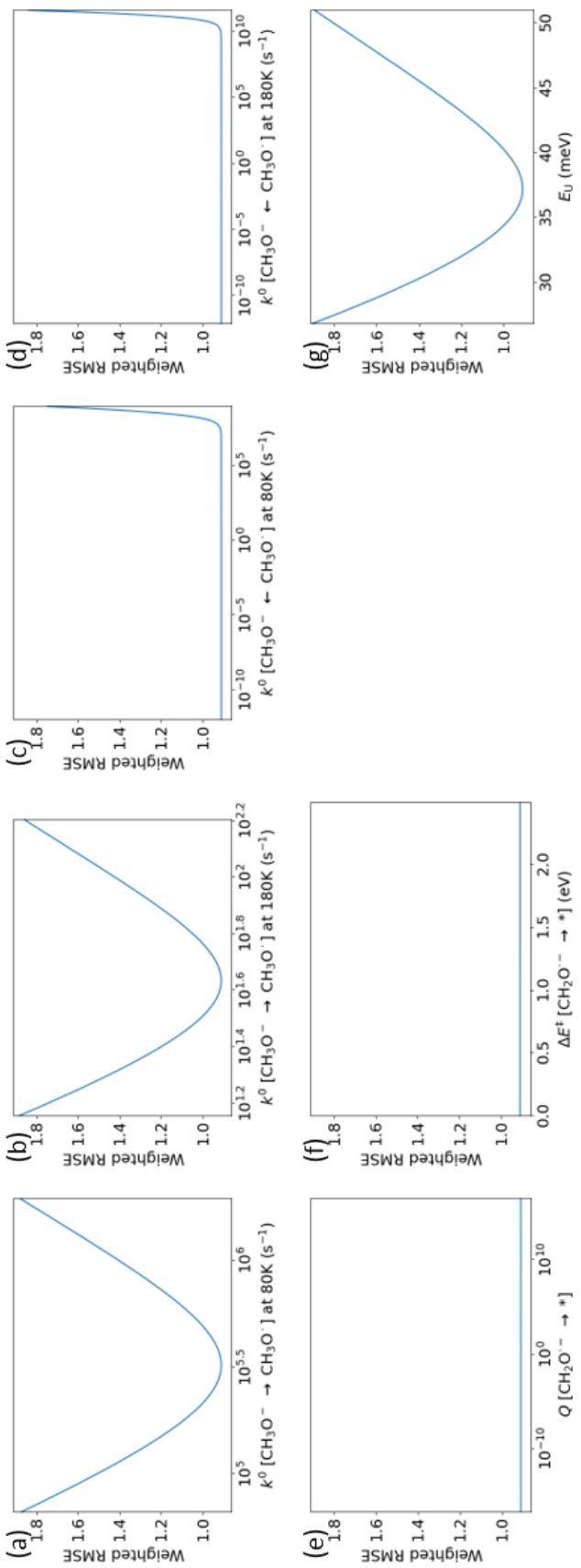

Figure A-13: Graphs of RMSNE in the modified model with HMF (1/2).

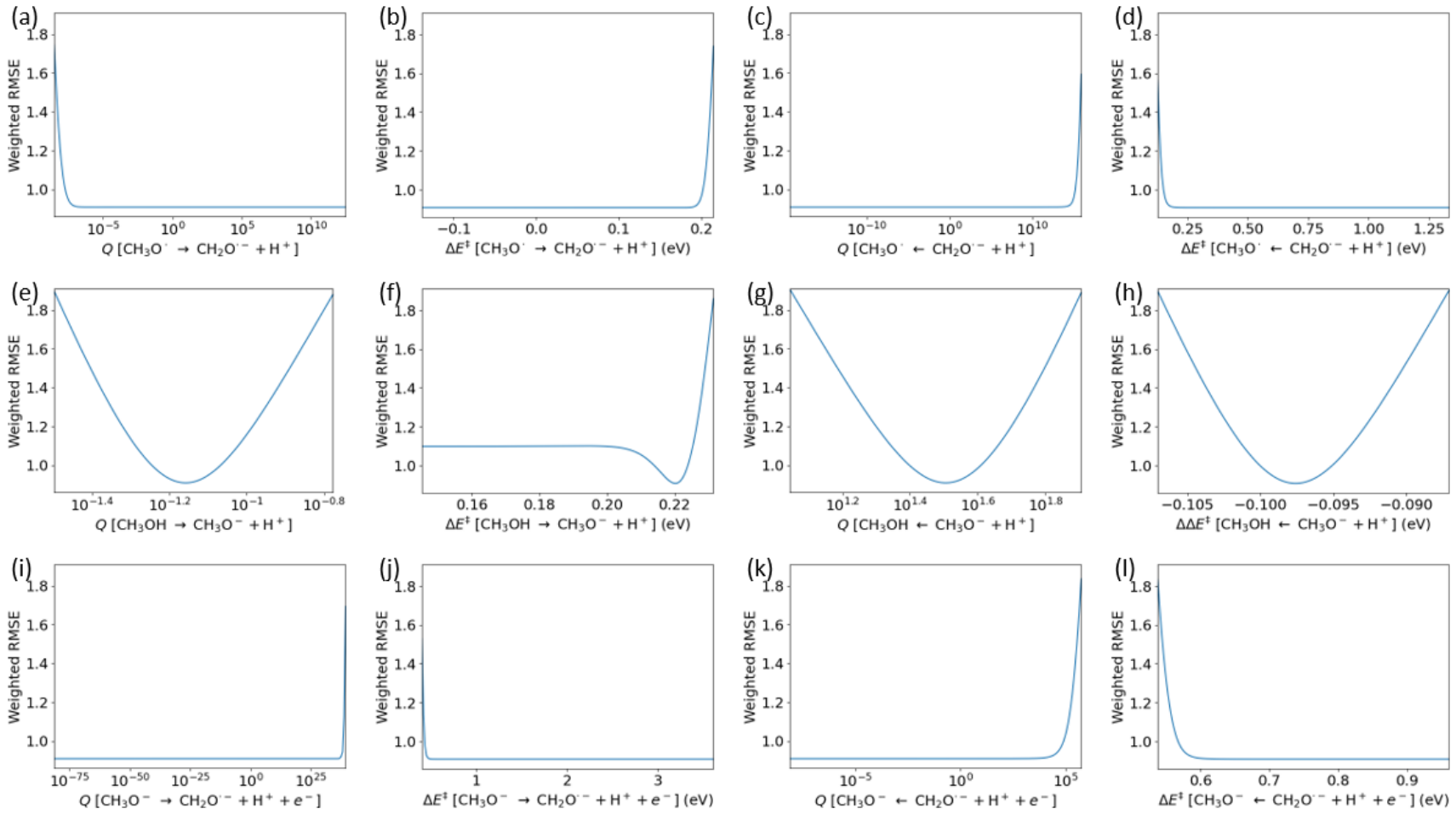

Figure A-14: Graphs of RMSNE in the modified model with HMF (2/2). Notice that we are using the reverse barrier (perturbed) minus the forward barrier (fixed) as the x-axis in panel (h) – hence, the double delta.

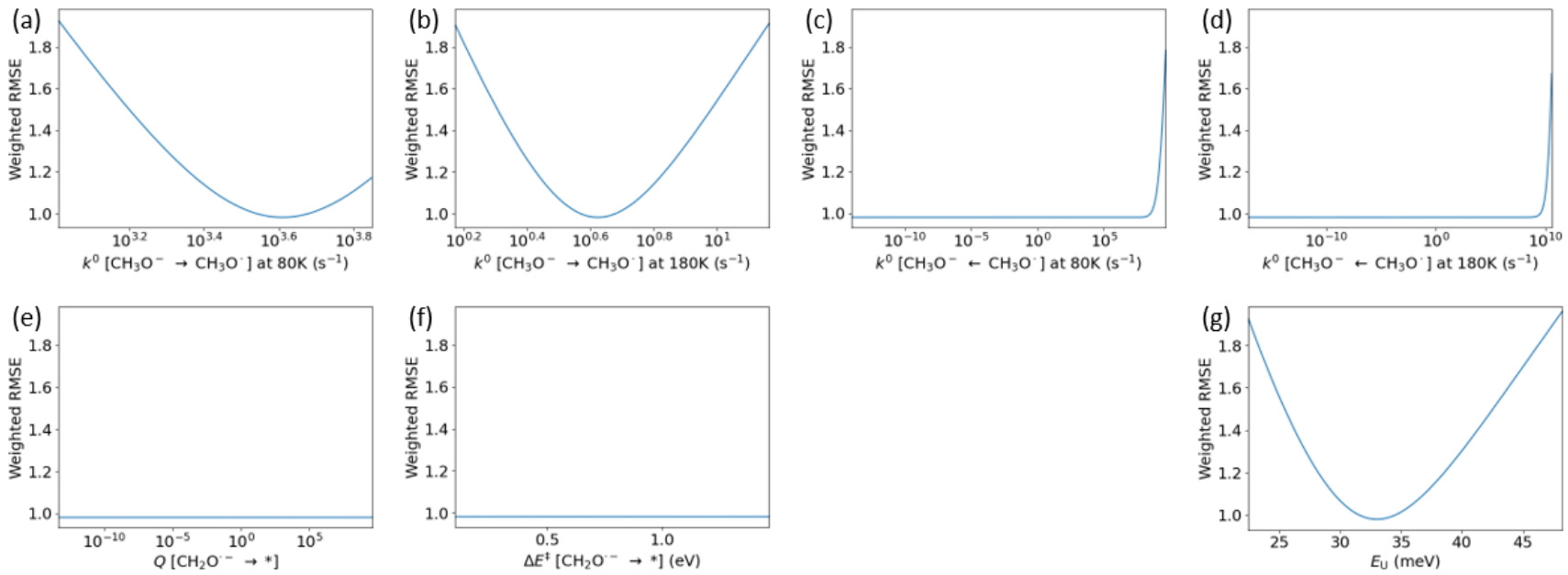

Figure A-15: Graphs of RMSNE in the modified model with HHPA (1/2).

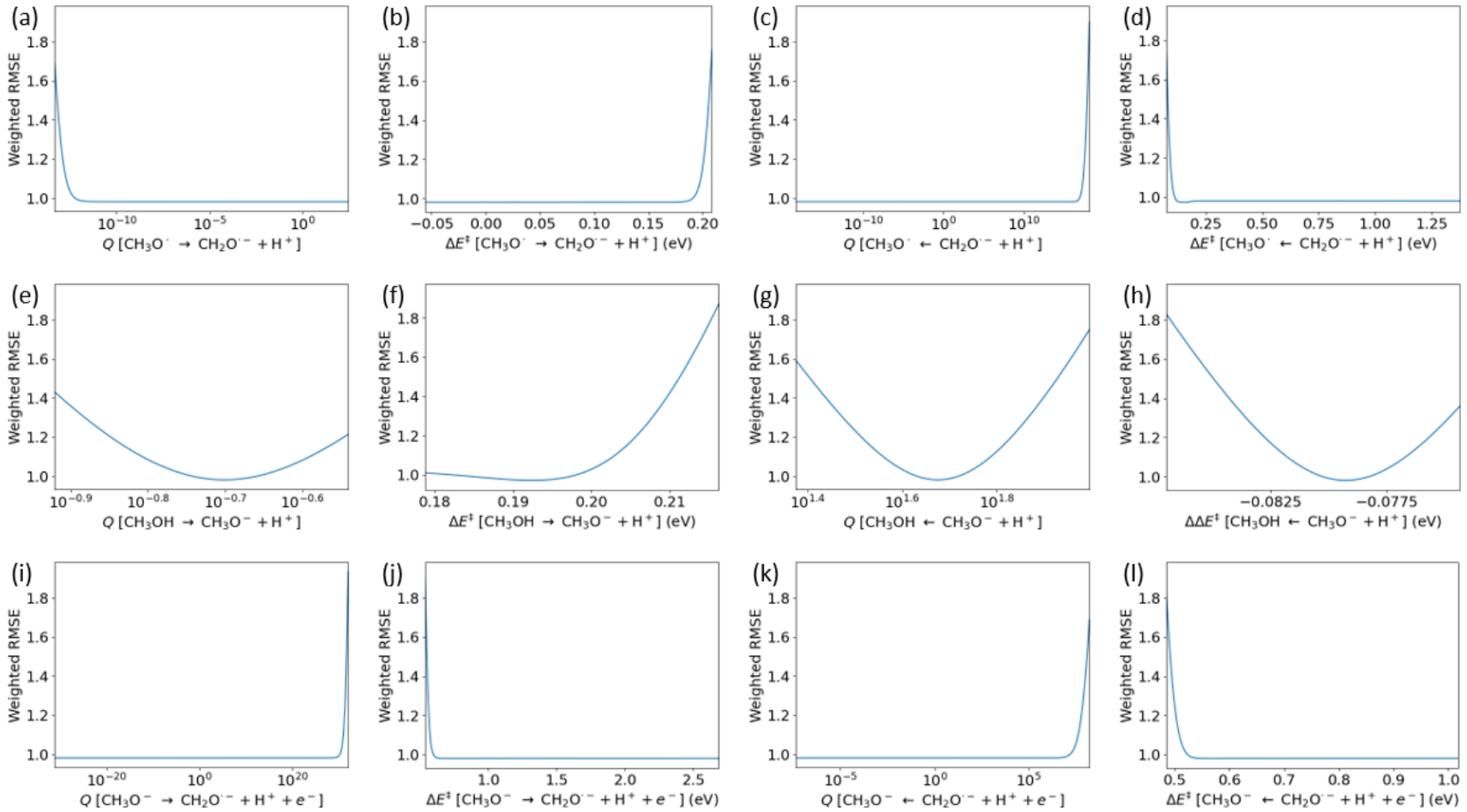

Figure A-16: Graphs of RMSNE in the modified model with HHPA (2/2). Notice that we are using the reverse barrier (perturbed) minus the forward barrier (fixed) as the x-axis in panel (h) – hence, the double delta.

Reaction	Parameter	Forward	Reverse
CH_3OH	$k^0(80\,\mathrm{K})$ (s^{-1})	0	0
$\rightleftharpoons CH_3OH^+$	$k^0(180\,\mathrm{K})$ (s^{-1})	parameter	0
CH_3O^-	$k^0(80\,\mathrm{K})$ (s^{-1})	parameter	0
$\rightleftharpoons CH_3O^{\cdot}$	$k^0(180\,\mathrm{K})$ (s^{-1})	0	0
$CH_2O^{\cdot -} + Ti_{5c}$	Q	1	
$\rightarrow Ti_{5c} + CH_2O^{\cdot -}$	$\Delta E^{\ddagger}$ (eV)	0.5	
$CH_3OH^+ + O_b$	Q	1	0
$\rightleftharpoons CH_3O^{\cdot} + H^+$	$\Delta E^{\ddagger}$ (eV)	0.1	-
$CH_3O^{\cdot} + O_b$	Q	1	0
$\rightleftharpoons CH_2O^{\cdot -} + H^+$	$\Delta E^{\ddagger}$ (eV)	0.0	-
$CH_3OH + O_b$	Q	parameter	parameter
$\rightleftharpoons CH_3O^- + H^+$	$\Delta E^{\ddagger}$ (eV)	parameter	parameter
$CH_3O^- + O_b$	Q	0	parameter
$\rightleftharpoons CH_2O^{\cdot -} + H^+$	$\Delta E^{\ddagger}$ (eV)	-	parameter
Urbach energy	E_U (meV)	parameter	

Table A.3: Construction of the compact model.

A.5 Compact Model

We constructed a compact model using only the 9 parameters that give a well-defined optimum when they are perturbed. The activation energies and the partition functions of the fast steps ensuing the rate-limiting steps and the diffusion of the formaldehyde were fixed at reasonable values, and the rate constants of the other steps were set to zero. Table A.3 summarizes the free and the fixed parameters.

As shown in Figure A-17, the compact model can attain RMSNEs on par with the original model. Although the transient in the simulated kinetics at 180 K appears to return in Figure A-17a,b, it is not as prominant as the transient in the uniform methods, and there are other solutions with similar RMSNEs that have negligible transients, as shown in Figure A-17c,d. Table A.4 summarizes the calibrated parameters and their deviations when we limit to solutions with RMSNE < 0.55 in HMF and RMSNE < 0.60 in HHPA. Considering the uncertainties in the density functional theory (DFT) estimates of the parameters, the parameters converge to a narrow range

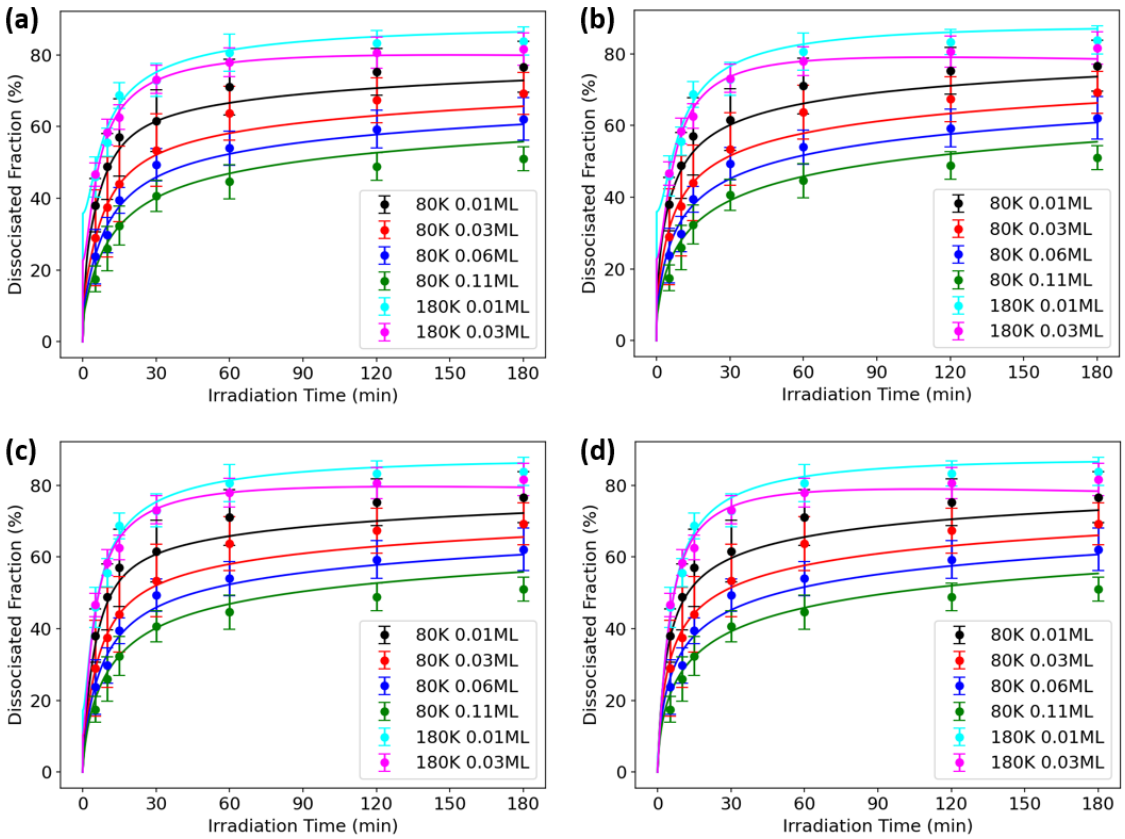

Figure A-17: Time-dependent dissociation fractions in the compact model with (a) HMF, RMSNE = 0.526; (b) HHPA, RMSNE = 0.581; (c) HMF, RMSNE = 0.541; and (d) HHPA, RMSNE = 0.595.

Reaction	Parameter	HMF	HHPA
$CH_3OH \rightarrow CH_3OH^+$	$k^0(180\,\mathrm{K})$ (s^{-1})	$10^{-2.12\pm0.03}$	$10^{-2.26\pm0.02}$
$CH_3O^- \rightarrow CH_3O^{\cdot}$	$k^0(80\,\mathrm{K})$ (s^{-1})	$10^{0.4\pm0.8}$	$10^{1\pm2}$
$CH_3OH + O_b$	Q	$10^{-1\pm1}$	$10^{-1.4\pm0.2}$
$\rightarrow CH_3O^- + H^+$	$\Delta E^{\ddagger}$ (eV)	0.22 ± 0.01	0.180 ± 0.003
$CH_3OH + O_b$	Q	$10^{1.3\pm0.7}$	$10^{0.6\pm0.5}$
$\leftarrow CH_3O^- + H^+$	$\Delta E^{\ddagger}$ (eV)	0.20 ± 0.02	0.14 ± 0.03
$CH_3O^- + O_b$	Q	$10^{\pm2}$	$10^{\pm1}$
$\leftarrow CH_2O^{\cdot -} + H^+$	$\Delta E^{\ddagger}$ (eV)	0.55 ± 0.06	0.56 ± 0.04
Urbach energy	E_U (meV)	32.2 ± 0.6	27.9 ± 0.5

Table A.4: Calibrated parameters in the compact model.

of values. Indeed, the 9 parameters appear to have a well-defined optimum in the multidimensional space.

We observe that the activation energies tend to be on the smaller end of the DFT estimates. The activation energy of the OH bond cleavage is 0.22 eV in HMF and 0.180 eV in HHPA, compared to the DFT estimates of 0.17–0.32 eV [79–81]. The activation energy of the CH bond reformation is 0.55 eV in HMF and 0.56 eV in HHPA, compared to the DFT estimates of 0.54–0.97 eV [79, 81]. Meanwhile, the activation energy of the OH bond reformation is 0.02 eV and 0.04 eV smaller than the OH bond cleavage in HMF and HHPA, respectively, inside the DFT estimate of 0.01–0.08 eV [79–81]. In spite of concerns about the underestimation of the barrier heights in some of the DFT studies [78, 81], the outcomes of the chemical kinetics appear to corroborate their results.

We were unable to find a reference on the Urbach energy in the reduced TiO_{2-x}. However, the Urbach energy of rutile TiO_2 nanoparticles has been reported to be 53 meV [350], and the band edge of the stoichiometric TiO_2 is known to be almost vertical at temperatures < 200 K [351]. We expect the Urbach energy of the reduced TiO_{2-x} to be somewhere between these limits. Thus, the Urbach energy of 32 meV in HMF and 28 meV in HHPA might be reasonable.

It is also worth noting that many of the parameters have nonoverlapping values in HMF and HHPA. In the hole transfer to the methanol molecule at 180 K, the HMF value of k^0 is somewhat greater than the HHPA value of k^0. Nonetheless, the ensemble average rate constants might be similar, since the Urbach energy is also greater in HMF. In the thermally activated cleavage and reformation of the OH bond, the activation energies in HMF are greater than those in HHPA. While the partition functions should counteract the differences at 180 K, the activation energies would dominate at 80 K, making the rate constants smaller in HMF. These results resonate the fact that MF and PA simulate somewhat different realities.

A.6 Distributions of Coverages and Rates

This section presents a complete collection of the time-averaged and the time-dependent distributions in the original, modified, and compact models.

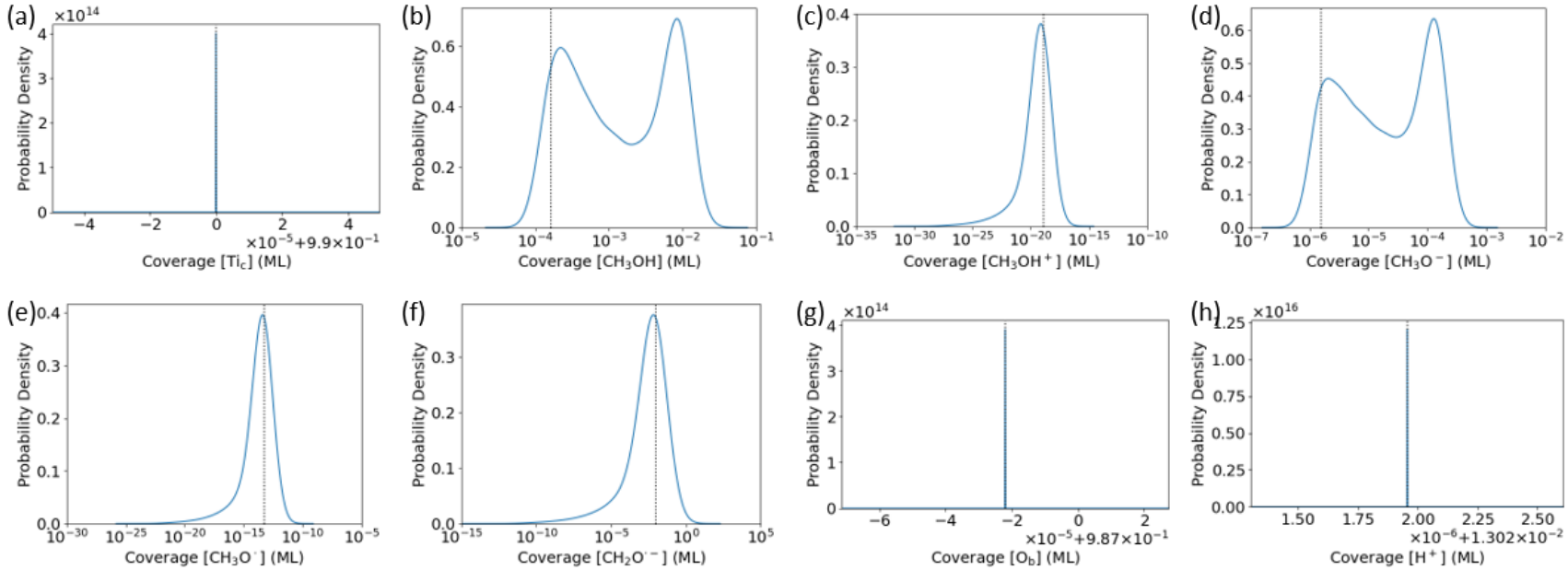

Figure A-18: Time-averaged distributions of the coverages at 80 K in HHPA.

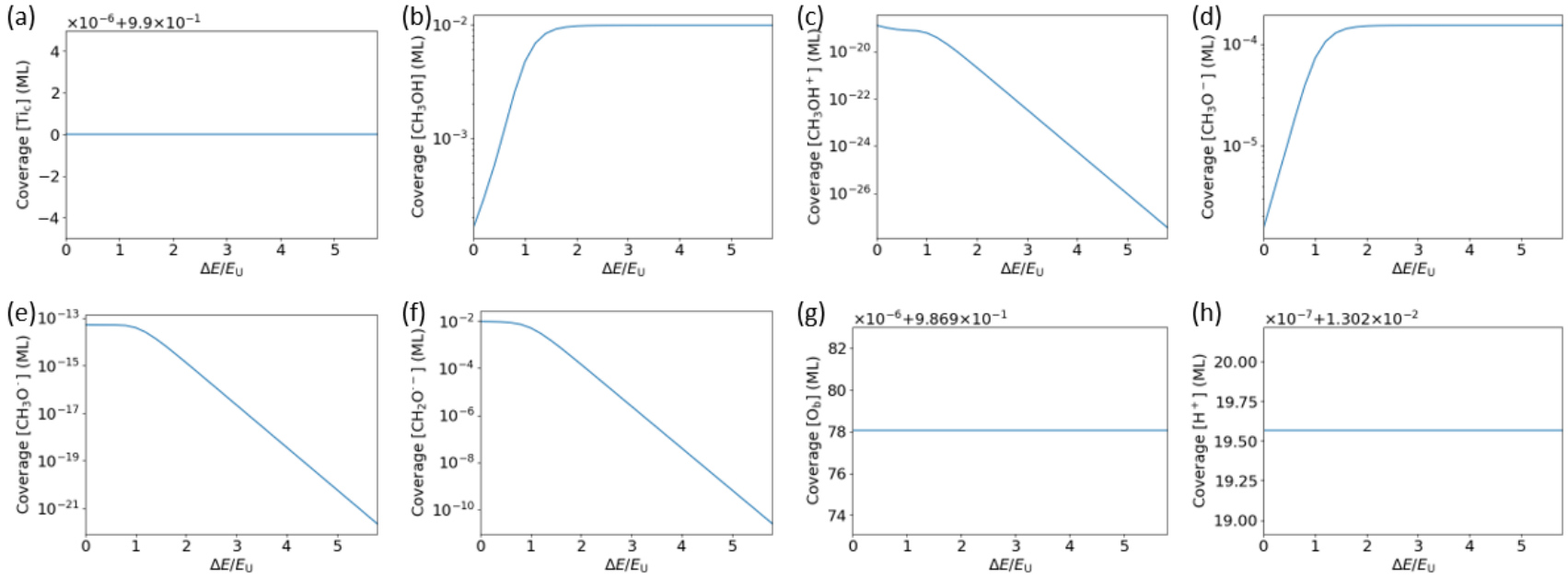

Figure A-19: Time-averaged coverages as a function of the trap energy at 80 K in HHPA.

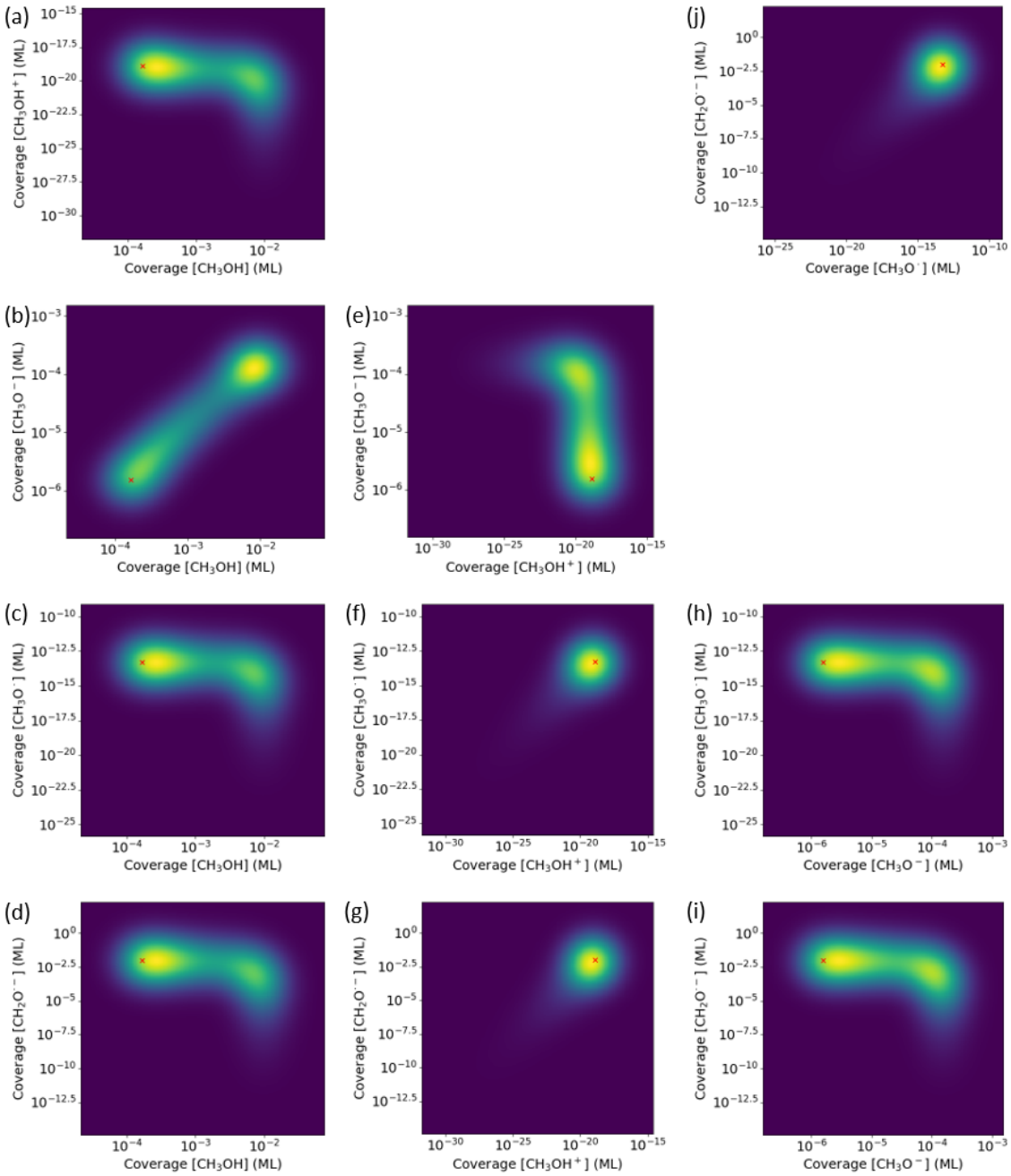

Figure A-20: Time-averaged 2D distributions of the coverages at 80 K in HHPA.

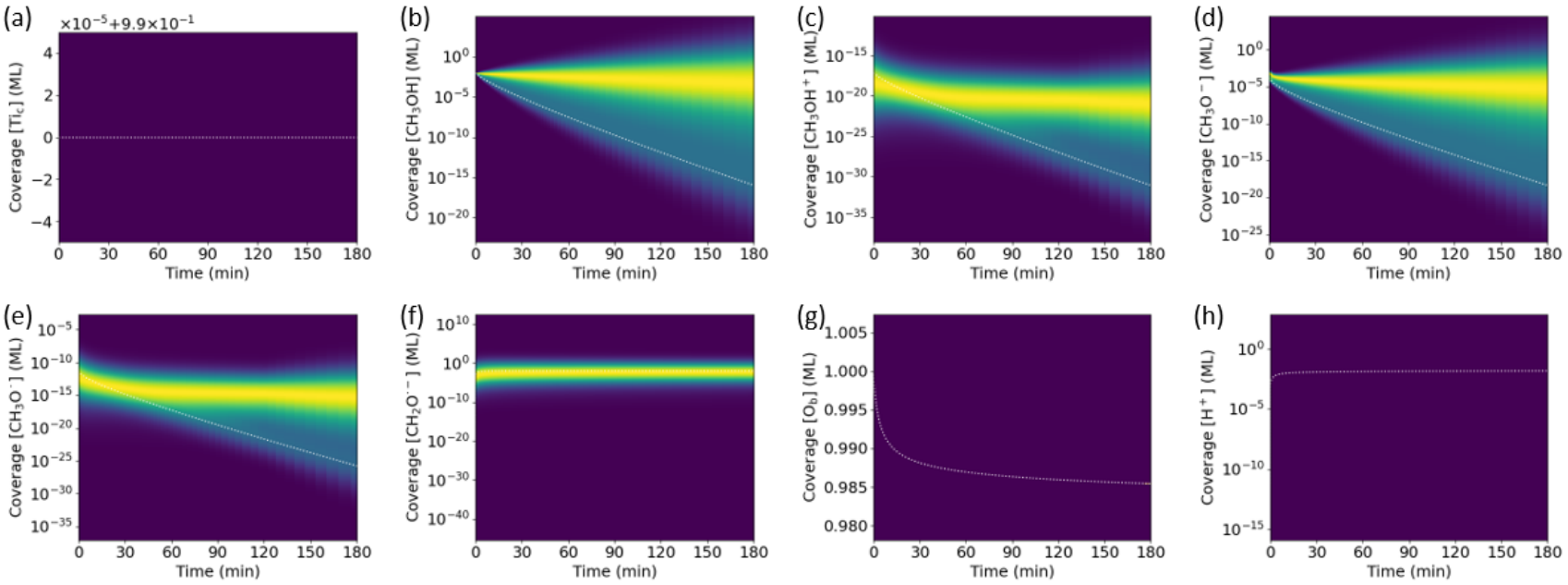

Figure A-21: Time-dependent distributions of the coverages at 80 K in HHPA.

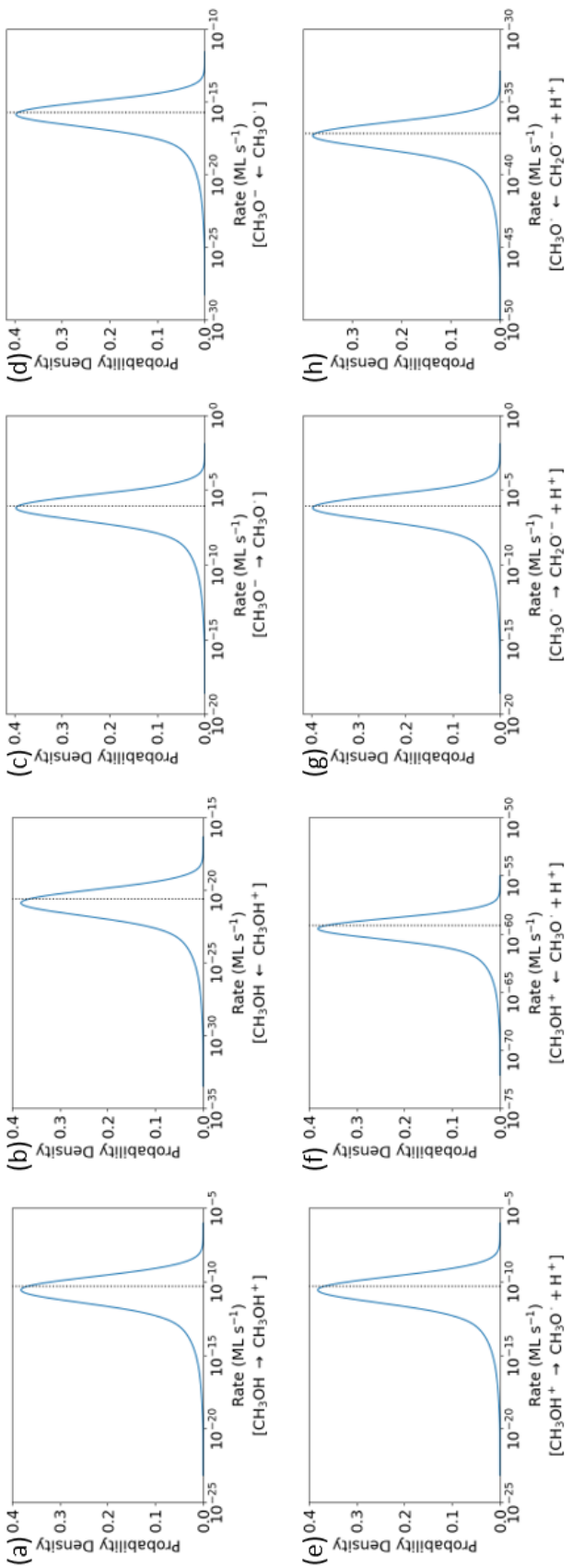

Figure A-22: Distributions of the rates at 80 K in HHPA (1/2).

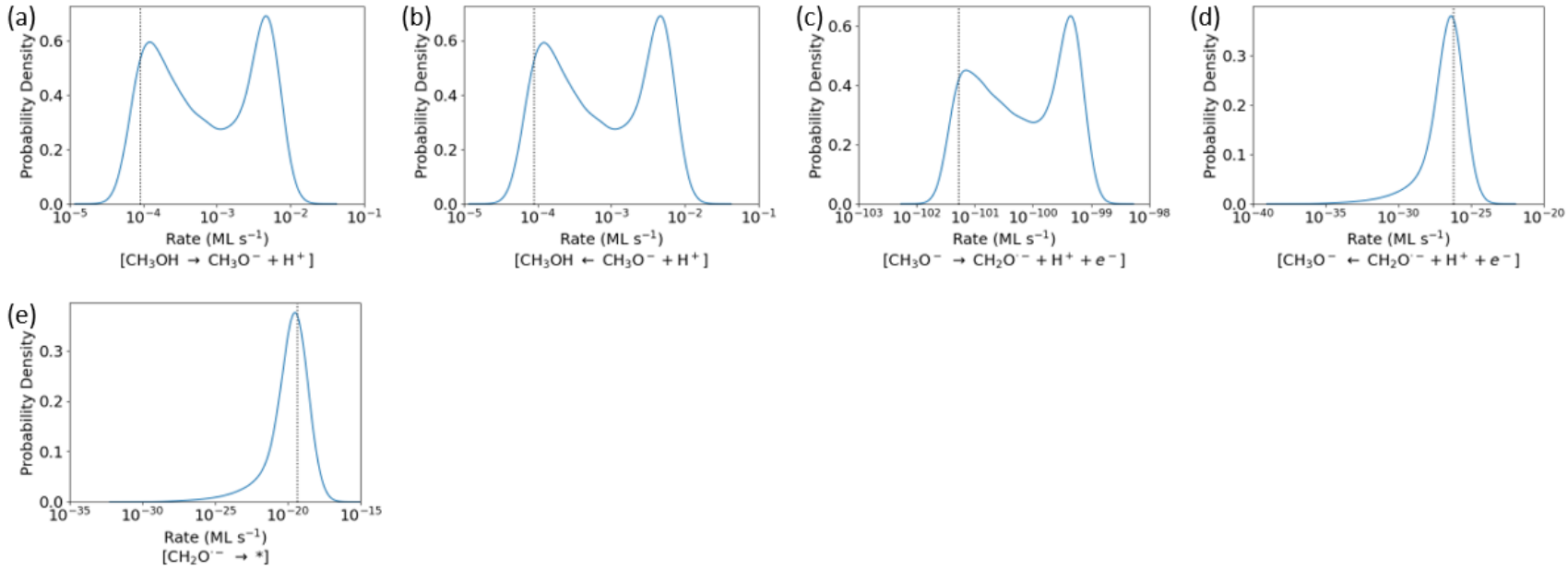

Figure A-23: Distributions of the rates at 80 K in HHPA (2/2).

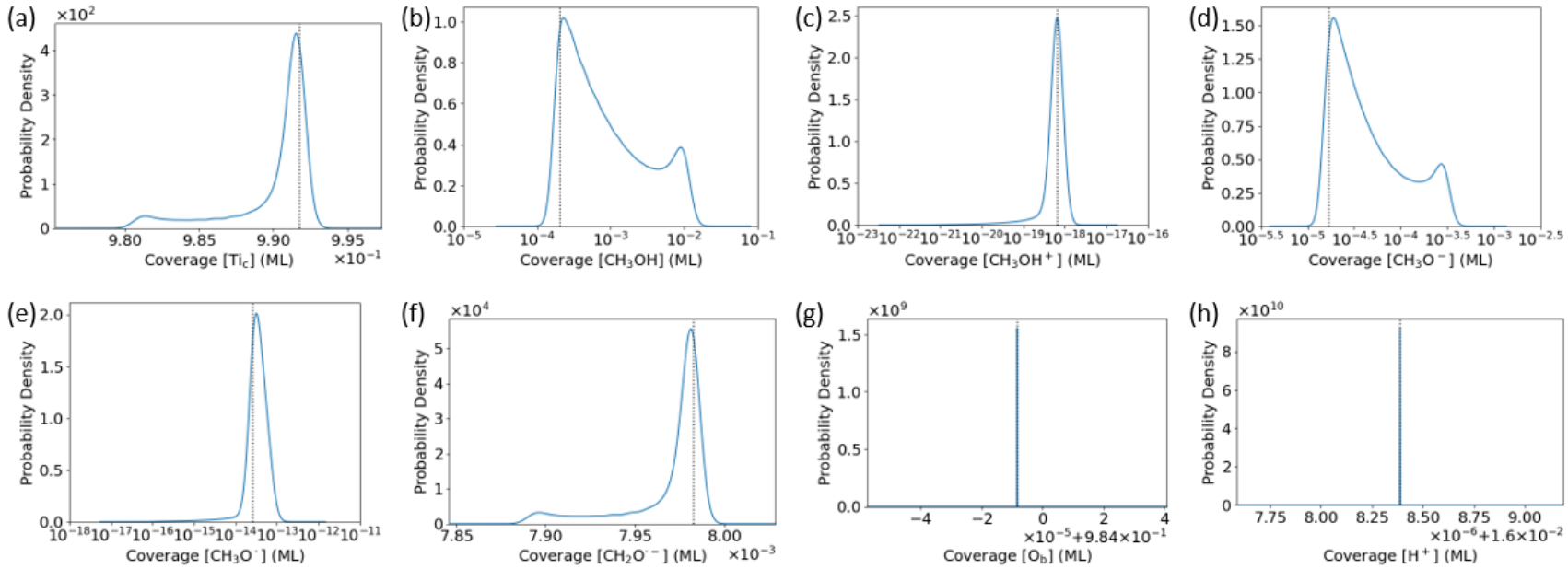

Figure A-24: Distributions of the coverages at 180 K in HHPA.

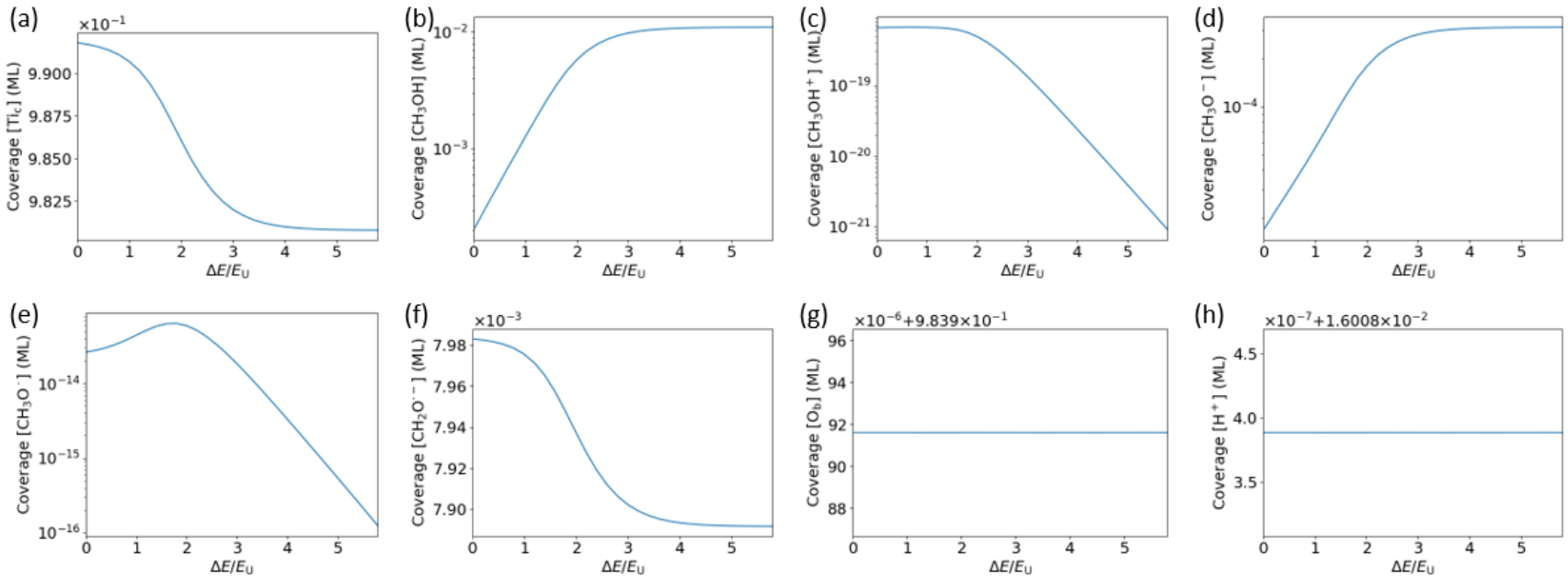

Figure A-25: Time-averaged coverages as a function of the trap energy at 180 K in HHPA.

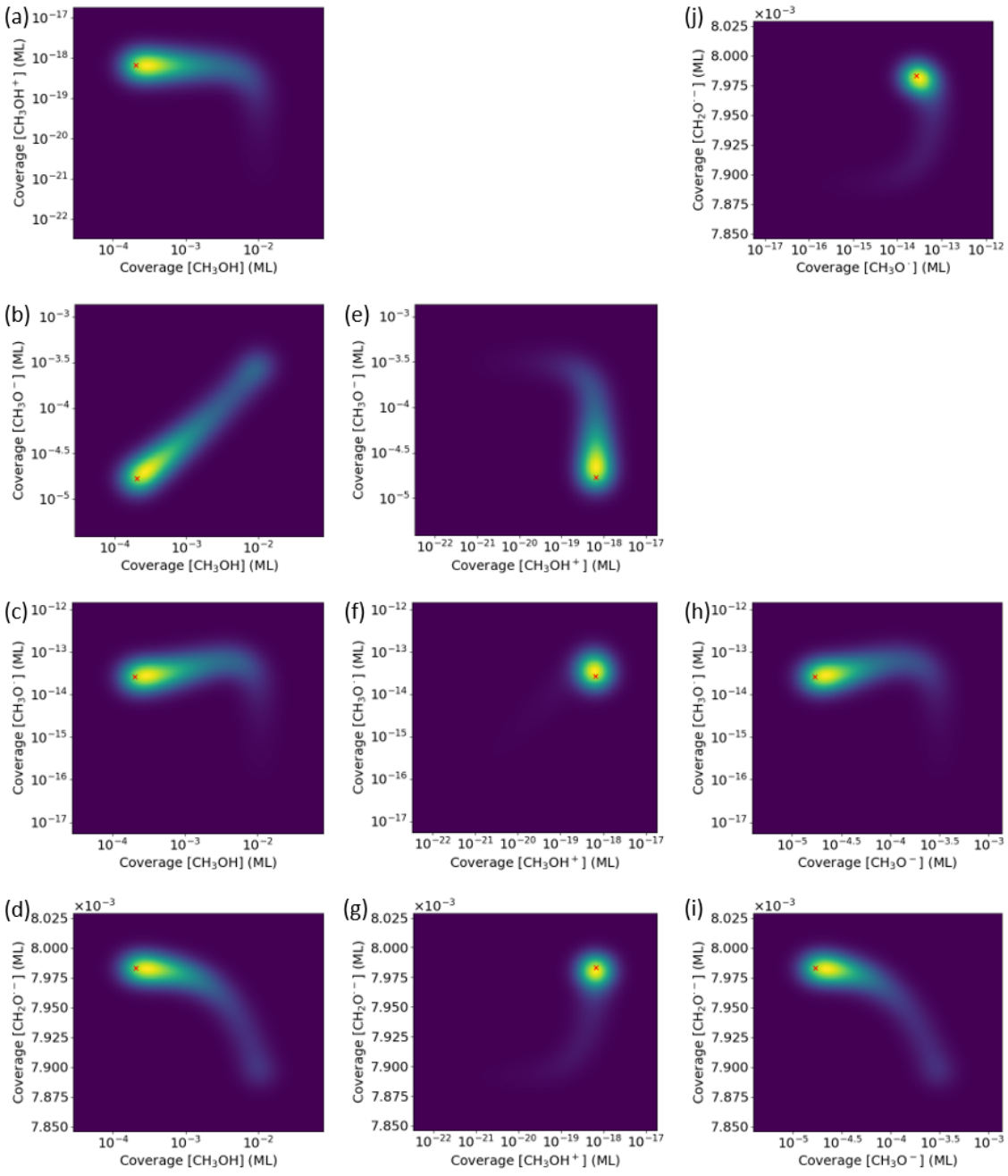

Figure A-26: Time-averaged 2D distributions of the coverages at 180 K in HHPA.

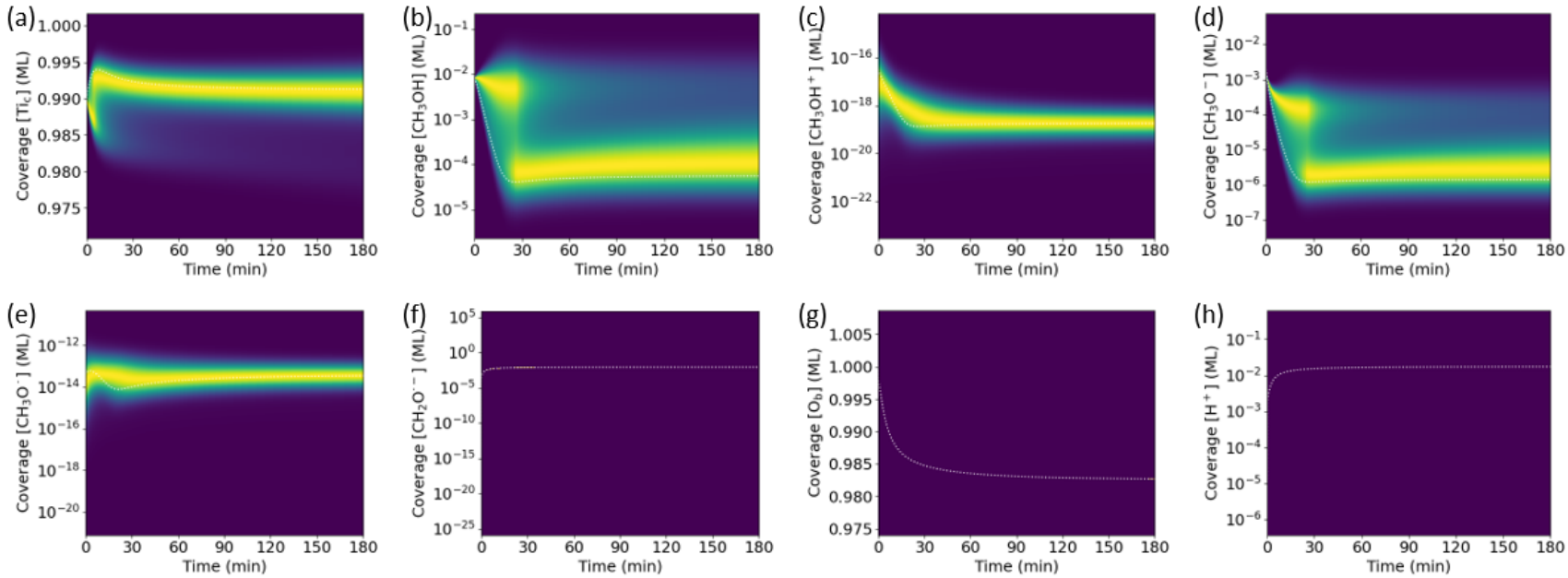

Figure A-27: Time-dependent distributions of the coverages at 180 K in HHPA.

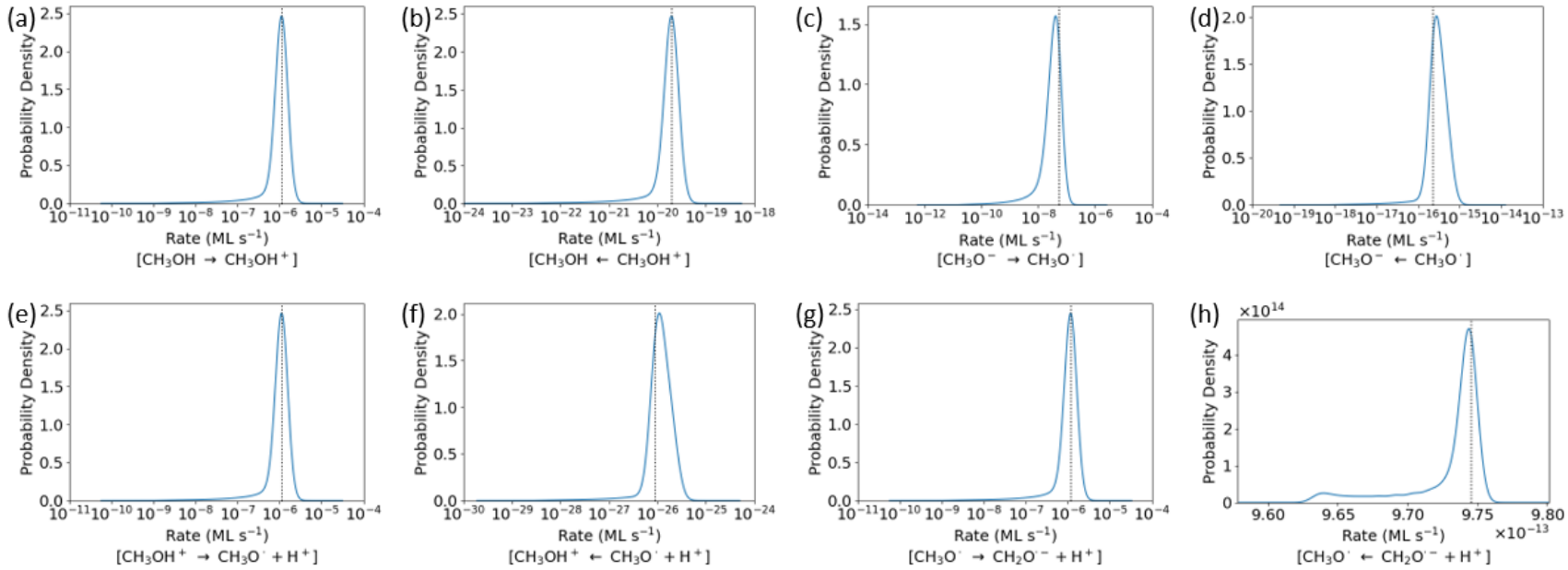

Figure A-28: Distributions of the rates at 180 K in HHPA (1/2).

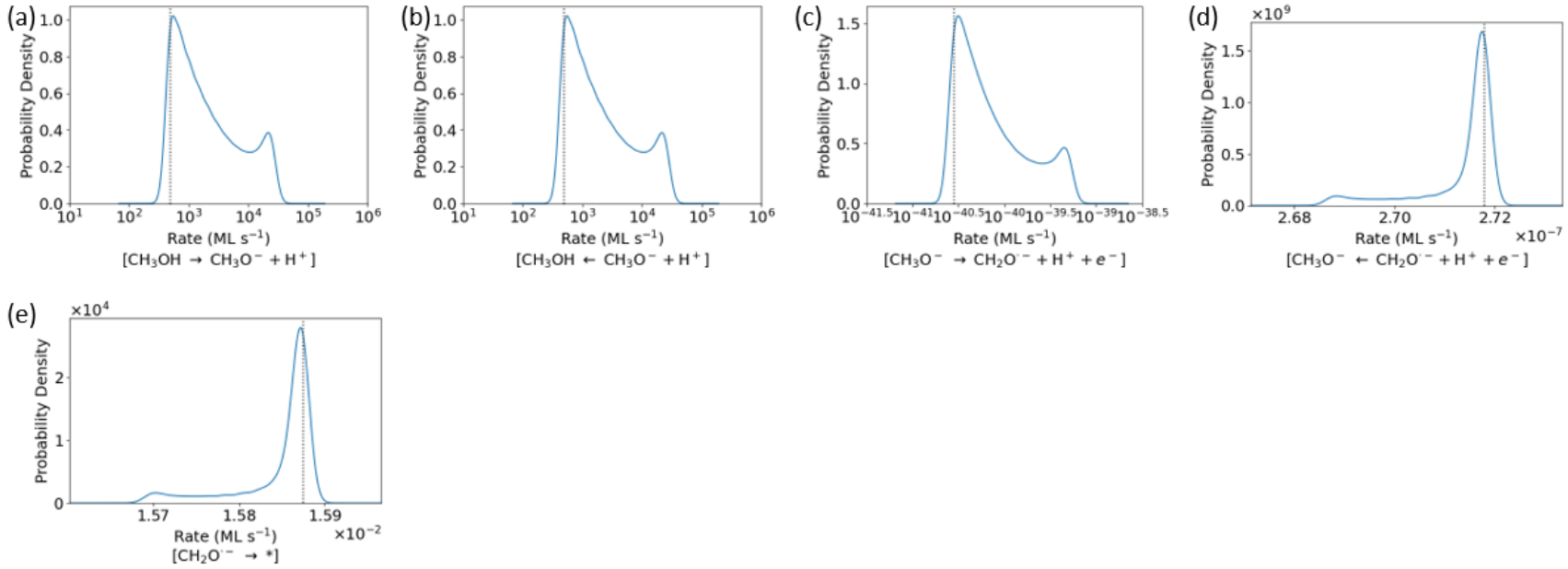

Figure A-29: Distributions of the rates at 180 K in HHPA (2/2).

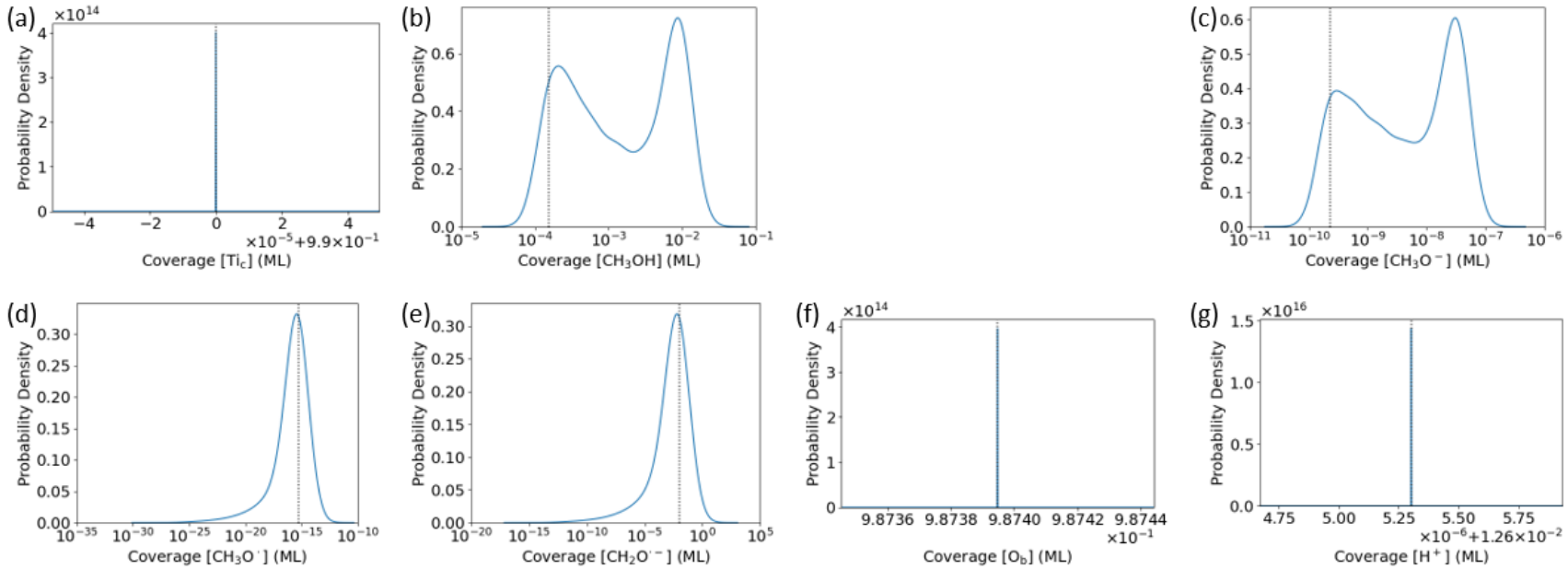

Figure A-30: Distributions of the coverages at 80 K in the modified model with HHPA.

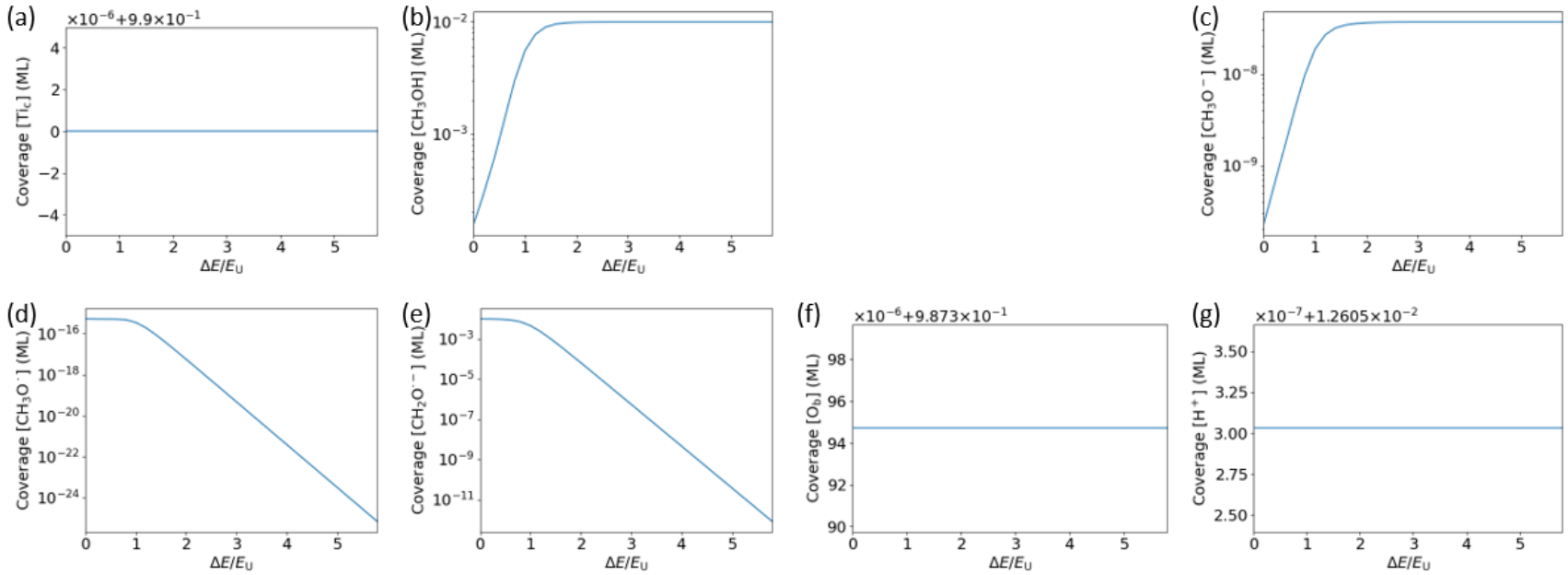

Figure A-31: Time-averaged coverages as a function of the trap energy at 80 K in the modified model with HHPA.

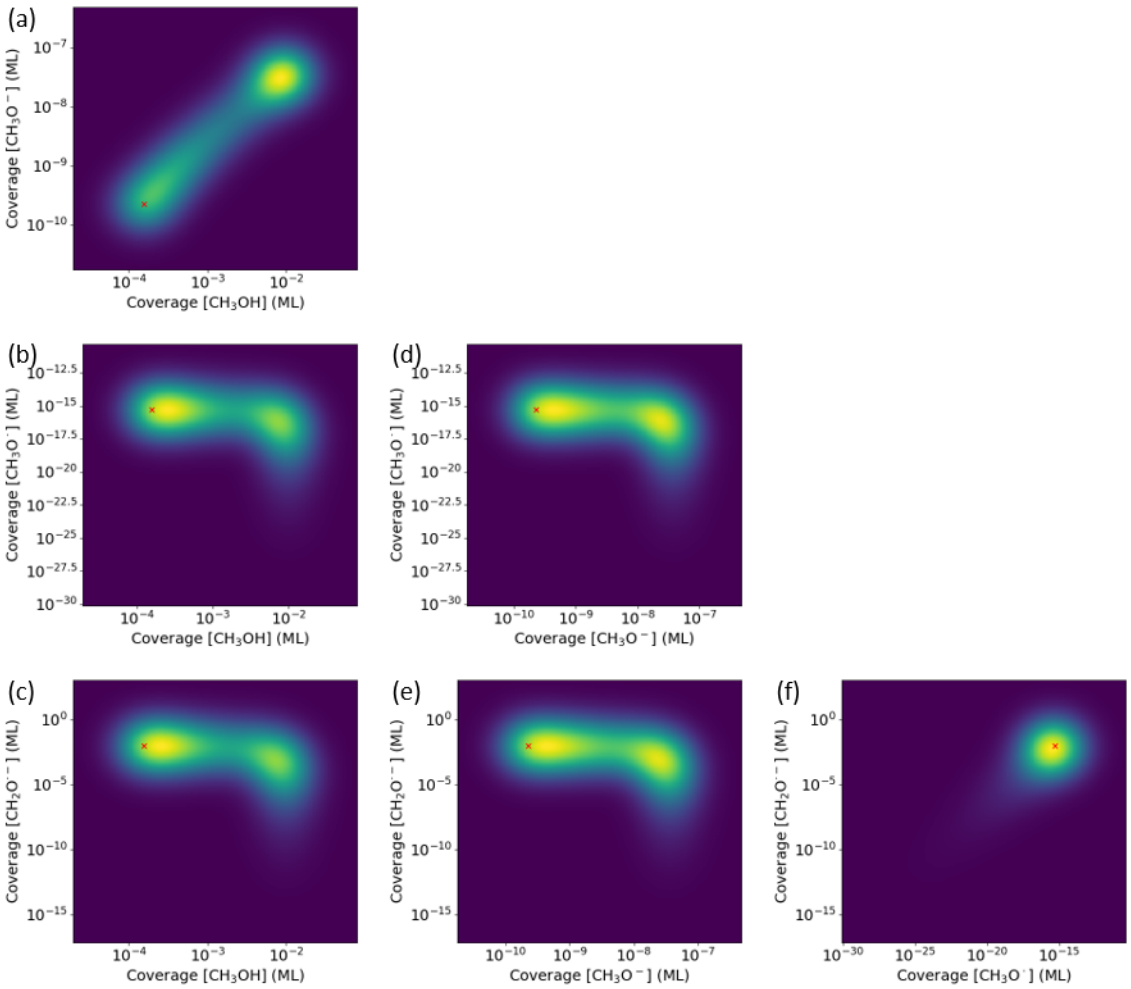

Figure A-32: Time-averaged 2D distributions of the coverages at 80 K in the modified model with HHPA.

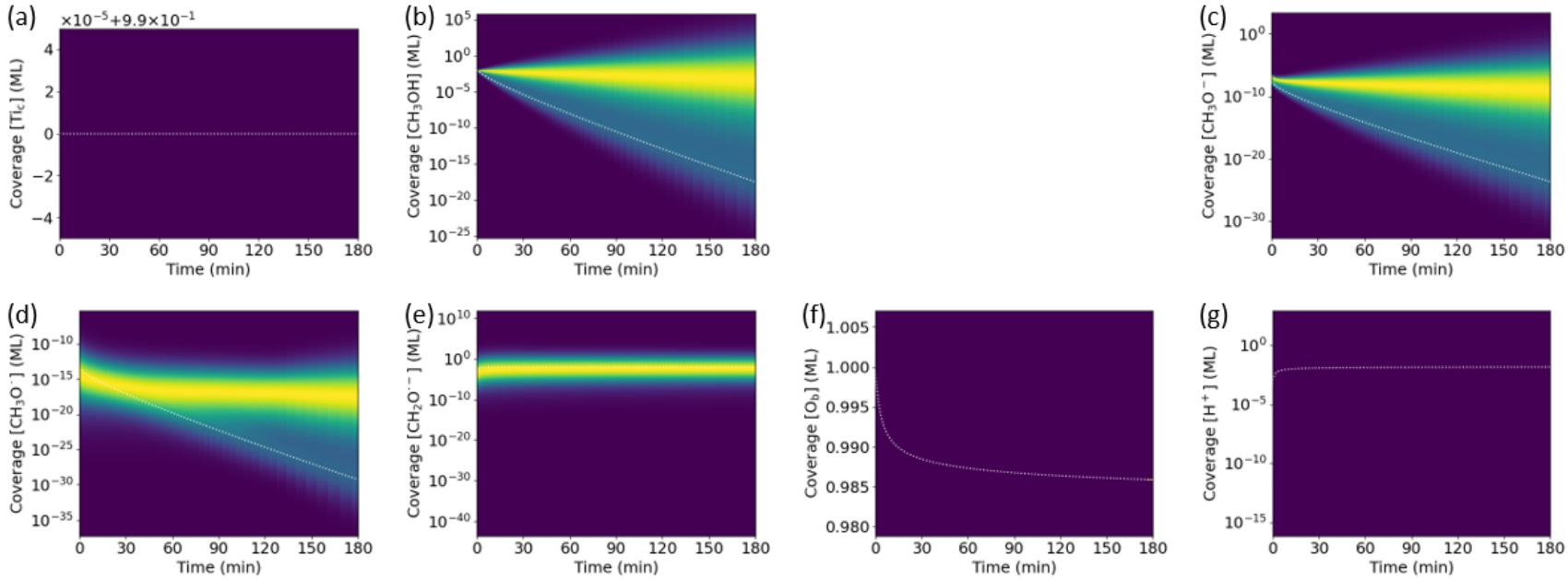

Figure A-33: Time-dependent distributions of the coverages at 80 K in the modified model with HHPA.

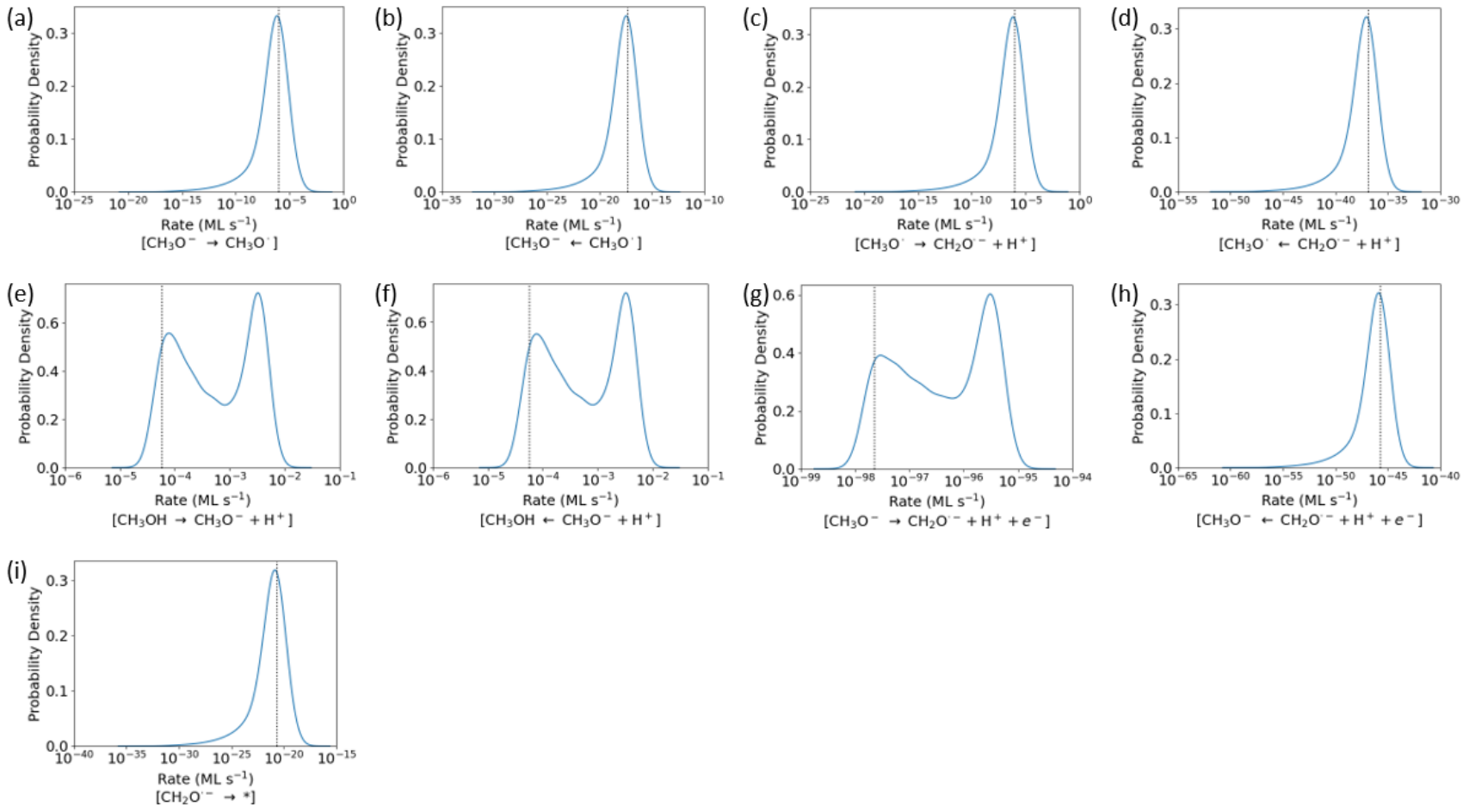

Figure A-34: Distributions of the rates at 80 K in the modified model with HHPA.

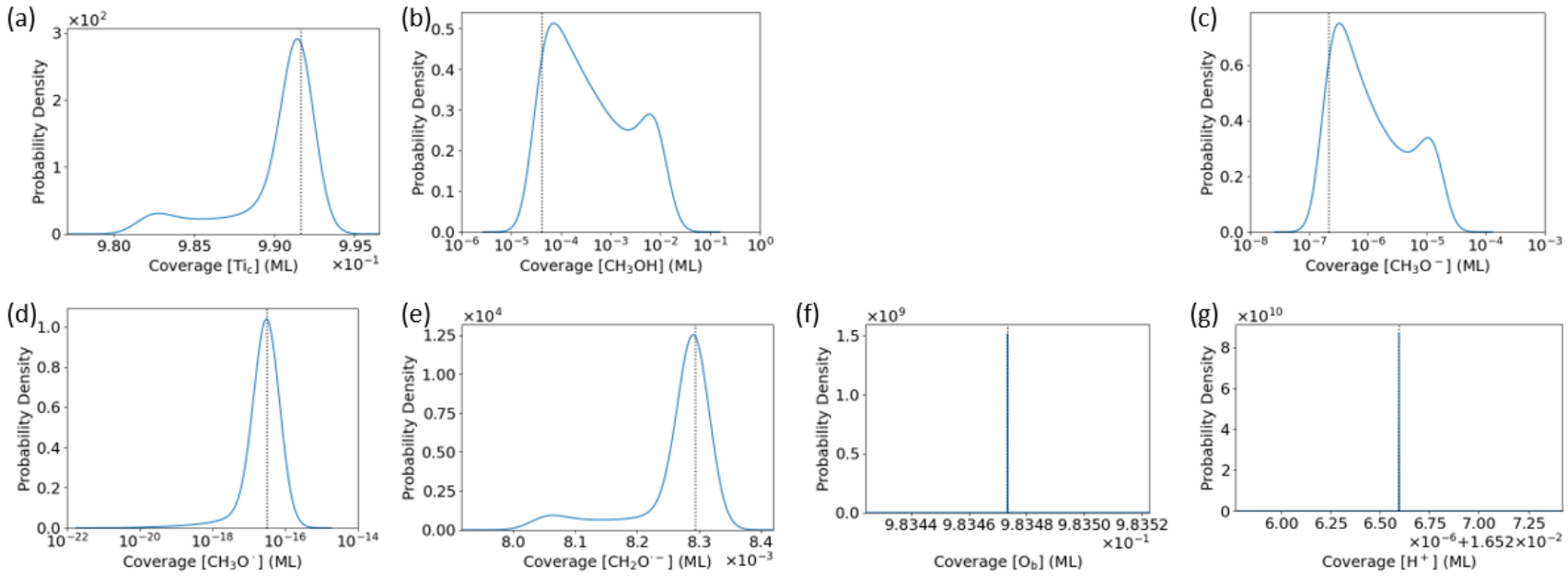

Figure A-35: Distributions of the coverages at 180 K in the modified model with HHPA.

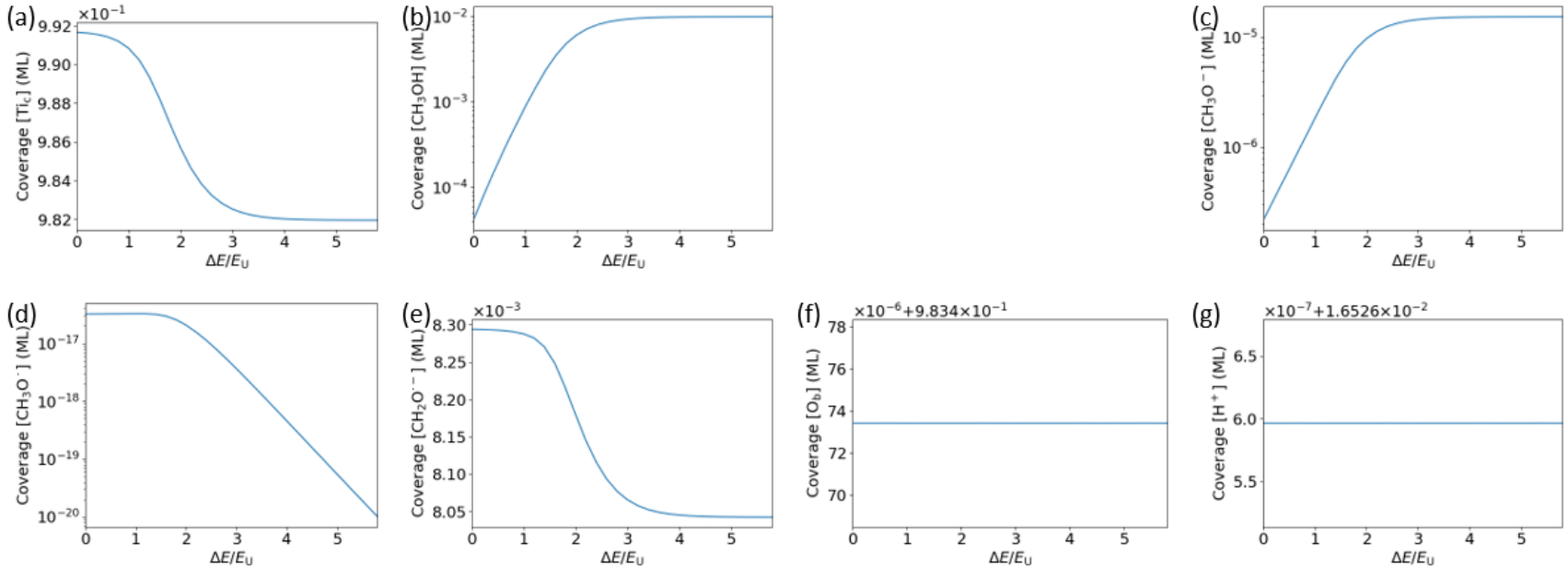

Figure A-36: Time-averaged coverages as a function of the trap energy at 180 K in the modified model with HHPA.

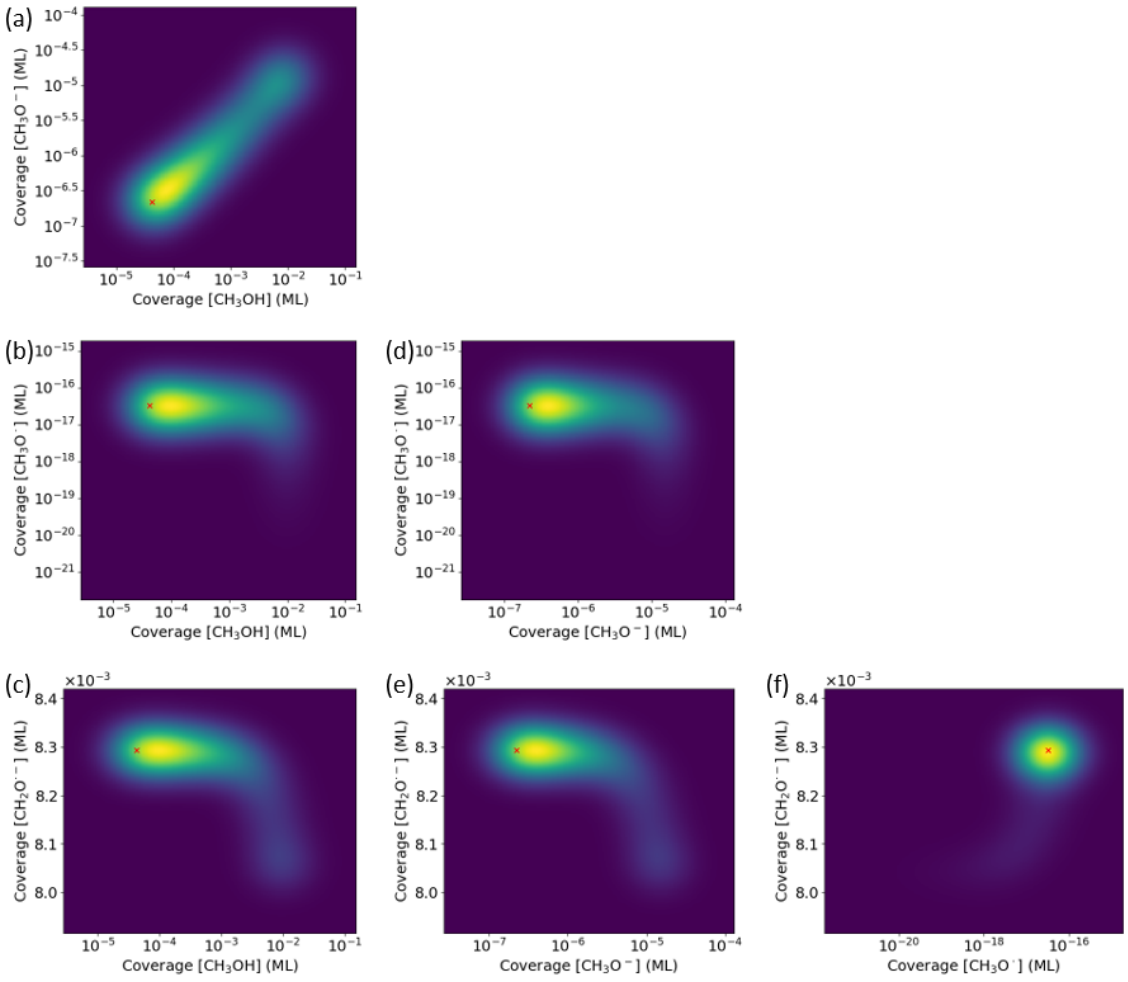

Figure A-37: Time-averaged 2D distributions of the coverages at 180 K in the modified model with HHPA.

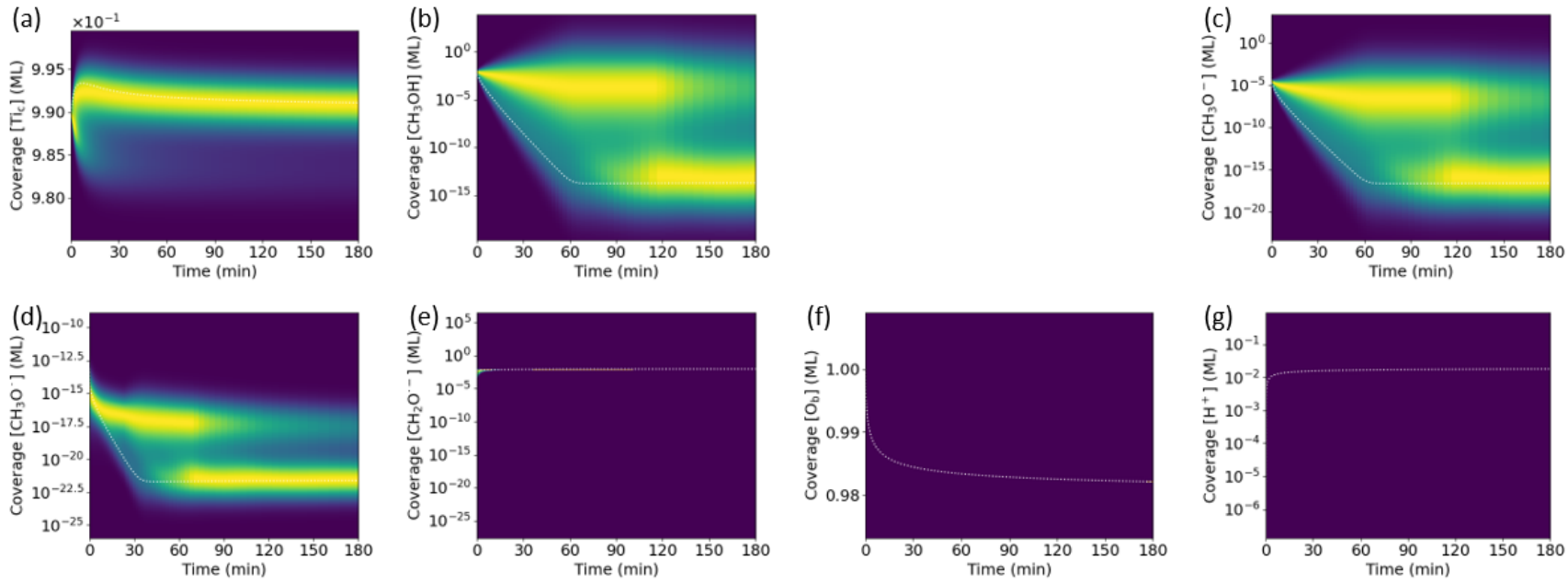

Figure A-38: Time-dependent distributions of the coverages at 180 K in the modified model with HHPA.

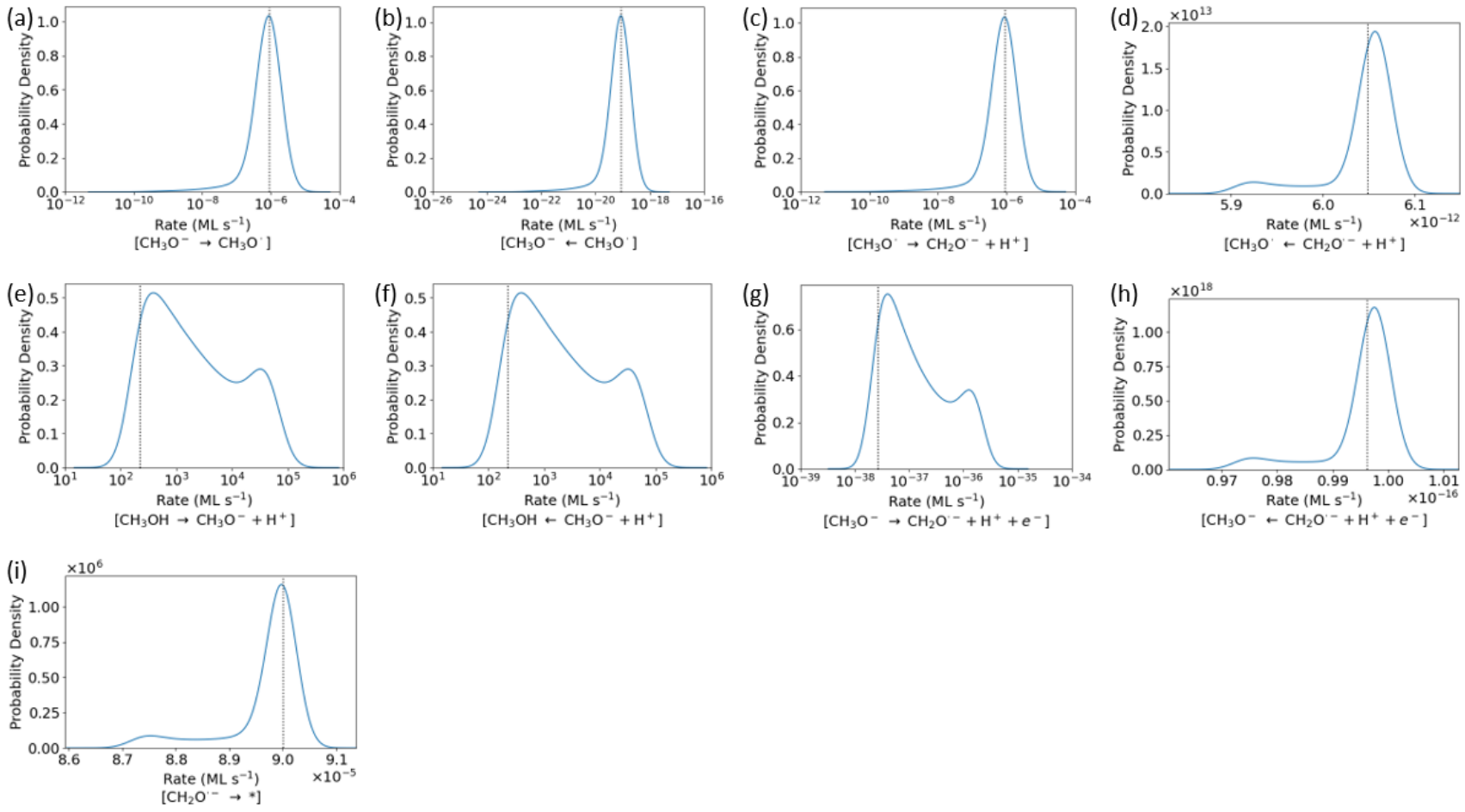

Figure A-39: Distributions of the rates at 180 K in the modified model with HHPA.

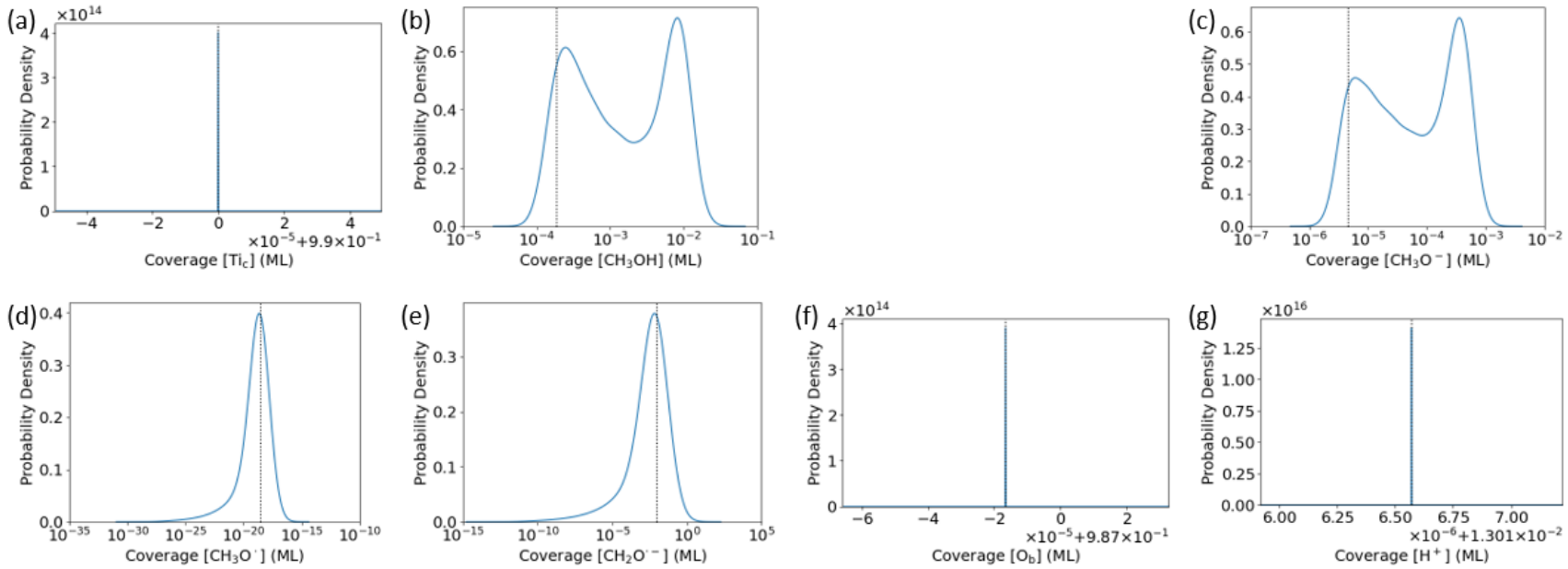

Figure A-40: Distributions of the coverages at 80 K in the compact model with HHPA.

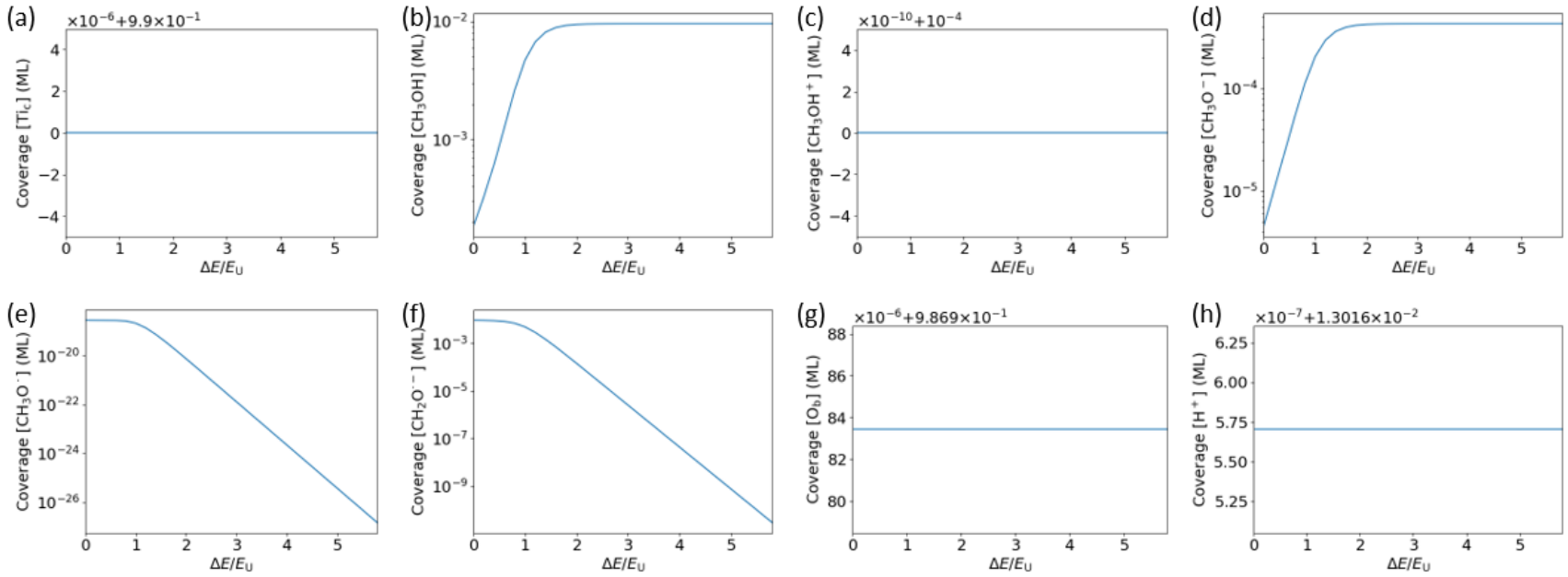

Figure A-41: Time-averaged coverages as a function of the trap energy at 80 K in the compact model with HHPA.

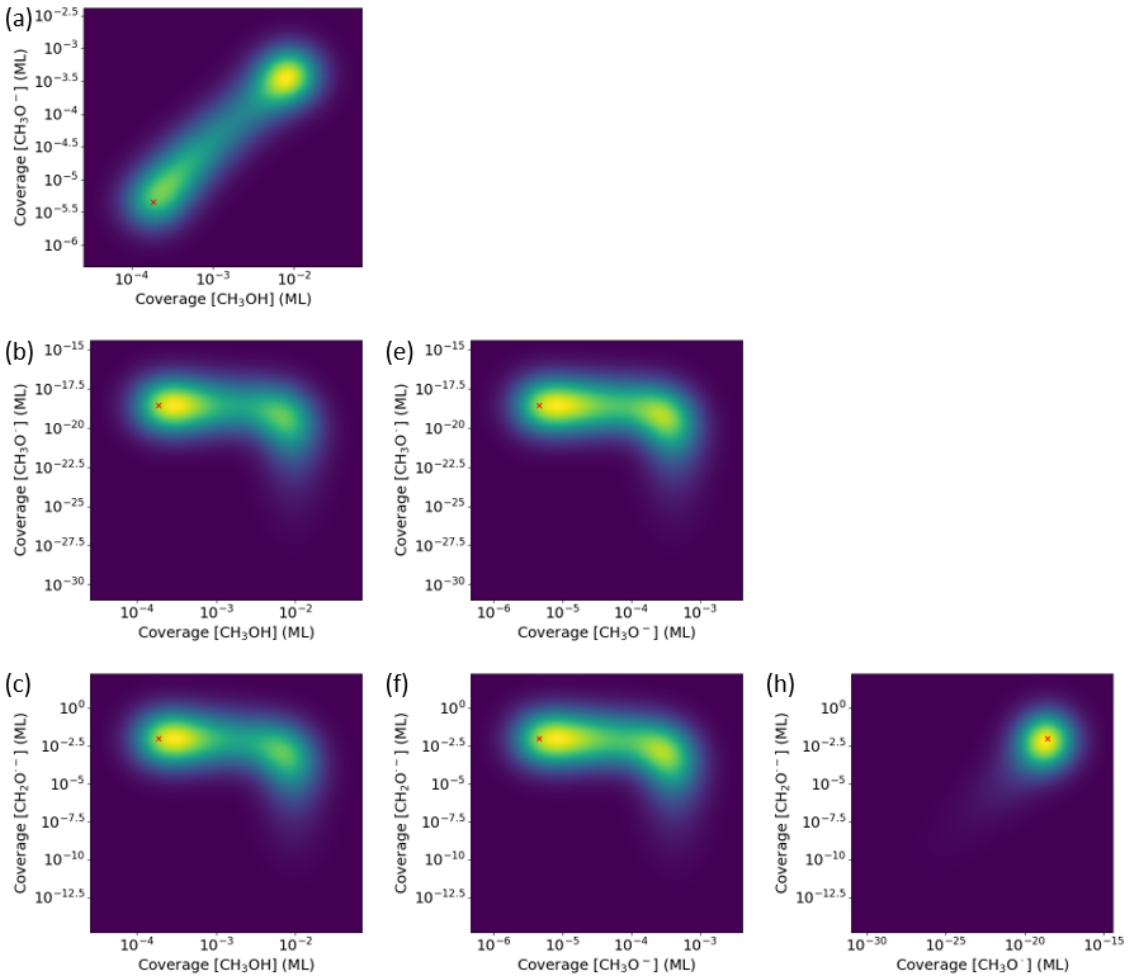

Figure A-42: Time-averaged 2D distributions of the coverages at 80 K in the compact model with HHPA.

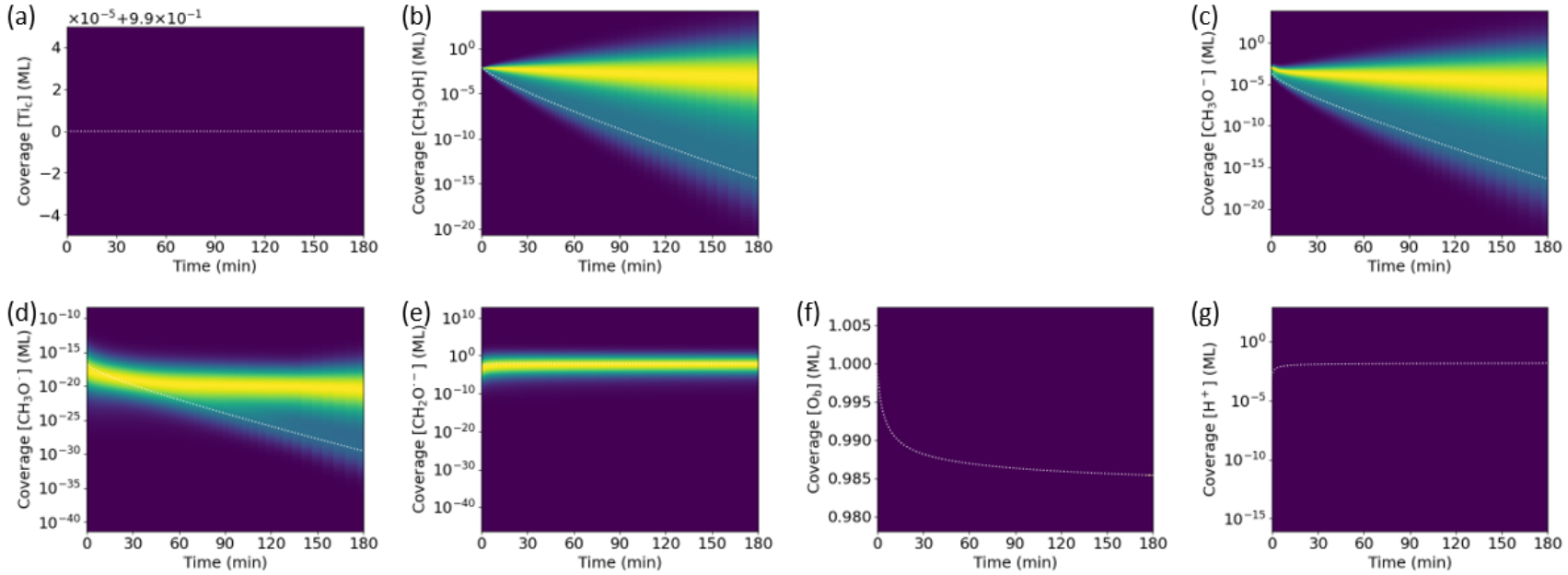

Figure A-43: Time-dependent distributions of the coverages at 80 K in the compact model with HHPA.

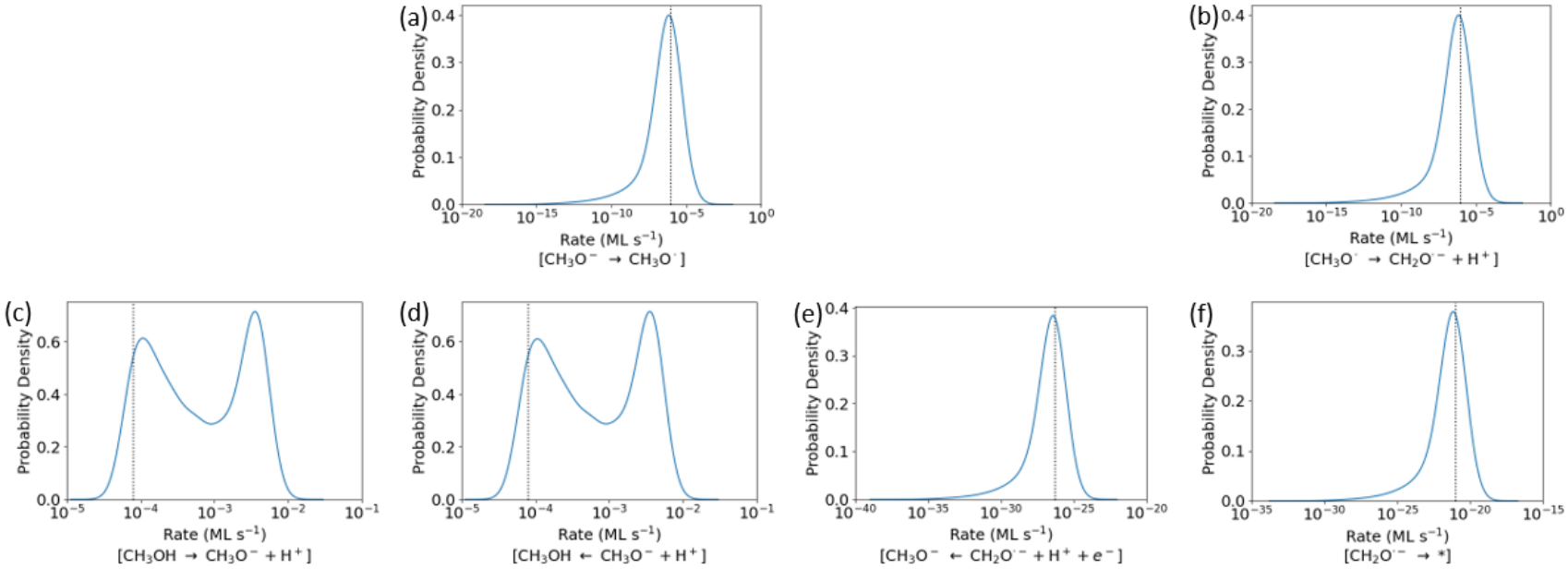

Figure A-44: Distributions of the rates at 80 K in the compact model with HHPA.

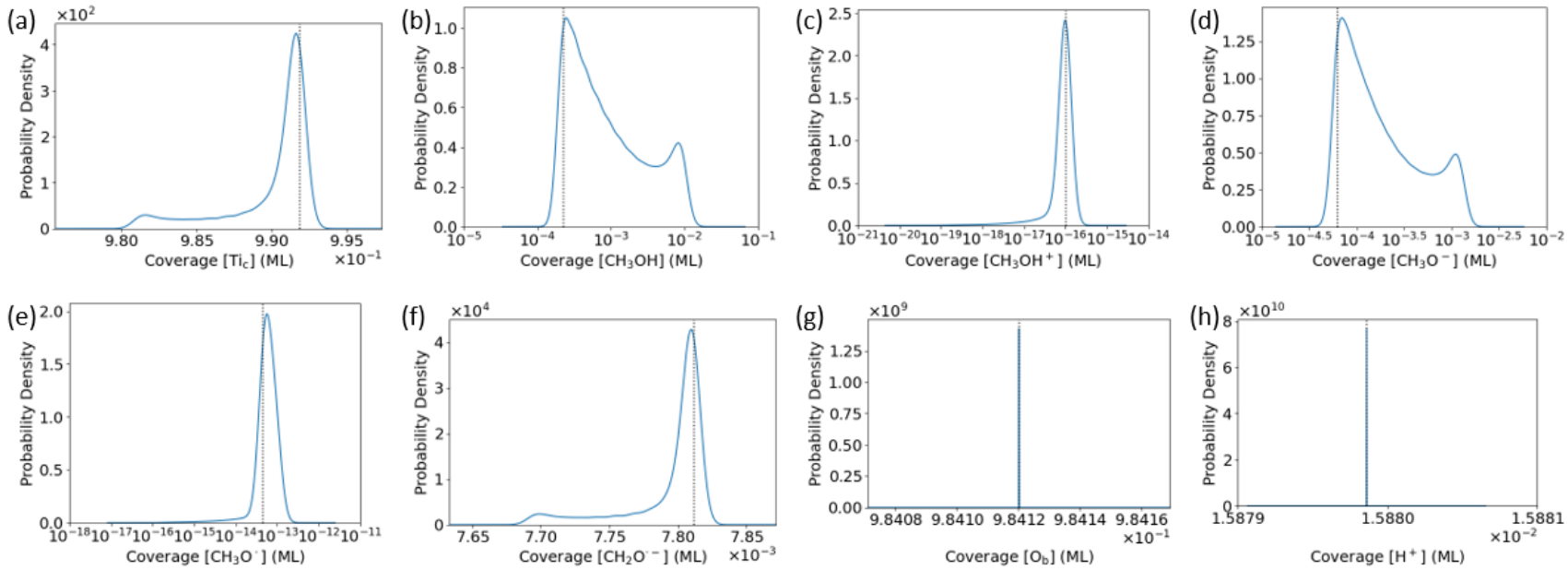

Figure A-45: Distributions of the coverages at 180 K in the compact model with HHPA.

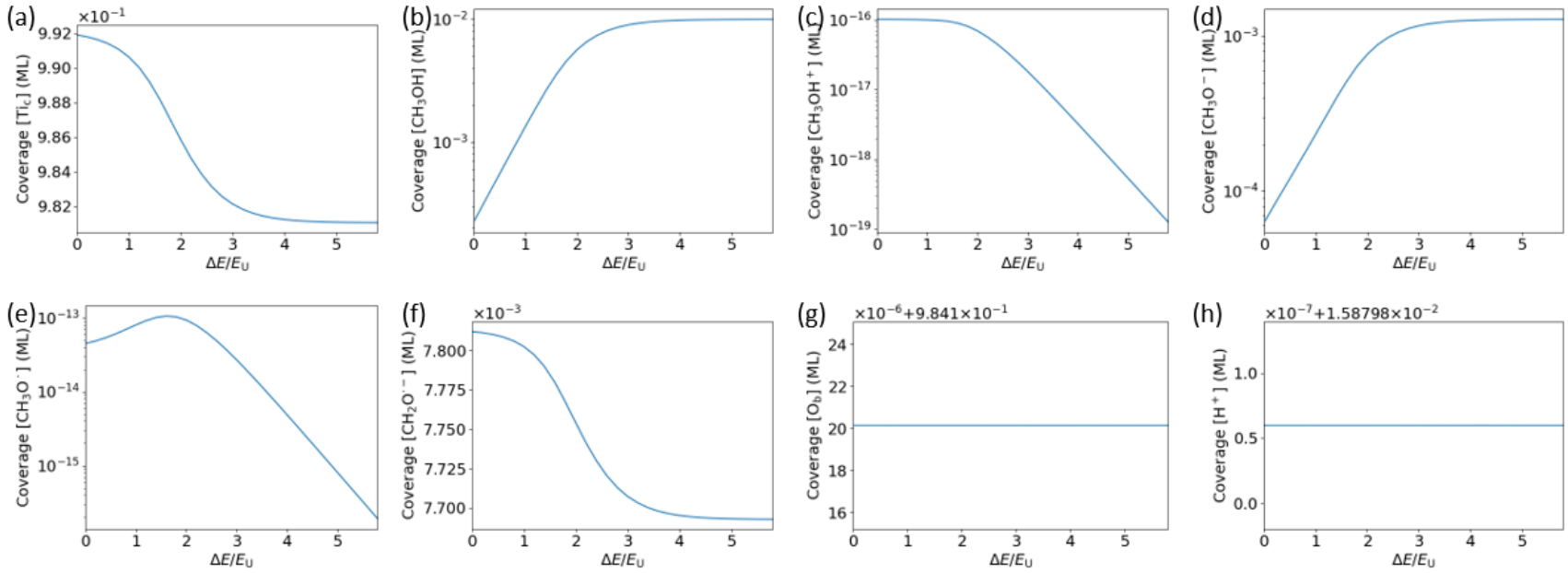

Figure A-46: Time-averaged coverages as a function of the trap energy at 180 K in the compact model with HHPA.

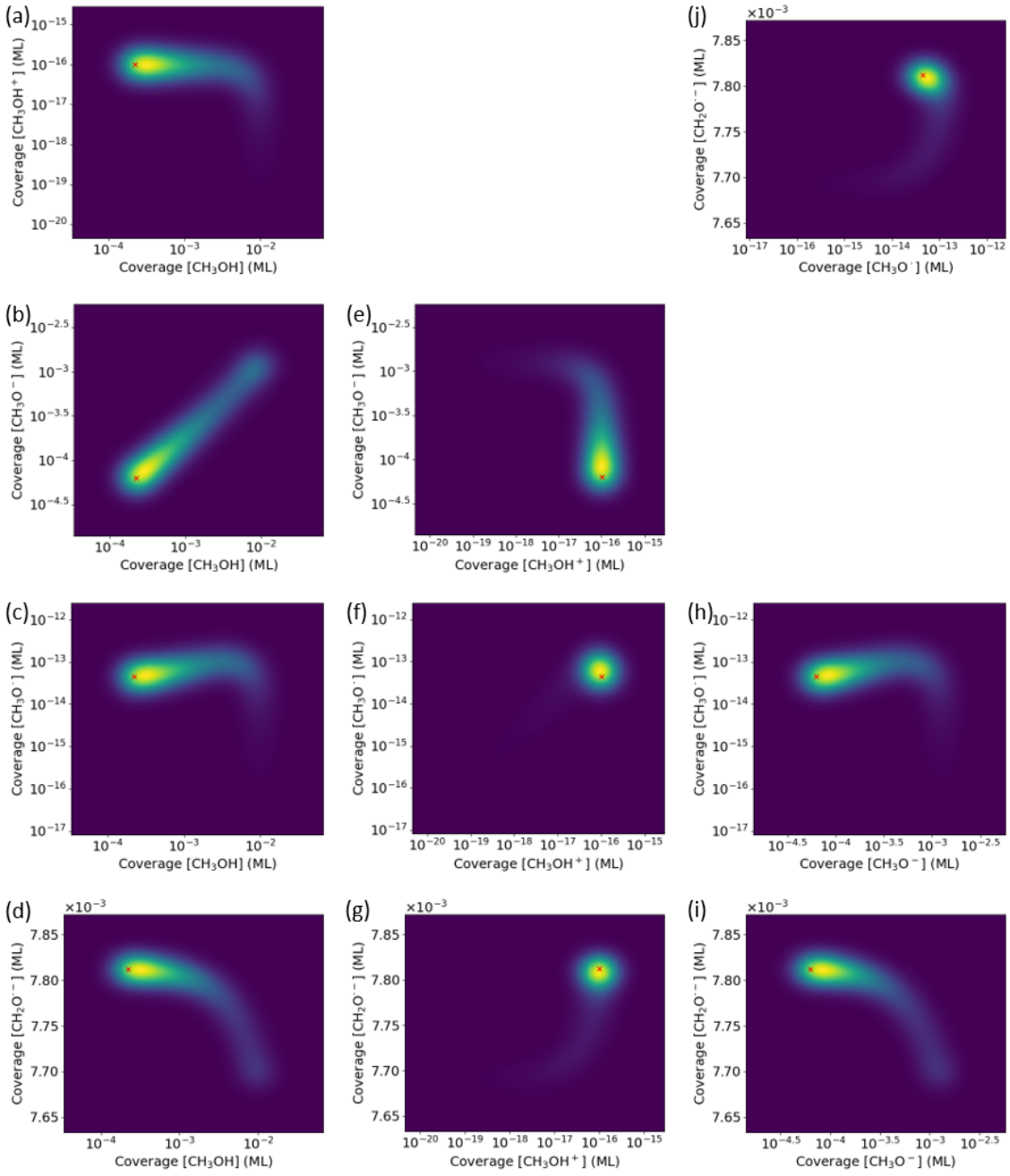

Figure A-47: Time-averaged 2D distributions of the coverages at 180 K in the compact model with HHPA.

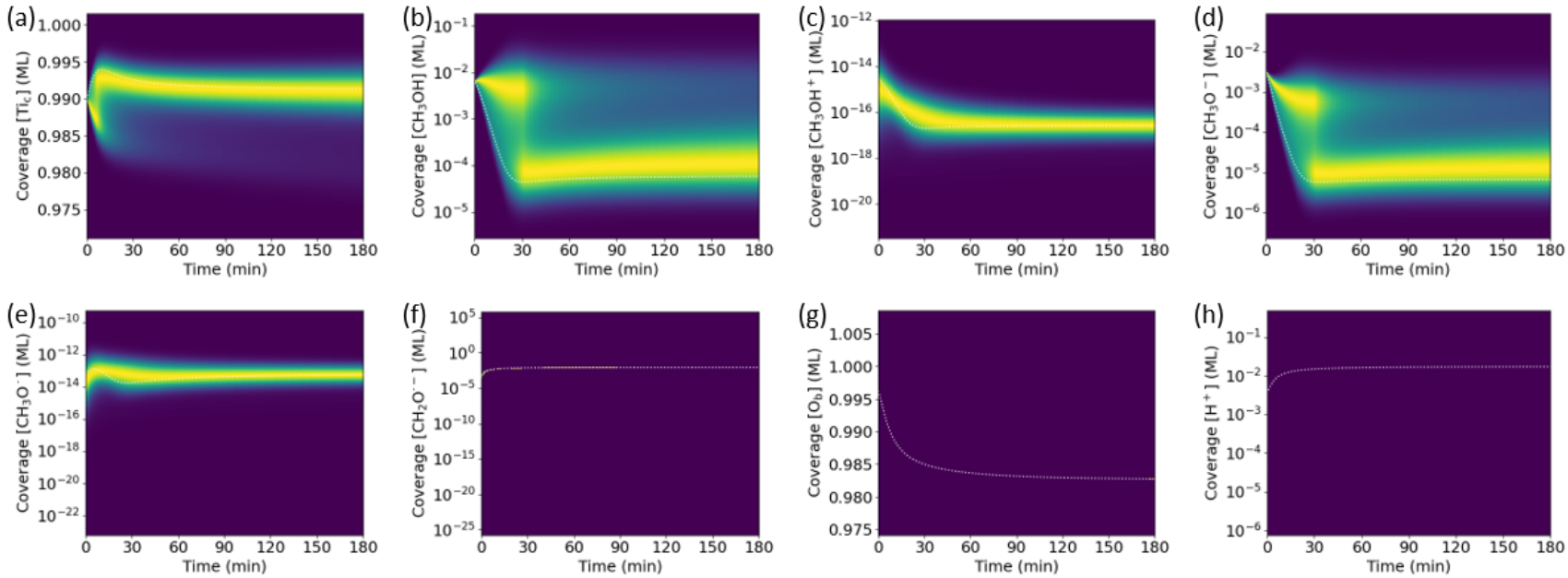

Figure A-48: Time-dependent distributions of the coverages at 180 K in the compact model with HHPA.

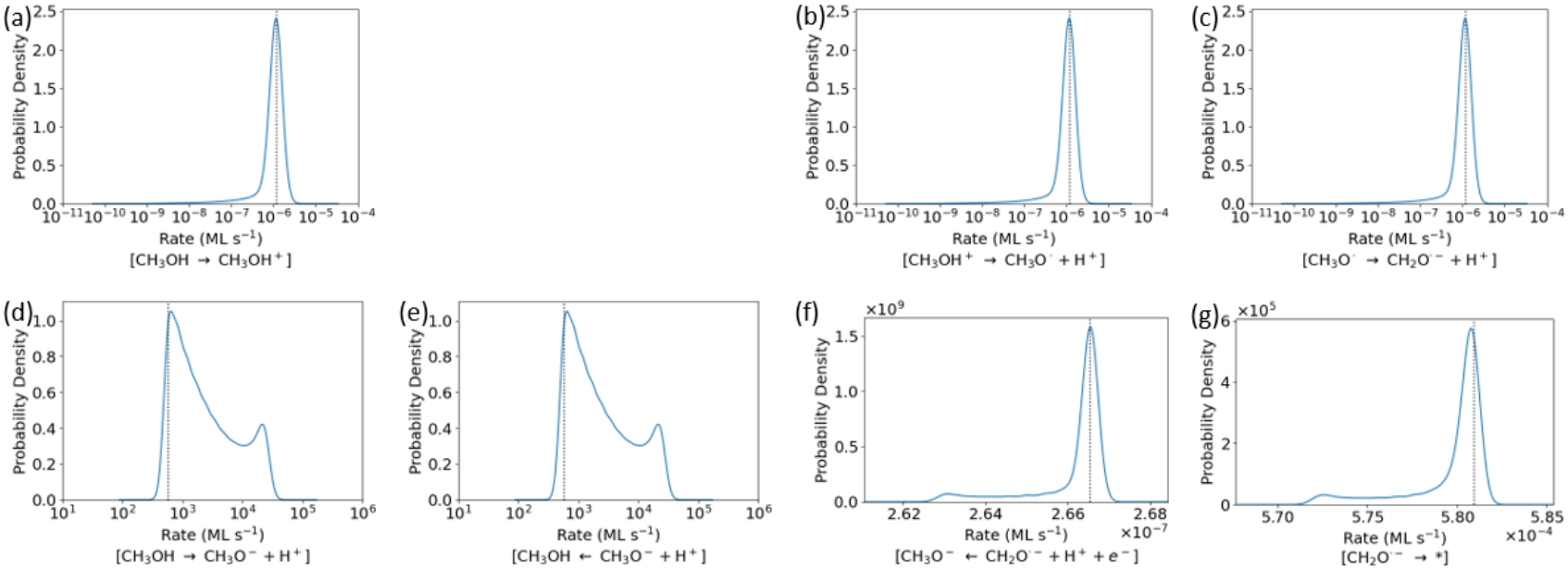

Figure A-49: Distributions of the rates at 180 K in the compact model with HHPA.

A.7 Distributions of Trap Energies

To establish the robustness of the high-activity and the low-activity groups, we considered the normal, Poisson ($k = 2$), and hyperbolic secant distributions in addition to the Poisson ($k = 0$) distribution of trap energies. The normal and the hyperbolic secant distributions are common in the physical sciences, and the Poisson ($k = 2$) distribution gives a smooth cutoff at ΔE_i, while retaining the exponential tail of the Poisson ($k = 0$) distribution. Unfortunately, it was cumbersome to employ HHPA with the normal and the hyperbolic secant distributions. Due to a significant fraction of sites that have much smaller trap energies and much greater rate constants than the mean, the kinetic equations were quite stiff, and the computational costs were considerable even with the preaveraging. For consistency across the types of static disorder, we use HMF in this section.

Distribution	PDF	Disorder	90 % CI
Poisson ($k = 0$)	$\rho(x) \propto e^{-x/\lambda}, x > 0$	$\lambda \approx 32\,\text{meV}$	$x < 2.303\lambda \approx 73\,\text{meV}$
normal	$\rho(x) \propto \exp\left[-\frac{x^2}{2\sigma^2}\right]$	$\sigma \approx 25\,\text{meV}$	$\lvert x\rvert < 1.645\sigma \approx 42\,\text{meV}$
Poisson ($k = 2$)	$\rho(x) \propto x^2 e^{-x/\lambda}, x > 0$	$\lambda \approx 16\,\text{meV}$	$x < 5.322\lambda \approx 84\,\text{meV}$
hyperbolic secant	$\rho(x) \propto \text{sech}\left[\frac{x}{\sigma}\right]$	$\sigma \approx 19\,\text{meV}$	$\lvert x\rvert < 2.542\sigma \approx 49\,\text{meV}$

Table A.5: Calibrated amounts of static disorder.

Figure A-50 shows the simulated kinetics in HMF with different distributions of trap energies. There are no significant differences in the overall kinetics. We note that the ranges of variations in the rate constants remain quite consistent across the types of static disorder, as shown in Table A.5. For example, the Poisson ($k = 0$) distribution predicts that 90 % of sites have trap energies within $2.303\lambda \approx 73\,\text{meV}$, and the normal distribution predicts that 90 % of sites have trap energies within $2 \times 1.645\sigma \approx 84\,\text{meV}$. Hence, the overall kinetics might not be as sensitive to the type of static disorder as it is to the amount of static disorder.

For reference, we begin by comparing the distributions of the coverages in HMF to those in HHPA with the Poisson ($k = 0$) distribution of trap states. Overall, the HMF results capture the qualitative trends in the HHPA results with minor

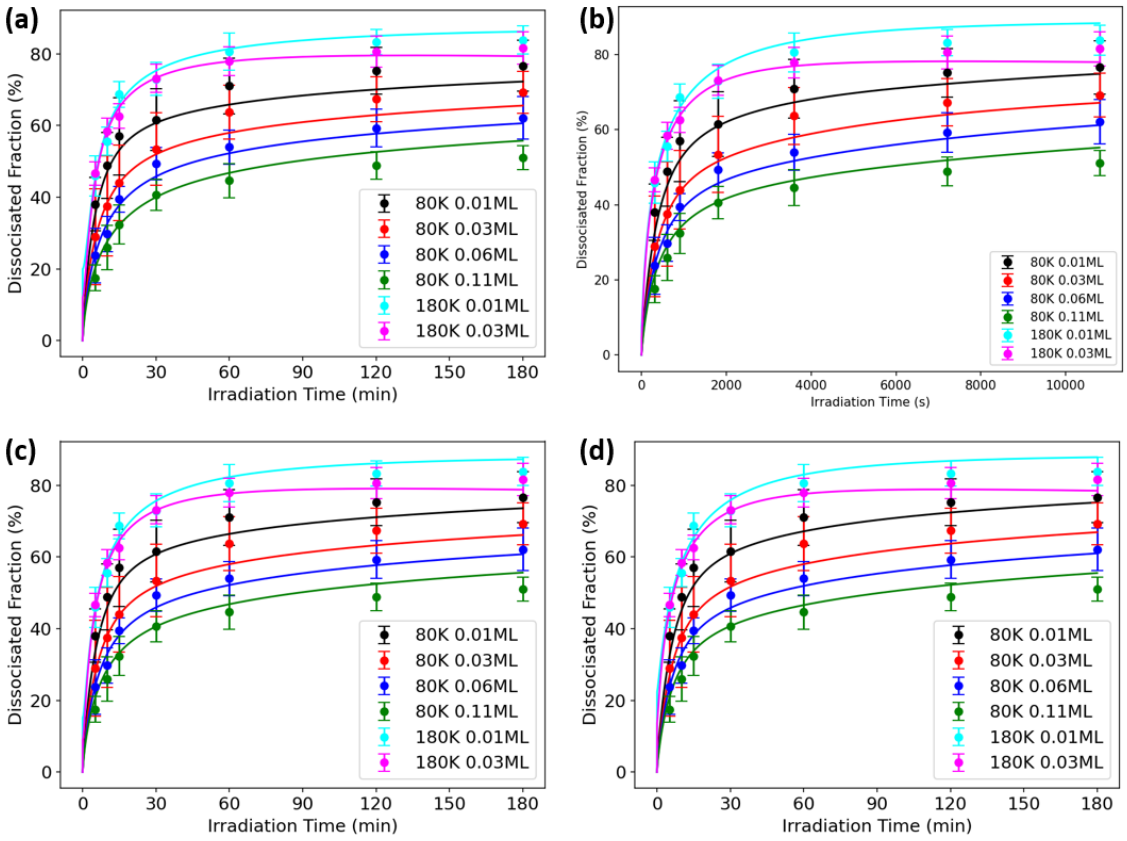

Figure A-50: Time-dependent dissociation fractions in HMF with (a) the Poisson ($k = 0$) disorder, RMSNE = 0.542; (b) the normal disorder, RMSNE = 0.576; (c) the Poisson ($k = 2$) disorder, RMSNE = 0.548; and (d) the hyperbolic secant disorder, RMSNE = 0.556.

deviations. Whereas HHPA predicts that the coverages of the methanol molecule and the methoxy anion have almost identical distributions, HMF predicts that the division is not as pronounced in the methoxy anion at 80 K, as shown in Figure A-51b,d. In addition, the methoxy anion at 80 K (Figure A-51d) and the methanol molecule and the methoxy anion at 180 K (Figure A-52b,d) have the position of the high-activity group offset with respect to the position of $k_r^i = k_r^0$. These deviations can be explained in terms of the dynamic correlation. When the OH bond breaks in HHPA, the coverage of the hydrogen is concentrated on the neighboring O_b sites. When the OH bond breaks in HMF, the coverage of the hydrogen is distributed on all of the O_b sites. Once the most active sites have reacted, the next sites in HMF do not have pristine O_b sites on which to deposit the hydrogen. Hence, a majority of the sites are not as active as their rate constants indicate, and the distributions of the coverages shift to the right. We keep these deviations in mind as we examine the other types of disorder.

The normal distribution of trap states gives a significant reduction of the division. As shown in Figure A-53b, there are two peaks in the coverage of the methanol molecule at 80 K, but the division of the high-activity and the low-activity groups is rather indistinct. The other coverages do not show any sign of division, as shown in Figures A-53d, A-54b, A-54d, and A-54f.

Interestingly, the Poission ($k = 2$) distribution enhances the division in the coverage of the methanol molecule at 80 K, as shown in Figure A-55b, while reducing the division in the other coverages. Nonetheless, the coverage of the methoxy anion at 80 K and the formaldehyde at 180 K retain a distinct shoulder, as shown in Figures A-55d and A-56f. The coverages of the methanol molecule and the methoxy anion at 180 K also retain a shoulder, as shown in Figures A-56b,d.

Finally, the hyperbolic secant distribution exhibits an intermediate behavior of the normal and the Poission ($k = 2$) distributions. It enhances the division in the coverage of the methanol molecule at 80 K, as shown in Figure A-57b. Among the other coverages, the coverage of the formaldehyde at 180 K retains a distinct shoulder, as shown in Figure A-58f.

Overall, the high-activity and the low-activity groups can be observed with various types of disorder, albeit with various extents of division. Based on the comparison of the HMF and the HHPA results, there is a chance that the shoulders in the distributions could have been distinct groups if we had employed HHPA. The emergence of the groups appears to be quite insensitive, even though the strength of the division depends on the type of static disorder. Only the normal distribution predicts a significant reduction of the division in all of the coverages. We suspect that the short Gaussian tail of the normal distribution does not give enough sites with trap energies $\gg k_{\mathrm{B}}T$, so the low-activity group fails to manifest on the distributions of the coverages.

The remainder of this section presents a complete collection of the time-averaged distributions in HMF with the Poisson ($k = 0$), normal, Poisson ($k = 2$), and hyperbolic secand distributions of trap energies.

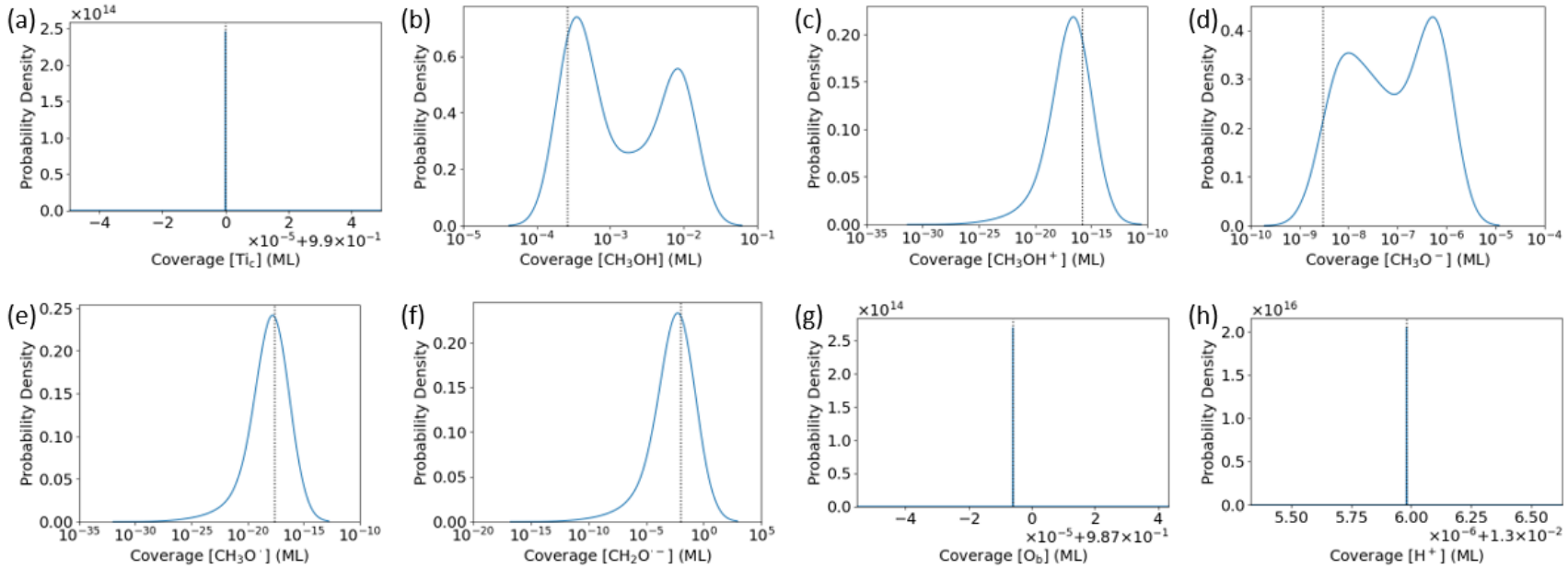

Figure A-51: Distributions of the coverages at 80 K in HMF with the Poisson ($k = 0$) distribution of trap states.

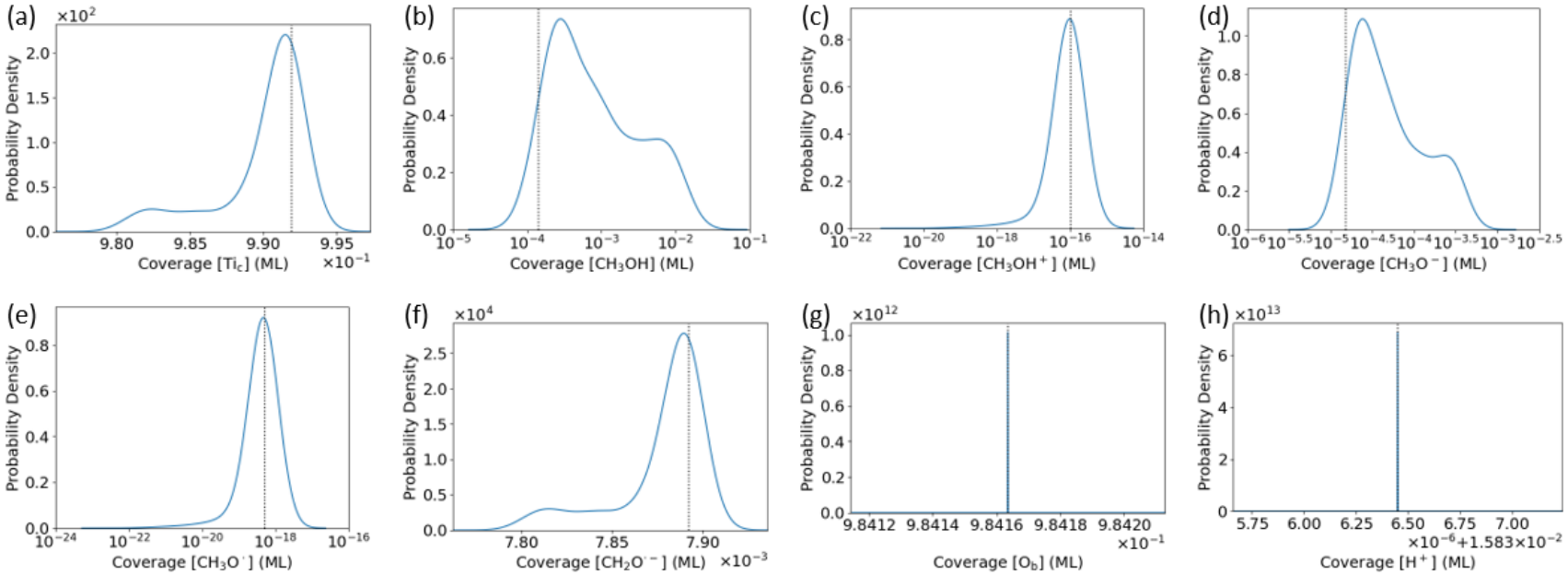

Figure A-52: Distributions of the coverages at 180 K in HMF with the Poisson ($k = 0$) distribution of trap states.

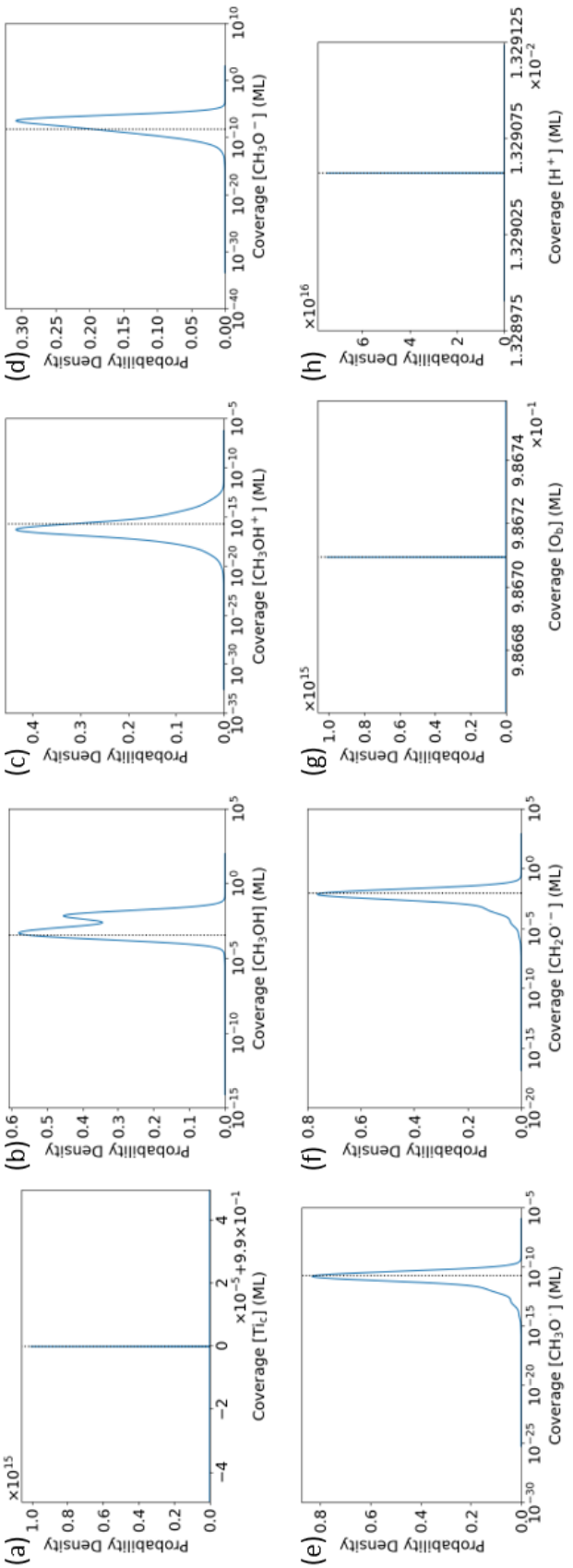

Figure A-53: Distributions of the coverages at 80 K in HMF with a normal distribution of trap states.

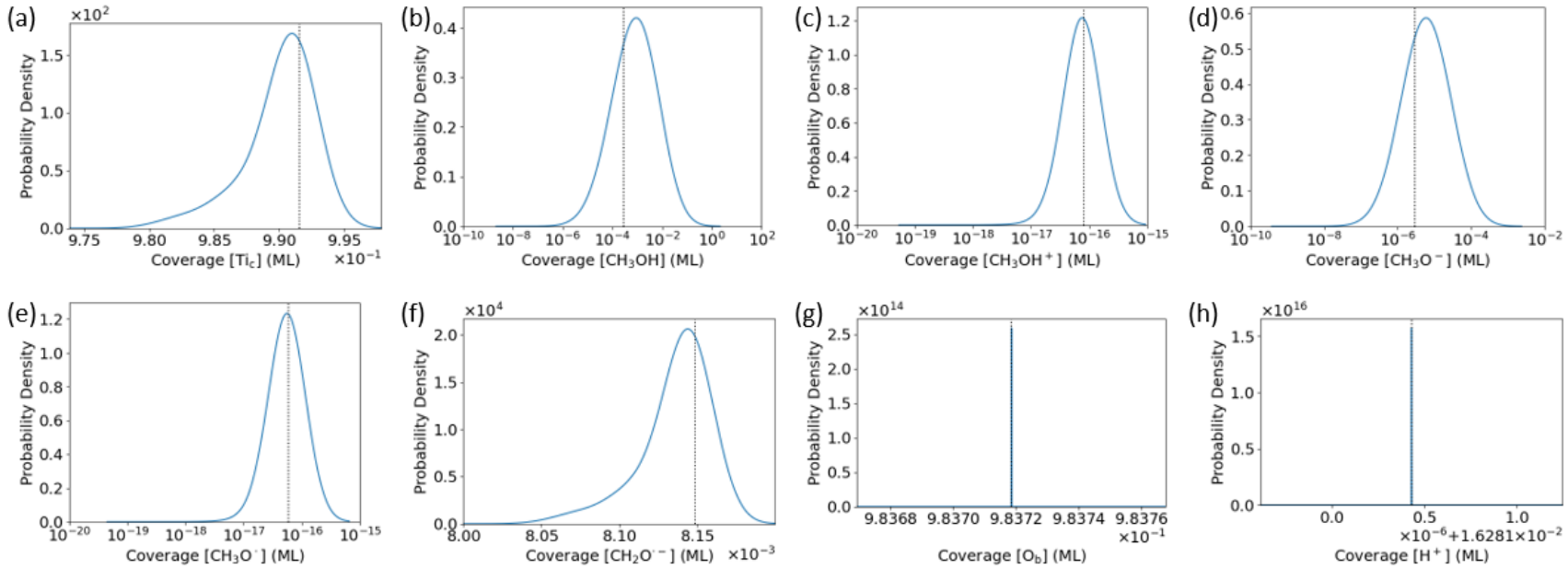

Figure A-54: Distributions of the coverages at 180 K in HMF with a normal distribution of trap states.

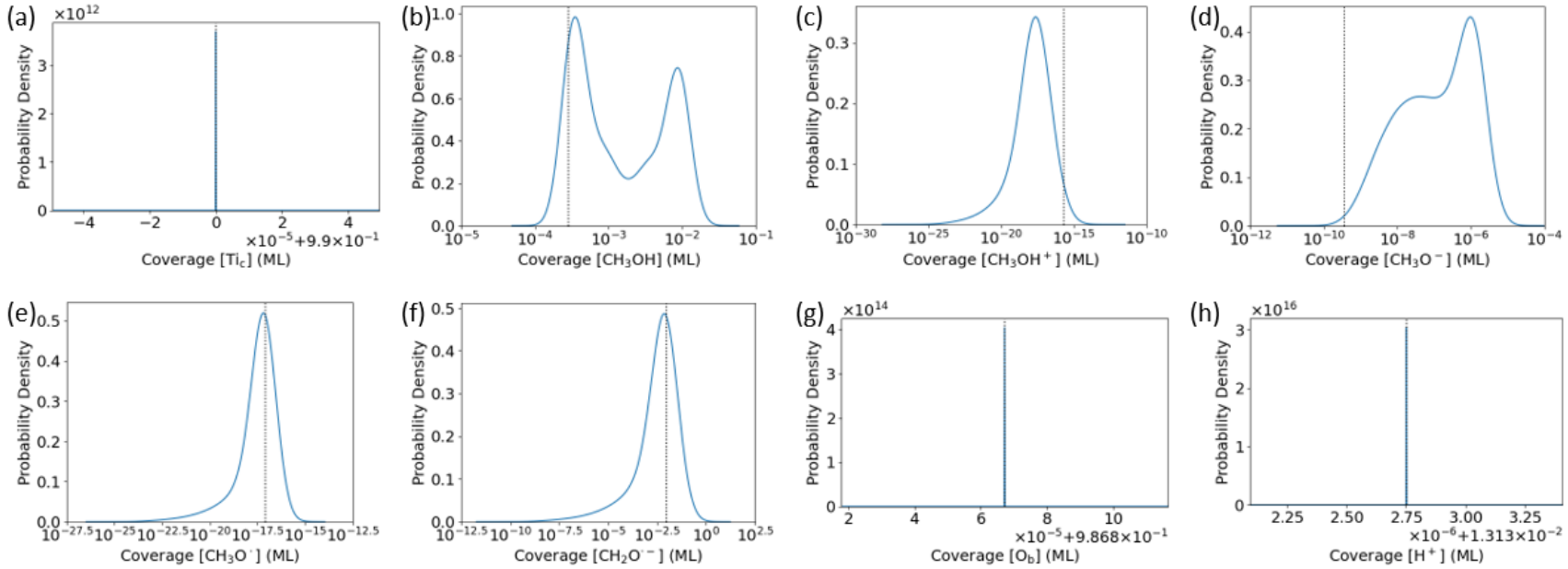

Figure A-55: Distributions of the coverages at 80 K in HMF with the Poisson ($k = 2$) distribution of trap states.

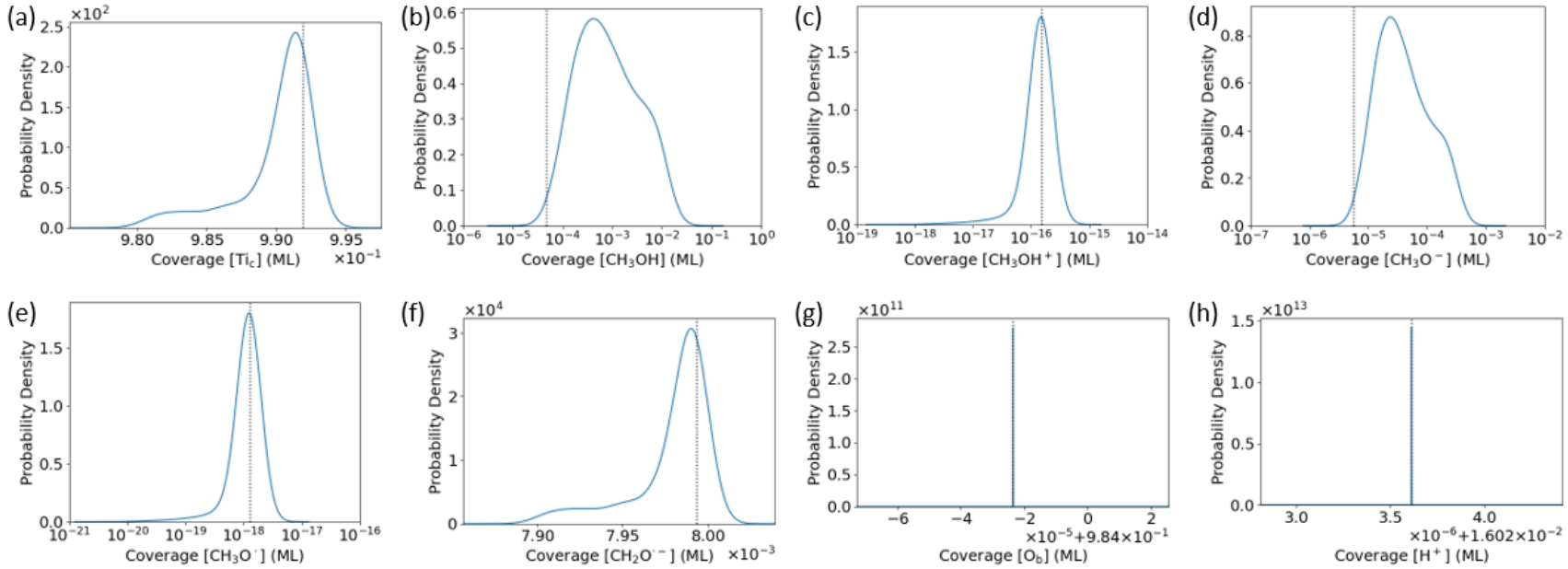

Figure A-56: Distributions of the coverages at 180 K in HMF with the Poisson ($k = 2$) distribution of trap states.

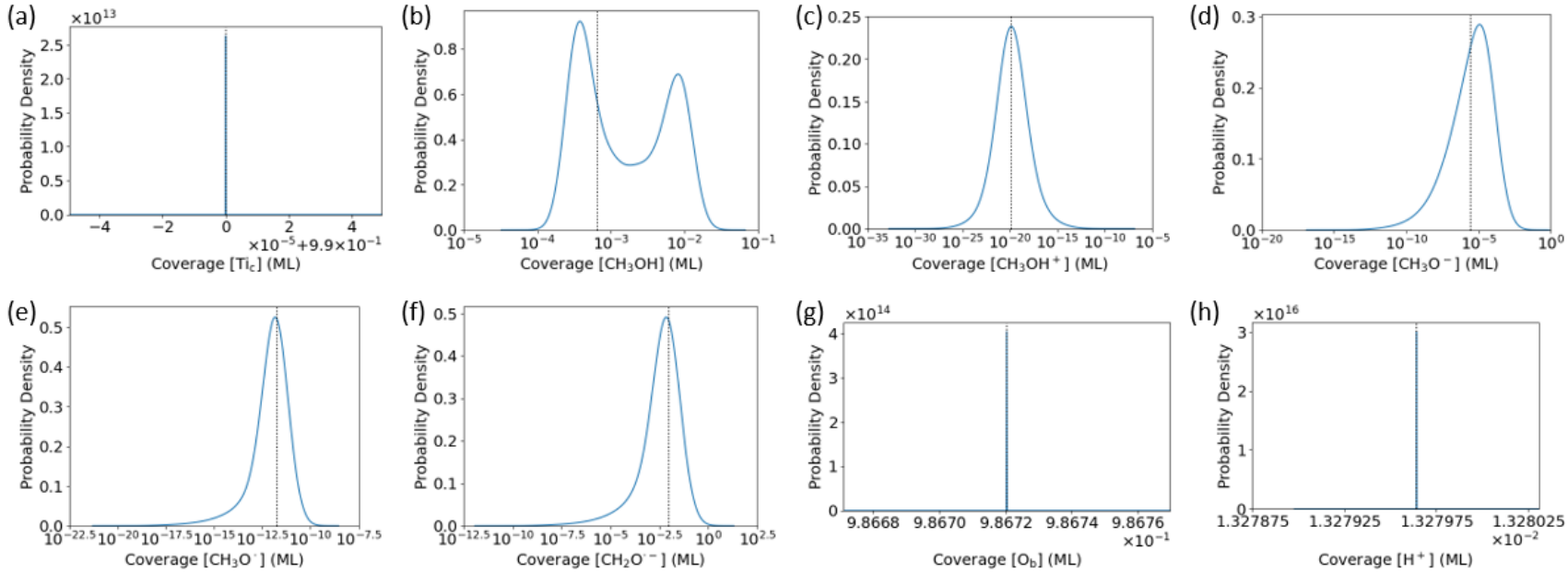

Figure A-57: Distributions of the coverages at 80 K in HMF with a hyperbolic secant distribution of trap states.

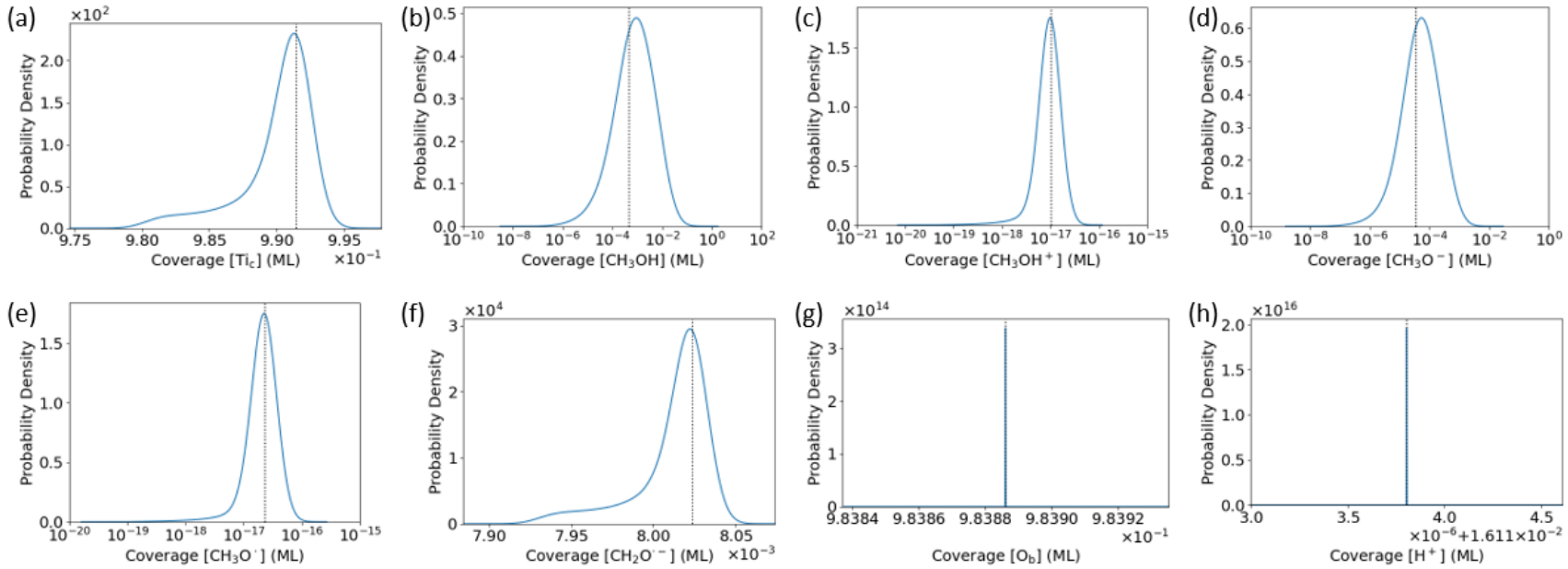

Figure A-58: Distributions of the coverages at 180 K in HMF with a hyperbolic secant distribution of trap states.

Appendix B

Supplementary Information: Machine Learning Dynamic Correlation in Lattice Lotka-Volterra Model

B.1 Concrete Examples of Chemical Master Equation

The chemical master equation (CME) of even simple model systems might be cumbersome to write down. For example, consider the lattice Lotka-Volterra model (LLVM) on a 2×2 lattice. There are already $3^{2\times 2} = 81$ possible configurations. Here, we examine just a couple of them.

For example, the probability of configuration $\begin{array}{|c|c|}\hline A & B \\ \hline O & B \\ \hline \end{array}$ obeys

$$\dot{P}(\begin{array}{|c|c|}\hline A & B \\ \hline O & B \\ \hline \end{array}) = + k_{AB\to BB} P(\begin{array}{|c|c|}\hline A & A \\ \hline O & B \\ \hline \end{array}) + k_{AB\to BB} P(\begin{array}{|c|c|}\hline A & B \\ \hline O & A \\ \hline \end{array}) + k_{B\to O} P(\begin{array}{|c|c|}\hline A & B \\ \hline B & B \\ \hline \end{array})$$
$$- k_{OA\to AA} P(\begin{array}{|c|c|}\hline A & B \\ \hline O & B \\ \hline \end{array}) - k_{AB\to BB} P(\begin{array}{|c|c|}\hline A & B \\ \hline O & B \\ \hline \end{array}) - 2k_{B\to O} P(\begin{array}{|c|c|}\hline A & B \\ \hline O & B \\ \hline \end{array}) \tag{B.1}$$

where $k_{AB\to BB}$ is the rate constant of the elementary step, $A+B \to B+B$, for example. The additive terms run over the configurations that can transform into $\begin{array}{|c|c|}\hline A & B \\ \hline O & B \\ \hline \end{array}$ in an elementary step. Meanwhile, the subractive terms run over the elementary steps that can take place on $\begin{array}{|c|c|}\hline A & B \\ \hline O & B \\ \hline \end{array}$.

Here is another example:

$$\dot{P}(\begin{array}{|c|c|}\hline A & A \\ \hline O & B \\ \hline \end{array}) = + k_{OA\to AA} P(\begin{array}{|c|c|}\hline O & A \\ \hline O & B \\ \hline \end{array}) + k_{OA\to AA} P(\begin{array}{|c|c|}\hline A & O \\ \hline O & B \\ \hline \end{array}) + k_{B\to O} P(\begin{array}{|c|c|}\hline A & A \\ \hline B & B \\ \hline \end{array})$$
$$- k_{OA\to AA} P(\begin{array}{|c|c|}\hline A & A \\ \hline O & B \\ \hline \end{array}) - k_{AB\to BB} P(\begin{array}{|c|c|}\hline A & A \\ \hline O & B \\ \hline \end{array}) - k_{B\to O} P(\begin{array}{|c|c|}\hline A & A \\ \hline O & B \\ \hline \end{array}) \tag{B.2}$$

B.2 Kinetic Equations of Lattice Lotka-Volterra Model

The kinetic equations of one-site clusters are

$$\frac{d[O]}{dt} = + k_{B\to O}[B] - Nk_{OA\to AA}[OA] \tag{B.3}$$
$$\frac{d[A]}{dt} = + Nk_{OA\to AA}[OA] - Nk_{AB\to BB}[AB] \tag{B.4}$$
$$\frac{d[B]}{dt} = + Nk_{AB\to BB}[AB] - k_{B\to O}[B] \tag{B.5}$$

where $k_{AB\to BB}$ is the rate constant of the elementary step, $A + B \to B + B$, for example; and N is the number of nearest neighbors.

The kinetic equations of two-site clusters are

$$\frac{d[OO]}{dt} = + 2k_{B\to O}[OB] - 2(N-1)k_{OA\to AA}[OOA] \tag{B.6}$$
$$\begin{aligned}\frac{d[OA]}{dt} =& + k_{B\to O}[AB] + (N-1)k_{OA\to AA}[OOA] \\ & - k_{OA\to AA}[OA] - (N-1)k_{OA\to AA}[AOA] - (N-1)k_{AB\to BB}[OAB]\end{aligned} \tag{B.7}$$
$$\begin{aligned}\frac{d[OB]}{dt} =& + k_{B\to O}[BB] + (N-1)k_{AB\to BB}[OAB] \\ & - k_{B\to O}[OB] - (N-1)k_{OA\to AA}[AOB]\end{aligned} \tag{B.8}$$
$$\begin{aligned}\frac{d[AA]}{dt} =& + 2k_{OA\to AA}[OA] + 2(N-1)k_{OA\to AA}[AOA] \\ & - 2(N-1)k_{AB\to BB}[AAB]\end{aligned} \tag{B.9}$$
$$\begin{aligned}\frac{d[AB]}{dt} =& + (N-1)k_{OA\to AA}[AOB] + (N-1)k_{AB\to BB}[AAB] \\ & - k_{B\to O}[AB] - k_{AB\to BB}[AB] - (N-1)k_{AB\to BB}[BAB]\end{aligned} \tag{B.10}$$
$$\frac{d[BB]}{dt} = + 2k_{AB\to BB}[AB] + 2(N-1)k_{AB\to BB}[BAB] - 2k_{B\to O}[BB] \tag{B.11}$$

B.3 NO+CO / Pt(110)-(1×1)

Here, we discuss how the NO + CO reaction on the Pt(100)-(1 × 1) surface might be coarse-grained on to LLVM. We base our coarse-graining scheme on the theoretical and experimental results of Imbihl *et al.* [1, 3, 143] The mechanism of the NO + CO reaction has been proposed to be

$$\mathrm{CO(g)} + * \leftrightharpoons \mathrm{CO(ad)} \tag{B.12}$$

$$\mathrm{NO(g)} + * \leftrightharpoons \mathrm{NO(ad)} \tag{B.13}$$

$$\mathrm{NO(ad)} + * \rightarrow \mathrm{N(ad)} + \mathrm{O(ad)} \tag{B.14}$$

$$2\mathrm{N(ad)} \rightarrow \mathrm{N_2(g)} + 2* \tag{B.15}$$

$$\mathrm{CO(ad)} + \mathrm{O(ad)} \rightarrow \mathrm{CO_2(g)} + 2* \tag{B.16}$$

where $*$ is a vacancy. Since N is not a strong adsorbant to Pt(100), we assume that it forms N_2 and desorbs as soon as it appears on the surface.

Combining Eq. (B.14), (B.15), and (B.16) reveals the auotocatalytic nature of the reaction

$$\mathrm{NO(ad)} + \mathrm{CO(ad)} + * \rightarrow \mathrm{CO_2(g)} + \frac{1}{2}\mathrm{N_2(g)} + 3* \tag{B.17}$$

The vacancy on the reactant side is needed to initiate the dissociation of NO. Notice that more vacancies are produced at the end of the reaction. On a surface that is covered in a mixed NO/CO adlayer, the vacancies would undergo explosive growth, starting with a few vacancies as seeds. Coarse-graining the lattice so that the minimal unit is a cluster of sites, the explosive growth of vacancies can be written as

$$\mathrm{NO/CO} + * \rightarrow * + * \tag{B.18}$$

When the surface has an abundance of vacancies, the dissociation of NO is no longer the rate-limiting step. Combining Eq. (B.13), (B.14), and(B.15) gives

$$\mathrm{NO(g)} + 2* \rightarrow \mathrm{O(ad)} + \frac{1}{2}\mathrm{N_2(g)} + * \tag{B.19}$$

However, the formation of an O adlayer is inhibited by its reaction with CO. In a neighborhood that is rich in O (in addition to vacancies), the inhibition can be suppressed to some extent. The excess of O excludes CO, reducing the likelihood that individual O atoms would react with CO and enabling O and NO to accumulate. In the coarse-graining scheme, the formation of the O adlayer can be written as

$$\mathrm{O} + * \rightarrow \mathrm{O} + \mathrm{O} \tag{B.20}$$

Hereinafter, the surface undergoes a gradual restoration of the mixed NO/CO adlayer. Combining Equations (B.12) and (B.16) gives

$$\mathrm{CO(g)} + \mathrm{O(ad)} + * \rightarrow \mathrm{CO_2(g)} + 2* \tag{B.21}$$

The above chemical equation may appear to represent an explosive growth of vacancies. However, the excess of O continues to exclude CO, and the new vacancies are occupied by NO, which then cannot dissociate due to the shortage of vacancies. Once enough O in the neighborhood has been replaced by NO, CO can begin to accumulate along with NO, which cannot react with CO by itself. In the coarse-graining scheme, the restoration of the NO/CO adlayer can be written as

$$\mathrm{O} \rightarrow \mathrm{NO/CO} \tag{B.22}$$

Together, Equations (B.18), (B.20), and (B.22) give LLVM.

B.4 Supplementary Figures and Tables

The following are the supplementary figures and tables that are referenced in Chapter 3.

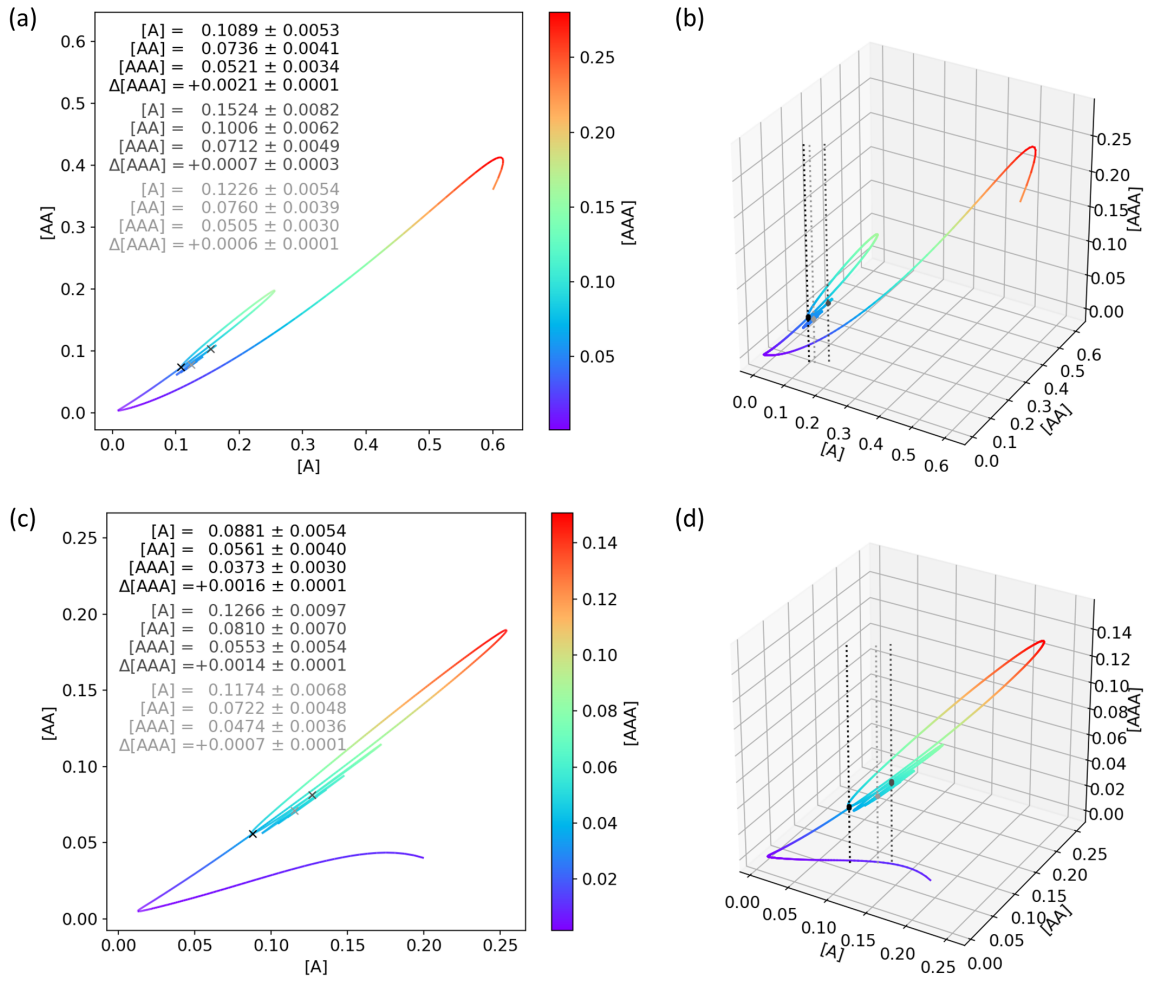

Figure B-1: Self-crossings of the time-dependent one-site, two-site, and three-site probabilities. The curve was obtained as an average over 20 KMC simulations on a 1000×1000 lattice. On the 2D plots in panels (a) and (c), the self-crossings on the xy-plane are indicated by crosses, and the coordinates and the standard deviations are provided on the upper left. On the 3D plots in panels (b) and (d), the self-crossings on the xy-plane are indicated by bold dots, and the vertical dotted lines are visual aids. The rate constants were $(k_1, k_2, k_3) = (0.5, 0.3, 0.1)$. For the plots in panels (a) and (b), the initial conditions were $([O], [A], [B]) = (0.2, 0.6, 0.2)$. For the plots in panels (c) and (d), the initial conditions were $(0.2, 0.2, 0.6)$.

Fixed	Dynamics	Varied	Simulations
$(y_1, y_2, y_3) = (0.4, 0.3, 0.3)$		$k_1, k_2, k_3 \in \{0.1, 0.3, 0.5, 0.7, 0.9\}$	125
$(k_1, k_2, k_3) = (0.5, 0.3, 0.1)$ $(k_1, k_2, k_3) = (0.1, 0.9, 0.5)$	damped oscillations	$[O], [A], [B] \in \{0.1, 0.2, ..., 0.8\}$ $[O] + [A] + [B] = 1.0$	7×36
$(k_1, k_2, k_3) = (0.7, 0.1, 0.1)$ $(k_1, k_2, k_3) = (0.7, 0.3, 0.5)$ $(k_1, k_2, k_3) = (0.3, 0.5, 0.7)$	simple decay and overshoot-undershoot		
$(k_1, k_2, k_3) = (0.3, 0.7, 0.1)$ $(k_1, k_2, k_3) = (0.1, 0.1, 0.3)$	depletion		

Table B.1: Selections of rate constants and initial conditions in the training data. The types of dynamics were assigned using the initial condition $([O], [A], [B]) = (0.4, 0.3, 0.3)$ as the reference. Depletion means that one or both of $[A]$ and $[B]$ go to zero.

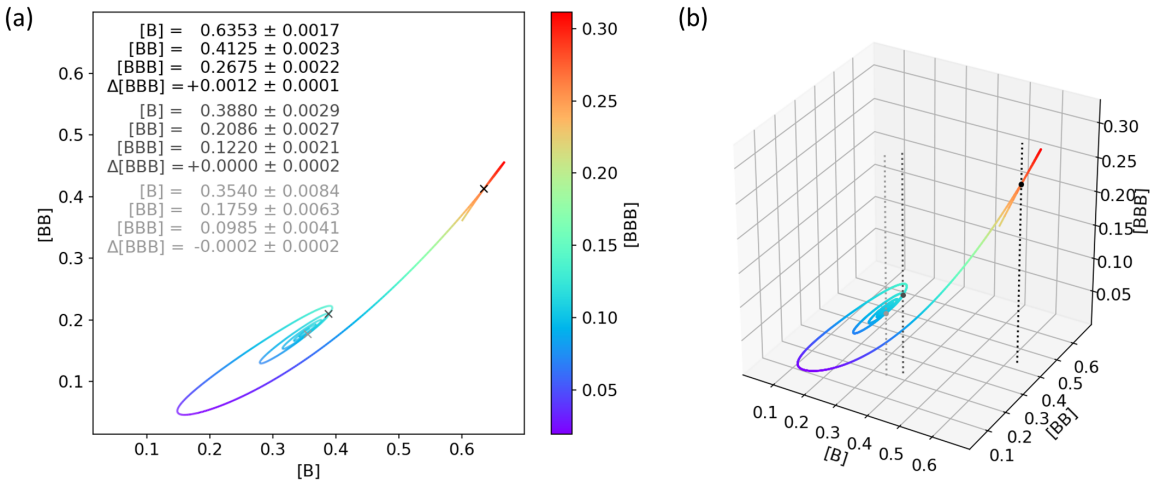

Figure B-2: Self-crossings of the time-dependent one-site, two-site, and three-site probabilities. The curve was obtained as an average over 20 KMC simulations on a 1000×1000 lattice. (a) On the 2D plot, the self-crossings on the xy-plane are indicated by crosses, and the coordinates and the standard deviations are provided on the upper left. (b) On the 3D plot, the self-crossings on the xy-plane are indicated by bold dots, and the vertical dotted lines are visual aids. The rate constants were $(k_1, k_2, k_3) = (0.5, 0.3, 0.1)$, and the initial conditions were $([O], [A], [B]) = (0.2, 0.2, 0.6)$.

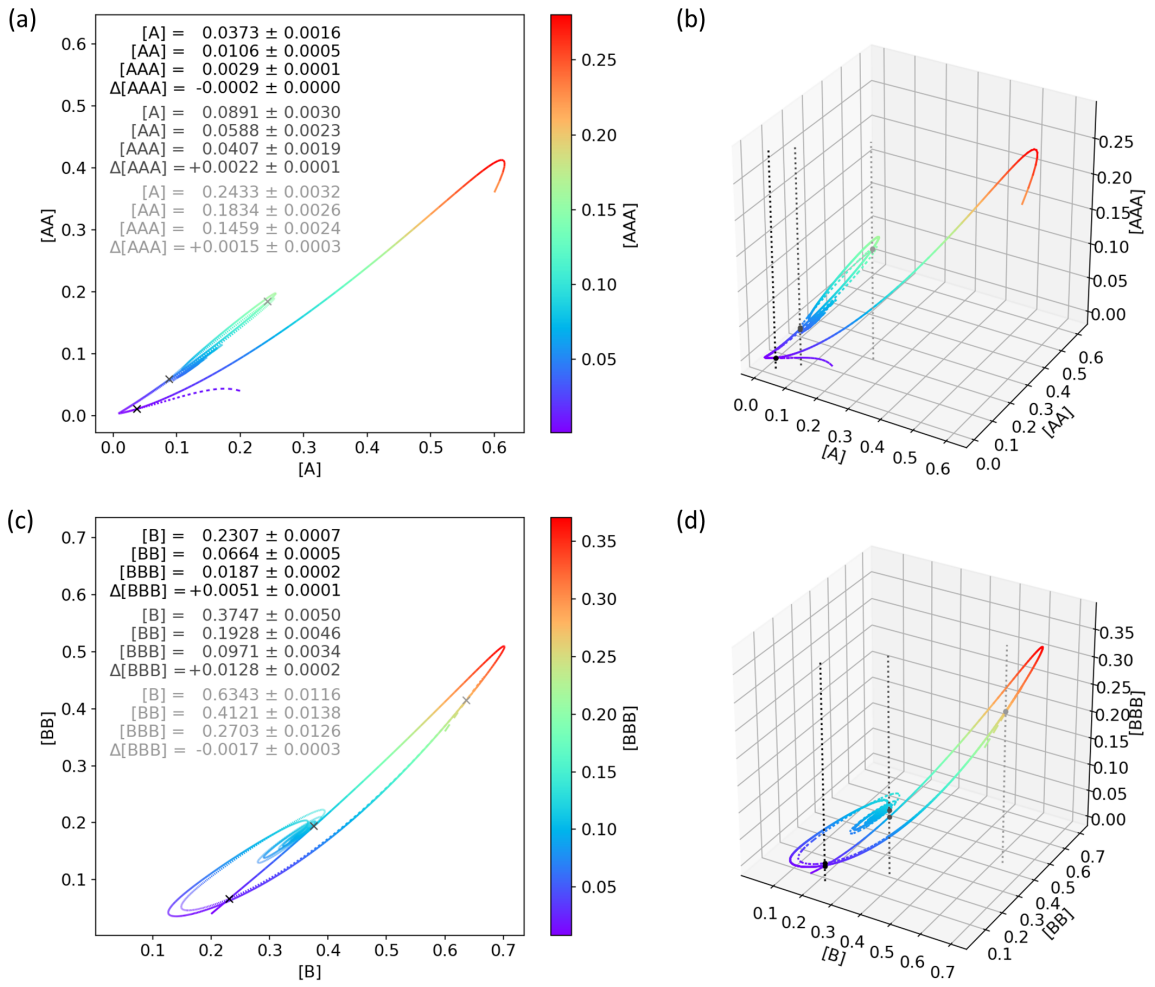

Figure B-3: Two-curve crossings of the time-dependent one-site, two-site, and three-site probabilities. The curves were obtained as averages over 20 KMC simulations on a 1000×1000 lattice. On the 2D plots in panels (a) and (c), the crossings of the two curves on the xy-plane are indicated by crosses, and the coordinates and the standard deviations are provided on the upper left. On the 3D plots in panels (b) and (d), the crossings of the two curves on the xy-plane are indicated by bold dots, and the vertical dotted lines are visual aids. The rate constants were $(k_1, k_2, k_3) = (0.5, 0.3, 0.1)$, and the solid and the dashed curves had the initial conditions of $([O], [A], [B]) = (0.2, 0.6, 0.2)$ and $(0.2, 0.2, 0.6)$, respectively.

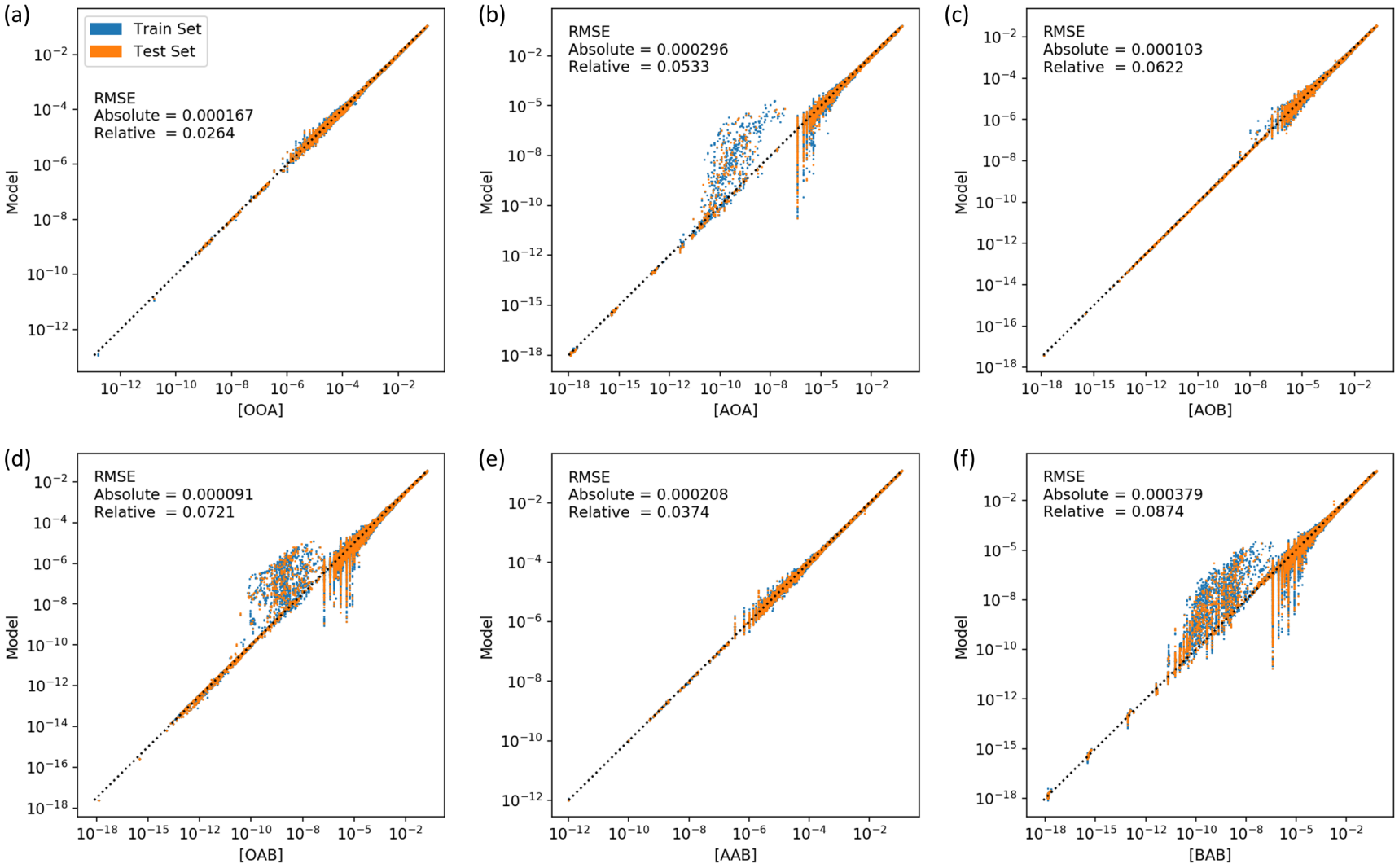

Figure B-4: Scatter plots of the ML against the KMC three-site probabilities. The panels correspond to the distinct three-site probabilities: (a) $[OOA]$; (b) $[AOA]$; (c) $[AOB]$; (d) $[OAB]$; (e) $[AAB]$; and (f) $[BAB]$. The training set is plotted in blue dots, and the test set is plotted in orange dots.

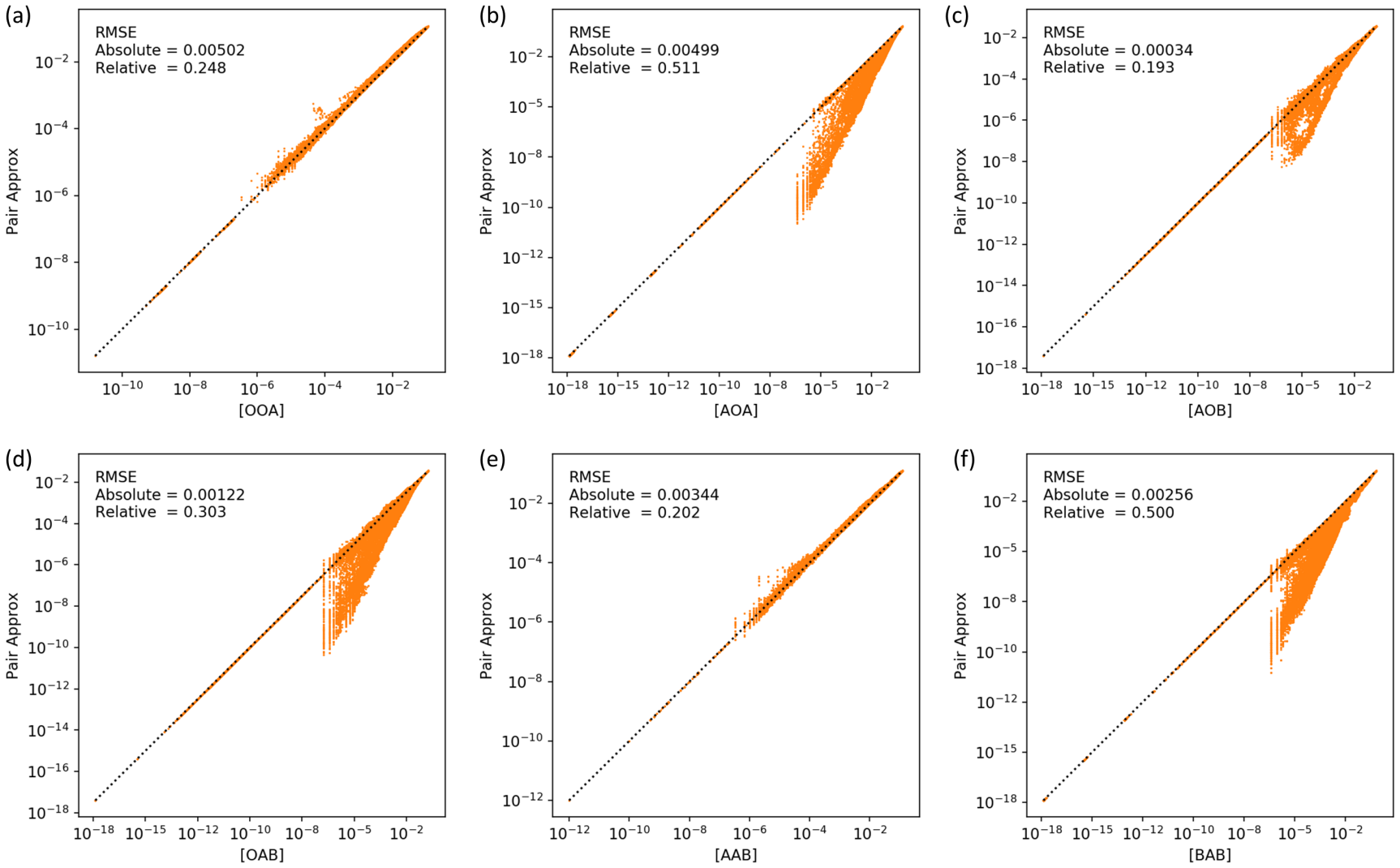

Figure B-5: Scatter plots of the PA against the KMC three-site probabilities. The panels correspond to the distinct three-site probabilities: (a) $[OOA]$; (b) $[AOA]$; (c) $[AOB]$; (d) $[OAB]$; (e) $[AAB]$; and (f) $[BAB]$. Only the test set is plotted, since PA is not a trained model.

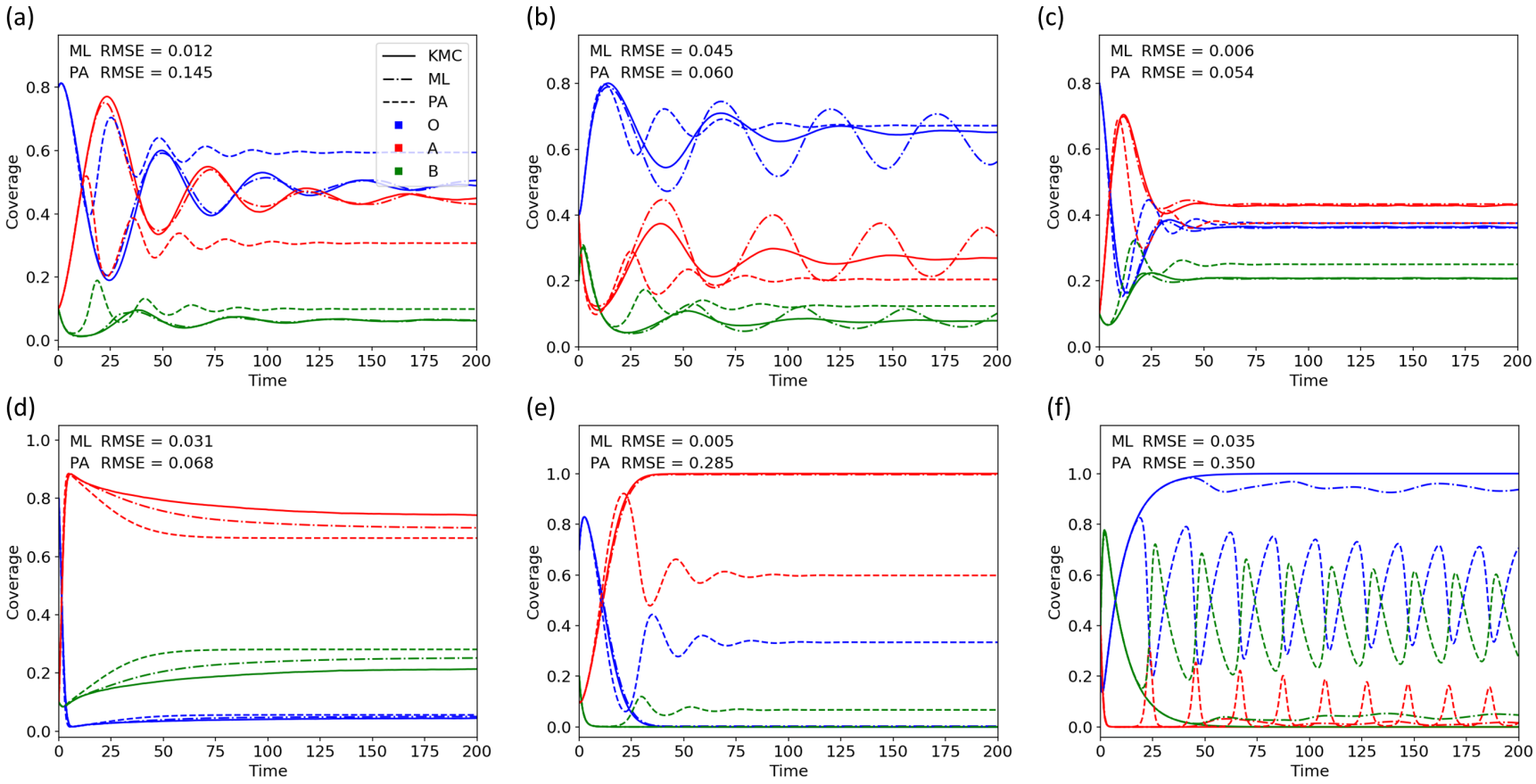

Figure B-6: Time-dependent coverages in PA (dashed lines), ML (dashed-dotted lines), and KMC (solid lines). (a) The rate constants were $(k_1, k_2, k_3) = (0.1, 0.7, 0.5)$, and the initial conditions were $([O], [A], [B]) = (0.8, 0.1, 0.1)$. (b) The rate constants and the initial conditions were $(0.1, 0.6, 0.3)$ and $(0.4, 0.4, 0.2)$, respectively. (c) The rate constants and the initial conditions were $(0.2, 0.3, 0.3)$ and $(0.8, 0.1, 0.1)$, respectively. (d) The rate constants and the initial conditions were $(0.6, 0.1, 0.2)$ and $(0.8, 0.1, 0.1)$, respectively. (e) The rate constants and the initial conditions were $(0.1, 0.6, 0.8)$ and $(0.7, 0.1, 0.2)$, respectively. (f) The rate constants and the initial conditions were $(0.8, 0.7, 0.1)$ and $(0.2, 0.4, 0.4)$, respectively.

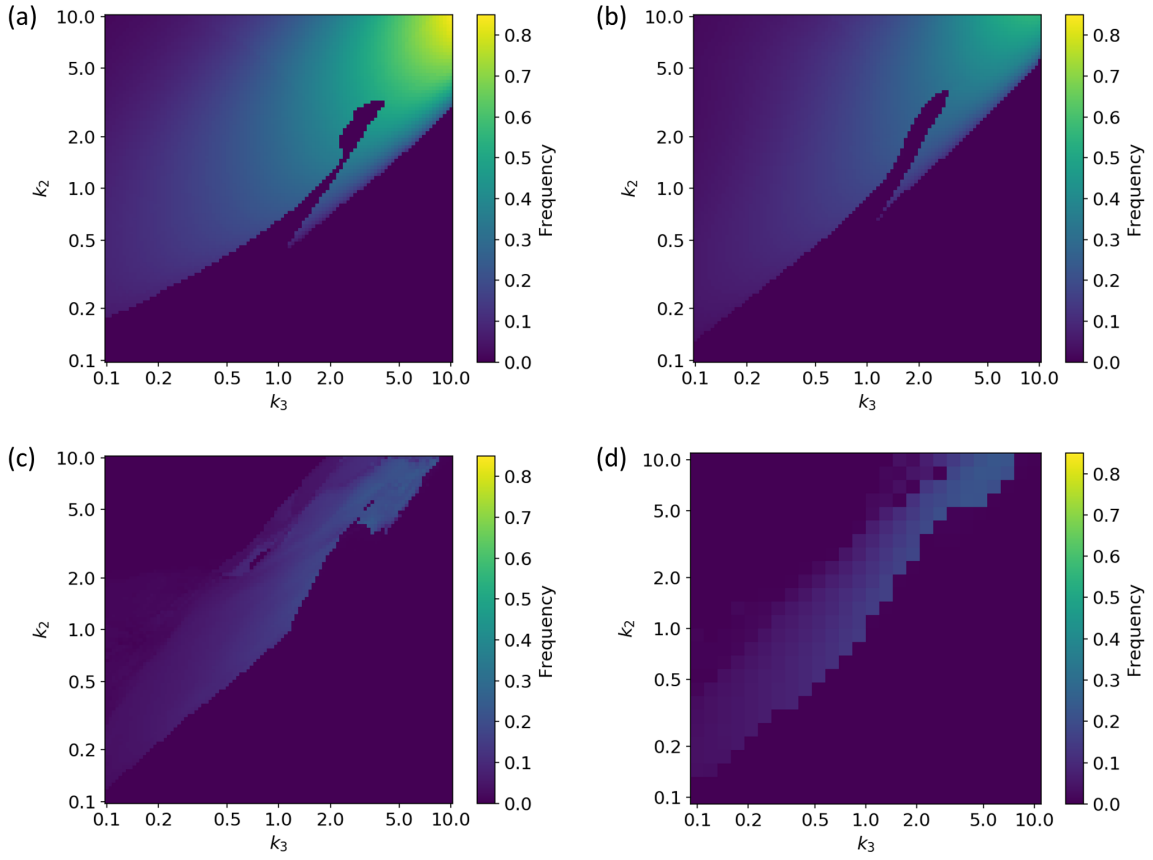

Figure B-7: Contour maps of the nonlinear oscillation frequencies in (a) MF, (b) PA, (c) ML, and (d) KMC. Given the nonlinear oscillation of the coverages, the frequency was defined as the inverse of the average crest-crest and trough-trough separation over the first two cycles (or three if resolvable). The rate constants were normalized to $k_1 = 1.0$, and the initial conditions were $([O], [A], [B]) = (0.5, 0.3, 0.2)$.

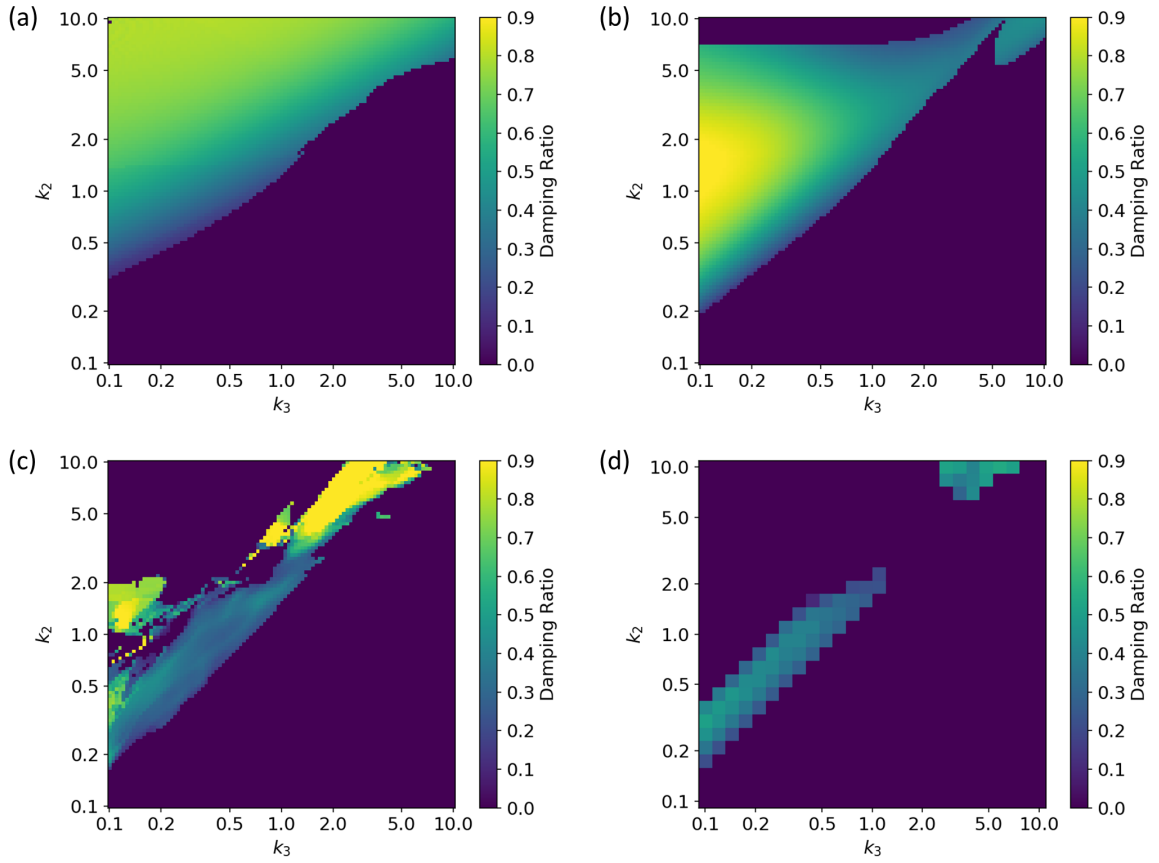

Figure B-8: Contour maps of the nonlinear oscillation damping ratios in (a) MF, (b) PA, (c) ML, and (d) KMC. Given the nonlinear oscillation of the coverages, the amplitude was defined as the crest-trough (and trough-crest) separation, and the damping ratio was define as the average ratio of consecutive crest-trough (and trough-crest) amplitudes over the first two cycles (or three if resolvable). The rate constants were normalized to $k_1 = 1.0$, and the initial conditions were $([O], [A], [B]) = (0.5, 0.3, 0.2)$.

Appendix C

Supplementary Information: Introduction to Part II

C.1 Rate of Fluorescence

We begin with the Hamiltonian of a particle in an electromagnetic field

$$\hat{H} = \frac{1}{2m}\left(\hat{\mathbf{p}} + q\mathbf{A}(\hat{\mathbf{r}})\right)^2 + V(\hat{\mathbf{r}}) \tag{C.1}$$

where m and q are the mass and the charge of the particle, respectively; $\hat{\mathbf{p}}$ and $\hat{\mathbf{r}}$ are the momentum and the position operators, respectively; V is the (unperturbed) potential energy; and A is the vector potential

$$\mathbf{A}(\hat{\mathbf{r}}) = \sum_{\mathbf{k},\boldsymbol{\epsilon}} \left(\frac{\hbar}{2\varepsilon_0 \omega_{\mathbf{k}} L^3}\right)^{1/2} \left(\hat{a}_{\mathbf{k},\boldsymbol{\epsilon}} e^{+i\mathbf{k}\cdot\hat{\mathbf{r}}}\boldsymbol{\epsilon} + \hat{a}^{\dagger}_{\mathbf{k},\boldsymbol{\epsilon}} e^{-i\mathbf{k}\cdot\hat{\mathbf{r}}}\boldsymbol{\epsilon}^*\right) \tag{C.2}$$

where $\mathbf{k}$ and $\boldsymbol{\epsilon}$ are the wave number and the polarization vectors, respectively; $\omega_{\mathbf{k}}$ is the frequency corresponding to $\mathbf{k}$; L is the length of the cubic box enclosing the system (for normalization); and $\hat{a}_{\mathbf{k},\boldsymbol{\epsilon}}$ and $\hat{a}^{\dagger}_{\mathbf{k},\boldsymbol{\epsilon}}$ are the annihilation and the creation operators, respectively. We divide the full Hamiltonian into the unperturbed Hamiltonian and

the first-order perturbation

$$\hat{H}^{(0)} = \frac{1}{2m}\hat{\mathbf{p}}^2 + V(\hat{\mathbf{r}}) \tag{C.3}$$

$$\hat{H}^{(1)} = \frac{q}{m}\mathbf{A}(\hat{\mathbf{r}}) \cdot \hat{\mathbf{p}} \tag{C.4}$$

To be precise, we are interested in emission, so we only need the part of the perturbation corresponding to the creation of a photon

$$\hat{H}^{(+)} = \sum_{\mathbf{k},\boldsymbol{\epsilon}} \frac{q}{m}\left(\frac{\hbar}{2\varepsilon_0\omega_{\mathbf{k}}L^3}\right)^{1/2} \hat{a}^\dagger_{\mathbf{k},\boldsymbol{\epsilon}} e^{-i\mathbf{k}\cdot\hat{\mathbf{r}}}\boldsymbol{\epsilon}^* \cdot \hat{\mathbf{p}} \tag{C.5}$$

We calculate the transition amplitudes in the interaction picture

$$\langle \mathrm{S}_0, n_{\mathbf{k},\boldsymbol{\epsilon}} + 1|\psi(t)\rangle = \frac{1}{i\hbar}\int_0^t \langle \mathrm{S}_0, n_{\mathbf{k},\boldsymbol{\epsilon}} + 1|H^{(+)}(t')|\mathrm{S}_1, n_{\mathbf{k},\boldsymbol{\epsilon}}\rangle \, dt' \tag{C.6}$$

On evaluating the matrix element, it is obvious that only the term corresponding to wave number $\mathbf{k}$ and polarization $\boldsymbol{\epsilon}$ survives.

$$\begin{aligned}&\langle \mathrm{S}_0, n_{\mathbf{k},\boldsymbol{\epsilon}} + 1|\psi(t)\rangle \\ &\quad = \frac{q}{im}\left(\frac{1}{2\varepsilon_0\hbar\omega_{\mathbf{k}}L^3}\right)^{1/2} \langle n_{\mathbf{k},\boldsymbol{\epsilon}} + 1|a^\dagger_{\mathbf{k},\boldsymbol{\epsilon}}|n_{\mathbf{k},\boldsymbol{\epsilon}}\rangle \, \boldsymbol{\epsilon}^* \cdot \langle \mathrm{S}_0|e^{-i\mathbf{k}\cdot\hat{\mathbf{r}}}\hat{\mathbf{p}}|\mathrm{S}_1\rangle \int_0^t e^{i(\omega_{\mathbf{k}}-\omega_{10})t'}dt'\end{aligned} \tag{C.7}$$

The first matrix element is given by the normalization of the creation operator

$$\langle n_{\mathbf{k},\boldsymbol{\epsilon}} + 1|\hat{a}^\dagger_{\mathbf{k},\boldsymbol{\epsilon}}|n_{\mathbf{k},\boldsymbol{\epsilon}}\rangle = (n_{\mathbf{k},\boldsymbol{\epsilon}} + 1)^{1/2} \tag{C.8}$$

In the second matrix element, we can assume $\mathbf{k}\cdot\hat{\mathbf{r}} \approx 0$, since the length scales of molecules are much smaller than the wavelength of visible light. Using the canonical commutation relation, the second matrix element becomes

$$\langle \mathrm{S}_0|\hat{\mathbf{p}}|\mathrm{S}_1\rangle = \frac{m}{i\hbar}\langle \mathrm{S}_0|[\hat{\mathbf{r}}, \hat{H}^{(0)}]|\mathrm{S}_1\rangle = im\omega_{10}\langle \mathrm{S}_0|\hat{\mathbf{r}}|\mathrm{S}_1\rangle \tag{C.9}$$

where we have used $\hbar\omega_{10} = E_{\mathrm{S}_1} - E_{\mathrm{S}_0}$; and $\langle \mathrm{S}_0|\hat{\mathbf{r}}|\mathrm{S}_1\rangle$ is the transition dipole moment (TDM). The last integral evaluates to

$$\int_0^t e^{i(\omega_{\mathbf{k}}-\omega_{10})t'}dt' = -i\,\frac{\sin((\omega_{\mathbf{k}}-\omega_{10})t/2)}{(\omega_{\mathbf{k}}-\omega_{10})/2}\,e^{i(\omega_{\mathbf{k}}-\omega_{10})t/2} \tag{C.10}$$

Therefore, the transition amplitudes are

$$\begin{aligned}&\langle \mathrm{S}_0, n_{\mathbf{k},\boldsymbol{\epsilon}}+1|\psi(t)\rangle \\ &\qquad = -iq\omega_{10}\left(\frac{n_{\mathbf{k},\boldsymbol{\epsilon}}+1}{2\varepsilon_0\hbar\omega_{\mathbf{k}}L^3}\right)^{1/2}\boldsymbol{\epsilon}^*\cdot\,\langle \mathrm{S}_0|\hat{\mathbf{r}}|\mathrm{S}_1\rangle\,\frac{\sin((\omega_{\mathbf{k}}-\omega_{10})t/2)}{(\omega_{\mathbf{k}}-\omega_{10})/2}\,e^{i(\omega_{\mathbf{k}}-\omega_{10})t/2}\end{aligned} \tag{C.11}$$

Since we are interested in spontaneous emission, we assume $n_{\mathbf{k},\boldsymbol{\epsilon}} = 0$.

We obtain the total $\mathrm{S}_1 \to \mathrm{S}_0$ transition probability by summing over the wave number and the polarization vectors

$$\begin{aligned}|\,\langle \mathrm{S}_0|\psi(t)\rangle\,|^2 &= \sum_{\mathbf{k},\boldsymbol{\epsilon}}|\,\langle \mathrm{S}_0, n_{\mathbf{k},\boldsymbol{\epsilon}}+1|\psi(t)\rangle\,|^2 \\ &= \frac{q^2}{2\varepsilon_0\hbar L^3}\sum_{\mathbf{k}}\frac{{\omega_{10}}^2}{\omega_{\mathbf{k}}}\left(\frac{\sin((\omega_{\mathbf{k}}-\omega_{10})t/2)}{(\omega_{\mathbf{k}}-\omega_{10})/2}\right)^2\sum_{\boldsymbol{\epsilon}}|\boldsymbol{\epsilon}^*\cdot\,\langle \mathrm{S}_0|\hat{\mathbf{r}}|\mathrm{S}_1\rangle\,|^2\end{aligned} \tag{C.12}$$

Since the polarization spans the plane perpendicular to the wave number, the sum over the polarizations reduces to

$$\sum_{\boldsymbol{\epsilon}}|\boldsymbol{\epsilon}^*\cdot\,\langle \mathrm{S}_0|\hat{\mathbf{r}}|\mathrm{S}_1\rangle\,|^2 = |\mathbf{n}\times\,\langle \mathrm{S}_0|\hat{\mathbf{r}}|\mathrm{S}_1\rangle\,|^2 \tag{C.13}$$

where $\mathbf{n}$ is a unit vector parallel to the wave number. We replace the sum over the wave numbers with an integral

$$\sum_{\mathbf{k}} \to \left(\frac{L}{2\pi}\right)^3\int d\mathbf{k} \tag{C.14}$$

Now, the transition probability is

$$|\langle S_0|\psi(t)\rangle|^2 = \frac{q^2}{16\pi^3\varepsilon_0\hbar}\int \frac{{\omega_{10}}^2}{\omega_{\mathbf{k}}}\left(\frac{\sin((\omega_{\mathbf{k}}-\omega_{10})t/2)}{(\omega_{\mathbf{k}}-\omega_{10})/2}\right)^2 |\mathbf{n}\times\langle S_0|\hat{\mathbf{r}}|S_1\rangle|^2 d\mathbf{k} \quad \text{(C.15)}$$

It is the convenient to evaluate this integral in spherical coordinates with the z-axis along the TDM

$$\int d\mathbf{k} = \int_0^\infty k^2 dk \int_0^\pi \sin\theta d\theta \int_0^{2\pi} d\phi \quad \text{(C.16)}$$

Further, we make a change of variables $\omega = kc$, where c is the speed of light. Now, the transition probability is

$$|\langle S_0|\psi(t)\rangle|^2 = \frac{q^2{\omega_{10}}^2}{8\pi^2\varepsilon_0\hbar c^3}|\langle S_0|\hat{\mathbf{r}}|S_1\rangle|^2 \int_0^\infty \left(\frac{\sin((\omega-\omega_{10})t/2)}{(\omega-\omega_{10})/2}\right)^2 \omega d\omega \int_0^\pi \sin^3\theta d\theta \quad \text{(C.17)}$$

In the radial integral, we make a change of variables $x = (\omega-\omega_{10})t/2$

$$\int_0^\infty \left(\frac{\sin((\omega-\omega_{10})t/2)}{(\omega-\omega_{10})/2}\right)^2 \omega d\omega = 2t\int_{-\omega_{10}t/2}^{+\infty}\left(\frac{\sin x}{x}\right)^2\left(\omega_{10}+\frac{2x}{t}\right)dx \quad \text{(C.18)}$$

For interactions of molecules with visible light, we can assume $\omega_{10}t \gg 1$. The radial integral reduces to

$$(C.18) \approx 2\omega_{10}t\int_{-\infty}^{+\infty}\left(\frac{\sin x}{x}\right)^2 dx = 2\pi\omega_{10}t \quad \text{(C.19)}$$

Meanwhile, the angular integral is

$$\int_0^\pi \sin^3\theta d\theta = \frac{4}{3} \quad \text{(C.20)}$$

Therefore, the total transition probaility is

$$|\langle S_0|\psi(t)\rangle|^2 = \frac{q^2{\omega_{10}}^3}{3\pi\varepsilon_0\hbar c^3}|\langle S_0|\hat{\mathbf{r}}|S_1\rangle|^2 t \quad \text{(C.21)}$$

We rewrite this expression as

$$| \langle \mathrm{S}_0 | \psi(t) \rangle |^2 = \frac{q^2 {\omega_{10}}^2}{2\pi\varepsilon_0 m c^3} f_{10} t \tag{C.22}$$

using the definition of the oscillator strength

$$f_{10} = \frac{2m\omega_{10}}{3\hbar} | \langle \mathrm{S}_0 | \hat{\mathbf{r}} | \mathrm{S}_1 \rangle |^2 \tag{C.23}$$

As desired, the rate of fluorescence is the same as the Einstein coefficient [191]

$$k_{\mathrm{F}} = \frac{q^2 {\omega_{10}}^2}{2\pi\varepsilon_0 m c^3} f_{10} \tag{C.24}$$

Appendix D

Supplementary Information: Simple Four-State Model of TADF

D.1 Approximations Behind the Four-State Hamiltonian

First, we consider the donor-acceptor system to be isolated; therefore, not interacting with other molecules in the environment. Next, we assume that there are only four excited diabatic states participating in the reverse intersystem crossing and fluorescence. These states can be effectively described by three orbitals localized on either donor or acceptor moieties. The conceptually simplest way to think about these states is to treat them as single electron configurations, which means that they result from some mean-field electronic structure approximation. Due to orthogonalization tails, the orbitals cannot be completely localized on the donor or acceptor. Assuming that such states can still be classified as charge transfer and local excitations, one obtains the four-state Hamiltonian (Equation 6.7) with coupling elements given by Equations 6.8-6.11. However, the form of the Hamiltonian in Equation 6.7 is not limited to the mean-field approximation, and the diabatic basis states can be treated as correlated many-body states. Such diabatic many-body representation would mean that the states are not necessarily strictly orthogonal and that, in addition to the

Hamiltonian, the system's description requires also an overlap matrix. We assume in the model that the off-diagonal overlaps can be neglected, so the expressions for coupling elements (Equations 6.8-6.11) still hold. In principle, there might be also some correlation effects that would break the symmetry between $\langle \mathrm{CT1}|\hat{H}|\mathrm{LE1}\rangle$ and $\langle \mathrm{CT2}|\hat{H}|\mathrm{LE2}\rangle$, as well as $\langle \mathrm{CT1}|\hat{H}|\mathrm{LE2}\rangle$ and $\langle \mathrm{CT2}|\hat{H}|\mathrm{LE1}\rangle$ coupling elements. In any case, we are assuming that these couplings do not change by flipping the spin of electrons in the excited orbitals.

D.2 Eigenvalues and Eigenvectors of the Four-State Hamiltonian

Eigenvalues:

$$E_{\mathrm{S}_1} = \frac{1}{2}(\Delta E + K_{\mathrm{LE}} + K_{\mathrm{CT}}) - \sqrt{\frac{1}{4}(\Delta E + K_{\mathrm{LE}} + K_{\mathrm{CT}})^2 - (\Delta E + K_{\mathrm{LE}})K_{\mathrm{CT}} + (t + K_{\mathrm{X}})^2} \tag{D.1}$$

$$E_{\mathrm{S}_2} = \frac{1}{2}(\Delta E + K_{\mathrm{LE}} + K_{\mathrm{CT}}) + \sqrt{\frac{1}{4}(\Delta E + K_{\mathrm{LE}} + K_{\mathrm{CT}})^2 - (\Delta E + K_{\mathrm{LE}})K_{\mathrm{CT}} + (t + K_{\mathrm{X}})^2} \tag{D.2}$$

$$E_{\mathrm{T}_1} = \frac{1}{2}(\Delta E - K_{\mathrm{LE}} - K_{\mathrm{CT}}) - \sqrt{\frac{1}{4}(\Delta E - K_{\mathrm{LE}} - K_{\mathrm{CT}})^2 + (\Delta E - K_{\mathrm{LE}})K_{\mathrm{CT}} + (t - K_{\mathrm{X}})^2} \tag{D.3}$$

$$E_{\mathrm{T}_1} = \frac{1}{2}(\Delta E - K_{\mathrm{LE}} - K_{\mathrm{CT}}) + \sqrt{\frac{1}{4}(\Delta E - K_{\mathrm{LE}} - K_{\mathrm{CT}})^2 + (\Delta E - K_{\mathrm{LE}})K_{\mathrm{CT}} + (t - K_{\mathrm{X}})^2} \tag{D.4}$$

Eigenvectors (unnormalized) in the basis of spin-pure diabatic states:

$$|\mathrm{S}_1\rangle = (t + K_\mathrm{X}) \left|{}^1\mathrm{LE}\right\rangle + \Bigg[-\frac{1}{2}(\Delta E + K_\mathrm{LE} - K_\mathrm{CT}) - \sqrt{\frac{1}{4}(\Delta E + K_\mathrm{LE} + K_\mathrm{CT})^2 - (\Delta E + K_\mathrm{LE})K_\mathrm{CT} + (t + K_\mathrm{X})^2} \Bigg] \left|{}^1\mathrm{CT}\right\rangle \quad \text{(D.5)}$$

$$|\mathrm{S}_2\rangle = (t + K_\mathrm{X}) \left|{}^1\mathrm{LE}\right\rangle + \Bigg[-\frac{1}{2}(\Delta E + K_\mathrm{LE} - K_\mathrm{CT}) + \sqrt{\frac{1}{4}(\Delta E + K_\mathrm{LE} + K_\mathrm{CT})^2 - (\Delta E + K_\mathrm{LE})K_\mathrm{CT} + (t + K_\mathrm{X})^2} \Bigg] \left|{}^1\mathrm{CT}\right\rangle \quad \text{(D.6)}$$

$$|\mathrm{T}_1\rangle = (t - K_\mathrm{X}) \left|{}^1\mathrm{LE}\right\rangle + \Bigg[-\frac{1}{2}(\Delta E - K_\mathrm{LE} + K_\mathrm{CT}) - \sqrt{\frac{1}{4}(\Delta E - K_\mathrm{LE} - K_\mathrm{CT})^2 + (\Delta E - K_\mathrm{LE})K_\mathrm{CT} + (t - K_\mathrm{X})^2} \Bigg] \left|{}^1\mathrm{CT}\right\rangle \quad \text{(D.7)}$$

$$|\mathrm{T}_2\rangle = (t - K_\mathrm{X}) \left|{}^1\mathrm{LE}\right\rangle + \Bigg[-\frac{1}{2}(\Delta E - K_\mathrm{LE} + K_\mathrm{CT}) + \sqrt{\frac{1}{4}(\Delta E - K_\mathrm{LE} - K_\mathrm{CT})^2 + (\Delta E - K_\mathrm{LE})K_\mathrm{CT} + (t - K_\mathrm{X})^2} \Bigg] \left|{}^1\mathrm{CT}\right\rangle \quad \text{(D.8)}$$

D.3 Monte Carlo Sampling of the Parameter Space

D.3.1 Sampling Ranges

To sample the parameter space of the four-state Hamiltonian, we made some arbitrary choices about the relevant ranges of parameters. Typically, the HOMO $\rightarrow$ LUMO transition would be a CT state and $\Delta E > 0$; however, we do not preclude a situation where the energy of the mixed LE is lower than CT and allow for either sign of ΔE. The different character of the CT and LE states is directly reflected in the exchange couplings which we fix to have positive values such that $K_\mathrm{CT} < K_\mathrm{LE}$. The distinction between a CT and LE state needs to be somewhat arbitrary, and we choose $K = 0.25\,\mathrm{eV}$ as the cutoff value for the CT/LE classification. The couplings t and K_X can have either sign which is to some extent arbitrary. Changing the phase of ϕ_L or $\phi_{\mathrm{L}+1}$ will flip the sign of both t and K_X simultaneously without changing the

other parameters, so only the relative sign matters for the model. We expect the average absolute value of t to be larger than K_{X} since it is a sum of a one-electron hopping integral and an exchange-like twoelectron integral, while K_{X} consists of only the latter. Based on these considerations we drew the Hamiltonian parameters from uniform distributions over the following ranges: $\Delta E \in [-2, 2]$eV; $K_{\mathrm{CT}} \in [0, 0.25]$eV; $K_{\mathrm{LE}} \in [0.25, 2]$eV; $t \in [-2, 2]$eV; $K_{\mathrm{S}} \in [-1, 1]$eV.

D.3.2 Data Filtering

We have set arbitrary cutoff values to keep only those combinations of parameters that lead to small singlet-triplet gaps, appreciable LE component in the S1 state, and significant difference in the electronic character of S_1 and T_1. Typically, the reported TADF emitters have singlet-triplet gaps up to 200 meV, and computational studies suggest that S_1^{LE} and ΔCT on the order of 10 % may be sufficient for TADF activity [236]. For this study we apply more stringent criteria, namely $\Delta E_{\mathrm{ST}} < 0.1$ eV, $S_1^{\mathrm{LE}} > 0.25$, and $\Delta\mathrm{CT} > 0.4$, where the latter two values approximately correspond to maxima in Figure 6-2b and Figure 6-2c.

D.3.3 Principal Component Analysis

The Principal Component Analysis (PCA) was performed on a covariance matrix of the parameter vectors in the filtered set. The original parameters of the four-state model were replaced by their combinations which appear directly in the singlet and triplet Hamiltonians, i.e.

$$x_1 = \Delta E + K_{\mathrm{LE}} \tag{D.9}$$

$$x_2 = \Delta E - K_{\mathrm{LE}} \tag{D.10}$$

$$x_3 = K_{\mathrm{CT}} \tag{D.11}$$

$$x_4 = t + K_{\mathrm{X}} \tag{D.12}$$

$$x_5 = t - K_{\mathrm{X}} \tag{D.13}$$

The resulting principal components c_i had the following coefficient in the original basis (coefficients smaller than 0.005 have been suppressed)

$$c_1 = 0.990x_4 + 0.143x_5 \tag{D.14}$$

$$c_2 = 0.959x_1 + 0.282x_2 \tag{D.15}$$

$$c_3 = 0.282x_1 - 0.959x_2 + 0.010x_5 \tag{D.16}$$

$$c_4 = 0.010x_2 - 0.143x_4 + 0.990x_5 \tag{D.17}$$

$$c_5 = 1.000x_3 \tag{D.18}$$

and the following singular values: $\lambda_1 = 255.29$, $\lambda_2 = 109.78$, $\lambda_3 = 55.04$, $\lambda_4 = 34.60$, and $\lambda_5 = 9.33$, which account for 0.799, 0.148, 0.037, 0.015, and 0.001 of the total variance, respectively.

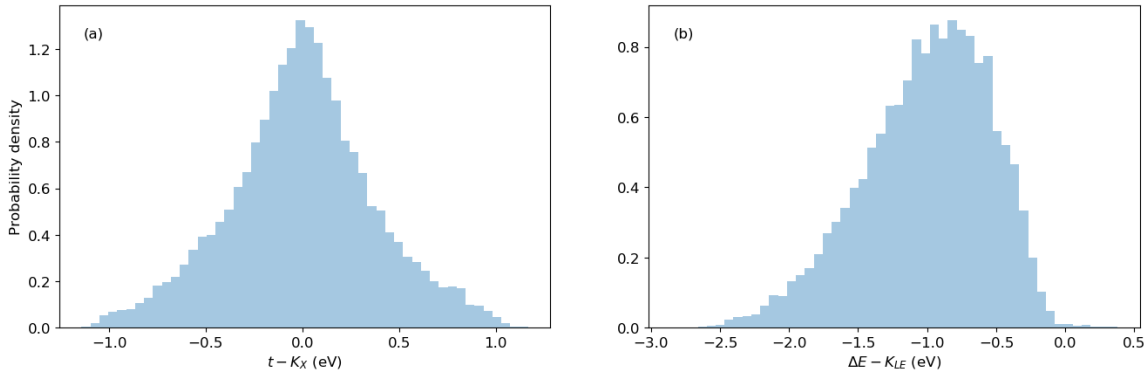

Figure D-1: Distributions of $t + K_{\mathrm{X}}$ and $\Delta E + K_{\mathrm{LE}}$ after filtering the data.

The principal components with the smallest singular values contribute the most to the satisfaction of the filtering criterion, so they represent the combinations of parameters that are prerequisites for TADF. The variability within the filtered set is explained the most by principal components with the largest singular values, so these combinations are responsible for fine-tuning of the TADF efficiency. The principal component with the smallest singular value and negligible contribution to the variance is K_{CT}. It reflects the fact that the exchange integral is in general small for CT states and efficient solutions can be found in the entire sampled range. The next component accounts for only 1.5 % of the variance and is dominated by the $t - K_{\mathrm{X}}$

combination, which means that along with K_{CT} this parameter determines whether TADF is possible at all. Indeed, the histogram in Figure D-1a reveals that the distribution of this parameter is strongly peaked around 0.00 eV with standard deviation 0.38 eV. The next smallest principal component accounts for 3.7 % of the variance and is dominated by the $\Delta E - K_{\mathrm{LE}}$ combination. Figure D-1b shows that the distribution of this parameter, which has a mean value -1.00 eV and standard deviation 0.46 eV. It also appears that K_{LE} has to be larger than ΔE as there are almost no solutions where the opposite is true, and the distribution is noticeably negatively skewed. The remaining two principal components correspond mostly to $\Delta E + K_{\mathrm{LE}}$ and $t + K_{\mathrm{X}}$ combinations, where the latter accounts for as much as 80 % of the variance, so it is the main source of variation in the filtered data.

This analysis of the importance of parameters is somewhat biased by the judicious but arbitrary choice of distribution ranges from which the parameters were sampled. Therefore, the analysis was repeated on normalized original parameters (z-scores): $z_i = \frac{x_i - \mu_i}{\sigma_i}$ to remove the initial bias introduced by different variances of original parameters. The resulting principal components are the following (coefficients smaller than 0.005 have been suppressed):

$$\tilde{c}_1 = 0.707t + 0.707K_{\mathrm{X}} \tag{D.19}$$

$$\tilde{c}_2 = 0.705\Delta E + 0.704K_{\mathrm{LE}} + 0.083K_{\mathrm{CT}} \tag{D.20}$$

$$\tilde{c}_3 = -0.041\Delta E - 0.076K_{\mathrm{LE}} + 0.996K_{\mathrm{CT}} \tag{D.21}$$

$$\tilde{c}_4 = -0.708\Delta E + 0.706K_{\mathrm{LE}} + 0.024K_{\mathrm{CT}} \tag{D.22}$$

$$\tilde{c}_5 = 0.707t - 0.707K_{\mathrm{X}} \tag{D.23}$$

with the following singular values $\tilde{\lambda}_1 = 186.334$, $\tilde{\lambda}_2 = 164.883$, $\tilde{\lambda}_3 = 132.840$, $\tilde{\lambda}_4 = 91.023$, and $\tilde{\lambda}_5 = 26.298$, accounting for 0.392, 0.307, 0.199, 0.094, and 0.008 of the total variance, respectively.

The compositions of principal components are essentially the same as in the non-standardized case, but the scaling of data changes the explained variance ratios so that $t - K_{\mathrm{X}}$ accounts for the least of the variance (0.8 %), followed by $\Delta E - K_{\mathrm{LE}}$

(9.4 %), K_{CT} (19.9 %), $\Delta E - K_{\mathrm{LE}}$ (30.7 %), and $t + K_{\mathrm{X}}$ (39.2 %). Therefore, if all the parameters are treated on an equal footing, clearly small values of $t + K_{\mathrm{X}}$ and to lesser extent moderately negative $\Delta E - K_{\mathrm{LE}}$ are necessary for TADF.

D.4 Molecular Dynamics

Ground state geometry optimization was carried out in the framework of density functional theory (DFT), using the B3LYP exchange-correlation functional [272–277] and the 6-31+G* basis set [278–280] as implemented in the Q-Chem 4.4 software package [297]. The CHELPG [352] charges were computed at the same level of theory. The Cartesian coordinates of the optimized geometry and the CHELPG charges have been provided in Table D.1.

Atom	x (Å)	y (Å)	z (Å)	CHELPG	Atom Type	Description
N	-0.1771724	0.1308221	-0.0536515	-0.7177610	opls_641	1,3,5-triazine N
C	-0.2907067	0.0594104	-0.0577637	0.7412900	opls_642	1,3,5-triazine C
N	-0.2951423	-0.0747524	-0.0593212	-0.7370840	opls_641	1,3,5-triazine N
C	-0.1764402	-0.1372672	-0.0562627	0.8040150	opls_642	1,3,5-triazine C
N	-0.0581012	-0.0741559	-0.0516787	-0.7356020	opls_641	1,3,5-triazine N
C	-0.0632419	0.0599753	-0.0505072	0.7320700	opls_642	1,3,5-triazine C
C	0.0650247	0.1344654	-0.0446425	-0.0582920	opls_145B	biphenyl C1
C	0.0655603	0.2748075	-0.0376595	-0.1251780	opls_145	benzene C
C	0.1861568	0.3446213	-0.0320655	-0.1262380	opls_145	benzene C
C	0.3076415	0.2753331	-0.0336096	-0.0920130	opls_145	benzene C
C	0.1874834	0.0655030	-0.0459690	-0.0744690	opls_145	benzene C
C	0.3079171	0.1356214	-0.0406489	-0.1281280	opls_145	benzene C
H	0.4020596	0.0813016	-0.0421523	0.1148450	opls_146	benzene H
H	0.1868097	-0.0428006	-0.0513049	0.1075690	opls_146	benzene H
H	0.1853611	0.4531580	-0.0264337	0.1204580	opls_146	benzene H
H	0.4015845	0.3298761	-0.0293961	0.1156810	opls_146	benzene H
H	-0.0290245	0.3278108	-0.0364674	0.1357560	opls_146	benzene H
C	-0.1759534	-0.2855269	-0.0574480	-0.1276070	opls_145B	biphenyl C1
C	-0.2965241	-0.3575297	-0.0615792	-0.1110500	opls_145	benzene C
C	-0.2962860	-0.4967235	-0.0614839	-0.1966050	opls_145	benzene C
C	-0.1748988	-0.5670871	-0.0586419	0.4028990	opls_918	N,N-dimethylaniline C(NH_2)
C	-0.0540563	-0.4958734	-0.0554877	-0.2577960	opls_145	benzene C
C	-0.0548582	-0.3566982	-0.0541884	-0.1166240	opls_145	benzene C
H	-0.3903387	-0.3032020	-0.0635794	0.1332380	opls_146	benzene H
H	-0.3900079	-0.5515554	-0.0619349	0.1355560	opls_146	benzene H
H	0.0400378	-0.5500398	-0.0555464	0.1535730	opls_146	benzene H

H	0.0385533	-0.3016960	-0.0519984	0.1464590	opls_146	benzene H
C	-0.4194147	0.1333345	-0.0601076	-0.0559090	opls_145B	biphenyl C1
C	-0.4207058	0.2738567	-0.0619985	-0.0843540	opls_145	benzene C
C	-0.5416996	0.3431940	-0.0637009	-0.1321960	opls_145	benzene C
C	-0.6628331	0.2732251	-0.0633679	-0.0905420	opls_145	benzene C
C	-0.6623286	0.1333685	-0.0615400	-0.1288670	opls_145	benzene C
C	-0.5414982	0.0637343	-0.0600341	-0.1128430	opls_145	benzene C
H	-0.5402709	-0.0446840	-0.0586540	0.1252090	opls_146	benzene H
H	-0.7570711	0.3274058	-0.0645889	0.1152140	opls_146	benzene H
H	-0.7561528	0.0785045	-0.0612874	0.1197590	opls_146	benzene H
H	-0.3263898	0.3273574	-0.0621695	0.1131400	opls_146	benzene H
H	-0.5415096	0.4518743	-0.0652907	0.1187370	opls_146	benzene H
N	-0.1743323	-0.7087744	-0.0587923	-0.3621580	opls_587	indole N1
C	-0.1100683	-0.7906475	0.0352199	0.2739950	opls_594	indole C8
C	-0.1339998	-0.9264327	0.0018879	-0.0149390	opls_595	indole C9
C	-0.2158921	-0.9266986	-0.1176433	-0.0119650	opls_595	indole C9
C	-0.3120495	-0.7559178	-0.2661347	-0.2717900	opls_593	indole C7
C	-0.3638388	-0.8591149	-0.3444576	-0.0788970	opls_592	indole C6
C	-0.3431816	-0.9941730	-0.3108205	-0.2075590	opls_591	indole C5
C	-0.2689765	-1.0284647	-0.1979432	-0.1527430	opls_590	indole C4
C	-0.0813888	-1.0278192	0.0829722	-0.1582400	opls_590	indole C4
C	-0.0068041	-0.9930365	0.1954527	-0.1963340	opls_591	indole C5
C	0.0147864	-0.8578391	0.2278818	-0.0957790	opls_592	indole C6
C	-0.0365160	-0.7550062	0.1487574	-0.2900690	opls_593	indole C7
C	-0.2390061	-0.7910665	-0.1521262	0.2533390	opls_594	indole C8
H	-0.0989574	-1.1323350	0.0587324	0.1423740	opls_599	indole H4
H	0.0346372	-1.0707802	0.2590432	0.1355690	opls_600	indole H5
H	0.0724471	-0.8325453	0.3164712	0.1257360	opls_601	indole H6
H	-0.0199339	-0.6510878	0.1753063	0.1599650	opls_602	indole H7
H	-0.3276138	-0.6521202	-0.2937596	0.1424250	opls_602	indole H7
H	-0.4210393	-0.8342520	-0.4334683	0.1193510	opls_601	indole H6
H	-0.3849812	-1.0721943	-0.3738366	0.1356040	opls_600	indole H5
H	-0.2520441	-1.1328719	-0.1728020	0.1420160	opls_599	indole H4
H	-0.3629621	0.0623256	0.2920560	0.1482280	opls_146	benzene H
H	-0.4094327	0.3049320	0.2826535	0.1569120	opls_146	benzene H
H	-0.1951850	-0.2894448	0.3104549	0.1619210	opls_146	benzene H
H	-0.3824010	-0.4515855	0.3092251	0.1226910	opls_146	benzene H
H	0.0251872	0.0312985	0.3065705	0.1697260	opls_146	benzene H
H	0.2586801	-0.0490898	0.3186254	0.1404710	opls_146	benzene H
C	-0.3074025	0.1300405	0.3561811	-0.2318230	opls_145	benzene C
C	-0.2835773	-0.2701037	0.3704517	-0.2903400	opls_145	benzene C
C	-0.3340177	0.2668022	0.3507469	-0.1453770	opls_145	benzene C
C	-0.3887857	-0.3615989	0.3695699	-0.0740760	opls_145	benzene C
C	0.0506771	-0.0492222	0.3747772	-0.3003650	opls_145	benzene C
C	0.1824429	-0.0943736	0.3812176	-0.0952270	opls_145	benzene C

C	-0.2611513	0.3542177	0.4314462	0.0789740	opls_263	chlorobenzene C(Cl)
C	0.2150726	-0.1994313	0.4670469	0.0526910	opls_263	chlorobenzene C(Cl)
C	-0.5032591	-0.3354795	0.4449634	0.0606780	opls_263	chlorobenzene C(Cl)
C	-0.2094671	0.0792910	0.4431227	0.3887900	opls_918	N,N-dimethylaniline C(NH_2)
C	-0.2908085	-0.1530699	0.4477933	0.4007680	opls_918	N,N-dimethylaniline C(NH_2)
C	-0.0490429	-0.1070993	0.4549987	0.4285840	opls_918	N,N-dimethylaniline C(NH_2)
N	-0.1831153	-0.0602986	0.4489654	-0.4642580	opls_902	tertiary amine N
Cl	-0.2933720	0.5270910	0.4239583	-0.1396110	opls_264	chlorobenzene Cl
Cl	0.3810083	-0.2575846	0.4745096	-0.1365380	opls_264	chlorobenzene Cl
Cl	-0.6369042	-0.4499010	0.4429752	-0.1369440	opls_264	chlorobenzene Cl
C	0.1173806	-0.2589631	0.5469530	-0.0757120	opls_145	benzene C
C	-0.1627541	0.3060616	0.5178761	-0.1060680	opls_145	benzene C
C	-0.5128685	-0.2194098	0.5218289	-0.1019440	opls_145	benzene C
C	-0.0138597	-0.2121586	0.5413605	-0.3212080	opls_145	benzene C
C	-0.4065416	-0.1292215	0.5237448	-0.2987640	opls_145	benzene C
C	-0.1378692	0.1689937	0.5241048	-0.2932570	opls_145	benzene C
H	0.1436894	-0.3401015	0.6140856	0.1336590	opls_146	benzene H
H	-0.6019486	-0.2002259	0.5808083	0.1401700	opls_146	benzene H
H	-0.1069738	0.3746853	0.5808106	0.1393450	opls_146	benzene H
H	-0.0897067	-0.2575724	0.6043950	0.1609010	opls_146	benzene H
H	-0.4134755	-0.0394764	0.5844489	0.1550840	opls_146	benzene H
H	-0.0621588	0.1312941	0.5921804	0.1557080	opls_146	benzene H

Table D.1: Cartesian coordinates of the optimized geometry, CHELPG charges, and atom type assignments.

The molecular dynamics (MD) simulations were carried out using the OPLS-aa force field [271] as implemented in the GROMACS 5.1.2 software package [353]. Since not every atom could be assigned to the exact atom type, assignments were made to best describe the chemical environment of each atom. The atom type assignments can be found in Table D.1. The equilibrium bond lengths, bond angles, and dihedral angles were parametrized to the DFT optimized geometry, and the default charges were replaced with the CHELPG charges. Periodic boundary conditions were enforced so that the complex was 1.0 nm from the walls of the cubic box at the beginning of the simulation. Although an NVT ensemble was used, a separate equilibration stage was deemed unnecessary, since the focus was not on the thermodynamics. The Nose-Hoover thermostat [354–356] was set at 300 K during regular MD runs and at 400 K during runs with modified Lennard-Jones parameters.

Since the initial results of TDDFT suggested that the oscillator strength, rather

than ΔE_{ST}, was the limiting factor of the TADF rate, many of the MD simulations had the Lennard-Jones parameters of the OPLS-aa force field modified to push the donor and the acceptor moieties closer together and increase the HOMO-LUMO overlap. The Lennard-Jones potential has the form:

$$V_{\mathrm{LJ}}(r) = 4\varepsilon \left[\left(\frac{\sigma}{r} \right)^{12} - \left(\frac{\sigma}{r} \right)^{6} \right] \tag{D.24}$$

where ε and σ are atom-specific parameters that control the depth and the position of the potential well, respectively. Keeping the ε-parameter of each atom at 1.5 times the default value, the σ-parameters were scaled down by a number of different factors.

Unless otherwise mentioned, snapshots were taken at rather short intervals of 0.1 ps, but they were sampled at longer intervals for TDDFT calculations. After the initial sampling, the temporal correlation between snapshots was used to select the intervals on which to focus the search. Whenever a simulation exhibited a transition between a large oscillator strength and a small ΔE_{ST} or an extended period of either, the more frames in that part of the simulation were submitted to TDDFT, with the hope that the trajectory would encounter a conformation of both a large oscillator strength and a small ΔE_{ST}.

D.5 Rate of Thermally Activated Delayed Fluorescence

Equation 6.20 assumes that the excited state populations have thermalized and that only the S_1 and the T_1 states are populated to a significant extent. On the other hand, if the T_2 state were lower in energy than the S_1 state, then the T_2 state should be included in the denominator [215]. The formula becomes

$$k_{\mathrm{TADF}} = \frac{k_{\mathrm{F}}[\mathrm{S}_1]}{[\mathrm{S}_1] + [\mathrm{T}_1] + [\mathrm{T}_2]} = \frac{k_{\mathrm{F}}}{1 + K_1 + K_2} \tag{D.25}$$

$$K_1 \equiv \frac{[\mathrm{T}_1]}{[\mathrm{S}_1]} = 3 \exp\left(\frac{\Delta E_{\mathrm{S}_1 - \mathrm{T}_1}}{k_{\mathrm{B}} T} \right) \tag{D.26}$$

$$K_2 \equiv \frac{[\mathrm{T}_2]}{[\mathrm{S}_1]} = 3 \exp\left(\frac{\Delta E_{\mathrm{S}_1-\mathrm{T}_2}}{k_\mathrm{B} T}\right) \tag{D.27}$$

However, the correction was neglected in Chapter 6, because taking the T2 state into consideration neither entailed an order-of-magnitude correction to a TADF rate nor altered the statistics in a meaningful way. Examples can be found in the following section.

D.6 Time-Dependent Density Functional Theory

The excited states in the selected conformations were computed in the framework of time-dependent density functional theory (TDDFT), using the same level of theory as geometry optimization. In the first MD simulation, which used the default Lennard-Jones parameters, some twenty conformations were sampled. The TDDFT results and the estimated rates have been provided in Table D.2. The TADF rate could already be seen undergoing order-of-magnitude fluctuations. The shortest TADF lifetime to be obtained at this point was 13 µs (oscillator strength of 1.1×10^{-3} and ΔE_ST of 0.01 eV), to be contrasted with the DFT optimized geometry, which was estimated to have a TADF lifetime of 1.6 ms (oscillator strength of 1.8×10^{-5} and ΔE_ST of 0.02 eV). Since $\Delta E_\mathrm{ST} < k_B T = 25.7$ meV was not difficult to obtain in the model system, it was decided that the oscillator strength, rather than ΔE_ST, was the limiting factor of the TADF rate.

In the MD simulations with modified Lennard-Jones parameters, the ε-parameter of each atom was kept at 1.5 times the default value, while the σ-parameter was scaled down by a number of different values (see Section D.4). Over a thousand conformations have been sampled. As such, only the conformations with the fastest TADF in each simulation have been listed in Tables D.3–D.7.

Frame	T_1 (eV)	T_2 (eV)	$T_n < S_1$	S_1 (eV)	f_{10}	τ_F (µs)	τ_{TADF} (µs)[a]	τ_{TADF} (µs)[b]
401	2.64	2.66	2	2.66	1.1×10^{-3}	2.8	1.3×10^{1}	1.4×10^{1}
0	2.77	2.83	1	2.78	1.8×10^{-3}	1.7	1.5×10^{1}	1.6×10^{1}
800	2.68	2.74	1	2.70	7.9×10^{-4}	3.7	2.5×10^{1}	2.6×10^{1}
201	2.80	2.89	1	2.81	5.5×10^{-4}	6.1	3.1×10^{1}	4.4×10^{1}
300	2.61	2.63	1	2.62	4.8×10^{-4}	6.0	3.3×10^{1}	3.4×10^{1}
400	2.84	2.93	1	2.85	6.4×10^{-4}	4.2	4.0×10^{1}	5.3×10^{1}
200	2.90	2.92	1	2.92	6.1×10^{-4}	4.6	4.9×10^{1}	6.0×10^{1}
202	2.82	2.86	1	2.85	7.7×10^{-4}	3.3	6.7×10^{1}	1.2×10^{2}
901	2.94	2.95	2	2.99	3.1×10^{-4}	8.9	8.2×10^{1}	1.0×10^{2}
2	2.87	2.91	1	2.90	9.5×10^{-5}	2.6×10^{1}	1.3×10^{2}	2.1×10^{2}
601	3.05	3.05	1	3.05	4.0×10^{-4}	6.7	2.9×10^{3}	2.9×10^{3}
701	2.81	2.90	3	2.94	5.2×10^{-4}	4.9	3.2×10^{3}	3.2×10^{3}
301	2.88	3.00	3	3.02	5.1×10^{-4}	4.7	5.0×10^{3}	5.1×10^{3}
100	2.92	3.02	4	3.07	3.9×10^{-3}	6.0×10^{-1}	9.4×10^{3}	1.4×10^{4}
500	2.93	2.95	4	3.15	1.3×10^{-3}	1.9	1.9×10^{4}	1.9×10^{4}
101	2.87	3.03	3	3.08	8.2×10^{-5}	3.2×10^{1}	2.9×10^{4}	3.0×10^{4}
102	2.81	2.92	3	2.96	1.1×10^{-2}	1.9×10^{-1}	5.6×10^{4}	5.6×10^{4}
501	2.69	2.97	2	2.99	6.4×10^{-4}	3.8	1.1×10^{5}	1.2×10^{5}
600	2.87	2.92	5	3.10	2.7×10^{-3}	1.0	4.0×10^{5}	4.0×10^{5}
1	2.61	2.89	3	2.92	1.6×10^{-4}	1.6×10^{1}	9.7×10^{5}	9.7×10^{5}
700	2.72	2.96	2	2.97	4.8×10^{-5}	4.6×10^{1}	1.0×10^{6}	1.5×10^{6}
801	3.00	3.01	5	3.23	1.7×10^{-4}	1.5×10^{1}	1.7×10^{6}	1.7×10^{6}
900	2.76	2.95	3	3.03	4.4×10^{-4}	5.0	6.6×10^{7}	7.4×10^{7}
opt[c]	2.86	2.91	4	3.25	1.8×10^{-5}	1.8×10^{2}	1.6×10^{3}	2.2×10^{3}

[a] The TADF lifetime according to Equation 6.20.
[b] The TADF lifetime according to Equation D.25.
[c] The DFT-optimized geometry.

Table D.2: TDDFT results on the MD simulation with the default Lennard-Jones parameters. Here, the snapshots were taken at 1 ps intervals. Except for the DFT-optimized geometry, the conformations have been sorted in the order of increasing TADF lifetime.

Frame	T_1 (eV)	T_2 (eV)	$T_n < S_1$	S_1 (eV)	f_{10}	τ_F (µs)	τ_{TADF} (µs)[a]	τ_{TADF} (µs)[b]
0	2.49	2.55	1	2.53	8.4×10^{-3}	4.3×10^{-1}	6.1	6.6
20	2.53	2.54	1	2.53	1.7×10^{-3}	2.2	1.0×10^{1}	1.5×10^{1}
8	2.58	2.66	1	2.60	2.7×10^{-3}	1.3	1.2×10^{1}	1.2×10^{1}
160	2.54	2.67	1	2.55	1.2×10^{-3}	3.0	1.6×10^{1}	1.6×10^{1}
12	2.57	2.65	1	2.58	1.4×10^{-3}	3.0	1.7×10^{1}	1.7×10^{1}
2	2.43	2.47	2	2.49	4.6×10^{-3}	8.1×10^{-1}	2.4×10^{1}	3.0×10^{1}
4	2.19	2.28	1	2.21	8.6×10^{-4}	5.5	3.6×10^{1}	3.6×10^{1}
110	2.17	2.57	1	2.17	4.8×10^{-4}	1.0×10^{1}	4.4×10^{1}	4.4×10^{1}

[a] The TADF lifetime according to Equation 6.20.
[b] The TADF lifetime according to Equation D.25.

Table D.3: TDDFT results on the MD simulation with modified Lennard-Jones parameters. The σ-parameter of each atom was set to 0.9 times the default value.

Frame	T_1 (eV)	T_2 (eV)	$T_n < S_1$	S_1 (eV)	f_{10}	τ_F (µs)	τ_{TADF} (µs)[a]	τ_{TADF} (µs)[b]
51	2.38	2.75	1	2.41	9.9×10^{-3}	4.0×10^{-1}	3.6	3.6
81	2.60	2.67	1	2.63	7.3×10^{-3}	4.6×10^{-1}	5.0	5.3
90	2.11	2.52	1	2.12	3.6×10^{-3}	1.4	1.0×10^{1}	1.0×10^{1}
150	2.52	2.59	1	2.57	5.0×10^{-3}	7.0×10^{-1}	1.3×10^{1}	1.4×10^{1}
53	2.65	2.68	2	2.69	3.4×10^{-3}	9.3×10^{-1}	1.4×10^{1}	1.8×10^{1}
92	2.68	2.74	2	2.77	2.2×10^{-2}	1.4×10^{-1}	1.4×10^{1}	1.5×10^{1}
65	2.57	2.82	1	2.66	2.2×10^{-2}	1.5×10^{-1}	1.4×10^{1}	1.4×10^{1}
88	2.27	2.45	1	2.28	1.6×10^{-3}	2.8	1.6×10^{1}	1.6×10^{1}

[a] The TADF lifetime according to Equation 6.20.
[b] The TADF lifetime according to Equation D.25.

Table D.4: TDDFT results on the MD simulation with modified Lennard-Jones parameters. The σ-parameter of each atom was set to 0.8 times the default value.

Frame	T_1 (eV)	T_2 (eV)	$T_n < S_1$	S_1 (eV)	f_{10}	τ_F (µs)	τ_{TADF} (µs)[a]	τ_{TADF} (µs)[b]
212	2.38	2.40	1	2.40	7.4×10^{-3}	5.4×10^{-1}	3.7	5.2
165	2.47	2.73	1	2.48	3.7×10^{-3}	1.0	5.0	5.0
191	2.57	2.63	1	2.58	4.0×10^{-3}	8.7×10^{-1}	5.4	5.8
10	2.31	2.42	1	2.36	1.2×10^{-2}	3.5×10^{-1}	8.2	8.3
213	2.67	2.69	2	2.74	1.7×10^{-2}	1.8×10^{-1}	8.2	1.2×10^{1}
214	2.32	2.52	1	2.42	4.1×10^{-2}	9.7×10^{-2}	9.2	9.2
163	2.66	2.72	1	2.67	2.1×10^{-3}	1.6	9.9	1.1×10^{1}
190	2.44	2.60	1	2.46	2.5×10^{-3}	1.6	1.0×10^{1}	1.0×10^{1}

[a] The TADF lifetime according to Equation 6.20.
[b] The TADF lifetime according to Equation D.25.

Table D.5: TDDFT results on the MD simulation with modified Lennard-Jones parameters. The σ-parameter of each atom was set to 0.75 times the default value.

Frame	T_1 (eV)	T_2 (eV)	$T_n < S_1$	S_1 (eV)	f_{10}	τ_F (µs)	τ_{TADF} (µs)[a]	τ_{TADF} (µs)[b]
438	2.41	2.43	2	2.43	9.6×10^{-3}	4.1×10^{-1}	2.7	4.1
363	2.07	2.44	1	2.10	1.8×10^{-2}	2.9×10^{-1}	2.8	2.8
368	1.96	2.22	1	2.00	2.6×10^{-2}	2.2×10^{-1}	3.1	3.1
366	2.23	2.59	1	2.24	9.0×10^{-3}	5.1×10^{-1}	3.4	3.4
173	2.36	2.42	1	2.39	1.2×10^{-2}	3.5×10^{-1}	3.5	3.8
361	2.16	2.38	1	2.22	4.1×10^{-2}	1.1×10^{-1}	3.6	3.6
185	2.19	2.42	1	2.24	1.7×10^{-2}	2.8×10^{-1}	5.2	5.2
171	2.56	2.60	1	2.59	6.2×10^{-3}	5.5×10^{-1}	5.5	6.6
749	2.46	2.53	1	2.48	1.4×10^{-2}	2.8×10^{-1}	2.0	2.1
800	2.48	2.51	1	2.51	2.4×10^{-2}	1.5×10^{-1}	2.1	2.6
819	2.21	2.47	1	2.25	1.9×10^{-2}	2.4×10^{-1}	3.2	3.2
657	2.21	2.37	1	2.22	1.0×10^{-2}	4.6×10^{-1}	3.3	3.3
315	2.35	2.41	1	2.40	2.1×10^{-2}	1.9×10^{-1}	3.7	4.1
666	2.30	2.55	1	2.32	9.5×10^{-3}	4.5×10^{-1}	3.8	3.8
219	2.40	2.48	1	2.42	5.1×10^{-3}	7.8×10^{-1}	4.4	4.5
801	2.25	2.42	1	2.30	2.1×10^{-2}	2.1×10^{-1}	4.4	4.4

[a] The TADF lifetime according to Equation 6.20.
[b] The TADF lifetime according to Equation D.25.

Table D.6: TDDFT results on the MD simulation with modified Lennard-Jones parameters. The σ-parameter of each atom was set to 0.7 times the default value.

Frame	T_1 (eV)	T_2 (eV)	$T_n < S_1$	S_1 (eV)	f_{10}	τ_F (µs)	τ_{TADF} (µs)[a]	τ_{TADF} (µs)[b]
155	1.94	2.20	1	2.04	2.0×10^{-2}	2.8×10^{-1}	4.2×10^{1}	4.2×10^{1}
115	2.02	2.33	1	2.06	1.1×10^{-3}	4.8	8.4×10^{1}	8.4×10^{1}
195	1.92	2.10	1	2.06	1.4×10^{-2}	3.9×10^{-1}	3.5×10^{2}	3.5×10^{2}
125	2.12	2.17	3	2.28	1.9×10^{-2}	2.3×10^{-1}	3.9×10^{2}	4.4×10^{2}
455	1.51	1.65	1	1.58	1.0×10^{-3}	9.2	4.1×10^{2}	4.1×10^{2}
305	1.55	1.85	1	1.71	2.9×10^{-2}	2.7×10^{-1}	5.0×10^{2}	5.0×10^{2}
185	1.15	1.18	2	1.23	1.7×10^{-3}	8.7	7.8×10^{2}	9.6×10^{2}
6	1.95	2.11	2	2.12	1.3×10^{-2}	3.8×10^{-1}	7.9×10^{2}	7.9×10^{2}

[a] The TADF lifetime according to Equation 6.20.
[b] The TADF lifetime according to Equation D.25.

Table D.7: TDDFT results on the MD simulation with modified Lennard-Jones parameters. The σ-parameter of each atom was set to 0.7 times the default value.

D.7 Polarizable Continuum Model

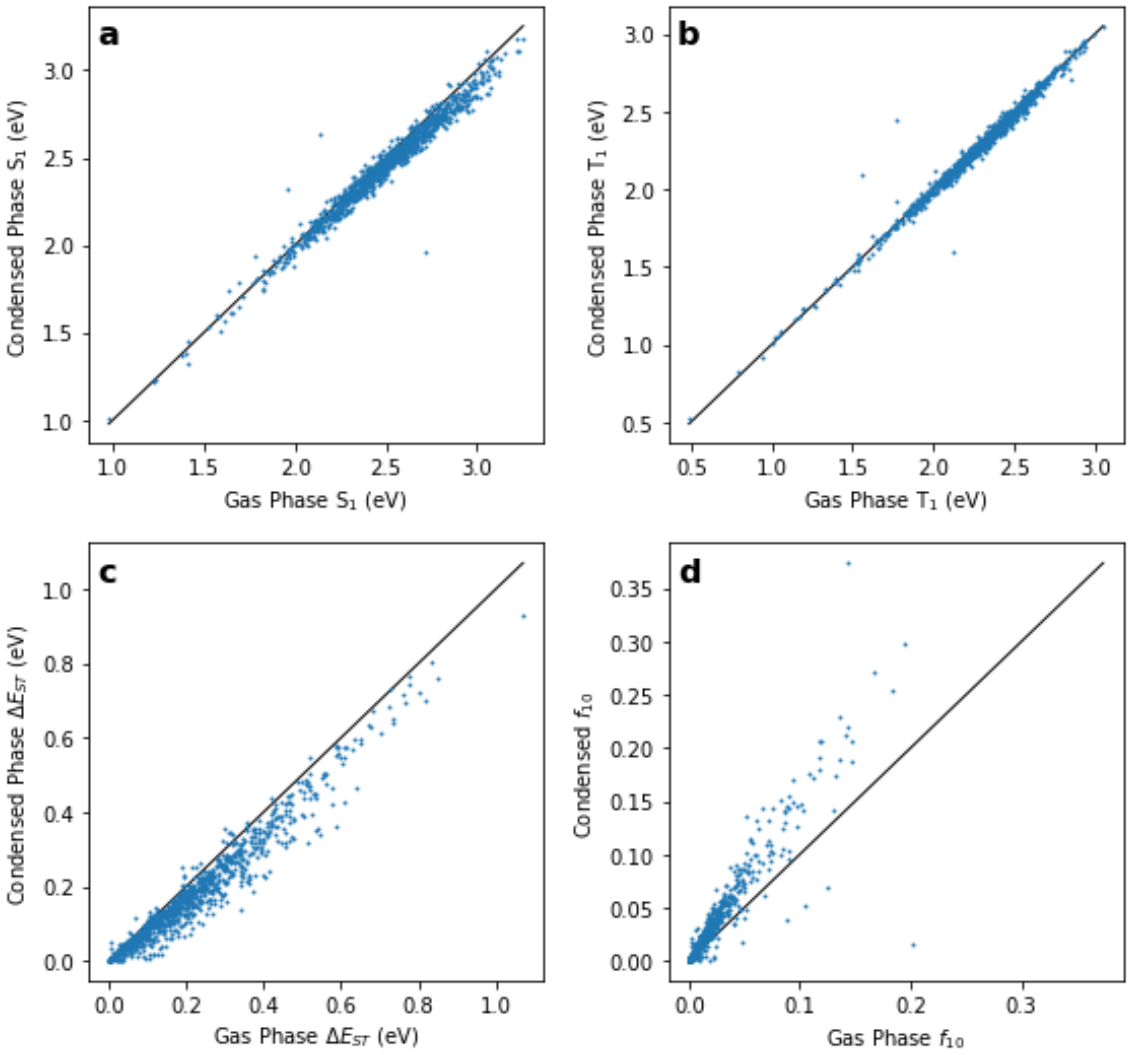

Figure D-2: Scatter plots of the condensed phase against the gas phase (a) S_1 excitation energy, (b) T_1 excitation energy, (c) ΔE_{ST}, and (d) $S_1 - S_0$ oscillator strength. The black lines have unit slope ($x = y$).

The condensed phase effects were examined at the level of linear-response conductor-like polarizable continuum model (LR-CPCM) [282, 283]. On the same set of conformations as the gas phase calculations, TDDFT/LR-CPCM calculations were carried out, assuming a dielectric constant of 3.0, which is quite common in the OLED matrix materials [245]. The results have been summarized in Figure S5. While LR-CPCM tended to stabilize the S_1 and the T_1 states, decrease ΔE_{ST}, and increase the oscillator

strength, it was not enough to induce qualitative changes in the statistics.

D.8 Natural Transition Orbitals

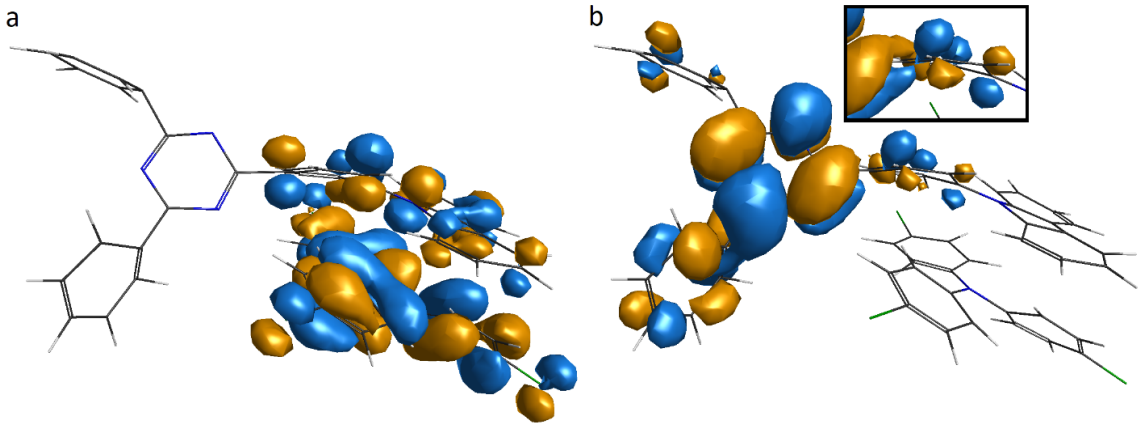

Figure D-3: (a) Hole and (b) particle orbitals of the S_1 state. The inset are the corresponding NTOs of the T_1 state.

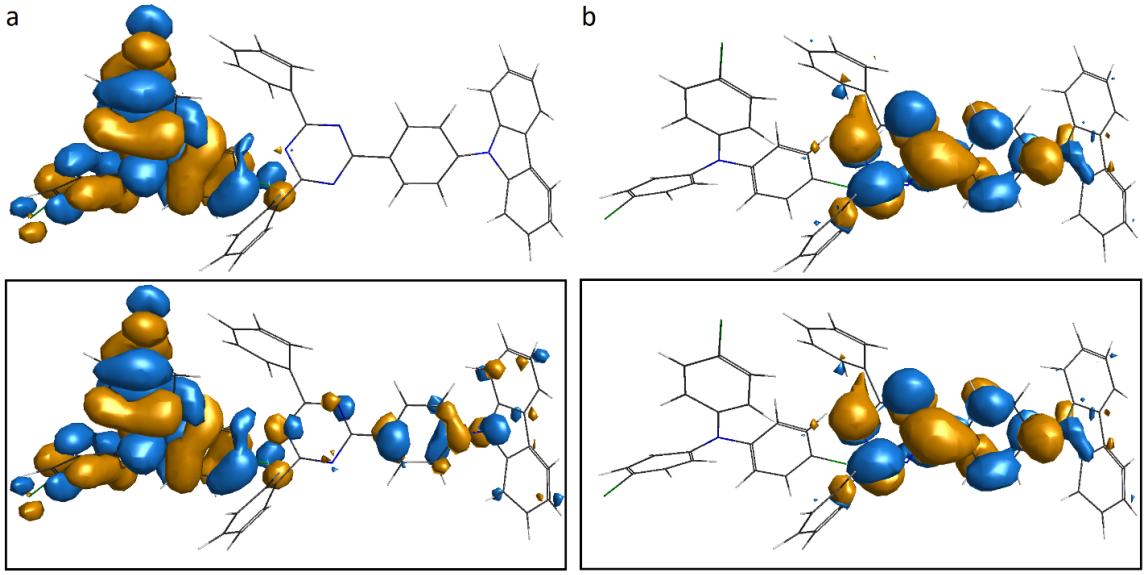

Figure D-4: (a) Hole and (b) particle orbitals of the S_1 state. The insets are the corresponding NTOs of the T_1 state.

The conformers in Figure 6-6 correspond to frames 438 and 819 in Table D.6. Here, two more representative conformations are examined. With the ISO value fixed at 0.02, the dominant NTO pairs in the S_1 and the T_1 excited states have been visualized in Figure D-3 and D-4.

D.9 Analysis of the Orbital Transitions

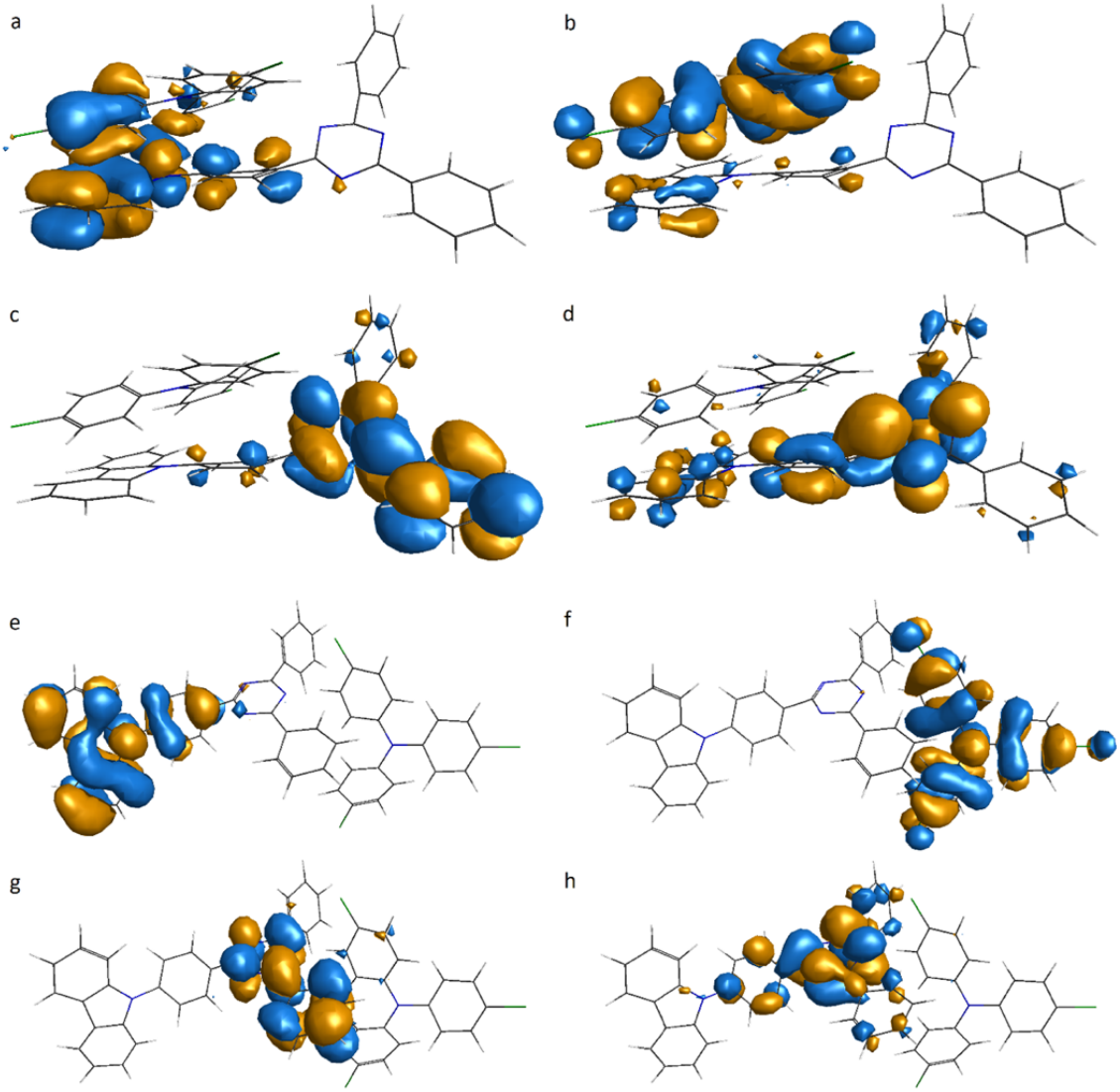

Figure D-5: Kohn-Sham orbitals: (a,e) HOMO − 1, (b,d) HOMO, (c,f) LUMO, and (d,h) LUMO + 1.

Among the conformers that exhibited the highest TADF rates ($\tau_{\mathrm{TADF}} < 10\,\mu\mathrm{s}$), the average HOMO → LUMO transition amplitude was 0.99 in the S_1 excitation and 0.94 in the T_1 excitation. The secondary contributions often came from the HOMO → LUMO + 1 and the HOMO − 1 → LUMO transitions, with the HOMO → LUMO + 1 transition being more important in the S_1 excitation and vice versa in the T_1 excitation. Figure D-5 depicts the relevant KS orbitals of the same conformers

as in Figure 6-6. The slight delocalization of the HOMO in the first conformer should not be a surprise, since the KS orbitals have been optimized in the adiabatic representation. With that said, the HOMO and the HOMO $-$ 1 of the second conformer are localized on the donor moiety and the CZ group, respectively. In either case, the HOMO $-$ 1 $\rightarrow$ LUMO transition increases the LE character of the excitation, since the bulk of the HOMO $-$ 1 resides on the carbazole group of the acceptor moiety. On the other hand, the HOMO $\rightarrow$ LUMO + 1 transition contributes more CT character. With cancellation between the delocalization of the HOMO and the CT contribution of the HOMO $\rightarrow$ LUMO + 1 transition, the HOMO $\rightarrow$ LUMO transition amplitude should provide a reasonable relative measure of the CT/LE character.

On the other end of the spectrum, among the conformers that exhibited low TADF rates ($\tau_{\mathrm{TADF}} > 1\,\mathrm{ms}$), the transitions became much more complicated, making detailed interpretation difficult. Fortunately, the KS orbitals HOMO $-$ 1 through LUMO + 1 retained their characteristics throughout the conformation space, so some insight could be extracted in terms of the HOMO $\rightarrow$ LUMO transition. In the S_1 excitation, the HOMO $\rightarrow$ LUMO transition still dominated, although the average transition amplitude was reduced to 0.94. Meanwhile, the T_1 excitation contained varying amounts of the HOMO $\rightarrow$ LUMO transition. In fact, some conformations exhibited negligible HOMO $\rightarrow$ LUMO transition in their T_1 excitation. In such cases, there had been a switch in the energy ordering of the CT-like and the LE-like triplet states, and some higher triplet state could be found with a dominant HOMO $\rightarrow$ LUMO transition. Due to the decreased CT character in the S_1 and the T_1 states, more than 80 % of these conformers had an oscillator strength $> 10^{-3}$, but they also had a $\Delta E_{\mathrm{ST}} > 100\,\mathrm{meV}$. The change in the limiting factor of TADF from the oscillator strength to the ΔE_{ST} highlights that the S_1 and the T_1 states should contain some LE character, but no more than a small fraction.

Appendix E

Supplementary Information: Maximizing TADF via Conformational Optimization

E.1 Variation of Nelder-Mead Simplex Method

We want to maximize the TADF rate of a molecule in a subspace of the Z-matrix coordinates. Let $\mathbf{x}_0$ be the vector of the n coordinates at the initial geometry.

1. **Initialization** Prepare $n+1$ geometries $\mathbf{x}_0, \mathbf{x}_1, ..., \mathbf{x}_n$, where $\mathbf{x}_{i>0}$ are generated by displacing the ith coordinate of $\mathbf{x}_0$. We displaced the bond lengths by 0.05 Å and the bond and the dihedral angles by 5.0°. The geometries correspond to the vertices of a n-simplex. Calculate the electronic structure at each geometry, and evaluate the TADF rate.

2. **Termination** Compute the center of the simplex $\mathbf{x}_c$. If every coordinate at every vertex is within some tolerance, then the maximization has converged. We required the bond lengths to be within 0.005 Å and the bond and dihetral angles to be within 0.5° of the corresponding value at the center.

3. **Reflection, Expansion, and Contraction** Sort the vertices in the order of

descending TADF rate. Let $\mathbf{x}_n$ denote the worst vertex. Compute the center of the facet $\mathbf{x}_o$ consisting of the first n vertices. Sample candidate vertices on the line $\mathbf{x}_0 + \alpha(\mathbf{x}_n - \mathbf{x}_o)$. We chose four points: $\alpha = -0.5, +0.5, +1.0, +2.0$. Calculate the electronic structure at each geometry, and evaluate the TADF rate.

4. **Shrink** Sort the candidate vertices in the order of descending TADF rate. Let $\mathbf{x}'_n$ denote the best candidate vertex. If $\mathbf{x}'_n$ has a higher TADF rate than $\mathbf{x}_{n-1}$, then replace $\mathbf{x}_n$ with $\mathbf{x}'_n$ and return to step 2. Otherwise, replace $\mathbf{x}_{i>0}$ with $(\mathbf{x}_{i>0}+\mathbf{x}_0)/2$, calculate the electronic structure at each geometry, evaluate the TADF rate, and return to step 2.

A notable feature of the above algorithm is that the function evaluations corresponding to Reflection, Expansion, and Contraction are performed in parallel, whereas they are performed in series in the original algorithm of Nelder and Mead [312]. The parallel algorithm does not make the most efficient use of the CPU time, since the serial algorithm would use heuristics to avoid function evaluations at one or more of the candidate vertices. However, knowing the TADF rate of every candidate vertex might help convergence as the differences in the TADF rates approach the uncertainty of the electronic structure method. Moreover, even though the CPU time might increase, the wall time can be reduced by assigning each electronic structure calculation to a separate set of CPU cores. Depending on the number of molecules to optimize and the real world time constraints, either the serial or parallel algorithm might be more useful than the other.

E.2 Rate of Reverse Intersystem Crossing

The rate of reverse intersystem crossing (RISC) was estimated using Fermi's golden rule

$$k_{\mathrm{T}_n \to \mathrm{S}_1} = \frac{2\pi}{\hbar} |\langle \mathrm{S}_1 | \hat{H}_{\mathrm{SO}} | \mathrm{T}_n \rangle|^2 \rho_{\mathrm{T}_n \to \mathrm{S}_1} \tag{E.1}$$

where $\rho_{T_n \to S_1}$ is the Franck-Condon weighted density of states (FCWD). One of the simplest ways to estimate the FCWD is Marcus theory [192, 193]

$$\rho_{T_n \to S_1} = \frac{1}{(4\pi\lambda_M k_B T)^{1/2}} \exp\left[-\frac{(\Delta E_{S_1 - T_n} + \lambda_M)^2}{4\lambda_M k_B T}\right] \tag{E.2}$$

where λ_M is the Marcus reorganization energy. Since conformational optimization considers a single conformer of a definite geometry, it is incompatible with geometric relaxation. Hence, we just used a typical value of the reorganization energy $\lambda_M = 0.2\,\text{eV}$ [195, 196, 290]. We expected that the simplified approach would give accuracies to the correct order of magnitude, which would suffice to assess the extent to which a finite RISC rate slows down TADF.

Since Equation 7.2 represents the limit of fast RISC, we consider the opposite limit of slow RISC, i.e. $k_{RISC} \ll k_F + k_{ISC}$. Assuming that internal conversion (IC) is fast enough that only the S_1, T_1, and T_2 states remain populated after a transient, the kinetic equation of the S_1 state becomes

$$\frac{d[S_1]}{dt} = -k_F[S_1] - k_{S_1 \to T_1}[S_1] + k_{T_1 \to S_1}[T_1] - k_{S_1 \to T_2}[S_1] + k_{T_2 \to S_1}[T_2] \tag{E.3}$$

Furthermore, assume that IC maintains a quasi-equilibrium between the triplet states with the equilibrium cosntant

$$K_{12} = \exp\left(\frac{\Delta E_{T_1 - T_2}}{k_B T}\right) \tag{E.4}$$

Then, the equation simplifies to

$$\frac{d[S_1]}{dt} = -k_F[S_1] - k_{ISC}[S_1] + k_{RISC}[T_1] \tag{E.5}$$

where $k_{ISC} = k_{S_1 \to T_1} + k_{S_1 \to T_2}$ and $k_{RISC} = k_{T_1 \to S_1} + k_{T_2 \to S_1} K_{12}$. Using the steady state approximation, we extract the quasi-steady-state population of the S_1 state

$$\frac{[S_1]}{[T_1]} = \frac{k_{RISC}}{k_F + k_{ISC}} \tag{E.6}$$

Returning to the definition of the TADF rate, we rearrange the expression

$$k_{\mathrm{TADF}} \equiv \frac{k_{\mathrm{F}}[\mathrm{S}_1]}{[\mathrm{S}_1]+[\mathrm{T}_1]+[\mathrm{T}_2]} = \left[\frac{1}{k_{\mathrm{F}}} + \frac{1+K_{12}}{k_{\mathrm{F}}} \cdot \frac{[\mathrm{T}_1]}{[\mathrm{S}_1]}\right]^{-1} \tag{E.7}$$

Substituting Equation E.6 and rearranging, we get

$$k_{\mathrm{TADF}} = \left[\frac{1}{k_{\mathrm{F}}} + \frac{1+K_{12}}{k_{\mathrm{F}}} \cdot \frac{k_{\mathrm{ISC}}}{k_{\mathrm{RISC}}} + \frac{1+K_{12}}{k_{\mathrm{RISC}}}\right]^{-1} \tag{E.8}$$

Detailed balance among the S_1, T_1, and T_2 states implies that $k_{\mathrm{ISC}}/k_{\mathrm{RISC}} = K_1$. The TADF rate becomes

$$k_{\mathrm{TADF}} = \left[\frac{1+K_1+K_2}{k_{\mathrm{F}}} + \frac{1+K_{12}}{k_{\mathrm{T}_1\to\mathrm{S}_1} + k_{\mathrm{T}_2\to\mathrm{S}_1}K_{12}}\right]^{-1} \tag{E.9}$$

where we have also used $K_{12} = K_2/K_1$ and $k_{\mathrm{RISC}} = k_{\mathrm{T}_1\to\mathrm{S}_1} + k_{\mathrm{T}_2\to\mathrm{S}_1}K_{21}$. Interestingly, Equation 7.2 appears in an intact form inside Equation E.9, and the RISC correction is additive to the reciprocal of the idealized TADF rate. For the assumption of fast RISC to be valid, the RISC rate only needs to be fast compared to the idealized TADF rate, which is much easier than fast compared to the fluorescence rate.

Table E.1 summarizes the energetics of the model systems at the maximum TADF geometries with various energy penalties. The electronic structures were calculated using the B3LYP exchange-correlation functional [272–277] and the 6-31+G* basis set [278–280, 296], and the spin-orbit coupling (SOC) matrix elements were computed using the one-electron Breit-Pauli Hamiltonian as implemented in the Q-Chem 5.1 software package [297]. Among the optimized geometries, the RISC correction entails upto 42 % decrease in the TADF rate. Although 42 % might seem like a large change, the RISC correction is insignificant compared to the orders-of-magnitude enhancement in the TADF rate between the energy minimum and the TADF maximum. Besides, the RISC correction is less than 5 % in most cases, and one of the DCzTrz geometries continue to exhibit a TADF rate in the submicrosecond time scales. The RISC correction might be important in a quantitative prediction of the TADF rate, but it does not alter the qualitative outcomes of conformational optimization.

	Λ ($\mu s^{-1} E_h^{-1}$)	ΔE_{DFT} ($kJ\,mol^{-1}$)	EE (eV) S$_1$ / T$_1$ / T$_2$	f_{10}	SOC (cm^{-1}) T$_1$ / T$_2$ $\leftrightarrow$ S$_1$	Rate (μs^{-1}) S$_1$ $\rightarrow$ S$_0$	TADF[a]	T$_1$ / T$_2$ $\rightarrow$ S$_1$	TADF[b]
DCzTrz	∞	0	2.84 / 2.71 / 2.74	0.017	0.31 / 1.49	5.9	0.0094	0.26 / 18	0.0094
	8.0	211	2.86 / 2.83 / 2.93	0.026	0.20 / 1.64	9.4	0.88	1.8 / 660	0.84
	4.0	278	2.94 / 2.91 / 3.00	0.029	0.25 / 1.61	11	1.06	2.8 / 580	1.01
	2.0	409	2.86 / 2.84 / 2.95	0.026	0.14 / 1.75	9.3	1.08	1.0 / 1000	0.99
	0.8	542	2.79 / 2.76 / 2.87	0.029	0.092 / 1.77	9.9	1.04	0.40 / 920	0.96
	0.0	594	2.79 / 2.77 / 2.90	0.028	0.10 / 1.72	9.3	1.07	0.46 / 1200	0.92
Cz2BP	∞	0	2.99 / 2.67 / 2.78	0.345	1.15 / 0.34	130	1.9×10^{-4}	0.002 / 0.021	1.7×10^{-4}
	8.0	162	2.67 / 2.63 / 2.64	0.061	0.20 / 0.12	19	0.66	1.3 / 0.54	0.40
	4.0	181	2.66 / 2.62 / 2.62	0.062	0.20 / 0.10	19	0.69	1.3 / 0.45	0.40
	0.0	193	2.64 / 2.60 / 2.61	0.060	0.20 / 0.10	18	0.69	1.3 / 0.40	0.40
Ac-MPM	∞	0	2.47 / 2.46 / 2.47	3.4×10^{-5}	0.014 / 0.0067	0.0090	0.0012	0.014 / 0.0038	0.0010
	8.0	51	2.51 / 2.49 / 2.49	0.036	0.12 / 0.156	10.0	0.59	0.70 / 1.2	0.36
	4.0	365	2.54 / 2.51 / 2.67	0.022	0.19 / 0.060	6.2	0.58	1.6 / 1.6	0.42
	0.0	420	2.55 / 2.52 / 2.61	0.028	0.20 / 0.049	8.0	0.63	1.6 / 0.49	0.45
SpiroAC-TRZ	∞	0	2.41 / 2.41 / 2.66	7.9×10^{-6}	0.0063 / 0.45	0.0020	4.2×10^{-4}	0.0029 / 110	4.0×10^{-4}
	8.0	104	2.56 / 2.54 / 2.75	0.012	0.18 / 0.58	3.5	0.49	1.8 / 190	0.39
	4.0	294	2.48 / 2.46 / 2.75	0.017	0.19 / 0.46	4.5	0.50	1.8 / 99	0.39
	0.0	475	2.50 / 2.48 / 2.67	0.019	0.15 / 0.09	5.1	0.61	1.1 / 4.8	0.39

[a] The TADF rate according to Equation 7.2, i.e. $k_{RISC} \gg k_F$.
[b] The TADF rate according to Equation E.9, i.e. $k_{RISC} \ll k_F + k_{ISC}$.

Table E.1: Energetics of the model systems at the maximum TADF geometries with various energy penalties.

It is remarkable that the RISC rate increases along with the idealized TADF rate, even though the TADF rate maximization did not consider the RISC rate in an explicit manner. The simultaneous enhancement of the RISC rate makes sense, given the parallel between the idealized TADF rate and the RISC rate: a high RISC rate requires a small singlet-triplet (ST) gap and a large SOC matrix element, which are expected to be contraindicated functions of the HOMO-LUMO overlap. Changes to the HOMO and the LUMO that increase the transition dipole moment (TDM) are likely to also increase the SOC matrix element, though the increases need not be proportional. Indeed, the TDMs of Ac-MPM and SpiroAC-TRZ increase by factors of 1000 and 2000, whereas the SOC matrix elements increase by factors of 15 and 25, respectively. On the other extreme, the RISC step appears even less likely to be the bottleneck in the TADF process as the ST gap becomes smaller. As shown by the minimum energy conformations of Ac-MPM and SpiroAC-TRZ, the $T_1 \rightarrow S_1$ RISC rate alone is enough to overtake the prompt fluorescence rate in the regime of vanishing ST gap.

Finally, as Brédas et al. have pointed out [290], the T_2 state appears to make an important contribution to the total RISC rate in some systems. In the cases of DCzTrz and SpiroAC-TRZ, the $T_2 \rightarrow S_1$ RISC rates are orders of magnitude greater than the respective $T_1 \rightarrow S_1$ RISC rates. Even if the T_2 state is higher in energy than the T_1 and the S_1 states, the T_2 contributions to the total RISC rate can be significant.

Tables E.2–E.4 summarize the energetics of the model systems, recomputed with PBE0 [300–302], M06-2X [303], and LRC-ω^*PBE [304–306]. Tables E.5 and E.6 are the outcomes of M06-2X and LRC-ω^*PBE with integral equation formalism polarizable continuum model (IEF-PCM) [307–309] and first order, perturbative state-specific (ptSS) [283] treatment of the excited states. We used the dielectric constant and the optical dielectric constant of toluene at 25 °C: $\varepsilon = 2.379$ and $\varepsilon_\infty = 2.232$ [310]. Remember that we have not reoptimized the geometries and just recalculated the electronic structures.

It is remarkable that various functionals exhibit such similar behaviors. For max-

	Λ ($\mu s^{-1} Ha^{-1}$)	ΔE_{DFT} ($kJ\,mol^{-1}$)	EE (eV) S_1 / T_1 / T_2	f_{10}	SOC (cm^{-1}) T_1 / $T_2 \leftrightarrow S_1$	Rate (μs^{-1}) $S_1 \rightarrow S_0$	TADF[a]	T_1 / $T_2 \rightarrow S_1$	TADF[b]
DCzTrz	∞	0	3.03 / 2.78 / 2.86	0.020	1.49 / 0.28	8.2	1.6×10^{-4}	0.071 / 0.051	1.6×10^{-4}
	8.0	229	3.09 / 3.02 / 3.05	0.030	0.46 / 0.52	12	0.18	3.1 / 10	0.17
	4.0	297	3.18 / 3.03 / 3.05	0.034	0.71 / 0.49	15	0.010	0.73 / 0.81	0.010
	2.0	423	3.10 / 2.93 / 2.98	0.030	0.77 / 0.042	13	0.0045	0.40 / 0.0067	0.0044
	0.8	548	3.02 / 2.79 / 2.84	0.034	0.27 / 0.98	14	5.1×10^{-4}	0.0052 / 0.43	5.1×10^{-4}
	0.0	604	3.02 / 2.79 / 2.86	0.031	0.21 / 0.85	12	4.0×10^{-4}	0.0024 / 0.74	3.9×10^{-4}
Cz2BP	∞	0	3.18 / 2.70 / 2.88	0.392	1.48 / 0.48	170	4.4×10^{-7}	2.1×10^{-7} / 4.7×10^{-4}	2.8×10^{-7}
	8.0	174	2.90 / 2.81 / 2.84	0.063	0.49 / 0.21	23	0.22	2.9 / 0.98	0.20
	4.0	193	2.88 / 2.80 / 2.83	0.062	0.48 / 0.19	22	0.23	2.9 / 0.84	0.21
	0.0	205	2.87 / 2.79 / 2.81	0.061	0.49 / 0.17	22	0.25	3.2 / 0.73	0.23
Ac-MPM	∞	0	2.65 / 2.65 / 2.65	3.4×10^{-5}	0.023 / 0.010	0.010	0.0012	0.037 / 0.0086	0.0012
	8.0	53	2.70 / 2.65 / 2.66	0.032	0.493 / 0.072	10	0.32	7.1 / 0.21	0.30
	4.0	359	2.73 / 2.67 / 2.68	0.024	0.378 / 0.201	7.7	0.16	3.3 / 1.2	0.15
	0.0	416	2.75 / 2.62 / 2.69	0.032	0.083 / 0.421	10	0.021	0.020 / 3.5	0.020
SpiroAC-TRZ	∞	0	2.60 / 2.59 / 2.90	8.6×10^{-6}	0.010 / 0.39	0.0025	4.9×10^{-4}	0.0064 / 49	4.6×10^{-4}
	8.0	105	2.75 / 2.72 / 2.92	0.014	0.34 / 0.20	4.4	0.42	5.1 / 22	0.38
	4.0	284	2.66 / 2.62 / 2.65	0.018	0.42 / 0.14	5.7	0.26	5.5 / 1.4	0.25
	0.0	458	2.69 / 2.60 / 2.65	0.021	0.10 / 0.34	6.5	0.054	0.10 / 4.5	0.049

[a] The TADF rate according to Equation 7.2, i.e. $k_{RISC} \gg k_F$.
[b] The TADF rate according to Equation E.9, i.e. $k_{RISC} \ll k_F + k_{ISC}$.

Table E.2: Energetics of the model systems recomputed with PBE0 at the maximum TADF geometries optimized with B3LYP.

	Λ ($\mu s^{-1}Ha^{-1}$)	ΔE_{DFT} ($kJ\,mol^{-1}$)	EE (eV) S_1 / T_1 / T_2	f_{10}	SOC (cm^{-1}) T_1 / $T_2 \leftrightarrow S_1$	Rate (μs^{-1}) $S_1 \rightarrow S_0$	TADF[a]	T_1 / $T_2 \rightarrow S_1$	TADF[b]
DCzTrz	∞	0	3.79 / 3.41 / 3.53	0.0420	1.186 / 0.36	26	2.7×10^{-6}	4.7×10^{-5} / 0.0027	2.6×10^{-6}
	8.0	227	3.94 / 3.62 / 3.62	0.0127	0.295 / 0.38	8.6	5.5×10^{-6}	9.4×10^{-5} / 1.6×10^{-4}	5.3×10^{-6}
	4.0	297	3.95 / 3.62 / 3.62	0.0022	0.413 / 0.30	1.5	7.0×10^{-7}	1.1×10^{-4} / 7.4×10^{-5}	6.9×10^{-7}
	2.0	426	3.81 / 3.48 / 3.62	0.0010	0.060 / 1.05	0.60	6.4×10^{-7}	3.2×10^{-6} / 0.35	6.4×10^{-7}
	0.8	557	3.76 / 3.23 / 3.50	0.0041	0.095 / 4.36	2.5	8.6×10^{-10}	2.5×10^{-11} / 0.35	8.6×10^{-10}
	0.0	610	3.76 / 3.24 / 3.53	8.4×10^{-4}	0.077 / 3.25	0.51	2.6×10^{-10}	3.5×10^{-11} / 0.61	2.6×10^{-10}
Cz2BP	∞	0	3.57 / 3.08 / 3.45	0.0061	14.3 / 10.3	3.4	5.1×10^{-9}	8.0×10^{-6} / 400	5.1×10^{-9}
	8.0	174	3.61 / 3.29 / 3.60	0.0014	3.1 / 13.2	0.81	1.0×10^{-6}	0.011 / 1.2×10^{4}	1.0×10^{-6}
	4.0	194	3.62 / 3.29 / 3.60	0.0018	3.4 / 12.2	1.0	1.2×10^{-6}	0.011 / 8300	1.2×10^{-6}
	0.0	206	3.60 / 3.28 / 3.59	0.0019	3.5 / 12.1	1.1	1.2×10^{-6}	0.011 / 9000	1.2×10^{-6}
Ac-MPM	∞	0	3.49 / 3.49 / 3.49	2.9×10^{-5}	0.10 / 0.032	0.015	0.0019	0.75 / 0.079	0.0019
	8.0	52	3.49 / 3.38 / 3.46	0.033	1.19 / 0.081	17	0.088	8.6 / 0.28	0.087
	4.0	372	3.55 / 3.26 / 3.44	0.034	0.11 / 0.795	19	6.9×10^{-5}	4.8×10^{-5} / 4.0	6.8×10^{-5}
	0.0	429	3.55 / 3.19 / 3.47	0.011	3.29 / 0.965	6.1	2.1×10^{-6}	0.0020 / 12	2.1×10^{-6}
SpiroAC-TRZ	∞	0	3.43 / 3.42 / 3.45	8.6×10^{-6}	0.061 / 1.14	0.0044	7.1×10^{-4}	2.7 / 150	7.1×10^{-4}
	8.0	101	3.58 / 3.50 / 3.52	0.019	1.02 / 0.34	10	0.10	13 / 2.5	0.10
	4.0	289	3.44 / 3.22 / 3.35	0.025	0.10 / 0.94	13	7.9×10^{-4}	0.0011 / 9.1	7.7×10^{-4}
	0.0	470	3.50 / 3.10 / 3.37	0.030	0.12 / 0.82	16	1.1×10^{-6}	2.4×10^{-7} / 1.9	1.1×10^{-6}

[a] The TADF rate according to Equation 7.2, i.e. $k_{RISC} \gg k_F$.
[b] The TADF rate according to Equation E.9, i.e. $k_{RISC} \ll k_F + k_{ISC}$.

Table E.3: Energetics of the model systems recomputed with M06-2X at the maximum TADF geometries optimized with B3LYP.

	ω^* (a_0^{-1})	Λ ($\mu s^{-1} Ha^{-1}$)	ΔE_{DFT} (kJ mol^{-1})	EE (eV) S_1 / T_1 / T_2	f_{10}	SOC (cm^{-1}) T_1 / $T_2 \leftrightarrow S_1$	Rate (μs^{-1}) $S_1 \rightarrow S_0$	TADF[a]	T_1 / $T_2 \rightarrow S_1$	TADF[b]
DCzTRZ	0.169	∞	0	3.39 / 3.07 / 3.14	0.0310	1.55 / 0.40	16	1.5×10^{-5}	0.0021 / 0.0039	1.5×10^{-5}
		8.0	202	3.49 / 3.27 / 3.29	0.0133	1.06 / 0.42	7.0	2.8×10^{-4}	0.11 / 0.040	2.8×10^{-4}
		4.0	267	3.49 / 3.26 / 3.27	0.0018	0.62 / 1.13	0.95	2.4×10^{-5}	0.026 / 0.15	2.4×10^{-5}
		2.0	394	3.37 / 3.15 / 3.20	3.5×10^{-4}	0.61 / 3.49	0.17	7.1×10^{-6}	0.029 / 7.7	7.1×10^{-6}
		0.8	524	3.33 / 2.95 / 3.09	0.0027	0.47 / 3.71	1.3	1.4×10^{-7}	7.9×10^{-6} / 0.51	1.4×10^{-7}
		0.0	573	3.33 / 2.93 / 3.11	3.9×10^{-4}	0.43 / 2.83	0.19	1.1×10^{-8}	2.8×10^{-6} / 0.70	1.1×10^{-8}
Cz2BP	0.186	∞	0	3.43 / 2.82 / 3.15	0.0083	12.57 / 5.06	4.3	5.0×10^{-11}	6.3×10^{-10} / 0.14	5.0×10^{-11}
		8.0	154	3.53 / 3.08 / 3.28	0.016	1.67 / 7.78	8.6	7.1×10^{-8}	1.9×10^{-6} / 2.0	7.1×10^{-8}
		4.0	172	3.52 / 3.09 / 3.27	0.037	1.41 / 5.83	20	3.0×10^{-7}	3.6×10^{-6} / 1.2	3.0×10^{-7}
		0.0	184	3.51 / 3.07 / 3.26	0.028	1.53 / 6.55	15	2.0×10^{-7}	3.5×10^{-6} / 1.8	2.0×10^{-7}
Ac-MPM	0.174	∞	0	3.15 / 3.13 / 3.14	1.3×10^{-5}	0.07 / 0.03	0.0056	4.4×10^{-4}	0.24 / 0.074	4.4×10^{-4}
		8.0	48	3.15 / 3.05 / 3.11	0.029	1.05 / 0.11	12	0.074	7.8 / 0.40	0.073
		4.0	342	3.19 / 2.89 / 3.08	0.031	0.11 / 0.82	14	3.2×10^{-5}	2.6×10^{-5} / 3.5	3.2×10^{-5}
		0.0	394	3.17 / 2.82 / 3.09	0.005	3.39 / 2.96	2.3	9.1×10^{-7}	0.0026 / 110	9.1×10^{-7}
SpiroAC-TRZ	0.167	∞	0	3.02 / 3.00 / 3.13	8.2×10^{-6}	0.03 / 0.99	0.0032	5.1×10^{-4}	0.065 / 400	5.1×10^{-4}
		8.0	95	3.16 / 3.10 / 3.15	0.018	0.76 / 0.75	7.6	0.17	11 / 36	0.17
		4.0	278	3.05 / 2.85 / 2.97	0.024	0.12 / 0.69	9.5	0.0017	0.0044 / 6.1	1.6×10^{-3}
		0.0	450	3.10 / 2.75 / 3.00	0.029	0.13 / 0.72	12	4.7×10^{-6}	4.0×10^{-6} / 3.4	4.6×10^{-6}

[a] The TADF rate according to Equation 7.2, i.e. $k_{RISC} \gg k_F$.
[b] The TADF rate according to Equation E.9, i.e. $k_{RISC} \ll k_F + k_{ISC}$.

Table E.4: Energetics of the model systems recomputed with LRC-ω^*PBE at the maximum TADF geometries optimized with B3LYP.

	Λ ($\mu s^{-1} Ha^{-1}$)	ΔE_{DFT} (kJ mol^{-1})	EE (eV) S$_1$ / T$_1$ / T$_2$	f_{10}	SOC (cm^{-1}) T$_1$ / T$_2$ $\leftrightarrow$ S$_1$	Rate (μs^{-1}) S$_1$ $\rightarrow$ S$_0$	TADF[a]	T$_1$ / T$_2$ $\rightarrow$ S$_1$	TADF[b]
DCzTRZ	∞	0	3.70 / 3.41 / 3.47	0.0407	1.14 / 0.37	24	8.2×10^{-5}	0.0054 / 0.010	8.1×10^{-5}
	8.0	224	3.81 / 3.63 / 3.63	0.0147	0.42 / 0.46	9.3	0.0012	0.075 / 0.096	0.0012
	4.0	292	3.83 / 3.63 / 3.63	0.0027	0.36 / 0.25	1.7	9.2×10^{-5}	0.022 / 0.013	9.2×10^{-5}
	2.0	421	3.71 / 3.47 / 3.62	0.0011	0.055 / 1.81	0.67	1.9×10^{-5}	1.4×10^{-4} / 31	1.9×10^{-5}
	0.8	552	3.66 / 3.22 / 3.50	0.0046	0.10 / 4.36	2.6	3.4×10^{-8}	1.5×10^{-8} / 20	3.4×10^{-8}
	0.0	605	3.67 / 3.23 / 3.53	0.0013	0.13 / 2.78	0.75	9.7×10^{-9}	2.2×10^{-8} / 17	9.7×10^{-9}
Cz2BP	∞	0	3.62 / 3.13 / 3.42	0.0077	15.24 / 4.62	4.4	5.7×10^{-9}	6.9×10^{-6} / 4.6	5.7×10^{-9}
	8.0	174	3.63 / 3.31 / 3.61	0.0011	2.77 / 11.70	0.61	1.0×10^{-6}	0.012 / 8900	1.0×10^{-6}
	4.0	194	3.63 / 3.31 / 3.60	0.0013	2.99 / 11.98	0.73	8.8×10^{-7}	0.0090 / 6400	8.8×10^{-7}
	0.0	206	3.62 / 3.30 / 3.58	0.0013	2.94 / 13.24	0.74	9.0×10^{-7}	0.0088 / 6400	9.0×10^{-7}
Ac-MPM	∞	0	3.28 / 3.45 / 3.37	2.8×10^{-5}	1.04 / 0.05	0.013	0.012	590 / 0.86	0.012
	8.0	52	3.29 / 3.32 / 3.40	0.036	1.32 / 0.12	17	8.1	240 / 5.3	7.8
	4.0	371	3.36 / 3.25 / 3.37	0.038	0.26 / 0.91	19	0.099	0.40 / 81	0.092
	0.0	428	3.44 / 3.19 / 3.47	0.013	3.36 / 2.82	6.6	1.1×10^{-4}	0.29 / 1100	1.1×10^{-4}
SpiroAC-TRZ	∞	0	3.22 / 3.45 / 3.21	9.5×10^{-6}	1.12 / 0.05	0.0043	9.9×10^{-4}	690 / 0.23	9.8×10^{-4}
	8.0	101	3.38 / 3.46 / 3.53	0.019	1.11 / 0.39	9.6	8.6	370 / 76	8.4
	4.0	290	3.24 / 3.22 / 3.26	0.026	0.10 / 1.00	12	1.5	0.64 / 120	1.4
	0.0	470	3.32 / 3.11 / 3.37	0.032	0.13 / 0.94	16	0.0010	0.0019 / 150	9.0×10^{-4}

[a] The TADF rate according to Equation 7.2, i.e. $k_{RISC} \gg k_F$.
[b] The TADF rate according to Equation E.9, i.e. $k_{RISC} \ll k_F + k_{ISC}$.

Table E.5: Energetics of the model systems recomputed with M06-2X/IEF-PCM at the maximum TADF geometries optimized with B3LYP.

	ω^*	Λ	ΔE_{DFT}	EE (eV)		SOC (cm^{-1})	Rate ($\mu\mathrm{s}^{-1}$)			
	(a_0^{-1})	($\mu\mathrm{s}^{-1}\mathrm{Ha}^{-1}$)	($\mathrm{kJ\,mol}^{-1}$)	S_1 / T_1 / T_2	f_{10}	T_1 / $T_2 \leftrightarrow S_1$	$S_1 \rightarrow S_0$	TADF[a]	T_1 / $T_2 \rightarrow S_1$	TADF[b]
DCzTrz	0.169	∞	0	3.30 / 3.07 / 3.08	0.0312	1.48 / 0.39	15	3.1×10^{-4}	0.13 / 0.012	3.1×10^{-4}
		8.0	199	3.37 / 3.27 / 3.27	0.0146	0.68 / 0.78	7.2	0.024	3.1 / 4.6	0.023
		4.0	262	3.39 / 3.27 / 3.27	0.0021	0.49 / 0.78	1.0	0.0019	1.0 / 2.9	0.0019
		2.0	389	3.28 / 3.14 / 3.21	4.2×10^{-4}	0.55 / 3.58	0.20	2.5×10^{-4}	0.62 / 200	2.5×10^{-4}
		0.8	519	3.25 / 2.95 / 3.10	0.0015	2.49 / 3.99	0.70	1.9×10^{-6}	0.017 / 24	1.9×10^{-6}
		0.0	568	3.24 / 2.93 / 3.12	3.4×10^{-4}	0.93 / 3.05	0.16	2.7×10^{-7}	0.0014 / 35	2.7×10^{-7}
Cz2BP	0.186	∞	0	3.48 / 2.86 / 3.12	0.0102	13.42 / 4.88	5.4	6.6×10^{-11}	8.2×10^{-10} / 0.0046	6.6×10^{-11}
		8.0	154	3.56 / 3.10 / 3.27	0.0023	2.09 / 0.86	1.3	6.9×10^{-9}	1.5×10^{-6} / 0.0039	6.9×10^{-9}
		4.0	173	3.56 / 3.10 / 3.27	0.0039	2.29 / 1.07	2.2	1.5×10^{-8}	2.6×10^{-6} / 0.0051	1.5×10^{-8}
		0.0	184	3.54 / 3.09 / 3.27	0.0029	2.21 / 1.42	1.6	1.0×10^{-8}	2.3×10^{-6} / 0.019	1.0×10^{-8}
Ac-MPM	0.174	∞	0	3.04 / 3.09 / 3.06	5.0×10^{-5}	0.13 / 0.089	0.020	0.0073	3.3 / 0.94	0.0073
		8.0	48	2.97 / 2.98 / 3.07	0.031	1.27 / 0.15	12	3.8	160 / 8.1	3.7
		4.0	341	3.02 / 2.89 / 3.02	0.034	0.25 / 0.96	13	0.026	0.17 / 80	0.025
		0.0	393	3.08 / 2.82 / 3.08	0.0059	3.48 / 3.09	2.4	3.4×10^{-5}	0.25 / 830	3.4×10^{-5}
SpiroAC-TRZ	0.167	∞	0	2.82 / 2.81 / 3.13	7.8×10^{-6}	0.049 / 0.97	0.0027	5.1×10^{-4}	0.17 / 290	5.1×10^{-4}
		8.0	95	2.97 / 2.99 / 3.16	0.018	0.86 / 0.89	7.0	2.9	87 / 450	2.8
		4.0	278	2.86 / 2.86 / 2.85	0.024	0.12 / 0.73	8.5	1.1	1.2 / 41	1.1
		0.0	450	2.93 / 2.75 / 3.00	0.030	0.13 / 0.93	11	0.0041	0.011 / 230	0.0035

[a] The TADF rate according to Equation 7.2, i.e. $k_{\mathrm{RISC}} \gg k_{\mathrm{F}}$.
[b] The TADF rate according to Equation E.9, i.e. $k_{\mathrm{RISC}} \ll k_{\mathrm{F}} + k_{\mathrm{ISC}}$.

Table E.6: Energetics of the model systems recomputed with LRC-ω^*PBE/IEF-PCM at the maximum TADF geometries optimized with B3LYP.

imum TADF geometries with little or no energy penalties, the functionals predict that the TADF rate would be similar to or even worse than the the minimum energy geometry. For maximum TADF geometries with sufficient energy penalties ($\Lambda \geq 4.0\,\mu s^{-1} {E_h}^{-1}$), the functionals agree with B3LYP that the TADF rate could be orders of magnitude greater than the minimum energy geometry. It would seem that the TADF rate maximization tended to exploit some quirk of the B3LYP functional, but the imposition of energy penalties mitigated the issue.

It is also remarkable that the functionals predict a simultaneous improvement of the ST gap and TDM. The simulataneous improvement is not observed in M06-2X and LRC-ω^*PBE without solvent models, but it is observed in M06-2X/IEF-PCM and LRC-ω^*PBE/IEF-PCM with a toluene-like environment. In the latter case, the maximized TADF rates of Ac-MPM and SpiroAC-TRZ are quite impressive, as they are well within the submicrosecond time scales.

Finally, the functionals predict the RISC correction to be even less important than B3LYP did. With a few excpetions, the RISC corrections are less than 10 % of the TADF rates. The finite rate of RISC does not seem to overturn the qualitative trends of conformational optimization.

E.3 Geometries of Cz2BP, Ac-MPM, and SpiroAC-TRZ

The 3D images of the geometries were generated in Avogadro 1.2.0 [298].

The maximum TADF geometries of Cz2BP have been illustrated in Figure E-1. Figure E-1a shows the minimum energy conformation with arrows indicating the degrees of freedom (DOFs) that are the most active in the TADF rate maximization. Going to the maximum TADF conformation in Figure E-1b, the carbazole (Cz, donor) and the phenyl groups in the benzophenone (BP, acceptor) group have rotated to increase the dihedral angles between the adjacent aromatic ring systems. The adjacent aromatic units are 73.7° (left), 57.2° (center), and 71.5° (right) to each other, respectively, in contrast to 52.6° (left), 52.9° (center), and 52.8° (right) at the energy minimum. While the increase in the DA dihedral angle is consistent with the decreases in the ST gap and the TDM, the benefit of increasing the dihedral angle between the phenyl rings in the acceptor group is not clear.

Meanwhile, the Cz and the phenyl groups also tilt in the direction of the carboxyl group so the overall molecule looks less bent in the maximum TADF rate conformation. In particular, the Cz group ends up with a gooseneck, as shown in Figure E-1c. The differences in the C_{Cz}-N_{Cz}-C_{Ph} angles at each carbazole group are 18.3° (left) and 15.7° (right), respectively, whereas the C_{Cz}-N_{Cz}-C_{Ph} angles in the minimum energy conformation are the same $125.8 \pm 0.1°$. As shown in Figure E-1d, the gooseneck persists even with an energy penalty of $\Lambda = 8.0\,\mu s^{-1} {E_h}^{-1}$, retaining 17.1° (left) and 14.5° (right) differences in the C_{Cz}-N_{Cz}-C_{Ph} angles. Figure E-1e shows the geometry after the hydrogen atoms and the aromatic ring systems have been relaxed. Visually, the relaxation of the aromatic units seems to somewhat undo the overall twist.

The maximum TADF geometries of Ac-MPM have been illustrated in Figure E-2. Figure E-2a shows the minimum energy conformation with arrows indicating the DOFs that are the most active in the TADF rate maximization. Unlike the cases of DCzTrz and Cz2BP, the dihedral angles between the donor and the acceptor groups decrease, consistent with the increases in the ST gap (albeit slight) and the TDM.

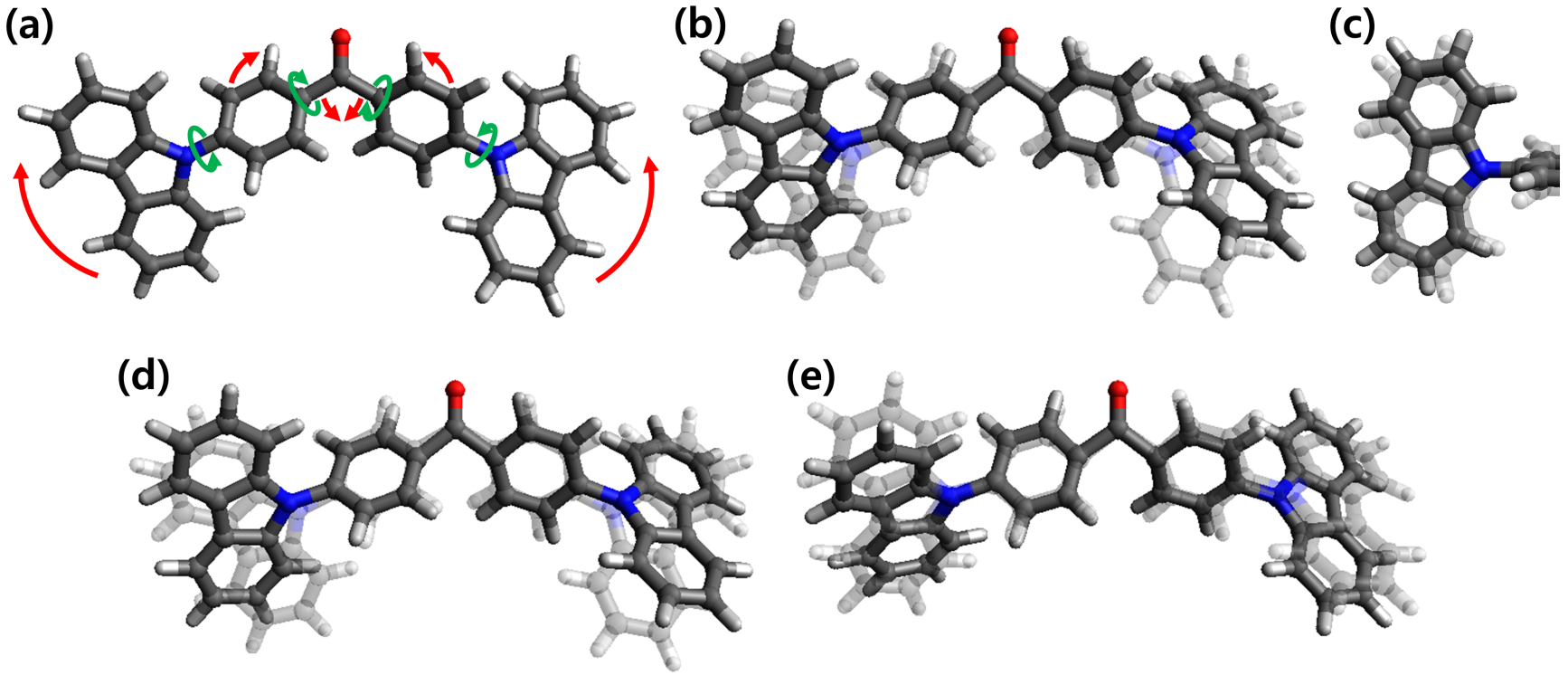

Figure E-1: Geometries of Cz2BP: (a) the energy minimum, $\Lambda = \infty$; (b) the TADF maximum with no energy penalty, $\Lambda = 0$; (c) a magnified view of the donor-acceptor bond; (d) the TADF maximum with energy penalty, $\Lambda = 8.0\,\mu s^{-1} {E_h}^{-1}$; and (e) after the relaxation of the hydrogen atoms and the aromatic ring systems. The arrows in panel (a) indicate the DOFs that are the most active in the TADF rate maximization, and the translucent geometries in the background are the energy minimum in panels (b)–(d) and the TADF maximum with no energy penalty in panel (e).

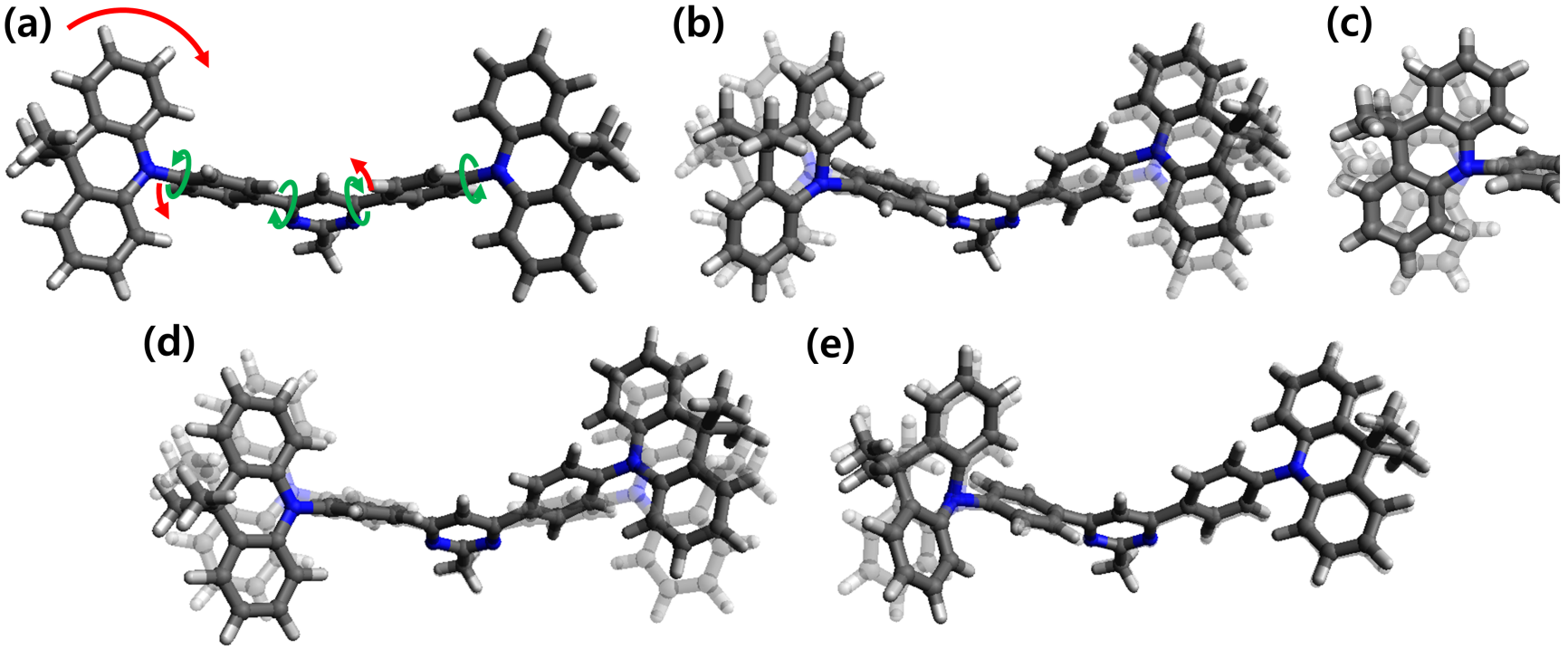

Figure E-2: Geometries of Ac-MPM: (a) the energy minimum, $\Lambda = \infty$; (b) the TADF maximum with no energy penalty, $\Lambda = 0$; (c) a maginfied view of the donor-acceptor bond; (d) the TADF maximum with energy penalty, $\Lambda = 8.0\,\mu\mathrm{s}^{-1}{E_\mathrm{h}}^{-1}$; and (e) after the relaxation of the hydrogen atoms and the aromatic ring systems. The arrows in panel (a) indicate the DOFs that are the most active in the TADF rate maximization, and the translucent geometries in the background are the energy minimum in panels (b)–(d) and the TADF maximum with no energy penalty in panel (e).

The acridine (Ac) groups are 75.2° (left) and 74.8° (right) to the phenyl rings of the 2-methylpyrimidine (MPM, acceptor) group, respectively, in contrast to 90.0° (left) and 90.4° (right) in the minimum energy conformation.

Nonetheless, familiar motifs appear in the maximum TADF rate conformation (Figure E-2b). One of the Ac groups tilts towards MPM group in a sharp gooseneck, as shown in Figure E-2c. The differences in the C_{Ac}-N_{Ac}-C_{Ph} angles at each acridine group are 55.0° (left) and 7.9° (right), respectively, whereas the C_{Ac}-N_{Ac}-C_{Ph} angles in the minimum energy conformation are the same $119.2 \pm 0.2°$. In addition, the MPM group twists in an asymmetric manner. One of the phenyl rings twists out of plane. While the other phenyl ring also reorients itself, it maintains a moderate angle to the plane of the pyrimidine ring. The phenyl rings are 48.4° (left) and 19.3° (right) to the pyrimidine ring, respectively, in contrast to 18.7° (left) and 17.7° (right) in the minimum energy conformation.

As shown in Figure E-2d, the twist in the acceptor group persists even with an energy penalty of $\Lambda = 8.0\,\mu s^{-1} {E_h}^{-1}$, though the angles between the phenyl rings and the pyrimidine ring change to 30.0° (left) and 17.2° (right), respectively. However, the sharp gooseneck dissipates at some point between $4.0\,\mu s^{-1} {E_h}^{-1}$ and $8.0\,\mu s^{-1} {E_h}^{-1}$, the differences in the C_{Ac}-N_{Ac}-C_{Ph} angles reduced to 5.0° (left) and 4.2° (right), respectively. We conjecture that the gooseneck provides negligible benefit to TADF in the case of Ac-MPM. Indeed, the twist in the acceptor group would skew the distribution of the LUMO towards the Ac group on the right, so the Ac group on the left would have limited impact on the TADF rate. Hence, it becomes favorable to unroll the gooseneck under even moderate energy penalties.

As shown in Figure E-2e, relaxing the hydrogen atoms and the aromatic ring systems puckers the Ac group on the left. In spite of the obvious disruption to the structure, the TADF rate only decreases by 16 %, in line with the conjecture that the Ac group on the right dominates the TADF process in the maximum TADF rate conformation of Ac-MPM.

The maximum TADF geometries of SpiroAC-TRZ have been illustrated in Figure E-3. Figure E-3a shows the minimum energy conformation with arrows indicating

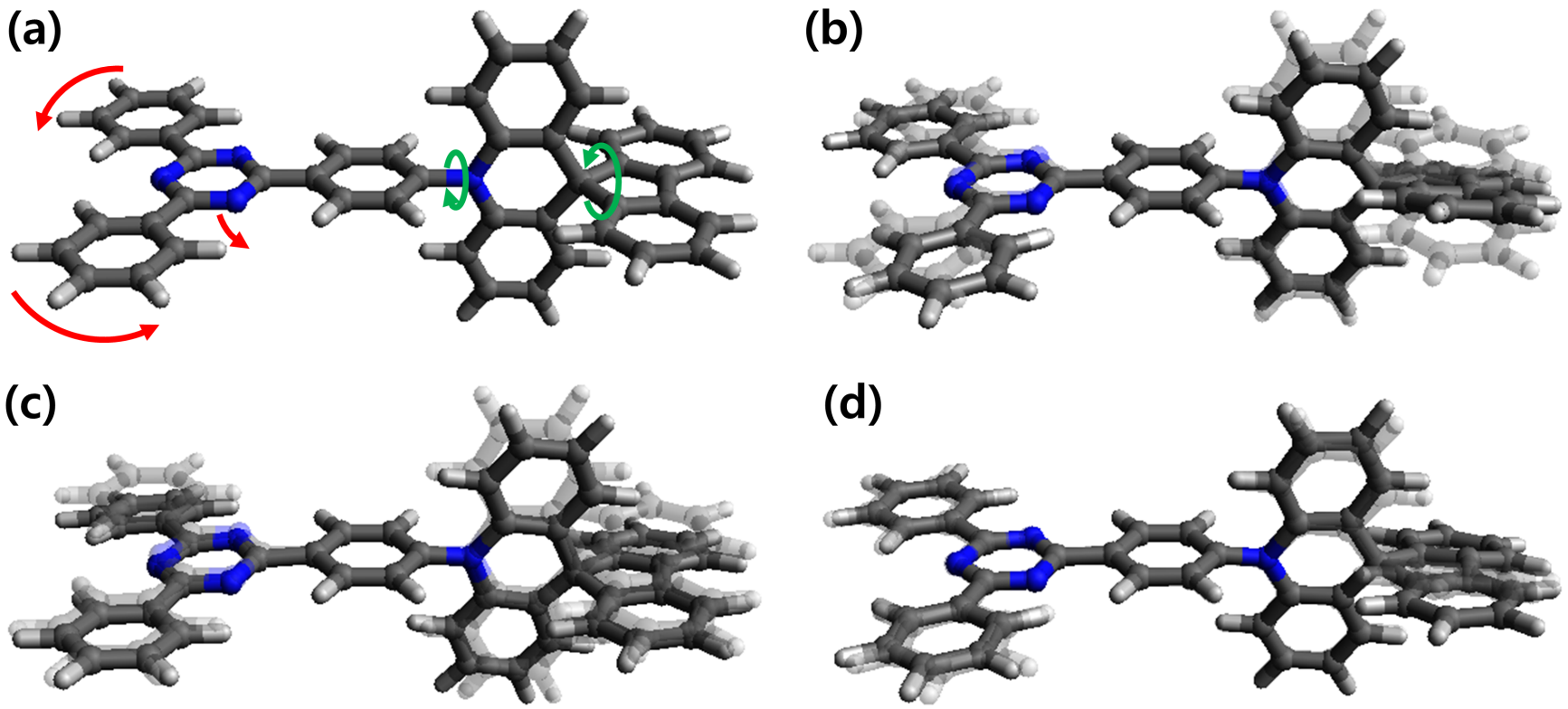

Figure E-3: Geometries of SpiroAC-TRZ: (a) the energy minimum, $\Lambda = \infty$; (b) the TADF maximum with no energy penalty, $\Lambda = 0$; (c) the TADF maximum with energy penalty, $\Lambda = 8.0\,\mu\mathrm{s}^{-1}{E_\mathrm{h}}^{-1}$; and (d) after the relaxation of the hydrogen atoms and the aromatic ring systems. The arrows in panel (a) indicate the DOFs that are the most active in the TADF rate maximization, and the translucent geometries in the background are the energy minimum in panel (b)–(c) and the TADF maximum with no energy penalty in panel (d).

the DOFs that are the most active in the TADF rate maximization. Once again, the dihedral angle between the donor group and the acceptor group decreases, consistent with the increases in the ST gap (albeit slight) and the TDM. The adjacent aromatic units are 83.9° and 62.2° to each other, respectively, in contrast to 90.1° and 90.0° in the minimum energy conformation. Unlike any of the previous cases, the maximum TADF rate conformation in Figure E-3b shows neither a gooseneck nor a twist in the acceptor group. In fact, most of the distortion is contained in the wagging of the phenyl groups in the plane of the Trz group. As shown in Figure E-3d, relaxing the hydrogen atoms and the aromatic ring systems appears to restore the relative positions of the atoms in the minimum energy conformation. Given that the effect of the constrained energy minimization on the TADF rate is not severe, it must be the case that the relaxation does not affect the orbital overlap. Indeed, the dihedral angles between aromatic units have been constrained, and SpiroAC-TRZ does not contain a goose neck. Distortions within aromatic ring systems would have minimal effect on the orbital overlaps.

E.4 Natural Transition Orbitals

The 3D images of the natural transition orbitals (NTOs) [284] were generated in MacMolPlt 7.7 [299].

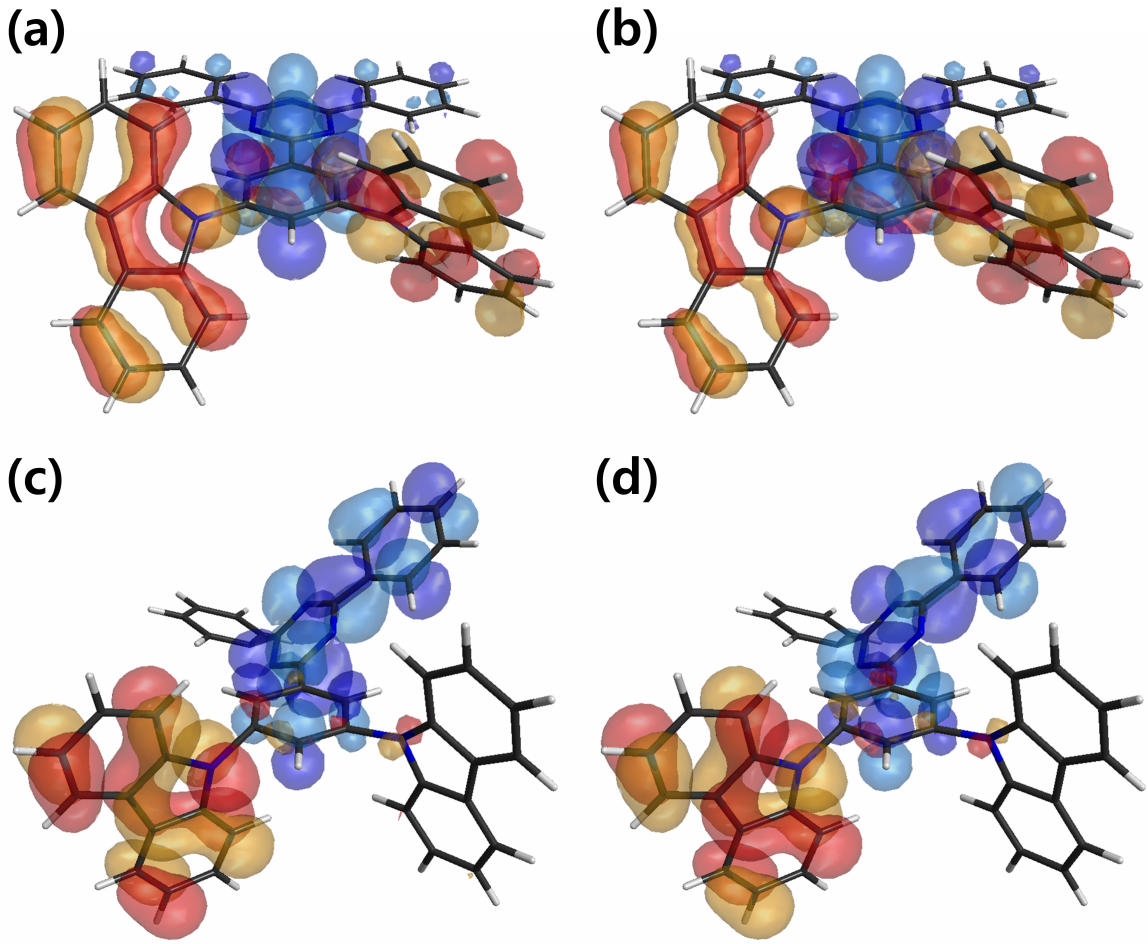

Figure E-4: NTO pairs of DCzTrz in (a) the S_1 state and (b) the T_1 state at the energy minimum, $\Lambda = \infty$; and (c) the S_1 state and (d) the T_1 state at the TADF maximum with no energy penalty, $\Lambda = 0$. The hole orbitals are shown in red and orange, and the electron orbitals are shown in sky blue and indigo. ISO value: 0.025.

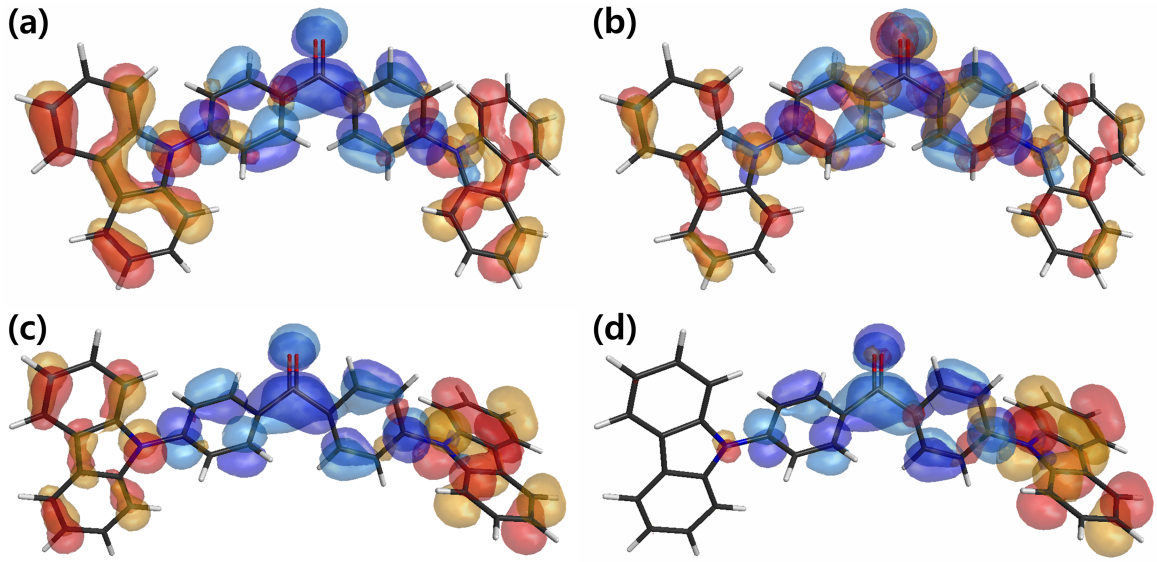

Figure E-5: NTO pairs of Cz2BP in (a) the S_1 state and (b) the T_1 state at the energy minimum, $\Lambda = \infty$; and (c) the S_1 state and (d) the T_1 state at the TADF maximum with no energy penalty, $\Lambda = 0$. The hole orbitals are shown in red and orange, and the electron orbitals are shown in sky blue and indigo. ISO value: 0.025.

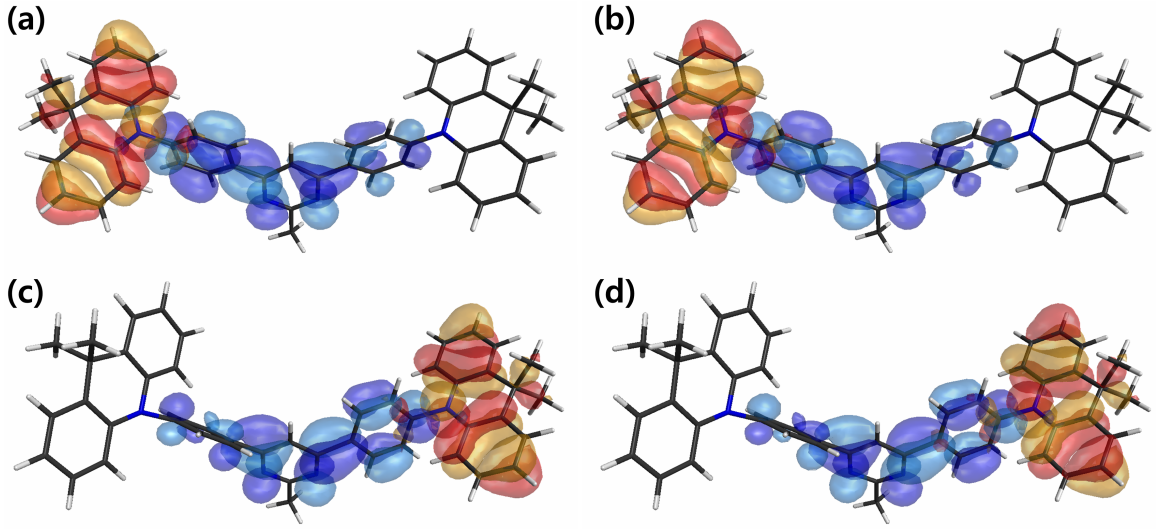

Figure E-6: NTO pairs of Ac-MPM in (a) the S_1 state and (b) the T_1 state at the energy minimum, $\Lambda = \infty$; and (c) the S_1 state and (d) the T_1 state at the TADF maximum with no energy penalty, $\Lambda = 0$. The hole orbitals are shown in red and orange, and the electron orbitals are shown in sky blue and indigo. ISO value: 0.025.

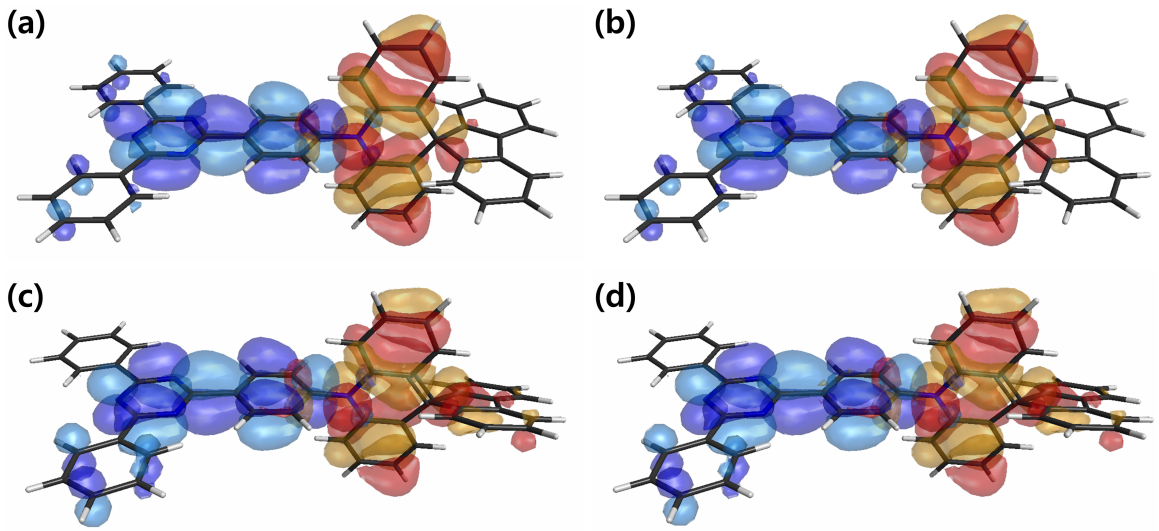

Figure E-7: NTO pairs of SpiroAC-TRZ in (a) the S_1 state and (b) the T_1 state at the energy minimum, $\Lambda = \infty$; and (c) the S_1 state and (d) the T_1 state at the TADF maximum with no energy penalty, $\Lambda = 0$. The hole orbitals are shown in red and orange, and the electron orbitals are shown in sky blue and indigo. ISO value: 0.025.

E.5 Z-Matrices

Tables E.7–E.28 show the Z-matrices of the model systems at the energy minimum, at the TADF maxima with various energy penalties, and after the relaxation of the hydrogen atoms and the aromatic ring systems. Note that Q-Chem reorders the Z-matrix during the constrained energy minimization.

C							C	41	1.40726	40	120.54922	39	359.65191
C	1	1.39881					C	42	1.39528	41	121.40346	40	0.34748
C	2	1.39425	1	120.16424			C	43	1.39880	42	117.72197	41	0.21165
C	3	1.40529	2	120.33344	1	0.05219	C	9	1.48313*	8	118.15009*	7	180.02562*
C	4	1.40538	3	119.18851	2	359.95385	C	45	1.40530	9	120.41287*	8	0.46503*
C	5	1.39442	4	120.32961	3	0.02562	C	46	1.39433	45	120.33164	9	179.97438*
C	4	1.48313*	3	120.37194*	2	179.97438*	C	47	1.39877	46	120.16975	45	0.02562
N	7	1.34191	4	118.12045*	3	1.04697*	C	48	1.39863	47	119.81686	46	359.97438
C	8	1.34180	7	116.19320	4	179.97438*	C	49	1.39441	48	120.16153	47	359.97438
N	9	1.34395	8	123.87602	7	0.15279	H	1	1.08713	2	120.08954	3	179.97438
C	10	1.33948	9	115.76541	8	359.79882	H	2	1.08691	1	120.09233	3	179.97438
N	11	1.33944	10	124.53015	9	0.03803	H	3	1.08429	2	120.63089	1	180.02562
C	11	1.48822*	10	117.70003*	9	180.02562*	H	5	1.08423	4	119.14092	3	180.02562
C	13	1.40145	11	120.08922*	10	3.55655*	H	6	1.08684	5	119.70222	4	180.02562
C	14	1.39772	13	120.10899	11	180.54975*	H	14	1.08328	13	119.60739	18	-178.97627
C	15	1.40041	14	120.13438	13	359.12975	H	16	1.08513	15	120.13739	14	180.33415
C	16	1.40041	15	119.75732	14	0.36550	H	18	1.08335	17	120.27300	16	178.51517
C	17	1.39763	16	120.17535	15	0.52083	H	21	1.08557	20	121.49918	19	1.06266
N	17	1.42043*	16	119.84005*	15	179.97438*	H	22	1.08691	21	119.07827	20	180.02562
C	19	1.40078	17	125.61232*	16	122.71268*	H	23	1.08658	22	119.59854	21	180.02562
C	20	1.39884	19	129.44131	17	358.59290*	H	24	1.08723	23	120.41591	22	179.42469
C	21	1.39526	20	117.71657	19	181.18901	H	27	1.08723	26	120.40812	25	359.13361
C	22	1.40729	21	121.40581	20	0.17108	H	28	1.08654	27	119.85378	26	179.90485
C	23	1.39379	22	120.54855	21	0.35645	H	29	1.08685	28	119.52324	27	180.49587
C	24	1.40103	23	119.18251	22	359.67902	H	30	1.08561	29	120.75101	28	180.51128
C	25	1.44891	24	133.61296	23	178.87145	H	34	1.08554	33	121.53615	32	0.80805
C	26	1.40095	25	133.59767	24	1.68791	H	35	1.08685	34	119.07160	33	180.09013
C	27	1.39372	26	119.17823	25	178.91015	H	36	1.08654	35	119.59660	34	180.12953
C	28	1.40722	27	120.55061	26	359.62121	H	37	1.08722	36	120.42035	35	179.37317
C	29	1.39519	28	121.40591	27	0.41068	H	40	1.08723	39	120.40225	38	359.28562
C	30	1.39882	29	117.72369	28	0.19095	H	41	1.08658	40	119.85209	39	179.97438
N	15	1.42021*	14	119.96093*	13	179.64405*	H	42	1.08690	41	119.52479	40	180.44541
C	32	1.40113	15	125.95848*	14	122.96261*	H	43	1.08550	42	120.77406	41	180.30187
C	33	1.39881	32	129.47780	15	358.32390*	H	46	1.08430	45	119.05000	50	-179.97489
C	34	1.39520	33	117.72493	32	181.18158	H	47	1.08692	46	119.73749	45	180.02562
C	35	1.40718	34	121.40971	33	0.18689	H	48	1.08712	47	120.08957	46	180.02562
C	36	1.39370	35	120.54803	34	0.41641	H	49	1.08684	48	120.13668	47	179.97438
C	37	1.40094	36	119.17491	35	359.62614	H	50	1.08420	49	120.52043	48	179.97438
C	38	1.44896	37	133.57589	36	178.74217							
C	39	1.40108	38	133.61407	37	1.67108							
C	40	1.39378	39	119.17892	38	179.07456							

* Z-matrix coordinates that were chosen as variables in the TADF rate maximization.

Table E.7: Z-matrix of DCzTrz at the energy minimum ($\Lambda = \infty$).

C							C	41	1.40726	40	120.54922	39	359.65191
C	1	1.39881					C	42	1.39528	41	121.40346	40	0.34748
C	2	1.39425	1	120.16424			C	43	1.39880	42	117.72197	41	0.21165
C	3	1.40529	2	120.33344	1	0.05219	C	9	1.51545*	8	120.31769*	7	187.62982*
C	4	1.40538	3	119.18851	2	359.95385	C	45	1.40530	9	118.82577*	8	8.44666*
C	5	1.39442	4	120.32961	3	0.02562	C	46	1.39433	45	120.33164	9	186.10948*
C	4	1.55254*	3	123.01669*	2	188.11414*	C	47	1.39877	46	120.16975	45	0.02562
N	7	1.34191	4	125.74810*	3	22.70005*	C	48	1.39863	47	119.81686	46	359.97438
C	8	1.34180	7	116.19320	4	185.88731*	C	49	1.39441	48	120.16153	47	359.97438
N	9	1.34395	8	123.87602	7	0.15279	H	1	1.08713	2	120.08954	3	179.97438
C	10	1.33948	9	115.76541	8	359.79882	H	2	1.08691	1	120.09233	3	179.97438
N	11	1.33944	10	124.53015	9	0.03803	H	3	1.08429	2	120.63089	1	180.02562
C	11	1.67136*	10	105.77128*	9	191.66687*	H	5	1.08423	4	119.14092	3	180.02562
C	13	1.40145	11	122.86105*	10	-35.58294*	H	6	1.08684	5	119.70222	4	180.02562
C	14	1.39772	13	120.10899	11	186.10056*	H	14	1.08328	13	119.60739	18	-178.97627
C	15	1.40041	14	120.13438	13	359.12975	H	16	1.08513	15	120.13739	14	180.33415
C	16	1.40041	15	119.75732	14	0.36550	H	18	1.08335	17	120.27300	16	178.51517
C	17	1.39763	16	120.17535	15	0.52083	H	21	1.08557	20	121.49918	19	1.06266
N	17	1.54738*	16	112.25142*	15	150.89825*	H	22	1.08691	21	119.07827	20	180.02562
C	19	1.40078	17	113.61400*	16	111.03754*	H	23	1.08658	22	119.59854	21	180.02562
C	20	1.39884	19	129.44131	17	351.29158*	H	24	1.08723	23	120.41591	22	179.42469
C	21	1.39526	20	117.71657	19	181.18901	H	27	1.08723	26	120.40812	25	359.13361
C	22	1.40729	21	121.40581	20	0.17108	H	28	1.08654	27	119.85378	26	179.90485
C	23	1.39379	22	120.54855	21	0.35645	H	29	1.08685	28	119.52324	27	180.49587
C	24	1.40103	23	119.18251	22	359.67902	H	30	1.08561	29	120.75101	28	180.51128
C	25	1.44891	24	133.61296	23	178.87145	H	34	1.08554	33	121.53615	32	0.80805
C	26	1.40095	25	133.59767	24	1.68791	H	35	1.08685	34	119.07160	33	180.09013
C	27	1.39372	26	119.17823	25	178.91015	H	36	1.08654	35	119.59660	34	180.12953
C	28	1.40722	27	120.55061	26	359.62121	H	37	1.08722	36	120.42035	35	179.37317
C	29	1.39519	28	121.40591	27	0.41068	H	40	1.08723	39	120.40225	38	359.28562
C	30	1.39882	29	117.72369	28	0.19095	H	41	1.08658	40	119.85209	39	179.97438
N	15	1.52703*	14	120.55488*	13	180.39188*	H	42	1.08690	41	119.52479	40	180.44541
C	32	1.40113	15	127.53646*	14	119.81345*	H	43	1.08550	42	120.77406	41	180.30187
C	33	1.39881	32	129.47780	15	338.24020*	H	46	1.08430	45	119.05000	50	-179.97489
C	34	1.39520	33	117.72493	32	181.18158	H	47	1.08692	46	119.73749	45	180.02562
C	35	1.40718	34	121.40971	33	0.18689	H	48	1.08712	47	120.08957	46	180.02562
C	36	1.39370	35	120.54803	34	0.41641	H	49	1.08684	48	120.13668	47	179.97438
C	37	1.40094	36	119.17491	35	359.62614	H	50	1.08420	49	120.52043	48	179.97438
C	38	1.44896	37	133.57589	36	178.74217							
C	39	1.40108	38	133.61407	37	1.67108							
C	40	1.39378	39	119.17892	38	179.07456							

* Z-matrix coordinates that were chosen as variables in the TADF rate maximization.

Table E.8: Z-matrix of DCzTrz at the TADF maximum with energy penalty ($\Lambda = 8.0\,\mu s^{-1} {E_h}^{-1}$).

C							C	41	1.40726	40	120.54922	39	359.65191
C	1	1.39881					C	42	1.39528	41	121.40346	40	0.34748
C	2	1.39425	1	120.16424			C	43	1.39880	42	117.72197	41	0.21165
C	3	1.40529	2	120.33344	1	0.05219	C	9	1.54946*	8	126.01449*	7	184.13810*
C	4	1.40538	3	119.18851	2	359.95385	C	45	1.40530	9	119.08048*	8	9.22708*
C	5	1.39442	4	120.32961	3	0.02562	C	46	1.39433	45	120.33164	9	185.67989*
C	4	1.54033*	3	120.90286*	2	203.26320*	C	47	1.39877	46	120.16975	45	0.02562
N	7	1.34191	4	127.05008*	3	33.08534*	C	48	1.39863	47	119.81686	46	359.97438
C	8	1.34180	7	116.19320	4	186.18443*	C	49	1.39441	48	120.16153	47	359.97438
N	9	1.34395	8	123.87602	7	0.15279	H	1	1.08713	2	120.08954	3	179.97438
C	10	1.33948	9	115.76541	8	359.79882	H	2	1.08691	1	120.09233	3	179.97438
N	11	1.33944	10	124.53015	9	0.03803	H	3	1.08429	2	120.63089	1	180.02562
C	11	1.63865*	10	104.46643*	9	192.70549*	H	5	1.08423	4	119.14092	3	180.02562
C	13	1.40145	11	123.91052*	10	-54.10297*	H	6	1.08684	5	119.70222	4	180.02562
C	14	1.39772	13	120.10899	11	185.98014*	H	14	1.08328	13	119.60739	18	-178.97627
C	15	1.40041	14	120.13438	13	359.12975	H	16	1.08513	15	120.13739	14	180.33415
C	16	1.40041	15	119.75732	14	0.36550	H	18	1.08335	17	120.27300	16	178.51517
C	17	1.39763	16	120.17535	15	0.52083	H	21	1.08557	20	121.49918	19	1.06266
N	17	1.56185*	16	111.52353*	15	151.87254*	H	22	1.08691	21	119.07827	20	180.02562
C	19	1.40078	17	109.10124*	16	109.76245*	H	23	1.08658	22	119.59854	21	180.02562
C	20	1.39884	19	129.44131	17	352.60995*	H	24	1.08723	23	120.41591	22	179.42469
C	21	1.39526	20	117.71657	19	181.18901	H	27	1.08723	26	120.40812	25	359.13361
C	22	1.40729	21	121.40581	20	0.17108	H	28	1.08654	27	119.85378	26	179.90485
C	23	1.39379	22	120.54855	21	0.35645	H	29	1.08685	28	119.52324	27	180.49587
C	24	1.40103	23	119.18251	22	359.67902	H	30	1.08561	29	120.75101	28	180.51128
C	25	1.44891	24	133.61296	23	178.87145	H	34	1.08554	33	121.53615	32	0.80805
C	26	1.40095	25	133.59767	24	1.68791	H	35	1.08685	34	119.07160	33	180.09013
C	27	1.39372	26	119.17823	25	178.91015	H	36	1.08654	35	119.59660	34	180.12953
C	28	1.40722	27	120.55061	26	359.62121	H	37	1.08722	36	120.42035	35	179.37317
C	29	1.39519	28	121.40591	27	0.41068	H	40	1.08723	39	120.40225	38	359.28562
C	30	1.39882	29	117.72369	28	0.19095	H	41	1.08658	40	119.85209	39	179.97438
N	15	1.53426*	14	115.57431*	13	182.04354*	H	42	1.08690	41	119.52479	40	180.44541
C	32	1.40113	15	125.98606*	14	117.87548*	H	43	1.08550	42	120.77406	41	180.30187
C	33	1.39881	32	129.47780	15	338.92970*	H	46	1.08430	45	119.05000	50	-179.97489
C	34	1.39520	33	117.72493	32	181.18158	H	47	1.08692	46	119.73749	45	180.02562
C	35	1.40718	34	121.40971	33	0.18689	H	48	1.08712	47	120.08957	46	180.02562
C	36	1.39370	35	120.54803	34	0.41641	H	49	1.08684	48	120.13668	47	179.97438
C	37	1.40094	36	119.17491	35	359.62614	H	50	1.08420	49	120.52043	48	179.97438
C	38	1.44896	37	133.57589	36	178.74217							
C	39	1.40108	38	133.61407	37	1.67108							
C	40	1.39378	39	119.17892	38	179.07456							

* Z-matrix coordinates that were chosen as variables in the TADF rate maximization.

Table E.9: Z-matrix of DCzTrz at the TADF maximum with energy penalty ($\Lambda = 4.0\,\mu s^{-1} {E_h}^{-1}$).

C							C	41	1.40726	40	120.54922	39	359.65191
C	1	1.39881					C	42	1.39528	41	121.40346	40	0.34748
C	2	1.39425	1	120.16424			C	43	1.39880	42	117.72197	41	0.21165
C	3	1.40529	2	120.33344	1	0.05219	C	9	1.44082*	8	130.39469*	7	185.92006*
C	4	1.40538	3	119.18851	2	359.95385	C	45	1.40530	9	104.38526*	8	8.43189*
C	5	1.39442	4	120.32961	3	0.02562	C	46	1.39433	45	120.33164	9	188.28194*
C	4	1.54711*	3	130.32246*	2	216.04060*	C	47	1.39877	46	120.16975	45	0.02562
N	7	1.34191	4	125.93354*	3	29.60538*	C	48	1.39863	47	119.81686	46	359.97438
C	8	1.34180	7	116.19320	4	187.01069*	C	49	1.39441	48	120.16153	47	359.97438
N	9	1.34395	8	123.87602	7	0.15279	H	1	1.08713	2	120.08954	3	179.97438
C	10	1.33948	9	115.76541	8	359.79882	H	2	1.08691	1	120.09233	3	179.97438
N	11	1.33944	10	124.53015	9	0.03803	H	3	1.08429	2	120.63089	1	180.02562
C	11	1.67937*	10	100.40804*	9	191.87496*	H	5	1.08423	4	119.14092	3	180.02562
C	13	1.40145	11	123.28155*	10	-52.66865*	H	6	1.08684	5	119.70222	4	180.02562
C	14	1.39772	13	120.10899	11	186.79199*	H	14	1.08328	13	119.60739	18	-178.97627
C	15	1.40041	14	120.13438	13	359.12975	H	16	1.08513	15	120.13739	14	180.33415
C	16	1.40041	15	119.75732	14	0.36550	H	18	1.08335	17	120.27300	16	178.51517
C	17	1.39763	16	120.17535	15	0.52083	H	21	1.08557	20	121.49918	19	1.06266
N	17	1.53919*	16	109.12161*	15	145.98502*	H	22	1.08691	21	119.07827	20	180.02562
C	19	1.40078	17	115.10068*	16	110.02287*	H	23	1.08658	22	119.59854	21	180.02562
C	20	1.39884	19	129.44131	17	353.40779*	H	24	1.08723	23	120.41591	22	179.42469
C	21	1.39526	20	117.71657	19	181.18901	H	27	1.08723	26	120.40812	25	359.13361
C	22	1.40729	21	121.40581	20	0.17108	H	28	1.08654	27	119.85378	26	179.90485
C	23	1.39379	22	120.54855	21	0.35645	H	29	1.08685	28	119.52324	27	180.49587
C	24	1.40103	23	119.18251	22	359.67902	H	30	1.08561	29	120.75101	28	180.51128
C	25	1.44891	24	133.61296	23	178.87145	H	34	1.08554	33	121.53615	32	0.80805
C	26	1.40095	25	133.59767	24	1.68791	H	35	1.08685	34	119.07160	33	180.09013
C	27	1.39372	26	119.17823	25	178.91015	H	36	1.08654	35	119.59660	34	180.12953
C	28	1.40722	27	120.55061	26	359.62121	H	37	1.08722	36	120.42035	35	179.37317
C	29	1.39519	28	121.40591	27	0.41068	H	40	1.08723	39	120.40225	38	359.28562
C	30	1.39882	29	117.72369	28	0.19095	H	41	1.08658	40	119.85209	39	179.97438
N	15	1.53780*	14	116.90182*	13	183.59926*	H	42	1.08690	41	119.52479	40	180.44541
C	32	1.40113	15	128.71968*	14	115.09179*	H	43	1.08550	42	120.77406	41	180.30187
C	33	1.39881	32	129.47780	15	334.79222*	H	46	1.08430	45	119.05000	50	-179.97489
C	34	1.39520	33	117.72493	32	181.18158	H	47	1.08692	46	119.73749	45	180.02562
C	35	1.40718	34	121.40971	33	0.18689	H	48	1.08712	47	120.08957	46	180.02562
C	36	1.39370	35	120.54803	34	0.41641	H	49	1.08684	48	120.13668	47	179.97438
C	37	1.40094	36	119.17491	35	359.62614	H	50	1.08420	49	120.52043	48	179.97438
C	38	1.44896	37	133.57589	36	178.74217							
C	39	1.40108	38	133.61407	37	1.67108							
C	40	1.39378	39	119.17892	38	179.07456							

* Z-matrix coordinates that were chosen as variables in the TADF rate maximization.

Table E.10: Z-matrix of DCzTrz at the TADF maximum with energy penalty ($\Lambda = 2.0\,\mu s^{-1} {E_h}^{-1}$).

C							C	41	1.40726	40	120.54922	39	359.65191
C	1	1.39881					C	42	1.39528	41	121.40346	40	0.34748
C	2	1.39425	1	120.16424			C	43	1.39880	42	117.72197	41	0.21165
C	3	1.40529	2	120.33344	1	0.05219	C	9	1.32650*	8	130.03798*	7	184.96724*
C	4	1.40538	3	119.18851	2	359.95385	C	45	1.40530	9	99.57363*	8	9.43006*
C	5	1.39442	4	120.32961	3	0.02562	C	46	1.39433	45	120.33164	9	187.96114*
C	4	1.53739*	3	127.63667*	2	226.69667*	C	47	1.39877	46	120.16975	45	0.02562
N	7	1.34191	4	126.30255*	3	39.17326*	C	48	1.39863	47	119.81686	46	359.97438
C	8	1.34180	7	116.19320	4	187.46366*	C	49	1.39441	48	120.16153	47	359.97438
N	9	1.34395	8	123.87602	7	0.15279	H	1	1.08713	2	120.08954	3	179.97438
C	10	1.33948	9	115.76541	8	359.79882	H	2	1.08691	1	120.09233	3	179.97438
N	11	1.33944	10	124.53015	9	0.03803	H	3	1.08429	2	120.63089	1	180.02562
C	11	1.64376*	10	99.62198*	9	184.92074*	H	5	1.08423	4	119.14092	3	180.02562
C	13	1.40145	11	121.81041*	10	-40.14115*	H	6	1.08684	5	119.70222	4	180.02562
C	14	1.39772	13	120.10899	11	187.84869*	H	14	1.08328	13	119.60739	18	-178.97627
C	15	1.40041	14	120.13438	13	359.12975	H	16	1.08513	15	120.13739	14	180.33415
C	16	1.40041	15	119.75732	14	0.36550	H	18	1.08335	17	120.27300	16	178.51517
C	17	1.39763	16	120.17535	15	0.52083	H	21	1.08557	20	121.49918	19	1.06266
N	17	1.51043*	16	111.76928*	15	142.24754*	H	22	1.08691	21	119.07827	20	180.02562
C	19	1.40078	17	115.61874*	16	111.91426*	H	23	1.08658	22	119.59854	21	180.02562
C	20	1.39884	19	129.44131	17	352.85551*	H	24	1.08723	23	120.41591	22	179.42469
C	21	1.39526	20	117.71657	19	181.18901	H	27	1.08723	26	120.40812	25	359.13361
C	22	1.40729	21	121.40581	20	0.17108	H	28	1.08654	27	119.85378	26	179.90485
C	23	1.39379	22	120.54855	21	0.35645	H	29	1.08685	28	119.52324	27	180.49587
C	24	1.40103	23	119.18251	22	359.67902	H	30	1.08561	29	120.75101	28	180.51128
C	25	1.44891	24	133.61296	23	178.87145	H	34	1.08554	33	121.53615	32	0.80805
C	26	1.40095	25	133.59767	24	1.68791	H	35	1.08685	34	119.07160	33	180.09013
C	27	1.39372	26	119.17823	25	178.91015	H	36	1.08654	35	119.59660	34	180.12953
C	28	1.40722	27	120.55061	26	359.62121	H	37	1.08722	36	120.42035	35	179.37317
C	29	1.39519	28	121.40591	27	0.41068	H	40	1.08723	39	120.40225	38	359.28562
C	30	1.39882	29	117.72369	28	0.19095	H	41	1.08658	40	119.85209	39	179.97438
N	15	1.53976*	14	112.36550*	13	184.77971*	H	42	1.08690	41	119.52479	40	180.44541
C	32	1.40113	15	132.04926*	14	115.61344*	H	43	1.08550	42	120.77406	41	180.30187
C	33	1.39881	32	129.47780	15	333.27152*	H	46	1.08430	45	119.05000	50	-179.97489
C	34	1.39520	33	117.72493	32	181.18158	H	47	1.08692	46	119.73749	45	180.02562
C	35	1.40718	34	121.40971	33	0.18689	H	48	1.08712	47	120.08957	46	180.02562
C	36	1.39370	35	120.54803	34	0.41641	H	49	1.08684	48	120.13668	47	179.97438
C	37	1.40094	36	119.17491	35	359.62614	H	50	1.08420	49	120.52043	48	179.97438
C	38	1.44896	37	133.57589	36	178.74217							
C	39	1.40108	38	133.61407	37	1.67108							
C	40	1.39378	39	119.17892	38	179.07456							

* Z-matrix coordinates that were chosen as variables in the TADF rate maximization.

Table E.11: Z-matrix of DCzTrz at the TADF maximum with energy penalty ($\Lambda = 0.8\,\mu s^{-1} {E_h}^{-1}$).

C							C	41	1.40726	40	120.54922	39	359.65191
C	1	1.39881					C	42	1.39528	41	121.40346	40	0.34748
C	2	1.39425	1	120.16424			C	43	1.39880	42	117.72197	41	0.21165
C	3	1.40529	2	120.33344	1	0.05219	C	9	1.35542*	8	138.93351*	7	183.91568*
C	4	1.40538	3	119.18851	2	359.95385	C	45	1.40530	9	98.66481*	8	9.05117*
C	5	1.39442	4	120.32961	3	0.02562	C	46	1.39433	45	120.33164	9	188.22049*
C	4	1.54804*	3	121.94919*	2	225.88712*	C	47	1.39877	46	120.16975	45	0.02562
N	7	1.34191	4	125.80883*	3	25.06701*	C	48	1.39863	47	119.81686	46	359.97438
C	8	1.34180	7	116.19320	4	187.65876*	C	49	1.39441	48	120.16153	47	359.97438
N	9	1.34395	8	123.87602	7	0.15279	H	1	1.08713	2	120.08954	3	179.97438
C	10	1.33948	9	115.76541	8	359.79882	H	2	1.08691	1	120.09233	3	179.97438
N	11	1.33944	10	124.53015	9	0.03803	H	3	1.08429	2	120.63089	1	180.02562
C	11	1.68377*	10	98.08918*	9	192.76451*	H	5	1.08423	4	119.14092	3	180.02562
C	13	1.40145	11	123.00369*	10	-47.05700*	H	6	1.08684	5	119.70222	4	180.02562
C	14	1.39772	13	120.10899	11	187.90564*	H	14	1.08328	13	119.60739	18	-178.97627
C	15	1.40041	14	120.13438	13	359.12975	H	16	1.08513	15	120.13739	14	180.33415
C	16	1.40041	15	119.75732	14	0.36550	H	18	1.08335	17	120.27300	16	178.51517
C	17	1.39763	16	120.17535	15	0.52083	H	21	1.08557	20	121.49918	19	1.06266
N	17	1.55824*	16	113.04495*	15	143.34604*	H	22	1.08691	21	119.07827	20	180.02562
C	19	1.40078	17	116.70497*	16	109.81953*	H	23	1.08658	22	119.59854	21	180.02562
C	20	1.39884	19	129.44131	17	351.89001*	H	24	1.08723	23	120.41591	22	179.42469
C	21	1.39526	20	117.71657	19	181.18901	H	27	1.08723	26	120.40812	25	359.13361
C	22	1.40729	21	121.40581	20	0.17108	H	28	1.08654	27	119.85378	26	179.90485
C	23	1.39379	22	120.54855	21	0.35645	H	29	1.08685	28	119.52324	27	180.49587
C	24	1.40103	23	119.18251	22	359.67902	H	30	1.08561	29	120.75101	28	180.51128
C	25	1.44891	24	133.61296	23	178.87145	H	34	1.08554	33	121.53615	32	0.80805
C	26	1.40095	25	133.59767	24	1.68791	H	35	1.08685	34	119.07160	33	180.09013
C	27	1.39372	26	119.17823	25	178.91015	H	36	1.08654	35	119.59660	34	180.12953
C	28	1.40722	27	120.55061	26	359.62121	H	37	1.08722	36	120.42035	35	179.37317
C	29	1.39519	28	121.40591	27	0.41068	H	40	1.08723	39	120.40225	38	359.28562
C	30	1.39882	29	117.72369	28	0.19095	H	41	1.08658	40	119.85209	39	179.97438
N	15	1.54035*	14	112.75538*	13	183.54298*	H	42	1.08690	41	119.52479	40	180.44541
C	32	1.40113	15	133.50170*	14	115.24717*	H	43	1.08550	42	120.77406	41	180.30187
C	33	1.39881	32	129.47780	15	333.24938*	H	46	1.08430	45	119.05000	50	-179.97489
C	34	1.39520	33	117.72493	32	181.18158	H	47	1.08692	46	119.73749	45	180.02562
C	35	1.40718	34	121.40971	33	0.18689	H	48	1.08712	47	120.08957	46	180.02562
C	36	1.39370	35	120.54803	34	0.41641	H	49	1.08684	48	120.13668	47	179.97438
C	37	1.40094	36	119.17491	35	359.62614	H	50	1.08420	49	120.52043	48	179.97438
C	38	1.44896	37	133.57589	36	178.74217							
C	39	1.40108	38	133.61407	37	1.67108							
C	40	1.39378	39	119.17892	38	179.07456							

* Z-matrix coordinates that were chosen as variables in the TADF rate maximization.

Table E.12: Z-matrix of DCzTrz at the TADF maximum with no energy penalty ($\Lambda = 0$).

N							C	40	1.40776	38	121.49768	33	-0.19363
C	1	1.39715					H	42	1.08669	40	119.47861	38	179.87531
C	2	1.40059	1	128.08763			C	42	1.39503	40	120.73377	38	-0.43570
H	3	1.08661	2	120.89219	1	6.22986	H	44	1.08746	42	120.34182	40	-179.41015
C	3	1.39404	2	118.01950	1	-174.79928	C	44	1.40055	42	118.98874	40	0.16284
H	5	1.08702	3	119.29731	2	-178.96277	C	36	1.40788	34	121.38328	32	-0.24697
C	5	1.40821	3	121.15761	2	1.73175	H	47	1.08662	36	119.51569	34	-179.78312
H	7	1.08664	5	119.62178	3	179.69452	C	47	1.39441	36	120.72017	34	0.23228
C	7	1.39322	5	120.53529	3	0.51213	H	49	1.08742	47	120.31667	36	179.91844
H	9	1.08727	7	120.38059	5	178.38025	C	49	1.40128	47	119.33377	36	0.14530
C	9	1.40204	7	119.34762	5	-1.00314	C	27	1.68377	25	123.00369	22	-172.09436
C	1	1.40934	2	106.96002	3	174.75427	N	52	1.30812	27	130.37186	25	138.34722
C	12	1.40020	1	129.11246	2	177.88175	N	52	1.33917	27	98.08918	25	-47.05700
H	13	1.08549	12	121.40933	1	-0.89885	C	53	1.36622	52	110.55943	27	176.42112
C	13	1.39509	12	118.02510	1	178.91960	N	55	1.31685	53	122.37831	52	-11.65370
H	15	1.08702	13	119.07912	12	-179.85155	C	56	1.34588	55	124.68780	53	9.02535
C	15	1.40721	13	121.41803	12	0.15051	C	57	1.35542	56	138.93351	55	-176.08432
H	17	1.08662	15	119.65233	13	-179.89989	C	58	1.38990	57	137.54173	56	-165.19630
C	17	1.39324	15	120.42436	13	0.31805	H	59	1.08384	58	120.85823	57	-6.81857
H	19	1.08732	17	120.43921	15	179.55994	C	59	1.39655	58	116.81444	57	171.83610
C	19	1.40120	17	119.11258	15	-0.10102	H	61	1.08654	59	119.34839	58	-179.97582
C	1	1.54035	2	133.50170	3	-26.75062	C	61	1.40349	59	121.18804	58	-1.25623
C	22	1.38612	1	123.45264	2	-53.48839	H	63	1.08729	61	118.87945	59	-178.24461
H	23	1.08453	22	121.70607	1	-11.73523	C	63	1.40483	61	121.63628	59	1.59947
C	22	1.40122	1	112.75538	2	115.24717	H	65	1.08792	63	119.52146	61	179.62340
H	25	1.08315	22	120.04252	1	4.89140	C	65	1.39524	63	119.15931	61	0.72990
C	25	1.39502	22	118.80625	1	-176.45702	H	67	1.07957	65	121.57635	63	-179.21725
C	23	1.40373	22	115.99598	1	-177.28969	C	55	1.54804	53	111.80084	52	169.53991
C	28	1.39009	23	121.85589	22	-10.99868	C	69	1.40658	55	114.82150	53	50.14069
H	29	1.08623	28	119.94876	23	173.89023	H	70	1.08546	69	119.34690	55	-26.77523
N	28	1.55824	23	113.04495	22	143.34604	C	70	1.39965	69	120.14358	55	147.06989
C	31	1.38549	28	131.44943	23	-84.83705	H	72	1.08695	70	119.55619	69	-179.39527
C	31	1.39249	28	116.70497	23	109.81953	C	72	1.39769	70	120.07094	69	-5.31187
C	32	1.39733	31	130.22670	28	12.21503	H	74	1.08697	72	120.07336	70	-171.83935
H	34	1.08578	32	121.23334	31	-1.54333	C	74	1.40333	72	119.65564	70	7.69409
C	34	1.39492	32	117.50912	31	178.39517	H	76	1.08672	74	120.49182	72	176.61201
H	36	1.08694	34	119.14495	32	179.89710	C	76	1.39203	74	119.16030	72	3.18384
C	33	1.39750	31	130.25039	28	-8.10999	H	78	1.08834	76	118.90623	74	-178.38346
H	38	1.08633	33	121.39499	31	0.22764							
C	38	1.39591	33	117.49611	31	-179.57768							
H	40	1.08707	38	119.09589	33	179.85210							

Table E.13: Z-matrix of DCzTrz after the relaxation of the hydrogen atoms and the aromatic ring systems

C														
C	1	1.40702												
C	2	1.39528	1	121.41976										
C	3	1.39880	2	117.72862	1	0.32396								
C	4	1.41828	3	121.57666	2	358.87175	C	34	1.44897	33	133.48140	32	178.56871
C	1	1.39358	2	120.53453	3	0.49165	C	35	1.40084	34	133.47401	33	2.23639
C	5	1.44898	4	106.92382	3	181.89637	C	36	1.39360	35	119.15384	34	178.59739
C	7	1.40083	5	133.49249	4	181.16482	C	37	1.40700	36	120.52443	35	359.50984
C	8	1.39371	7	119.18480	5	178.57492	C	38	1.39527	37	121.42667	36	0.49654
C	9	1.40691	8	120.51336	7	359.52293	C	39	1.39887	38	117.73226	37	0.29911
C	10	1.39536	9	121.40126	8	0.49943	H	1	1.08653	2	119.60585	3	180.09595
C	11	1.39880	10	117.78429	9	0.28109	H	2	1.08683	1	119.51664	6	-179.30384
N	12	1.40257	11	129.52416	10	181.46160	H	3	1.08526	2	120.70564	1	180.77694
C	13	1.41654*	12	125.85864*	11	357.77120*	H	6	1.08716	1	120.43948	2	179.20861
C	14	1.40458	13	120.26704*	12	126.58292*	H	8	1.08717	7	120.39801	5	358.89829
C	15	1.39063	14	120.07901	13	179.16190*	H	9	1.08652	8	119.86397	7	179.97438
C	16	1.40552	15	120.85450	14	2.00484	H	10	1.08691	9	119.51021	8	180.71322
C	17	1.40455	16	118.67759	15	358.33054	H	11	1.08530	10	120.70276	9	180.75962
C	18	1.39418	17	120.73164	16	359.86866	H	15	1.08573	14	119.52089	19	178.90871
C	17	1.49856*	16	118.23050*	15	181.96209*	H	16	1.08569	15	120.42221	14	181.14493
O	20	1.22892	17	119.76853*	16	27.87786*	H	18	1.08575	17	120.11789	16	182.64318
C	20	1.49834*	17	120.43467*	16	207.93748*	H	19	1.08571	18	120.29449	17	182.70446
C	22	1.40564	20	118.22455*	17	207.11683*	H	23	1.08569	22	118.71556	27	179.20878
C	23	1.39053	22	120.86830	20	181.98179*	H	24	1.08572	23	120.38584	22	182.55906
C	24	1.40466	23	120.09228	22	1.94707	H	26	1.08568	25	119.57715	24	177.64791
C	25	1.40196	24	119.46666	23	359.49957	H	27	1.08573	26	119.06349	25	178.78661
C	26	1.39414	25	120.13386	24	358.77673	H	30	1.08528	29	121.51383	28	1.03633
N	25	1.41630*	24	120.28946*	23	179.24517*	H	31	1.08690	30	119.08389	29	180.02562
C	28	1.40278	25	125.84628*	24	126.64966*	H	32	1.08651	31	119.62354	30	180.09641
C	29	1.39881	28	129.53406	25	357.93284*	H	33	1.08716	32	120.41659	31	179.19601
C	30	1.39540	29	117.78877	28	181.52004	H	36	1.08715	35	120.40432	34	358.91372
C	31	1.40688	30	121.40300	29	0.27912	H	37	1.08651	36	119.86334	35	179.91071
C	32	1.39369	31	120.50917	30	0.49056	H	38	1.08684	37	119.51523	36	180.69978
C	33	1.40084	32	119.18459	31	359.52181	H	39	1.08525	38	120.68850	37	180.78166

* Z-matrix coordinates that were chosen as variables in the TADF rate maximization.

Table E.14: Z-matrix of Cz2BP at the energy minimum ($\Lambda = \infty$).

C														
C	1	1.40702												
C	2	1.39528	1	121.41976										
C	3	1.39880	2	117.72862	1	0.32396								
C	4	1.41828	3	121.57666	2	358.87175	C	34	1.44897	33	133.48140	32	178.56871
C	1	1.39358	2	120.53453	3	0.49165	C	35	1.40084	34	133.47401	33	2.23639
C	5	1.44898	4	106.92382	3	181.89637	C	36	1.39360	35	119.15384	34	178.59739
C	7	1.40083	5	133.49249	4	181.16482	C	37	1.40700	36	120.52443	35	359.50984
C	8	1.39371	7	119.18480	5	178.57492	C	38	1.39527	37	121.42667	36	0.49654
C	9	1.40691	8	120.51336	7	359.52293	C	39	1.39887	38	117.73226	37	0.29911
C	10	1.39536	9	121.40126	8	0.49943	H	1	1.08653	2	119.60585	3	180.09595
C	11	1.39880	10	117.78429	9	0.28109	H	2	1.08683	1	119.51664	6	-179.30384
N	12	1.40257	11	129.52416	10	181.46160	H	3	1.08526	2	120.70564	1	180.77694
C	13	1.52498*	12	133.05604*	11	356.46919*	H	6	1.08716	1	120.43948	2	179.20861
C	14	1.40458	13	122.39514*	12	112.68901*	H	8	1.08717	7	120.39801	5	358.89829
C	15	1.39063	14	120.07901	13	171.80382*	H	9	1.08652	8	119.86397	7	179.97438
C	16	1.40552	15	120.85450	14	2.00484	H	10	1.08691	9	119.51021	8	180.71322
C	17	1.40455	16	118.67759	15	358.33054	H	11	1.08530	10	120.70276	9	180.75962
C	18	1.39418	17	120.73164	16	359.86866	H	15	1.08573	14	119.52089	19	178.90871
C	17	1.59118*	16	104.29281*	15	187.83050*	H	16	1.08569	15	120.42221	14	181.14493
O	20	1.22892	17	127.75694*	16	35.17061*	H	18	1.08575	17	120.11789	16	182.64318
C	20	1.59317*	17	106.09812*	16	204.05523*	H	19	1.08571	18	120.29449	17	182.70446
C	22	1.40564	20	105.62123*	17	208.49072*	H	23	1.08569	22	118.71556	27	179.20878
C	23	1.39053	22	120.86830	20	187.96988*	H	24	1.08572	23	120.38584	22	182.55906
C	24	1.40466	23	120.09228	22	1.94707	H	26	1.08568	25	119.57715	24	177.64791
C	25	1.40196	24	119.46666	23	359.49957	H	27	1.08573	26	119.06349	25	178.78661
C	26	1.39414	25	120.13386	24	358.77673	H	30	1.08528	29	121.51383	28	1.03633
N	25	1.51968*	24	123.46821*	23	178.37136*	H	31	1.08690	30	119.08389	29	180.02562
C	28	1.40278	25	134.33802*	24	110.84007*	H	32	1.08651	31	119.62354	30	180.09641
C	29	1.39881	28	129.53406	25	352.87971*	H	33	1.08716	32	120.41659	31	179.19601
C	30	1.39540	29	117.78877	28	181.52004	H	36	1.08715	35	120.40432	34	358.91372
C	31	1.40688	30	121.40300	29	0.27912	H	37	1.08651	36	119.86334	35	179.91071
C	32	1.39369	31	120.50917	30	0.49056	H	38	1.08684	37	119.51523	36	180.69978
C	33	1.40084	32	119.18459	31	359.52181	H	39	1.08525	38	120.68850	37	180.78166

* Z-matrix coordinates that were chosen as variables in the TADF rate maximization.

Table E.15: Z-matrix of Cz2BP at the TADF maximum with energy penalty ($\Lambda = 8.0\,\mu s^{-1} {E_h}^{-1}$).

C														
C	1	1.40702												
C	2	1.39528	1	121.41976										
C	3	1.39880	2	117.72862	1	0.32396								
C	4	1.41828	3	121.57666	2	358.87175	C	34	1.44897	33	133.48140	32	178.56871
C	1	1.39358	2	120.53453	3	0.49165	C	35	1.40084	34	133.47401	33	2.23639
C	5	1.44898	4	106.92382	3	181.89637	C	36	1.39360	35	119.15384	34	178.59739
C	7	1.40083	5	133.49249	4	181.16482	C	37	1.40700	36	120.52443	35	359.50984
C	8	1.39371	7	119.18480	5	178.57492	C	38	1.39527	37	121.42667	36	0.49654
C	9	1.40691	8	120.51336	7	359.52293	C	39	1.39887	38	117.73226	37	0.29911
C	10	1.39536	9	121.40126	8	0.49943	H	1	1.08653	2	119.60585	3	180.09595
C	11	1.39880	10	117.78429	9	0.28109	H	2	1.08683	1	119.51664	6	-179.30384
N	12	1.40257	11	129.52416	10	181.46160	H	3	1.08526	2	120.70564	1	180.77694
C	13	1.52984*	12	133.24419*	11	356.78070*	H	6	1.08716	1	120.43948	2	179.20861
C	14	1.40458	13	121.88521*	12	113.29183*	H	8	1.08717	7	120.39801	5	358.89829
C	15	1.39063	14	120.07901	13	172.20389*	H	9	1.08652	8	119.86397	7	179.97438
C	16	1.40552	15	120.85450	14	2.00484	H	10	1.08691	9	119.51021	8	180.71322
C	17	1.40455	16	118.67759	15	358.33054	H	11	1.08530	10	120.70276	9	180.75962
C	18	1.39418	17	120.73164	16	359.86866	H	15	1.08573	14	119.52089	19	178.90871
C	17	1.60329*	16	102.71849*	15	187.37262*	H	16	1.08569	15	120.42221	14	181.14493
O	20	1.22892	17	126.65875*	16	35.68912*	H	18	1.08575	17	120.11789	16	182.64318
C	20	1.59325*	17	107.44506*	16	203.85027*	H	19	1.08571	18	120.29449	17	182.70446
C	22	1.40564	20	103.32982*	17	209.01788*	H	23	1.08569	22	118.71556	27	179.20878
C	23	1.39053	22	120.86830	20	188.26234*	H	24	1.08572	23	120.38584	22	182.55906
C	24	1.40466	23	120.09228	22	1.94707	H	26	1.08568	25	119.57715	24	177.64791
C	25	1.40196	24	119.46666	23	359.49957	H	27	1.08573	26	119.06349	25	178.78661
C	26	1.39414	25	120.13386	24	358.77673	H	30	1.08528	29	121.51383	28	1.03633
N	25	1.52128*	24	123.56957*	23	178.71464*	H	31	1.08690	30	119.08389	29	180.02562
C	28	1.40278	25	134.57269*	24	110.20700*	H	32	1.08651	31	119.62354	30	180.09641
C	29	1.39881	28	129.53406	25	353.19649*	H	33	1.08716	32	120.41659	31	179.19601
C	30	1.39540	29	117.78877	28	181.52004	H	36	1.08715	35	120.40432	34	358.91372
C	31	1.40688	30	121.40300	29	0.27912	H	37	1.08651	36	119.86334	35	179.91071
C	32	1.39369	31	120.50917	30	0.49056	H	38	1.08684	37	119.51523	36	180.69978
C	33	1.40084	32	119.18459	31	359.52181	H	39	1.08525	38	120.68850	37	180.78166

* Z-matrix coordinates that were chosen as variables in the TADF rate maximization.

Table E.16: Z-matrix of Cz2BP at the TADF maximum with energy penalty ($\Lambda = 4.0\,\mu s^{-1} {E_h}^{-1}$).

C														
C	1	1.40702												
C	2	1.39528	1	121.41976										
C	3	1.39880	2	117.72862	1	0.32396								
C	4	1.41828	3	121.57666	2	358.87175	C	34	1.44897	33	133.48140	32	178.56871
C	1	1.39358	2	120.53453	3	0.49165	C	35	1.40084	34	133.47401	33	2.23639
C	5	1.44898	4	106.92382	3	181.89637	C	36	1.39360	35	119.15384	34	178.59739
C	7	1.40083	5	133.49249	4	181.16482	C	37	1.40700	36	120.52443	35	359.50984
C	8	1.39371	7	119.18480	5	178.57492	C	38	1.39527	37	121.42667	36	0.49654
C	9	1.40691	8	120.51336	7	359.52293	C	39	1.39887	38	117.73226	37	0.29911
C	10	1.39536	9	121.40126	8	0.49943	H	1	1.08653	2	119.60585	3	180.09595
C	11	1.39880	10	117.78429	9	0.28109	H	2	1.08683	1	119.51664	6	-179.30384
N	12	1.40257	11	129.52416	10	181.46160	H	3	1.08526	2	120.70564	1	180.77694
C	13	1.53387*	12	133.65481*	11	356.64144*	H	6	1.08716	1	120.43948	2	179.20861
C	14	1.40458	13	122.33817*	12	112.71677*	H	8	1.08717	7	120.39801	5	358.89829
C	15	1.39063	14	120.07901	13	171.83207*	H	9	1.08652	8	119.86397	7	179.97438
C	16	1.40552	15	120.85450	14	2.00484	H	10	1.08691	9	119.51021	8	180.71322
C	17	1.40455	16	118.67759	15	358.33054	H	11	1.08530	10	120.70276	9	180.75962
C	18	1.39418	17	120.73164	16	359.86866	H	15	1.08573	14	119.52089	19	178.90871
C	17	1.59797*	16	101.37122*	15	187.60954*	H	16	1.08569	15	120.42221	14	181.14493
O	20	1.22892	17	126.79618*	16	36.28006*	H	18	1.08575	17	120.11789	16	182.64318
C	20	1.59503*	17	107.72494*	16	203.19350*	H	19	1.08571	18	120.29449	17	182.70446
C	22	1.40564	20	103.14411*	17	208.97514*	H	23	1.08569	22	118.71556	27	179.20878
C	23	1.39053	22	120.86830	20	188.69261*	H	24	1.08572	23	120.38584	22	182.55906
C	24	1.40466	23	120.09228	22	1.94707	H	26	1.08568	25	119.57715	24	177.64791
C	25	1.40196	24	119.46666	23	359.49957	H	27	1.08573	26	119.06349	25	178.78661
C	26	1.39414	25	120.13386	24	358.77673	H	30	1.08528	29	121.51383	28	1.03633
N	25	1.52078*	24	123.44516*	23	179.40816*	H	31	1.08690	30	119.08389	29	180.02562
C	28	1.40278	25	134.91195*	24	109.47571*	H	32	1.08651	31	119.62354	30	180.09641
C	29	1.39881	28	129.53406	25	353.47814*	H	33	1.08716	32	120.41659	31	179.19601
C	30	1.39540	29	117.78877	28	181.52004	H	36	1.08715	35	120.40432	34	358.91372
C	31	1.40688	30	121.40300	29	0.27912	H	37	1.08651	36	119.86334	35	179.91071
C	32	1.39369	31	120.50917	30	0.49056	H	38	1.08684	37	119.51523	36	180.69978
C	33	1.40084	32	119.18459	31	359.52181	H	39	1.08525	38	120.68850	37	180.78166

* Z-matrix coordinates that were chosen as variables in the TADF rate maximization.

Table E.17: Z-matrix of Cz2BP at the TADF maximum with no energy penalty ($\Lambda = 0$).

N														
C	1	1.39467												
C	2	1.40007	1	128.43849										
H	3	1.08648	2	121.01022	1	1.20228								
C	3	1.39415	2	117.88388	1	-178.80979	C	34	1.38583	32	134.75808	31	30.17071
H	5	1.08697	3	119.27817	2	-179.81656	H	35	1.08578	34	121.91596	32	-6.70568
C	1	1.40672	2	107.33630	3	177.95123	C	35	1.40010	34	117.11559	32	169.30457
C	7	1.40020	1	129.18183	2	178.99092	H	37	1.08564	35	120.31821	34	-176.42799
H	8	1.08550	7	121.48354	1	0.39734	C	37	1.40048	35	120.50703	34	0.50967
C	8	1.39504	7	117.93312	1	-179.57432	C	39	1.39848	37	121.62174	35	2.25902
H	10	1.08699	8	119.06799	7	-179.84472	H	40	1.08686	39	119.44551	37	179.25874
C	10	1.40736	8	121.43896	7	0.23061	C	40	1.39726	39	118.77815	37	-3.07417
H	12	1.08660	10	119.64422	8	-179.96272	H	42	1.08182	40	120.69312	39	-175.83788
C	12	1.39318	10	120.45216	8	0.20760	N	39	1.53387	37	115.85904	35	-172.95908
H	14	1.08729	12	120.45646	10	179.64437	C	44	1.39363	39	133.65481	37	-72.10270
C	14	1.40137	12	119.13279	10	-0.22740	C	45	1.39992	44	128.64143	39	-3.35856
C	5	1.40819	3	121.19535	2	0.50517	H	46	1.08653	45	121.05826	44	0.36681
H	17	1.08655	5	119.60927	3	179.88813	C	46	1.39428	45	117.85045	44	-179.45681
C	17	1.39327	5	120.56185	3	0.24361	H	48	1.08698	46	119.26486	45	-179.94844
H	19	1.08723	17	120.38633	5	179.36981	C	44	1.40438	39	118.60592	37	105.38481
C	19	1.40207	17	119.38429	5	-0.35695	C	50	1.40011	44	129.37268	39	0.76030
C	1	1.52078	2	134.91195	3	-6.52186	H	51	1.08541	50	121.49554	44	0.49755
C	22	1.39932	1	123.44516	2	109.47571	C	51	1.39496	50	117.90476	44	-179.40507
H	23	1.08718	22	119.32241	1	-1.44824	H	53	1.08699	51	119.05285	50	-179.89037
C	23	1.39613	22	119.28693	1	179.40816	C	53	1.40744	51	121.45671	50	0.21337
H	25	1.08083	23	120.75467	22	-178.36391	H	55	1.08658	53	119.63983	51	-179.95710
C	22	1.40154	1	115.48031	2	-71.26083	C	55	1.39320	53	120.45494	51	0.24104
H	27	1.08571	22	119.01719	1	0.01606	H	57	1.08729	55	120.45551	53	179.60875
C	27	1.39929	22	120.53530	1	-177.54372	C	57	1.40143	55	119.15336	53	-0.24812
H	29	1.08628	27	120.66318	22	175.52679	C	48	1.40816	46	121.21954	45	0.26876
C	29	1.38713	27	117.60677	22	-1.80432	H	60	1.08656	48	119.59809	46	179.93524
C	31	1.59503	29	133.40400	27	170.83099	C	60	1.39344	48	120.57493	46	0.14624
O	32	1.20478	31	124.09683	29	-155.76847	H	62	1.08725	60	120.38628	48	179.62986
C	32	1.59797	31	107.72495	29	36.87906	C	62	1.40193	60	119.35952	48	-0.23046

Table E.18: *Z*-matrix of Cz2BP after the relaxation of the hydrogen atoms and the aromatic ring systems

C							C	47	1.41102	46	119.50875	43	-179.83838
C	1	1.50583					C	48	1.39122	47	121.04682	46	-0.04531
N	2	1.33850	1	117.65244			C	49	1.39540	48	120.06786	47	0.02562
C	3	1.34777	2	117.53683	1	180.67270	C	50	1.39389	49	118.72214	48	0.03143
C	4	1.39892	3	120.61082	2	0.41799	H	1	1.09183	2	110.52815	3	358.89572
C	5	1.40148	4	118.04691	3	358.33898	H	1	1.09596	2	110.21152	3	237.75877
N	6	1.34435	5	120.55549	4	1.62323	H	1	1.09643	2	110.19187	3	119.89113
C	6	1.48802*	5	122.56083*	4	180.89240*	H	5	1.08254	4	120.95348	3	176.04645
C	8	1.40558	6	121.90024*	5	19.05584*	H	9	1.08583	8	120.47543	13	-178.20401
C	9	1.39449	8	120.84388	6	179.53663*	H	10	1.08642	9	120.48286	8	180.73154
C	10	1.39844	9	120.19424	8	0.05385	H	12	1.08655	11	119.26092	10	180.02562
C	11	1.39913	10	119.47151	9	359.93454	H	13	1.08450	12	120.47333	11	180.62790
C	12	1.39339	11	120.28598	10	359.85119	H	17	1.08648	16	118.84331	15	180.02562
N	11	1.43526*	10	120.18493*	9	180.62019*	H	18	1.08639	17	120.30937	16	179.97438
C	14	1.40881	11	119.03804*	10	89.30318*	H	19	1.08707	18	120.64944	17	179.88956
C	15	1.41140	14	120.68266	11	180.23342*	H	20	1.08329	19	119.12749	18	179.90649
C	16	1.40257	15	117.86250	14	179.88235	H	22	1.09518	21	111.14838	16	301.25129
C	17	1.39386	16	122.78512	15	0.04971	H	22	1.09524	21	111.11557	16	181.42759
C	18	1.39532	17	118.72603	16	0.05845	H	22	1.09541	21	110.68218	16	61.34003
C	19	1.39115	18	120.05390	17	359.92503	H	23	1.09534	21	111.10718	16	58.89841
C	16	1.53400	15	122.77663	14	359.87960	H	23	1.09540	21	110.68742	16	298.83261
C	21	1.55448	16	109.06563	15	239.34748	H	23	1.09535	21	111.12222	16	178.72351
C	21	1.55432	16	109.08608	15	120.20691	H	26	1.08348	25	119.74985	24	-179.99781
C	21	1.53437	16	111.41054	15	359.76800	H	27	1.08710	26	119.30079	25	179.97438
C	24	1.41163	21	122.76259	16	0.39126	H	28	1.08640	27	120.95898	26	179.97438
C	25	1.41099	24	119.51131	21	179.83170	H	29	1.08639	28	118.41477	27	180.02562
C	26	1.39124	25	121.06066	24	0.08325	H	31	1.08452	30	118.76935	35	-179.29891
C	27	1.39543	26	120.05288	25	359.97438	H	32	1.08655	31	120.45969	30	179.57257
C	28	1.39398	27	118.72283	26	359.96278	H	34	1.08644	33	119.33823	32	180.78326
C	4	1.48749*	3	116.79359*	2	179.58587*	H	35	1.08590	34	118.70349	33	181.45095
C	30	1.40577	4	119.71610*	3	341.30782*	H	39	1.08637	38	118.79129	37	180.02562
C	31	1.39350	30	120.76369	4	180.26535*	H	40	1.08639	39	120.32407	38	179.97438
C	32	1.39900	31	120.29692	30	359.53888	H	41	1.08710	40	120.64008	39	179.97438
C	33	1.39851	32	119.47468	31	359.97355	H	42	1.08344	41	119.15881	40	179.97438
C	34	1.39437	33	120.18402	32	0.29666	H	44	1.09533	43	111.11629	38	300.83187
N	33	1.43519*	32	120.31726*	31	180.29743*	H	44	1.09539	43	111.14247	38	180.96782
C	36	1.40820	33	119.15858*	32	269.89360*	H	44	1.09543	43	110.67794	38	60.89850
C	37	1.41146	36	120.69701	33	180.13193*	H	45	1.09526	43	111.13974	38	59.28773
C	38	1.40242	37	117.88065	36	179.97438	H	45	1.09543	43	110.68503	38	299.19004
C	39	1.39394	38	122.78422	37	0.03726	H	45	1.09525	43	111.13650	38	179.11870
C	40	1.39538	39	118.71530	38	359.97438	H	48	1.08339	47	119.80377	46	179.88065
C	41	1.39120	40	120.06452	39	359.97438	H	49	1.08707	48	119.29068	47	179.97438
C	38	1.53410	37	122.77223	36	359.89121	H	50	1.08640	49	120.95506	48	179.97438
C	43	1.55442	38	109.04047	37	239.86052	H	51	1.08643	50	118.43815	49	179.97438
C	43	1.55435	38	109.08347	37	120.72677							
C	43	1.53418	38	111.40551	37	0.26477							
C	46	1.41147	43	122.77468	38	-0.28109							

* Z-matrix coordinates that were chosen as variables in the TADF rate maximization.

Table E.19: Z-matrix of Ac-MPM at the energy minimum ($\Lambda = \infty$).

C							C	47	1.41102	46	119.50875	43	-179.83838
C	1	1.50583					C	48	1.39122	47	121.04682	46	-0.04531
N	2	1.33850	1	117.65244			C	49	1.39540	48	120.06786	47	0.02562
C	3	1.34777	2	117.53683	1	180.67270	C	50	1.39389	49	118.72214	48	0.03143
C	4	1.39892	3	120.61082	2	0.41799	H	1	1.09183	2	110.52815	3	358.89572
C	5	1.40148	4	118.04691	3	358.33898	H	1	1.09596	2	110.21152	3	237.75877
N	6	1.34435	5	120.55549	4	1.62323	H	1	1.09643	2	110.19187	3	119.89113
C	6	1.58773*	5	121.03757*	4	166.64874*	H	5	1.08254	4	120.95348	3	176.04645
C	8	1.40558	6	124.72347*	5	2.92038*	H	9	1.08583	8	120.47543	13	-178.20401
C	9	1.39449	8	120.84388	6	185.77137*	H	10	1.08642	9	120.48286	8	180.73154
C	10	1.39844	9	120.19424	8	0.05385	H	12	1.08655	11	119.26092	10	180.02562
C	11	1.39913	10	119.47151	9	359.93454	H	13	1.08450	12	120.47333	11	180.62790
C	12	1.39339	11	120.28598	10	359.85119	H	17	1.08648	16	118.84331	15	180.02562
N	11	1.47465*	10	120.62338*	9	186.87893*	H	18	1.08639	17	120.30937	16	179.97438
C	14	1.40881	11	120.85874*	10	93.65843*	H	19	1.08707	18	120.64944	17	179.88956
C	15	1.41140	14	120.68266	11	190.85584*	H	20	1.08329	19	119.12749	18	179.90649
C	16	1.40257	15	117.86250	14	179.88235	H	22	1.09518	21	111.14838	16	301.25129
C	17	1.39386	16	122.78512	15	0.04971	H	22	1.09524	21	111.11557	16	181.42759
C	18	1.39532	17	118.72603	16	0.05845	H	22	1.09541	21	110.68218	16	61.34003
C	19	1.39115	18	120.05390	17	359.92503	H	23	1.09534	21	111.10718	16	58.89841
C	16	1.53400	15	122.77663	14	359.87960	H	23	1.09540	21	110.68742	16	298.83261
C	21	1.55448	16	109.06563	15	239.34748	H	23	1.09535	21	111.12222	16	178.72351
C	21	1.55432	16	109.08608	15	120.20691	H	26	1.08348	25	119.74985	24	-179.99781
C	21	1.53437	16	111.41054	15	359.76800	H	27	1.08710	26	119.30079	25	179.97438
C	24	1.41163	21	122.76259	16	0.39126	H	28	1.08640	27	120.95898	26	179.97438
C	25	1.41099	24	119.51131	21	179.83170	H	29	1.08639	28	118.41477	27	180.02562
C	26	1.39124	25	121.06066	24	0.08325	H	31	1.08452	30	118.76935	35	-179.29891
C	27	1.39543	26	120.05288	25	359.97438	H	32	1.08655	31	120.45969	30	179.57257
C	28	1.39398	27	118.72283	26	359.96278	H	34	1.08644	33	119.33823	32	180.78326
C	4	1.48160*	3	122.27281*	2	176.73015*	H	35	1.08590	34	118.70349	33	181.45095
C	30	1.40577	4	120.09702*	3	339.35727*	H	39	1.08637	38	118.79129	37	180.02562
C	31	1.39350	30	120.76369	4	166.85606*	H	40	1.08639	39	120.32407	38	179.97438
C	32	1.39900	31	120.29692	30	359.53888	H	41	1.08710	40	120.64008	39	179.97438
C	33	1.39851	32	119.47468	31	359.97355	H	42	1.08344	41	119.15881	40	179.97438
C	34	1.39437	33	120.18402	32	0.29666	H	44	1.09533	43	111.11629	38	300.83187
N	33	1.40817*	32	124.40266*	31	187.07618*	H	44	1.09539	43	111.14247	38	180.96782
C	36	1.40820	33	116.63137*	32	274.09461*	H	44	1.09543	43	110.67794	38	60.89850
C	37	1.41146	36	120.69701	33	183.00945*	H	45	1.09526	43	111.13974	38	59.28773
C	38	1.40242	37	117.88065	36	179.97438	H	45	1.09543	43	110.68503	38	299.19004
C	39	1.39394	38	122.78422	37	0.03726	H	45	1.09525	43	111.13650	38	179.11870
C	40	1.39538	39	118.71530	38	359.97438	H	48	1.08339	47	119.80377	46	179.88065
C	41	1.39120	40	120.06452	39	359.97438	H	49	1.08707	48	119.29068	47	179.97438
C	38	1.53410	37	122.77223	36	359.89121	H	50	1.08640	49	120.95506	48	179.97438
C	43	1.55442	38	109.04047	37	239.86052	H	51	1.08643	50	118.43815	49	179.97438
C	43	1.55435	38	109.08347	37	120.72677							
C	43	1.53418	38	111.40551	37	0.26477							
C	46	1.41147	43	122.77468	38	-0.28109							

* Z-matrix coordinates that were chosen as variables in the TADF rate maximization.

Table E.20: Z-matrix of Ac-MPM at the TADF maximum with energy penalty ($\Lambda = 8.0\,\mu s^{-1}{E_h}^{-1}$).

C							C	47	1.41102	46	119.50875	43	-179.83838
C	1	1.50583					C	48	1.39122	47	121.04682	46	-0.04531
N	2	1.33850	1	117.65244			C	49	1.39540	48	120.06786	47	0.02562
C	3	1.34777	2	117.53683	1	180.67270	C	50	1.39389	49	118.72214	48	0.03143
C	4	1.39892	3	120.61082	2	0.41799	H	1	1.09183	2	110.52815	3	358.89572
C	5	1.40148	4	118.04691	3	358.33898	H	1	1.09596	2	110.21152	3	237.75877
N	6	1.34435	5	120.55549	4	1.62323	H	1	1.09643	2	110.19187	3	119.89113
C	6	1.56286*	5	124.04279*	4	178.33480*	H	5	1.08254	4	120.95348	3	176.04645
C	8	1.40558	6	123.50612*	5	6.07434*	H	9	1.08583	8	120.47543	13	-178.20401
C	9	1.39449	8	120.84388	6	184.40876*	H	10	1.08642	9	120.48286	8	180.73154
C	10	1.39844	9	120.19424	8	0.05385	H	12	1.08655	11	119.26092	10	180.02562
C	11	1.39913	10	119.47151	9	359.93454	H	13	1.08450	12	120.47333	11	180.62790
C	12	1.39339	11	120.28598	10	359.85119	H	17	1.08648	16	118.84331	15	180.02562
N	11	1.52472*	10	115.91129*	9	188.25346*	H	18	1.08639	17	120.30937	16	179.97438
C	14	1.40881	11	113.53090*	10	96.71973*	H	19	1.08707	18	120.64944	17	179.88956
C	15	1.41140	14	120.68266	11	186.06754*	H	20	1.08329	19	119.12749	18	179.90649
C	16	1.40257	15	117.86250	14	179.88235	H	22	1.09518	21	111.14838	16	301.25129
C	17	1.39386	16	122.78512	15	0.04971	H	22	1.09524	21	111.11557	16	181.42759
C	18	1.39532	17	118.72603	16	0.05845	H	22	1.09541	21	110.68218	16	61.34003
C	19	1.39115	18	120.05390	17	359.92503	H	23	1.09534	21	111.10718	16	58.89841
C	16	1.53400	15	122.77663	14	359.87960	H	23	1.09540	21	110.68742	16	298.83261
C	21	1.55448	16	109.06563	15	239.34748	H	23	1.09535	21	111.12222	16	178.72351
C	21	1.55432	16	109.08608	15	120.20691	H	26	1.08348	25	119.74985	24	-179.99781
C	21	1.53437	16	111.41054	15	359.76800	H	27	1.08710	26	119.30079	25	179.97438
C	24	1.41163	21	122.76259	16	0.39126	H	28	1.08640	27	120.95898	26	179.97438
C	25	1.41099	24	119.51131	21	179.83170	H	29	1.08639	28	118.41477	27	180.02562
C	26	1.39124	25	121.06066	24	0.08325	H	31	1.08452	30	118.76935	35	-179.29891
C	27	1.39543	26	120.05288	25	359.97438	H	32	1.08655	31	120.45969	30	179.57257
C	28	1.39398	27	118.72283	26	359.96278	H	34	1.08644	33	119.33823	32	180.78326
C	4	1.53670*	3	121.24252*	2	180.15153*	H	35	1.08590	34	118.70349	33	181.45095
C	30	1.40577	4	128.05927*	3	309.16618*	H	39	1.08637	38	118.79129	37	180.02562
C	31	1.39350	30	120.76369	4	182.96308*	H	40	1.08639	39	120.32407	38	179.97438
C	32	1.39900	31	120.29692	30	359.53888	H	41	1.08710	40	120.64008	39	179.97438
C	33	1.39851	32	119.47468	31	359.97355	H	42	1.08344	41	119.15881	40	179.97438
C	34	1.39437	33	120.18402	32	0.29666	H	44	1.09533	43	111.11629	38	300.83187
N	33	1.48910*	32	124.28356*	31	188.02574*	H	44	1.09539	43	111.14247	38	180.96782
C	36	1.40820	33	90.81682*	32	277.91899*	H	44	1.09543	43	110.67794	38	60.89850
C	37	1.41146	36	120.69701	33	188.91668*	H	45	1.09526	43	111.13974	38	59.28773
C	38	1.40242	37	117.88065	36	179.97438	H	45	1.09543	43	110.68503	38	299.19004
C	39	1.39394	38	122.78422	37	0.03726	H	45	1.09525	43	111.13650	38	179.11870
C	40	1.39538	39	118.71530	38	359.97438	H	48	1.08339	47	119.80377	46	179.88065
C	41	1.39120	40	120.06452	39	359.97438	H	49	1.08707	48	119.29068	47	179.97438
C	38	1.53410	37	122.77223	36	359.89121	H	50	1.08640	49	120.95506	48	179.97438
C	43	1.55442	38	109.04047	37	239.86052	H	51	1.08643	50	118.43815	49	179.97438
C	43	1.55435	38	109.08347	37	120.72677							
C	43	1.53418	38	111.40551	37	0.26477							
C	46	1.41147	43	122.77468	38	-0.28109							

* Z-matrix coordinates that were chosen as variables in the TADF rate maximization.

Table E.21: Z-matrix of Ac-MPM at the TADF maximum with energy penalty ($\Lambda = 4.0\,\mu s^{-1} {E_h}^{-1}$).

C							C	47	1.41102	46	119.50875	43	-179.83838
C	1	1.50583					C	48	1.39122	47	121.04682	46	-0.04531
N	2	1.33850	1	117.65244			C	49	1.39540	48	120.06786	47	0.02562
C	3	1.34777	2	117.53683	1	180.67270	C	50	1.39389	49	118.72214	48	0.03143
C	4	1.39892	3	120.61082	2	0.41799	H	1	1.09183	2	110.52815	3	358.89572
C	5	1.40148	4	118.04691	3	358.33898	H	1	1.09596	2	110.21152	3	237.75877
N	6	1.34435	5	120.55549	4	1.62323	H	1	1.09643	2	110.19187	3	119.89113
C	6	1.62393*	5	125.04929*	4	165.95375*	H	5	1.08254	4	120.95348	3	176.04645
C	8	1.40558	6	127.44863*	5	-2.38961*	H	9	1.08583	8	120.47543	13	-178.20401
C	9	1.39449	8	120.84388	6	186.72320*	H	10	1.08642	9	120.48286	8	180.73154
C	10	1.39844	9	120.19424	8	0.05385	H	12	1.08655	11	119.26092	10	180.02562
C	11	1.39913	10	119.47151	9	359.93454	H	13	1.08450	12	120.47333	11	180.62790
C	12	1.39339	11	120.28598	10	359.85119	H	17	1.08648	16	118.84331	15	180.02562
N	11	1.55891*	10	118.00157*	9	190.37380*	H	18	1.08639	17	120.30937	16	179.97438
C	14	1.40881	11	114.96625*	10	98.39991*	H	19	1.08707	18	120.64944	17	179.88956
C	15	1.41140	14	120.68266	11	188.32512*	H	20	1.08329	19	119.12749	18	179.90649
C	16	1.40257	15	117.86250	14	179.88235	H	22	1.09518	21	111.14838	16	301.25129
C	17	1.39386	16	122.78512	15	0.04971	H	22	1.09524	21	111.11557	16	181.42759
C	18	1.39532	17	118.72603	16	0.05845	H	22	1.09541	21	110.68218	16	61.34003
C	19	1.39115	18	120.05390	17	359.92503	H	23	1.09534	21	111.10718	16	58.89841
C	16	1.53400	15	122.77663	14	359.87960	H	23	1.09540	21	110.68742	16	298.83261
C	21	1.55448	16	109.06563	15	239.34748	H	23	1.09535	21	111.12222	16	178.72351
C	21	1.55432	16	109.08608	15	120.20691	H	26	1.08348	25	119.74985	24	-179.99781
C	21	1.53437	16	111.41054	15	359.76800	H	27	1.08710	26	119.30079	25	179.97438
C	24	1.41163	21	122.76259	16	0.39126	H	28	1.08640	27	120.95898	26	179.97438
C	25	1.41099	24	119.51131	21	179.83170	H	29	1.08639	28	118.41477	27	180.02562
C	26	1.39124	25	121.06066	24	0.08325	H	31	1.08452	30	118.76935	35	-179.29891
C	27	1.39543	26	120.05288	25	359.97438	H	32	1.08655	31	120.45969	30	179.57257
C	28	1.39398	27	118.72283	26	359.96278	H	34	1.08644	33	119.33823	32	180.78326
C	4	1.49463*	3	119.33252*	2	182.48917*	H	35	1.08590	34	118.70349	33	181.45095
C	30	1.40577	4	132.45115*	3	308.63468*	H	39	1.08637	38	118.79129	37	180.02562
C	31	1.39350	30	120.76369	4	182.38989*	H	40	1.08639	39	120.32407	38	179.97438
C	32	1.39900	31	120.29692	30	359.53888	H	41	1.08710	40	120.64008	39	179.97438
C	33	1.39851	32	119.47468	31	359.97355	H	42	1.08344	41	119.15881	40	179.97438
C	34	1.39437	33	120.18402	32	0.29666	H	44	1.09533	43	111.11629	38	300.83187
N	33	1.52926*	32	123.30528*	31	187.49014*	H	44	1.09539	43	111.14247	38	180.96782
C	36	1.40820	33	90.95333*	32	279.84399*	H	44	1.09543	43	110.67794	38	60.89850
C	37	1.41146	36	120.69701	33	189.91067*	H	45	1.09526	43	111.13974	38	59.28773
C	38	1.40242	37	117.88065	36	179.97438	H	45	1.09543	43	110.68503	38	299.19004
C	39	1.39394	38	122.78422	37	0.03726	H	45	1.09525	43	111.13650	38	179.11870
C	40	1.39538	39	118.71530	38	359.97438	H	48	1.08339	47	119.80377	46	179.88065
C	41	1.39120	40	120.06452	39	359.97438	H	49	1.08707	48	119.29068	47	179.97438
C	38	1.53410	37	122.77223	36	359.89121	H	50	1.08640	49	120.95506	48	179.97438
C	43	1.55442	38	109.04047	37	239.86052	H	51	1.08643	50	118.43815	49	179.97438
C	43	1.55435	38	109.08347	37	120.72677							
C	43	1.53418	38	111.40551	37	0.26477							
C	46	1.41147	43	122.77468	38	-0.28109							

* Z-matrix coordinates that were chosen as variables in the TADF rate maximization.

Table E.22: Z-matrix of Ac-MPM at the TADF maximum with no energy penalty ($\Lambda = 0$).

N							C	45	1.49463	44	119.33252	43	-177.51083
C	1	1.39492					C	48	1.40109	45	132.45115	44	-51.36532
C	1	1.40606	2	123.86563			H	49	1.08819	48	119.14962	45	-0.11540
C	2	1.41014	1	120.06970	3	176.76796	C	49	1.39137	48	122.92650	45	-177.61011
H	4	1.08446	2	119.46348	1	-0.59736	H	51	1.08678	49	118.82096	48	179.26608
C	4	1.39104	2	120.82014	1	179.73867	C	51	1.39402	49	121.36525	48	-6.70756
H	6	1.08716	4	119.37775	2	-179.97600	C	53	1.39837	51	117.00914	49	6.99678
C	6	1.39641	4	120.04190	2	0.26546	H	54	1.08503	53	120.09983	51	177.58479
H	8	1.08641	6	120.87055	4	-179.89703	C	54	1.39386	53	120.87110	51	-2.54281
C	8	1.39483	6	118.86485	4	0.36831	H	56	1.08689	54	117.77377	53	-179.31256
H	10	1.08659	8	118.42861	6	179.75655	C	43	1.50532	42	117.04247	41	-178.37930
C	10	1.40198	8	122.66206	6	-0.37475	H	58	1.09173	43	110.39053	42	-178.88128
C	3	1.41053	1	121.77466	2	-179.22538	H	58	1.09607	43	110.32153	42	-57.71734
H	13	1.08173	3	120.27071	1	0.51441	H	58	1.09641	43	110.15633	42	60.25819
C	13	1.39226	3	121.05607	1	-179.14797	N	53	1.52926	51	123.30528	49	-172.50986
H	15	1.08718	13	119.06078	3	-179.81869	C	62	1.40745	53	123.82777	51	153.26124
C	15	1.39433	13	120.32161	3	0.43428	C	63	1.40226	62	122.38376	53	-32.67906
H	17	1.08642	15	121.02120	13	179.94722	H	64	1.08442	63	120.11781	62	2.90016
C	17	1.39437	15	118.59709	13	0.27549	C	64	1.39461	63	119.68471	62	-176.72385
H	19	1.08655	17	118.38210	15	179.36341	H	66	1.08693	64	119.45179	63	-179.64103
C	19	1.40139	17	122.70865	15	-0.22368	C	66	1.39595	64	120.10564	63	0.06935
C	12	1.53525	10	119.92979	8	179.80224	H	68	1.08661	66	120.45728	64	-178.95848
C	22	1.55437	12	108.91626	10	61.06124	C	68	1.39792	66	119.64646	64	2.38055
H	23	1.09539	22	111.09687	12	-178.62200	H	70	1.08466	68	118.60975	66	177.86466
H	23	1.09548	22	110.73700	12	61.28365	C	70	1.39989	68	121.46694	66	-0.99074
H	23	1.09555	22	110.98833	12	-58.73843	C	62	1.51487	53	90.95333	51	-80.15601
C	22	1.55463	12	108.90794	10	-57.80838	C	73	1.40962	62	131.88412	53	6.79107
H	27	1.09512	22	111.22484	12	178.69936	H	74	1.07583	73	123.46927	62	0.18000
H	27	1.09515	22	111.10678	12	58.94291	C	74	1.39994	73	121.29412	62	-178.78308
H	27	1.09535	22	110.66369	12	-61.13313	H	76	1.08708	74	117.82284	73	-179.29101
C	1	1.55891	2	120.93535	3	174.17348	C	76	1.38615	74	121.47328	73	2.04883
C	31	1.39045	1	120.90202	2	107.00982	H	78	1.08664	76	121.14059	74	179.18096
H	32	1.08579	31	120.17590	1	-4.77128	C	78	1.39483	76	118.27227	74	-0.41964
C	31	1.39063	1	118.00157	2	-76.26487	H	80	1.08355	78	118.46797	76	179.29834
H	34	1.08529	31	120.16114	1	4.14856	C	80	1.39725	78	121.63178	76	-1.11616
C	32	1.39552	31	118.99501	1	173.70503	C	72	1.53176	70	124.67563	68	171.66243
H	36	1.08377	32	119.96267	31	179.15524	C	83	1.53950	72	111.50064	70	17.84573
C	34	1.39616	31	119.03268	1	-169.62620	H	84	1.09403	83	110.99160	72	-175.29677
H	38	1.08827	34	118.46941	31	176.64603	H	84	1.09409	83	110.20597	72	-57.91606
C	38	1.40029	34	121.30539	31	-7.36039	H	84	1.09608	83	112.34529	72	62.95181
C	40	1.62393	38	127.44863	34	-173.27680	C	83	1.56137	72	108.22008	70	-99.69020
N	41	1.33847	40	114.25813	38	171.42509	H	88	1.09281	83	111.72145	72	-58.61578
C	42	1.34004	41	117.94743	40	-170.49978	H	88	1.09647	83	109.97681	72	61.71336
N	43	1.34098	42	125.30167	41	2.78534	H	88	1.09655	83	109.86750	72	-178.88577
C	44	1.34374	43	117.23561	42	-4.84949								
C	41	1.39410	40	125.04929	38	-2.38961								
H	46	1.08481	41	121.19248	40	-6.80598								

Table E.23: *Z*-matrix of Ac-MPM after the relaxation of the hydrogen atoms and the aromatic ring systems

C							C	42	1.40158	41	120.58139	40	359.97438
C	1	1.39864					C	43	1.40051	42	120.50910	41	-0.01063
C	2	1.39443	1	120.16574			C	40	1.47063*	39	108.64466*	44	179.96928*
C	3	1.40511	2	120.36404	1	0.02562	C	45	1.40777	40	108.62415*	39	0.02562*
C	4	1.40517	3	119.15050	2	359.97438	C	46	1.39054	45	120.59798	40	180.02562*
C	5	1.39446	4	120.35081	3	359.97438	C	47	1.40062	46	119.00287	45	359.97438
C	4	1.48397*	3	120.41209*	2	180.02562*	C	48	1.40125	47	120.52755	46	359.97438
N	7	1.34295	4	117.98695*	3	0.24845*	C	49	1.39825	48	120.55950	47	0.03294
C	8	1.34095	7	115.86057	4	179.86002*	H	1	1.08713	2	120.10348	3	179.97438
N	9	1.34093	8	124.28585	7	0.15796	H	2	1.08693	1	120.09391	3	180.02562
C	10	1.34317	9	115.83276	8	359.89831	H	3	1.08427	2	120.59577	1	180.02562
N	11	1.34192	10	123.98178	9	-0.04540	H	5	1.08430	4	119.02626	3	179.97438
C	11	1.48397*	10	118.00583*	9	180.02562*	H	6	1.08694	5	119.73537	4	180.02562
C	13	1.40515	11	120.45847*	10	359.59226*	H	14	1.08428	13	119.03859	18	179.95982
C	14	1.39448	13	120.35439	11	179.97438*	H	15	1.08693	14	119.73768	13	179.97438
C	15	1.39867	14	120.16896	13	359.97438	H	16	1.08713	15	120.09936	14	180.02562
C	16	1.39868	15	119.79481	14	0.02562	H	17	1.08694	16	120.08859	15	180.02562
C	17	1.39438	16	120.17167	15	0.02562	H	18	1.08428	17	120.62263	16	179.97438
C	9	1.48607*	8	117.80484*	7	180.32489*	H	20	1.08418	19	119.09929	24	-179.99032
C	19	1.40442	9	120.43777*	8	359.63072*	H	21	1.08639	20	120.54881	19	180.13849
C	20	1.39361	19	120.44951	9	179.64292*	H	23	1.08648	22	119.31321	21	179.97438
C	21	1.39882	20	120.21264	19	359.97438	H	24	1.08427	23	120.43211	22	180.12133
C	22	1.39970	21	119.67264	20	0.15218	H	28	1.08664	27	118.40112	26	180.02562
C	23	1.39353	22	120.16856	21	359.85828	H	29	1.08626	28	120.33044	27	180.14617
N	22	1.43589*	21	119.88295*	20	180.45092*	H	30	1.08710	29	120.53882	28	180.02562
C	25	1.40845*	22	119.15861*	21	91.66166*	H	31	1.08354	30	119.21243	29	179.76689
C	26	1.40940	25	120.78333*	22	181.82435*	H	34	1.08358	33	119.76961	38	-179.94501
C	27	1.40190	26	118.64931	25	180.26182*	H	35	1.08709	34	119.20891	33	179.97438
C	28	1.39189	27	122.26296	26	359.76559	H	36	1.08626	35	120.89328	34	179.97438
C	29	1.39740	28	118.76420	27	359.97438	H	37	1.08669	36	119.32083	35	180.33624
C	30	1.39055	29	120.26866	28	0.20004	H	41	1.08750	40	120.85913	39	180.02562
C	27	1.53331*	26	122.20037*	25	2.53202*	H	42	1.08715	41	119.71334	40	179.97438
C	25	1.40831*	22	119.29754*	21	267.79859*	H	43	1.08705	42	119.74014	41	179.97438
C	33	1.41195	25	120.09902*	22	358.19701*	H	44	1.08743	43	120.37776	42	-179.99848
C	34	1.39060	33	120.94302	25	180.13352*	H	47	1.08744	46	120.72099	45	179.97438
C	35	1.39745	34	120.25391	33	0.10523	H	48	1.08708	47	119.73759	46	180.02562
C	36	1.39186	35	118.78061	34	359.78995	H	49	1.08711	48	119.71986	47	180.02562
C	37	1.40196	36	122.26388	35	0.05250	H	50	1.08755	49	120.25204	48	179.97980
C	32	1.53844*	27	111.35488*	26	225.32217*							
C	39	1.40745	32	111.13284*	27	242.74082*							
C	40	1.39861	39	120.41622	32	179.97438*							
C	41	1.39810	40	118.87226	39	0.02562							

* Z-matrix coordinates that were chosen as variables in the TADF rate maximization.

Table E.24: Z-matrix of SpiroAC-TRZ at the energy minimum ($\Lambda = \infty$).

C														
C	1	1.39864												
C	2	1.39443	1	120.16574										
C	3	1.40511	2	120.36404	1	0.02562								
C	4	1.40517	3	119.15050	2	359.97438	C	42	1.40158	41	120.58139	40	359.97438
C	5	1.39446	4	120.35081	3	359.97438	C	43	1.40051	42	120.50910	41	-0.01063
C	4	1.49978*	3	124.94879*	2	173.42101*	C	40	1.48760*	39	107.69736*	44	189.99573*
N	7	1.34295	4	108.77141*	3	0.27177*	C	45	1.40777	40	107.38631*	39	0.75640*
C	8	1.34095	7	115.86057	4	180.26046*	C	46	1.39054	45	120.59798	40	180.78082*
N	9	1.34093	8	124.28585	7	0.15796	C	47	1.40062	46	119.00287	45	359.97438
C	10	1.34317	9	115.83276	8	359.89831	C	48	1.40125	47	120.52755	46	359.97438
N	11	1.34192	10	123.98178	9	-0.04540	C	49	1.39825	48	120.55950	47	0.03294
C	11	1.58946*	10	118.14211*	9	179.30103*	H	1	1.08713	2	120.10348	3	179.97438
C	13	1.40515	11	120.84298*	10	372.87065*	H	2	1.08693	1	120.09391	3	180.02562
C	14	1.39448	13	120.35439	11	167.44939*	H	3	1.08427	2	120.59577	1	180.02562
C	15	1.39867	14	120.16896	13	359.97438	H	5	1.08430	4	119.02626	3	179.97438
C	16	1.39868	15	119.79481	14	0.02562	H	6	1.08694	5	119.73537	4	180.02562
C	17	1.39438	16	120.17167	15	0.02562	H	14	1.08428	13	119.03859	18	179.95982
C	9	1.58104*	8	122.52945*	7	182.48646*	H	15	1.08693	14	119.73768	13	179.97438
C	19	1.40442	9	116.79138*	8	361.16568*	H	16	1.08713	15	120.09936	14	180.02562
C	20	1.39361	19	120.44951	9	176.57457*	H	17	1.08694	16	120.08859	15	180.02562
C	21	1.39882	20	120.21264	19	359.97438	H	18	1.08428	17	120.62263	16	179.97438
C	22	1.39970	21	119.67264	20	0.15218	H	20	1.08418	19	119.09929	24	-179.99032
C	23	1.39353	22	120.16856	21	359.85828	H	21	1.08639	20	120.54881	19	180.13849
N	22	1.39728*	21	121.04382*	20	185.09586*	H	23	1.08648	22	119.31321	21	179.97438
C	25	1.42786*	22	114.89611*	21	94.81547*	H	24	1.08427	23	120.43211	22	180.12133
C	26	1.40940	25	119.71894*	22	181.45209*	H	28	1.08664	27	118.40112	26	180.02562
C	27	1.40190	26	118.64931	25	179.68903*	H	29	1.08626	28	120.33044	27	180.14617
C	28	1.39189	27	122.26296	26	359.76559	H	30	1.08710	29	120.53882	28	180.02562
C	29	1.39740	28	118.76420	27	359.97438	H	31	1.08354	30	119.21243	29	179.76689
C	30	1.39055	29	120.26866	28	0.20004	H	34	1.08358	33	119.76961	38	-179.94501
C	27	1.53922*	26	119.94814*	25	5.69563*	H	35	1.08709	34	119.20891	33	179.97438
C	25	1.43477*	22	121.02129*	21	275.12326*	H	36	1.08626	35	120.89328	34	179.97438
C	33	1.41195	25	122.53828*	22	360.56800*	H	37	1.08669	36	119.32083	35	180.33624
C	34	1.39060	33	120.94302	25	178.78098*	H	41	1.08750	40	120.85913	39	180.02562
C	35	1.39745	34	120.25391	33	0.10523	H	42	1.08715	41	119.71334	40	179.97438
C	36	1.39186	35	118.78061	34	359.78995	H	43	1.08705	42	119.74014	41	179.97438
C	37	1.40196	36	122.26388	35	0.05250	H	44	1.08743	43	120.37776	42	-179.99848
C	32	1.51266*	27	107.26540*	26	222.26042*	H	47	1.08744	46	120.72099	45	179.97438
C	39	1.40745	32	110.92204*	27	227.29839*	H	48	1.08708	47	119.73759	46	180.02562
C	40	1.39861	39	120.41622	32	175.77397*	H	49	1.08711	48	119.71986	47	180.02562
C	41	1.39810	40	118.87226	39	0.02562	H	50	1.08755	49	120.25204	48	179.97980

* Z-matrix coordinates that were chosen as variables in the TADF rate maximization.

Table E.25: Z-matrix of SpiroAC-TRZ at the TADF maximum with energy penalty ($\Lambda = 8.0\,\mu s^{-1} {E_h}^{-1}$).

C							C	42	1.40158	41	120.58139	40	359.97438
C	1	1.39864					C	43	1.40051	42	120.50910	41	-0.01063
C	2	1.39443	1	120.16574			C	40	1.44129*	39	109.00697*	44	176.22851*
C	3	1.40511	2	120.36404	1	0.02562	C	45	1.40777	40	106.13967*	39	0.22415*
C	4	1.40517	3	119.15050	2	359.97438	C	46	1.39054	45	120.59798	40	181.07432*
C	5	1.39446	4	120.35081	3	359.97438	C	47	1.40062	46	119.00287	45	359.97438
C	4	1.46986*	3	118.86981*	2	181.49791*	C	48	1.40125	47	120.52755	46	359.97438
N	7	1.34295	4	112.02339*	3	1.54776*	C	49	1.39825	48	120.55950	47	0.03294
C	8	1.34095	7	115.86057	4	180.05888*	H	1	1.08713	2	120.10348	3	179.97438
N	9	1.34093	8	124.28585	7	0.15796	H	2	1.08693	1	120.09391	3	180.02562
C	10	1.34317	9	115.83276	8	359.89831	H	3	1.08427	2	120.59577	1	180.02562
N	11	1.34192	10	123.98178	9	-0.04540	H	5	1.08430	4	119.02626	3	179.97438
C	11	1.66172*	10	119.62692*	9	180.44673*	H	6	1.08694	5	119.73537	4	180.02562
C	13	1.40515	11	123.23214*	10	359.40282*	H	14	1.08428	13	119.03859	18	179.95982
C	14	1.39448	13	120.35439	11	179.64214*	H	15	1.08693	14	119.73768	13	179.97438
C	15	1.39867	14	120.16896	13	359.97438	H	16	1.08713	15	120.09936	14	180.02562
C	16	1.39868	15	119.79481	14	0.02562	H	17	1.08694	16	120.08859	15	180.02562
C	17	1.39438	16	120.17167	15	0.02562	H	18	1.08428	17	120.62263	16	179.97438
C	9	1.51262*	8	116.29851*	7	181.09967*	H	20	1.08418	19	119.09929	24	-179.99032
C	19	1.40442	9	118.25573*	8	360.39622*	H	21	1.08639	20	120.54881	19	180.13849
C	20	1.39361	19	120.44951	9	180.22357*	H	23	1.08648	22	119.31321	21	179.97438
C	21	1.39882	20	120.21264	19	359.97438	H	24	1.08427	23	120.43211	22	180.12133
C	22	1.39970	21	119.67264	20	0.15218	H	28	1.08664	27	118.40112	26	180.02562
C	23	1.39353	22	120.16856	21	359.85828	H	29	1.08626	28	120.33044	27	180.14617
N	22	1.33022*	21	117.27093*	20	185.06677*	H	30	1.08710	29	120.53882	28	180.02562
C	25	1.42105*	22	122.74351*	21	96.43530*	H	31	1.08354	30	119.21243	29	179.76689
C	26	1.40940	25	120.42310*	22	184.17002*	H	34	1.08358	33	119.76961	38	-179.94501
C	27	1.40190	26	118.64931	25	180.82942*	H	35	1.08709	34	119.20891	33	179.97438
C	28	1.39189	27	122.26296	26	359.76559	H	36	1.08626	35	120.89328	34	179.97438
C	29	1.39740	28	118.76420	27	359.97438	H	37	1.08669	36	119.32083	35	180.33624
C	30	1.39055	29	120.26866	28	0.20004	H	41	1.08750	40	120.85913	39	180.02562
C	27	1.54975*	26	123.65876*	25	2.19957*	H	42	1.08715	41	119.71334	40	179.97438
C	25	1.41944*	22	118.67674*	21	274.26073*	H	43	1.08705	42	119.74014	41	179.97438
C	33	1.41195	25	122.02268*	22	361.07643*	H	44	1.08743	43	120.37776	42	-179.99848
C	34	1.39060	33	120.94302	25	180.41148*	H	47	1.08744	46	120.72099	45	179.97438
C	35	1.39745	34	120.25391	33	0.10523	H	48	1.08708	47	119.73759	46	180.02562
C	36	1.39186	35	118.78061	34	359.78995	H	49	1.08711	48	119.71986	47	180.02562
C	37	1.40196	36	122.26388	35	0.05250	H	50	1.08755	49	120.25204	48	179.97980
C	32	1.60938*	27	100.02180*	26	222.74965*							
C	39	1.40745	32	112.13108*	27	232.40907*							
C	40	1.39861	39	120.41622	32	172.65959*							
C	41	1.39810	40	118.87226	39	0.02562							

* Z-matrix coordinates that were chosen as variables in the TADF rate maximization.

Table E.26: Z-matrix of SpiroAC-TRZ at the TADF maximum with energy penalty ($\Lambda = 4.0\,\mu s^{-1} {E_h}^{-1}$).

C													
C	1	1.39864											
C	2	1.39443	1	120.16574									
C	3	1.40511	2	120.36404	1	0.02562							
C	4	1.40517	3	119.15050	2	359.97438	C	42	1.40158	41	120.58139	40	359.97438
C	5	1.39446	4	120.35081	3	359.97438	C	43	1.40051	42	120.50910	41	-0.01063
C	4	1.47554*	3	111.98727*	2	181.37311*	C	40	1.44517*	39	108.45973*	44	183.12696*
N	7	1.34295	4	110.24980*	3	1.19506*	C	45	1.40777	40	104.91216*	39	-0.59160*
C	8	1.34095	7	115.86057	4	180.05717*	C	46	1.39054	45	120.59798	40	182.56593*
N	9	1.34093	8	124.28585	7	0.15796	C	47	1.40062	46	119.00287	45	359.97438
C	10	1.34317	9	115.83276	8	359.89831	C	48	1.40125	47	120.52755	46	359.97438
N	11	1.34192	10	123.98178	9	-0.04540	C	49	1.39825	48	120.55950	47	0.03294
C	11	1.66300*	10	120.93424*	9	180.35447*	H	1	1.08713	2	120.10348	3	179.97438
C	13	1.40515	11	124.11850*	10	359.49472*	H	2	1.08693	1	120.09391	3	180.02562
C	14	1.39448	13	120.35439	11	179.89436*	H	3	1.08427	2	120.59577	1	180.02562
C	15	1.39867	14	120.16896	13	359.97438	H	5	1.08430	4	119.02626	3	179.97438
C	16	1.39868	15	119.79481	14	0.02562	H	6	1.08694	5	119.73537	4	180.02562
C	17	1.39438	16	120.17167	15	0.02562	H	14	1.08428	13	119.03859	18	179.95982
C	9	1.56142*	8	114.34246*	7	181.06750*	H	15	1.08693	14	119.73768	13	179.97438
C	19	1.40442	9	116.94103*	8	360.76368*	H	16	1.08713	15	120.09936	14	180.02562
C	20	1.39361	19	120.44951	9	179.87608*	H	17	1.08694	16	120.08859	15	180.02562
C	21	1.39882	20	120.21264	19	359.97438	H	18	1.08428	17	120.62263	16	179.97438
C	22	1.39970	21	119.67264	20	0.15218	H	20	1.08418	19	119.09929	24	-179.99032
C	23	1.39353	22	120.16856	21	359.85828	H	21	1.08639	20	120.54881	19	180.13849
N	22	1.36424*	21	119.09386*	20	185.15793*	H	23	1.08648	22	119.31321	21	179.97438
C	25	1.42155*	22	123.85158*	21	96.64759*	H	24	1.08427	23	120.43211	22	180.12133
C	26	1.40940	25	120.17878*	22	183.92301*	H	28	1.08664	27	118.40112	26	180.02562
C	27	1.40190	26	118.64931	25	180.19737*	H	29	1.08626	28	120.33044	27	180.14617
C	28	1.39189	27	122.26296	26	359.76559	H	30	1.08710	29	120.53882	28	180.02562
C	29	1.39740	28	118.76420	27	359.97438	H	31	1.08354	30	119.21243	29	179.76689
C	30	1.39055	29	120.26866	28	0.20004	H	34	1.08358	33	119.76961	38	-179.94501
C	27	1.54636*	26	124.27689*	25	2.51236*	H	35	1.08709	34	119.20891	33	179.97438
C	25	1.41821*	22	119.59668*	21	275.55572*	H	36	1.08626	35	120.89328	34	179.97438
C	33	1.41195	25	122.43565*	22	360.93879*	H	37	1.08669	36	119.32083	35	180.33624
C	34	1.39060	33	120.94302	25	179.81468*	H	41	1.08750	40	120.85913	39	180.02562
C	35	1.39745	34	120.25391	33	0.10523	H	42	1.08715	41	119.71334	40	179.97438
C	36	1.39186	35	118.78061	34	359.78995	H	43	1.08705	42	119.74014	41	179.97438
C	37	1.40196	36	122.26388	35	0.05250	H	44	1.08743	43	120.37776	42	-179.99848
C	32	1.65550*	27	97.68815*	26	219.33790*	H	47	1.08744	46	120.72099	45	179.97438
C	39	1.40745	32	111.98606*	27	225.06535*	H	48	1.08708	47	119.73759	46	180.02562
C	40	1.39861	39	120.41622	32	173.05428*	H	49	1.08711	48	119.71986	47	180.02562
C	41	1.39810	40	118.87226	39	0.02562	H	50	1.08755	49	120.25204	48	179.97980

* Z-matrix coordinates that were chosen as variables in the TADF rate maximization.

Table E.27: Z-matrix of SpiroAC-TRZ at the TADF maximum with no energy penalty ($\Lambda = 0$).

N													
C	1	1.36424											
C	2	1.40282	1	121.50867									
H	3	1.08683	2	119.04460	1	-2.85476							
C	3	1.39572	2	120.37391	1	176.08647	C	42	1.44517	40	133.05254	38	-179.27285
H	5	1.08541	3	120.95971	2	-179.56036	C	43	1.40109	42	129.17557	40	16.93548
C	5	1.39647	3	119.56328	2	-0.24994	H	44	1.08775	43	120.53838	42	-12.49670
C	7	1.40257	5	120.87229	3	0.99276	C	44	1.39849	43	119.15790	42	169.74197
H	8	1.08173	7	120.03060	5	179.94059	H	46	1.08719	44	119.87457	43	178.01097
C	8	1.39379	7	119.18353	5	0.28161	C	46	1.40050	44	120.30729	43	-2.72602
H	10	1.08679	8	120.66254	7	-179.43165	H	48	1.08730	46	119.80167	44	178.79374
C	1	1.41821	2	119.59668	3	97.72603	C	48	1.40228	46	120.53386	44	-2.41667
C	12	1.41557	1	125.79177	2	-178.46516	H	50	1.08727	48	119.95908	46	-176.86033
C	13	1.40520	12	122.54747	1	175.74373	C	50	1.39000	48	119.30294	46	-0.66100
H	14	1.08609	13	117.18512	12	-178.90174	C	7	1.56142	5	122.18538	3	-178.58008
C	14	1.38342	13	122.95496	12	4.31697	N	53	1.33856	7	114.34246	5	-179.64759
H	16	1.08584	14	121.41073	13	178.27902	N	53	1.34014	7	119.33362	5	0.89565
C	16	1.39360	14	116.48146	13	-0.10751	C	55	1.33044	53	115.32737	7	178.85780
H	18	1.08671	16	121.35447	14	178.71368	N	56	1.34112	55	124.49184	53	0.10657
C	18	1.38560	16	119.96574	14	-4.14850	C	57	1.33300	56	115.11477	55	0.28381
H	20	1.08751	18	116.54086	16	-177.01436	C	58	1.47554	57	123.69594	56	179.58234
C	1	1.42155	2	123.85158	3	-81.18211	C	59	1.39518	58	126.12386	57	2.23938
C	22	1.40887	1	118.75145	2	4.93037	H	60	1.08585	59	119.54809	58	-1.03588
H	23	1.08414	22	119.31195	1	-0.74919	C	60	1.39678	59	119.19866	58	178.69563
C	23	1.38819	22	120.90003	1	179.57028	H	62	1.08679	60	119.94071	59	-179.93415
H	25	1.08693	23	119.69170	22	179.82401	C	62	1.39846	60	119.94165	59	-0.11219
C	25	1.39637	23	119.41787	22	0.02276	H	64	1.08727	62	119.74224	60	-179.79482
H	27	1.08637	25	120.89368	23	179.42376	C	64	1.40230	62	120.42595	60	0.25201
C	27	1.39125	25	119.28133	23	-0.33138	H	66	1.08767	64	119.40856	62	179.78621
H	29	1.08484	27	117.89135	25	178.27800	C	66	1.39716	64	120.75541	62	-0.03680
C	29	1.40956	27	123.53932	25	0.04169	H	68	1.07301	66	120.20625	64	179.76333
C	13	1.47692	12	120.16292	1	-13.86355	C	56	1.66301	55	120.93424	53	-179.64553
C	32	1.47373	13	114.34423	12	-119.78432	C	70	1.39583	56	124.11850	55	-0.50528
C	33	1.40067	32	121.96391	13	55.54923	H	71	1.08690	70	119.41936	56	-0.05058
H	34	1.08843	33	119.73017	32	10.04678	C	71	1.39636	70	120.21958	56	179.89436
C	34	1.40136	33	121.14814	32	-170.93155	H	73	1.08686	71	119.55158	70	-179.98149
H	36	1.08714	34	119.75233	33	-178.14280	C	73	1.39741	71	120.18337	70	0.03111
C	36	1.39786	34	120.42619	33	2.99037	H	75	1.08706	73	120.12163	71	-179.99708
H	38	1.08711	36	120.03855	34	179.26135	C	75	1.39825	73	119.67097	71	0.00890
C	38	1.39906	36	120.20297	34	0.02928	H	77	1.08711	75	120.12302	73	179.98530
H	40	1.08734	38	120.48219	36	178.44057	C	77	1.39603	75	120.17494	73	-0.01384
C	40	1.39177	38	119.11562	36	-0.88343	H	79	1.08416	77	120.67450	75	179.98837

Table E.28: Z-matrix of SpiroAC-TRZ after the relaxation of the hydrogen atoms and the aromatic ring systems

Appendix F

Supplementary Information: Enhancing TTA Upconversion via High-Level Intersystem Crossing

F.1 Calculation of ISC Rates

We calculated the intersystem crossing (ISC) rates in the framework of Marcus theory [192, 337]

$$k_{R\to P} = \frac{2\pi}{\hbar}|\langle P|\hat{H}_{\mathrm{SOC}}|R\rangle|^2 \frac{1}{(4\pi\lambda_{\mathrm{M}}k_{\mathrm{B}}T)^{1/2}} \exp\left[-\frac{(\Delta E_{P-R}+\lambda_{\mathrm{M}})^2}{4\lambda_{\mathrm{M}}k_{\mathrm{B}}T}\right] \tag{F.1}$$

where R and P are the initial (reactant) and the final (product) states, respectively; $\langle P|\hat{H}_{\mathrm{SOC}}|R\rangle$ is the spin-orbit coupling (SOC); ΔE_{P-R} is the minimum-to-minimum energy; and λ_{M} is the reorganization energy. SOC can be obtained in TDDFT using the Breit-Pauli Hamiltonian as implemented in the Q-Chem 5.1 software package [297]. To obtain ΔE_{P-R} and λ_{M}, the geometries of the initial and the final states must be optimized. In the case of T_1, we employed the Tamm-Dancoff approximation (TDA) [209], because the full TDDFT ran into imaginary roots.

To capture the effects of tunneling, we also calculated the rates in Marcus-Levich-

Jortner (MLJ) theory [194]

$$k_{R\to P} = \frac{2\pi}{\hbar}|\langle P|\hat{H}_{\mathrm{SOC}}|R\rangle|^2 \frac{1}{(4\pi\lambda_{\mathrm{M}}k_{\mathrm{B}}T)^{1/2}} \sum_n \frac{S^n}{n!} e^{-S} \exp\left[-\frac{(\Delta E_{P-R} + \lambda_{\mathrm{M}} + n\hbar\omega)^2}{4\lambda_{\mathrm{M}}k_{\mathrm{B}}T}\right] \tag{F.2}$$

where S is the effective Huang-Rhys factor and ω is the effective frequency. These are obtained by mode-averaging

$$S = \sum_v^{S_v<10} S_v \tag{F.3}$$

$$\omega = \frac{1}{S} \sum_v^{S_v<10} S_v\omega_v \tag{F.4}$$

where we have enforced a cutoff of $S_v < 10$ to remove modes with unreasonable values of Huang-Rhys factors. For each vibrational mode v, the Huang-Rhys factor is defined as

$$S_v = \frac{k_v(q_{P,v} - q_{R,v})^2}{2\hbar\omega_v} \tag{F.5}$$

where k_v is the spring constant of the mode; and $q_{R,v}$ and $q_{P,v}$ are the coordinates of the initial and the final state minima along the mode, respectively. For simplicity, we assume that the vibrational modes of the excited states are the same as the ground state. Using the harmonic approximation, we can rewrite $q_{P,v} - q_{R,v}$ in terms of the gradients

$$\frac{dE_R}{dq_v} = \frac{dE_R}{dq_v}(q_v = q_{0,v}) + k_v(q_v - q_{0,v}) \tag{F.6}$$

$$\frac{dE_P}{dq_v} = \frac{dE_P}{dq_v}(q_v = q_{0,v}) + k_v(q_v - q_{0,v}) \tag{F.7}$$

where $q_{0,v}$ is some reference coordinate, which we choose to be the ground state minimum. The Huang-Rhys factors become

$$S_v = \frac{1}{2k_v\hbar\omega_v}\left(\frac{dE_P}{dq_v}(q_v = q_{0,v}) - \frac{dE_R}{dq_v}(q_v = q_{0,v})\right)^2 \tag{F.8}$$

Tables F.1 and F.2 summarize the values of ΔE, λ_M, S, ω, SOC, and ISC rates

in the $T_2 \rightarrow S_1$ and $T_1 \rightarrow S_0$ transitions, respectively. The excited state energies in Tables F.1 and F.2 are minimum-to-minimum energies, so they are not the same as the vertical excitation energies in Table 8.1.

Molecule	T_2 (eV)	S_1 (eV)	λ_M (eV)	S	ω (rad s^{-1})	SOC (cm^{-1})	ISC Rate (s^{-1})	
							Marcus	MLJ
Anthracene	3.05	3.06	0.14	0.89	8256	3.27×10^{-2}	1.48×10^{5}	6.13×10^{4}
DPA	3.03	2.89	0.20	3.25	2274	2.33×10^{-1}	2.71×10^{7}	7.41×10^{6}
Diamide	3.02	2.82	0.24	5.75	1470	4.61×10^{-2}	1.04×10^{6}	2.68×10^{5}
Diamine	3.03	2.77	0.24	2.40	3403	8.37×10^{-1}	3.64×10^{8}	1.79×10^{8}
Tetracene	2.31	2.32	0.11	0.39	8057	2.81×10^{-2}	1.53×10^{5}	1.03×10^{5}
Rubrene	2.12	1.98	0.14	3.07	1352	1.56	1.68×10^{9}	1.13×10^{9}
Tetraamide	2.13	1.98	0.14	4.92	896	1.45	1.44×10^{9}	9.00×10^{8}
Tetraamine	2.11	1.93	0.12	3.32	1075	1.23	7.59×10^{8}	1.03×10^{9}
DPBF	2.89	2.70	0.14	6.94	1067	1.60	1.46×10^{9}	9.86×10^{8}
DPBTP	2.98	2.71	0.18	7.65	1168	9.95	3.80×10^{10}	3.91×10^{10}

Table F.1: $T_2 \rightarrow S_1$ energetics in B3LYP/6-31G*. The excitation energies are minimum-to-minium energies with the ground state minimum as the reference.

Molecule	T_1 (eV)	λ_M (eV)	S	ω (rad s^{-1})	SOC (cm^{-1})	ISC Rate (s^{-1})	
						Marcus	MLJ
Anthracene	1.44	0.28	1.60	7495	1.68×10^{-2}	2.63×10^{-16}	1.64×10^{2}
DPA	1.38	0.28	4.30	2962	1.64×10^{-1}	9.18×10^{-12}	4.78×10^{2}
Diamide	1.37	0.28	5.21	2547	1.01×10^{-1}	1.12×10^{-11}	1.36×10^{2}
Diamine	1.37	0.28	1.75	7012	3.34×10^{-1}	5.84×10^{-11}	1.24×10^{5}
Tetracene	0.72	0.22	1.93	7449	1.21×10^{-2}	1.29	2.07×10^{4}
Rubrene	0.43	0.23	4.51	3135	3.17×10^{-2}	9.19×10^{4}	3.29×10^{5}
Tetraamide	0.45	0.23	4.05	3447	1.53×10^{-1}	1.54×10^{6}	7.80×10^{6}
Tetraamine	0.46	0.23	4.80	2811	2.06×10^{-1}	2.16×10^{6}	1.53×10^{7}
DPBF	1.15	0.25	9.26	2091	1.14	3.05×10^{-5}	6.58×10^{6}
DPBTP	1.17	0.34	4.79	4895	1.27	1.23	1.17×10^{8}

Table F.2: $T_1 \rightarrow S_0$ energetics in B3LYP/6-31G*. The T_1 energy is minimum-to-minium energy with the ground state minimum as the reference.

Interestingly, substitution of the electron-withdrawing (EW) amide and the electron-donating (ED) amine groups does not appear to have a significant effect on the $T_2 \rightarrow S_1$ SOC and ISC rate of rubrene. As shown in Figure F-1, the natural transition orbital (NTO) pairs [284] of rubrene do not have the same symmetries as DPA. The S_1 and the T_2 orbitals localize or delocalize together, and the excitaton characters do not differentiate on substitution of EW or ED groups. Instead, the enhancement

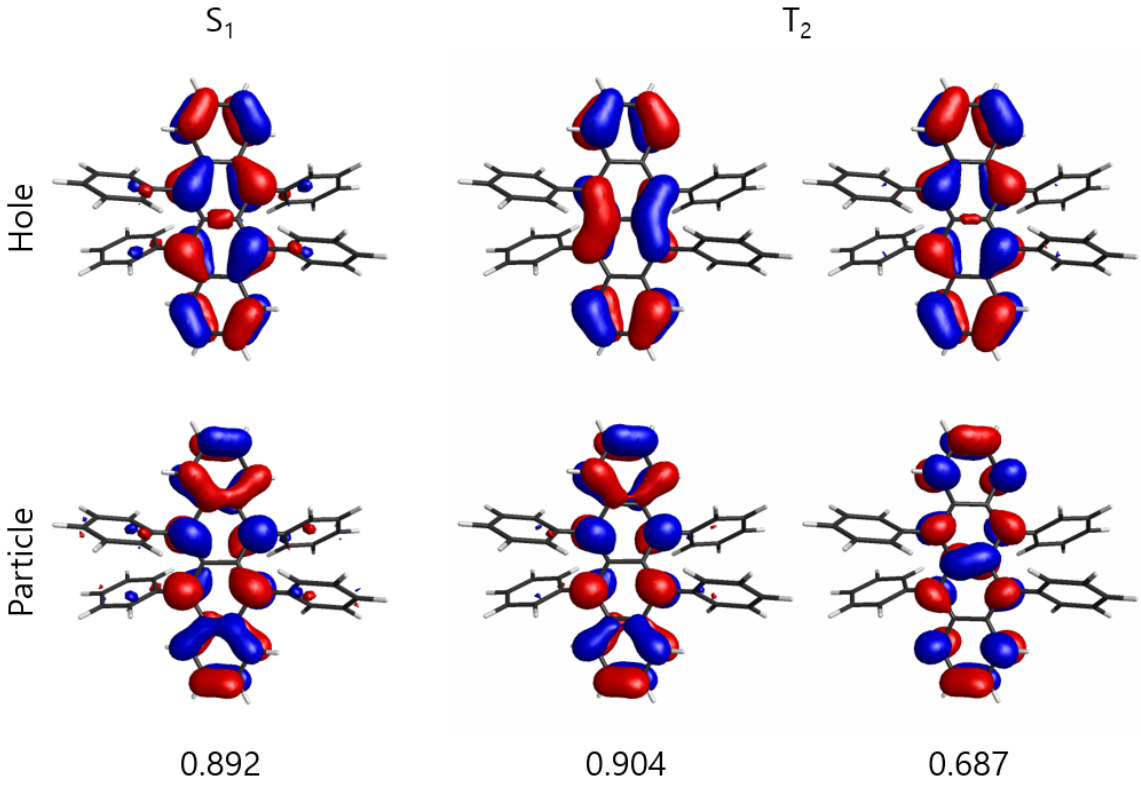

Figure F-1: NTO pairs of S_1 and T_2 in rubrene and their eigenvalues.

of the $T_2 \rightarrow S_1$ SOC and ISC rate might be associated with the twist in the tetracene core of rubrene. Unfortunately, there does not appear to be an intuitive way to modulate the twist.

In addition to B3LYP [272–277], we repeated the calculations of the $T_2 \rightarrow S_1$ ISC rates in PBE [300], PBE0 [301, 302], LRC-ωPBEh [305, 357], and M06-2X [303], continuing to use the 6-31G* basis set [278, 279, 335, 336]. As shown in Figure F-2, the qualitative trends in ISC are reproduced. The $T_2 - S_1$ SOC is stronger in DPA and rubrene than anthracene and tetracene, respectively, which gives higher $T_2 \rightarrow S_1$ ISC rates. Substituting the electron-donating (ED) amine groups in DPA and substituting the oxygen with sulfur in DPBF increase the $T_2 - S_1$ SOC and ISC rates. The only exception is PBE, which reverses the trends in the DPA derivatives. This might be attributed to the self-interaction error, especially since the SOC in the DPA derivatives depends on orbital delocalization.

Figure F-3 shows the $T_1 \rightarrow S_0$ SOC and ISC rates. The differences between Marcus theory and MLJ theory indicate that tunneling might play a significant role in the $T_1 \rightarrow S_0$ ISC. In this case, we must use MLJ theory to obtain qualitative predictions of the rates. Comparing Figures F-2 and F-3 suggests a correlation between the $T_2 \rightarrow S_1$ and the $T_1 \rightarrow S_0$ ISC. A molecule with a higher $T_2 \rightarrow S_1$ SOC and ISC rate also tends to have a higher $T_1 \rightarrow S_0$ SOC and ISC rate. In particular, the $T_1 \rightarrow S_0$ ISC rate remains similar from anthracene to DPA, but it increases by orders of magnitude from DPA to Diamine. This might explain why ϕ_{TTA} increases from anthracene to DPA, but does not improve from DPA to Diamine in our experiments.

F.2 Fabrication of Photon Upconverters

To exclude solvent effects on the candidates, upconversion thin films are fabricated as follows: The sensitizers are mixed with the candidates at 0.5 wt.% in chloroform. Polystyrene (PS) is added at 10 wt.% to improve the uniformity of the film, forming an overall $20\,\mathrm{mg\,mL^{-1}}$ solution ($10\,\mathrm{mg\,mL^{-1}}$ for DPA-Diamine due to limited solubility). Next, the solution is spin-coated at 750 rpm for 90 s and annealed at 65 °C

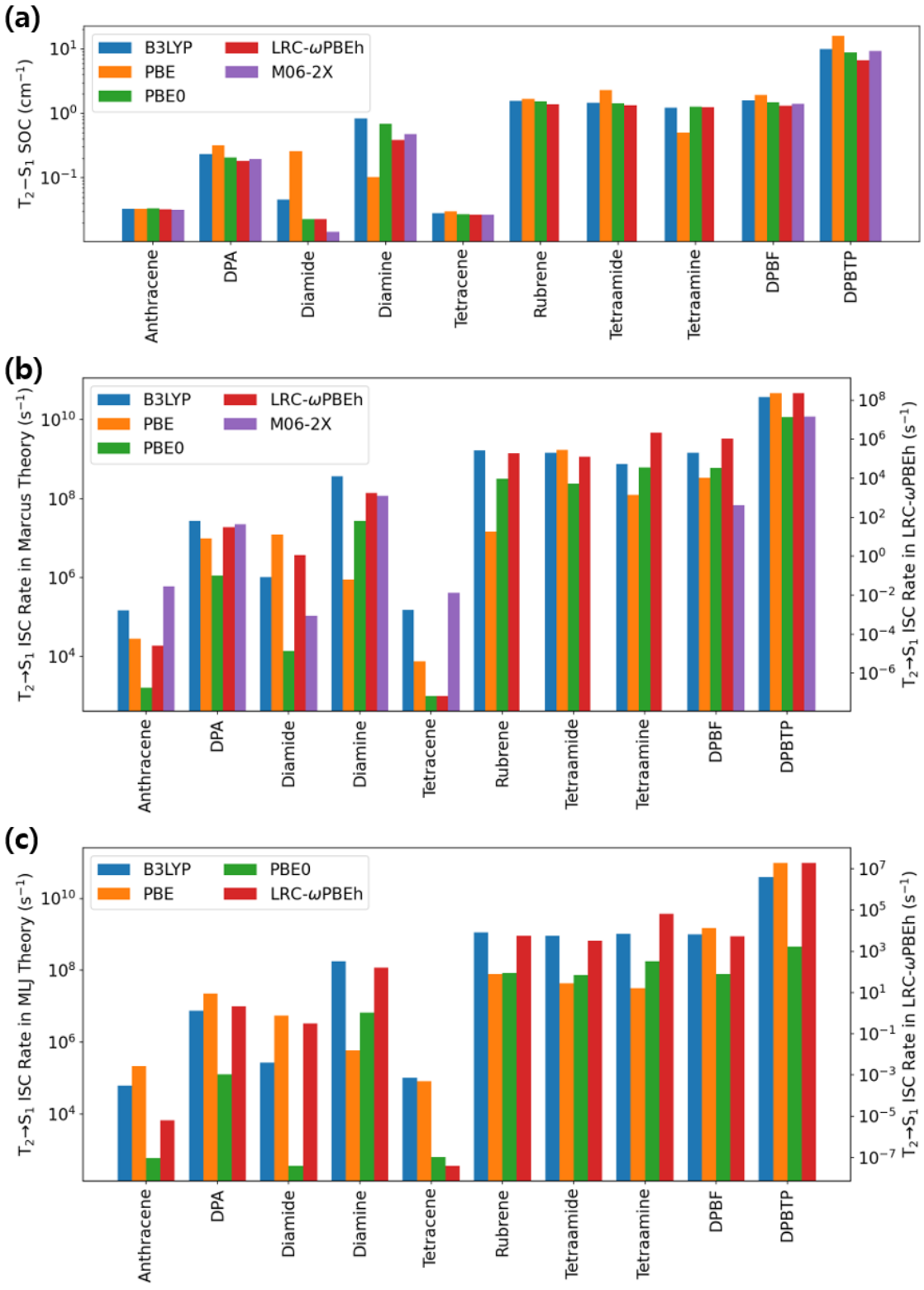

Figure F-2: (a) $T_2 - S_1$ SOC. (b) $T_2 \rightarrow S_1$ ISC rates in Marcus theory. (c) $T_2 \rightarrow S_1$ ISC rates in MLJ theory.

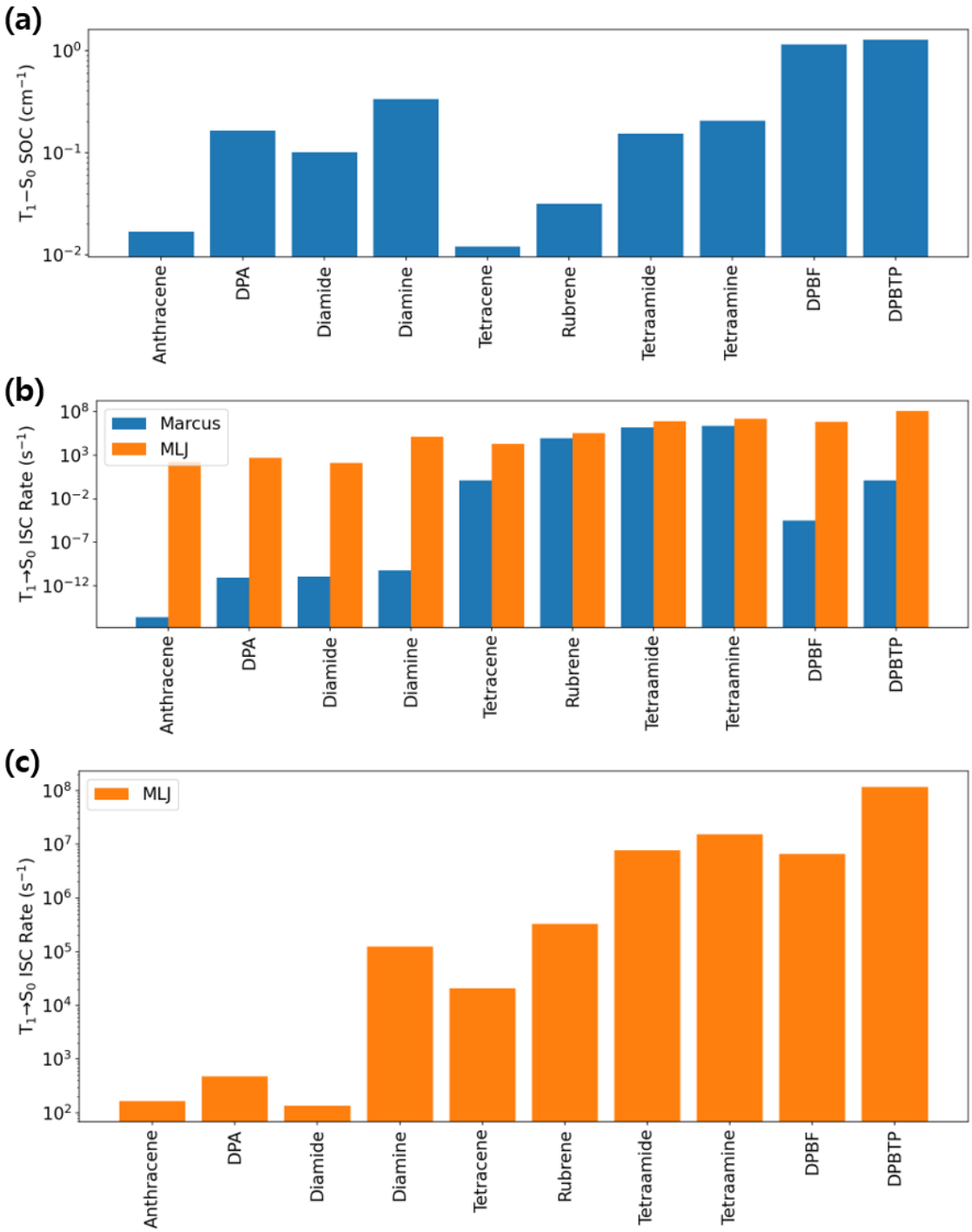

Figure F-3: (a) $T_1 - S_0$ SOC. (b) $T_1 \rightarrow S_0$ ISC rates in Marcus theory and MLJ theory. (c) $T_1 \rightarrow S_0$ ISC rates in MLJ theory only.

for 5 min. The spin-coating and annealing process are repeated 3 times (6 times for DPA-Diamine) to obtain thick upconversion films that give sufficient absorption from the sensitizers for reliable measurements. Indeed, absorption spectra of PS:0.5 wt.% sensitizer films show Q-band absorption of $> 1\,\%$, and upconverted emission is clearly observed when exciting the PtOEP-sensitized and PtTPBP-sensitized upconversion systems at $\lambda = 532\,\text{nm}$ and $\lambda = 635\,\text{nm}$, respectively (Figure 8-4b-c).

F.3 Dependence of Upconverted PL Intensity on Incident Intensity

Upconverted emission due to TTA has a distinct dependence ion incident intensity [341], which can be understood from the triplet exciton dynamics in the candidates:

$$\frac{d[\mathrm{T}_1]}{dt} = G - k_\mathrm{T}[\mathrm{T}_1] - k_\mathrm{TTA}[\mathrm{T}_1]^2 \tag{F.9}$$

where $[\mathrm{T}_1]$ is the triplet density; G is the generation rate of triplet excitons, which is proportional to the incident intensity; k_T is the decay rate of T_1; and k_TTA is the rate of TTA. At steady state, we have

$$G = k_\mathrm{T}[\mathrm{T}_1] + k_\mathrm{TTA}[\mathrm{T}_1]^2 \tag{F.10}$$

At low incident intensities where k_T dominates triplet decay, the generation rate is proportional to triplet density ($G \propto [\mathrm{T}_1]$). Since upconverted PL depends quadratically on triplet density ($\mathrm{UCPL} \propto [\mathrm{T}_1]^2$), the linear relationship between triplet density, and generation rate gives a quadratic relationship between the upconverted PL and the incident intensity. As the incident intensity increases, k_TTA dominates the triplet decay, and the generation rate becomes quadratic in triplet density ($G \propto [\mathrm{T}_1]^2$), which in turn gives a linear relationship between the upconverted PL and the incident intensity. Therefore, the threshold intensity at which TTA reaches its maximal efficiency is defined as the transition point from the quadratic to the linear dependence

of the upconverted PL on the incident intensity.

All but one of the devices show a transition from a quadratic to a linear dependence with increasing incident intensity (Figure 8-4c). This indicates that the measured ϕ_{TTA} represent the optimal performances of the three devices but a suboptimal performance of the fourth device containing DPBTP. Fortunately, this does not affect our conclusions, since DPBTP appears to be the best annihilator in any case.

Bibliography

[1] R. Imbihl and G. Ertl. Oscillatory Kinetics in Heterogeneous Catalysis. *Chem. Rev.*, 95(3):697–733, 1995.

[2] K. Krischer, M. Eiswirth, and G. Ertl. Oscillatory CO oxidation on Pt(110): Modeling of temporal self-organization. *J. Chem. Phys.*, 96(12):9161–9172, 1992.

[3] R. Imbihl, T. Fink, and K. Krischer. Bifurcation analysis of the three-variable model for the NO+CO reaction on Pt surfaces. *J. Chem. Phys.*, 96(8):6236–6248, 1992.

[4] G. Veser and R. Imbihl. Synchronization and spatiotemporal self-organization in the NO+CO reaction on Pt(100). I. Unsynchronized oscillations on the 1×1 substrate. *J. Chem. Phys.*, 100(11):8483–8491, 1994.

[5] G. Veser and R. Imbihl. Synchronization and spatiotemporal self-organization in the NO+CO reaction on Pt(100). II. Synchronized oscillations on the hex-substrate. *J. Chem. Phys.*, 100(11):8492–8500, 1994.

[6] M. Eiswirth, K. Krischer, and G. Ertl. Transition to chaos in an oscillating surface reaction. *Surf. Sci.*, 202(3):565–591, 1988.

[7] M. Eiswirth, T.-M. Kruel, G. Ertl, and F. Schneider. Hyperchaos in a chemical reaction. *Chem. Phys. Lett.*, 193(4):305–310, 1992.

[8] F. Horn and R. Jackson. General mass action kinetics. *Arch. Rational Mech. Anal.*, 47(2):81–116, 1972.

[9] F. Horn. Necessary and sufficient conditions for complex balancing in chemical kinetics. *Arch. Rational Mech. Anal.*, 49(3):172–186, 1972.

[10] M. Feinberg. Complex balancing in general kinetic systems. *Arch. Rational Mech. Anal.*, 49(3):187–194, 1972.

[11] M. A. Grela and A. J. Colussi. Kinetics of Stochastic Charge Transfer and Recombination Events in Semiconductor Colloids. Relevance to Photocatalysis Efficiency. *J. Phys. Chem.*, 100(46):18214–18221, 1996.

[12] T. L. Thompson and J. T. Yates. Control of a Surface Photochemical Process by Fractal Electron Transport Across the Surface: O_2 Photodesorption from TiO_2(110). *J. Phys. Chem. B*, 110(14):7431–7435, 2006.

[13] M. Haerifar and S. Azizian. Fractal-Like Adsorption Kinetics at the Solid/Solution Interface. *J. Phys. Chem. C*, 116(24):13111–13119, 2012.

[14] M. O. Vlad, R. Metzler, and J. Ross. Generalized Huber kinetics for nonlinear rate processes in disordered systems: Nonlinear analogs of stretched exponential. *Phys. Rev. E*, 57(6):6497–6505, 1998.

[15] R. Kopelman. Rate processes on fractals: Theory, simulations, and experiments. *J. Stat. Phys.*, 42(1):185–200, 1986.

[16] R. Kopelman. Fractal Reaction Kinetics. *Science*, 241(4873):1620–1626, 1988.

[17] D. L. Huber. Dynamical model for stretched exponential relaxation in solids. *Phys. Rev. E*, 53(6):6544–6546, 1996.

[18] F. Moiny, M. Dumont, and R. Dagonnier. Fractal kinetics and surface reactions. *J. Chem. Phys.*, 108(11):4572–4581, 1998.

[19] B. Peters and S. L. Scott. Single atom catalysts on amorphous supports: A quenched disorder perspective. *J. Chem. Phys.*, 142(10):104708, 2015.

[20] N. Geva, V. Vaissier, J. Shepherd, and T. Van Voorhis. Mean field treatment of heterogeneous steady state kinetics. *Chem. Phys. Lett.*, 685:185–190, 2017.

[21] S. A. Khan, C. A. Vandervelden, S. L. Scott, and B. Peters. Grafting metal complexes onto amorphous supports: from elementary steps to catalyst site populations via kernel regression. *React. Chem. Eng.*, 5(1):66–76, 2020.

[22] A. R. McIsaac, V. Vaissier Welborn, M. Einzinger, N. Geva, H. Weir, M. A. Baldo, and T. Van Voorhis. Investigation of External Quantum Efficiency Roll-Off in OLEDs Using the Mean-Field Steady-State Kinetic Model. *J. Phys. Chem. C*, 124(27):14424–14431, 2020.

[23] C. A. Vandervelden, S. A. Khan, S. L. Scott, and B. Peters. Site-averaged kinetics for catalysts on amorphous supports: an importance learning algorithm. *React. Chem. Eng.*, 5(1):77–86, 2020.

[24] R. H. Wells, S. An, P. Patel, C. Liu, and R. T. Skodje. Single-Molecule Kinetics of Styrene Hydrogenation on Silica-Supported Vanadium: The Role of Disorder for Single-Atom Catalysts. *J. Phys. Chem. C*, 125(37):20286–20300, 2021.

[25] M. V. Smoluchowski. Versuch einer mathematischen Theorie der Koagulationskinetik kolloider Lösungen. *Z. Phys. Chem.*, 92U(1):129–168, 1918.

[26] R. B. Getman and W. F. Schneider. DFT-Based Coverage-Dependent Model of Pt-Catalyzed NO Oxidation. *ChemCatChem*, 2(11):1450–1460, 2010.

[27] A. Chatterjee and D. G. Vlachos. An overview of spatial microscopic and accelerated kinetic Monte Carlo methods. *J. Comput. Aided Mater. Des.*, 14(2):253–308, 2007.

[28] M. Andersen, C. Panosetti, and K. Reuter. A Practical Guide to Surface Kinetic Monte Carlo Simulations. *Front. Chem.*, 7:202, 2019.

[29] B. Temel, H. Meskine, K. Reuter, M. Scheffler, and H. Metiu. Does phenomenological kinetics provide an adequate description of heterogeneous catalytic reactions? *J. Chem. Phys.*, 126(20):204711, 2007.

[30] D. T. Gillespie. A General Method for Numerically Simulating the Stochastic Time Evolution of Coupled Chemical Reactions. *J. Comput. Phys.*, 22(4):403–434, 1976.

[31] B. Munsky and M. Khammash. The finite state projection algorithm for the solution of the chemical master equation. *J. Chem. Phys.*, 124(4):044104, 2006.

[32] A. Hellander and P. Lötstedt. Hybrid method for the chemical master equation. *J. Comput. Phys.*, 227(1):100–122, 2007.

[33] P. Smadbeck and Y. N. Kaznessis. A closure scheme for chemical master equations. *Proc. Natl. Acad. Sci. U.S.A.*, 110(35):14261–14265, 2013.

[34] D. Schnoerr, G. Sanguinetti, and R. Grima. Comparison of different moment-closure approximations for stochastic chemical kinetics. *J. Chem. Phys.*, 143(18):185101, 2015.

[35] M. Pineda and M. Stamatakis. Beyond mean-field approximations for accurate and computationally efficient models of on-lattice chemical kinetics. *J. Chem. Phys.*, 147(2):024105, 2017.

[36] O. K. Ernst, T. Bartol, T. Sejnowski, and E. Mjolsness. Deep Learning Moment Closure Approximations using Dynamic Boltzmann Distributions, 2019. arXiv:1905.12122 [cs.LG].

[37] A. F. Voter. Introduction to the Kinetic Monte Carlo Method. In K. E. Sickafus, E. A. Kotomin, and B. P. Uberuaga, editors, *Radiation Effects in Solids*, volume 235 of *NATO Science Series*, pages 1–23. Springer, Dordrecht, Netherlands, 2007.

[38] A. B. Bortz, M. H. Kalos, and J. L. Lebowitz. A new algorithm for Monte Carlo simulation of Ising spin systems. *J. Comput. Phys.*, 17(1):10–18, 1975.

[39] S. A. Serebrinsky. Physical time scale in kinetic Monte Carlo simulations of continuous-time Markov chains. *Phys. Rev. E*, 83(3):037701, 2011.

[40] D. T. Gillespie. Approximate accelerated stochastic simulation of chemically reacting systems. *J. Chem. Phys.*, 115(4):1716–1733, 2001.

[41] H. Resat, H. S. Wiley, and D. A. Dixon. Probability-Weighted Dynamic Monte Carlo Method for Reaction Kinetics Simulations. *J. Phys. Chem. B*, 105(44):11026–11034, 2001.

[42] J. P. DeVita, L. M. Sander, and P. Smereka. Multiscale kinetic Monte Carlo algorithm for simulating epitaxial growth. *Phys. Rev. B*, 72(20):205421, 2005.

[43] D. R. Jefferson. Virtual Time. *ACM Trans. Program. Lang. Syst.*, 7(3):404–425, 1985.

[44] B. D. Lubachevsky. Efficient parallel simulations of dynamic Ising spin systems. *J. Comput. Phys.*, 75(1):103–122, 1988.

[45] Y. Shim and J. G. Amar. Semirigorous synchronous sublattice algorithm for parallel kinetic Monte Carlo simulations of thin film growth. *Phys. Rev. B*, 71(12):125432, 2005.

[46] E. Martínez, J. Marian, M. H. Kalos, and J. M. Perlado. Synchronous parallel kinetic Monte Carlo for continuum diffusion-reaction systems. *J. Computat. Phys.*, 227(8):3804–3823, 2008.

[47] J. D. Weeks and G. H. Gilmer. Pair approximation equations for interfaces and free surfaces in the Ising model. *J. Chem. Phys.*, 63(7):3136–3143, 1975.

[48] R. Dickman. Kinetic phase transitions in a surface-reaction model: Mean-field theory. *Phys. Rev. A*, 34(5):4246–4250, 1986.

[49] H. Matsuda. Conditions for the Evolution of Altruism. In Y. Ito, J. P. Brown, and J. Kikkawa, editors, *Animal Societies: Theories and Facts*, pages 67–80. Japan Scientific Societies Press, Tokyo, Japan, 1987.

[50] H. Matsuda, N. Ogita, A. Sasaki, and K. Satō. Statistical Mechanics of Population: The Lattice Lotka-Volterra Model. *Prog. Theor. Phys.*, 88(6):1035–1049, 1992.

[51] M. J. Keeling, D. A. Rand, and A. J. Morris. Correlation models for childhood epidemics. *Proc. R. Soc. Lond. B*, 264(1385):1149–1156, 1997.

[52] C. Chow and C. Liu. Approximating discrete probability distributions with dependence trees. *IEEE Trans. Inf. Theory*, 14(3):462–467, 1968.

[53] H.-J. Kang, K. Kim, and J. H. Kim. Optimal approximation of discrete probability distribution with kth-order dependency and its application to combining multiple classifiers. *Pattern Recognit. Lett.*, 18(6):515–523, 1997.

[54] D. E. Hiebeler and N. E. Millett. Pair and triplet approximation of a spatial lattice population model with multiscale dispersal using Markov chains for estimating spatial autocorrelation. *J. Theor. Biol.*, 279(1):74–82, 2011.

[55] V. Marceau, P.-A. Noël, L. Hébert-Dufresne, A. Allard, and L. J. Dubé. Adaptive networks: Coevolution of disease and topology. *Phys. Rev. E*, 82(3):036116, 2010.

[56] J. Lindquist, J. Ma, P. van den Driessche, and F. H. Willeboordse. Effective degree network disease models. *J. Math. Biol.*, 62(2):143–164, 2011.

[57] P. Whittle. On the Use of the Normal Approximation in the Treatment of Stochastic Processes. *J. R. Stat. Soc. B*, 19(2):268–281, 1957.

[58] C. A. Gómez-Uribe and G. C. Verghese. Mass fluctuation kinetics: Capturing stochastic effects in systems of chemical reactions through coupled mean-variance computations. *J. Chem. Phys.*, 126(2):024109, 2007.

[59] I. Nåsell. An extension of the moment closure method. *Theor. Popul. Biol.*, 64(2):233–239, 2003.

[60] M. J. Keeling. Multiplicative Moments and Measures of Persistence in Ecology. *J. Theor. Biol.*, 205(2):269–281, 2000.

[61] S. Chatterjee and R. Durrett. Contact processes on random graphs with power law degree distributions have critical value 0. *Ann. Probab.*, 37(6):2332–2356, 2009.

[62] A. V. Goltsev, S. N. Dorogovtsev, J. G. Oliveira, and J. F. F. Mendes. Localization and Spreading of Diseases in Complex Networks. *Phys. Rev. Lett.*, 109(12):128702, 2012.

[63] H. K. Lee, P.-S. Shim, and J. D. Noh. Epidemic threshold of the susceptible-infected-susceptible model on complex networks. *Phys. Rev. E*, 87(6):062812, 2013.

[64] M. Boguñá, C. Castellano, and R. Pastor-Satorras. Nature of the Epidemic Threshold for the Susceptible-Infected-Susceptible Dynamics in Networks. *Phys. Rev. Lett.*, 111(6):068701, 2013.

[65] R. Pastor-Satorras and C. Castellano. Distinct types of eigenvector localization in networks. *Sci. Rep.*, 6(1):18847, 2016.

[66] E. Pugliese and C. Castellano. Heterogeneous pair approximation for voter models on networks. *EPL*, 88(5):58004, 2009.

[67] A. S. Mata, R. S. Ferreira, and S. C. Ferreira. Heterogeneous pair-approximation for the contact process on complex networks. *New J. Phys.*, 16(5):053006, 2014.

[68] B. Emonts, J. Bøgild Hansen, S. Lægsgaard Jorgensen, B. Höhlein, and R. Peters. Compact methanol reformer test for fuel-cell powered light-duty vehicles. *J. Power Sources*, 71(1):288–293, 1998.

[69] W. Wiese, B. Emonts, and R. Peters. Methanol steam reforming in a fuel cell drive system. *J. Power Sources*, 84(2):187–193, 1999.

[70] R. Peters, H. G. Düsterwald, and B. Höhlein. Investigation of a methanol reformer concept considering the particular impact of dynamics and long-term stability for use in a fuel-cell-powered passenger car. *J. Power Sources*, 86(1):507–514, 2000.

[71] G. A. Olah. Beyond Oil and Gas: The Methanol Economy. *Angew. Chem. Int. Ed.*, 44(18):2636–2639, 2005.

[72] T. Kawai and T. Sakata. Photocatalytic hydrogen production from liquid methanol and water. *J. Chem. Soc., Chem. Comm.*, 1980(15):694–695, 1980.

[73] M. Kawai, S. Naito, K. Tamaru, and T. Kawai. The mechanism of photocatalytic hydrogen production from gaseous methanol and water: IR spectroscopic approach. *Chem. Phys. Lett.*, 98(4):377–380, 1983.

[74] A. Dickinson, D. James, N. Perkins, T. Cassidy, and M. Bowker. The photocatalytic reforming of methanol. *J. Mol. Catal. A*, 146(1):211–221, 1999.

[75] C. Zhou, Z. Ren, S. Tan, Z. Ma, X. Mao, D. Dai, H. Fan, X. Yang, J. LaRue, R. Cooper, A. M. Wodtke, Z. Wang, Z. Li, B. Wang, J. Yang, and J. Hou. Site-specific photocatalytic splitting of methanol on TiO_2(110). *Chem. Sci.*, 1(5):575–580, 2010.

[76] C. Zhou, Z. Ma, Z. Ren, X. Mao, D. Dai, and X. Yang. Effect of defects on photocatalytic dissociation of methanol on TiO_2(110). *Chem. Sci.*, 2(10):1980–1983, 2011.

[77] H. Feng, S. Tan, H. Tang, Q. Zheng, Y. Shi, X. Cui, X. Shao, A. Zhao, J. Zhao, and B. Wang. Temperature- and Coverage-Dependent Kinetics of Photocatalytic Reaction of Methanol on TiO_2 (110)-(1 $\times$ 1) Surface. *J. Phys. Chem. C*, 120(10):5503–5514, 2016.

[78] S. Tan, H. Feng, Y. Ji, Q. Zheng, Y. Shi, J. Zhao, A. Zhao, J. Yang, Y. Luo, B. Wang, and J. G. Hou. Visualizing Elementary Reactions of Methanol by Electrons and Holes on TiO_2(110) Surface. *J. Phys. Chem. C*, 122(50):28805–28814, 2018.

[79] Q. Guo, C. Xu, Z. Ren, W. Yang, Z. Ma, D. Dai, H. Fan, T. K. Minton, and X. Yang. Stepwise Photocatalytic Dissociation of Methanol and Water on TiO_2(110). *J. Am. Chem. Soc.*, 134(32):13366–13373, 2012.

[80] A. Migani and L. Blancafort. Excitonic Interfacial Proton-Coupled Electron Transfer Mechanism in the Photocatalytic Oxidation of Methanol to Formaldehyde on TiO_2(110). *J. Am. Chem. Soc.*, 138(49):16165–16173, 2016.

[81] J. Zhang, C. Peng, H. Wang, and P. Hu. Identifying the Role of Photogenerated Holes in Photocatalytic Methanol Dissociation on Rutile TiO_2(110). *ACS Catal.*, 7(4):2374–2380, 2017.

[82] F. Jin, X. Zhang, M. Wei, T. Chen, H. Ma, and Y. Ma. Critical role of the defect state in the photo-oxidation of methanol on TiO_2(110). *J. Mater. Chem. A*, 8(38):20082–20090, 2020.

[83] O. Micic, Y. Zhang, K. R. Cromack, A. Trifunac, and M. Thurnauer. Photoinduced hole transfer from titanium dioxide to methanol molecules in aqueous solution studied by electron paramagnetic resonance. *J. Phys. Chem.*, 97(50):13284–13288, 1993.

[84] A. Yamakata, T. Ishibashi, and H. Onishi. Electron- and Hole-Capture Reactions on Pt/TiO_2 Photocatalyst Exposed to Methanol Vapor Studied with Time-Resolved Infrared Absorption Spectroscopy. *J. Phys. Chem. B*, 106(35):9122–9125, 2002.

[85] Y. Tamaki, A. Furube, M. Murai, K. Hara, R. Katoh, and M. Tachiya. Direct Observation of Reactive Trapped Holes in TiO_2 Undergoing Photocatalytic Oxidation of Adsorbed Alcohols: Evaluation of the Reaction Rates and Yields. *J. Am. Chem. Soc.*, 128(2):416–417, 2006.

[86] T. Wang, Q. Hao, Z. Wang, X. Mao, Z. Ma, Z. Ren, D. Dai, C. Zhou, and X. Yang. Deuterium Kinetic Isotope Effect in the Photocatalyzed Dissociation of Methanol on TiO_2(110). *J. Phys. Chem. C*, 122(46):26512–26518, 2018.

[87] X. Mao, D. Wei, Z. Wang, X. Jin, Q. Hao, Z. Ren, D. Dai, Z. Ma, C. Zhou, and X. Yang. Recombination of Formaldehyde and Hydrogen Atoms on TiO_2(110). *J. Phys. Chem. C*, 119(2):1170–1174, 2015.

[88] T. L. Thompson and J. T. Yates. Monitoring Hole Trapping in Photoexcited TiO_2(110) Using a Surface Photoreaction. *J. Phys. Chem. B*, 109(39):18230–18236, 2005.

[89] C. L. Pang, R. Lindsay, and G. Thornton. Chemical reactions on rutile TiO_2(110). *Chem. Soc. Rev.*, 37(10):2328–2353, 2008.

[90] S. Wendt, P. T. Sprunger, E. Lira, G. K. H. Madsen, Z. Li, J. Ø. Hansen, J. Matthiesen, A. Blekinge-Rasmussen, E. Lægsgaard, B. Hammer, and F. Besenbacher. The Role of Interstitial Sites in the Ti_{3d} Defect State in the Band Gap of Titania. *Science*, 320(5884):1755–1759, 2008.

[91] N. A. Deskins, R. Rousseau, and M. Dupuis. Defining the Role of Excess Electrons in the Surface Chemistry of TiO_2. *J. Phys. Chem. C*, 114(13):5891–5897, 2010.

[92] J. Haubrich, E. Kaxiras, and C. M. Friend. The Role of Surface and Subsurface Point Defects for Chemical Model Studies on TiO_2: A First-Principles Theoretical Study of Formaldehyde Bonding on Rutile TiO_2(110). *Chem. Eur. J.*, 17(16):4496–4506, 2011.

[93] Z. Zhang, M. Tang, Z.-T. Wang, Z. Ke, Y. Xia, K. T. Park, I. Lyubinetsky, Z. Dohnálek, and Q. Ge. Imaging of Formaldehyde Adsorption and Diffusion on TiO_2(110). *Top. Catal.*, 58(2):103–113, 2015.

[94] Y. Gao, C. S. S. Sandeep, J. M. Schins, A. J. Houtepen, and L. D. A. Siebbeles. Disorder strongly enhances Auger recombination in conductive quantum-dot solids. *Nat. Commun.*, 4:2329, 2013.

[95] W. O. Kermack, A. G. McKendrick, and G. T. Walker. A contribution to the mathematical theory of epidemics. *Proc. R. Soc. Lond. A*, 115(772):700–721, 1927.

[96] R. A. Holley and T. M. Liggett. Ergodic Theorems for Weakly Interacting Infinite Systems and the Voter Model. *Ann. Probab.*, 3(4):643–663, 1975.

[97] U. Diebold. The surface science of titanium dioxide. *Surf. Sci. Rep.*, 48(5):53–229, 2003.

[98] S. P. Bates, M. J. Gillan, and G. Kresse. Adsorption of Methanol on TiO_2(110): A First-Principles Investigation. *J. Phys. Chem. B*, 102(11):2017–2026, 1998.

[99] M. A. Henderson, S. Otero-Tapia, and M. E. Castro. The chemistry of methanol on the TiO_2(110) surface: the influence of vacancies and coadsorbed species. *Faraday Discuss.*, 114:313–329, 1999.

[100] R. S. de Armas, J. Oviedo, M. A. San Miguel, and J. F. Sanz. Methanol Adsorption and Dissociation on TiO_2(110) from First Principles Calculations. *J. Phys. Chem. C*, 111(27):10023–10028, 2007.

[101] J. Zhao, J. Yang, and H. Petek. Theoretical study of the molecular and electronic structure of methanol on a TiO_2(110) surface. *Phys. Rev. B*, 80(23):235416, 2009.

[102] Q. Yuan, Z. Wu, Y. Jin, L. Xu, F. Xiong, Y. Ma, and W. Huang. Photocatalytic Cross-Coupling of Methanol and Formaldehyde on a Rutile TiO_2(110) Surface. *J. Am. Chem. Soc.*, 135(13):5212–5219, 2013.

[103] M. Shen and M. A. Henderson. Identification of the Active Species in Photochemical Hole Scavenging Reactions of Methanol on TiO_2. *J. Phys. Chem. Lett.*, 2(21):2707–2710, 2011.

[104] J. Nelson. Continuous-time random-walk model of electron transport in nanocrystalline TiO_2 electrodes. *Phys. Rev. B*, 59(23):15374–15380, 1999.

[105] J. Pascual, J. Camassel, and H. Mathieu. Fine structure in the intrinsic absorption edge of TiO_2. *Phys. Rev. B*, 18(10):5606–5614, 1978.

[106] A. Amtout and R. Leonelli. Optical properties of rutile near its fundamental band gap. *Phys. Rev. B*, 51(11):6842–6851, 1995.

[107] F. Urbach. The Long-Wavelength Edge of Photographic Sensitivity and of the Electronic Absorption of Solids. *Phys. Rev.*, 92(5):1324–1324, 1953.

[108] M. Shen and M. A. Henderson. Impact of Solvent on Photocatalytic Mechanisms: Reactions of Photodesorption Products with Ice Overlayers on the TiO_2(110) Surface. *J. Phys. Chem. C*, 115(13):5886–5893, 2011.

[109] C. A. Kim and T. Van Voorhis. Heterogeneous Pair Approximation of Methanol Oxidation on TiO_2 Reveals Two Reaction Pathways. *J. Phys. Chem. C*, 126(4):1845–1856, 2022.

[110] M. Rupp, A. Tkatchenko, K.-R. Müller, and O. A. von Lilienfeld. Fast and Accurate Modeling of Molecular Atomization Energies with Machine Learning. *Phys. Rev. Lett.*, 108(5):058301, 2012.

[111] K. Hansen, G. Montavon, F. Biegler, S. Fazli, M. Rupp, M. Scheffler, O. A. von Lilienfeld, A. Tkatchenko, and K.-R. Müller. Assessment and Validation of Machine Learning Methods for Predicting Molecular Atomization Energies. *J. Chem. Theory Comput.*, 9(8):3404–3419, 2013.

[112] G. Montavon, M. Rupp, V. Gobre, A. Vazquez-Mayagoitia, K. Hansen, A. Tkatchenko, K.-R. Müller, and O. A. von Lilienfeld. Machine learning of molecular electronic properties in chemical compound space. *New J. Phys.*, 15(9):095003, 2013.

[113] E. O. Pyzer-Knapp, K. Li, and A. Aspuru-Guzik. Learning from the Harvard Clean Energy Project: The Use of Neural Networks to Accelerate Materials Discovery. *Adv. Funct. Mater.*, 25(41):6495–6502, 2015.

[114] J. P. Janet and H. J. Kulik. Predicting electronic structure properties of transition metal complexes with neural networks. *Chem. Sci.*, 8(7):5137–5152, 2017.

[115] H. Gelernter, J. R. Rose, and C. Chen. Building and refining a knowledge base for synthetic organic chemistry via the methodology of inductive and deductive machine learning. *J. Chem. Inf. Comput. Sci.*, 30(4):492–504, 1990.

[116] Q.-Y. Zhang and J. Aires-de-Sousa. Structure-Based Classification of Chemical Reactions without Assignment of Reaction Centers. *J. Chem. Inf. Model.*, 45(6):1775–1783, 2005.

[117] C. W. Coley, R. Barzilay, T. S. Jaakkola, W. H. Green, and K. F. Jensen. Prediction of Organic Reaction Outcomes Using Machine Learning. *ACS Cent. Sci.*, 3(5):434–443, 2017.

[118] P. Di Lena, K. Nagata, and P. Baldi. Deep architectures for protein contact map prediction. *Bioinformatics*, 28(19):2449–2457, 2012.

[119] J. Eickholt and J. Cheng. Predicting protein residue–residue contacts using deep networks and boosting. *Bioinformatics*, 28(23):3066–3072, 2012.

[120] E. Faraggi, T. Zhang, Y. Yang, L. Kurgan, and Y. Zhou. SPINE X: Improving protein secondary structure prediction by multistep learning coupled with prediction of solvent accessible surface area and backbone torsion angles. *J. Comput. Chem.*, 33(3):259–267, 2012.

[121] J. C. Snyder, M. Rupp, K. Hansen, K.-R. Müller, and K. Burke. Finding Density Functionals with Machine Learning. *Phys. Rev. Lett.*, 108(25):253002, 2012.

[122] L. Li, J. C. Snyder, I. M. Pelaschier, J. Huang, U.-N. Niranjan, P. Duncan, M. Rupp, K.-R. Müller, and K. Burke. Understanding machine-learned density functionals. *Int. J. Quantum Chem.*, 116(11):819–833, 2016.

[123] F. Brockherde, L. Vogt, L. Li, M. E. Tuckerman, K. Burke, and K.-R. Müller. Bypassing the Kohn-Sham equations with machine learning. *Nat. Commun.*, 8:872, 2017.

[124] A. Grisafi, A. Fabrizio, B. Meyer, D. M. Wilkins, C. Corminboeuf, and M. Ceriotti. Transferable Machine-Learning Model of the Electron Density. *ACS Cent. Sci.*, 5(1):57–64, 2019.

[125] J. Behler and M. Parrinello. Generalized Neural-Network Representation of High-Dimensional Potential-Energy Surfaces. *Phys. Rev. Lett.*, 98(14):146401, 2007.

[126] A. Seko, A. Takahashi, and I. Tanaka. Sparse representation for a potential energy surface. *Phys. Rev. B*, 90(2):024101, 2014.

[127] Z. Li, J. R. Kermode, and A. De Vita. Molecular Dynamics with On-the-Fly Machine Learning of Quantum-Mechanical Forces. *Phys. Rev. Lett.*, 114(9):096405, 2015.

[128] S. Chmiela, H. E. Sauceda, K.-R. Müller, and A. Tkatchenko. Towards exact molecular dynamics simulations with machine-learned force fields. *Nat. Commun.*, 9:3887, 2018.

[129] O. K. Ernst, T. Bartol, T. Sejnowski, and E. Mjolsness. Learning dynamic Boltzmann distributions as reduced models of spatial chemical kinetics. *J. Chem. Phys.*, 149(3):034107, 2018.

[130] O. K. Ernst, T. M. Bartol, T. J. Sejnowski, and E. Mjolsness. Learning moment closure in reaction-diffusion systems with spatial dynamic Boltzmann distributions. *Phys. Rev. E*, 99(6):063315, 2019.

[131] M. Abadi, P. Barham, J. Chen, Z. Chen, A. Davis, J. Dean, M. Devin, S. Ghemawat, G. Irving, M. Isard, M. Kudlur, J. Levenberg, R. Monga, S. Moore, D. G. Murray, B. Steiner, P. Tucker, V. Vasudevan, P. Warden, M. Wicke, Y. Yu, and X. Zheng. TensorFlow: A System for Large-Scale Machine Learning. In *12th USENIX Symposium on Operating Systems Design and Implementation (OSDI 16)*, pages 265–283, Savannah, GA, 2016. USENIX Association.

[132] F. Pedregosa, G. Varoquaux, A. Gramfort, V. Michel, B. Thirion, O. Grisel, M. Blondel, P. Prettenhofer, R. Weiss, V. Dubourg, J. Vanderplas, A. Passos, D. Cournapeau, M. Brucher, M. Perrot, and E. Duchesnay. Scikit-learn: Machine Learning in Python. *J. Mach. Learn. Res.*, 12:2825–2830, 2011.

[133] A. J. Lotka. Contribution to the Theory of Periodic Reactions. *J. Phys. Chem.*, 14(3):271–274, 1910.

[134] A. J. Lotka. Analytical Note on Certain Rhythmic Relations in Organic Systems. *Proc. Nat. Acad. Sci. U.S.A.*, 6(7):410–415, 1920.

[135] A. J. Lotka. *Elements of Physical Biology.* Williams & Wilkins Co., Baltimore, MD, 1925.

[136] V. Volterra. Variazioni e fluttuazioni del numero d'individui in specie animali conviventi. *Mem. Acad. Lincei Roma.*, 2:31–113, 1926.

[137] A. Lipowski and D. Lipowska. Nonequilibrium phase transition in a lattice prey–predator system. *Physica A*, 276(3):456–464, 2000.

[138] T. Antal and M. Droz. Phase transitions and oscillations in a lattice prey-predator model. *Phys. Rev. E*, 63(5):056119, 2001.

[139] M. Kowalik, A. Lipowski, and A. L. Ferreira. Oscillations and dynamics in a two-dimensional prey-predator system. *Phys. Rev. E*, 66(6):066107, 2002.

[140] M. Mobilia, I. T. Georgiev, and U. C. Täuber. Phase Transitions and Spatio-Temporal Fluctuations in Stochastic Lattice Lotka-Volterra Models. *J. Stat. Phys.*, 128(1):447–483, 2007.

[141] T. H. Keitt and A. R. Johnson. Spatial Heterogeneity and Anomalous Kinetics: Emergent Patterns in Diffusion-Limited Predatory-Prey Interaction. *J. Theor. Biol.*, 172(2):127–139, 1995.

[142] A. Provata, G. Nicolis, and F. Baras. Oscillatory dynamics in low-dimensional supports: A lattice Lotka–Volterra model. *J. Chem. Phys.*, 110(17):8361–8368, 1999.

[143] G. Veser and R. Imbihl. Synchronization and spatiotemporal self-organization in the NO+CO reaction on Pt(100). I. Unsynchronized oscillations on the 1×1 substrate. *J. Chem. Phys.*, 100(11):8483–8491, 1994.

[144] T. Fink, J.-P. Dath, R. Imbihl, and G. Ertl. Kinetic oscillations in the NO + CO reaction on Pt(100): Experiments and mathematical modeling. *J. Chem. Phys.*, 95(3):2109–2126, 1991.

[145] G. D. Byrne and A. C. Hindmarsh. A Polyalgorithm for the Numerical Solution of Ordinary Differential Equations. *ACM Trans. Math. Softw.*, 1(1):71–96, 1975.

[146] P. N. Brown, G. D. Byrne, and A. C. Hindmarsh. VODE: A Variable-Coefficient ODE Solver. *SIAM J. Sci. Stat. Comput.*, 10(5):1038–1051, 1989.

[147] A. C. Hindmarsh, P. N. Brown, K. E. Grant, S. L. Lee, R. Serban, D. E. Shumaker, and C. S. Woodward. SUNDIALS: Suite of Nonlinear and Differential/Algebraic Equation Solvers. *ACM Trans. Math. Softw.*, 31(3):363–396, 2005.

[148] M. Galassi, B. Gough, F. Rossi, J. Theiler, G. Jungman, M. Booth, and J. Davies. *GNU Scientific Library Reference Manual*. Network Theory Ltd., Godalming, England, 2001.

[149] D. P. Kingma and J. Ba. Adam: A Method for Stochastic Optimization. In Y. Bengio and Y. LeCun, editors, *3rd International Conference on Learning Representations*, San Diego, CA, 2015.

[150] B.-G. Hu, H.-B. Qu, Y. Wang, and S.-H. Yang. A generalized-constraint neural network model: Associating partially known relationships for nonlinear regressions. *Inf. Sci.*, 179(12):1929–1943, 2009.

[151] Y.-J. Qu and B.-G. Hu. Generalized Constraint Neural Network Regression Model Subject to Linear Priors. *IEEE Trans. on Neural Netw.*, 22(12):2447–2459, 2011.

[152] Z. Long, Y. Lu, X. Ma, and B. Dong. PDE-Net: Learning PDEs from Data. In J. Dy and A. Krause, editors, *Proceedings of the 35th International Conference on Machine Learning*, volume 80 of *Proceedings of Machine Learning Research*, pages 3208–3216. PMLR, 2018.

[153] M. Raissi and G. E. Karniadakis. Hidden physics models: Machine learning of nonlinear partial differential equations. *J. Comput. Phys.*, 357:125–141, 2018.

[154] C. Rackauckas, Y. Ma, J. Martensen, C. Warner, K. Zubov, R. Supekar, D. Skinner, A. Ramadhan, and A. Edelman. Universal Differential Equations for Scientific Machine Learning, 2020. arXiv:2001.04385 [cs.LG].

[155] C. A. Kim, N. D. Ricke, and T. Van Voorhis. Machine learning dynamic correlation in chemical kinetics. *J. Chem. Phys.*, 155(14):144107, 2021.

[156] C. W. Tang and S. A. VanSlyke. Organic electroluminescent diodes. *Appl. Phys. Lett.*, 51(12):913–915, 1987.

[157] P. E. Burrows, G. Gu, V. Bulovic, Z. Shen, S. R. Forrest, and M. E. Thompson. Achieving full-color organic light-emitting devices for lightweight, flat-panel displays. *IEEE Trans. Electron Devices*, 44(8):1188–1203, 1997.

[158] B. Geffroy, P. le Roy, and C. Prat. Organic light-emitting diode (OLED) technology: materials, devices and display technologies. *Polym. Int.*, 55(6):572–582, 2006.

[159] L. Xiao, Z. Chen, B. Qu, J. Luo, S. Kong, Q. Gong, and J. Kido. Recent Progresses on Materials for Electrophosphorescent Organic Light-Emitting Devices. *Adv. Mater.*, 23(8):926–952, 2011.

[160] A. de Almeida, G. Zissis, M. Quicheron, and P. Bertldi. *Accelerating the Deployment of Solid State Lighting (SSL) in Europe*. EUR 25596 EN. European Commission Joint Research Centre, Ispra (VA), Italy, 2012.

[161] J. Penning, K. Stober, V. Taylor, and M. Yamada. *Energy Savings Forecast of Solid-State Lighting in General Illumination Applications*. DOE/EE-1467. U.S. Department of Energy Office of Energy Efficiency and Renewable Energy, Washington D.C., 2016.

[162] H. Sasabe and J. Kido. Recent Progress in Phosphorescent Organic Light-Emitting Devices. *Eur. J. Org. Chem.*, 34:7653–7663, 2013.

[163] M. Y. Wong and E. Zysman-Colman. Purely Organic Thermally Activated Delayed Fluorescence Materials for Organic Light-Emitting Diodes. *Adv. Mater.*, 29(22):1605444, 2017.

[164] M. A. Baldo, D. F. O'Brien, Y. You, A. Shoustikov, S. Sibley, M. E. Thompson, and S. R. Forrest. Highly efficient phosphorescent emission from organic electroluminescent devices. *Nature*, 395(6698):151–154, 1998.

[165] B. Minaev, G. Baryshnikov, and H. Agren. Principles of phosphorescent organic light emitting devices. *Phys. Chem. Chem. Phys.*, 16(5):1719–1758, 2014.

[166] Y. Zhang, J. Lee, and S. R. Forrest. Tenfold increase in the lifetime of blue phosphorescent organic light-emitting diodes. *Nat. Commun.*, 5:1–7, 2014.

[167] C. A. Parker and C. G. Hatchard. Triplet-singlet emission in fluid solutions. Phosphorescence of eosin. *Trans. Faraday Soc.*, 57:1894–1904, 1961.

[168] A. Endo, M. Ogasawara, A. Takahashi, D. Yokoyama, Y. Kato, and C. Adachi. Thermally Activated Delayed Fluorescence from Sn^{4+}–Porphyrin Complexes and Their Application to Organic Light Emitting Diodes — A Novel Mechanism for Electroluminescence. *Adv. Mater.*, 21(47):4802–4806, 2009.

[169] A. Endo, K. Sato, K. Yoshimura, T. Kai, A. Kawada, H. Miyazaki, and C. Adachi. Efficient up-conversion of triplet excitons into a singlet state and its application for organic light emitting diodes. *Appl. Phys. Lett.*, 98(8):083302, 2011.

[170] H. Uoyama, K. Goushi, K. Shizu, H. Nomura, and C. Adachi. Highly efficient organic light-emitting diodes from delayed fluorescence. *Nature*, 492(7428):234–238, 2012.

[171] J. Lee, K. Shizu, H. Tanaka, H. Nomura, T. Yasuda, and C. Adachi. Oxadiazole- and triazole-based highly-efficient thermally activated delayed fluorescence emitters for organic light-emitting diodes. *J. Mater. Chem. C*, 1(30):4599–4604, 2013.

[172] K. Kawasumi, T. Wu, T. Zhu, H. S. Chae, T. Van Voorhis, M. A. Baldo, and T. M. Swager. Thermally Activated Delayed Fluorescence Materials Based on Homoconjugation Effect of Donor–Acceptor Triptycenes. *J. Am. Chem. Soc.*, 137(37):11908–11911, 2015.

[173] Y. Liu, G. Xie, K. Wu, Z. Luo, T. Zhou, X. Zeng, J. Yu, S. Gong, and C. Yang. Boosting reverse intersystem crossing by increasing donors in triarylboron/phenoxazine hybrids: TADF emitters for high-performance solution-processed OLEDs. *J. Mater. Chem. C*, 4(20):4402–4407, 2016.

[174] R. S. Nobuyasu, Z. Ren, G. C. Griffiths, A. S. Batsanov, P. Data, S. Yan, A. P. Monkman, M. R. Bryce, and F. B. Dias. Rational Design of TADF Polymers Using a Donor–Acceptor Monomer with Enhanced TADF Efficiency Induced by the Energy Alignment of Charge Transfer and Local Triplet Excited States. *Adv. Opt. Mater.*, 4(4):597–607, 2016.

[175] M. Sarma and K.-T. Wong. Exciplex: An Intermolecular Charge-Transfer Approach for TADF. *ACS Appl. Mater. Interfaces*, 10(23):19279–19304, 2018.

[176] M. A. El-Sayed. Spin—Orbit Coupling and the Radiationless Processes in Nitrogen Heterocyclics. *J. Chem. Phys.*, 38(12):2834–2838, 1963.

[177] Y. Y. Cheng, T. Khoury, R. G. C. R. Clady, M. J. Y. Tayebjee, N. J. Ekins-Daukes, M. J. Crossley, and T. W. Schmidt. On the efficiency limit of triplet–triplet annihilation for photochemical upconversion. *Phys. Chem. Chem. Phys.*, 12(1):66–71, 2010.

[178] T. Ogawa, N. Yanai, A. Monguzzi, and N. Kimizuka. Highly Efficient Photon Upconversion in Self-Assembled Light-Harvesting Molecular Systems. *Sci. Rep.*, 5(1):10882, 2015.

[179] D. Di, L. Yang, J. M. Richter, L. Meraldi, R. M. Altamimi, A. Y. Alyamani, D. Credgington, K. P. Musselman, J. L. MacManus-Driscoll, and R. H. Friend. Efficient Triplet Exciton Fusion in Molecularly Doped Polymer Light-Emitting Diodes. *Adv. Mater.*, 29(13):1605987, 2017.

[180] T. N. Singh-Rachford and F. N. Castellano. Photon upconversion based on sensitized triplet–triplet annihilation. *Coord. Chem. Rev.*, 254(21):2560–2573, 2010.

[181] V. Gray, D. Dzebo, M. Abrahamsson, B. Albinsson, and K. Moth-Poulsen. Triplet–triplet annihilation photon-upconversion: towards solar energy applications. *Phys. Chem. Chem. Phys.*, 16(22):10345–10352, 2014.

[182] B. S. Richards, D. Hudry, D. Busko, A. Turshatov, and I. A. Howard. Photon Upconversion for Photovoltaics and Photocatalysis: A Critical Review. *Chem. Rev.*, 121(15):9165–9195, 2021.

[183] M. Majek, U. Faltermeier, B. Dick, R. Pérez-Ruiz, and A. Jacobi von Wangelin. Application of Visible-to-UV Photon Upconversion to Photoredox Catalysis: The Activation of Aryl Bromides. *Chem. Eur. J.*, 21(44):15496–15501, 2015.

[184] B. D. Ravetz, A. B. Pun, E. M. Churchill, D. N. Congreve, T. Rovis, and L. M. Campos. Photoredox catalysis using infrared light via triplet fusion upconversion. *Nature*, 565(7739):343–346, 2019.

[185] B. Pfund, D. M. Steffen, M. R. Schreier, M.-S. Bertrams, C. Ye, K. Börjesson, O. S. Wenger, and C. Kerzig. UV Light Generation and Challenging Photoreactions Enabled by Upconversion in Water. *J. Am. Chem. Soc.*, 142(23):10468–10476, 2020.

[186] D. Yildiz, C. Baumann, A. Mikosch, A. J. C. Kuehne, A. Herrmann, and R. Göstl. Anti-Stokes Stress Sensing: Mechanochemical Activation of Triplet–Triplet Annihilation Photon Upconversion. *Angew. Chem. Int. Ed.*, 58(37):12919–12923, 2019.

[187] L. Huang, T. Le, K. Huang, and G. Han. Enzymatic enhancing of triplet–triplet annihilation upconversion by breaking oxygen quenching for background-free biological sensing. *Nat. Commun.*, 12:1898, 2021.

[188] Q. Dou, L. Jiang, D. Kai, C. Owh, and X. J. Loh. Bioimaging and biodetection assisted with TTA-UC materials. *Drug Discov. Today*, 22(9):1400–1411, 2017.

[189] X. Xiao, W. Tian, M. Imran, H. Cao, and J. Zhao. Controlling the triplet states and their application in external stimuli-responsive triplet–triplet-annihilation photon upconversion: from the perspective of excited state photochemistry. *Chem. Soc. Rev.*, 50(17):9686–9714, 2021.

[190] L. Huang, Y. Zhao, H. Zhang, K. Huang, J. Yang, and G. Han. Expanding Anti-Stokes Shifting in Triplet–Triplet Annihilation Upconversion for In Vivo Anticancer Prodrug Activation. *Angew. Chem. Int. Ed.*, 56(46):14400–14404, 2017.

[191] R. C. Hilborn. Einstein coefficients, cross sections, f values, dipole moments, and all that. *Am. J. Phys.*, 50(11):982–986, 1982.

[192] R. A. Marcus. On the Theory of Oxidation-Reduction Reactions Involving Electron Transfer. I. *J. Chem. Phys.*, 24(5):966–978, 1956.

[193] R. A. Marcus. Chemical and Electrochemical Electron-Transfer Theory. *Annu. Rev. Phys. Chem.*, 15:155–196, 1964.

[194] J. Jortner. Temperature dependent activation energy for electron transfer between biological molecules. *J. Chem. Phys.*, 64(12):4860–4867, 1976.

[195] D. Beljonne, Z. Shuai, G. Pourtois, and J.-L. Brédas. Spin-Orbit Coupling and Intersystem Crossing in Conjugated Polymers: A Configuration Interaction Description. *J. Phys. Chem. A*, 105(15):3899–3907, 2001.

[196] K. Schmidt, S. Brovelli, V. Coropceanu, D. Beljonne, J. Cornil, C. Bazzini, T. Caronna, R. Tubino, F. Meinardi, Z. Shuai, and J.-L. Brédas. Intersystem Crossing Processes in Nonplanar Aromatic Heterocyclic Molecules. *J. Phys. Chem. A*, 111(42):10490–10499, 2007.

[197] P. K. Samanta, D. Kim, V. Coropceanu, and J.-L. Brédas. Up-Conversion Intersystem Crossing Rates in Organic Emitters for Thermally Activated Delayed Fluorescence: Impact of the Nature of Singlet vs Triplet Excited States. *J. Am. Chem. Soc.*, 139(11):4042–4051, 2017.

[198] R. R. Valiev, V. N. Cherepanov, G. V. Baryshnikov, and D. Sundholm. First-principles method for calculating the rate constants of internal-conversion and intersystem-crossing transitions. *Phys. Chem. Chem. Phys.*, 20(9):6121–6133, 2018.

[199] M. Born and R. Oppenheimer. Zur Quantentheorie der Molekeln. *Ann. Phys.*, 389(20):457–484, 1927.

[200] R. Car and M. Parrinello. Unified Approach for Molecular Dynamics and Density-Functional Theory. *Phys. Rev. Lett.*, 55(22):2471–2474, 1985.

[201] J. C. Slater. The Theory of Complex Spectra. *Phys. Rev.*, 34(10):1293–1322, 1929.

[202] F. Jensen. Atomic orbital basis sets. *Wiley Interdiscip. Rev.: Comput. Mol. Sci.*, 3(3):273–295, 2013.

[203] P. Hohenberg and W. Kohn. Inhomogeneous Electron Gas. *Phys. Rev.*, 136(3B):B864–B871, 1964.

[204] J. P. Perdew and K. Schmidt. Jacob's ladder of density functional approximations for the exchange-correlation energy. *AIP Conf. Proc.*, 577(1):1–20, 2001.

[205] J. P. Perdew, A. Ruzsinszky, J. Tao, V. N. Staroverov, G. E. Scuseria, and G. I. Csonka. Prescription for the design and selection of density functional approximations: More constraint satisfaction with fewer fits. *J. Chem. Phys.*, 123(6):062201, 2005.

[206] E. Runge and E. K. U. Gross. Density-Functional Theory for Time-Dependent Systems. *Phys. Rev. Lett.*, 52(12):997–1000, 1984.

[207] M. E. Casida. Time-Dependent Density Functional Response Theory of Molecular Systems: Theory, Computational Methods, and Functionals. In J. M. Seminario, editor, *Recent Developments and Applications of Modern Density Functional Theory*, volume 4 of *Theoretical and Computational Chemistry*, pages 391–439. Elsevier Science B.V., Amsterdam, Netherlands, 1996.

[208] A. Dreuw and M. Head-Gordon. Single-Reference ab Initio Methods for the Calculation of Excited States of Large Molecules. *Chem. Rev.*, 105(11):4009–4037, 2005.

[209] S. Hirata and M. Head-Gordon. Time-dependent density functional theory within the Tamm–Dancoff approximation. *Chem. Phys. Lett.*, 314(3):291–299, 1999.

[210] Perrin, Francis. La fluorescence des solutions. *Ann. Phys.*, 10(12):169–275, 1929.

[211] K. Goushi, K. Yoshida, K. Sato, and C. Adachi. Organic light-emitting diodes employing efficient reverse intersystem crossing for triplet-to-singlet state conversion. *Nat. Photonics*, 6(4):253–258, 2012.

[212] H. Tanaka, K. Shizu, H. Miyazaki, and C. Adachi. Efficient green thermally activated delayed fluorescence (TADF) from a phenoxazine–triphenyltriazine (PXZ–TRZ) derivative. *Chem. Commun.*, 48(93):11392–11394, 2012.

[213] Q. Zhang, J. Li, K. Shizu, S. Huang, S. Hirata, H. Miyazaki, and C. Adachi. Design of Efficient Thermally Activated Delayed Fluorescence Materials for Pure Blue Organic Light Emitting Diodes. *J. Am. Chem. Soc.*, 134(36):14706–14709, 2012.

[214] F. B. Dias, K. N. Bourdakos, V. Jankus, K. C. Moss, K. T. Kamtekar, V. Bhalla, J. Santos, M. R. Bryce, and A. P. Monkman. Triplet Harvesting with 100% Efficiency by Way of Thermally Activated Delayed Fluorescence in Charge Transfer OLED Emitters. *Adv. Mater.*, 25(27):3707–3714, 2013.

[215] Q. Zhang, B. Li, S. Huang, H. Nomura, H. Tanaka, and C. Adachi. Efficient blue organic light-emitting diodes employing thermally activated delayed fluorescence. *Nat. Photonics*, 8(4):326–332, 2014.

[216] S. Hirata, Y. Sakai, K. Masui, H. Tanaka, S. Y. Lee, H. Nomura, N. Nakamura, M. Yasumatsu, H. Nakanotani, Q. Zhang, K. Shizu, H. Miyazaki, and C. Adachi. Highly efficient blue electroluminescence based on thermally activated delayed fluorescence. *Nat. Mater.*, 14(3):330–336, 2015.

[217] W. Huang, M. Einzinger, T. Zhu, H. S. Chae, S. Jeon, S.-G. Ihn, M. Sim, S. Kim, M. Su, G. Teverovskiy, T. Wu, T. Van Voorhis, T. M. Swager, M. A. Baldo, and S. L. Buchwald. Molecular Design of Deep Blue Thermally Activated Delayed Fluorescence Materials Employing a Homoconjugative Triptycene Scaffold and Dihedral Angle Tuning. *Chem. Mater.*, 30(5):1462–1466, 2018.

[218] Y. Liu, C. Li, Z. Ren, S. Yan, and M. R. Bryce. All-organic thermally activated delayed fluorescence materials for organic light-emitting diodes. *Nat. Rev. Mater.*, 3(4):18020, 2018.

[219] P. L. dos Santos, J. S. Ward, M. R. Bryce, and A. P. Monkman. Using Guest–Host Interactions To Optimize the Efficiency of TADF OLEDs. *J. Phys. Chem. Lett.*, 7(17):3341–3346, 2016.

[220] L.-S. Cui, H. Nomura, Y. Geng, J. U. Kim, H. Nakanotani, and C. Adachi. Controlling Singlet–Triplet Energy Splitting for Deep-Blue Thermally Activated Delayed Fluorescence Emitters. *Angew. Chem. Int. Ed.*, 56(6):1571–1575, 2017.

[221] S. Huang, Q. Zhang, Y. Shiota, T. Nakagawa, K. Kuwabara, K. Yoshizawa, and C. Adachi. Computational Prediction for Singlet- and Triplet-Transition Energies of Charge-Transfer Compounds. *J. Chem. Theory Comput.*, 9(9):3872–3877, 2013.

[222] T. Chen, L. Zheng, J. Yuan, Z. An, R. Chen, Y. Tao, H. Li, X. Xie, and W. Huang. Understanding the Control of Singlet-Triplet Splitting for Organic Exciton Manipulating: A Combined Theoretical and Experimental Approach. *Sci. Rep.*, 5(1):10923, 2015.

[223] M. Moral, L. Muccioli, W.-J. Son, Y. Olivier, and J. C. Sancho-García. Theoretical Rationalization of the Singlet–Triplet Gap in OLEDs Materials: Impact of Charge-Transfer Character. *J. Chem. Theory Comput.*, 11(1):168–177, 2015.

[224] T. J. Penfold. On Predicting the Excited-State Properties of Thermally Activated Delayed Fluorescence Emitters. *J. Phys. Chem. C*, 119(24):13535–13544, 2015.

[225] H. Sun, C. Zhong, and J.-L. Brédas. Reliable Prediction with Tuned Range-Separated Functionals of the Singlet–Triplet Gap in Organic Emitters for Thermally Activated Delayed Fluorescence. *J. Chem. Theory Comput.*, 11(8):3851–3858, 2015.

[226] D. Hait, T. Zhu, D. P. McMahon, and T. Van Voorhis. Prediction of Excited-State Energies and Singlet–Triplet Gaps of Charge-Transfer States Using a Restricted Open-Shell Kohn–Sham Approach. *J. Chem. Theory Comput.*, 12(7):3353–3359, 2016.

[227] G. Valchanov, A. Ivanova, A. Tadjer, D. Chercka, and M. Baumgarten. Understanding the Fluorescence of TADF Light-Emitting Dyes. *J. Phys. Chem. A*, 120(35):6944–6955, 2016.

[228] Y. Shu and B. G. Levine. Simulated evolution of fluorophores for light emitting diodes. *J. Chem. Phys.*, 142(10):104104, 2015.

[229] R. Gómez-Bombarelli, J. Aguilera-Iparraguirre, T. D. Hirzel, D. Duvenaud, D. Maclaurin, M. A. Blood-Forsythe, H. S. Chae, M. Einzinger, D.-G. Ha, T. Wu, G. Markopoulos, S. Jeon, H. Kang, H. Miyazaki, M. Numata, S. Kim, W. Huang, S. I. Hong, M. Baldo, R. P. Adams, and A. Aspuru-Guzik. Design of efficient molecular organic light-emitting diodes by a high-throughput virtual screening and experimental approach. *Nat. Mater.*, 15(10):1120–1127, 2016.

[230] C. Rupakheti, R. Al-Saadon, Y. Zhang, A. M. Virshup, P. Zhang, W. Yang, and D. N. Beratan. Diverse Optimal Molecular Libraries for Organic Light-Emitting Diodes. *J. Chem. Theory Comput.*, 12(4):1942–1952, 2016.

[231] F. B. Dias, J. Santos, D. R. Graves, P. Data, R. S. Nobuyasu, M. A. Fox, A. S. Batsanov, T. Palmeira, M. N. Berberan-Santos, M. R. Bryce, and A. P. Monkman. The Role of Local Triplet Excited States and D-A Relative Orientation in Thermally Activated Delayed Fluorescence: Photophysics and Devices. *Adv, Sci.*, 3(12):1600080, 2016.

[232] L. Gan, K. Gao, X. Cai, D. Chen, and S.-J. Su. Achieving Efficient Triplet Exciton Utilization with Large ΔE_{ST} and Nonobvious Delayed Fluorescence by Adjusting Excited State Energy Levels. *J. Phys. Chem. Lett.*, 9(16):4725–4731, 2018.

[233] T. Hosokai, H. Noda, H. Nakanotani, T. Nawata, Y. Nakayama, H. Matsuzaki, and C. Adachi. Solvent-dependent investigation of carbazole benzonitrile derivatives: does the ^{3}LE–^{1}CT energy gap facilitate thermally activated delayed fluorescence? *J. Photonics Energy*, 8(3):1–9, 2018.

[234] D. Kim. Effects of Intermolecular Interactions on the Singlet–Triplet Energy Difference: A Theoretical Study of the Formation of Excimers in Acene Molecules. *J. Phys. Chem. C*, 119(22):12690–12697, 2015.

[235] D. Kim. A theoretical understanding of the energy difference between singlet and triplet states of oligoacene molecules. *Int. J. Quantum Chem.*, 116(8):651–655, 2016.

[236] K. Lee and D. Kim. Local-Excitation versus Charge-Transfer Characters in the Triplet State: Theoretical Insight into the Singlet–Triplet Energy Differences of Carbazolyl-Phthalonitrile-Based Thermally Activated Delayed Fluorescence Materials. *J. Phys. Chem. C*, 120(49):28330–28336, 2016.

[237] Y. Gao, T. Su, L. Zhao, Y. Geng, Y. Wu, M. Zhang, and Z.-M. Su. How does a little difference in structure determine whether molecules have thermally activated delayed fluorescence characteristic or not? *Org. Electron.*, 50:70–76, 2017.

[238] Y.-C. Duan, L.-L. Wen, Y. Gao, Y. Wu, L. Zhao, Y. Geng, G.-G. Shan, M. Zhang, and Z.-M. Su. Fluorescence, Phosphorescence, or Delayed Fluorescence?—A Theoretical Exploration on the Reason Why a Series of Similar Organic Molecules Exhibit Different Luminescence Types. *J. Phys. Chem. C*, 122(40):23091–23101, 2018.

[239] X.-K. Chen, S.-F. Zhang, J.-X. Fan, and A.-M. Ren. Nature of Highly Efficient Thermally Activated Delayed Fluorescence in Organic Light-Emitting Diode Emitters: Nonadiabatic Effect between Excited States. *J. Phys. Chem. C*, 119(18):9728–9733, 2015.

[240] M. K. Etherington, J. Gibson, H. F. Higginbotham, T. J. Penfold, and A. P. Monkman. Revealing the spin–vibronic coupling mechanism of thermally activated delayed fluorescence. *Nat. Commun.*, 7:13680, 2016.

[241] J. Gibson, A. P. Monkman, and T. J. Penfold. The Importance of Vibronic Coupling for Efficient Reverse Intersystem Crossing in Thermally Activated Delayed Fluorescence Molecules. *ChemPhysChem*, 17(19):2956–2961, 2016.

[242] L. Lin, L. Cai, J. Fan, and C.-K. Wang. Electroluminescent Mechanism of Thermally Activated Delayed Fluorescence Emitters: Conformational Effect. *J. Phys. Chem. C*, 122(34):19953–19961, 2018.

[243] C. M. Marian. Mechanism of the Triplet-to-Singlet Upconversion in the Assistant Dopant ACRXTN. *J. Phys. Chem. C*, 120(7):3715–3721, 2016.

[244] T. Northey, J. Stacey, and T. J. Penfold. The role of solid state solvation on the charge transfer state of a thermally activated delayed fluorescence emitter. *J. Mater. Chem. C*, 5(42):11001–11009, 2017.

[245] H. Sun, Z. Hu, C. Zhong, X. Chen, Z. Sun, and J.-L. Brédas. Impact of Dielectric Constant on the Singlet–Triplet Gap in Thermally Activated Delayed Fluorescence Materials. *J. Phys. Chem. Lett.*, 8(11):2393–2398, 2017.

[246] L. Lv, K. Liu, K. Yuan, Y. Zhu, and Y. Wang. Thermally activated delayed fluorescence processes for Cu(I) complexes in solid-state: a computational study using quantitative prediction. *RSC Adv.*, 8(50):28421–28432, 2018.

[247] J.-M. Mewes. Modeling TADF in organic emitters requires a careful consideration of the environment and going beyond the Franck–Condon approximation. *Phys. Chem. Chem. Phys.*, 20(18):12454–12469, 2018.

[248] Y. Olivier, B. Yurash, L. Muccioli, G. D'Avino, O. Mikhnenko, J. C. Sancho-García, C. Adachi, T.-Q. Nguyen, and D. Beljonne. Nature of the singlet and triplet excitations mediating thermally activated delayed fluorescence. *Phys. Rev. Mater.*, 1(7):075602, 2017.

[249] P. de Silva and T. Van Voorhis. QM/MM Study of Static and Dynamic Energetic Disorder in the Emission Layer of an Organic Light-Emitting Diode. *J. Phys. Chem. Lett.*, 9(6):1329–1334, 2018.

[250] F. B. Dias, T. J. Penfold, and A. P. Monkman. Photophysics of thermally activated delayed fluorescence molecules. *Methods Appl. Fluoresc.*, 5(1):012001, 2017.

[251] X.-K. Chen, D. Kim, and J.-L. Brédas. Thermally Activated Delayed Fluorescence (TADF) Path toward Efficient Electroluminescence in Purely Organic Materials: Molecular Level Insight. *Acc. Chem. Res.*, 51(9):2215–2224, 2018.

[252] Y. Olivier, J.-C. Sancho-Garcia, L. Muccioli, G. D'Avino, and D. Beljonne. Computational Design of Thermally Activated Delayed Fluorescence Materials: The Challenges Ahead. *J. Phys. Chem. Lett.*, 9(20):6149–6163, 2018.

[253] T. J. Penfold, F. B. Dias, and A. P. Monkman. The theory of thermally activated delayed fluorescence for organic light emitting diodes. *Chem. Commun.*, 54(32):3926–3935, 2018.

[254] C. M. Marian. Spin–orbit coupling and intersystem crossing in molecules. *Wiley Interdiscip. Rev.: Comput. Mol. Sci.*, 2(2):187–203, 2012.

[255] J. S. Ward, R. S. Nobuyasu, A. S. Batsanov, P. Data, A. P. Monkman, F. B. Dias, and M. R. Bryce. The interplay of thermally activated delayed fluorescence (TADF) and room temperature organic phosphorescence in sterically-constrained donor–acceptor charge-transfer molecules. *Chem. Commun.*, 52(12):2612–2615, 2016.

[256] X.-K. Chen, Y. Tsuchiya, Y. Ishikawa, C. Zhong, C. Adachi, and J.-L. Brédas. A New Design Strategy for Efficient Thermally Activated Delayed Fluorescence Organic Emitters: From Twisted to Planar Structures. *Adv. Mater.*, 29(46):1702767, 2017.

[257] H. Yersin, L. Mataranga-Popa, S.-W. Li, and R. Czerwieniec. Design strategies for materials showing thermally activated delayed fluorescence and beyond: Towards the fourth-generation OLED mechanism. *J. Soc. Inf. Disp.*, 26(4):194–199, 2018.

[258] W. Zhang, J. Jin, Z. Huang, S. Zhuang, and L. Wang. A new way towards high-efficiency thermally activated delayed fluorescence devices via external heavy-atom effect. *Sci. Rep.*, 6(1):30178, 2016.

[259] M. Einzinger, T. Zhu, P. de Silva, C. Belger, T. M. Swager, T. Van Voorhis, and M. A. Baldo. Shorter Exciton Lifetimes via an External Heavy-Atom Effect: Alleviating the Effects of Bimolecular Processes in Organic Light-Emitting Diodes. *Adv. Mater.*, 29(40):1701987, 2017.

[260] J. Gibson and T. J. Penfold. Nonadiabatic coupling reduces the activation energy in thermally activated delayed fluorescence. *Phys. Chem. Chem. Phys.*, 19(12):8428–8434, 2017.

[261] I. Lyskov and C. M. Marian. Climbing up the Ladder: Intermediate Triplet States Promote the Reverse Intersystem Crossing in the Efficient TADF Emitter ACRSA. *J. Phys. Chem. C*, 121(39):21145–21153, 2017.

[262] T. J. Penfold, E. Gindensperger, C. Daniel, and C. M. Marian. Spin-Vibronic Mechanism for Intersystem Crossing. *Chem. Rev.*, 118(15):6975–7025, 2018.

[263] S. Difley, D. Beljonne, and T. Van Voorhis. On the Singlet–Triplet Splitting of Geminate Electron–Hole Pairs in Organic Semiconductors. *J. Am. Chem. Soc.*, 130(11):3420–3427, 2008.

[264] Q. Wu and T. Van Voorhis. Direct optimization method to study constrained systems within density-functional theory. *Phys. Rev. A*, 72(2):024502, 2005.

[265] Q. Wu and T. Van Voorhis. Direct Calculation of Electron Transfer Parameters through Constrained Density Functional Theory. *J. Phys. Chem. A*, 110(29):9212–9218, 2006.

[266] Q. Wu and T. Van Voorhis. Extracting electron transfer coupling elements from constrained density functional theory. *J. Chem. Phys.*, 125(16):164105, 2006.

[267] B. Kaduk, T. Kowalczyk, and T. Van Voorhis. Constrained Density Functional Theory. *Chem. Rev.*, 112(1):321–370, 2012.

[268] A. T. B. Gilbert, N. A. Besley, and P. M. W. Gill. Self-Consistent Field Calculations of Excited States Using the Maximum Overlap Method (MOM). *J. Phys. Chem. A*, 112(50):13164–13171, 2008.

[269] T. Kowalczyk, S. R. Yost, and T. V. Voorhis. Assessment of the ΔSCF density functional theory approach for electronic excitations in organic dyes. *J. Chem. Phys.*, 134(5):054128, 2011.

[270] Y. Im, M. Kim, Y. J. Cho, J.-A. Seo, K. S. Yook, and J. Y. Lee. Molecular Design Strategy of Organic Thermally Activated Delayed Fluorescence Emitters. *Chem. Mater.*, 29(5):1946–1963, 2017.

[271] W. L. Jorgensen, D. S. Maxwell, and J. Tirado-Rives. Development and Testing of the OPLS All-Atom Force Field on Conformational Energetics and Properties of Organic Liquids. *J. Am. Chem. Soc.*, 118(45):11225–11236, 1996.

[272] S. H. Vosko, L. Wilk, and M. Nusair. Accurate spin-dependent electron liquid correlation energies for local spin density calculations: a critical analysis. *Can. J. Phys.*, 58(8):1200–1211, 1980.

[273] A. D. Becke. Density-functional exchange-energy approximation with correct asymptotic behavior. *Phys. Rev. A*, 38(6):3098–3100, 1988.

[274] C. Lee, W. Yang, and R. G. Parr. Development of the Colle-Salvetti correlation-energy formula into a functional of the electron density. *Phys. Rev. B*, 37(2):785–789, 1988.

[275] A. D. Becke. Density-functional thermochemistry. III. The role of exact exchange. *J. Chem. Phys.*, 98(7):5648–5652, 1993.

[276] P. J. Stephens, F. J. Devlin, C. F. Chabalowski, and M. J. Frisch. Ab Initio Calculation of Vibrational Absorption and Circular Dichroism Spectra Using Density Functional Force Fields. *J. Phys. Chem.*, 98(45):11623–11627, 1994.

[277] K. Kim and K. D. Jordan. Comparison of Density Functional and MP2 Calculations on the Water Monomer and Dimer. *J. Phys. Chem.*, 98(40):10089–10094, 1994.

[278] P. C. Hariharan and J. A. Pople. The influence of polarization functions on molecular orbital hydrogenation energies. *Theor. Chim. Acta*, 28(3):213–222, 1973.

[279] M. M. Francl, W. J. Pietro, W. J. Hehre, J. S. Binkley, M. S. Gordon, D. J. DeFrees, and J. A. Pople. Self-consistent molecular orbital methods. XXIII. A polarization-type basis set for second-row elements. *J. Chem. Phys.*, 77(7):3654–3665, 1982.

[280] T. Clark, J. Chandrasekhar, G. W. Spitznagel, and P. V. R. Schleyer. Efficient diffuse function-augmented basis sets for anion calculations. III. The 3-21+G basis set for first-row elements, Li–F. *J. Comput. Chem.*, 4(3):294–301, 1983.

[281] A. Dreuw and M. Head-Gordon. Failure of Time-Dependent Density Functional Theory for Long-Range Charge-Transfer Excited States: The Zincbacteriochlorin–Bacteriochlorin and Bacteriochlorophyll–Spheroidene Complexes. *J. Am. Chem. Soc.*, 126(12):4007–4016, 2004.

[282] Z.-Q. You, J.-M. Mewes, A. Dreuw, and J. M. Herbert. Comparison of the Marcus and Pekar partitions in the context of non-equilibrium, polarizable-continuum solvation models. *J. Chem. Phys.*, 143(20):204104, 2015.

[283] J.-M. Mewes, Z.-Q. You, M. Wormit, T. Kriesche, J. M. Herbert, and A. Dreuw. Experimental Benchmark Data and Systematic Evaluation of Two a Posteriori, Polarizable-Continuum Corrections for Vertical Excitation Energies in Solution. *J. Phys. Chem. A*, 119(21):5446–5464, 2015.

[284] R. L. Martin. Natural transition orbitals. *J. Chem. Phys.*, 118(11):4775–4777, 2003.

[285] P. de Silva, C. A. Kim, T. Zhu, and T. Van Voorhis. Extracting Design Principles for Efficient Thermally Activated Delayed Fluorescence (TADF) from a Simple Four-State Model. *Chem. Mater.*, 31(17):6995–7006, 2019.

[286] R. Gómez-Bombarelli, J. Aguilera-Iparraguirre, T. D. Hirzel, D. Duvenaud, D. Maclaurin, M. A. Blood-Forsythe, H. S. Chae, M. Einzinger, D.-G. Ha, T. Wu, G. Markopoulos, S. Jeon, H. Kang, H. Miyazaki, M. Numata, S. Kim, W. Huang, S. I. Hong, M. Baldo, R. P. Adams, and A. Aspuru-Guzik. Design of efficient molecular organic light-emitting diodes by a high-throughput virtual screening and experimental approach. *Nat. Mater.*, 15(10):1120–1127, 2016.

[287] M. Kim, S. K. Jeon, S.-H. Hwang, and J. Y. Lee. Stable Blue Thermally Activated Delayed Fluorescent Organic Light-Emitting Diodes with Three Times Longer Lifetime than Phosphorescent Organic Light-Emitting Diodes. *Adv. Mater.*, 27(15):2515–2520, 2015.

[288] P. L. dos Santos, J. S. Ward, M. R. Bryce, and A. P. Monkman. Using Guest–Host Interactions To Optimize the Efficiency of TADF OLEDs. *J. Phys. Chem. Lett.*, 7(17):3341–3346, 2016.

[289] T.-A. Lin, T. Chatterjee, W.-L. Tsai, W.-K. Lee, M.-J. Wu, M. Jiao, K.-C. Pan, C.-L. Yi, C.-L. Chung, K.-T. Wong, and C.-C. Wu. Sky-Blue Organic Light Emitting Diode with 37% External Quantum Efficiency Using Thermally Activated Delayed Fluorescence from Spiroacridine-Triazine Hybrid. *Adv. Mater.*, 28(32):6976–6983, 2016.

[290] P. K. Samanta, D. Kim, V. Coropceanu, and J.-L. Brédas. Up-Conversion Intersystem Crossing Rates in Organic Emitters for Thermally Activated Delayed Fluorescence: Impact of the Nature of Singlet vs Triplet Excited States. *J. Am. Chem. Soc.*, 139(11):4042–4051, 2017.

[291] Z. Tu, G. Han, T. Hu, R. Duan, and Y. Yi. Nature of the Lowest Singlet and Triplet Excited States of Organic Thermally Activated Delayed Fluorescence Emitters: A Self-Consistent Quantum Mechanics/Embedded Charge Study. *Chem. Mater.*, 31(17):6665–6671, 2019.

[292] E. W. Evans, Y. Olivier, Y. Puttisong, W. K. Myers, T. J. H. Hele, S. M. Menke, T. H. Thomas, D. Credgington, D. Beljonne, R. H. Friend, and N. C. Greenham. Vibrationally Assisted Intersystem Crossing in Benchmark Thermally Activated Delayed Fluorescence Molecules. *J. Phys. Chem. Lett.*, 9(14):4053–4058, 2018.

[293] T. Hu, G. Han, Z. Tu, R. Duan, and Y. Yi. Origin of High Efficiencies for Thermally Activated Delayed Fluorescence Organic Light-Emitting Diodes: Atomistic Insight into Molecular Orientation and Torsional Disorder. *J. Phys. Chem. C*, 122(48):27191–27197, 2018.

[294] H. Sun, C. Zhong, and J.-L. Brédas. Reliable Prediction with Tuned Range-Separated Functionals of the Singlet–Triplet Gap in Organic Emitters for Thermally Activated Delayed Fluorescence. *J. Chem. Theory Comput.*, 11(8):3851–3858, 2015.

[295] M. Saigo, K. Miyata, S. Tanaka, H. Nakanotani, C. Adachi, and K. Onda. Suppression of Structural Change upon S_1–T_1 Conversion Assists the Thermally Activated Delayed Fluorescence Process in Carbazole-Benzonitrile Derivatives. *J. Phys. Chem. Lett.*, 10(10):2475–2480, 2019.

[296] R. Krishnan, J. S. Binkley, R. Seeger, and J. A. Pople. Self-consistent molecular orbital methods. XX. A basis set for correlated wave functions. *J. Chem. Phys.*, 72(1):650–654, 1980.

[297] Y. Shao, Z. Gan, E. Epifanovsky, A. T. Gilbert, M. Wormit, J. Kussmann, A. W. Lange, A. Behn, J. Deng, X. Feng, D. Ghosh, M. Goldey, P. R. Horn, L. D. Jacobson, I. Kaliman, R. Z. Khaliullin, T. Kuś, A. Landau, J. Liu, E. I. Proynov, Y. M. Rhee, R. M. Richard, M. A. Rohrdanz, R. P. Steele, E. J. Sundstrom, H. L. W. III, P. M. Zimmerman, D. Zuev, B. Albrecht, E. Alguire, B. Austin, G. J. O. Beran, Y. A. Bernard, E. Berquist, K. Brandhorst, K. B. Bravaya, S. T. Brown, D. Casanova, C.-M. Chang, Y. Chen, S. H. Chien, K. D. Closser, D. L. Crittenden, M. Diedenhofen, R. A. D. Jr., H. Do, A. D. Dutoi, R. G. Edgar, S. Fatehi, L. Fusti-Molnar, A. Ghysels, A. Golubeva-Zadorozhnaya, J. Gomes, M. W. Hanson-Heine, P. H. Harbach, A. W. Hauser, E. G. Hohenstein, Z. C. Holden, T.-C. Jagau, H. Ji, B. Kaduk, K. Khistyaev, J. Kim, J. Kim, R. A. King, P. Klunzinger, D. Kosenkov, T. Kowalczyk, C. M. Krauter, K. U. Lao, A. D. Laurent, K. V. Lawler, S. V. Levchenko, C. Y. Lin, F. Liu, E. Livshits, R. C. Lochan, A. Luenser, P. Manohar, S. F. Manzer, S.-P. Mao, N. Mardirossian, A. V. Marenich, S. A. Maurer, N. J. Mayhall, E. Neuscamman, C. M. Oana, R. Olivares-Amaya, D. P. O'Neill, J. A. Parkhill, T. M. Perrine, R. Peverati, A. Prociuk, D. R. Rehn, E. Rosta, N. J. Russ, S. M. Sharada, S. Sharma, D. W. Small, A. Sodt, T. Stein, D. Stück, Y.-C. Su, A. J. Thom, T. Tsuchimochi, V. Vanovschi, L. Vogt, O. Vydrov, T. Wang, M. A. Watson, J. Wenzel, A. White, C. F. Williams, J. Yang, S. Yeganeh, S. R. Yost, Z.-Q. You, I. Y. Zhang, X. Zhang, Y. Zhao, B. R. Brooks, G. K. Chan, D. M. Chipman, C. J. Cramer, W. A. G. III, M. S. Gordon, W. J. Hehre, A. Klamt, H. F. S. III, M. W. Schmidt, C. D. Sherrill, D. G. Truhlar, A. Warshel, X. Xu, A. Aspuru-Guzik, R. Baer, A. T. Bell, N. A. Besley, J.-D. Chai, A. Dreuw, B. D. Dunietz, T. R. Furlani, S. R. Gwaltney, C.-P. Hsu, Y. Jung, J. Kong, D. S. Lambrecht, W. Liang, C. Ochsenfeld, V. A. Rassolov, L. V. Slipchenko, J. E. Subotnik, T. V. Voorhis, J. M. Herbert, A. I. Krylov, P. M. Gill, and M. Head-Gordon. Advances in molecular quantum chemistry contained in the Q-Chem 4 program package. *Mol. Phys.*, 113(2):184–215, 2015.

[298] M. D. Hanwell, D. E. Curtis, D. C. Lonie, T. Vandermeersch, E. Zurek, and

G. R. Hutchison. Avogadro: an advanced semantic chemical editor, visualization, and analysis platform. *J. Cheminform.*, 4:No. 17, 2012.

[299] B. M. Bode and M. S. Gordon. MacMolPlt: a graphical user interface for GAMESS. *J. Mol. Graph. Model.*, 16(3):133–138, June 1998.

[300] J. P. Perdew, K. Burke, and M. Ernzerhof. Generalized Gradient Approximation Made Simple. *Phys. Rev. Lett.*, 77(18):3865–3868, 1996.

[301] J. P. Perdew, M. Ernzerhof, and K. Burke. Rationale for mixing exact exchange with density functional approximations. *J. Chem. Phys.*, 105(22):9982–9985, 1996.

[302] C. Adamo and V. Barone. Toward reliable density functional methods without adjustable parameters: The PBE0 model. *J. Chem. Phys.*, 110(13):6158–6170, 1999.

[303] Y. Zhao and D. G. Truhlar. The M06 suite of density functionals for main group thermochemistry, thermochemical kinetics, noncovalent interactions, excited states, and transition elements: two new functionals and systematic testing of four M06-class functionals and 12 other functionals. *Theor. Chem. Acc.*, 120(1):215–241, 2008.

[304] M. A. Rohrdanz and J. M. Herbert. Simultaneous benchmarking of ground- and excited-state properties with long-range-corrected density functional theory. *J. Chem. Phys.*, 129(3):No. 034107, 2008.

[305] T. M. Henderson, B. G. Janesko, and G. E. Scuseria. Generalized gradient approximation model exchange holes for range-separated hybrids. *J. Chem. Phys.*, 128(19):No. 194105, 2008.

[306] U. Salzner and R. Baer. Koopmans' springs to life. *J. Chem. Phys*, 131(23):No. 231101, 2009.

[307] E. Cancès, B. Mennucci, and J. Tomasi. A new integral equation formalism for the polarizable continuum model: Theoretical background and applications to isotropic and anisotropic dielectrics. *J. Chem. Phys.*, 107(8):3032–3041, 1997.

[308] D. M. Chipman. Reaction field treatment of charge penetration. *J. Chem. Phys.*, 112(13):5558–5565, 2000.

[309] E. Cancès and B. Mennucci. Comment on "Reaction field treatment of charge penetration" [J. Chem. Phys. 112, 5558 (2000)]. *J. Chem. Phys.*, 114(10):4744–4745, 2001.

[310] J. Marchal and C. Lapp. Dielectric properties of polymethyl methacrylate in dilute solution previous results. *J. Polym. Sci.*, 27(115):571–573, 1958.

[311] W. Spendley, G. R. Hext, and F. R. Himsworth. Sequential Application of Simplex Designs in Optimisation and Evolutionary Operation. *Technometrics*, 4(4):441–461, 1962.

[312] J. A. Nelder and R. Mead. A Simplex Method for Function Minimization. *Comput. J.*, 7(4):308–313, 1965.

[313] S. Y. Lee, T. Yasuda, Y. S. Yang, Q. Zhang, and C. Adachi. Luminous Butterflies: Efficient Exciton Harvesting by Benzophenone Derivatives for Full-Color Delayed Fluorescence OLEDs. *Angew. Chem. Int. Ed.*, 53(25):6402–6406, 2014.

[314] R. Komatsu, H. Sasabe, Y. Seino, K. Nakao, and J. Kido. Light-blue thermally activated delayed fluorescent emitters realizing a high external quantum efficiency of 25% and unprecedented low drive voltages in OLEDs. *J. Mater. Chem. C*, 4(12):2274–2278, 2016.

[315] W. Huang, M. Einzinger, A. Maurano, T. Zhu, J. Tiepelt, C. Yu, H. S. Chae, T. Van Voorhis, M. A. Baldo, and S. L. Buchwald. Large Increase in External Quantum Efficiency by Dihedral Angle Tuning in a Sky-Blue Thermally Activated Delayed Fluorescence Emitter. *Adv. Opt. Mater.*, 7(20):1900476, 2019.

[316] L. Zhan, Y. Xiang, Z. Chen, K. Wu, S. Gong, G. Xie, and C. Yang. Fine-tuning the photophysical properties of thermally activated delayed fluorescent emitters using torsion angles: high performance sky-blue OLEDs. *J. Mater. Chem. C*, 7(44):13953–13959, 2019.

[317] G. Ohlendorf, C. W. Mahler, S.-S. Jester, G. Schnakenburg, S. Grimme, and S. Höger. Highly Strained Phenylene Bicyclophanes. *Angew. Chem. Int. Ed.*, 52(46):12086–12090, 2013.

[318] Y.-Y. Liu, J.-Y. Lin, Y.-F. Bo, L.-H. Xie, M.-D. Yi, X.-W. Zhang, H.-M. Zhang, T.-P. Loh, and W. Huang. Synthesis and Crystal Structure of Highly Strained [4]Cyclofluorene: Green-Emitting Fluorophore. *Org. Lett.*, 18(2):172–175, 2016.

[319] C. A. Kim and T. Van Voorhis. Maximizing TADF via Conformational Optimization. *J. Phys. Chem. A*, 125(35):7644–7654, 2021.

[320] H. Kuma and C. Hosokawa. Blue fluorescent OLED materials and their application for high-performance devices. *Sci. Technol. Adv. Mater*, 15(3):034201, 2014.

[321] T. Suzuki, Y. Nonaka, T. Watabe, H. Nakashima, S. Seo, S. Shitagaki, and S. Yamazaki. Highly efficient long-life blue fluorescent organic light-emitting diode exhibiting triplet–triplet annihilation effects enhanced by a novel hole-transporting material. *Jpn. J. Appl. Phys.*, 53(5):052102, 2014.

[322] A. Salehi, C. Dong, D.-H. Shin, L. Zhu, C. Papa, A. Thy Bui, F. N. Castellano, and F. So. Realization of high-efficiency fluorescent organic light-emitting diodes with low driving voltage. *Nat. Commun.*, 10:2305, 2019.

[323] W. Sun, A. Ronchi, T. Zhao, J. Han, A. Monguzzi, and P. Duan. Highly efficient photon upconversion based on triplet–triplet annihilation from bichromophoric annihilators. *J. Mater. Chem. C*, 9(40):14201–14208, 2021.

[324] A. J. Carrod, A. Cravcenco, C. Ye, and K. Börjesson. Modulating TTA efficiency through control of high energy triplet states. *J. Mater. Chem. C*, 10(12):4923–4928, 2022.

[325] D. G. Bossanyi, Y. Sasaki, S. Wang, D. Chekulaev, N. Kimizuka, N. Yanai, and J. Clark. Spin Statistics for Triplet–Triplet Annihilation Upconversion: Exchange Coupling, Intermolecular Orientation, and Reverse Intersystem Crossing. *JACS Au*, 1(12):2188–2201, 2021.

[326] R. Ieuji, K. Goushi, and C. Adachi. Triplet–triplet upconversion enhanced by spin–orbit coupling in organic light-emitting diodes. *Nat. Commun.*, 10:5283, 2019.

[327] N. Nijegorodov, V. Ramachandran, and D. P. Winkoun. The dependence of the absorption and fluorescence parameters, the intersystem crossing and internal conversion rate constants on the number of rings in polyacene molecules. *Spectrochim. Acta A*, 53(11):1813–1824, 1997.

[328] J. S. Brinen and J. G. Koren. The lowest triplet state of 9, 10 diphenylanthracene. *Chem. Phys. Lett.*, 2(8):671–672, 1968.

[329] Y. H. Meyer, R. Astier, and J. M. Leclercq. Triplet-Triplet Spectroscopy of Polyacenes. *J. Chem. Phys.*, 56(2):801–815, 1972.

[330] Photoelectric Spectrometry Group England Staff. *UV Atlas of Organic Compounds*. Springer, Boston, MA, 1967.

[331] G. M. Badger and R. S. Pearce. Absorption spectrum of rubrene in different solvents. *Spectrochim. Acta*, 4(4):280–283, 1951.

[332] D. K. K. Liu and L. R. Faulkner. P-Type delayed fluorescence from rubrene. *J. Am. Chem. Soc.*, 99(14):4594–4599, 1977.

[333] W. G. Herkstroeter and P. B. Merkel. The triplet state energies of rubrene and diphenylisobenzofuran. *J. Photochem.*, 16(4):331–341, 1981.

[334] J.-F. Longevial, M. Lo, A. Lebrun, D. Laurencin, S. Clément, and S. Richeter. Molecular complexes and main-chain organometallic polymers based on Janus bis(carbenes) fused to metalloporphyrins. *Dalton Trans.*, 49(21):7005–7014, 2020.

[335] V. A. Rassolov, J. A. Pople, M. A. Ratner, and T. L. Windus. 6-31G* basis set for atoms K through Zn. *J. Chem. Phys.*, 109(4):1223–1229, 1998.

[336] V. A. Rassolov, M. A. Ratner, J. A. Pople, P. C. Redfern, and L. A. Curtiss. 6-31G* basis set for third-row atoms. *J. Comput. Chem.*, 22(9):976–984, 2001.

[337] R. A. Marcus. Exchange reactions and electron transfer reactions including isotopic exchange. Theory of oxidation-reduction reactions involving electron transfer. Part 4.—A statistical-mechanical basis for treating contributions from solvent, ligands, and inert salt. *Discuss. Faraday Soc.*, 29:21–31, 1960.

[338] T. W. Schmidt and F. N. Castellano. Photochemical Upconversion: The Primacy of Kinetics. *J. Phys. Chem. Lett.*, 5(22):4062–4072, 2014.

[339] B. Joarder, N. Yanai, and N. Kimizuka. Solid-State Photon Upconversion Materials: Structural Integrity and Triplet–Singlet Dual Energy Migration. *J. Phys. Chem. Lett.*, 9(16):4613–4624, 2018.

[340] J. C. de Mello, H. F. Wittmann, and R. H. Friend. An improved experimental determination of external photoluminescence quantum efficiency. *Adv. Mater.*, 9(3):230–232, 1997.

[341] D. Y. Kondakov. Characterization of triplet-triplet annihilation in organic light-emitting diodes based on anthracene derivatives. *J. Appl. Phys.*, 102(11):114504, 2007.

[342] S. Rashev. Calculation of internal conversion rate constants of single vibronic levels in S_1 benzene. *J. Chem. Phys.*, 101(8):6632–6639, 1994.

[343] T. Nakajima and S. Kato. An ab initio study of the internal conversion rate from the first singlet excited state to the ground state in formaldehyde. *J. Chem. Phys.*, 105(14):5927–5938, 1996.

[344] R. Islampour and M. Miralinaghi. Theoretical Study of Internal Conversion Decay Rates Associated with the Three Lowest Singlet Electronic States in Pyrazine. *J. Phys. Chem. A*, 113(11):2340–2349, 2009.

[345] R. S. H. Liu and J. R. Edman. Triplet-Triplet Energy Transfer from the Second Triplet States of Anthracenes. Chemical Studies. *J. Am. Chem. Soc.*, 91(6):1492–1497, 1969.

[346] R. O. Campbell and R. S. H. Liu. More on the Second Triplet States of Anthracenes in Sensitized Reactions of Olefins. Evidence against the Singlet-Triplet Energy-Transfer Process. *J. Am. Chem. Soc.*, 95(20):6560–6562, 1973.

[347] W. G. McGimpsey and J. C. Scaiano. Photochemistry and Photophysics from Upper Triplet Levels of 9,10-Dibromoanthracene. *J. Am. Chem. Soc.*, 111(1):335–340, 1989.

[348] C. Bohne, S. R. Kennedy, R. Boch, F. Negri, G. Orlandi, W. Siebrand, and J. C. Scaiano. Determination of the Lifetime of the Second Excited Triplet State of Anthracenes. *J. Phys. Chem.*, 95(25):10300–10306, 1991.

[349] W. Yang, J. Zhao, G. Tang, X. Li, and G. G. Gurzadyan. Direct Observation of Long-Lived Upper Excited Triplet States and Intersystem Crossing in Anthracene-Containing Pt^{II} Complexes. *J. Phys. Chem. Lett.*, 10(24):7767–7773, 2019.

[350] B. Choudhury and A. Choudhury. Oxygen defect dependent variation of band gap, Urbach energy and luminescence property of anatase, anatase–rutile mixed phase and of rutile phases of TiO_2 nanoparticles. *Physica E*, 56:364–371, 2014.

[351] H. Tang, F. Lévy, H. Berger, and P. E. Schmid. Urbach tail of anatase TiO_2. *Phys. Rev. B*, 52(11):7771–7774, 1995.

[352] C. M. Breneman and K. B. Wiberg. Determining atom-centered monopoles from molecular electrostatic potentials. The need for high sampling density in formamide conformational analysis. *J. Comput. Chem.*, 11(3):361–373, 1990.

[353] M. J. Abraham, T. Murtola, R. Schulz, S. Páll, J. C. Smith, B. Hess, and E. Lindahl. GROMACS: High performance molecular simulations through multi-level parallelism from laptops to supercomputers. *SoftwareX*, 1-2:19–25, 2015.

[354] S. Nosé. A molecular dynamics method for simulations in the canonical ensemble. *Mol. Phys.*, 52(2):255–268, 1984.

[355] S. Nosé. A unified formulation of the constant temperature molecular dynamics methods. *J. Chem. Phys.*, 81(1):511–519, 1984.

[356] W. G. Hoover. Canonical dynamics: Equilibrium phase-space distributions. *Phys. Rev. A*, 31(3):1695–1697, 1985.

[357] M. A. Rohrdanz, K. M. Martins, and J. M. Herbert. A long-range-corrected density functional that performs well for both ground-state properties and time-dependent density functional theory excitation energies, including charge-transfer excited states. *J. Chem. Phys.*, 130(5):054112, 2009.